REVIEW OF THE VKI DOCTORAL RESEARCH

2017 - 2018



von Karman Institute for Fluid Dynamics

Front cover: Comparison of the numerically computed field of the density gradient around a static pressure probe with a Schlieren image obtained during a helium test in the VKI Longshot hypersonic gun tunnel. The contours in the upper half of the picture correspond to the free-stream Mach number 34.6, resulting from a conventional nozzle rebuilding method, which assumes that the nozzle expansion is isentropic and adiabatic. The lower contours are computed for the free-stream Mach number 25.4 as given by a newly developed free-stream rebuilding method.
Back cover: The VKI Longshot hypersonic gun tunnel, capable of partially duplicating atmospheric entry flows in terms of Mach and Reynolds numbers. The left figure shows the piston held by a primary diaphragm in its initial position. The right figure depicts the unique system of check valves, which extends the useful testing time.
Picture of Zdeněk Ilich

©2018 by the von Karman Institute for Fluid Dynamics
Waterloosesteenweg 72, B-1640 Sint-Genesius-Rode
To order: https://www.vki.ac.be

ISBN 978-2-87516-135-2

D/2018/0238/704, T. Magin, Editor-in-Chief

The contents of this book are the property of the von Karman Institute for Fluid Dynamics. No part of this book may be reproduced or distributed in any form of by any means, or stored in a database or retrieval system, without the prior written permission from the Publisher.

PREFACE

The ninth symposium on the doctoral research of the von Karman Institute for Fluid Dynamics took place during the period March 5 to 7, 2018. The doctoral students have presented the progress of their research work carried out in the three departments: Aeronautics and Aerospace, Environmental and Applied Fluid Dynamics, Turbomachinery and Propulsion. The first year students have presented a poster on their research plans and some preliminary results, while the most advanced students have proposed a presentation followed by a session of questions.

This event was attended by the faculty of the von Karman Institute, as well as by colleagues from universities and industrial partners. The Symposium is open to external attendees free of charge. In addition to the presentations of the PhD candidates, we had the pleasure to welcome three prominent keynote lecturers who have opened each day the Symposium:

- Dr. Pietro Marco Congedo, INRIA Paris-Saclay, France, "*Uncertainty quantification for computational fluid dynamics applications,*"
- Prof. GertJan van Heijst, Department of Applied Physics, Technische Universiteit Eindhoven, The Netherlands, *"Laboratory modelling of environmental flows,"*
- Prof. Piero Colonna, Faculty of Aerospace Engineering, Technische Universiteit Delft, The Netherlands, *"Organic Rankine cycle technology in general and technical aspects."*

A special IFAR virtual conference (International Forum for Aviation Research) was organized in collaboration with NASA. This virtual conference was broadcasted among the IFAR members and associated universities with interaction during the question session. Firstly Prof. Dr.-Ing. Joachim Szodruch, IFAR founder and chairman, presented the Young Researchers Network. Two PhD members have presented their work related to IFAR activities.

This year, the best presentation award has been attributed to Zdeněk Ilich for his research on "Design of experiments to assess non-equilibrium nozzle flow phenomena in the VKI Longshot hypersonic tunnel." We would like to congratulate him on this achievement. The illustrated cover art of these proceedings is based on his research results. The best poster presentation has been attributed to Adriana Enache for a work on "*Analytical and experimental investigation of icing phenomena on wind turbine blades*" and to Maxim Van Cappellen for his work on "*Modeling turbulent polydispersed multiphase flows in stirring tank reactors*".

This proceedings volume contains 39 papers, which are divided into the following topics: "*Numerical Approach for Hypersonic and Plasma Flows*," "*Ground and Flight Experiments*," "*Stability and Transition in Hypersonic Flows*," "*Multiscale and Multiphase Flow Problems*," "*Noise and Aeroacoustics*," "*Aero-Thermal Investigations in Turbomachinery*," and "*Development of Advanced CFD and Optimization*."

We would like to emphasize that this publication serves as a tool for communication and aims to enhance exchange between the doctoral candidates, the faculty and external attendees. The annual publication of their results in proceedings is of crucial importance to the VKI research providing a thorough review of the different activities within the three departments.

As such, the doctoral candidate students play a key role in strengthening the expertise in experimental research, computational methods, and physical modelling. In addition to basic research, works carried out at the von Karman Institute often leads to implementation of real life industrial applications critical to the fluid dynamics community.

Andrea Attavino	Thierry Magin	Christelle Debeer
Francisco Torres Herrador	Professor	Evelyne Crochard
Phd Representatives		Organizer / Editor

The contribution of all VKI members who helped with this event is deeply acknowledged in particular the faculty, library and printing office staff.

TABLE OF CONTENTS

Editorial notes i

Table of contents iii

NUMERICAL APPROACH FOR HYPERSONIC AND PLASMA FLOWS

Federico BARISELLI 3
Development of a coupled DSMC-SPH solver for the study of melting in rarefied gas flows

Stefano BOCCELLI (1st year phD) 13
Modeling of rarefied and ionized flows for electric space propulsion

Joffrey COHEUR 15
A first step towards the Bayesian inference of uncertain kinetic parameters of pyrolysis decomposition laws

Andrea CORTESI 25
Rebuilding freestream conditions in atmospheric entry flows from wall pressure and heat flux data

Simon DEMANGE 35
Absolute instability in plasma jet

Vincent FITZGERALD GIANGASPERO 37
Higher-order shock-fitting methods for high-speed simulations

Bruno DIAS 39
Ablation modelling for the simulation of the atmospheric entry of meteors

Ray VANDENHOECK (1st year phD) 49
Massively parallel and robust high-order methods for transitional hypersonic flow modelling on unstructured grids application to reusable launcher stages

Quentin WARGNIER 51
Numerical treatment of the nonconservative product in a multiscale fluid model for plasmas in thermal nonequilibrium: application to solar physics

GROUND AND FLIGHT EXPERIMENTS

Ana DEL VAL BENÍTEZ 65
Stochastic inference of the catalytic properties of thermal protection materials from plasma wind tunnel experiments

Zdeněk ILICH 75
Design of experiments to assess non-equilibrium nozzle flow phenomena in the VKI longshot hypersonic tunnel

Francisco TORRES HERRADOR (1st year phD) 87
Experimental characterization and numerical modelling of space debris degradation during atmospheric re-entry

STABILITY AND TRANSITION IN HYPERSONIC FLOWS

Florian DANVIN 91
Modeling transition to turbulence for hypersonic flows with metamodels of linear stability theory

Ludovico ZANUS 99
Nonlinear parabolized stability analysis of hypersonic flows in presence of curvature effects

Iván PADILLA MONTERO 109
Analysis of the stability of a flat plate high-speed boundary layer with discrete roughness

Fernando MIRÓ MIRÓ 121
Blowing and chemical non-equilibrium effects on hypersonic boundary-layer stability

Jorge SAAVEDRA GARCIA 135
Analysis of the mean flow unsteadiness impact on the near wall flow region

MULTISCALE AND MULTIPHASE FLOW PROBLEMS

Andrea ATTAVINO 153
CFD analysis of erosion of a light gas stratification by means of a hot air jet in the MiniPanda facility

Nicolas COUDOU 163
Development of wake meandering detection algorithms and their application to large eddy simulation results of wind turbine

Adriana ENACHE (1st year phD) 173
Analytical and experimental investigation of icing phenomena on wind turbine blades

Claudia ESPOSITO 175
Experimental study of different cavitating regimes through an orifice

Charline FOUCHIER 185
Scaled model of the pollutant dispersion driven by a condensed-phase explosion in an urban environment

Yoshiyuki NISHIO (1st year phD) 195
Multiphase flow modeling for CBRN applications

Sara PORCHETTA 197
Offshore wind wave interaction: a new roughness parameterization

Maria Teresa SCELZO 205
Experimental characterization of a solid-liquid mixture flowing in circular pipes

Maxim VAN CAPPELLEN (1st Year PhD) 215
Modeling turbulent polydispersed multiphase flows in stirring tank reactors

Agustín VILLA ORTIZ 217
Turbulent heat transfer at different prandtl number fluids in natural convection boundary layer on a vertical plate

NOISE AND AEROACOUSTICS

Nicolas BOUANATI 235
Leakage characterization through structural vibration analysis

Dominique JOACHIM (1st year phD) 245
Towards quieter compressors : investigation of installation effects and noise mitigation strategies

Riccardo ZAMPONI (1st year phD) 247
Investigation of turbulence-surface interaction noise mechanisms and their reduction using porous materials

Alessandro ZARRI (1st year phD) 249
SMARTANSWER - Flow and acoustic control of low-speed cooling fans

AERO-THERMAL INVESTIGATIONS IN TURBOMACHINERY

Elissavet BOUFIDI 253
On the dynamic response of constant temperature hot wire anemometers (CTHWA)

Tânia Sofia CAÇÃO FERREIRA 265
Influence of gas-to-wall temperature on bypass transition

Bogdan Cezar CERNAT 275
On the time-resolved flow field downstream of a turbine stage mounting optimized rotor tip geometries

Gian Luca GORI 287
LIF temperature field measurement for internal forced convection blade cooling

Marco VIRGILIO 299
Advanced experimental aero-thermal investigations of wall-bounded swirling flows in three-dimensional ribbed tubes

DEVELOPMENT OF ADVANCED CFD AND OPTIMIZATION

GIACOMO ALESSI 313
Adjoint surface optimization for internal and external aerodynamics applications by means of OpenFoam®

Arnaud CHÂTEL 323
Single-point optimization of the LS89 turbine cascade using a hybrid algorithm

Maria FARUOLI (1st year phD) 335
Adjoint method with thermal constraints for the optimization of fluid machinery

NUMERICAL APPROACH FOR HYPERSONIC AND PLASMA FLOWS

Development of a coupled DSMC-SPH solver for the study of melting in rarefied gas flows

Federico Bariselli

Aeronautics and Aerospace Department, von Karman Institute for Fluid Dynamics, Belgium, federico.bariselli@vki.ac.be

Supervisor: Thierry Magin

Associate Professor, Aeronautics and Aerospace Department, von Karman Institute for Fluid Dynamics, Belgium, thierry.magin@vki.ac.be

University Supervisor: Aldo Frezzotti

Professor, Aerospace Science and Technology Department, Politecnico di Milano, Italy, aldo.frezzotti@polimi.it

University Supervisor: Annick Hubin

Professor, Electrochemical and Surface Engineering Department, Vrije Universiteit Brussel, Belgium, annick.hubin@vub.ac.be

Abstract

Describing the entrainment of a molten layer into a hypersonic rarefied flow is relevant to predict the demise of space debris. Here, the different fluid phases cannot be described by the same models: the liquid can be treated as a continuous medium whereas a kinetic treatment is needed for the gas. In our approach, both models rely on particle schemes: the DSMC method for the gas phase and the SPH method for the solid and liquid phases. Preliminary results are presented to describe the main features of the methodology, the interface tracking and gas-liquid coupling procedures.

Keywords: Multiphase flow, atmospheric entry flow, liquid entrainment, particle method

1. Introduction

To date, the exact mechanisms of the demise of space systems are not understood. Debris from launcher stages and satellites at end-of-life is increasingly becoming a threat to other space systems while still in orbit, but may also be a direct threat for humans when remains, that have not fully disintegrated during descent, impact Earth's surface [1].

During their destructive re-entry, end-of-life space systems could experience significant melting in the highest layers of the atmosphere. Hence, the development of prediction tools for space debris demise and risk assessment requires developing a description of the entrainment of the molten layer into the hypersonic rarefied flow surrounding the body, where the different fluid phases cannot be described by the same models. On the contrary, the Knudsen number of these flows, i.e. the ratio of the mean free path of the molecules and the characteristic length, is such that the Boltzmann equation needs to be solved to describe the gas phase, while the Navier-Stokes equations are adequate to model the liquid phase [2].

More in general, interactions among gas, liquid, and solid phases at nano scales play a significant role in a variety of industrial processes. Gas-liquid flows in small scale geometries have received considerable attention in the past few years, especially due to the rapid developments in micro- and nanofluidics [3]. Atomization of droplets influences the coating properties and should be well understood to control and improve the quality of the process [4]. The stiction phenomenon is the major failure mode in microdevices [5].

In our approach, all the phases rely on particle schemes: the Direct Simulation Monte Carlo (DSMC)

[6] for the gas/vapour phase and the Smoothed Particle Hydrodynamics (SPH) [7] for the solid and liquid phases. While DSMC is the dominant technique for rarefied gas flows simulations, SPH has been selected, among other two-phase flows numerical techniques, because of its easier coupling with DSMC and its natural treatment of the free surface.

In the stochastic DSMC method, a kinetic particle simulates a large number of identical real molecules and the dynamics of the gas is solved under the assumption that the streaming operator of the Boltzmann equation can be decoupled from the collision term. On the other hand, in the SPH method, every particle represents a fluid parcel, subject to pressure, viscous and surface tension forces, and free to move in the domain. The properties of every particle depend on the properties of the neighbours through an interpolation kernel.

In comparison with mesh-dependent approaches, the SPH method significantly facilitates the handling of the problems with free or interfacial surfaces, whose locations are a priori unknown and have to be computed during the solution of the problem. Therefore, it is a particularly powerful tool to study multiphase fluid flow problems [8].

To the best of our knowledge, this is one of the first attempts to couple the Boltzmann and Navier-Stokes equations in an unsteady simulation with a deformable gas-liquid interface. In [9], a hybrid DSMC-SPH approach is employed to study the flow in hydrogen separation membranes. The steady solution is obtained by an iterative process in which the two solvers are run separately over two different domains and an overlapping buffer at their interface is used to update the free-stream boundary conditions. Tiwari et al. [10] couple the Finite Pointset method, which is similar in character to SPH, to simulate a nanobubble in shear flow, keeping the interface fixed.

In the next section, we present the physico-mathematical models employed to solve the different phases. A certain attention is given to the description of the interface. Section 3 delineates the numerical methods. After a description of the main features of the two methods, further details about the coupling procedure are provided. Finally, in Section 4, preliminary results are presented to describe the main characteristics of the methodology, the interface tracking and gas-liquid coupling procedures.

2. Physico-mathematical models

2.1. Incompressible Navier-Stokes equations for the liquid phase

The mathematical modelling of the liquid phase is based on the incompressible Navier-Stokes equations which can be derived by macroscopic local mass, momentum and energy balances. In the case of a single component fluid, this set of equations can be solved in function of the velocity, pressure and temperature field in the liquid ($\boldsymbol{v}_L$, p_L and T_L) and can be written as:

$$\begin{aligned} \nabla \cdot \boldsymbol{v}_L &= 0 \\ \rho_L \, \mathcal{D}_t \boldsymbol{v}_L &= -\nabla p_L + \mu_L \nabla^2 \boldsymbol{v}_L \\ c_{p_L} \rho_L \, \mathcal{D}_t T_L &= k_L \nabla^2 T_L \end{aligned} \tag{1}$$

where all liquid physical properties are denoted with the index $_L$ and the operator $\mathcal{D}_t()$ refers to the material derivative $\partial_t() + \boldsymbol{v}_l \cdot \nabla()$. The density of the liquid ρ_L is assumed constant and viscous heating is considered negligible, which results in a simplified energy equation, which is decoupled from the rest of the system [11].

2.2. Boltzmann equation for the gas phase

As long as the hypothesis of continuum is valid, a hydrodynamic model, such as the one described in Section 2.1, can be applied. However, when the rate of the collisions is too low for the gas to reach local thermodynamic equilibrium [2], the gas has to be described at a molecular scale. This scale does not allow a fully deterministic approach and a statistical description is more suitable.

The function $f(\boldsymbol{x}, \boldsymbol{\xi}, t)$ is defined as the one-particle velocity distribution function and its evolution over time is described by an integro-differential equation, the Boltzmann equation, which for a single atomic species reads as:

$$\partial_t f + \boldsymbol{\xi} \cdot \nabla f = \int \left(f' f'_1 - f f_1 \right) |\boldsymbol{\xi}' - \boldsymbol{\xi}| \, \sigma \, d\omega \, d\boldsymbol{\xi} \tag{2}$$

The streaming operator on the left hand side describes the result of macroscopic gradients over the velocity distribution function evolution in the physical and molecular velocity space $(\boldsymbol{x}, \boldsymbol{\xi})$, while the integral at the right hand side models the effect of the binary collisions in a dilute gas characterized by a collision cross-section σ [12].

For the gas phase, any quantity of interest at the macroscopic level, $\Psi_G(\boldsymbol{x},t) = (\rho_G, \rho_G \boldsymbol{v}_G, E_G)$, can be obtained from the related microscopic quantity, $\psi(\boldsymbol{x},\boldsymbol{\xi},t) = (m, m\boldsymbol{\xi}, \frac{1}{2}m|\boldsymbol{\xi}|^2)$, as a moment of f:

$$\Psi_G(\boldsymbol{x},t) = \int \psi(\boldsymbol{x},\boldsymbol{\xi},t) f d\boldsymbol{\xi} \tag{3}$$

where the macroscopic quantity of interest are, in this case, the density, ρ_G, the bulk velocity, $\boldsymbol{v}_G$, and the energy of the gas, E_G.

2.3. Interface boundary conditions

To couple the liquid and gas phases one has to first determine the interface between the two phases and then prescribe the interface boundary conditions. From a microscopic point of view, the vapour-liquid interface is a finite region whose thickness is 10-20 nominal molecular diameters. At a kinetic scale, its detailed physical structure is neglected and reduced to a surface, Σ, bounding the vapour.

For solving the Boltzmann and the incompressible Navier-Stokes equations, the free surface of the liquid domain has to be determined and tracked over time. The two phases are coupled by means of surface mass, momentum and energy balances. In this work, we deal with two immiscible phases, with no mass exchange from one to the other, hence, the surface mass balance is trivial. Therefore, we have the following conditions for the surface momentum and energy fluxes:

$$\boldsymbol{P}_L \cdot \boldsymbol{n}_\Sigma - \gamma_\Sigma \kappa_\Sigma \boldsymbol{n}_\Sigma = \boldsymbol{P}_G \cdot \boldsymbol{n}_\Sigma \tag{4}$$

$$\boldsymbol{q}_L \cdot \boldsymbol{n}_\Sigma = \boldsymbol{q}_G \cdot \boldsymbol{n}_\Sigma \tag{5}$$

where on the right hand side, the contribution coming from the gas appears, while the left hand side consists of all the terms from the liquid, including the one related to the surface tension γ_Σ and proportional to the local curvature of the surface κ_Σ.

The stress tensors, $\boldsymbol{P}(\boldsymbol{x},t)$, are defined for the liquid and the gas in the following way:

$$\boldsymbol{P}_G = \int m(\boldsymbol{\xi} - \boldsymbol{v}_G) \otimes (\boldsymbol{\xi} - \boldsymbol{v}_G) f d\boldsymbol{\xi} \tag{6}$$

$$\boldsymbol{P}_L = p_L \boldsymbol{I} + \mu_L (\nabla \boldsymbol{v}_L + \nabla \boldsymbol{v}_L^T) \tag{7}$$

while the heat fluxes, $\boldsymbol{q}(\boldsymbol{x},t)$, read as:

$$\boldsymbol{q}_G = \int \frac{1}{2} m |\boldsymbol{\xi} - \boldsymbol{v}_G|^2 (\boldsymbol{\xi} - \boldsymbol{v}_G) f d\boldsymbol{\xi} \tag{8}$$

$$\boldsymbol{q}_L = k_L \nabla T_L \tag{9}$$

depending if we look it from the vapour or the liquid side.

While the quantities available on the gas side of the interface are enough to determine all of the quantities needed on the liquid side, the same is not true in the opposite direction. Therefore, additional assumptions have to be made when computing the interfacial phase-space distribution in the gas from the density, velocity and temperature in the liquid.

The molecular flux emerging from Σ, which moves at $\boldsymbol{v}_\Sigma = \boldsymbol{v}_L$ and is characterized by a normal unit vector, $\boldsymbol{n}_\Sigma$ pointing in the direction of the gas, is classically modelled by the following inhomogeneous linear boundary condition [13]:

$$f[\boldsymbol{\xi} - \boldsymbol{v}_L] \cdot \boldsymbol{n}_\Sigma = \int_{[\boldsymbol{\xi}' - \boldsymbol{v}_L] \cdot \boldsymbol{n} < 0} \mathcal{K}_B(\boldsymbol{\xi}' \to \boldsymbol{\xi}) f[\boldsymbol{\xi}' - \boldsymbol{v}_L] \cdot \boldsymbol{n}_\Sigma \, d\boldsymbol{\xi}', \quad [\boldsymbol{\xi} - \boldsymbol{v}_L] \cdot \boldsymbol{n}_\Sigma > 0 \tag{10}$$

which is valid for two immiscible fluids. The molecules in the gas phase which, interacting with the wall and not condensing, are scattered back and whose velocity is instantaneously changed from $\boldsymbol{\xi}'$ to $\boldsymbol{\xi}$ with probability driven by the scattering kernel:

$$\mathcal{K}_B(\boldsymbol{\xi}' \to \boldsymbol{\xi}) = \frac{[\boldsymbol{\xi} - \boldsymbol{v}_L] \cdot \boldsymbol{n}_w}{2\pi (R T_L)^2} \, exp \left\{ - \frac{|\boldsymbol{\xi} - \boldsymbol{v}_L|^2}{2 R T_L} \right\} \tag{11}$$

in which R is the gas constant defined as k_B/m, k_B being the Boltzmann constant and m the atomic mass of the species. In this case, the kernel is written as if all the impinging particles were fully thermalized to the temperature of the liquid.

3. Numerical methods

3.1. Smoothed Particle Hydrodynamics for the liquid phase

Originally developed to model partial differential equations in astrophysics [7], the Smoothed Particle Hydrodynamics (SPH) method has been extended to model a wide variety of problems in computational physics, among which it has shown to be capable to model complicated and dynamic boundaries [8].

SPH is a fully Lagrangian technique, in which the fluid is represented by an ensemble of discrete particles, typically of fixed mass, M, which move with the local fluid velocity, $\boldsymbol{v}_L(\boldsymbol{x}, t)$ and carry other fluid quantities specific to the given problem. Field variables in a certain point, $\Psi_L(\boldsymbol{x}, t)$, are calculated through an interpolation function (the weighting smoothing kernel) from the field variables of surrounding neighbour particles. Hence, the particles can also be regarded as interpolation points:

$$\Psi_L(\boldsymbol{x}, t) = \int \Psi_L(\boldsymbol{x}', t)\, \mathcal{W}(\boldsymbol{x} - \boldsymbol{x}', h)\, d\boldsymbol{x}' \approx \Psi_{L_i}(t) = \sum_j \Psi_{L_j} \mathcal{W}_{ij} M_j \qquad (12)$$

where $\mathcal{W}_{ij} = \mathcal{W}(\boldsymbol{x}_i - \boldsymbol{x}_j, h)$ is the smoothing kernel with smoothing length h which controls the number of active neighbour particles within the support domain.

Particles are integrated along their trajectories following the Newton's second law of motion, with the net force which is computed according to the right hand side of the momentum in 1. In the SPH formalism, the momentum and energy equations are written as follows:

$$\mathcal{D}_t \boldsymbol{v}_{L_i} = -\sum_j M \left(\frac{p_{L_j}}{\rho_{L_j}^2} + \frac{p_{L_i}}{\rho_{L_i}^2} + \Pi_{ij} \right) \nabla_i \mathcal{W}_{ij} + \gamma_{\Sigma_i} \kappa_{\Sigma_i} \boldsymbol{n}_{\Sigma_i} \delta^{\Sigma} \qquad (13)$$

$$c_{p_{L_i}} \mathcal{D}_t T_i = \sum_j M \frac{2k_L}{\rho_{L_i} \rho_{L_j}} (T_{L_i} - T_{L_j}) \frac{\boldsymbol{x}_i - \boldsymbol{x}_j}{|\boldsymbol{x}_i - \boldsymbol{x}_j|^2} \nabla_i \mathcal{W}_{ij} \qquad (14)$$

where Π_{ij} is an artificial viscosity term [8] and the effect of surface tension forces is taken into account by adding a volume term to the momentum equation [14], which is proportional to the local curvature of the interface:

$$\kappa_{\Sigma_i} = -(\nabla \cdot \boldsymbol{n})_i = \sum_j \frac{M}{\rho_{L_j}} (\boldsymbol{n}_j - \boldsymbol{n}_i) \cdot \nabla_i \mathcal{W}_{ij} \qquad (15)$$

and it is different from zero only at the boundary.

3.2. Direct Simulation Monte Carlo for the gas phase

Direct Simulation Monte Carlo (DSMC) is a particle-based method for the numerical solution of the Boltzmann equation [6]. This technique has been widely used in the aerospace community over the last 50 years to simulate hypersonic flows with a high degree of thermo-chemical non-equilibrium [16].

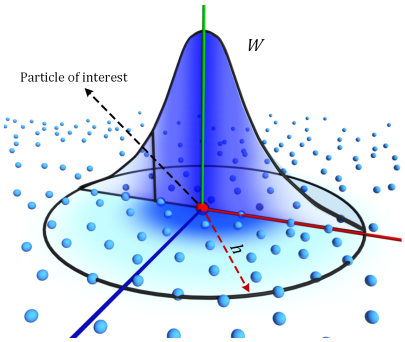

Figure 1: Schematic of the SPH kernel interpolation function and its support domain. The particles can be regarded as interpolation points [15].

The trajectories of a representative number of molecules are simulated in the physical space. Each simulated particle corresponds to a certain number of real particles according to a statistical weight W_p. Each molecule is initialized in position, velocity, internal state and species. The advection phase of the particles is treated deterministically using finite differences, while the local homogeneous relaxation $\partial_t f = J(f, f)$, where $J(f, f)$ represents the right hand side of Equation 2, is solved by means of Monte Carlo technique.

The splitting of the operators leads to accurate results only if the employed time step, Δt, is a fraction of the mean collision time that exist between two consecutive collisions. The domain is discretized with a grid, whose cells have a characteristic length which must be a fraction of the mean free path. In DSMC, the grid is used for an efficient choice of collisions partners, i.e., only the particles belonging to the same cell can potentially collide. The grid is also used to compute the properties at a macroscopic level, such as density, temperature and bulk velocities as described by Equation 3. These properties are computed by sampling the averages of the microscopic properties on the particles of the same cell.

3.3. Details of the DSMC-SPH coupling procedure

DSMC routines are developed in-house and have been embedded in the framework of the open source

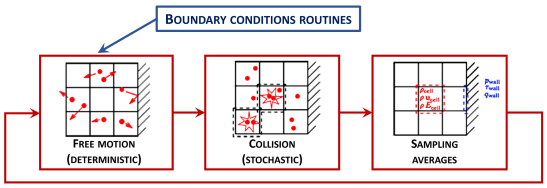

Figure 2: Schematic of the DSMC algorithm. The gas-surface interactions routines are implemented in the free advection phase.

SPHysics software [17]. This tool had been validated against experimental results in dam break and sloshing type flows [18]. We take advantage of the established capabilities of this tool while others, such as the implementation of the energy equation and its Neumann boundary conditions [19], or surface tension effects, have been added. SPHysics performs the integration in time explicitly with a Verlet procedure and employs a Tait's equation of state with artificial compressibility to model a quasi-incompressible fluid.

We aim to reach the dynamic and thermal coupling between the gas and the condensed phases. The gas feels the change in the geometry by deforming the boundaries, while the liquid feels the presence of the gas due to the net exchange of momentum and energy. At each time step, the coupling procedure consists of the following points:

- Point 1. The SPH particles are moved according to mass, momentum and energy balances following the incompressible formulation of the Navier-Stokes equations as sketched in Section 3.1.

- Point 2. The SPH particles in the proximity of the gas-liquid interface can be distinguished from the ones in the bulk of the liquid. In fact, particles near free surfaces are characterized by a truncated kernel because of the absence of neighbours in their compact support (see Figure 1). The method used here was proposed by Doring [20] and exploits the fact that the eigenvalues of the renormalization matrix, as defined by Equation 16, depends on the spatial organization of the particles in the neighbourhood of a considered point:

$$\boldsymbol{B}(\boldsymbol{x}_i) = \left[\sum_j \nabla \mathcal{W}_j(\boldsymbol{x}_i) \otimes (\boldsymbol{x}_j - \boldsymbol{x}_i) \frac{M}{\rho_{L_j}} \right]^{-1} \quad (16)$$

  Doring showed that the value of the minimum eigenvalue of the matrix $\boldsymbol{B}$ depends on the spatial organization of the particles j in the neighbourhood of the considered calculation point i. When going away from the fluid domain this eigenvalue tends theoretically to 0 while inside this domain, it tends theoretically to 1. This allows to determine regions of the fluid domain where the free surface lies.

- Point 3. The normals to the free surface are computed. The normal is aligned with the gradient of the density of the SPH particles. As shown in [21], inside the liquid domain, the sum of the kernel gradient over the neighbours is very close to zero. When a particle, instead, is near the free surface, such sum is a good approximation of the local normal to the interface. Since the accuracy of the evaluation of this vector depends on the particle disorder, it is possible to get a more accurate evaluation by using again the renormalization matrix:

$$\boldsymbol{n}_\Sigma(\boldsymbol{x}_i) = \frac{\boldsymbol{r}(\boldsymbol{x}_i)}{|\boldsymbol{r}(\boldsymbol{x}_i)|}$$

$$\boldsymbol{r}(\boldsymbol{x}_i) = -\boldsymbol{B}(\boldsymbol{x}_i) \sum_j \nabla \mathcal{W}_j(\boldsymbol{x}_i) \frac{M}{\rho_{L_j}} \quad (17)$$

- Point 4. The DSMC particles are moved in the physical space. The gas-liquid interactions routines are part of the advection phase, with the particles which interact with the interface being reflected according to the implemented scattering kernel. Gas-liquid interactions are performed, as described in Point 5, 6, 7.

- Point 5. The new position of the gas-liquid interface is identified by finding the intersection point of the DSMC trajectories with the free surface of the liquid. The DSMC cells containing the liquid interface are tagged. When one of these cells is crossed, the SPH particle which is the closest to the trajectory and belongs to the interface is selected. The intersection point is computed as the point of minimum distance between this SPH particle and the DSMC particle trajectory. The full procedure is presented in the flowchart of Figure 3.

- Point 6. The gas-surface interactions are performed. DSMC particles are scattered back, fully thermalized as described by Equation 10 and 11, following the normal associated to the SPH particle selected on the interface at Point 5.

- Point 7. Momentum and energy are exchanged between the gas and the liquid. The net force and energy are included in the balances for the computation of the trajectory and thermal response of the SPH particles computed at Point 1:

$$M\mathcal{D}_t \boldsymbol{v}_{L_i} = \boldsymbol{F}_i^{SPH} + \boldsymbol{F}_i^{DSMC} \tag{18}$$

$$M\mathcal{D}_t T_{L_i} = E_i^{SPH} + E_i^{DSMC} \tag{19}$$

$\boldsymbol{F}_i^{SPH}$ and E_i^{SPH} are nothing else than the right hand sides in Equation 13 and 14, while $\boldsymbol{F}_i^{DSMC}$ and E_i^{DSMC} are the net contribution resulting from momentum and energy exchange of the gas molecules impinging on the liquid surface and can be expressed in the following way:

$$\boldsymbol{F}_i^{DSMC} = \frac{-W_p \sum m(\boldsymbol{\xi}^{post} - \boldsymbol{\xi}^{pre})}{N_s \Delta t} \tag{20}$$

$$E_i^{DSMC} = \frac{W_p \sum (e_{int}^{post} - e_{int}^{pre})}{N_s \Delta t} + \frac{W_p \sum \frac{m}{2}(|\boldsymbol{\xi}^{post}|^2 - |\boldsymbol{\xi}^{pre}|^2)}{N_s \Delta t} \tag{21}$$

where ^{pre} and ^{post} stands for pre- and post- surface collision properties, e_{int} represents the internal energy of each molecule and the sum $\sum$ is accumulated from all the DSMC molecules impinging a certain SPH particle over N_s sampling time steps.

- Point 8. The DSMC particles in the same cell can collide among each others. The velocities and internal energy states are updated according to the local homogeneous relaxation equation as described in Section 3.2.

As a final remark, we can recall that, since the gas time scale is usually much faster than the one characterizing the liquid, the gas and the condensed phases would not need to be coupled at every DSMC time step. The possibility of averaging in a wider time window would reduce the statistical noise introduced at Point 7 due to the stochastic nature of the DSMC methodology.

4. Results

4.1. Test case 1: 2D hypersonic rarefied flow around a cylinder made of fixed SPH particles

A hypersonic cross-flow developing around a solid cylinder is a common test case employed in rarefied gas dynamics for the purpose of verification. Here, we compare the results obtained with a classic DSMC boundary condition with those obtained through a DSMC-SPH static coupling as described in Section 3.3 at Point 5 and 6 and better detailed in Figure 3.

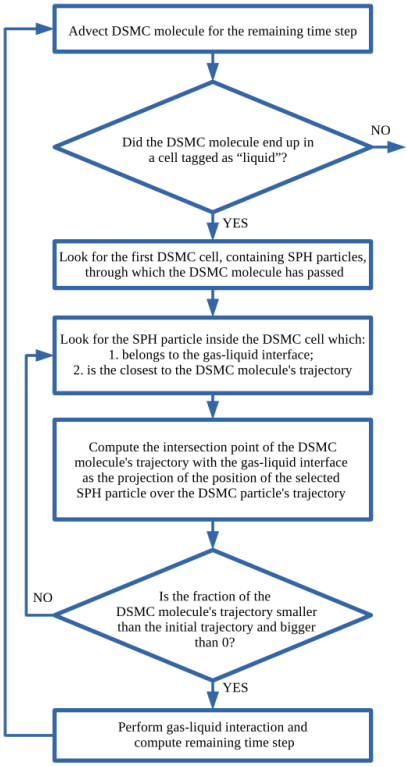

Figure 3: Description of the algorithm developed for Point 5 in the coupling procedure.

While the new boundary condition is approximated in nature, in the classic boundary condition, both the normal to the surface and the point of intersection of the DSMC molecule trajectory with the solid wall are computed analytically. The new boundary condition tends to the exact one as the number of SPH particles increase.

The cylinder is formed by a system of SPH particles which are kept fixed along the simulation. For the same degree of rarefaction, $Kn = 0.25$, two different Mach number conditions have been chosen: argon free-stream $M = 10$ and 25. The numerical parameters selected for these simulation are: $\Delta t = 0.5 \times 10^{-6}$ s, $\Delta x = 3.5 \times 10^{-4}$ m and $N_p = 20$ per DSMC cell. The number of SPH particles per DSMC cell is about 10.

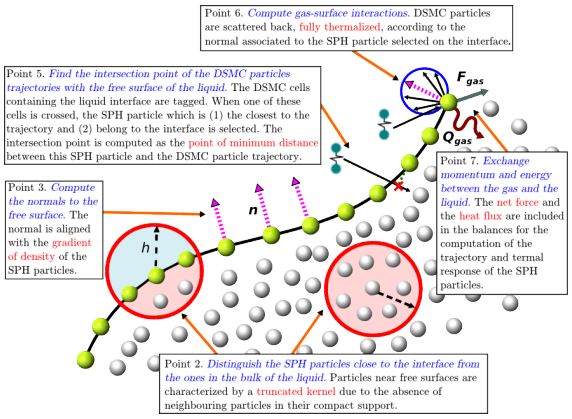

Figure 4: Schematic of the DSMC-SPH coupling procedure as described in Section 3.3.

Figure 5 shows gas temperature, number density and velocity along the stagnation line in the front and in the rear of the cylinder. As reference, Lofthouse results have been also reported [22]. The implemented boundary condition proves to perform well for the chosen conditions. The comparison is not perfect but fair and seems to be better for the condition at a lower Mach number (Figure 5-a).

4.2. *Test case 2: 2D droplet oscillation due to surface tension effects*

The free oscillation of a 2D droplet with an initial square shape constitutes an ordinary benchmark for the scientific community interested in multiphase flows. Here, we want to test the ability of the SPH method to deal with surface tension effects and, at the same time, to provide a validation case for SPHysics which is more relevant to our field of interest.

This simulation concerns SPH without the use of DSMC. The gas-liquid interface effect is contained inside the tension force applied at the surface. The initial square of side l is such that the curvature is null everywhere except at corners (see Figure 6). Surface tension leads to the deformation of the square toward an equilibrium circular shape of radius:

$$R_{eq} = \sqrt{l^2/\pi} \tag{22}$$

Inertia produces an overshoot with respect to this position such that the droplet reaches a square shape that is just the initial shape rotated by $\pi/4$. The same process takes the droplet back to its starting condition. In

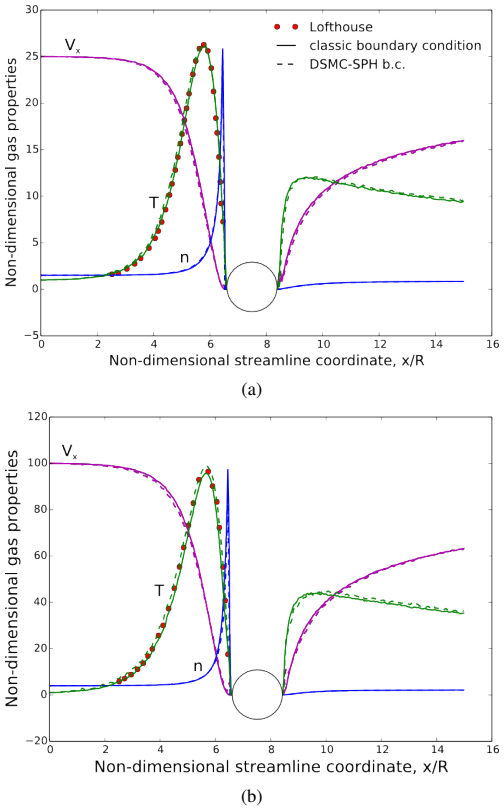

Figure 5: Comparison of stagnation line properties for a hypersonic argon flow over a cylinder for $Kn = 0.25$, $M = 10$ (a) and $M = 25$ (b). Reference solution provided by Lofthouse [22].

the case of an inviscid fluid, this oscillation is characterized by a constant period

$$\omega = \sqrt{\frac{n(n^2-1)\gamma_\Sigma}{\rho_L R_{eq}^3}} \tag{23}$$

which is a classic result of hydrodynamics and was derived by Lamb [23] already in 1885. The period is well predicted by the inviscid theory and the oscillations are damped out due to viscous effects till the final curvature

$$\kappa_{fin} = 1/R_{eq} \tag{24}$$

remains constant (see Figure 7). At this point, the pressure jump across the interface satisfies the Laplace equation

$$\Delta p = \gamma_\Sigma \kappa_{fin} \tag{25}$$

which is a direct result of Equation 4 when equilibrium is reached.

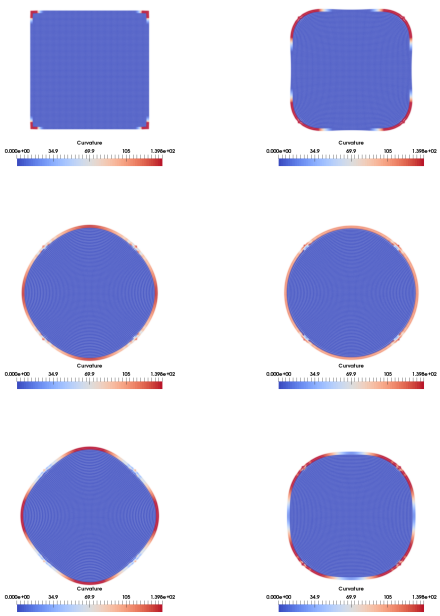

Figure 6: SPH simulation of a 2D liquid droplet which starts from an initial square shape. The color depends on the curvature of the surface, computed with the formula of Equation 15.

4.3. Simulation of a 2D hypersonic rarefied flow around a droplet

A coupled DSMC-SPH simulation for a liquid droplet being deformed due to a nitrogen gas jet impinging on its wall has been performed. Surface tension effects have been switched off so that the Weber number can be considered infinite, while the gas free-stream conditions are M=15 and Kn=0.1.

Due to the deformation of the droplet the position of the diffuse bow shock wave which develops in front of the body evolves as it can be appreciated in Figure 8 where both the density and translational temperature (b) fields are presented. The gas molecules get accumulated in the region close to the stagnation point which moves as the surface recedes. The noise in the gas temperature field is due to the fact that for this simulation no time averaging has been carried out.

The detail provided by Figure 9 shows the proper tracking of the gas-liquid interface (Point 2 in Section 3.3) and the correct computation of the normals to the surface, described at Point 3, along the simulation. The color of the SPH particles depends on the minimum eigenvalue of the renormalization matrix in Equation 16. The normals are computed only for those SPH particle which are considered as part of the interface.

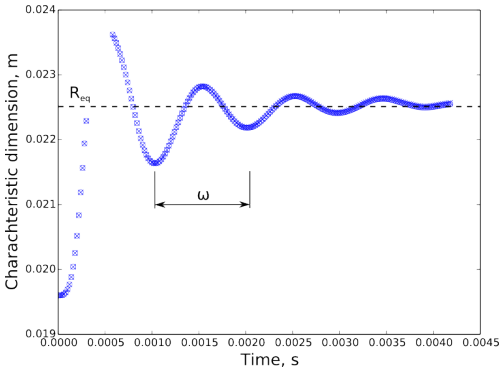

Figure 7: Oscillations characterizing a 2D liquid droplet which starts from an initial square shape. The period of the oscillation is well predicted by the inviscid theory [23].

5. Conclusions

An approach to couple DSMC with SPH method has been introduced. The flexibility of the latter in the description of deformable free surfaces has been exploited to model a gas-liquid multiphase flow, in which the vapour phase, due to strong non equilibrium effects, has to be described by a kinetic equation. Preliminary results have been presented to verify the main features of the methodology, the interface tracking and gas-liquid coupling procedures. In the next future, the coupling will be tested against available analytical solutions starting from a Couette flow.

Acknowledgments

The research presented here was funded by a PhD grant of the Research Foundation Flanders (FWO).

References

[1] G. Koppenwallner, T. Lips, Influence of rarefied gas flow on reentry survivability of space debris 1084 (2008) 740–747.
[2] E. Josyula, J. Burt, Review of rarefied gas effects in hypersonic applications, NATO tecnical report RTO-EN-AVT-194.
[3] J. M. Oh, T. Faez, S. de Beer, F. Mugele, Capillarity-driven dynamics of water–alcohol mixtures in nanofluidic channels, Microfluidics and Nanofluidics 9 (1) (2010) 123–129.
[4] M. Jadidi, S. Moghtadernejad, A. Dolatabadi, A comprehensive review on fluid dynamics and transport of suspension/liquid droplets and particles in High-Velocity Oxygen-Fuel (HVOF) thermal spray, Coatings Journal 5 (2015) 576–645.

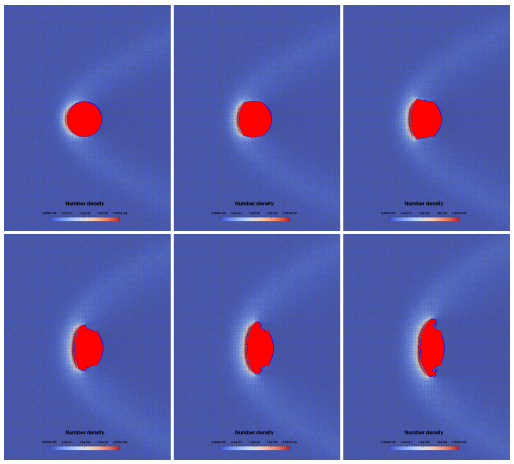

(a)

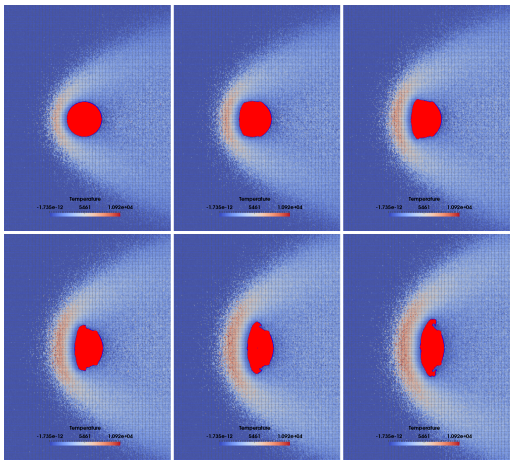

(b)

Figure 8: Simulation of a liquid droplet in gas jet by means of DSMC-SPH coupling. The droplet, characterized by a infinite Weber number, is being deformed by a hypersonic (M=15) rarefied (Kn=0.1) gas flow. The gas density (a) and translational temperature (b) fields are presented.

[5] N. Tas, T. Sonnenberg, H. Jansen, R. Legtenberg, M. Elwenspoek, Stiction in surface micromachining, Journal of Micromechanics and Microengineering 6 (4) (1996) 385.

[6] G. A. Bird, Molecular Gas Dynamics and the Direct Simulation of Gas Flows, Oxford University Press, 1994.

[7] R. A. Gingold, J. J. Monaghan, Smoothed particle hydrodynamics: Theory and application to non-spherical stars, Mon. Not. Roy. Astron. Soc. 181 (1977) 375.

[8] J. Monaghan, Simulating free surface flows with SPH, Journal of Computational Physics 110 (2) (1994) 399 – 406.

[9] J. Ye, J. Yang, J. Zheng, X. Ding, I. Wong, W. Li, C. Chen, A multi-scale flow analysis in hydrogen separation membranes using a coupled DSMC-SPH method, International Journal of Hydrogen Energy 37 (1) (2012) 894 – 902.

[10] S. Tiwari, A. Klar, S. Hardt, A. Donkov, Coupled solution of the boltzmann and navierstokes equations in gasliquid two phase flow, Computers and Fluids 71 (2013) 283–296.

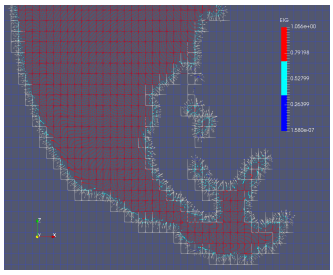

Figure 9: A detail of the DSMC-SPH simulation to show the proper operation of Point 2 and 3 in the coupling procedure. The color of the SPH particles has been chosen according to the minimum eigenvalue of the matrix in Equation 16. The DSMC grid is visible in the background.

[11] G. L. Morini, Viscous heating in liquid flows in microchannels, International Journal of Heat and Mass Transfer 48 (17) (2005) 3637 – 3647.

[12] J. H. Ferziger, H. G. Kaper, Mathematical Theory of Transport Processes in Gases, Elsevier Science Publishing, 1972.

[13] A. Frezzotti, Boundary Conditions at the Vapor-Liquid Interface, Physics of Fluids 23 (3).

[14] J. P. Morris, Simulating surface tension with Smoothed Particle Hydrodynamics, International Journal for Numerical Methods in Fluids 33 (3) (2000) 333–353.

[15] `http://docs.neutrinodynamics.com`.

[16] M. S. Ivanov, G. N. Markelov, S. F. Gimelshein, L. V. Mishina, A. N. Krylov and N. V. Grechko, High-Altitude Capsule Aerodynamics with Real Gas Effects, Journal of Spacecraft and Rockets 35 (1) (1998) 16–22.

[17] M. Gomez-Gesteira, B. D. Rogers, A. J. C. Crespo, R. A. Dalrymple, M. Narayanaswamy, J. M. Dominguez, Sphysics - development of a free-surface fluid solver - part 1: Theory and formulations, Computers and Geoscience 48 (2012) 289–299.

[18] M. Gomez-Gesteira, A. Crespo, B. Rogers, R. Dalrymple, J. Dominguez, A. Barreiro, Sphysics development of a free-surface fluid solver part 2: Efficiency and test cases, Computers and Geosciences 48 (2012) 300 – 307.

[19] M. E. Sikarudi, A. Nikseresht, Neumann and robin boundary conditions for heat conduction modeling using Smoothed Particle Hydrodynamics, Computer Physics Communications 198 (2016) 1 – 11.

[20] M. Doring, Dveloppement d'une mthode SPH pour les applications surface libre en hydrodynamique, Ph.D. thesis (2005).

[21] P. Randles, L. Libersky, Smoothed Particle Hydrodynamics: Some recent improvements and applications, Computer Methods in Applied Mechanics and Engineering 139 (1) (1996) 375 – 408.

[22] A. J. Lofthouse, Nonequilibrium hypersonic aerothermodynamics using the Direct Simulation Monte Carlo and Navier-Stokes models, Ph.D. thesis (2008).

[23] H. Lamb, Hydrodynamics, Cambridge University Press, 1885.

Modeling of Rarefied and Ionized Flows for Electric Space Propulsion

Stefano Boccelli

Aeronautics and Aerospace Department, von Karman Institute for Fluid Dynamics, Belgium, stefano.boccelli@vki.ac.be

Supervisor: Thierry E. Magin

Associate Professor, Aeronautics and Aerospace Department, von Karman Institute for Fluid Dynamics, Belgium, magin@vki.ac.be

University Supervisor: Aldo Frezzotti

Professor, Dipartimento di Scienze e Tecnologie Aerospaziali, Politecnico di Milano, Italy, aldo.frezzotti@polimi.it

Abstract

The large variety of altitudes at which aerospace vehicles operate poses serious limitations to the validity of present fluid dynamic models. In particular, continuum models based on the Navier-Stokes equations lose their accuracy as the degrees of rarefaction and non-equilibrium increase. Capsules entering planetary atmospheres, hypersonic vehicles and deorbiting satellites are a few of the many cases where the flow field needs to be computed taking into account the effects of rarefaction. This research project deals with the study of flows characterising electric propulsion systems mounted on satellites or spacecrafts, where the injected flow rapidly gets rarefied as it expands in the space environment. Such electric devices are currently in operation on a number of satellites, allowing cost-efficient orbital maneuvers, and are among the most promising propulsion strategies for upcoming manned missions to Mars.

Nowadays, the study of rarefied flows can be tackled almost exclusively in the framework of gaskinetic theory, employing particle-based methods such as the Direct Simulation Monte Carlo (DSMC) or the Particle-In-Cell (PIC) method. Such framework constitutes the most accurate approach to the problem, but is limited by its numerical cost, which becomes prohibitively high as the density increases.

This work aims at developing a class of fluid dynamic models termed “moment methods”, able to extend the validity of the Navier-Stokes system towards nonequilibrium conditions. A number of significant achievements have been obtained through the years by such methods, however a unified and global approach is not available yet. In order to apply moment methods to electric thrusters, first the formulation will be extended to include the effect of electric and magnetic fields; multispecies capabilities will then be added. The resulting set of equations will be tested on a real-world electric thruster of Hall type and compared to full kinetic simulations as well as experimental data.

The numerical tool that will be developed, will offer solutions with extended accuracy with respect to classical Navier-Stokes simulations, while keeping the numerical expense at the same order of magnitude. This will make the tool useful for iterative procedures of electric thrusters design. Moreover, the PDE nature of the method will pave the way to the application of stability analysis techniques. Finally, electric thrusters flows share a large number of features with hypersonic and atmospheric entry flows. The tools developed in this work will be easily applicable to such fields.

A First Step Towards the Bayesian Inference of Uncertain Kinetic Parameters of Pyrolysis Decomposition Laws

Joffrey Coheur

Aeronautics and Aerospace Department, von Karman Institute for Fluid Dynamics, Belgium, joffrey.coheur@vki.ac.be

Supervisor: Thierry Magin

Associate Professor, Aeronautics and Aerospace Department, von Karman Institute for Fluid Dynamics, Belgium, magin@vki.ac.be

University Supervisors:

Maarten Arnst

Assistant Professor, Aerospatial & Mechanical Engineering, Université de Liège, Belgium, maarten.arnst@uliege.be

Philippe Chatelain

Professor, Institute of mechanics, materials and civil engineering, Université Catholique de Louvain, Belgium, philippe.chatelain@uclouvain.be

Abstract

We present a Bayesian approach for the inference of uncertain kinetic parameters relevant to the pyrolysis of composite ablators. We present the random walk Metropolis algorithm for sampling from the posterior density in a Markov Chain Monte Carlo process and we discuss the choice of prior density, likelihood function, and proposal distribution. Correlations between parameters are identified and analyzed.

Keywords: inverse problem, bayesian, chemical kinetics, pyrolysis, thermal protection materials

1. Introduction

Ablative thermal protection materials are largely used for the heat shield of spacecraft of extra-orbital high-velocity entry missions. In particular, low density thermal protection materials have proven to be successful during atmospheric entries of several missions such as Stardust [1; 2] or the Mars Science Laboratory [3], and more recently for the SpaceX Dragon capsule. Ablative porous materials can accommodate the high heating rates and heat loads encountered during hypersonic entry [4] through phase change and mass loss. The ablation of reinforced fiber/resin composite materials occurs mainly in two steps [5]. First, the resin is progressively pyrolyzed, producing *pyrolysis gases* that percolate through the material and leave a carbonaceous residue on the fibers, the *char*. Then, this charred material is ablated simultaneously by heterogeneous chemical reactions, sublimation, and spallation (mechanical erosion).

The typical process for designing the thermal protection system is to calculate the nominal thickness by performing numerical simulations using predictive tools, apply mission margins, and verify the results with experimental testings. Although nowadays baseline predictions are performed using high-fidelity simulations tools, the estimation of their associated uncertainties receive little rigorous analysis. The first step in a quantification of uncertainty in numerical simulations is the characterization of input uncertainties, which can then be propagated through numerical solvers to assess error margins. In this paper, we propose a Bayesian approach to quantify the uncertainty in the parameters of laws governing pyrolysis process of thermal protection materials.

1.1. Literature review

Studies on ablative materials date back to the 60's with the development of early material response

codes [6; 7] based on the experiments of Goldstein and Sykes [8; 9]. Since then, these materials have been largely investigated from both the numerical and experimental sides. Regarding numerical developments, material response codes have been progressively coupled to computational fluid dynamic solvers, exchanging boundary conditions dynamically [10; 11; 12]. At the sime time, innovative approaches to simulate both the material and the flow in the same domain of computation (a *unified approach*) have been developed [13; 14; 15; 16]. For predicting the condensed phase thermal decomposition, those current models are still based on previous experiments from the 60's [8; 9] although nowadays computer solvers allow the use of more accurate models. On the experimental side, many experiments have been carried out more recently to get new insights into the pyrolysis of the resin [17; 18; 19; 20; 21] and improve models for numerical solvers. A large test campaign was also performed in the von Karman Institute (VKI) Plasmatron facility to test new lightweight ablative materials, providing a large comprehensive set of experimental data that will ultimately help to validate numerical models [22]. There have been several efforts to infer the kinetic parameters in order to update those models based on recent experiments. Most of the inference is performed in a deterministic framework, mainly by using optimization solvers to obtain best-fit estimates. Although those algorithms can be very efficient, results can hardly account for the uncertainty on the parameters, coming from experimental measurements, model inadequacy, parameter variability, etc. A correct estimation of those uncertainties will eventually lead to a robust estimation of errors on numerical simulations for better assessing safety margins. A few investigations on pyrolysis experiments in a stochastic view have been performed for fire technology [23], but to the author's knowledge no study of this kind has been performed in aerospace engineering for the pyrolysis of thermal protection materials.

1.2. Objectives

The objective of this work is therefore to determine in an uncertainty quantification framework the kinetic parameters in the physico-chemical laws used for simulating the pyrolysis of thermal protection materials. In this paper, we present a Bayesian inference method for determining kinetic parameters based on recent pyrolysis experiments.

1.3. Outline of the paper

The paper is structured as follows. In Section 2, we first start by presenting the mathematical description of the pyrolysis of a point-mass sample and we focus strictly on the thermal degradation of the material. Next in Section 3 we introduce the experimental results that we use for the data comparison and in Section 4 we present the methodology for the Bayesian inference of the parameters of the model. Then, in Section 5, we present the algorithm and the implementation of the Markov Chain Monte Carlo simulations for sampling from the posterior distribution, and, finally, in Section 6, we present the results of the inference process. Conclusions and suggestions for further work are given in Section 7.

2. Physico-Chemical Model for Pyrolysis

We address here the mathematical description of the pyrolysis of thermal protection materials. When these materials are heated, they first undergo pyrolysis, during which gaseous products are released and a char layer is left behind. In a second step, they undergo ablation of the char and the fibers by heterogeneous chemical reactions, mechanical erosion (spallation) and/or phase change. In this paper, we focus solely on the pyrolysis of the resin and do not consider gas production.

It is generally accepted that solid state reactions are often too complex to be described in terms of one single pair of Arrhenius parameters with the corresponding kinetic model [24; 25]. A comprehensive decomposition law for pyrolysis decomposition, as already proposed by Mansour and Lachaud [26], models reaction rates as follows:

$$\frac{d\xi_j}{dt} = A_j T^{m_j} \exp\left(\frac{-E_{\mathrm{a},j}}{RT}\right)(1-\xi_j)^{n_j}, \qquad (1)$$

where ξ is the extent of the pyrolysis reaction, R is the universal gas constant, and A, E_a, n, m the pre-exponential factor, activation energy, reaction rate, and temperature exponent, respectively. The subscript j denotes the different numbers of pyrolysis reactions and $j = 1, \ldots, N_\mathrm{p}$, where N_p is the number of pyrolysis decomposition processes in the solid resin (or the number of reactants). Assuming a point-mass model, sample mass is then given by

$$m = m_0 - \sum_{j=1}^{N_\mathrm{p}} F_j \xi_j (m_0 - m_\mathrm{c}), \qquad (2)$$

where m_0 is the initial mass of the sample and m_c is the residual mass of char and F_j is the fraction of mass that decomposes due to reaction j. Because at the end of the global pyrolysis process, $m = m_c$ and $\xi_j = 1$ $\forall j$, the following restriction must hold on the mass fractions

$$\sum_{j=1}^{N_p} F_j = 1. \tag{3}$$

In this preliminary study, we focus on the determination of the kinetic parameters for the decomposition of the reactants. Further work will investigate reaction mechanisms and stoechiometric coefficients for the pyrolysis gas production.

3. Pyrolysis Experiments

We use the experiments of Wong for the parameter inference [19]. In these experiments, production of pyrolysis products are quantified using gas chromatography (GC) techniques. A phenol-formaldehyde resin is heated in a reactor in a stepwise procedure with a temperature increment of 50 K from 320 K to 1290 K. The reactor is kept at the target temperature for 1 h to ensure that the pyrolysis reaction at this temperature is near completion. The amount of pyrolysis products formed in the gas phase is estimated at the end of the process. Then, the temperature is increased by 50 K to reach a new target temperature at which the sample is heated again for 1 h. This procedure is repeated until the maximum temperature is reached. Those experiments are very promising as they provide a quantification of mass species production from pyrolysis that could help for inferring reaction mechanisms.

This system also allows to measure the mass of the sample after each step without using a thermogravimetric analyzer. An electronic balance is used to weigh the reactor after each step increment but mass loss can also be deduced from the mass yield production as the system ensures that everything produced in the reactor is collected without loss and quantitatively analyzed. However, for the latter the possibility of secondary reactions exists in the reservoir and the batch-reactor approach does not lend itself well to nonequilibrium measurements of evolving products in real time.

The overall experimental procedure was repeated three times, allowing to define a mean value and a standard deviation for the measured quantities at each temperature. We use the results from the mass loss estimated from GC analyses to perform the parameter inference of the kinetic laws introduced in Section 2. This will allow to deduce the reaction kinetics but not the reaction mechanisms, for which we should use directly species product yields from the GC analyses.

3.1. Numerical Simulation of the Experiments

For the reconstruction of the sample mass from Eq. 2, we assume a point-mass material of 50 mg that is heated using the same procedure as in Wong experiments. Solving Eq. 2 involves the resolution of a system of independent first order differential equations. Finding an analytical solution can be particularly hard especially when the temperature is a complex function of time. In general, thermal analysis experiments are performed using either a linear heating rate or a (piecewise) constant temperature (isothermal conditions). The analytical solution of the extent of reaction, assuming a constant value T_i for the temperature during a time interval i of duration $\Delta t = [0, t_f]$ as described above is given by

$$\xi(t) = 1 - \left[(1-n)(C_i - A\exp\left(-\frac{E}{RT_i}\right)t)\right]^{1/(n-1)}, \tag{4}$$

$$C_i = \frac{(1-\xi_i(0))^{1-n}}{1-n}, \tag{5}$$

where $\xi_0(0) = 0$ in the first time interval, then the value for $\xi_i(0)$ in a given time interval is provided from $\xi_{i-1}(t = t_f)$ in the previous time interval. This equation holds for every reactant j that is involved in the pyrolysis decomposition process. More complex temperature function or more complex model for the thermal analysis of the material require numerical treatment of partial differential equations and the use of more sophisticated solvers.

4. Bayesian Inference for Parameter Estimation

Kennedy and O'Hagan [27] represent the relationship between the observed data d_i^{obs}, the true process $\zeta(\cdot)$ and the computer output $\eta(\cdot,\cdot)$ in the equation

$$d_i^{\text{obs}} = \zeta(\mathbf{x}_i) + \varepsilon_i = \eta(\mathbf{x}_i, \mathbf{p}) + \delta(\mathbf{x}_i) + \varepsilon_i, \tag{6}$$

where ε_i is the observation error for the ith observation, $\delta(\cdot)$ is the model inadequacy (or the model structure error) that is independent of the code output $\eta(\cdot,\cdot)$. There are two distinct groups of inputs in the computer model η. The first group is the calibration parameters, the one that we wish to learn about. Those

are for example in the case of the pyrolysis mass decomposition model (1)–(3) $\mathbf{p} = \left\{A_j, E_{\mathrm{a},j}, n_j, F_j\right\}$. The $\mathbf{x}_i$ are called the variable inputs whose value might change during the calibration process. These are for example time or temperature that are supposed to be known. The formulation of the model (6) is not unique and one could find different expressions.

Assuming no model structure error, there are only observation errors

$$d_i^{\mathrm{obs}} = \zeta(\mathbf{x}_i) + \varepsilon_i = \eta(\mathbf{x}_i, \mathbf{p}) + \varepsilon_i. \tag{7}$$

In the deterministic inverse problem, one assumes that there exists a true value of the parameter $\mathbf{p}_0$ obtained from the regression of a given law with a best fit approach. Lautenberger and Fernander-Pello [28] provide a good review of the existing optimization algorithms that have been applied for material pyrolysis property estimation for fire modeling.

In Bayesian inference, what differs significantly from frequentist perspective is that parameters are considered to be a vector of random variables $\mathbf{P}$ with realizations $\mathbf{p}$ and *there is no true parameter in the Bayesian approach*. Thus, $\mathbf{d}^{\mathrm{obs}}$ is also a realization of a random vector $\mathbf{D}^{\mathrm{obs}}$ for which randomness comes from both the error ε_i and the parameters through the computer model $\eta(\cdot, \cdot)$ in Eq. (6). In the following, let's assume that $\mathbf{P} = (P_1, \ldots, P_m)$ is a random vector with values in $\mathbb{R}^m$ and $\mathbf{D}^{\mathrm{obs}} = (D_1^{\mathrm{obs}}, \ldots, D_n^{\mathrm{obs}})$ a random vector with values in $\mathbb{R}^n$

Therefore, from a Bayesian perspective, there is no fundamental distinction between observables and parameters of a statistical model: all are considered random quantities. Bayesian theory is based on (Bayes' theorem)

$$\pi(\mathbf{p}|\mathbf{d}^{\mathrm{obs}}) = \frac{\pi(\mathbf{d}^{\mathrm{obs}}|\mathbf{p})\pi_0(\mathbf{p})}{\int_{\mathbb{R}^m} \pi(\mathbf{d}^{\mathrm{obs}}|\mathbf{p})\pi_0(\mathbf{p})d\mathbf{p}}, \tag{8}$$

where $\pi_0(\mathbf{p})$ is the prior density, $\pi(\mathbf{p}|\mathbf{d}^{\mathrm{obs}})$ is the posterior density, and $\pi(\mathbf{d}^{\mathrm{obs}}|\mathbf{p})$ is the likelihood. The likelihood function evaluates the plausibility of observing the data $\mathbf{d}^{\mathrm{obs}}$ given the parameters $\mathbf{p}$ through the model linking the observable and the parameters. The prior density should compile all the information we know about the parameters before any computation. It can stem from physical consideration (e.g. a mass can not be negative), or from personal knowledge about that parameter. When only a few or no information are available *à priori*, it is possible to specify a noninformative prior. We can express for example that the variable must be positive or not exceed a given limit. One way to do this is by means of an equiprobable density function whose support is the parameter space, and most of the time we will use such uniform noninformative priors. The posterior density is what we know about the parameters after observing the data and is what we want to know. The solution of the inverse problem is the posterior probability distribution function $\pi(\mathbf{p}|\mathbf{d}^{\mathrm{obs}})$ and this principle makes the statistical approach quite different from the classical approach. A good introduction to Bayesian approach towards inverse problems are discussed in Kaipio and Somersalo [29], Smith [30] or Gelman [31].

Thus, the most general solution of a stochastic inverse problem provides a probability distribution function over the model space. It is only when the probability distribution in the model space is very simple (for instance, when it has only one maximum) that analytic techniques can be used to characterize it. For more general probability distributions, one needs to perform an extensive exploration of the model space. This can be performed numerically by means of quadrature rules or random (stochastic) explorations. We see two main advantages of performing random explorations: first, they provide samples directly drawn from the posterior distribution that can be used to estimate statistics of the posterior distribution (by Monte Carlo integration), and second, they can be used for propagation through numerical solvers for uncertainty quantification. Random explorations can solve many complex problems and a type of methods that explore efficiently the posterior distribution are the *Markov chain simulations*.

5. Implementation

Markov chain simulation is a general sampling method that draws samples from a target distribution. It is most of the time called *Markov Chain Monte Carlo* simulation (MCMC). A Markov chain is a sequence of samples that possess the Markov property, that is every new sample θ^{t+1} drawn from a probability distribution depends only on the current iterate θ^t and not on the previous iterates $\theta^{t-1}, \ldots, \theta^0$. Under certain conditions, it can be proven that ultimately, samples will forget their initial state θ^0 and will eventually converge to a unique stationary distribution.

The question is now how to construct such a Markov Chain such that its stationary distribution is exactly the posterior distribution $\pi(\mathbf{p}|\mathbf{d}^{\mathrm{obs}})$ that we are looking for. This can be accomplished quite simply by means of the Metropolis–Hastings algorithm, that was first proposed by Metropolis et al. [32] and

later generalized by Hastings [33]. Implementing Markov Chain Monte Carlo is the subject of many textbooks [34; 35; 30; 31]. Metropolis–Hasting algorithm for a multivariate target distribution $\pi(\mathbf{p}|\mathbf{d}^{\text{obs}})$ may be summarized as follows.

Metropolis-Hastings algorithm

1: **Initialize** $\mathbf{p}_0$:
2: **Iteration** i:

a) Draw a new value $\mathbf{p}^*$ from proposal distribution $J(\cdot|\mathbf{p}_{i-1})$. J specifies $\mathbf{p}^*$ based on previous value $\mathbf{p}_{i-1}$, and $J(\cdot|\mathbf{p}_{i-1})$ should not be interpreted as a conditional density.

b) Construct acceptance probability

$$\alpha(\mathbf{p}^*|\mathbf{p}_{i-1}) = \min\left(1, \frac{\pi(\mathbf{p}^*|\mathbf{d})J(\cdot|\mathbf{p}_{i-1})}{\pi(\mathbf{p}_{i-1}|\mathbf{d})J(\mathbf{p}_{i-1}|\cdot)}\right). \tag{9}$$

c) Sample a Uniform(0,1) random variable U. Set

$$\mathbf{p}^i = \begin{cases} \mathbf{p}^* & \text{if } U \leq \alpha(\mathbf{p}^*|\mathbf{p}_{i-1}), \\ \mathbf{p}^{i-1} & \text{otherwise.} \end{cases} \tag{10}$$

3: **Continue** until convergence and enough samples are collected

The collected samples $\mathbf{p}^i$ characterize fully the posterior distribution. Replacing Eq. 8 in the acceptance ratio (9) we have

$$r = \frac{\pi(\mathbf{d}|\mathbf{p}^*)\pi_0(\mathbf{p}^*)J(\cdot|\mathbf{p}_{i-1})}{\pi(\mathbf{d}|\mathbf{p}_{i-1})\pi_0(\mathbf{p}_{i-1})J(\mathbf{p}_{i-1}|\cdot)}, \tag{11}$$

for which we need to specify the likelihood function $\pi(\mathbf{d}|\cdot)$, the prior density $\pi_0(\cdot)$ and the proposal distribution J.

5.1. Proposal Distribution

When the proposal distribution is taken to be symmetric $J(\mathbf{p}_{i-1}|\mathbf{p}^*) = J(\mathbf{p}^*|\mathbf{p}_{i-1})$, and if we assume a uniform prior density acceptance ratio simplifies to

$$r(\mathbf{p}^*|\mathbf{p}^{k-1}) = \frac{\pi(\mathbf{d}|\mathbf{p}^*)}{\pi(\mathbf{d}|\mathbf{p}^{i-1})}. \tag{12}$$

We only need to sample from J for determining the new value of the estimate $\mathbf{p}^*$. Specifically, when the proposal distribution is of the form $J(\mathbf{p}^*|\mathbf{p}_{i-1}) = J(|\mathbf{p}^* - \mathbf{p}_{i-1}|)$ such as a gaussian distribution, then the algorithm is called *Random Walk Metropolis*. Therefore, we choose the proposal distribution to be a multivariate gaussian distribution centered on $\mathbf{p}_{i-1}$ with covariance matrix Σ

$$J(\mathbf{p}^*|\mathbf{p}_{i-1}) = \frac{1}{\sqrt{(2\pi)^m \det\Sigma}} \cdot \exp\left(-\frac{1}{2}(\mathbf{p}^* - \mathbf{p}_{i-1})^{\mathrm{T}} \Sigma^{-1} (\mathbf{p}^* - \mathbf{p}_{i-1})\right), \tag{13}$$

$$\Sigma = \begin{pmatrix} \sigma_1^2 & \rho_{12}\sigma_1\sigma_2 & \cdots & \rho_{1m}\sigma_1\sigma_m \\ \rho_{21}\sigma_2\sigma_1 & \sigma_2^2 & \rho_{2m}\sigma_2\sigma_m & \\ \vdots & \vdots & \ddots & \vdots \\ \rho_{m1}\sigma_m\sigma_1 & \rho_{m2}\sigma_m\sigma_2 & \cdots & \sigma_m^2 \end{pmatrix}. \tag{14}$$

Covariance matrix Σ will generally be assumed to be a diagonal matrix where the diagonal elements are tuned by trial-and-error to reach a good acceptance rate for fast convergence.

5.2. Likelihood Function

For the likelihood function, we assume the observation errors to be independent and identically distributed (iid) following a Gaussian density of known mean and variance [30]. In Wong experiments, a different standard deviation is estimated at every temperature at which sample mass measured. We use the following likelihood distribution

$$\pi(\mathbf{d}^{\text{obs}}|\mathbf{p}) = \frac{1}{(\Pi_i \sigma_i)(2\pi)^{n/2}} e^{-SS_{\mathbf{p}}}, \tag{15}$$

$$SS_{\mathbf{p}} = \sum_{i=1}^{n} \frac{\left[d_i^{\text{obs}} - \eta(\mathbf{x}_i, \mathbf{p})\right]^2}{2\sigma_i^2}. \tag{16}$$

For now, σ_i is left as a fixed and known parameter as it is already estimated in Wong experiments. Considering σ as a hyperparameter as in Najm et al. [36] with the likelihood (15) would considerably increase the dimensionality of the problem. However, estimation of σ_i is questionable as it comes from 3 experimental runs.

5.3. Prior Distribution

Finally, if we assume a uniform prior density that is strictly positive, candidate $\mathbf{p}^*$ will be rejected if a negative value is sampled, thus $r(\mathbf{p}^*|\mathbf{p}^{k-1}) = 0$ if $\mathbf{p}^* < 0$. Ensuring positiveness is based on physical constraints. Upper bounds are taken to be very large.

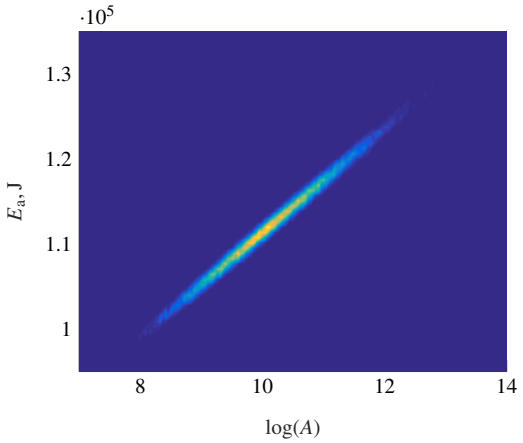

Figure 1: Join posterior pdf for the activation energy E_a and pre-exponential factor A.

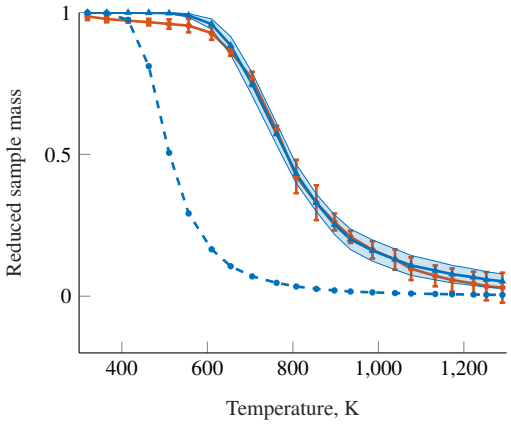

Figure 2: Sample mass as a function of temperature. MCMC samples are propagated through the model with one reactant in the pyrolysis process. Experimental data [19] (—●—), initial parameter guess (- -●- -), and median parameter (—▲—).

6. Results and Discussions

Kinetic parameters were calibrated using the random walk metropolis algorithm for the material tested in the experiments of Wong et al. [19] using a constant stepwise temperature heating. Solution of the system of pde from Eq. (1)–(3) is obtained using the analytical solution (4). We start by visualizing the joint posterior distribution for a simple model with one equation and with 2 uncertain parameter A and E_a to emphasize the correlation between them. We then infer on the parameters of models of increasing complexity and we present the propagation of the samples through the numerical model for checking the plausibility of the results.

6.1. Joint Posterior Distribution

Posterior distributions are useful for characterizing the parameters uncertainty, identifying correlation between them and evaluate point estimate like deterministic optimization solvers could find. However, as the number of parameters increase, it is impossible to visualize joint pdf.

The pdf in Fig. 1 was obtained using a 2 parameter inference $\mathbf{p} = \{A, E_a\}$ (with $n = 2$ fixed) after a 10^6 interation long MCMC chain. In Fig. 1 we can see a strong correlation between Arrhenius parameters $\log(A)$ and E_a. The result is known as the kinetic compensation effect (KCE) that has been observed in numerous kinetics studies [37; 38; 23]. This results in a wide variation of the pre-exponential factor A and activation energy E_a that can give satisfactory fits to the data. For this reason, convergence is achieved much faster using $\mathbf{p} = \{\log A, E_a\}$ rather than $\mathbf{p} = \{A, E\}$. In this case, the joint posterior for $\pi(\log A, E_a|\mathbf{d}^{\text{obs}})$ has the form of Fig. 1 and a proper choice for the covariance of the proposal distribution is a diagonal matrix. We then only have to tune the diagonal elements.

For monitoring the convergence of the MCMC chain, it is convenient to check multiple sequences that start at different positions in the parameter space.

6.2. Posterior predictive checks

We now specify the posterior estimated samples to be used as inputs of the model. The objective is to observe how well the new data fit to the observed experimental values we used for the inference process. The quantity of interest is the reduced sample mass

$$m' = \frac{m - m_c}{m_0 - m_c}, \tag{17}$$

where the mass of char m_c is assumed to be fixed and known from the experimental results.

6.2.1. One-equation model

Assuming that the resin is made up of one reactant, the decomposition of the sample is governed by a single ordinary differential equation and the total number of parameters that we need to infer is $n_p = 3$, with $\mathbf{p} = \{A, E, n\}$ ($F = 1$) having values in $\mathbb{R}^3$. Prior distribution is the uniform pdf of compact support $S = [10; 10^{10}] \times [1000; 10^{10}] \times [1; 10]$.

Results are shown in Fig. 2. The initial solution obtained from initial parameter guess used to start the

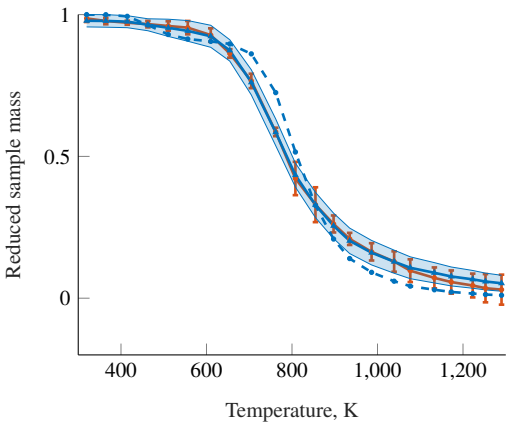

Figure 3: Sample mass as a function of temperature. MCMC samples are propagated through the model with two reactants in the pyrolysis process. Experimental data [19] (—●—), initial parameter guess (- -●- -), and median parameter (—▲—).

MCMC chain is represented by a dotted line. Different initial guesses are used to prove convergence of the solution to the same target pdf. The shaded area represents all the possible outcomes from the sampling distribution. The median parameter is the mean over all outcomes at a given temperature. We can see that the one-equation model reproduces well the steepest mass decrease between 600 K and 1200 K but fails to reproduces the mass decrease in the range [350 600] K. This suggests that more than one pyrolysis decomposition process should be assumed.

6.2.2. Two-equations model

If we add one reactant to the pyrolysis decomposition process, we have $n_p = 7$ unknown parameters $\mathbf{p} = \{A_1, E_1, n_1, F_1, A_2, E_2, n_2, \}$ ($F_2 = 1 - F_1$) having values in $\mathbb{R}^7$.

Result of the propagation of a 5×10^6 iteration long chain is shown in Fig. 3. We can see that now the mass decrease in the temperature range [350 600] K is better approximated. There is still a slight difference above 1050 K. We could use more equations in the model, however convergence is slower as we increase the number of parameters (more samples are rejected by the algorithm). To obtain chains that are converged, we need to perform much more iterations.

6.3. Discussion

The main drawback from the classical random walk metropolis algorithm presented before is the slow convergence of the chain as the number of parameters increases. Adaptative MCMC (AMCMC) could be a good alternative to classical MCMC as they use the information of previous iterates to update the covariance matrix of the proposal distribution. It can therefore approximate much better the posterior distribution leading to a faster convergence. AMCMC are easy to implement and should be a first path to investigate. The Hamiltonian Monte Carlo (HMC) method seems to be a good improvement as the algorithm can converge m times faster than classical MCMC (m being the number of parameters). However HMC requires the computation of derivatives of the log-likelihood function in every direction that can be challenging and computationally expensive if numerical methods are employed. Already implemented open source toolboxes featuring some of the most up-to-date algorithms exist and could be considered as well (STAN).

One of the main difficulties in these simulations is to make a balance between the complexity of the model and the accuracy of the prediction. On the one hand, complex models tend to make better predictions, but they are highly computationnaly expensive and not general and therefore can not be used for large scale flow-material simulations. On the other hand, simple models work faster and might be applicable to a larger variety of problems but these predictions currently lack of uncertainty quantification.

7. Conclusions and further work

In this paper, we were able to simulate pyrolysis experiments using a point-mass model where kinetic parameters were inferred from a Bayesian perspective. The likelihood function is made up of a set of independent Gaussian functions of iid samples of known variances from experimental results. The prior distribution is a noninformative uniform distribution of compact support to ensure positiveness of the data. The posterior distribution is sampled using MCMC method and we chose to implement a random walk metropolis algorithm for which we assume a proposal function to be a multivariate Gaussian function where the variance is a parameter to be tuned. All the three choices for the likelihood, prior and proposal distributions are not based on rigorous arguments and should be investigated in the future.

Propagating the posterior samples, we showed that with two reactant model we were able to simulate quite accurately the thermal decomposition of the material in the range [350 1300] K with appropriate error bars. Three or more reactant model should be investigated but increasing the number of reactants increases

the number of parameters to be inferred and deteriorates the convergence of the MCMC. Other implementations using AMCMC and HMC are proposed as a next step for improving algorithm efficiency.

Future work could investigate how we could evaluate the plausibility of a given model on an other, e.g. which model is the most plausible between one, two or three equations. This could be achieved for example by the Occam's razor principle [39].

We need to investigate how to characterize posterior distribution in order to be useful for flow-material solver as presented in the introduction. A convenient way is to define sample mean and variance but this is however inaccurate when the pdf is a complex function. In this work, we observed that parameters where highly correlated, due to the kinetic compensation effect, and posterior distribution were multimodals.

Finally, it must be questioned whether or not the parameter inferred from the point-mass model are applicable to multidimensional case as encountered during reentry problem. In particular it should be investigated if the evolution of the porosity must be taken into account in the inference process. To answer this question, we need to use more complex models than the simple point-mass material developed here. Then, the first step would be to use the parameters inferred from the point-mass material model in high-fidelity models and compare it with the initial experiments.

Acknowledgments

This work is supported by the Fund for Research Training in Industry and Agriculture (FRIA) provided by the Belgian Fund for Scientific Research (F.R.S.-FNRS). The first author would like to thank P. Schrooyen and K. Hillewaert (Cenaero) for valuable discussions and for their support. The first author would also like to thank A. Turchi (von Karman Institute) for valuable suggestions and discussions. The first author would also like to thank prof. H.-W. Wong (University of Massachussetts Lowell) for providing the experimental results, Nagi Mansour and Francesco Panerai (NASA Ames Research Center).

References

[1] M. Stackpoole, S. Sepka, I. Cozmuta, D. Kontinos, Post-Flight Evaluation of Stardus Sample Return Capsule Forebody Heatshield Material, Journal of Thermophysics and Heat Transfer 24 (4) (2010) 694–707.

[2] W. H. Willcockson, Stardust sample return capsule design experience, Journal of Spacecraft and Rockets 36 (1999) 470–474. doi:10.2514/2.3468.

[3] M. J. Wright, A. S. Beck, K. T. Edquist, D. Driver, S. A. Sepka, E. Slimko, W. H. Willcockson, sizing and margins assessment of mars science laboratory aeroshell thermal protection system, Journal of Spacecraft and Rockets 51 (4) (2014) 1125–1138. doi:10.2514/1.A32579.

[4] J. D. Anderson, Hypersonic and High Temperature Gas Dynamics, 2nd Edition, AIAA Education Series, 2006.

[5] G. Duffa, Ablative thermal protection systems modeling, American Institute of Aeronautics and Astronautics, Inc., Reston, Virginia, 2013.

[6] R. M. Kendall, E. P. Barlett, R. A. Rindal, C. B. Moyer, An Analysis of the Coupled Chemically Reacting Boundary Layer and Charring Ablator: Part I., CR-1060, NASA (1968).

[7] Y.-K. Chen, F. S. Milos, Ablation and thermal response program for spacecraft heatshield analysis, Journal of Spacecraft and Rockets 36 (3) (1999) 475–483.

[8] G. F. Sykes, Decomposition Characteristics of a Char-Forming Phenolic Polymer Used for Ablative Composites, Tech. rep., NASA TN D-3810 (1967).

[9] H. E. Goldstein, Pyrolysis Kinetics of Nylon 6-6, Phenolic Resin, and Their Composites, Journal of Macromolecular Science: Part A - Chemistry 3 (4) (1969) 649–673.

[10] D. Bianchi, A. Turchi, N. Francesco, O. Marcello, Coupled CFD analysis of thermochemical erosion and unsteady heat conduction in solid rocket nozzles, in: 48th AIAA/ASME/ASEE Joint Propulsion Conference & Exhibit, Atlanta, GA, US, 2012.

[11] Y.-K. Chen, T. Gökçen, Implicit coupling approach for simulation of charring carbon ablators, Journal of Spacecraft and Rockets 51 (3) (2014) 779–788.

[12] A. Martin, I. Boyd, Strongly coupled computation of material response and nonequilibrium flow for hypersonic ablation, Journal of Spacecraft and Rockets 52 (1) (2015) 89–104.

[13] A. Martin, Volume averaged modeling of the oxidation of porous carbon fiber material, in: 44th AIAA Thermophysics Conference, San Diego, CA, 2013.

[14] P. Schrooyen, K. Hillewaert, T. E. Magin, P. Chatelain, Fully Implicit Discontinuous Galerkin Solver to Study Surface and Volume Ablation Competition in Atmospheric Entry Flows, International Journal of Heat and Mass Transfer 103 (2016) 108–124.

[15] P. Schrooyen, J. Coheur, A. Turchi, T. Magin, Numerical simulation of a non-charring ablator in high enthalpy flows by means of a unified flow-material solver, in: 47th AIAA Thermophysics Conference, Denver, CO, US, 2017.

[16] J. Coheur, A. Turchi, P. Schrooyen, T. Magin, Development of a unifed model for flow-material interaction applied to porous charring ablators, in: 47th AIAA Thermophysics Conference, Denver, CO, US, 2017.

[17] K. A. Trick, T. E. Saliba, Mechanisms of the pyrolysis of phenolic resin in a carbon/phenolic composite, Carbon 33 (11) (1995) 1509–1515.

[18] K. A. Trick, T. E. Saliba, S. S. Sandhu, A kinetic model of the pyrolysis of phenolic resin in a carbon/phenolic composite, Carbon 35 (3) (1997) 393–401.

[19] H.-W. Wong, J. Peck, R. Bonomi, J. Assif, F. Panerai, G. Reinish, J. Lachaud, N. Mansour, Quantitative determination of species production from phenol-formaldehyde resin pyrolysis, Polymer Degradation and Stability 112 (2015) 122–131.

[20] B. K. Bessire, S. A. Lahankar, T. K. Minton, Pyrolysis of Phenolic Impregnated Carbon Ablator (PICA), ACS Appl. Mater. Interfaces 7 (3) (2015) 1383–1395.

[21] B. K. Bessire, T. K. Minton, Decomposition of phenolic impregnated carbon ablator (PICA) as a function of tempera-

ture and heating rate, ACS Appl. Mater. Interfaces 9 (2017) 21422–21437.
[22] B. Helber, A. Turchi, J. B. Scoggins, A. Hubin, T. E. Magin, Experimental investigation of ablation and pyrolysis processes of carbon-phenolic ablators in atmospheric entry plasmas, International Journal of Heat and Mass Transfer 100 (2016) 810–824.
[23] M. Bruns, Inferring and propagatin kinetic parameter uncertainty for condensed phase burning models, Fire Technology 52 (2016) 93–120.
[24] S. Vyazivkin, C. A. Wight, Kinetics in solids, Annual review of Physical Chemistry 48 (1997) 125–149.
[25] M. E. Brown, M. Maciejewski, S. Vyazovkin, R. Nomen, J. Sempere et al., Computational aspects of kinetic analysis. Part A: The ICTAC kinetics project-data, methods and results, Thermochimica Acto 355 (2000) 125–143.
[26] J. Lachaud, N. N. Mansour, Porous-material analysis toolbox based on OpenFOAM and applications, Journal of Thermophysics and Heat Transfer 28 (2) (2014) 191–202, ahead of print.
[27] M. C. Kennedy, A. O'Hagan, Bayesian calibration of computer models, Journal of the Royal Statistical Society 63 (3) (2001) 425–464.
[28] C. Lautenberger, C. Fernander-Pello, Optimization algorithms for material pyrolysis property estimation, Fire Safety Science 10 (2011) 751–764. doi:10.3801/IAFSS.FSS.10-751.
[29] J. Kaipio, E. Somersalo, Statistical and Computational Inverse Problems, Springer, New York, 2005.
[30] R. C. Smith, Uncertainty Quantification: Theory, Implementation, and Applications, Society for Industrial and Applied Mathematics, Philadelphia, 2014.
[31] A. Gelman, J. B. Carlin, H. S. Stern, D. B. Dunson, A. Vehtari, D. B. Rubin, Bayesian Data Analysis, 3rd Edition, Chapman & Hall/CRC, London, 2014.
[32] N. Metropolis, A. W. Rosenbluth, M. N. Rosenbluth, A. H. Teller, T. E., Equation of state calculations by fast computing machines, Journal of Chemical Physics 21 (1953) 1087–1092.
[33] W. K. Hastings, Monte Carlo sampling methods using Markov chains and their applications, Biometrika 5 (1) (1970) 97–109.
[34] W. R. Gilks, S. Richardson, D. J. Spiegelhalter, Markov Chain Monte Carlo in Practice, Chapman & Hall/CRC, London, 1996.
[35] S. Brooks, A. Gelman, G. L. Jones, X.-L. Meng, Handbook of Markov Chain Monte Carlo, Chapman & Hall/CRC, London, 2011.
[36] H. Najm, R. Berry, C. Safta, K. Sargsyan, B. Debusschere, Data-free inference of uncertain parameters in chemical models, International Journal for Uncertainty Quantification 4 (2014) 111–132.
[37] N. Koga, A review of the mutual dependence of Arrhenius parameters evaluated by the thermoanalytical study of solid-state reactions: the kinetic compensation effect, Thermochimica Acta 244 (1994) 1–20.
[38] A. K. Galwey, M. E. Brown, Thermal Decomposition of Ionic Solids, Elsevier, Amsterdam, 1999.
[39] D. MacKay, Information Theory, Inference, and Learning Algorithms, Cambridge University Press, 2003.

Rebuilding freestream conditions in atmospheric entry flows from wall pressure and heat flux data

Andrea F. Cortesi

CARDAMOM Team, Inria Bordeaux Sud-Ouest, France, andrea.cortesi@inria.fr

Supervisor: Thierry E. Magin

Professor, Aeronautics and Aerospace Department, von Karman Institute for Fluid Dynamics, Belgium, magin@vki.ac.be

University Supervisor: Pietro M. Congedo

CR-HDR, CARDAMOM Team, Inria Bordeaux Sud-Ouest, France, pietro.congedo@inria.fr

Abstract

The objective of this work is to assess the interest in exploiting heat flux measurements at the heat shield of an entry vehicle, together with pressure measurements, to rebuild freestream parameters and other uncertain model parameters. In particular, we will focus on the reconstruction of freestream density, flow angles and catalytic recombination coefficient. The reconstruction problem is solved in a Bayesian framework, to account for measurement errors and parameter uncertainties.

Keywords: Freestream reconstruction, hypersonic flows, atmospheric entry, uncertainty quantification, Bayesian inference, surrogate models

1. Introduction

Hypersonic aerodynamics plays a big role in the atmospheric entry of space vehicles and an accurate aerothermal simulation of the entry flow is crucial in the design of the vehicle and the entry trajectory. In fact, aerodynamic flows in the hypersonic regime are characterized by the presence of a strong bow shock in front of the vehicle forebody, which converts a big part of the kinetic energy of the flow into thermal energy. This causes a huge increase in the temperature of the shock layer, the part of the fluid flow between the shock and the body. For this reason, the surface of the vehicle is exposed to a strong heating, requiring the presence of a Thermal Protection System (TPS, also called heat shield) which needs to be designed to protect the structure and internal components from excessive temperatures. Also the design and reconstruction of Entry, Descent and Landing (EDL) trajectories is significantly affected by hypersonic aerodynamics. In fact, the aerodynamic drag produced during hypersonic phase of the entry trajectory provides a major contribution to the deceleration of the capsule. Therefore, an accurate prediction of the aerodynamic and thermal loads is fundamental for the success of an entry mission.

In order to produce accurate and predictive simulations, it is essential to provide accurate models but also representative values for the boundary conditions and model parameters, such as the composition and the thermodynamic state of the atmosphere at the freestream and flight speed. Unfortunately, the knowledge about atmospheric properties and thermodynamic state is generally characterized by a high degree of uncertainty, especially away from Earth. Furthermore, the variability of atmospheric conditions, in particular density, has important implications for EDL mission design and performance [1], since entry velocities are reduced mainly by aerodynamic drag. In fact, atmospheric fluctuations can cause random deviations from standard-atmospheric models, which can be very substantial also on reduced difference of altitudes of a few kilometers [2] (as shown in Figure 1). To improve the knowledge about freestream conditions, it is common practice to rebuild atmospheric parameters from flight data in post-flight analysis. This

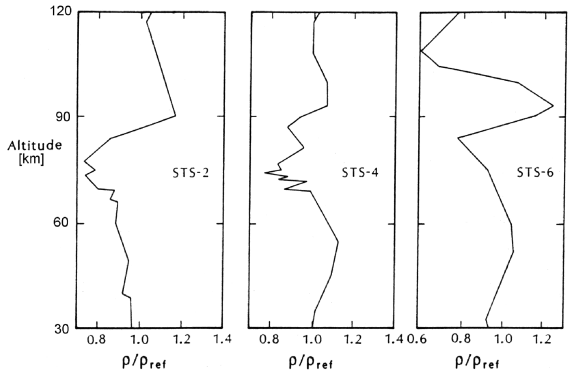

Figure 1: Deviations between atmospheric densities derived by Shuttle measurements and the 1962 U.S. standard atmosphere (from [1]).

allows to improve atmospheric models for the design and the analysis of EDL missions and to provide significant input boundary conditions for predictive CFD simulations. The reconstruction of atmospheric conditions and the state of the vehicle is also important for the control and guidance of operational manned vehicles [3].

Classical reconstruction techniques of the entry trajectory and atmospheric conditions are deterministic approaches based on linear accelerations and angular rotations measured by accelerometers and gyros composing the Inertial Measurement Unit (IMU), which is part of the standard instrumentation on entry vehicles. The post-flight analysis of the entry phase of many different space missions relied mainly on inertial data to rebuild the entry trajectory and characterize the atmospheric freestream conditions. Examples in literature can be found in [4; 5; 6; 7; 8; 9; 10], to cite some. A more modern formulation and review of IMU-based trajectory and atmosphere reconstruction approaches can be found in [11]. However, while inertial flight data are ideally suited for the entry trajectory reconstruction [12], they may not be sufficient to accurately characterize the atmospheric environment [13], since they do not include any direct information about the air flow around the capsule.

For this reason, on some other entry vehicles a Flush Air Data System (FADS) is also available, consisting of pressure ports (and other sensors in some cases) integrated into the heat shield [14]. Hence, FADS measurements normally consist of pressure data at several points of the vehicle forebody. This system is able to provide measurements that are complementary to those by IMU, since they contain direct information about the flow and the atmospheric environment to which the vehicle surface is exposed. FADS sensors were mounted on different entry vehicles, like Viking [15] and Mars Science Laboratory (MSL) [16] in case of Mars missions, or on the Space Shuttle [17] for Earth entry missions. Freestream reconstruction techniques have been developed in literature to exploit also surface pressure data, as a direct measurement of the flow given by the FADS. Often, these techniques do not take into account many high-temperature effects (*e.g.* chemical non-equilibrium, surface catalysis, ablation and radiative effects), and they usually rely on the calorically perfect gas approximation [18; 3] or Newtonian flow assumption [19; 20].

On some entry vehicles, flush-mounted sensors are able to provide also heat flux measurements. The Re-entry Aerodynamic Flow Experiment (RAFLEX) [21] instrumentation package, for example, is composed by several flush-mounted probes that are able to measure pressure and heat flux at the same location. This system equips different vehicles, such as MIRKA (Mikro-Rückkehrkapsel) [18] and EXPERT (European eXPErimental Re-entry Test-bed) [22]. However, at least up to the author's knowledge, heat flux measurements normally are not exploited in freestream reconstruction, probably due to the difficulty of realizing both accurate measurements [23] and significant simulations of the heating. Some efforts in this direction can be found in literature with the preliminary analysis of [24]. Another use of heat flux measurements can be found in [18], where it has been used, together with dynamic pressure measurements, to determine the freestream velocity for MIRKA vehicle through an analytic relation.

In order to account for measurement errors in the rebuilt values, which intrinsically affect flight data, many trajectory and freestream reconstruction techniques have been developed in literature. For example [25] used Monte Carlo methods to propagate uncertainties in the reconstruction inverse problem, in [26] instead, uncertainties have been propagated by linear covariance mapping. [27] proposed to use Kalman filtering to account for uncertainties in the freestream and trajectory rebuilding problem. A more advanced method for freestream characterization was discussed in [28; 29; 30], where different statistical estimation methods, namely Extended Kalman filter, Unscented Kalman filter, and adaptive filter, were used to statistically estimate trajectories and freestream conditions from flight data, containing pressure measurements together with gyroscope, accelerometer and radar al-

timeter data, as well as to quantify uncertainties in these estimates. This method was applied in the context of post-flight analysis for Mars Science Laboratory (MSL) mission.

This work is devoted to the study of an inverse uncertainty propagation problem within the framework of atmospheric entry. The goal is to understand the interest in using heat flux measurements at the heat shield of the vehicle, together with pressure measurements, for the rebuilding of freestream parameters and other uncertain model parameters. The statistical Bayesian approach [31; 32] is adopted to solve the inverse problem that leads to the results of the reconstruction. This allows to account for measurement errors and other uncertainties on model parameters in the rebuilt values, and to consider complex forward models able to describe the phenomena occurring during the entry flight.

The work is structured as follows: in Section 2, we describe how simulations of hypersonic entry flows are performed. Then, in Section 2.1 we give a description about the hypothesis and the model used in order to consider the effect of flow angles in the case where only axisymmetric computational models are available. Section 3 describes the Bayesian framework and the tools used to solve the inverse reconstruction problem. Finally, in Section 4, results are shown for several cases of parameter calibrations: using only pressure measurements, to reproduce classical reconstruction techniques in the Bayesian framework (Sec. 4.1), and exploiting both pressure and heat flux (Sec. 4.2).

2. Numerical simulation of the flow

The application proposed in this work is about the atmospheric entry flow around the forebody of the EXPERT vehicle from the European Space Agency [33; 22]. We focus on the part of the entry trajectory where the hypothesis of continuum regime is valid. Two specific points of the entry trajectory are considered for the freestream calibration. The first, at a higher altitude, is known to exhibit chemical non-equilibrium effects, while in the second, close to the peak heating point, the chemistry tends to be at equilibrium. Nominal freestream conditions for both trajectory points are reported in Table 1.

Axisymmetric reacting Navier-Stokes governing equations are used to describe the hypersonic entry flow, together with the physico-chemical models described in the work of Barbante [34]. The equations

Altitude, Km	T_∞, K	p_∞, Pa	ρ_∞, kg/m^3	u_∞ m/s	M_∞
60	245.5	20.3	2.8806e-04	4868.6	15.5
30	220	1200	0.0190	3657.3	12.3

Table 1: Freestream conditions for two points of the trajectory of the EXPERT vehicle.

are combined with the chemical mechanism introduced by Park et al. [35] applied to a mixture of five species air (N, O, NO, N_2 and O_2). Furthermore, we also account for chemical reactions at the wall promoted by the catalytic property of the reusable TPS material. A cell-centered shock-capturing finite volumes code, named COSMIC [34], is used to simulate the flow, using AUFS numerical scheme [36], and an automated mesh adaptation technique is adopted to align the shock with the grid, in order to improve the accuracy of the heat flux simulation. The deterministic simulation problem consists in computing the quantities of interest, which correspond to the pressure and heat flux measured by five sensors integrated in the nose heat shield. In practice, the solution, computed with the finite volume code, is available at the nodes of the computational grid, and it is interpolate at the desired locations. Figure 2 shows the $n \times m$ nominal computational grid, with labels for the bounds, and the solution temperature field computed for the 60km trajectory point. Supersonic inflow and outflow

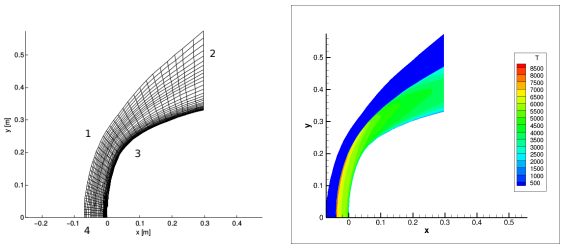

(a) (b)

Figure 2: Nominal computational grid (a) and nominal temperature field for the 60km trajectory point (b) of the EXPERT vehicle.

boundary conditions are again imposed respectively on boundaries 1 and 2. On boundary 3, a partially catalytic wall at radiative equilibrium and with no-slip condition is imposed. The nominal value of recombination probability is taken as $\gamma = 0.0015$. Finally, on boundary 4 the axisymmetry condition is imposed.

2.1. *Modelization of aerodynamic angles effect on measured quantities*

Aerodynamic angles reconstruction is one of the classical applications for FADS problems. Also here, one of the goals is to exploit the different pressure and heat flux measurements to infer the value of the angles of attack α and sideslip β (referred to as flow or aerodynamic angles). However, since simulations are performed with the axisymmetric code COSMIC, it is not possible to directly simulate the change in pressure and heat flux at each sensor location due to changes of aerodynamic angles. Instead, it could be rigorously done by the use of a 3D computational code. However, doing some hypothesis on the geometry of the EXPERT forebody, it is possible to exploit the output of the axisymmetric 2D simulation to evaluate the pressure and the heat flux at some measurement locations as function of the aerodynamic angles.

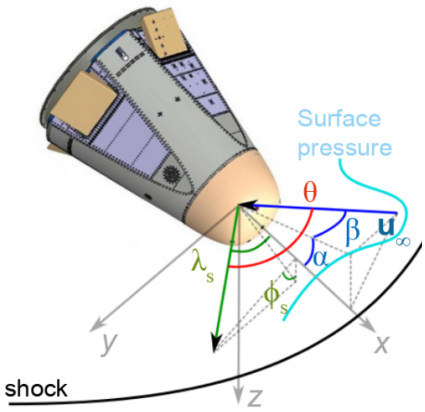

Figure 3: Graphical representation of the flow angles (α and β), total surface angle θ and of sensors clock ϕ_s and cone angles λ_s.

The supporting geometrical hypothesis consists in considering the nose of EXPERT vehicle as a half sphere. While this is not its actual geometry, it consists in a relatively good approximation, from a geometrical point of view, as can be noticed from figure 3. Since for a sphere the air flow does not change when changing the aerodynamic angles, a single axisymmetrical simulation performed at α and β equal to zero can just be rotated and used to describe the behavior at different angles values. By geometrically treating the EXPERT forebody as a hemisphere, we suppose that also for it the flow field is invariant with respect to some small changes in the aerodynamic angles, and the surface pressure and heat flux from the axisymmetric simulation can just be rotated to describe the surface values with non-zero aerodynamic angles. This hypothesis allows to run only an axisymmetric simulations for the actual geometry of the nose, and then properly rotate the pressure and heat flux distributions according to the aerodynamic angles we want to account for.

When considering the forebody geometry as a sphere, it is practical to describe the position of a point on the surface, and particular sensors locations, by means of its cone λ_s and clock ϕ_s angles (see Figure 3). With this convention, the locations of the $n_s = 5$ sensors in the EXPERT configuration are given by the values in Table 2. Then, the surface angle θ, namely the total angle from the sensor location to the velocity direction, can be computed from the flow angles and the sensor angles by means of the following trigonometric relation:

$$\begin{aligned}\cos(\theta) = &\cos(\alpha)\cos(\beta)\cos(\lambda_s)+\\ &+\sin(\beta)\sin(\phi_s)\sin(\lambda_s)+\\ &+\sin(\alpha)\cos(\beta)\cos(\phi_s)\sin(\lambda_s).\end{aligned} \quad (1)$$

This surface angle is used to rotate the axisymmetric solution at the wall to get the pressure and heat flux values at each sensor location. In practice, the axisymmetric solution, that is given at the Cartesian coordinates of the surface points, is rewritten with respect to the cone angle of this point, that coincides with the angle θ (see Figure 4). In fact, if $\theta = 0$ it means that the velocity and the sensor location vector are aligned, and therefore the sensor reads the stagnation values. When instead the sensor and the velocity are not aligned, the measurement will read a value of pressure or heat flux at an angle θ from the stagnation.

	Sensors				
	1 (stag.)	2 (top)	3 (left)	4 (bottom)	5 (right)
λ_s [deg]	0	45	45	45	45
ϕ_s [deg]	0	180	90	0	270

Table 2: Locations of the FADS sensors for the EXPERT vehicle expressed by means of the angles λ_s and ϕ_s.

3. Bayesian reconstruction of the freestream

The statistical Bayesian approach [31; 37] is adopted to solve the inverse problem that leads to the

results of the freestream reconstruction. Bayes rule, here recalled

$$\sigma^{\text{pos}}(\mathbf{x}|\boldsymbol{d}) = \frac{\ell(\boldsymbol{d}|\mathbf{x})\,\sigma(\mathbf{x})}{\int \ell(\boldsymbol{d}|\mathbf{x})\,\sigma(\mathbf{x})\,\mathrm{d}\mathbf{x}}, \tag{2}$$

is able to provide the posterior joint probability density function (PDF) $\sigma^{\text{pos}}(\mathbf{x}|\boldsymbol{d})$ of the inferred parameters ($\mathbf{x} = \{\rho_\infty, \gamma, \alpha, \beta\}$ in the case here considered), given the measurements of pressure and heat flux at the sensors locations $\boldsymbol{d} = \{p_i; q_i\}_{i=1}^{n_s}$. The prior probability density, denoted with $\sigma(\mathbf{x})$, represents the degree of belief about possible values of $\mathbf{x}$ before observing the data. The conditional probability $\ell(\boldsymbol{d}|\mathbf{x})$ is called the *likelihood* function, because it expresses the likelihood of a measurement outcome given a realization $\mathbf{x}$ of the inputs. The construction of the likelihood models the information about the measurement noise and other model uncertainties. Often, in the classical literature [37], measurement errors are considered as additive noise $\boldsymbol{\eta}$, mutually independent of $\mathbf{x}$, added to the model prediction $f(\mathbf{x})$:

$$\mathbf{d} = f(\mathbf{x}) + \boldsymbol{\eta}. \tag{3}$$

The probability density $p_{\boldsymbol{\eta}}(\boldsymbol{\eta})$ of the noise is assumed to be known. In this case the likelihood distribution becomes:

$$\ell(\boldsymbol{d}|\mathbf{x}) = \prod_{j=1}^{n_m} \ell_{d_j}(d_j|\mathbf{x}) = \prod_{j=1}^{n_m} p_{\eta_j}(d_j - f_j(\mathbf{x}))\,, \tag{4}$$

where $p_{\eta_j}(\eta_j)$ is the probability density representing the noise associated to the j-th measured quantity, and n_m is the number of independent measurements. In the present work, we will assume measurement errors as Gaussian noise with zero mean and a standard deviation that quantifies the experimental error. With this additive noise model, the likelihood models the discrepancy between the model output $\boldsymbol{f}(\mathbf{x})$ and the measured data, which is equal to the measurement error if the model is considered to be exact.

3.1. Markov Chain Monte Carlo sampling and surrogate models

Often, an analytical expression for the posterior PDF is not available, but it must be sampled in order to know its properties. The most common class of sampling methods for characterizing the posterior distribution, defined in eq. (2), are Markov Chain Monte Carlo (MCMC) methods [38; 39]. They are a broad class of methods used to draw samples from a probability density by constructing a Markov chain whose stationary distribution converges to the desired posterior. Several implementations of MCMC exist in literature, that differ in the way they construct a Markov chain such that the stationary distribution is exactly the distribution of interest. A well-known implementation of MCMC is the Metropolis-Hastings algorithm [40]. In following parts of this work, the Metropolis-Hastings algorithm with single-site updating and Gaussian proposal density [32] will be used to draw samples from the posterior distributions.

MCMC methods, as all sampling methods, require several thousand of model evaluations to achieve convergence. Furthermore, unlike in standard MC methods, the evaluation in different samples from the same chain can not be run in parallel. This makes impossible the direct application of MCMC methods to expensive computational modes, like in CFD applications. One possible way to reduce the computational cost in such cases is to replace the expensive model evaluation by the use of a surrogate model [41; 42]. In this case, in the likelihood expression (4) the exact model evaluation $f(\mathbf{x})$ is replaced by the prediction given by the surrogate model $\hat{f}(\mathbf{x})$. In this work, the PDD-UK technique introduced in [43; 44] is used to train surrogate models for the quantities of interest, which coincide with pressure and heat flux at sensors locations. These surrogates are needed to accelerate the MCMC algorithms.

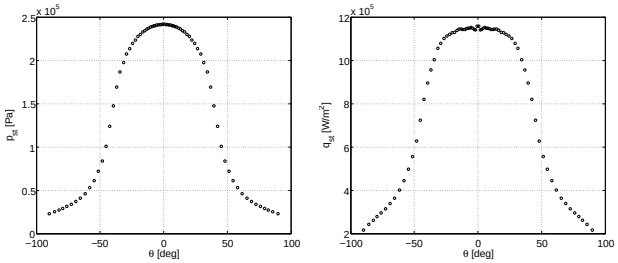

(a) Pressure (b) Heat flux

Figure 4: Output of the COSMIC simulations performed at nominal conditions for the 30km trajectory point. Axisymmetric simulations give results between 0° and 90°, and results for negative angles are obtained by symmetry.

Firstly, Latin Hypercube [45] training points are drawn in the space of the uniform prior distributions of ρ_∞ and γ. Sets containing $N_s = 72$ training points are created for each individual uncertain variable and for the bi-dimensional case that arises when consider-

ing both of them. Simulations of the COSMIC code are run for every training point, exploiting an automated mesh adaptation approach. The output of each simulation is the value of pressure and heat flux at the wall, given at each cell center of the computational grid, a shown in Figure 4 for the output obtained using nominal input values at the 30km trajectory point.

When creating the surrogate model, a decision has to be made on whether building it with respect to the flow angles (α, β) or the surface angle θ. We decide to create the surrogate in the angle θ, because in this way it is possible to reduce the input dimensionality.

3.1.1. Adopted methodology

Once the metamodels for the quantities of interest are available, it is possible to tackle different inverse problems relative to the freestream reconstruction for the entry trajectory of the EXPERT vehicle. In the cases shown in the results, freestream velocity and temperature are assumed to be known exactly and therefore fixed to their nominal value, given in Table 1. For the velocity, this can be justified by the fact that it can be rebuilt from IMU measurement with a very high accuracy. Related measurement errors are in the order of few meters per second and they do not influence the results of the reconstruction. Artificial measurements are produced by evaluating the surrogate models at the nominal values of ρ_∞ and γ. Regarding θ, the value is computed at each location of the sensors at the reference flow angles. No additional perturbation is added to the obtained value, because the main purpose of this work is to assess the interest of the reconstructions using heat flux measurement and not to reproduce a realistic case. Measurement errors are still accounted in the posterior distributions thanks to the formulation of the problem in the Bayesian framework.

For each case, a preliminary chain is run to adapt the values of the proposal distribution widths ω_i of the MCMC algorithm. They are chosen so that the resulting acceptance rate of the chain, namely the ratio between accepted and total steps, is close to an empirical optimal value, that is equal to 0.234 [46, Chapter 4]. After the adaptation process, MCMC chains are run for 250000 iterations. Then, for each final chain, the first 50000 iterations are discarded as burn-in time. The already small autocorrelation between samples of the obtained chain is already reduced by keeping in the final sampling point only one every 100 samples.

3.1.2. Characterization of the uncertainties

For the EXPERT entry problem, uncertainties are taken into account on the freestream values that we will try to rebuild by means of Bayesian inference and also on some parameters of the air chemistry mechanism. Concerning the freestream conditions, a uniformly distributed prior uncertainty in the ±20% interval around the nominal condition is considered on the density. The relatively wide uncertainty range is chosen arbitrarily to allow the rebuilt parameters to be mainly informed by the measurements rather than by the priors. Furthermore, an uncertainty on the catalytic recombination coefficient γ is taken into account. It is a uniform uncertainty of ±33% around the nominal value of 0.0015, as proposed by [47]. Finally, we consider we consider ±3 deg uniform prior intervals for the flow angles.

Experimental data are considered to be affected by Gaussian measurement noise. Pressure measurements are supposed to be affected by a noise with standard deviation $\sigma_p = 0.02\, p^*_{\mathrm{st}}$, and the standard deviation value for heat flux measurements is supposed to be $\sigma_q = 0.1\, q^*_{\mathrm{st}}$; where p^*_{st} and q^*_{st} are the measured values.

4. Results for freestream parameters reconstructions

In this section, results are presented for the reconstruction problem with and without including heat flux data. Each case represents a possible configuration of available measurements and quantities that are inferred exploiting the available information.

4.1. Reconstructions from pressure measurements

At first, the Bayesian approach is adopted to calibrate some freestream quantities, namely the atmospheric density and the flow angles, starting only from pressure measurements at the wall of the vehicle. This problem is equivalent to the typical reconstruction performed by means of FADS sensors. The difference is that the Bayesian approach naturally allows to account for priors uncertainties, error measurements and complex direct models (CFD) able to accurately describe the physics of entry flows.

The reference values for the inferred parameters are taken as $\rho_r = 1.9309 \cdot 10^{-2}$ kg/m^3, $\alpha_r = 5$ degrees and $\beta_r = -1$ degrees for the 30km trajectory point, and changing to $\rho_r = 2.8806 \cdot 10^{-4}$ kg/m^3 for the 60km point, and artificial measurements are created by evaluating the surrogate at those values for each sensor

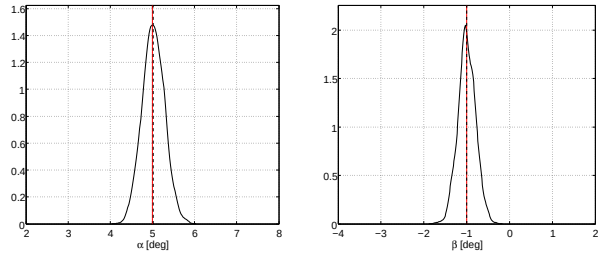

(a) Angle of attack

(b) Angle of sideslip

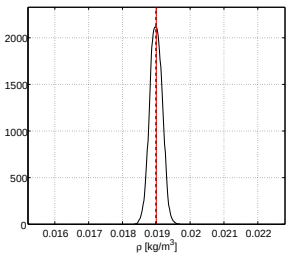

(c) Freestream density

Figure 5: PDFs of the freestream density and flow angles rebuilt from wall pressure measurements (solid black line) for the 30km trajectory points. The dashed line represents the posterior mean value and the red line the reference value. The x axis width shows the uniform prior interval.

location. The posterior probability densities of the inferred parameters are plotted in Figure 5 for the trajectory point at 30km, and their statistics are displayed in Table 3. The reconstruction is able to lead to good results, with standard deviations of 0.2 degrees for the angles and 0.9% for the density, and small errors with respect to the reference value. The support of the posterior of the rebuilt quantities is much more compact than the one of the prior, meaning that the data was able to provide knowledge about these quantities, thus reducing their uncertainties.

4.2. Reconstructions from both pressure and heat flux measurements

In this section, both pressure and heat flux measurements are exploited simultaneously. The global reconstruction of freestream density, flow angles and catalycity exploiting both pressure and heat flux measurements. The reconstruction is repeated for both the 30km and 60km trajectory points. The obtained posterior PDFs are shown in Figure 6 for the 30km case, and analogous plots, not reported here, are obtained

		30 km	60 km
ρ_∞ [kg/m^3]	μ	1.899502e-02	2.880108e-04
	σ	1.710478e-04	2.638375e-06
	σ/μ	0.903937 %	0.916068 %
	$\epsilon_{\%}$	0.037084 %	0.018024 %
α [deg]	μ	4.999603	5.004188
	σ	0.2611465	0.2592601
	ϵ_{deg}	0.000397	0.004188
β [deg]	μ	-0.995729	-0.982169
	σ	0.209720	0.197225
	ϵ_{deg}	0.004271	0.017831

Table 3: Posterior mean value, standard deviation and coefficient of variation of the inferred freestream density and flow angles computed with the MCMC samples for both trajectory points. The error $\epsilon_{\%}$ represents the relative error between the reference and the mean posterior values.

for the other condition. Posterior statistics are shown in Table 4 for both trajectory points.

		30km	60km
ρ_∞ [kg/m^3]	μ	1.900030e-02	2.886678e-04
	σ	1.676463e-04	2.597421e-06
	σ/μ	0.882 %	0.899796 %
	$\epsilon_{\%}$	0.009335 %	0.210063 %
γ	μ	1.495664e-03	1.484817e-03
	σ	0.000285	0.000283
	σ/μ	19.035 %	19.076693 %
	$\epsilon_{\%}$	0.289057 %	1.080869 %
α [deg]	μ	5.017937	4.945957
	σ	0.2672945	0.2673363
	ϵ_{deg}	0.017937	0.054043
β [deg]	μ	-1.003269	-0.976203
	σ	0.203691	0.190685
	ϵ_{deg}	0.003269	0.023797

Table 4: Posterior mean value, standard deviation and coefficient of variation of the inferred freestream density and flow angles computed with the MCMC samples for 30km and 60km trajectory point. The error $\epsilon_{\%}$ represents the relative error between the reference and the mean posterior values.

It is clear that the information added by the heating measurements is not sufficient to reduce the support of the probability density of γ, but it just slightly reduces its variance. However, better reconstruction results could be obtained if measurements with lower noise would be available, or the reconstruction could prove more useful in case of a wider prior distribution.

Comparing these results with the ones in Table 3, where just pressure had been used to reconstruct density and flow angles, it is possible to notice a small

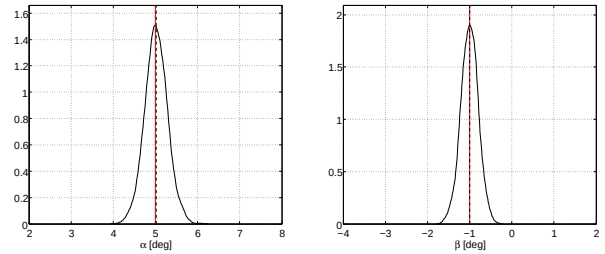

(a) Angle of attack (b) Angle of sideslip

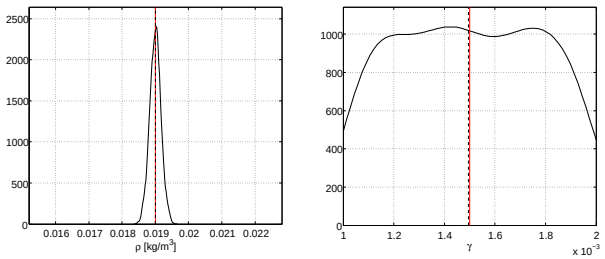

(c) Freestream density (d) Freestream density

Figure 6: PDFs of the freestream density and flow angles rebuilt from wall pressure measurements (solid black line) for the 30km trajectory points. The dashed line represents the posterior mean value and the red line the reference value. The x axis width shows the uniform prior interval.

reduction in the coefficient of variation of the density, while the posterior variance associated with flow angles remains substantially the same. From this, it is possible to deduce that density and flow angles are mainly reconstructed from pressure and not very influenced by heating data. Therefore, in the considered configuration, accounting for heat flux measurements does not seem to provide valuable improvements on reconstructions that can be done with only FADS pressure measurements.

5. Conclusions

This work focused on statistical inverse uncertainty propagation problems applied to atmospheric entry flows, with a particular interest in the assessment of the possibility to exploit heat flux measurements at the forebody of the vehicle to rebuild values of freestream conditions and uncertain parameters of the model. The reconstruction of freestream density, aerodynamic angles and catalytic coefficient has been performed in a Bayesian framework for the EXPERT vehicle, exploiting heat flux measurements at the forebody of the entry vehicle, together with the classically-available surface pressure measurements.

At the current level of accuracy for heat flux measurements (high measurement error, in the order of 10% the measured value), this kind of data does not provide enough information and, therefore, it is not able to reduce uncertainties on the rebuilt quantities with respect to reconstructions performed with only pressure measurements. Heat flux data do not bring substantial information on the catalycity either, with respect to the fairly precise expert-based prior information considered for this variable.

However, according to the results of a recent work [48], the expert-based prior distribution used for γ could be too optimistic, meaning that in practice wider prior PDFs could be expected for this parameter. In this case, it could be useful to show whether in-flight heat flux measurements could improve the characterization of γ. One last empirical test showed that the contribution of heat flux measurement could be more useful if measurement errors were substantially reduced. In a real-life scenario, benefits from including heat flux measurements will probably be obtained if, together with measurement accuracy, also prediction capabilities of numerical simulations were improved. In fact, when dealing with more complex flow, as the ones involved in Mars atmospheric entry, where ablation and irradiation affect the surface heating, all these contributions to the global wall heat flux should also be accurately modeled, in order for the reconstruction to be meaningful.

The reconstruction of freestream velocity and density using pressure and heat flux measurements, which has also been tested in another work [49] for the HEG cylinder experimental configuration, leads to results for the velocity that are much more uncertain, *i.e.* with a higher 1σ variation, than the classical reconstruction by inertial data (provided by the IMU) as usually done in the literature. The only scenario where heat flux measurements would become more useful is in the case of IMU malfunctioning: in the absence of inertial data, a relatively uncertain reconstruction by heat flux would be better than the complete impossibility of rebuilding this variable.

From the results of this work, freestream and parameter reconstruction possibilities given by heat flux forebody measurements were less useful than expected. Nevertheless, this does not mean that this kind of measurements are useless or that it is not worth trying to include different newly-available in-flight data

in the trajectory and atmospheric reconstruction process. On the contrary, this partially disappointing result should motivate the research on how to fully exploit the available in-flight data in a global framework to improve the information on uncertain parameters. Furthermore, the quality of surface heat flux measurements will probably improve in the future, since they are very useful for a direct monitoring of the TPS heating and performance. More accurate measurements will allow to improve also the predictive capabilities of numerical simulations. All these factors will eventually lead to progress in accuracy and robustness of predictions and freestream reconstruction.

To conclude, we assessed atmospheric reconstruction performed with heat flux. Moreover, this work allowed to identify some critical aspects for UQ problems in hypersonic entry flows. In particular, mesh adaptation for numerical simulations of the flow was a very critical aspect, since was causing major problems to get accurate yet automated simulations. While this may be obvious for experts in the field of numerical simulations of hypersonic flows, it becomes less evident when trying to perform a high number of simulations for UQ. This aspect needs an adequate collaboration between UQ people and experts in numerical simulations, in order to define a more general and rigorous operational framework. Another general conclusion that can be drawn from this work is that many further aspects in atmospheric entry are worth being analyzed in a UQ framework, for example the effect of ablation phenomena on surface heating, entry flows in atmospheres of different planets and entry trajectories of capsules and debris. All these problems involve complex models, with parameters that are difficult to estimate because of the lack of experimental data for a proper calibration, and therefore the whole validation and verification process could benefit from the quantification of uncertainties to robustly assess predictive capabilities of simulations.

Acknowledgments

The research of Andrea F. Cortesi has been supported by DGA (Direction Générale de l'Armement) from French Government.

References

[1] T. A. Talay, N. H. White, J. C. Naftel, Impact of atmospheric uncertainties and viscous interaction effects on the performance of aeroassisted orbital transfer vehicles, Progress in Astronautics and Aeronautics 96 (1985) 198–229, thermal Design of Aeroassisted Orbital Transfer Vehicles.

[2] A. Enzian, D. Devezeaux, A. Mohamed, F. Thivet, P. Tran, J.-P. Tribot, Flight experiments to address unsolved aerothermodynamic issues for a future european reusable space launcher, Tech. Rep. ESA SP-487, ESA (2002).

[3] G. Koppenwallner, Controlled hypersonic flight air data system and flight instrumentation, Flight Experiments for Hypersonic Vehicle Development, Educational Notes RTO-EN-AVT-130 (17) (2007) 1 – 30.

[4] L. M. Jones, J. W. Peterson, E. J. Schaefer, H. F. Schulte, Upper-air density and temperature: some variations and an abrupt warming in the mesosphere, Journal of Geophysical Research 64 (12) (1959) 2331–2340.

[5] A. Seiff, D. E. J. Reese, Use of entry vehicle responses to define the properties of the mars atmosphere, Tech. rep., NASA Ames Research Center (1965).

[6] D. A. Spencer, R. C. Blanchard, R. D. Braun, P. H. Kallemeyn, S. W. Thurman, Mars pathfinder entry, descent, and landing reconstruction, Journal of Spacecraft and Rockets 36 (3) (1999) 357–366.

[7] P. Withers, M. D. Smith, Atmospheric entry profiles from the mars exploration rovers spirit and opportunity, Icarus 185 (1) (2006) 133 – 142.

[8] R. C. Blanchard, P. N. Desai, Mars phoenix entry, descent, and landing trajectory and atmosphere reconstruction, Journal of Spacecraft and Rockets 48 (5) (2011) 511–518.

[9] P. N. Desai, P. C. Knocke, Mars exploration rovers entry, descent, and landing trajectory analysis, Journal of the Astronautical Sciences 55 (3) (2007) 311 – 323.

[10] G. Colombatti, P. Withers, F. Ferri, A. Aboudan, A. Ball, C. Bettanini, V. Gaborit, A. Harri, B. Hathi, M. Leese, T. Makinen, P. Stoppato, M. Towner, J. Zarnecki, F. Angrilli, M. Fulchignoni, Reconstruction of the trajectory of the huygens probe using the huygens atmospheric structure instrument (hasi), Planetary and Space Science 56 (2008) 586–600.

[11] P. Withers, M. Towner, B. Hathi, J. Zarnecki, Analysis of entry accelerometer data: A case study of mars pathfinder, Planetary and Space Science 51 (9) (2003) 541 – 561.

[12] P. N. Desai, J. L. Prince, E. M. Queen, M. M. Schoenenberger, J. R. Cruz, M. R. Grover, Entry, descent and landing performance of the mars phoenix lander, Journal of Spacecraft and Rockets 48 (5) (2011) 798 – 808.

[13] B. Van Hove, O. Karatekin, Mars entry, descent, and landing reconstruction from flight data: uncertainty quantification.

[14] B. R. Cobleigh, S. A. Whitmore, E. A. J. Haering, J. Borrer, V. E. Roback, Flush Airdata Sensing (FADS) System Calibration Procedures and Results for Blunt Forebodies, Tech. Rep. NASA-TP-1999-209012, NASA (1999).

[15] E. Euler, G. Adams, F. Hopper, Design and reconstruction of the viking lander descent trajectories, Journal of Guidance, Control, and Dynamics 1 (5) (1978) 372–378.

[16] C. D. Karlgaard, J. V. Norman, , P. M. Siemers, M. Schoenenberger, M. M. Munk, Mars entry atmospheric data system modeling, calibration, and error analysis, Tech. Rep. NASA/TM–2014–218535, NASA Langley Research Center (2014).

[17] C. D. Pruett, H. Wolf, M. L. Heck, P. M. Siemers III, Innovative air data system for the space shuttle orbiter, Journal of Spacecraft and Rockets 20 (1) (1983) 61 – 69.

[18] R. Müller-Eigner, G. Koppenwallner, B. Fritsche, Pressure and heat flux measurement with RAFLEX II during MIRKA re-entry, Third European Symposium on Aerothermodynamics for Space Vehicles ESA SP-426 (1999) 685 – 694.

[19] J. Häuser, W. Dai, G. Koppenwallner, J. Muylaert, Inverse problem solution for determining spacecraft orientation from pressure measurements, Proceedings of the Fifth European

Symposium on Aerothermodynamics for Space Vehicles ESA SP-563 (2004) 1 – 30.
[20] G. Koppenwallner, Definition of requirements and operational specifications for fads, Technical note WP1: Flush and Laser Air Data System HTG TN-03-6.
[21] R. Müller-Eigner, G. Koppenwallner, RAFLEX-an air data system for re-entry vehicles, Fourth European Symposium on Aerothermodynamics for Space Vehicles ESA SP-487.
[22] J. Thoemel, J.-M. Muylaert, F. Ratti, J. Gavira, In-flight testing of critical technologies and experimentation of aerothermodynamic phenomena, in: 16th AIAA/DLR/DGLR International Space Planes and Hypersonic Systems and Technologies Conference, American Institute of Aeronautics and Astronautics, 2009.
[23] S. Loehle, Review of heat flux measurements for high enthalpy flows, in: 32nd AIAA Aerodynamic Measurement Technology and Ground Testing Conference, American Institute of Aeronautics and Astronautics, 2016.
[24] A. K. Alekseev, G. A. Pavlov, Estimation of entry parameters from heat flux measurements, Journal of Spacecraft and Rockets 35 (4) (1998) 575–577.
[25] B. Van Hove, Ö. Karatekin, Atmospheric reconstruction with stagnation pressure flight data from mars science laboratory, Journal of Spacecraft and Rockets 54 (3) (2017) 609 – 620. doi:10.2514/1.A33627.
[26] P. M. Kutty, Reconstruction and uncertainty quantification of entry, descent and landing trajectories using vehicle aerodynamics, Master's thesis, Georgia Institute of Technology (2014).
[27] J. Christian, A. Verges, R. Braun, Statistical reconstruction of mars entry, descent, and landing trajectories and atmospheric profiles, in: AIAA SPACE Conference and Exposition, AIAA 2007-6192, 2007.
[28] S. Dutta, R. D. Braun, Statistical entry, descent, and landing performance reconstruction of the mars science laboratory, Journal of Spacecraft and Rockets 51 (4) (2014) 1048 – 1061.
[29] S. Dutta, R. D. Braun, R. P. Russell, S. A. Striepe, I. G. Clark, Comparison of statistical estimation techniques for mars entry, descent, and landing reconstruction, Journal of Spacecraft and Rockets 50 (6) (2013) 1207–1221.
[30] S. Dutta, R. D. Braun, C. D. Karlgaard, Uncertainty quantification for mars entry, descent, and landing reconstruction using adaptive filtering, Journal of Spacecraft and Rockets 51 (3) (2014) 967–977.
[31] D. Calvetti, E. Somersalo, Introduction to Bayesian Scientific Computing: Ten Lectures on Subjective Computing, Springer, New York, 2007.
[32] J. Tryoen, P. M. Congedo, R. Abgrall, N. Villedieu, T. Magin, Bayesian-based method with metamodels for rebuilding freestream conditions in atmospheric entry flows, AIAA Journal **52** (10) (2014) 2190 – 2197.
[33] J. Muylaert, L. Walpot, H. Ottens, F. Cipollini, Aerothermodynamic reentry flight experiments EXPERT, Tech. Rep. RTO-EN-AVT-130, NATO OTAN (2007).
[34] P. Barbante, Accurate and efficient modelling of high temperature non-equilibrium air flows, Ph.D. thesis, Von Karman Institute for Fluid Dynamics (2001).
[35] C. Park, R. Jaffe, H. Partridge, Chemical-kinetic parameters of hyperbolic earth entry, Journal of Thermophysics and Heat Transfer **15** (1) (2001) 76 – 90.
[36] M. Sun, K. Takayama, An artificially upstream flux vector splitting scheme for the euler equations, Journal of Computational Physics 189 (1) (2003) 305 – 329.
[37] J. Kaipio, E. Somersalo, Statistical and computational inverse problems, Vol. 160 of Applied Mathematical Sciences, Springer, 2005.
[38] W. R. Gilks, S. Richardson, D. J. Spiegelhalter, Markov Chain Monte Carlo in practice, Chapman & Hall/CRC Interdisciplinary Statistics, 1996.
[39] A. Tarantola, Inverse Problem Theory and Methods for Model Parameter Estimation, Society for Industrial and Applied Mathematics, 2005.
[40] W. K. Hastings, Monte carlo sampling methods using markov chains and their applications, Biometrika 57 (1) (1970) 97–109.
[41] Y. M. Marzouk, H. N. Najm, L. A. Rahn, Stochastic spectral methods for efficient bayesian solution of inverse problems, J. Comput. Physics 224 (2007) 560–586.
[42] A. Birolleau, G. Poëtte, D. Lucor, Adaptive bayesian inference for discontinuous inverse problems, application to hyperbolic conservation laws, Communications in Computational Physics 16 (1) (2014) 1–34. doi:10.4208/cicp.240113.071113a.
[43] A. F. Cortesi, P. M. Congedo, A kriging-pdd surrogate model for uncertainty quantification, in: VII European Congress on Computational Methods in Applied Sciences and Engineering, ECCOMAS 2016, ECCOMAS, 2016.
[44] A. F. Cortesi, P. M. Congedo, A kriging-PDD surrogate model for low-cost sensitivity analysis, in: 17th AIAA/ISSMO Multidisciplinary Analysis and Optimization Conference, AIAA AVIATION Forum, American Institute of Aeronautics and Astronautics, 2016.
[45] M. D. McKay, R. J. Beckman, W. J. Conover, A comparison of three methods for selecting values of input variables in the analysis of output from a computer code, Technometrics 21 (2) (1979) 239 – 245.
[46] S. Brooks, A. Gelman, G. Jones, X.-L. Meng, Handbook of Markov Chain Monte Carlo, Chapman & Hall / CRC, Boca Raton, 2011.
[47] N. Villedieu, F. Panerai, O. Chazot, T. Magin, Uncertainty quantification for gas-surface interaction in plasmatron, Tech. rep., ESA (2012).
[48] F. Sanson, T. E. Magin, F. Panerai, P. M. Congedo, Bayesian Reconstruction of Catalytic Properties of Thermal Protection Materials for Atmospheric Reentry, in: SIAM UQ, Lausanne, Switzerland, 2016.
[49] A. F. Cortesi, P. G. Constantine, T. E. Magin, P. M. Congedo, Forward and backward uncertainty quantification with active subspaces: application to hypersonic flows around a cylinder, Journal of Computational Physics.

Absolute instability in plasma jet

Simon Demange

Aeronautics and Aerospace Department, von Karman Institute for Fluid Dynamics, Belgium, simon.demange@vki.ac.be

Supervisor: Fabio Pinna

Research Engineer, Aeronautics and Aerospace Department, von Karman Institute for Fluid Dynamics, Belgium, fabio.pinna@vki.ac.be

Supervisor: Olivier Chazot

Head of department, Aeronautics and Aerospace Department, von Karman Institute for Fluid Dynamics, Belgium, chazot@vki.ac.be

University Supervisor: Gérard Degrez

Promoter, Aero-Thermo-Mechanics department, Université Libre de Bruxelles, Belgium, gdegrez@ulb.ac.be

Abstract

The stability of the plasma jet generated in the VKI Inductively Coupled Plasma wind tunnel Plasmatron is investigated numerically using the Linear Stability Theory, as a novel approach to quantify the uncertainties in the studies of ablative materials for TPS and high enthalpy flows. This study aims at developing a numerical tool using LST, matching available experimental results from Cipullo [1] including the instabilities shapes and frequencies for a wide range of operative conditions (stagnation pressure and power combinations) in the facility.

Jet flows can sustain two types of instabilities: either absolute or convective (see [2] among others). Previous LST studies conducted at VKI [3] [4] matched partially the experimental observations for some of the operative conditions of the facility. Unfortunately, the combination of extreme temperatures and low Reynold number of the plasma flow differ greatly from typical conditions studied in literature. For this study, the plasma flow is considered as a mixture of perfect gases in Local Thermodynamic Equilibrium and Chemical Equilibrium, which makes this study the first to investigate absolute instabilities in such conditions with LST.

The base flow is computed by fitting CFD simulations taking into account high temperature effects, and a spatio-temporal analysis is performed to determine the time-asymptotic behavior of the flow, concluding on the absolute/convective nature of instabilities at several streamwise positions. Preliminary results show that absolute intabilities dominate the stability beahvior of the jet for some experimental conditions. Moreover, the range of frequencies as well as the shape of the instabilities found by the LTE-LST model are coherent with the experimental observations. However, the growth-rate associated with these instabilities implies a rapid growth of the instabilities to the turbulent state which is not observed in the facility. So it seems possible that non-linear instability growth and non-parallel base flow effects would mitigate this growth.

Keywords: Jet instabilities, Absolute Instabilities, Inductively Coupled Plasma wind tunnel, Linear Stability Theory

References

[1] A. Cipullo, B. Helber, F. Panerai, L. Zeni, O. Chazot, *Investigation of freestream plasma flow produced by inductively coupled plasma wind tunnel.* Journal of Thermophysics and Heat Transfer, Vol. 28, Issue 3, pp 381-393, 2014.

[2] P. Huerre and P. A. Monkewitz, *Absolute and convective instabilities in free shear layers.* Journal of Fluid Mechanics 159, pp 151âĂŞ168, 1985.

[3] F. Garcia Rubio, *Numerical study of plasma jet unsteadiness for re-entry simulation in ground based facilities.* Stage report, von Karman Institute for fluid dynamics, 2013.

[4] M. Chiatto, *Spatio-temporal stability analysis of shear layers.* Stage report, von Karman Institute for fluid dynamics, 2014.

[5] N. Kumar, *Spatio-temporal stability analysis of shear layers.* Stage report, von Karman Institute for fluid dynamics, 2017.

Higher-order shock-fitting methods for high-speed simulations

Vincent Fitzgerald Giangaspero

Aeronautics & Aerospace department, von Karman Institute for Fluid Dynamics, Belgium, vincent.giangaspero@vki.ac.be

Supervisor: Herman Deconinck

Dean of the faculty, Aeronautics & Aerospace department, von Karman Institute for Fluid Dynamics, Belgium, deconinck @vki.ac.be

Co-supervisor: Andrea Lani

Research engineer,Plasma-astrophysics department, University of KU Leuven, Belgium, andrea.lani@kuleuven.be

Promoter: Gerard Degrez

Dean of the faculty, Aero-Thermo-Mechanics department Universite Libre de Bruxelles, Belgium, Gerard.Degrez@ulb.ac.be

Keywords: hypersonic flows, re-entry flows, CFD, shock-fitting, high-order methods, COOLFluiD

First year doctoral summary

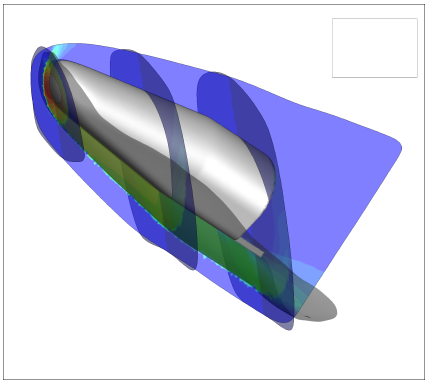

Figure 1: Shock fitting on IXV vehicle

The ability to provide simulations of hypersonic flows over planetary entry vehicles with well-defined uncertainties on the predicted aerothermal environments is critical to the success of solar system exploration. Hypersonic aerothermodynamics is characterized by high-speed flows and particular physical phenomena that do not appear in the supersonic regime. The analysis of such flows requires accurate and robust numerical techniques to properly handle strong shocks, thin shock layers, entropy layer, thermochemical and radiative phenomena. The vast majority of state-of-the-art CFD codes tackling hypersonic applications are based on Finite Volume (FV) shock-capturing solvers, mostly limited to second-order accuracy[1]. Problems such as extreme grid sensitivity, shock instabilities, noisy post-shock field and inaccurate stagnation heat flux prediction can still plague those methods especially on unstructured grids, even on relatively simple geometries and represent major obstacles for achieving the desired accuracy [2]. Shock-fitting methods represent a valid alternative to more traditional shock-capturing schemes for simulating hypersonic flows affected by strong shocks and can deliver superior accuracy at the price of an increased algorithmic complexity. In addition to this, modern higher-order numerical methods which are well consolidated for certain classes of CFD applications (e.g. turbulence, biological flows, low speed aerodynamics) are still rather immature for hypersonic simulations, mainly due to the lack of robustness of shock-capturing approaches when trying to resolve strong shocks [3]. Besides the higher accuracy, another desirable advantage of high-order methods is that they may require much coarser grid resolution in boundary layers, therefore simplifying considerably the mesh generation process for high-speed high-Reynolds re-entry flows, which is currently a very time-consuming activity for those kind of simulations.

The objective of the present PhD research project is to further develop and validate shock-fitting algorithms in order to improve the overall accuracy of 3D re-entry aerothermodynamics simulations, as resulting from a better characterization of the shock layer. The project takes profit of an existing open source C++ code, the Shock Fitting (SF) library [4], which couples shock- fitting algorithms to unstructured CFD solvers, based on the shock-fitting technique on unstructured grids proposed by Paciorri and Bonfiglioli [5]. In our preliminary work, SF has been coupled with an existing aerothermodynamics COOLFluiD solver, which is based upon a second-order accurate Residual Distribution (RD) method. The research project will start with the optimization and consolidation of the existing SF library in order to improve the performances and capabilities of the shock-fitting solver. First, the parallelization of the code is of paramount importance for the demanding 3-D algorithms needed by the shock-fitting technique. As a first step, this will be achieved via OpenMP for parallelizing the most critical portions of the code by integrating some macro directives and by reorganizing the data arrays in a more vectorization-friendly way. As a second step, a more intrusive parallelization involving data partitioning and MPI may be considered, depending on the actual performance of the most demanding target test-cases. The performance of the existing shock-fitting procedure will be further improved by implementing an ad-hoc boundary condition (far- field condition) to be imposed on the post-shock states. This will allow for performing more than one iteration with the CFD solver between consecutive shock-fitting steps and for speeding up convergence to steady state, once the shock reaches a steady location.The second part of the project will be the extension to high-order methods, coupling SF and the COOLFluiD-FR (Flux Reconstruction) solver [6]. A crucial aspect of this task will be the upgrade of the mesh generation process for generating high-order unstructured mesh as most existing mesh generators can exclusively create low-order meshes. As a consequence, a specific mesh generator need to be coupled with SF (Gmsh), along with the extension of COOLFluiD-FR solver to handle tetrahedral elements (P2-P2,P5-P2). During the third part of the project, the SF and FR solvers will be extended to handle viscous and non-equilibrium flows. To this end, both solvers will be interfaced with Mutation++, the Multicomponent Thermodynamic And Transport properties for Ionized gases C++ library [Mutation] developed at VKI, allowing for computing chemistry, thermodynamics and transport properties with beyond state-of-the-art models. The fourth and last task in the project, will include the verification and validation of the code against benchmark test-cases available in literature, existing experimental database (for supersonic Plasmatron experiments)[7] and flight data (for the ESA IXV vehicle).

References

[1] P. A. Gnoffo and J. A. White. "Computational Aerothermodynamic Simulation Issues on Unstructured Grids". In: 37th AIAA ThermoPhysics Conference. Portland, Oregon, 2004.

[2] P. A. Gnoffo. "Multi-dimensional, inviscid flux reconstruction for simulation of hypersonic heating on tetrahedral grids." In: 47th AIAA aerospace sciences meeting. Florida, Orlando, 2009.

[3] HT Huynh. "A flux reconstruction approach to high-order schemes including discontinuous galerkin methods". In: *AIAA paper* 4079 (2007).

[4] *Shock Fitting Solver C++ Library.* https://github.com/andrealani/ShockFitting/wiki.

[5] A. Bonfiglioli et al. "An unstructured, three-dimensional, shock-fitting solver for hypersonic flows". In: *Journal of Computer and Fluids* 73 (2013).

[6] Vandenhoeck R. Papen A. *Development of an Implicit High-Order Flux Reconstruction Solver for Compressible Flows on Unstructured Grids.* Master Thesis. KU Leuven, 2017.

[7] O. Chazot T.E. Magin B. Helber A. Turchi. *Preliminary experiments on wooden flat plate in supersonic plasma flow for ABLARADABLA TRP.* Technical report. von Karman Institute for Fluid Dynamics, January 2017.

Ablation modelling for the simulation of the atmospheric entry of meteors

Bruno Dias

Aeronautics and Aerospace Department, von Karman Institute for Fluid Dynamics, Belgium, barros@vki.ac.be

Supervisor: Thierry E. Magin

Associate Professor, Aeronautics and Aerospace Department, von Karman Institute for Fluid Dynamics, Belgium, magin@vki.ac.be

University Supervisor: Philippe Chatelain

Assistant professor, Thermodynamics and fluid mechanics - TFL, Université catholique de Louvain, Belgium, philippe.chatelain@uclouvain.be

Abstract

The meteor phenomenon occurs constantly into our planet. The discrepancy of meteoroid flux varies from 50 to 100 tonnes according to aeronomy experts. A better understating of the phenomenon allows to track the meteoroid to the parent comet/asteroid and eventually to prevent catastrophic events by knowing the respective trajectory and composition. This type of events are characterized by complex shock layer physics such as radiation, evaporation of the meteoroid surface and the resulting chemistry process with the air constituents. In this work we present the analysis of a meteor entry using Computational Fluid Dynamic tools where a boundary condition for evaporation is implemented. Moreover the radiative source terms are derived by solving a 1D radiative transfer equations using a tangent slab method. Form the preliminary results it is shown that for a small radius the radiative heating is negligible compared to the convective heating.

Keywords: radiation, evaporation, meteor, CFD

1. Introduction

The meteor phenomenon occurs daily around the planet Earth. From 50 to 100 tonnes of these interplanetary objects enters Earth's atmosphere every day with a range of velocities from 11.5 km/s to 72 km/s [1]. Although a large number of the arriving particles are considered dust (micron-size grains) occasionally a large bolide burst into the atmosphere. The latter may represent a threat to the population as experienced during the Chelyabinsk event in 2013 [2]. A better understanding of such phenomenon is important on a variety of fields such as aeronomy, astronomy, geophysics, evolutionary biology and planetology. Tracing a large number of meteoroid orbits in the Solar System allows to clarify the association of meteoroids with asteroids, comets, or the zodiacal cloud. At the range of velocities typical of meteor phenomena, radiation becomes highly significant, the intense light observed during a meteor entry is mainly due to the radiation of the air and metallic species, where the latter are coming from ablation products. The current models to study meteor entries are focus in the ablation of small particles in the upper atmosphere. They usually rely on a zero dimensional approach providing lack of an accurate treatment of the particle interaction with the atmosphere, from the fluid dynamic point of view. Therefore, for meteoroids big enough to survive this first phase of the atmospheric entry, a different approach has to be sought.

In this work we propose to study the meteor ablation with a numerical approach similar to those used in the aerospace community to model the gas-surface interaction over Thermal Protection System (TPS) materials. A 1D Stagnation-Line solver is used to resolve the multicomponent, reacting governing equations including radiative source terms computed by a tangent slab radiative transfer solver using the HSNB formulation (presented in the next section).

2. Model description

2.1. Physico-Chemical Models

The following sections describe briefly the physico-chemical models. These models are used to close the governing equations which in turn are solved by numerical methods. The evaporation model described is used as a boundary conditions between the gas and the surface. Finally the radiation model provides source terms to the governing equations.

2.1.1. Thermodynamics

From quantum mechanics it follows that the energy levels of atoms and molecules are discrete [3]. In the case of atoms this energy is contained into the translational movement of the particle (translational energy) and into the electronic energy modes (associtated to the electron orbit around the nucleus). In the case of molecules, they have two additional energy modes which corresponds to the rotational and vibrational energy levels. Even thoughh the translational energy levels are discrete, the spacing between them are generally very small therefore they are considered continuum [4]. The internal modes of molecules (electronic, rotational and vibrational modes) are dependent of each other. Very often for simplicity, one considers the separation between the internal modes by assuming that the molecule behaves as a rigid-rotator and an harmonic oscillator (RRHO).

The focus of this section concerns only with the derivation of the thermodynamics properties for metallic atoms. For atoms the separation between translational and electronic modes is valid since they are independent. Thermodynamic properties such as specific heat, enthalpy and entropy is computed based on the system partition function (eq. 1). Typically metallic species are characterised by having a low ionization energy and hundreds of energy levels, turning the evaluation of the partition function computational expensive due to its exponential nature.

To circumvent this problem a binning strategy [5] was employed, which consists in grouping the energy levels into bins over an energy grid $[\varepsilon_k, \varepsilon_{k+1}[$, (Fig. 1) follow:

$$I_k = \{i \in I_e \text{ such that } (\varepsilon_k \leq E_i < \varepsilon_{k+1})\}, \quad k \in K_e$$

where K_e is the set of the indices for the bins. An average energy for bin k follows:

$$\overline{E}_k = \frac{\sum_{i \in I_k} g_i E_i}{\overline{g}_K}, \quad k \in K_e$$

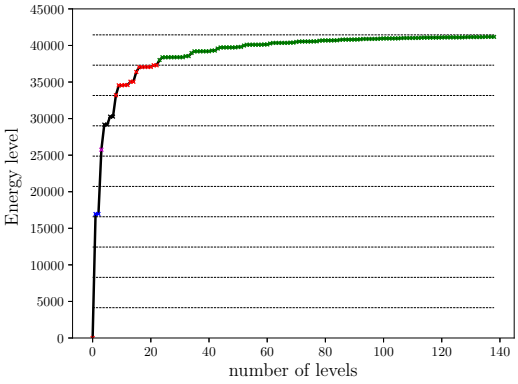

Figure 1: Energy Levels for Na

based on the degeneracy of the bin as $\overline{g}_k = \sum_{i \in I_k} g_i$. Finally the electronic partition function assuming a reduced number of energy levels estimated for each bin is computed by eq. 1.

$$\overline{Q}_i^E(T_{ele}) = \sum_{k \in K_e} \overline{g}_k \exp\left(\frac{-\overline{\theta}_k}{T}\right), \quad i \in N_s \tag{1}$$

where the characteristic temperature $\overline{\theta_k} = \overline{E}_k / k_b$ and k_b is the Boltzmann constant. As mentioned previously once the electronic partition function is known the computation of the thermodynamic properties become trivial. The electronic enthalpy follow:

$$h_i^E(T_{ele}) = R_i T^2 \frac{\partial \ln \overline{Q}_i^E}{\partial T}, \quad i \in N_s \tag{2}$$

where R_i is the specific gas constant for species i. The total enthalpy of the atom as:

$$h = \sum_{i \in N_s} y_i (h_i^T + h_i^E) \tag{3}$$

where the translational contribution is defined as $h_i^T(T) = 5/2 R_i T$.

The electronic levels for atoms are either observed through spectroscopy measurements or computed from quantum mechanics. The Nist database [6] comprises a big amount of data regarding the electronic levels for several atoms. In fig. 1 the total 140 electronic levels for Na are shown. The bars shown in the same figure represent the bins and the symbols concerns the total number electronic levels per bin. Using the reduction technique mentioned above it was possible to pass from 140 to 6 electronic levels. The non-dimensional enthalpy for Na is show in 2 for the

total number of electronic levels extracted from Nist and for the reduced number.

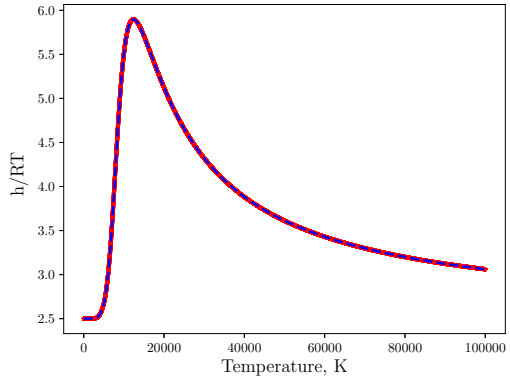

Figure 2: Non-dimensional total enthalpy for Na; line: 140 electronic levels, broken line: 6 electronic levels

From the figure one can conclude that the reduction system works well being able to reproduce the same thermodynamic quantity as the entire number of electronic levels. Finally fig. 3 shows the equilibrium composition based on the Gibbs free energy minimization [7] for a Na elemental system. A comparison was made between the RRHO model and the Nasa polynomials database [8], where the later is more accurate up to 20000 K. Initially only NaO is present in the mixture, around 2500 K the species starts to dissociate forming Na and O. Around 5000 K Na starts to ionize forming Na^+ and finally at 12000 K the mixture becomes fully ionized. The agreement between both models is very good up to 17000 K , limit where the Nasa polynomials become invalid and the composition becomes unrealistic.

2.1.2. *Hybrid Statistical Narrow Band Model*

By solving the radiative transfer equations (RTE) one can determine the spectral radiative intensity, therefore, the radiative source terms, $\mathcal{P}^{rad}$ and $\mathcal{P}^{rad,VE}$ and $\dot{\omega}_i^{rad}$. The production or destruction of species, $\dot{\omega}_i^{rad}$, due to radiative processes such as photoionization and photodissociation and the radiative source terms. Solving the RTE by conventional methods such as Line-by-Line (LBL) becomes computationally very expensive for complex molecular spectra. Recently, [9] presented a hybrid statistical narrow band model (HSNB) showing an accurate description of the radiative flux with low CPU costs for non-ablative materials. Later [10], extended this approach for ablative TPS material.

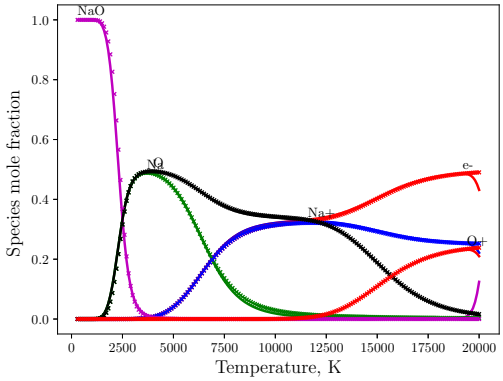

Figure 3: Equilibrium composition for {NaO, Na, O, Na^+, O^+, e^-}; lines: Nasa database, symbols: RRHO

The feature of the HSNB is that if the radiative mechanisms are statistically uncorrelated one can divide the spectra into narrow bands and compute the intensity in terms of averages. The different mechanism can be separated into 3 contributions: optically thick molecular systems, optically thin molecular systems and continua, atomic lines. Due to the weak spectral density of atomic lines, this contribution has to be solved by LBL methods. Details about the HSNB can be found in Refs. [9; 10].

2.1.3. *Gas-Surface Interaction*

The evaporation of a molten layer can be modeled by limiting the control volume to a infinitesimal thin lamina where the surface is located. Typically mass conservation for the generic species i can be written in terms of a surface mass balance (SMB):

$$J_{i,w} + \dot{m}_{evap,i} = (\rho v)_w y_{i,w} \quad \mathrm{i} \in \mathrm{N_s} \tag{4}$$

where $(\rho v)_w$ is the gas blowing, $y_{i,w}$ is the mass fraction of species i in the gaseous mixture at the wall, $\dot{m}_{evap}$ is the evaporation/condensation rate and $J_{i,w}$ is the species mass diffusion.

To solve this balance a suitable model to compute the surface reactions is needed, which in general can be solved by heterogeneous finite-rate chemistry. The evaporation/condensation of the material $\dot{m}_{evap,i}$ is estimated by the Knudsen-Langmuir law:

$$\dot{m}_{evap,i} = \left(\frac{\mathcal{M}_i}{2\pi\mathcal{R}T}\right)^{\frac{1}{2}} (\alpha_{evap} p_{vap,i} - \alpha_{cond} p_i) \quad \mathrm{i} \in \mathrm{N_s} \tag{5}$$

where the equilibrium vapor pressure , $p_{vap,i}$, can be compute through a multiphase equilibrium solver

such as Magma [11]. The Magma solver has been extensively validated for silicate melt compositions. The solver it uses the ideal mixing of complex components (IMCC) model which considers the deviation of ideal mixture into the melt. In another words it uses complex pseudospecies to compute activity coefficients of metal oxides in non-ideal molten compositions. In fig. 4 is shown the equilibrium vapour pressure of each species for a wide range of temperatures.

The term $(\mathcal{M}/2\pi\mathcal{R}T)^{1/2}\, p_i$ represents the flux of incident particles on the surface while the therm $(\mathcal{M}/2\pi\mathcal{R}T)^{1/2}\, p_{vap,i}$ represents the mass flux emerging from the wall. The α_{evap} and α_{cond} are respectively the evaporation and condensation coefficient. In equilibrium both coefficients are the same and the net flux of evaporating and condensating particles is zero [12]. The non-equilibrium evaporation implies a formation a of layer called Knudsen layer where the rarefaction effects become dominant thus the use of continuum methods becomes impossible [13]. [14] defines the α_{evap} coefficient as the ratio of the number of particles evaporated with respect to the equilibrium conditions, while the α_{cond} is the ratio of the number of particles condensating with respect to the impinging particles at the wall (both coefficients are bounded between 0 and 1). He observed these coefficients experimentally for water and concluded that they can vary significantly depending on the conditions. One possible way to estimate these coefficients is trough molecular dynamics (MD) [15] which becomes prohibited expensive for a large system. Hereafter a sensitivity analysis was made to these coefficients which will be shown later on.

By summing Eq. 4 over all species, one obtains:

$$\dot{m}_{evap} = (\rho u)_w$$

Once the gas composition is known and the mass blowing rate, $\dot{m}_{evap}$, is computed, the surface blowing velocity can be easily.

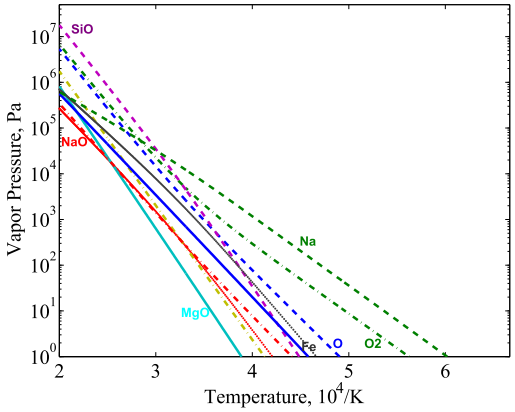

Figure 4: Vapor pressure for a silicate composition

2.2. *Numerical tools*

The flow governing equations are solved through a CFD code where the SMB boundary condition, explained the in previous section, is implemented. The flow properties are computed with the VKI physico-chemical library (Mutation^{++}). Energy and chemical (photoionization and photodissociation) source terms to account for radiation are included into the Navier-Stokes. These source terms are computed by solving the radiative transfer equations (RTE).

2.2.1. *Stagnation-Line Code CFD Solver*

The 1D Stagnation-Line solver developed at the VKI by Munafò [16], resolves the Navier-Stokes equations along the stagnation line of spherical or cylindrical bodies, where an illustration is shown by Fig. 5. This model leads to an efficient way to calculate hypersonic flows with low computational costs.

In this code the three-dimensional Navier-Stokes equations are reduced to a one-dimensional approximation for the stagnation streamline by a system called "Dimensionally Reduced Navier Stokes Equations" (DRNSE). The spatial discretization is done by finite volume method and the time integration is computed by a Backward-Euler method. The stagnation-line equations read as:

$$\frac{\partial}{\partial t}\mathbf{U} + \frac{\partial}{\partial r}\mathbf{F^{inv}} + \frac{\partial}{\partial r}\mathbf{F^{vis}} + \frac{\mathbf{G^{inv}} + \mathbf{G^{vis}}}{r} = \mathbf{S^c} + \mathbf{S^r} \quad (6)$$

Where $\mathbf{U}$ denotes the volume-specific balance quantities, $\mathbf{F^{inv}}$ are the inviscid fluxes, $\mathbf{F^{vis}}$ the viscous terms, $\mathbf{S^c}$ and $\mathbf{S^r}$ are respectively the chemical and radiative source terms:

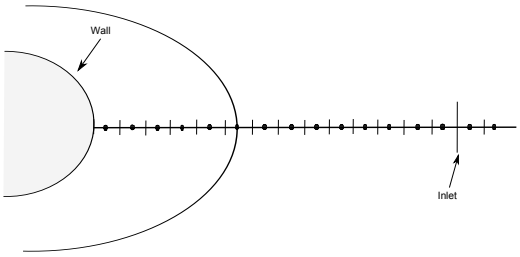

Figure 5: 1D Stagnation-Line illustration

$$
\begin{aligned}
\mathbf{U} &= \left[\rho_i,\ \rho u,\ \rho v,\ \rho E,\ \rho e^{VE}\right]^T \\
\mathbf{F^{inv}} &= \left[\rho_i u,\ \rho u^2 + p,\ \rho uv,\ \rho uH,\ \rho u e^{VE}\right]^T \\
\mathbf{F^{vis}} &= \left[\mathrm{J}_{ri},\ \bar{\tau}_{rr},\ \bar{\tau}_{r\theta},\ q_r + \bar{\tau}_{rr}u,\ q_r^{VE}\right]^T \\
\mathbf{G^{inv}} &= \left[2\rho_i(u+v),\ 2\rho u(u+v),\ 3\rho v(u+v) - 2\bar{p},\ 2\rho H(u+v),\ \rho e^{VE}\right]^T \\
\mathbf{G^{vis}} &= \left[\mathrm{J}_{ri},\ 2(\bar{\tau}_{rr} - \bar{\tau}_{\theta\theta} + \bar{\tau}_{r\theta}),\ -\bar{\tau}_{\theta\theta} + 3\bar{\tau}_{r\theta},\ 2(q_r + \bar{\tau}_{rr}u + \bar{\tau}_{\theta\theta}u + \bar{\tau}_{r\theta}v),\ 2q_r^{VE}\right]^T \\
\mathbf{S^c} &= \left[\dot{\omega}_i^{\mathbf{c}},\ 0,\ 0,\ 0,\ \Omega^{VE}\right]^T \\
\mathbf{S^r} &= \left[\dot{\omega}_i^{\mathbf{rad}},\ 0,\ 0,\ \mathcal{P}^{rad},\ \mathcal{P}^{rad,VE}\right]^T
\end{aligned}
$$

The variables $\mathbf{G^{inv}}$ and $\mathbf{G^{vis}}$ are inviscid and viscous source terms arising from the DRNSE transformation, respectively. The therm ρe^{VE} stands for vibrational-electronic-electron energy. Details regarding the radial heat fluxes, q_r and q_r^{VE} as well the energy transfer source term, Ω^{VE} are given by [10].

2.2.2. *MUlticomponent Thermodynamic And Transport properties for IONized plasmas in C++ (Mutation^{++})*

The closure of the multi-temperature Navier-Stokes equations is done by computing thermodynamic and transport properties. Mutation^{++} is a library built at the VKI by [17] where thermodynamic properties are computed by the Rigid Rotor Harmonic Oscillator model while transport properties are derived by the Chapman-Enskog expansion from Kinetic Theory [18].

3. Results and Discussion

A two-temperature model was used for these simulations, i.e., T = T_{rot} and T_{vib} =T_{ele} and the wall temperature was imposed at 2600 K. The choice of this temperature was based on experimental and numerical observations of a melting ordinary chondrite [19].

The first analysis concerns a sensibility study of both the evaporation and condensation coefficient (respectively α_{evap} and α_{cond}) in eq. 5. This analysis is made to understand the influence of such coefficients in terms of the overall mass blowing rate. The concept of these coefficients is explained in section 2.1.3 as well the difficulty to access such properties, which motivates the following study. It was considered a 0.1 meter radius object with a 15 km/s velocity at 60 km altitude.

The second part of the discussion concerns the influence of radiation coupled to the flow/ablation and the overall effects for two different sizes (0.1 and 1 meter radii). The radiation source terms (section 2.1.2) are computed and updated to the flow after a determined number of iterations. The conditions were the same as the previous analysis.

3.1. *Sensitivity analysis on the evaporation law*

The choice of the Knudsen-Langmuir (eq. 5) parameters is shown by table 1. For all the cases the major vapour species are Na followed by NaO being in agreement with meteor observations since these species are considered the most volatiles.

Figure 6 shows a comparison between case 1 and 2 of Na and Na^+ along the stagnation streamline. It is

Table 1: Eq. 5 coefficient parameters

Case #	coefficient
Case 1	$\alpha_{evap} = 0.1$
	$\alpha_{cond} = 0.1$
Case 2	$\alpha_{evap} = 0.1$
	α_{cond} =0.0
Case 3	$\alpha_{evap} = 1.0$
	$\alpha_{cond} = 1.0$

seen a large difference between both cases regarding the concentration of Na at the surface. Even if both cases have the same evaporation coefficient the null condensation coefficient, for case 2, does not allow for this species to condensate. The species Na^+ is not a direct product from the evaporation but instead from the ionization of Na. The choice of a different condensation/evaporation coefficient not only influences the ablation rate but also changes the behaviour of the shock layer increasing substantially the electron concentration. The low ionization coefficient for this type of species leads to a fast ionization making the electron concentration a the wall different than zero, which can make an impact to the material (material electric conductivity). Moreover due to the high evaporation rate of Na for the case 2, the composition becomes strongly ionized close to the wall.

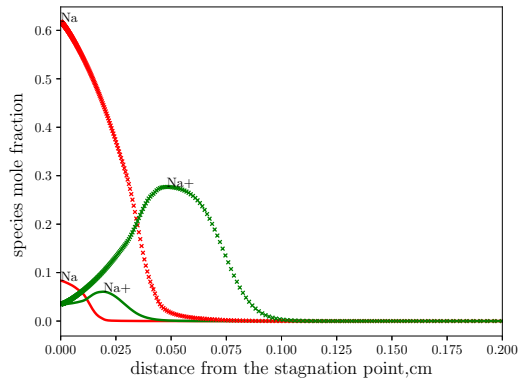

Figure 6: Evaporated species along the stagnation streamline; —— case 1, , $*$ case 2

In figure 7 the temperature profile along the stagnation streamline is shown. The shock translation temperature reaches a maximum of 70000 followed by a decrease to a plateau of 12000 K where both the internal and translational reaches equilibrate. This decrease is due to a transfer of energy between translational to internal mode caused by chemical reactions of dissociation and ionization. For the case 1 the shock is roughly located at 0.7 cm while for the case 2 it is slight shifted upstream. The thermal boundary layer is also affected. These effects are a consequence of a stronger blowing rate from the material shown in table 2.

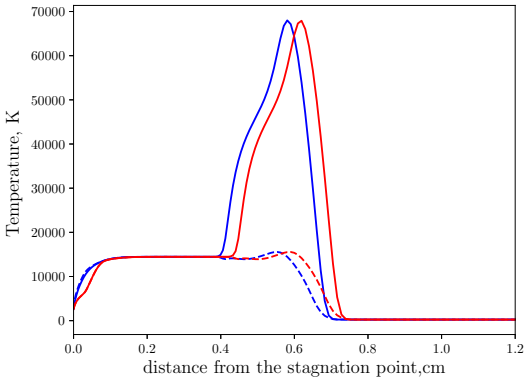

Figure 7: Temperature profile along the stagnation streamline at 60 km; —— translational temperature, −− internal temperature; case 1, case 2

For case 1 and 3 the evaporation rates are similar (around 10 % of Na at the surface, fig 8). The blowing rates for the evaporated species are slightly higher for the case 3, when compared with case 1, explaining why the concentration of Na is higher leading also to a higher ionization. Even though in the case 3 the evaporation coefficient is ten times higher than case 1 also the condensation coefficient follows the same trend. Meaning a balance between evaporation/condensation fluxes is established.

In figure 9 the temperature profile for both case 1 and 3 are shown. The difference at the thermal boundary layer is quite small and the position of the shock for case 3 is slightly shifted upstream due to a higher blowing rate

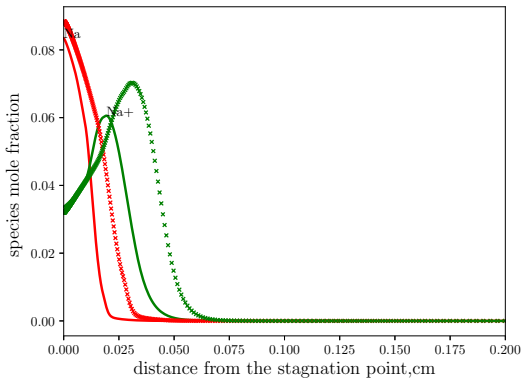

Figure 8: Evaporated species along the stagnation streamline; —— without radiation, , $*$ with radiation

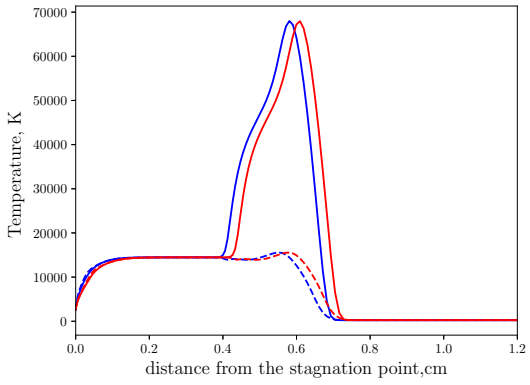

Figure 9: Temperature profile along the stagnation streamline at 60 km; —— translational temperature, −− internal temperature; case 1, case 3

Table 2: Blowing rates for major species

Case #	blowing rates
Case 1	$\dot{m}_{Na} = 0.133 \times 10^{-1}$
	$\dot{m}_{NaO} = 0.296 \times 10^{-2}$
	$\dot{m}_{SiO} = 0.597 \times 10^{-2}$
Case 2	$\dot{m}_{Na} = 0.226$
	$\dot{m}_{NaO} = 0.232 \times 10^{-2}$
	$\dot{m}_{SiO} = 0.597 \times 10^{-2}$
Case 3	$\dot{m}_{Na} = 0.119 \times 10^{-1}$
	$\dot{m}_{NaO} = 0.218 \times 10^{-1}$
	$\dot{m}_{SiO} = 0.297 \times 10^{-2}$

3.2. Radiation coupling with the flow

The final analysis was to include radiative source terms and to compare a 1 dm to a 1 m radius OC at the same conditions as the case 1 mentioned above

In figure 10 the temperature profile is shown. he shock position is roughly located at 0.6 cm showing a smaller shock layer when compared to the non-radiative case (fig 7) for the same conditions. The reduction of the shock layer is explained by a cooling down due to a strong emission (also observed by the equilibrium plateau after the shock). The highly excited particles emit photons in all the directions due to a decrease of the electronic levels. The emitted photons is absorbed by thermal boundary layer (increasing the internal energy of the particles) and also by the free-stream. A departure of non-equilibrium is also observed in the free-stream, where the internal temperature is higher than the translational. Since the atmosphere at 60 km is optically thin, this departure of non-equilibrium is observed up to 12 cm way from the surface. Once the free-stream particles absorbs this energy it result in photochemical processes such as photoionization and photodissociation.

The consequence of the photochemical processes is shown by fig. 11 where free stream is no longer formed by only N_2 and O_2 but also atoms and ions.

The effects of the shock layer coll down is also seen by fig 12. For a non-radiative field a constant plateau until the thermal boundary layer is expect for the species composition, meaning chemical equilibrium, which in this case is not observed.

For a bigger radius the radiation effects become stronger. For the 1 m radius body this departure is strong enough to have an exchange of energy between the internal and translation mode rising the translation temperature (fig. 13). The non-equilibrium departure

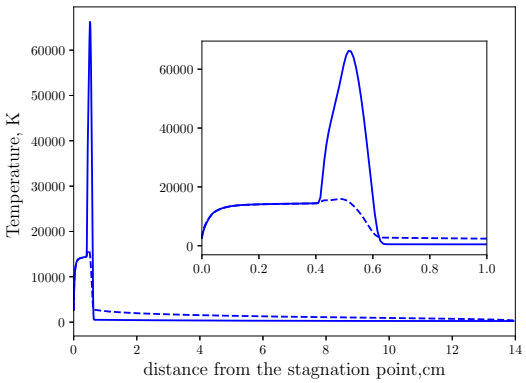

Figure 10: Temperature profile along the stagnation streamline at 60 km for 0.1 meter; —— translational temperature, −− internal temperature

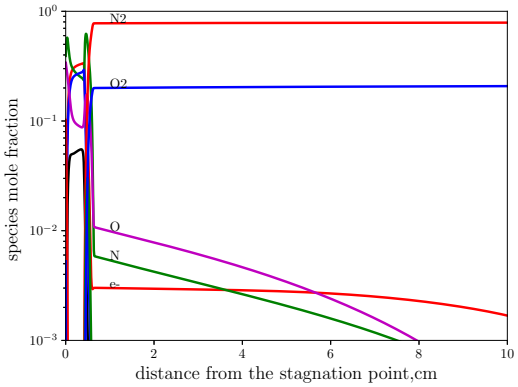

Figure 11: Air composition along the stagnation streamline at 60 km for 0.1 meter (log scale)

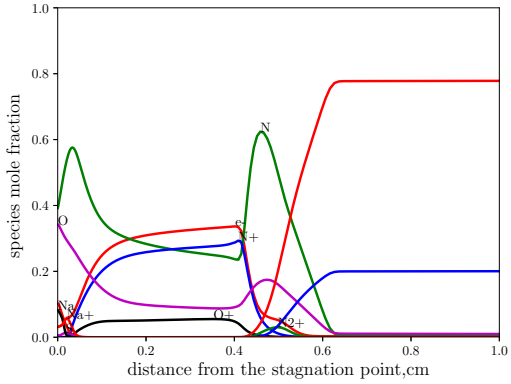

Figure 12: Air composition along the stagnation streamline at 60 km for 0.1 meter

becomes more pronounced than for the smaller radius.

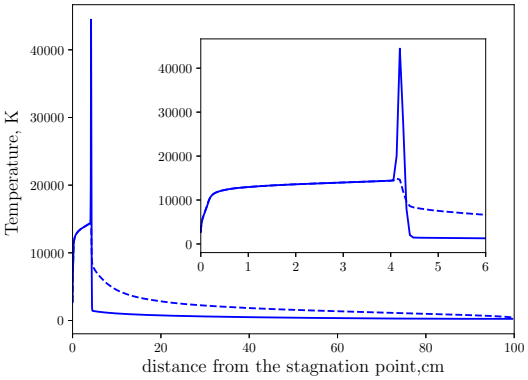

Figure 13: Temperature profile along the stagnation streamline at 60 km for 1 meter; —— translational temperature, −− internal temperature

This rise of the translation temperature leads to a strong dissociation of O_2 (fig 14) since the chemical rate is controlled by a geometrical temperature $T = \sqrt{TT_i}$.

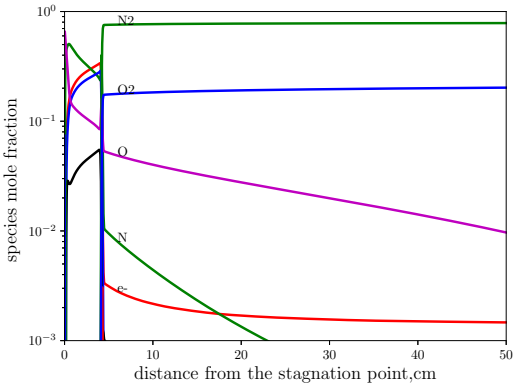

Figure 14: Air composition along the stagnation streamline at 60 km for 1 meter (log scale)

The composition of the shock layer is also shown in fig 15 where the chemical non-equilibrium becomes also stronger.

In terms of evaporation rate not substantially differences were noticed comparing with the non-radiative flow because the surface temperature was imposed to be same for all the cases. In reality the surface temperature should be estimated by an surface energy balance (SEB), similar to the surface mass balance. For

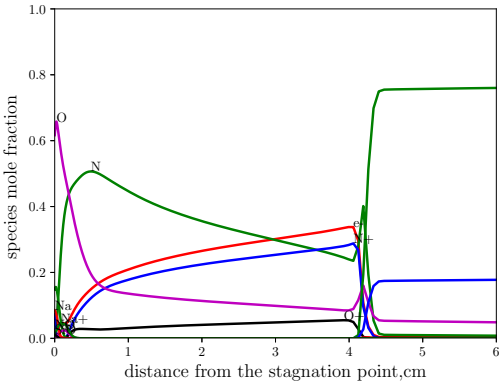

Figure 15: Air composition along the stagnation streamline at 60 km for 1 meter

the calculation of the SEB the incoming radiative flux will enter to the balance which might change significantly the surface temperature, deepening how strong the radiative field is.

4. Conclusion

A model to study the meteor ablation at low altitude has been proposed and implemented. The chosen parameters (trajectory, entry velocity and material size) were selected arbitrarily with the purpose of presenting a different approach from the one proposed by the state of the art. The model takes the clue from the strategy used to evaluate the gas-surface interaction on the heat shields of re-entry capsules.

The first step was to gather thermodynamic properties for the metallic species produced by evaporation. Taking the full electronic levels can become computationally expensive when used by CFD solvers. A reduction method was presented which has shown to preserve its accuracy when compared with the full data set.

An evaporation model based on kinetic-theory was also presented. Do to the kinetic nature of the evaporation processes, approximations are made when extended to macroscopic properties. A sensitivity analysis was made to the evaporation and condensation coefficients from the Knudsen-Langmuir law. These coefficients range from 0 to 1 and not big difference was observed when both coefficients are the same for lowest and highest bond. On the other hand if both coefficients are different a significant effects is observed in the flow field.

In this work a flow/radiation/ablation methodology was presented to study the meteor entry. It was observed that a stronger radiative field for bigger bodies which explains the stronger luminosity for bolides. For both radii it was observed a decrease of temperature in the shock layer due to the radiant emission increasing of the heat flux at the surface. The radiative field becomes stronger for the 1 m case due to a larger shock layer. The ablation rate did not change significantly since the wall temperature as chosen to be the same as the first analysis. Interestingly, due to the strong shock emission the flow upstream of the shock undergoes photochemical processes. These processes leads to photoionization and photodissociation reactions increasing the electron density. In our case only photoionization mechanisms are considered. Moreover a departure from thermal equilibrium is also observed in the free-stream. In this case the surface energy balance was not considered. Further analyses will be made to compute the energy balance considering the incoming radiative flux to the surface.

Acknowledgments

This research is sponsored by the Belgian Research Action Through Interdisciplinary Networks “METRO: Meteor trajectories and origins”. Research of B. Dias is sponsored by fellowship from the “Fonds pour la Formation à la Recherche dans l’Industrie et dans l’Agriculture.”.

References

[1] Z. Ceplecha, J. Borovicka, W. Elford, D. ReVelle, R. Hawkes, V. Porubcan, M. Simek, Meteor phenomena and bodies, Space Science Reviews 84 (3-4) (1998) 327–471.

[2] O. P. Popova, P. Jenniskens, V. Emel’yanenko, A. Kartashova, E. Biryukov, S. Khaibrakhmanov, V. Shuvalov, Y. Rybnov, A. Dudorov, V. I. Grokhovsky, et al., Chelyabinsk airburst, damage assessment, meteorite recovery, and characterization, Science 342 (6162) (2013) 1069–1073.

[3] N. Laurendeau, Statistical thermodynamics: fundamentals and applications, Cambridge University Press, 2005.

[4] A. D. Mario Capitelli, Gianpiero Colonna, Fundamental Aspects of Plasma Chemical Physics: Thermodynamics, 1st Edition, Springer Series on Atomic, Optical, and Plasma Physics 66, Springer-Verlag New York, 2012.

[5] T. E. Magin, M. Panesi, A. Bourdon, R. L. Jaffe, D. W. Schwenke, Coarse-grain model for internal energy excitation and dissociation of molecular nitrogen, Chemical Physics 398 (2012) 90 – 95.

[6] Atomic spectra database, https://www.nist.gov/pml/atomic-spectra-database.

[7] J. Scoggins, T. Magin, The gibbs function continuation method for linearly constrained multiphase equilibria, Combustion and Flame 162 (12) (2015) 4514–4522.

[8] B. J. McBride, S. Gordon, M. A. Reno, Thermodynamic data for fifty reference elements, NASA TP-3287-REV1, Glenn Research Center, Cleveland, Ohio (February 2001).

[9] J. Lamet, P. Rivière, M. Perrin, A. Soufiani, Narrow-band model for nonequilibrium air plasma radiation, Journal of Quantitative Spectroscopy and Radiative Transfer 111 (1) (2010) 87–104.

[10] J. Scoggins, L. Soucasse, P. Riviere, S. Soufiani, T. Magin, Coupled flow, radiation, and ablation simulations of atmospheric entry vehicles using the hybrid statistical narrow band model, in: 45th AIAA Thermophysics Conference, Dallas, Texas, 2015, AIAA 2015–3112.

[11] L. Schaefer, B. Fegley, A thermodynamic model of high temperature lava vaporization on io, Icarus 169 (2004) 216–241.

[12] Y. Zudin, Non-equilibrium evaporation and condensation processes : analytical solutions, Mathematical engineering, Springer, 2017.

[13] T. Ytrehus, S. Østmo, Kinetic theory approach to interphase processes, International Journal of Multiphase Flow 22 (1) (1996) 133 – 155.

[14] R. Marek, J. Straub, Analysis of the evaporation coefficient and the condensation coefficient of water, International Journal of Heat and Mass Transfer 44 (1) (2001) 39 – 53.

[15] A. Frezzotti, P. Barbante, Kinetic theory aspects of non-equilibrium liquid-vapor flows, Mechanical Engineering Reviews.

[16] A. Munafò, T. E. Magin, Modeling of stagnation-line nonequilibrium flows by means of quantum based collisional models, Physics of Fluids 26 (9) (2014) 097102. doi:10.1063/1.4894842.

[17] J. Scoggins, Development of Mutation++: MUlticomponent Thermodynamics And Transport properties for IONized gases library in C++, Tech. Rep. VKI PhD Symposium (2013).

[18] T. E. Magin, G. Degrez, Transport algorithms for partially ionized and unmagnetized plasmas, Journal of Computational Physics 198 (2004) 424–449.

[19] B. Dias, F. Bariselli, A. Turchi, A. Frezzotti, P. Chatelain, T. Magin, Development of a melting model for meteors, AIP Conference Proceedings 1786 (1) (2016) 160004.

Massively Parallel and Robust High-Order Methods for Transitional Hypersonic Flow Modelling on Unstructured Grids Application to Reusable Launcher Stages

Ray Vandenhoeck

PhD Candidate, Aeronautics & Aerospace Department, von Karman Institute for Fluid Dynamics, Belgium, vandenhoeck@vki.ac.be

Supervisor: Andrea Lani

Research Expert, Centre for Mathematical Plasma Astrophysics, KU Leuven, Belgium,
Research Expert, Aeronautics & Aerospace Department, von Karman Institute for Fluid Dynamics, Belgium, lani@vki.ac.be

Supervisor: Johan Steelant

Professor, Department of Mechanical Engineering, KU Leuven, Belgium,
Senior Research Engineer, Aerothermodynamics and Propulsion Analysis Section, ESA-ESTEC, Netherlands, johan.steelant@esa.int

Keywords: high-order computational fluid dynamics, hypersonics, laminar-turbulent transition, reusable launcher stages

First Year Doctoral Summary

During their ascent and descent trajectories, reusable space vehicles travel primarily in the hypersonic regime ($5 < \text{Mach} < 25$) which is characterized by high speeds, strong shocks, chemical dissociation, radiation, viscous interaction, gas-surface interaction, etc. Additionally, along the trajectory, the flow experiences various changes in regimes i.e. laminar, transitional and turbulent. Prediction of the onset and extent of the transition from laminar to turbulent regime is particularly challenging and a main subject of ongoing research activities.

The present project consists in developing a fast parallel flow solver based on Finite Element-type high-order methods. Such methods reduce the computational time considerably and allow for calculating more accurate solutions on relatively coarser computational grids than traditional low-order methods. More specifically, the high-order Flux Reconstruction approach [1] is used. This method provides a unifying framework for other Finite Element-type methods such as Discontinuous Galerkin, Spectral Finite Difference and Spectral Finite Volume. The Flux Reconstruction method is robuster and more economical than the original methods and is particularly well-adapted to massively parallel environments as well as to GPU-enabled computing [2].

Robust shock capturing methods for high-speed flows is the main pacing item for high-order Finite Element-type methods. Two promising schemes are used to stabilize the Flux Reconstruction method in hypersonic flows: the Multi-Dimensional Limiting Process [3] and Localized Laplacian Artificial Viscosity [4].

Furthermore, the novel $\gamma - \alpha$ model [5] to predict the onset and extent of laminar-turbulent transition will be incorporated. This local correlation-based transition model is independent of the turbulence model and can readily be used in parallel environments. Furthermore, this model has been verified in simple hypersonic test cases.

The developed solver will be applied to the hypersonic flow around representative reusable launcher stages, e.g. the Hexafly-INT [6] and IXV [7] vehicles of the European Space Agency. The results will be compared to experimental and flight data. The final result will provide the first open-source high-order solver able to simulate transitional hypersonic flows and will significantly improve the current state-of-the-art of CFD methods for these challenging applications.

Acknowledgment

This research is supported by SB PhD fellowship 1S19918N of the Research Foundation Flanders (FWO).

References

[1] H T Huynh. "A flux reconstruction approach to high-order schemes including discontinuous Galerkin methods". In: *18th AIAA Computational Fluid Dynamics Conference*. 2007.

[2] Jerry E Watkins, Joshua Romero, and Antony Jameson. "Multi-GPU, Implicit Time Stepping for High-order Methods on Unstructured Grids". In: *46th AIAA Fluid Dynamics Conference*. 2016.

[3] Jin Seok Park, Hojun You, and Chongam Kim. "Higher-order multi-dimensional limiting process for DG and FR/CPR methods on tetrahedral meshes". In: *Computers & Fluids* 154 (2017).

[4] ML Yu et al. "Localized artificial viscosity stabilization of discontinuous Galerkin methods for nonhydrostatic mesoscale atmospheric modeling". In: *Monthly Weather Review* 143.12 (2015).

[5] Jeroen Van den Eynde, Johan Steelant, and Andrea Passaro. "Intermittency-based Transition Model with Local Empirical Correlations". In: *21st AIAA International Space Planes and Hypersonics Technologies Conference*. 2017.

[6] Marco Marini et al. "Numerical and Experimental Aerodynamic Characterization of the HEXAFLY-INT Hypersonic Glider". In: *21st AIAA International Space Planes and Hypersonics Technologies Conference*. 2017.

[7] Pietro Roncioni et al. "Experimental and numerical investigation of aerothermal characteristics of hypersonic intermediate experimental vehicle". In: *Journal of Spacecraft and Rockets* 48.2 (2011).

Numerical treatment of the nonconservative product in a multiscale fluid model for plasmas in thermal nonequilibrium: application to solar physics

Quentin Wargnier

CMAP, Ecole polytechnique, CNRS, Université Paris-Saclay, Route de Saclay, 91128 Palaiseau Cedex, quentin.wargnier@polytechnique.edu

Marc Massot

CMAP, Ecole polytechnique, CNRS, Université Paris-Saclay, Route de Saclay, 91128 Palaiseau Cedex, marc.massot@polytechnique.edu

Benjamin Graille

Laboratoire de Mathématiques d'Orsay, Univ. Paris-Sud, CNRS, Université Paris-Saclay, 91405 Orsay, France, benjamin.graille@u-psud.fr

Thierry Magin

von Karman Institute for Fluid Dynamics, Chaussée de Waterloo 72, 1640, Rhode-Saint-Genèse, Belgium, magin@vki.ac.be

Abstract

This contribution is based on the work done by Wargnier *et al.* [16]. The latter deals with the modeling of collisional multicomponent magnetized plasmas in thermal and chemical nonequilibrium aiming at simulating and predicting magnetic reconnections in the chromosphere of the sun. We focus on the numerical simulation of a simplified fluid model in order to properly investigate the influence on shock solutions of a nonconservative product present in the electron energy equation. Then, we derive jump conditions based on travelling wave solutions and propose an original numerical treatment in order to avoid non-physical shocks for the solution, that remains valid in the case of coarse-resolution simulations. A key element for the numerical scheme proposed is the presence of diffusion in the electron variables, consistent with the physically-sound scaling used in the model developed by Graille *et al.* following a multiscale Chapman-Enskog expansion method [M3AS, 19 (2009) 527–599]. The numerical strategy is eventually assessed in the framework of a solar physics test case. The computational method is able to capture the travelling wave solutions in both the highly- and coarsely-resolved cases.

Keywords: Fluid model from kinetic theory, plasma out of thermal equilibrium, solar physics, nonconservative product, shock wave, travelling wave, jump conditions, finite volume schemes.

1. Introduction

This contribution deals with the modeling of collisional multicomponent magnetized plasmas in thermal and chemical nonequilibrium, aiming at simulating and predicting magnetic reconnections in the chromosphere of the sun. If multicomponent Magneto-HydroDynamic (MHD) simulations are still scarce in solar physics, in recent years, the study of partially ionized plasmas has become an important topic because solar structures, such as prominences [1] as well as layers of the solar atmosphere (photosphere and chromosphere) [2; 3], are made of partially ionized plasmas. Multicomponent plasmas introduce physical effects which are not described by means of models for fully ionized mixtures, *i.e.*, Cowling's resistivity, isotropic thermal conduction, heating due to ion-neutral friction, heat transfer due to collisions, charge exchange, and ionization, which are important to better understand the behavior of plasmas in the sun chromosphere.

In this context, Graille *et al.* [4] have derived from kinetic theory a model for multicomponent plasmas in thermal nonequilibrium accounting for the influence of the electro-magnetic field, that can be applied to the sun chromosphere conditions. The model is obtained by seeking a generalized Chapman-Enskog solution

to the Boltzmann equation using a multiscale perturbation method. These developments provide a model with an extended range of validity from partially- to fully-ionized plasmas, for the non-, weakly-, and strongly- magnetized regimes, together with an entropy inequality and Onsager reciprocity relations for the transport properties. At the zeroth order of the expansion, this development yields a hyperbolic system of equations with a parabolic regularization of the electron variables due to dissipative terms such as the electron diffusion velocity and heat flux. When weak solutions (shocks) are considered, the total energy equation is used regarding its conservative form suitable for the development of a numerical scheme. Both the electron and heavy-particle energy equations exhibit non conservative terms leading to some numerical difficulties. Although our model directly inspired from [4] is well identified and applicable to the sun chromosphere conditions, it is still necessary to understand how to treat the nonconservative term present in the hyperbolic convection part of the system.

Indeed, solving nonconservative hyperbolic systems is a delicate problem because of the definition of weak admissible solutions. First, from a theoretical point of view, Dal Maso *et al.* have proposed in [5] a new theory to define nonconservative products based on the intoduction of paths, that generalizes in the sense of distributions the notion of weak solution for conservative systems. In this context, Parès [6] have developed path-conservative schemes for nonconservative hyperbolic systems. However, it has been proved by Abgrall and Karni [7] that these numerical schemes fail to converge to the right solutions. In fact, even if the correct path is known, the numerical solution obtained can be far from the expected solution, depending mainly on the numerical dissipation of the scheme. In [8], Chalons and Coquel have proposed a different strategy for nonconservative hyperbolic systems using Roe-type conservative schemes. Even if progress has been made in the field, the design of accurate and efficient schemes for shock solutions to nonconservative systems of equations and their numerical analysis still lacks completeness. More specifically, in the field of plasma physics, the problem has already been investigated. Coquel and Marmignon [9] have replaced the equation of thermal energy of electrons by an equation of conservation of entropy for a model applicable to weakly ionized hypersonic flows in thermal non-equilibrium. Candler and MacCormack [10] have considered the nonconservative product in the equation of thermal energy for electrons as a source term for a model applicable to weakly ionized flows. These methods lead to conservative system of equations where the structure of the shock waves is identified, but the link with the original system of equations is still incomplete. In [11], [12], Lowrie *et al.* have defined semi-analytic solutions for planar radiative shock waves, which can be used for verifying codes for thermal equilibrium diffusion-radiation models. Besides, in references [13] by Shafranov, [14] by Zel'dovich and Raizer, and [15] by Mihalas and Mihalas, the shock wave structure has been identified for a nonequilibrium fully ionized plasma. Even if we know what to expect in terms of physics, such waves structure and jump conditions have not been obtained in the framework of a one-fluid model exhibiting a nonconservative product. In summary, no fully satisfactory solution has yet been achieved to handle both theoretically and numerically the nonconservative product appearing in a one-fluid model and it remains an open problem.

We focus on the model derived by Graille *et al.* [4] at the zeroth order of the Chapman-Enskog expansion. First, we identify a simplified model, which inherits the same difficulty of dealing with nonconservative products and proper shock numerical solution as the original system, but which is tractable mathematically. A decoupling of the governing equations is proposed and we look for piecewise smooth traveling wave solutions to the decoupled problem, as it is coherent with [14; 13]. This analysis leads to a complete analytical solution, as well as an explicit expression of the missing jump relation for the thermal energy of electrons. The ability of conducting the full analysis strongly relies on a regularizing effect in the electron variables at this order of the expansion. For the numerical solution, we first use a standard finite volume Godunov scheme based on a consistent discretization of the nonconservative product, in order to resolve the traveling wave. When the level of resolution is too coarse, some artificial and non-physical additional shock appears in the solution, whereas for fine resolution, the proper and expected travelling wave solution is reproduced. We thus identify the characteristic scales associated with the compatibility conditions related to the analytic solution for the travelling wave in order to define the limit between the coarse and fine resolutions. A new scheme based on a specific treatment of the nonconservative product is developed to verify the compatibility equations in a discretized sense. It is able to capture the proper travelling wave even in weakly-resolved cases without

generating unexpected additional and artificial numerical shocks. The proposed numerical strategy is assessed for a travelling wave test case based on the sun chromosphere conditions, for which the characteristic scales are identified and for which the resolution of the finest diffusion scales is out of reach. Using the new scheme combined to a Strang operator splitting technique, we obtain an accurate resolution of the test case with two main advantages: we do not have to resolve the smallest diffusion spatial scales, and the timestep is not limited by the Fourier stability condition based on the largest diffusion coefficient. Following the work in [16], we eventually investigate the structure of the travelling wave for the original coupled system of equations and prove that: 1- the structure is similar to the one of the decoupled problem, which allow us to have a precious insight on the wave structure and jump conditions; and 2- in a regime of Mach numbers close to one, the missing jump condition for the decoupled and coupled problems are very close to one another, thus fully justifying our strategy to focus on a simplified problem.

The paper is organized as follows: in Section 2 the model derived by Graille *et al.* [4] is presented and briefly compared to other models used by the solar physics community. Then, the decoupling of the governing equations is discussed. In Section 3, piecewise smooth travelling wave solutions to the decoupled problem are derived, as well as the missing jump condition associated with the equation of thermal energy of electrons. InSection 4, a 1D finite volume Godunov scheme with a standard discretization of the nonconservative product is developed, as well as a new scheme based on a specific treatment of the nonconservative product. In Section 5, a test case based on the sun chromosphere conditions is fully investigated and our numerical strategy assessed.

2. Modeling and governing equations

In this section, we present a multiscale and multicomponent one-fluid model and explain its advantages and differences compared to the conventional models that are used for describing collisional plasmas in thermal non-equilibrium, such as those found in the sun chromosphere. We identify a simplified system of equations, which reproduces the difficulty due to the nonconservative product encountered in the general model. An approximation of this system will allow us to conduct analytical studies in 3 and also to highlight the proper paths in the theoretical approach.

2.1. One simplified model for solar physics

The non-equilibrium model is developed based on a thorough kinetic theory derivation by Graille *et al.* [4]. It is a generalized Chapman-Enskog solution to the Boltzmann equation by means of a multiscale perturbation method. To achieve a fluid limit, the Knudsen number is assumed to scale as a small parameter ε equal to the square root of the ratio of electron mass to a characteristic heavy-particle mass, that drives thermal non-equilbrium. The model is general and can be used for multicomponent, non- to weakly- and strongly-ionized plasmas including reactive binary collisions between species.

Considering the level of complexity of the general model shown in [4] that we propose to use for solar physics applications, some simplified model is now introduced. We consider the system of equations associated to the zeroth-order of the Chapman-Enskog expansion, where neither Soret-Dufour effects nor electromagnetic forces have been considered. Thermal energy relaxation and chemical processes are assumed to be negligible. Both heavy particles (multiple species can be considered) and electrons have a common adiabatic coefficient $\gamma = 5/3$, since the internal energy modes are neglected. While diffusion can be anisotropic in the strongly magnetized case, we assume isotropic diffusion since no magnetic field is present. The electron diffusion coefficient and thermal conductivity are assumed to be constant. Under these assumptions, the simplified system of equations is made up of the conservation equations for the heavy-particle mass, mixture momentum and total energy, and the electron mass and thermal energy. In nondimensional form (assuming a unit reference Mach number, see [4]), this system reads:

$$
\left\{
\begin{aligned}
&\partial_t \rho_{\mathfrak{h}} + \boldsymbol{\partial_x}\cdot(\rho_{\mathfrak{h}}\boldsymbol{v}_{\mathfrak{h}}) = 0,\\
&\partial_t(\rho_{\mathfrak{h}}\boldsymbol{v}_{\mathfrak{h}}) + \boldsymbol{\partial_x}\cdot(\rho_{\mathfrak{h}}\boldsymbol{v}_{\mathfrak{h}}\otimes\boldsymbol{v}_{\mathfrak{h}} + p\mathbb{I}) = 0,\\
&\partial_t\mathcal{E} + \boldsymbol{\partial_x}\cdot(\mathcal{E}\boldsymbol{v}_{\mathfrak{h}} + p\boldsymbol{v}_{\mathfrak{h}}) = \boldsymbol{\partial_x}\cdot(\lambda\boldsymbol{\partial_x}T_{\mathfrak{e}} + \tfrac{\gamma}{\gamma-1}D\boldsymbol{\partial_x}p_{\mathfrak{e}}),\\
&\partial_t\rho_{\mathfrak{e}} + \boldsymbol{\partial_x}\cdot(\rho_{\mathfrak{e}}\boldsymbol{v}_{\mathfrak{h}}) = \boldsymbol{\partial_x}\cdot(D\tfrac{1}{T_{\mathfrak{e}}}\boldsymbol{\partial_x}p_{\mathfrak{e}}),\\
&\partial_t(\rho_{\mathfrak{e}}e_{\mathfrak{e}}) + \boldsymbol{\partial_x}\cdot(\rho_{\mathfrak{e}}e_{\mathfrak{e}}\boldsymbol{v}_{\mathfrak{h}}) = -p_{\mathfrak{e}}\boldsymbol{\partial_x}\cdot\boldsymbol{v}_{\mathfrak{h}}\\
&\qquad\qquad + \boldsymbol{\partial_x}\cdot(\lambda\boldsymbol{\partial_x}T_{\mathfrak{e}} + \tfrac{\gamma}{\gamma-1}D\boldsymbol{\partial_x}p_{\mathfrak{e}}),
\end{aligned}
\right. \qquad (S)
$$

where quantity $\rho_{\mathfrak{h}}$ stands for the heavy-particle density, $\boldsymbol{v}_{\mathfrak{h}}$ the heavy-particle velocity, p the mixture pressure, $\mathcal{E}$ the mixture total energy, λ the electron thermal conductivity, $T_{\mathfrak{e}}$ the electron temperature, D the electron diffusion coefficient, $p_{\mathfrak{e}}$ the electron pressure, $\rho_{\mathfrak{e}}$ the electron density, $\rho_{\mathfrak{e}}e_{\mathfrak{e}}$ the electron thermal energy. Notice that the mixture pressure is com-

posed of both the electron and heavy-particle partial pressures $p = p_e + p_h$, obeying the perfect gas law $p_e = (\gamma-1)\rho_e e_e$, $p_h = (\gamma-1)\rho_h e_h$, where $\rho_h e_h$ is the heavy-particle thermal energy. The mixture total energy $\mathcal{E}$ is defined as $\mathcal{E} = \rho_h |\boldsymbol{v}_h|^2/2 + p/(\gamma-1)$. The term $-p_e \boldsymbol{\partial_x}\cdot\boldsymbol{v}_h$ in the electron energy equation is a nonconservative product examined in great details in this paper. The simplified model S inherits the difficulty of dealing with nonconservative products and proper shock numerical solution from the original system, but it remains mathematically tractable.

2.2. Structure of the system

System S is hyperbolic in the open set of admissible states $\Omega = \{\rho_h > 0, \quad \rho_e > 0, \quad \boldsymbol{v}_h \in \mathbb{R}^3, \quad p > 0, \quad p_e > 0\}$ with a parabolic regularization on the electron variables. For any direction defined by the unit vector $\boldsymbol{n}$, the matrix $\boldsymbol{n}\cdot\mathbf{A}$, where $\mathbf{A}$ is the Jacobian matrix of the hyperbolic part (removing the second order diffusion terms) is shown to be diagonalizable with real eigenvalues and a complete set of eigenvectors. The eigenvalue $\boldsymbol{v}_h\cdot\boldsymbol{n}$ is linearly degenerate of multiplicity $d+2$, where d is the space dimension, and the eigenvalues $\boldsymbol{v}_h\cdot\boldsymbol{n}\pm c$ are genuinely nonlinear, where c is the sound speed defined by $c = \sqrt{\gamma p/\rho_h}$. Electrons participate in the momentum balance through the pressure gradient. As a result, the sound speed includes as well the electron contribution to the pressure. In system S, the heavy-particle velocity is chosen as the reference frame velocity instead of the mixture hydrodynamic velocity. Finally, the structure of the entropy is well identified, so the second law of thermodynamics is satisfied.

We recall that the equation of electron thermal energy is nonconservative in system S. This leads to the difficulties mentioned in the introduction when looking for discontinuous solutions to the hyperbolic part of the problem. For shock wave solutions, one possibility would be to transform the system S into a conservative system. For instance, the equation of electronic thermal energy can be exchanged with a conservative equation for the electron entropy [9]. This method works only for smooth solutions when there is no dissipation in the electron energy equation. Another possibility would be to consider the nonconservative product as a source term [10]. However, this strategy modifies the eigenstructure of the system and, as a consequence, the electronic temperature remains constant through a shock wave. Our approach is different: we want to make use of the sound structure of system S in order to derive general jump conditions involving neither simplifications nor modifications of the system.

2.3. Approximate decoupled problem

This section is devoted to an approximate decoupled system obtained by removing the electronic diffusion in the conservation equation for the total energy. This modified system is so-called decoupled since the first three conservation equations constitute the Euler system and the electronic equations are then solved, once the heavy part velocity $\boldsymbol{v}_h$ is known. We derive analytical expressions for travelling wave solutions. The wave structure of the decoupled problem obtained will be shown to be very close to the fully coupled problem of system S in a Mach number regime close to 1, shedding some light on the structure of travelling wave solutions for the fully coupled system.

The approximate decoupled system splits then into the Euler system

$$\begin{cases} \partial_t(\bar\rho_h) + \boldsymbol{\partial_x}\cdot(\bar\rho_h\bar{\boldsymbol{v}}_h) = 0, \\ \partial_t(\bar\rho_h\bar{\boldsymbol{v}}_h) + \boldsymbol{\partial_x}\cdot(\bar\rho_h\bar{\boldsymbol{v}}_h\otimes\bar{\boldsymbol{v}}_h + \bar p\mathbb{I}) = 0, \\ \partial_t\bar{\mathcal{E}} + \boldsymbol{\partial_x}\cdot(\bar{\mathcal{E}}\bar{\boldsymbol{v}}_h + \bar p\bar{\boldsymbol{v}}_h) = 0, \end{cases} \qquad (\bar S_1)$$

and a nonconservative drift-diffusion system

$$\begin{cases} \partial_t\bar\rho_e + \boldsymbol{\partial_x}\cdot(\bar\rho_e\bar{\boldsymbol{v}}_h) = \boldsymbol{\partial_x}\cdot(\frac{1}{\bar T_e} D\boldsymbol{\partial_x}\bar p_e), \\ \partial_t(\bar\rho_e\bar e_e) + \boldsymbol{\partial_x}\cdot(\bar\rho_e\bar e_e\bar{\boldsymbol{v}}_h) = -\bar p_e\boldsymbol{\partial_x}\cdot\bar{\boldsymbol{v}}_h \\ \qquad\qquad + \boldsymbol{\partial_x}\cdot(\lambda\boldsymbol{\partial_x}\bar T_e + \frac{\gamma}{\gamma-1}D\boldsymbol{\partial_x}\bar p_e). \end{cases} \qquad (\bar S_2)$$

The mixture pressure is introduced as before, $\bar p = \bar p_e + \bar p_h$, with the partial pressures $\bar p_e = (\gamma-1)\bar\rho_e\bar e_e$, $\bar p_h = (\gamma-1)\bar\rho_h\bar e_h$. We also have $\bar p_e = \bar\rho_e\bar T_e$. The mixture total energy is given by $\bar{\mathcal{E}} = \bar\rho_h|\bar{\boldsymbol{v}}_h|^2/2 + \bar p/(\gamma-1)$. One can find a global solution to this decoupled problem. The first part $\bar S_1$ admits discontinous solutions for which the discontinuity is propagating with the velocity prescribed by the usual Rankine-Hugoniot jump relations and Lax's condition. One can then calculate a solution to the sub-system of electron $\bar S_2$ as one piecewise smooth travelling wave, and determine the missing jump condition, with a heavy-particle velocity field previously solved from system $\bar S_1$.

3. Jump relations and travelling wave solutions to the approximate decoupled problem

In this section, we determine travelling wave solutions for the system $\bar S_2$, being given the velocity

$\bar{\boldsymbol{v}}_\mathfrak{h}$ as a piecewise constant function. The variables $(\bar{\rho}_\mathfrak{h}, \bar{\rho}_\mathfrak{h}\bar{\boldsymbol{v}}_\mathfrak{h}, \bar{\mathcal{E}})$ are assumed to be a shock wave solution to the Euler System $\bar{S}_1$ with velocity σ, which satisfies the Rankine-Hugoniot jump relations and the Lax entropy condition. We are subsequently looking for a piecewise smooth travelling wave solution in the variables $(\bar{\rho}_\mathfrak{e}, \bar{e}_\mathfrak{e})$, moving with the same velocity σ, solution to the system $\bar{S}_2$. Since the electron variables experience nonlinear heat and mass diffusion, their profile is expected to exhibit only weak discontinuities, that is discontinuities in their gradients. We derive boundary conditions at left and right infinities and show that they do not depend on the (constant) diffusion coefficients λ and D, hence they can be used as jump conditions associated with the electronic variables $\bar{\rho}_\mathfrak{e}$ and $\bar{\rho}_\mathfrak{e}\bar{e}_\mathfrak{e}$. It is consistent with the work of Zel'dovich and Raizer in [14]. A onedimensional case (d=1) is considered.

We consider that the heavy-particle variables read as piecewise constant functions depending only on $\xi = \boldsymbol{x}\cdot\boldsymbol{n} - \sigma t$ with $\sigma > 0$ and $\boldsymbol{n}$, a unit vector in the first direction, such that $\boldsymbol{x}\cdot\boldsymbol{n} = x$. The same notation is used for functions depending on time and space and for functions depending on ξ as there is no ambiguity. Superscript R denotes the right state and L denotes the left state. For example, the density and hydrodynamic velocity of heavy particle are defined as

$$\bar{\rho}_\mathfrak{h}(\xi) = \begin{cases} \bar{\rho}_\mathfrak{h}^\mathrm{L} & \text{if } \xi < 0, \\ \bar{\rho}_\mathfrak{h}^\mathrm{R} & \text{if } \xi > 0, \end{cases} \quad \bar{\boldsymbol{v}}_\mathfrak{h}(\xi) = \begin{cases} \bar{\boldsymbol{v}}_\mathfrak{h}^\mathrm{L} & \text{if } \xi < 0, \\ \bar{\boldsymbol{v}}_\mathfrak{h}^\mathrm{R} & \text{if } \xi > 0, \end{cases} \tag{1}$$

We consider a 3-shock wave that propagates at velocity $\sigma > 0$. The case of a 1-shock wave is symmetric and can be solved in a similar way.

Based on the sub-system of electrons $\bar{S}_2$, we look for piecewise smooth travelling wave for the electron variables that propagate at the velocity σ. More precisely, the functions $\bar{\rho}_\mathfrak{e}$ and $\bar{p}_\mathfrak{e}$ solutions to $\bar{S}_2$ are assumed to satisfy

- $\bar{\rho}_\mathfrak{e} : \xi \mapsto \bar{\rho}_\mathfrak{e}(\xi) \in C^0(\mathbb{R})$, $\bar{p}_\mathfrak{e} : \xi \mapsto \bar{p}_\mathfrak{e}(\xi) \in C^0(\mathbb{R})$,
- $\bar{\rho}_\mathfrak{e}$ and $\bar{p}_\mathfrak{e}$ are C^∞ on $(-\infty, 0)$ and $(0, +\infty)$,
- $\bar{\rho}_\mathfrak{e}$ and $\bar{p}_\mathfrak{e}$ admit limits in $\pm\infty$ denoted by

$$\lim_{\xi\to-\infty} \bar{\rho}_\mathfrak{e}(\xi) = \bar{\rho}_\mathfrak{e}^\mathrm{L}, \lim_{\xi\to+\infty} \bar{\rho}_\mathfrak{e}(\xi) = \bar{\rho}_\mathfrak{e}^\mathrm{R}, \lim_{\xi\to\pm\infty} \bar{\rho}_\mathfrak{e}'(\xi) = 0,$$
$$\lim_{\xi\to-\infty} \bar{p}_\mathfrak{e}(\xi) = \bar{p}_\mathfrak{e}^\mathrm{L}, \lim_{\xi\to+\infty} \bar{p}_\mathfrak{e}(\xi) = \bar{p}_\mathfrak{e}^\mathrm{R}, \lim_{\xi\to\pm\infty} \bar{p}_\mathfrak{e}'(\xi) = 0.$$

The goal of this section is to exhibit the structure of these solutions in order to understand the relations between the left and right states according to the travelling wave velocity σ and structure of the diffusion (in particular the value of the coefficients D and λ). We assume that the right state R is known, and we look for state L connected to the state R. For the purpose of the work, we do not exhibit the full resolution of the system. Further details can be found in [16].

After some algebra the system $\bar{S}_2$ of partial differential equations becomes a system of ordinary differential equations. Finally, for $\xi > 0$ one gets an analytical expression of the solution that combines decreasing exponential functions. Moreover, for $\xi < 0$, similar algebraic relations as those found in the case $\xi > 0$ are obtained by replacing state R by state L. It leads to similar eigenvalues by replacing state R by state L. However, the only way for having a non diverging solution is to get constant functions equal to the left constant state L. Indeed, the only bounded solutions when ξ goes to $-\infty$ are constant solutions.

At $\xi = 0$, since $\bar{p}_\mathfrak{e}$ and $\bar{\rho}_\mathfrak{e}$ (and $\bar{T}_\mathfrak{e}$) are continuous functions, the system $\bar{S}_2$ leads to

$$[\bar{p}_\mathfrak{e}']_{(0)} = \tfrac{1}{L_D}\bar{p}_\mathfrak{e}(0), \qquad [\bar{T}_\mathfrak{e}']_{(0)} = 0. \tag{2}$$

where $[\cdot]_{(0)}$ denotes for the value of the jump in $\xi = 0$, $L_D = D/[\bar{\boldsymbol{v}}_\mathfrak{h}]_{(0)}$, $L_\lambda = (\gamma-1)\lambda\bar{\rho}_\mathfrak{e}^\mathrm{R}/\gamma\,[\bar{\boldsymbol{v}}_\mathfrak{h}]_{(0)} = \kappa^\mathrm{R}/\,[\bar{\boldsymbol{v}}_\mathfrak{h}]_{(0)}$, κ^R is the electron thermal diffusivity. In this context, since $\bar{p}_\mathfrak{e}$ is continuous and the derivative $\bar{\boldsymbol{v}}_\mathfrak{h}'$ has a jump at $\xi = 0$, the nonconservative product is not ambiguous. The second relation of Eq. 2 provides the continuity of the derivative of $T_\mathfrak{e}$ in the discontinuity (at $\xi = 0$). In other words, $T_\mathfrak{e}$ is a C^1 function. This result is consistent with the work of Zel'dovich and Raizer in [14], showing that the temperature of electron is smooth in the shock wave of a nonequilibrium fully ionized plasma. Moreover, the first relation of Eq. 2 can be seen as a relation between the jump of the pressure gradient in the discontinuity, the jump of the velocity and the diffusion coefficient D. This result is also consistent with the work of Zel'dovich and Raizer in [14], showing that the discontinuity of the shock wave in a plasma depend on the dissipative process.

The jump compatibility relations for the pressure of electron $\bar{p}_\mathfrak{e}$ and for the electron temperature $\bar{T}_\mathfrak{e}$ link the states R and L at infinity. They are obtained by integrating the system of ordinary differential equations (further details in [16]) from 0^+ to ∞. One gets

$$\frac{\bar{p}_\mathfrak{e}^\mathrm{L}}{\bar{p}_\mathfrak{e}^\mathrm{R}} = \frac{(\gamma+1)M_\mathrm{R}^2}{(1-\gamma)M_\mathrm{R}^2 + 2\gamma}, \quad \frac{\bar{T}_\mathfrak{e}^\mathrm{L}}{\bar{T}_\mathfrak{e}^\mathrm{R}} = \frac{(\gamma-1)M_\mathrm{R}^2 + 2}{(1-\gamma)M_\mathrm{R}^2 + 2\gamma}, \tag{3}$$

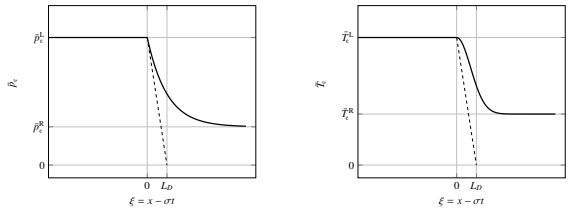

Figure 1: Scheme of the travelling wave with the characteristic diffusion length L_D

where $M_R = (\sigma - \bar{v}_b^R)/c^R$. The state L at infinity does not depend on the diffusion coefficients D and λ. Let us underline however that the relations of Eq. 3 are valid only for $M_R^2 < 2\gamma/(\gamma-1)$, and a singularity is present when M_R goes to $\sqrt{2\gamma/(\gamma-1)}$. Thus, the obtained relations are valid for a Mach number range close to one. Notice that the jump condition $\bar{\rho}_e^L/\bar{\rho}_e^R$ is the same as for $\bar{\rho}_b^L/\bar{\rho}_b^R$ and is compatible with the Rankine-Hugoniot jump relations.

As a conclusion, by looking for piecewise smooth travelling wave solutions, we were able to get an analytical expression of the missing jump condition associated with the thermal energy of electrons, and the analytical travelling wave solution of the electron variables valid for a Mach number regime close to one. For that purpose, we had to decouple the problem: a discontinuity propagating at velocity σ where the jump conditions are prescribed by the usual Rankine-Hugoniot relations solution to the sub-system $\bar{S}_1$ and a continuous travelling wave propagating at the same velocity σ, solution to the sub-system $\bar{S}_2$. The resulting jump conditions are valid in a neighborhood of Mach one and then lead to a singularity for larger Mach numbers. At the end of this contribution, we will prove that the analytical expression obtained for the decoupled system is a very good approximation in a Mach range close to the one of the jump conditions for the fully coupled problem S.The next step is to verify numerically the jump conditions and if we can capture the analytical travelling waves.

4. Numerical scheme for the decoupled system

In the previous section, we show the existence of a travelling wave for system $\bar{S}_2$. The aim of this section is to develop numerical methods able to capture the dynamic of the travelling wave. First, we introduce a standard scheme based on a finite volume Godunov method with a standard discretization of the nonconservative product and then a specific treatment.

Note that the proposed method to treat the nonconservative term is independant of the chosen finite volume scheme. Numerical experiments for a Lax-Friedrichs scheme and an upwind scheme have been performed and led to the same conclusions.

4.1. Finite volume scheme with a standard discretization for the nonconservative product

The electron variables $\bar{\rho}_e$ and $\bar{\rho}_e\bar{e}_e$ are initialized by using the analytical solution found in the previous section. The heavy variables $\bar{\rho}_b$, $\bar{v}_b$, and $\bar{\mathcal{E}}$ are discontinuities propagating at velocity σ, where the conditions are fixed by the Rankine-Hugoniot conditions.

A monodimensional finite volume Godunov method is used to discretize the electron sub-system $\bar{S}_2$. We consider a finite domain of length L with N cells of length $\Delta x = L/N$. The position of each cell C_j, $1 \le j \le N$ is defined by its center x_j at the middle of the interfaces $x_{j+1/2}$ and $x_{j-1/2}$. The bounds of the domain are not taken into account as the simulations are stopped before any interaction occurs between the travelling wave and the boundary. Left and right Dirichlet conditions are then used. The time is also discretized with a timestep Δt.

We denote by U_j^n, $n \ge 0$, $1 \le j \le N$, the vector of the natural variables at time t^n in the cell C_j $U_j^n = (U_{j,1}^n, U_{j,2}^n) = (\bar{\rho}_{e,j}^n, \bar{\rho}_{e,j}^n \bar{e}_{e,j}^n)$. The general scheme reads

$$U_j^{n+1} = U_j^n - \frac{\Delta t}{\Delta x}(F_{j+1/2}^n - F_{j-1/2}^n) + \frac{\Delta t}{\Delta x}(G_{j+1/2}^n - G_{j-1/2}^n) + N_j^n, \tag{4}$$

where $F_{j\pm1/2}^n$ are the convective fluxes at interfaces $j \pm 1/2$, $G_{j\pm1/2}^n$ the diffusive fluxes at interfaces $j \pm 1/2$, and N_j^n the value of the nonconservative term in the cell j.

The convective flux $F_{j+1/2}^n$ is computed by means of Godunov's scheme, by solving the Riemann problem with the left and the right values given by the cells j and $j+1$ and by taking the value of the flux at the interface. Then, the diffusive flux is calculated by using a second-order centered scheme

$$G_{j+1/2}^n = \frac{1}{\Delta x}\Big(D\frac{\gamma-1}{\bar{T}_{e,j+1/2}^n}(U_{j+1,2}^n - U_{j,2}^n), \\ \lambda(\bar{T}_{e,j+1}^n - \bar{T}_{e,j}^n) + D\gamma(U_{j+1,2}^n - U_{j,2}^n)\Big),$$

where $\bar{T}_{e,j}^n = (\gamma-1)\bar{e}_{e,j}^n = (\gamma-1)U_{j,2}^n/U_{j,1}^n$ and the interface temperature $\bar{T}_{e,j+1/2}^n = 1/2(\bar{T}_{e,j+1}^n + \bar{T}_{e,j}^n)$. Finally, the second composant of the nonconservative term $N_j^n = (0, N_{j,2}^n)$ is computed as an approximation (as accurate as possible) of the integral over $[t^n, t^{n+1}] \times C_j$ of the nonconservative contribution

$$\int_{t^n}^{t^{n+1}} \int_{C_j} \bar{p}_e \partial_x \bar{v}_b \, dx \, dt \simeq (\gamma-1)U_{j,2}^n \int_{t^n}^{t^{n+1}} \int_{C_j} \partial_x \bar{v}_b \, dx \, dt,$$

where the integral of $\partial_x \bar{v}_\mathfrak{h}$ is exactly computed as the velocity $\bar{v}_\mathfrak{h}$ is prescribed. The proposed scheme is then a consistent numerical scheme with a standard discretization of the nonconservative product that can be tested for capturing the travelling wave.

4.2. Numerical results

In this section, we present some numerical experiments, using the finite volume scheme with standard discretization for the non-conservative product proposed in the previous section. Different resolutions of the travelling wave are presented with a double objective: first, to capture the dynamic of the travelling wave with a fine enough mesh; second, to visualize the behaviour with a coarse mesh in order to understand how the scheme can capture a shock discontinuity. We focus on the 3-wave with respect to the wave structure of the Euler system $\bar{S}_1$, so that the right state R is known.

The number of nodes N and the length of the domain L are fixed: $N = 2000$ and $L = 10$. The initial position of the travelling wave is $0.2L$. The time discretization Δt is fixed by a Fourier condition $\Delta t \leq \frac{1}{2}\beta\Delta x^2$ where $\beta = \max(D, \kappa^{\mathrm{R}})$. All the simulations are stopped at $t = t_f = 1$, corresponding to a displacement of the travelling wave to $0.373L$. The electron thermal conductivity $\lambda = 0.001$ is fixed, so the associated characteristic length $L_\lambda = 7.6 \times 10^{-2}$ is fixed. This value has been chosen as a good compromise between the length of the domain, which is fixed, and the regularization of the profile of the electron temperature. However, the electron diffusion coefficient D (or the characteristic length L_D) is going to vary in our numerical experiments changing the resolution of the travelling wave. This leads to a change in the resolution of the travelling wave since the length of the domain and the number of nodes are fixed. Simulations are conducted for diffusion coefficient D between 10^{-3} and 10^{-1} corresponding to $L_D = 3.055{\times}10^{-1}$ and $3.055{\times}10^{-3}$ respectively (or in other words a number of nodes in $L_D = 61.1$ and 0.611 respectively). The two extreme cases, denoted by case **HD** (highly-discretized) and case **WD** (weakly-discretized): in case **HD**, $L_D > L_\lambda$ whereas in case **WD**, $L_D \ll L_\lambda$. In 5, we will see that the physical test case in sun chromosphere conditions corresponds to cases where $L_D \ll L_\lambda$. The right state and the left state have been initialized with the values given in 1. The left state of the travelling wave has been computed using Rankine-Hugoniot relations for the heavy particles variables and jump conditions given in Eq. 3 for the electronic variables.

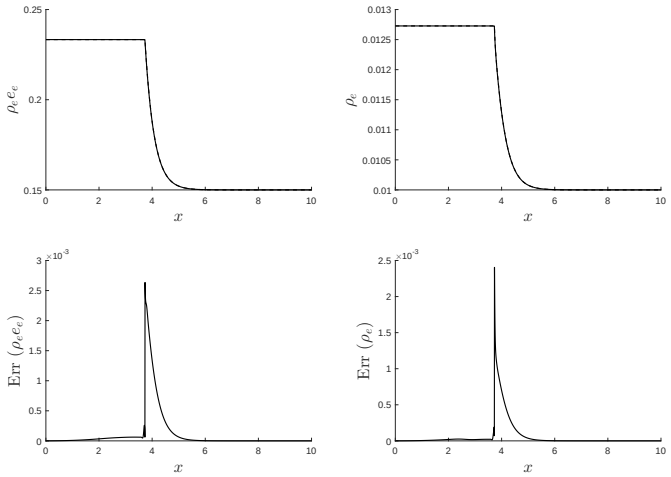

(a) Case **HD**

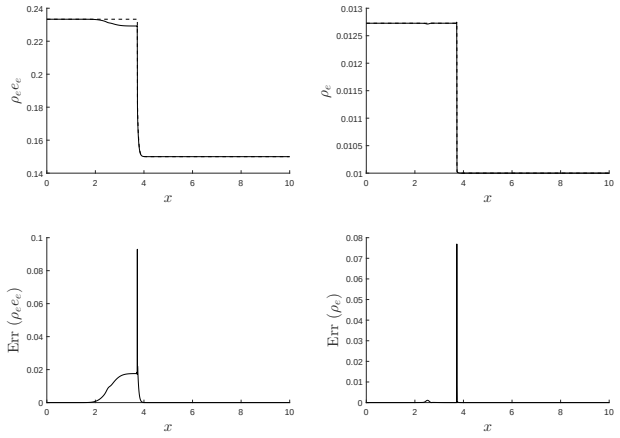

(b) Case **WD**

Figure 2: Analytical solution (dashed line), numerical solution (full line), and relative error (Err) for the travelling wave at $t = t_f = 1$

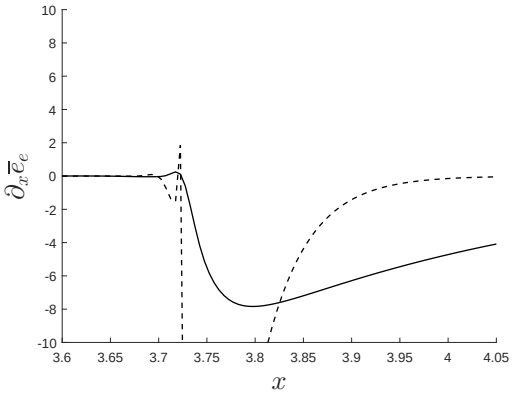

Figure 3: Quantity $\partial_x \bar{e}_\mathfrak{e}$ for case **HD** (full line) and case **WD** (dashed line) at $t = t_f = 1$.

Table 1: Right and left states of the travelling wave

	$\bar{\rho}_{\mathfrak{h}}$	$\bar{\rho}_{\mathfrak{e}}$	$\bar{p}$	$\bar{p}_{\mathfrak{e}}$	Mach number
State R	1	0.01	1	0.1	1.1832
State L	1.274	0.01274	1.5	0.1556	0.8563

Fig. 2 show first that the travelling wave is well captured in the case **HD**: the dynamic of the travelling wave is preserved if the number of nodes in the length L_D is large enough; second, that a non-expected artificial numerical shock appears in the case **WD**. Two main contributions to the difference between the numerical and analytical solutions can be exhibited: a contribution upstream of the shock due to the numerical dissipation in the regular part of the travelling wave; a contribution downstream of the shock due to the error on the gradients in the discontinuity.

Fig. 3 represents the gradient of the electron energy $\boldsymbol{\partial_x}\bar{e}_{\mathfrak{e}} = (\gamma-1)\boldsymbol{\partial_x}\bar{T}_{\mathfrak{e}}$ close to the discontinuity for the cases **HD** and **WD** at $t = t_f = n_f\Delta t$, where n_f is the total number of iterations at the final time t_f. For each cell $1 \leq j \leq N$, the gradient is computed by means of a centered finite difference formula such as $(\boldsymbol{\partial_x}\bar{e}_{\mathfrak{e}})_j^{n_f} = (\bar{e}_{\mathfrak{e},j+1}^{n_f} - \bar{e}_{\mathfrak{e},j-1}^{n_f})/2\Delta x$. One can see that in the case **HD**, the gradient is small whereas in the case **WD**, a numerical artefact appears in the discontinuity. If the equality $\bar{T}_{\mathfrak{e}}'(0^+) = \bar{T}_{\mathfrak{e}}'(0^-)$ is verified numerically, one gets the proper travelling wave with the right jump condition. If not, an artefact is produced in the discontinuity, due to the poor resolution of the gradient in the discontinuity, resulting in an artificial numerical shock.

The conclusive remark of these numerical experiments is the following. If the gradients in the discontinuity are well resolved (that is the case when the spatial mesh is fine enough),then, the travelling wave is well captured; if not, an artificial numerical shock is produced and, in this case, the numerical dissipation is responsible of the dynamic of the travelling wave. While the wave is regularized, having a nonlinear model with diffusion coming from physics implies that the conditions for solving the wave are identified. On the contrary, in systems based on general nonconservative hyperbolic equations, it is difficult to clearly identify how numerical dissipation impacts the resolution of the wave [7], [17]. Since the conditions for capturing the travelling wave have been identified, one wants to improve these results and build a new way for discretizing the nonconservative product allowing us to capture properly the travelling wave, even in weakly resolved cases. This is particularly relevant in solar physics where the characteristic length are very small.

4.3. Specific treatment of the nonconservative product

In this section, we develop an original method for discretizing the nonconservative term $N_{j,2}^n$. The idea is to express in a discretized sense the compatibility conditions Eq. 2 for the discontinuity, and deduce a new expression of the nonconservative term $N_{j,2}^n$ in order to satisfy these conditions. In that way, we aim at capturing the travelling wave even when the gradients are not fully resolved.

We consider the general scheme written in term of finite volumes Eq. 4 and specify the two vectorial coordinates by means of an index

$$\begin{cases} U_{j,1}^{n+1} - U_{j,1}^n + \frac{\Delta t}{\Delta x}(F_{j+1/2,1}^n - F_{j-1/2,1}^n) = \\ \qquad\qquad \frac{\Delta t}{\Delta x}(G_{j+1/2,1}^n - G_{j-1/2,1}^n), \\ U_{j,2}^{n+1} - U_{j,2}^n + \frac{\Delta t}{\Delta x}(F_{j+1/2,2}^n - F_{j-1/2,2}^n) = \\ \qquad\qquad N_{j,2}^n + \frac{\Delta t}{\Delta x}(G_{j+1/2,2}^n - G_{j-1/2,2}^n). \end{cases} \tag{5}$$

According to the relation found in 2, the jump of the gradient of $\bar{p}_{\mathfrak{e}}$ in the discontinuity is the same in the electron mass and electron thermal energy equations. In the discretized sense, one can simply link these two equations by multiplying the electron mass equation by a temperature $\bar{T}_{\mathfrak{e},j}^n = (\gamma-1)U_{j,2}^n/U_{j,1}^n$. According to Eq. 2, the derivative of the temperature $\bar{T}_{\mathfrak{e}}$ is continuous in the discontinuity so we have:

$$\bar{T}_{\mathfrak{e},j+1}^n - \bar{T}_{\mathfrak{e},j}^n = \bar{T}_{\mathfrak{e},j}^n - \bar{T}_{\mathfrak{e},j-1}^n \iff \bar{T}_{\mathfrak{e},j+1}^n - 2\bar{T}_{\mathfrak{e},j}^n + \bar{T}_{\mathfrak{e},j-1}^n = 0. \tag{6}$$

Consequently, the second-order terms of the electron thermal energy equation can be simplified as

$$G_{j+1/2,2}^n - G_{j-1/2,2}^n = \frac{D\gamma}{\Delta x}\left(U_{j+1,2}^n - 2U_{j,2}^n + U_{j-1,2}^n\right), \tag{7}$$

and coupled to second-order terms of the electron mass equation defined as

$$G_{j+1/2,1}^n - G_{j-1/2,1}^n = \frac{2D(\gamma-1)}{\Delta x}\left[\frac{\left(U_{j+1,2}^n - U_{j,2}^n\right)}{\left(\bar{T}_{\mathfrak{e},j+1}^n + \bar{T}_{\mathfrak{e},j}^n\right)} - \frac{\left(U_{j,2}^n - U_{j-1,2}^n\right)}{\left(\bar{T}_{\mathfrak{e},j}^n + \bar{T}_{\mathfrak{e},j-1}^n\right)}\right], \tag{8}$$

Besides, the time derivative terms are not playing a role in the compatibility of Eq. 2. We couple the electron mass equation with the electron thermal energy

equation, providing a new expression for the nonconservative product:

$$N^n_{j,2} = \frac{\Delta t}{\Delta x}(F^n_{j+1/2,2} - F^n_{j-1/2,2}) - \frac{\gamma}{\gamma-1}\bar{T}^n_{\mathrm{e},j}\frac{\Delta t}{\Delta x}(F^n_{j+1/2,1} - F^n_{j-1/2,1}) - \frac{\Delta t}{\Delta x}(H^n_{j+1/2} - H^n_{j-1/2}), \tag{9}$$

where the second-order terms of 9 are given by $H^n_{j\pm1/2} = \frac{\gamma}{2}(\bar{T}^n_{\mathrm{e},j\pm1} - \bar{T}^n_{\mathrm{e},j})G^n_{j\pm1/2,1}$. This expression of the nonconservative product $N^n_{j,2}$ verifies Eq. 2 in the discretized sense, that is to say: 1- the continuity of $\bar{T}_\mathrm{e}$ in the discontinuity of the travelling wave, 2- the conditions on the jump of the gradient of $\bar{p}_\mathrm{e}$ in the discontinuity.

However, the expression found in 9 for $N^n_{j,2}$ makes the global scheme not consistent. It is necessary to add correction terms in order to get the consistency property. It is important to make sure that these additional correction terms are not playing any role in discontinuities, which could violate Eq. 2 in the discretized sense. We limit the impact of these additional terms in the discontinuities. The main idea of this numerical scheme is to get proper compensations of the different terms in discontinuities in order to verify Eq. 2 in the discretized sense, and at the same time, to add correction terms for getting the consistency in order to capture properly the regular parts of the travelling wave. By adding first order correction terms, the expression of the nonconservative product 9 reads:

$$N^{n\,*}_{j,2} = N^n_{j,2} - (\gamma-1)\bar{\boldsymbol{v}}^n_{\mathfrak{h},j}\frac{U^n_{j,2} - U^n_{j-1,2}}{\Delta x} + \gamma\bar{\boldsymbol{v}}^n_{\mathfrak{h},j}U^n_{j,1}\frac{\bar{T}^n_{\mathrm{e},j} - \bar{T}^n_{\mathrm{e},j+1}}{\Delta x}. \tag{10}$$

Fig. 4 represent the L^2 norm of $\bar{p}_\mathrm{e}$ in function of the number of nodes in L_D for three different way of discretizing the nonconservative product $N^n_{j,2}$. Results are presented for three methods: the standard way of discretizing $N^n_{j,2}$ described in 3, without correction terms of 9, and with correction terms $N^{n\,*}_{j,2}$ of 10. The formulation of the nonconservative product $N^n_{j,2}$ without correction terms is working well in the weakly discretized case for the travelling wave test cases. However, in the regularized case, an additional numerical shock is appearing and the L_2 norm is increasing with the number of nodes in L_D, because the scheme is not consistent. By adding correction terms and using the formulation of the nonconservative term $N^{n\,*}_{j,2}$ from 10, we have built a scheme which is able to capture the travelling wave in both the highly- and coarsely-resolved cases. We could have built this numerical scheme because of the thorough understanding of the travelling wave linked to a good structure of the diffusion, as well as system allowing us to derive compatibility equations in the discontinuity.

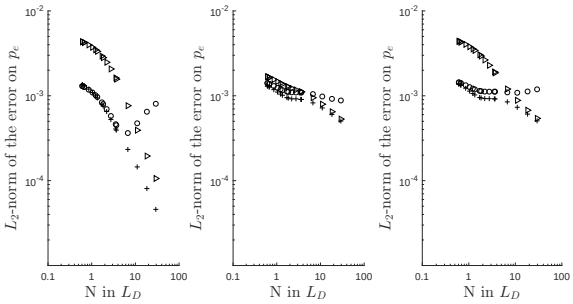

Figure 4: L^2-norm of the error on $\bar{p}_\mathrm{e}$ with respect to the number of nodes in L_D, ▷ standard discretization, ○ discretization without correction terms from 9, and + discretization with correction terms from 10. Left: downstream domain contribution; middle: upstream domain contribution; right: full domain contribution.

5. Application to solar physics

In this section, we apply the previous development to a test case chosen so as to reproduce typical scales from sun chromosphere conditions. We study the ability of our scheme to resolve shock solutions in such conditions and design a specific numerical strategy based on the new scheme in order to cope with the nonconservative term. A 3-wave is considered by using the system $\bar{S}_2$ with non-dimensional quantities for building the travelling wave in the sun chromosphere conditions.

First, we use atmospheric parameters from the model C of Vernazza *et al.* [18] where the values of these parameters are given at 52 depth in the atmosphere from the low corona to the photosphere. For the purpose of the work, we have focused on the photospheric level at the heigth $h = 0\,km$. We consider $\bar{p}^\mathrm{R}_\mathrm{e} = \bar{p}^\mathrm{R}_\mathfrak{h}$ at the right state, with only two species: electrons and protons H^+ as heavy particles. The transport coefficients D and λ are computed using third-order Sonine polynomials approximation based on a spectral Galerkin method used in [19; 20] considering local thermodynamic equilibrium for the fully ionized gas.

Then, we non-dimensionalize these quantities with reference quantities. The characteristic length of diffusion $L_0 = L_D = 1.747 \times 10^{-6}$ is chosen as the reference length. The density of heavy particle is chosen

as the reference density $\rho_0 = 1.873 \times 10^{-4}$. The reference velocity $v_0 = 6.518 \times 10^2$ is the Alfvén velocity defined as $v_0 = B_0/\sqrt{\mu_0 \rho_0}$ where B_0 is the reference magnetic field, chosen as $B_0 = 100$ G, and μ_0 the vacuum permeability.

Finally, after non-dimensionalizing the governing equations with reference quantities, the travelling wave is investigated using values from Table 2 and 3. We have chosen a number of nodes of either $N = 1000$ or $N = 5000$ and a length of the domain $L/L_0 = 2{\times}10^5$.

Table 2: Right and left states at infinity of the travelling wave

	$\bar{\rho}_\mathfrak{h}$	$\bar{\rho}_\mathfrak{e}$	$\bar{p}$	$\bar{p}_\mathfrak{e}$	$\bar{v}_\mathfrak{h}$
State R	1	$5.44{\times}10^{-4}$	0.5974	0.2987	0.07
State L	1.6962	$9.23{\times}10^{-4}$	1.5	0.9454	0.6787

Table 3: Diffusion coefficients and related typical lengths

D	κ^{R}	L_D/L_0	L_λ/L_0	L/L_0
10.7853	121 970.96	1	11309	200 000

After initializing the travelling wave, three numerical schemes are compared. The first scheme, denoted **scheme A**, is the standard scheme based on a standard discretization of the nonconservative product introduced in Section 4, where the timestep, denoted Δt_F, is limited by a Fourier stability condition, thus involving the largest diffusion coefficient, that is the electron thermal diffusivity κ^{R}. The second scheme, denoted **scheme B**, is based on the formulation of the nonconservative product described in Eq. 10, where the timestep is also limited by the same Fourier stability condition. The third scheme, denoted **scheme C**, is based on the formulation of the nonconservative product defined in 10, using an operator splitting approach based on a second-order Strang formalism in order to separate the convection and diffusion operators [21; 22; 23; 24]. The idea is to not be limited by the small timesteps Δt_F imposed by the Fourier stability condition, due to the electron thermal diffusivity. Concerning the **scheme C**, there are two possibilities for the operators : one can 1- gather diffusive terms and the nonconservative product, or 2- gather convective terms and the nonconservative product. In this work, we have focused on the second case. Indeed, according to Eq. 10, the expression of the nonconservative product depends on the thermal energy and density convective fluxes, which makes the second case a rather more natural choice.

The operators are splitted: one operator X corresponds to convective terms and the nonconservative product defined by Eq. 10, where the convective timestep, called Δt, is simply limited by a CFL condition; an other operator Y regroups diffusion terms, where the timestep Δt_F is computed based on the Fourier condition and integrated over several subtimesteps in order to reach the convective timestep. The general scheme is summarized as follows:

$$U^{n+1} = Y^{\frac{\Delta t}{2}} X^{\Delta t} Y^{\frac{\Delta t}{2}} U^n.$$

In the proposed schemes, the values used for the convective timestep Δt and the diffusive timestep Δt_F are presented in Table 4. In order to perform the comparison between the timesteps used, we have compared them to the convective timestep $\Delta t = C{\times}\Delta x/\max(\bar{\boldsymbol{v}}_\mathfrak{h}^{\mathrm{R}} + c^{\mathrm{R}}, \bar{\boldsymbol{v}}_\mathfrak{h}^{\mathrm{L}} + c^{\mathrm{L}})$ for $N = 1000$ and $N = 5000$, where the Courant number is $C = 0.2$.

Table 4: Timesteps used for the three schemes for $N = 1000$ and $N = 5000$

N	Δt	Δt_F
1000	2.233×10^1	4.095×10^{-1}
5000	4.466	1.64×10^{-2}

Results are presented in Fig. 5a and 5b for the electron energy $\bar{e}_\mathfrak{e}$, comparing the three schemes, at the final time $t = t_f = 30000$, for $N = 1000$ and $N = 5000$. In the sun chromosphere conditions, the characteristic scales are such that $L_\lambda \gg L_D$, because the electron diffusivity is much higher than the electron diffusion coefficient in such conditions. In the test case, the smallest spatial scale to be resolved is the length L_D, which is the characteristic scale related to the resolution of the travelling wave. By fixing the number of nodes N and the length of the domain L based on 3, the test case can be identified as a very weakly-resolved travelling wave test case.

In Fig. 5a and 5b, the standard scheme exhibits artificial numerical shock since the smallest scale is not properly resolved and small timesteps Δt_F have to be used, as expected. Switching to a proper treatment of the nonconservative term allows to reduce by a factor of 9, for $N = 5000$, the amplitude of the error on the electron temperature and to reduce drastically the artificial numerical shock, thus leading to a satisfactory level of resolution. However, using the new scheme based on Strang splitting operator techniques combined to the new formulation of the nonconservative product (**scheme C**) leads to an additional im-

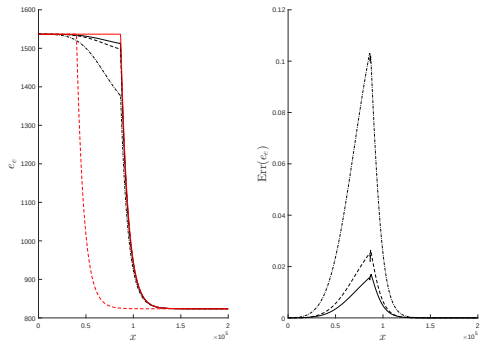

(a) $N = 1000$

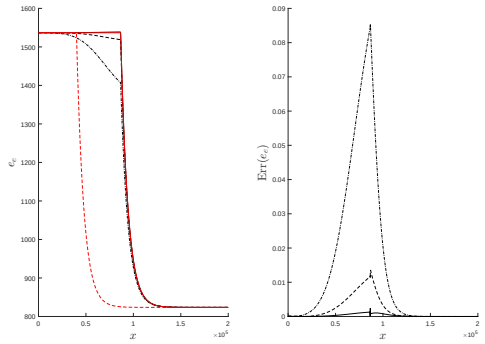

(b) $N = 5000$

Figure 5: Electron energy ($\bar{e}_e$) and relative error (Err) for the solar test case based on the values from 2 and 3. Exact solution at $t = 0$ (red dashed line) and $t = 30000$ (red full line). Numerical solution for **scheme A** (semi-dashed line), **scheme B** (dashed line), and **scheme C** (full line), at the final time $t = 30000$.

provement of the resolution of all the scales of the travelling wave. The travelling wave can be well captured, while using splitting timesteps of the order of the convective CFL stability limitation, thus leading to a minimal amount of numerical dissipation in the convective step. In fact, based on the results obtained in the previous section, a good approximation of the travelling wave obtained with the **scheme A** would require several nodes in the characteristic length L_D thus leading to about a million nodes. In this context, the corresponding convective timestep and the diffusive timestep would be respectively $\Delta t = 8.94 \times 10^{-2}$ and $\Delta t_F = 4.01 \times 10^{-7}$ and the original scheme would become useless.

6. Conclusion

The general plasma model derived in [4] has been presented in a simplified model, without considering the electro-magnetic forces and under several assumptions, which inherits the difficulties of the general case in terms of evaluating jump conditions and simulating shock solutions. We have proposed a decoupling of the governing equations in order to derive an analytic expression of the missing jump condition on the electron temperature. In order to reproduce numerically the structure of the travelling wave solution with the proper jump conditions, we have used a finite volume method of Godunov type. A naive consistant treatment of the nonconservative product proves that, for a fine resolution, the expected wave is well reproduced. We have verified the jump condition as well as the structure of the travelling wave obtained analytically and identified the required level of resolution in order to prevent the appearance of an additional artificial jump due to the numerical dissipation of the numerical scheme.

In this context, we have developed a numerical scheme with a specific treatment of the nonconservative product. The idea is to express the compatibility equations at the discontinuity of the travelling wave in a discretized sense. It gives the ability to predict the proper travelling wave even when the gradients are not fully resolved. We have thus built a scheme, which is able to capture the travelling wave in the highly- or weakly-resolved cases. Such a scheme is important since the weakly-discretized case is particularly relevant in the sun chromosphere conditions. We have also applied a Strang operator splitting technique in order to prevent the use of small time-steps limited by the presence of large diffusion terms and a Fourier stability condition. Eventually, a 1D travelling wave test case has been presented based on conditions found in the sun chromosphere, which allowed us to assess the numerical scheme and numerical strategy based on operator splitting. Such a strategy should prove very useful for applications in solar physics in order to gain computational cost, as well as obtain physically accurate simulations.

Furthermore, following the work in [16], jump conditions based on our knowledge of the decoupled problem have been derived numerically for the fully coupled system and we were able to justify that studying the decoupled problem provides a good approximation of the original system in a range of Mach number close to one, as well as a good insight on the resolution of the problem for the general system of equations. The contributions proposed in this paper should also be extended to the case where electromagnetic forces are present and the system is coupled to Maxwell's equations. This is the subject of our cur-

rent research.

Acknowledgments

The authors would like to warmly thank Nagi Mansour (NASA Ames Research Center), Frédéric Coquel and Alejandro Alvarez-Laguna (Ecole Polytechnique) for several helpful discussions

References

[1] S. Parenti, Solar prominences: Observations, S. Living Review Sol. Phys.

[2] T. Wiegelmann, J. Thalmann, S. Solanki, The magnetic field in the solar atmosphere, Astron Astrophys Review.

[3] E. Khomenko, M. Collados, A. Diaz, N. Vitas, Fluid description of multi-component solar partially ionized plasma, Physics of Plasmas 21 (2014) 635–725.

[4] B. Graille, T. E. Magin, M. Massot, Kinetic theory of plasmas: translational energy, Mathematical Models and Methods in Applied Sciences 19 (4) (2009) 527–599.

[5] G. D. Maso, P. L. Floch, F. Murat, Definition and weak stability of nonconservative products, J. Math. Pures et Appl 74 (1995) 483¢–548.

[6] C. Pares, Numerical methods for nonconservative hyperbolic systems: a theoretical framework, SIAM J. Numer. Anal. 44 (2006) 300¢–321.

[7] R. Abgrall, S. Karni, A comment on the computation of nonconservative products, Journal of Computational Physics 229 (2010) 2759–2763.

[8] C. Chalons, F. Coquel, A new comment on the computation of non-conservative products using roe-type path conservative schemes, Journal of Computational Physics 335 (2017) 592–604.

[9] F. Coquel, C. Marmignon, A roe-type linearization for the euler equations for weakly ionized multi-component and multi-temperature gas, 12th Computational Fluid Dynamics Conference, Fluid Dynamics and Co-located Conferences.

[10] G. V. Candler, R. W. Maccormack, Computation of weakly ionized hypersonic flows in thermochemical nonequilibrium, Journal of Thermophysics and Heat Transfer (1991) 266–273.

[11] R. B. Lowrie, R. M. Rauenzahn, Radiative shock solutons in the equilibrium diffusion limit, Shock waves 16 (2007) 445–453.

[12] R. B. Lowrie, J. Edwards, Radiative shock solutons with grey nonequilibrium diffusion, Shock waves 18 (2008) 129–143.

[13] V. Shafranov, The structure of shock waves in a plasma, Soviet Phys. JETP 5.

[14] Y. B. Zeldovich, Y. P. Raizer, Physics of Shock Waves and High-Temperature Hydrodynamic Phenomena, Vol. 2, Academic Press, New York and London, 1967, w.D. Hayes and R.F. Probstein Editors.

[15] D. Mihalas, B. W. Mihalas, Foundations of radiation hydrodynamics, Oxford University Press, New York, 1984.

[16] Q. Wargnier, S. Faure, B. Graille, T. Magin, M. Massot, Numerical treatment of the nonconservative product in a multiscale fluid model for plasmas in thermal nonequilibrium: application to solar physics, SIAM J. Sci Comp. in revision, available on ArXivHttps://arxiv.org/abs/1806.10436. arXiv:1806.10436.

[17] D. A. Driollet, J. Breil, Modelling and numerical approximation for the nonconservative bitemperature euler model, Mathematical modelling and numerical analysis.

[18] J. E. Vernazza, E. H. Avrett, R.Loeser, Structure of the solar chromosphere. iii. models of the euv brightness components of the quiet sun, The astrophysical journal supplement series 45 (1981) 635–725.

[19] T. E. Magin, G. Degrez, Transport algorithms for partially ionized and unmagnetized plasmas, Journal of computational Physics 198 (2004) 424–449.

[20] Q. Wargnier, A. Alvarez-Laguna, N. N. Mansour, M. Massot, T. Magin, Consistent transport properties in a two temperature multicomponent plasma model: Application to the magnetized sun chromosphere, Astronomy and Astrophysics-sSubmitted.

[21] G. Strang, On the construction and comparison of difference schemes, SIAM Journal on Numerical Analysis 5 (3) (1968) 506–517.

[22] M. Duarte, M. Massot, S. Descombes, C. Tenaud, T. Dumont, V. Louvet, F. Laurent, New resolution strategy for multiscale reaction waves using time operator splitting, space adaptive multiresolution, and dedicated high order implicit/explicit time integrators, SIAM Journal on Scientific Computing 34 (1) (2012) A76–A104.

[23] S. Descombes, M. Duarte, T. Dumont, F. Laurent, V. Louvet, M. Massot, Analysis of operator splitting in the nonasymptotic regime for nonlinear reaction-diffusion equations. Application to the dynamics of premixed flames, SIAM Journal on Numerical Analysis 52 (3) (2014) 1311–1334.

[24] M. Duarte, Adaptive time-space numerical methods for the simulations of multi-scale reaction waves, Ph.D. thesis, Ecole Centrale Paris, France, https://tel.archives-ouvertes.fr/tel-00667857 (2011).

GROUND AND FLIGHT EXPERIMENTS

Stochastic Inference of the Catalytic Properties of Thermal Protection Materials from Plasma Wind Tunnel Experiments

Ana Isabel del Val Benítez

Aeronautics and Aerospace Department, von Karman Institute for Fluid Dynamics, Belgium, delvalbeni@vki.ac.be

Supervisors: Olivier Chazot and Thierry E. Magin

Professor and Associate Professor, Aeronautics and Aerospace Department, von Karman Institute for Fluid Dynamics, Belgium, chazot@vki.ac.be, magin@vki.ac.be

University Supervisor: Pietro M. Congedo

Research Scientist, DEFI team (INRIA Saclay Île-de-France, École Polytechnique), France, pietro.congedo@inria.fr

Abstract

Aerothermodynamics ground testing in high-enthalpy flow facilities is essential for the development and design of aerospace vehicles. It is a convenient step regarding the intensive cost of flight experiments. The determination of catalytic properties of thermal protection materials is subjected to experimental and model uncertainties which must be evaluated during the design phase of reusable atmospheric entry vehicles. As a result of the uncertainties reported in the rebuilding of the catalytic parameter for copper reference probes, this work focuses on the Mini-Max testing methodology originally adopted to better assess copper probe catalysis. A fully Bayesian approach is proposed in previous works and extended to the Mini-Max testing framework for different sets of experimental data. This will help pave the way to the computation of the optimal testing conditions for the characterization of reusable thermal protection systems, regarded as future work.

Keywords: Uncertainty Quantification, Bayesian Inference, Plasma Flows, Catalysis, Thermal Protection Systems

1. Introduction

After the successful manned missions to the Moon and many probe entries into the atmosphere of outer planets, the next challenges of space exploration include bringing samples back to Earth by means of robotic missions, as well as continuing the manned space program to send human beings to Mars and bring them home safely. Facing these problems requires in-depth knowledge of the systems and phenomena involved. Different experimental and numerical methodologies are adopted to study particular phenomena that occurs during the re-entry flight.

An important step towards the design of reusable thermal protection materials is using ground testing facilities to assess the thermal behavior and perform the extrapolation to flight. The properties of these materials quantify the recombination of oxygen and nitrogen atoms into molecules, and allow for accurate computation of the heat flux to the spacecraft. Their rebuilding combines direct measurements using various diagnostics and a numerical reconstruction based on computational fluid dynamics (CFD) simulations subjected to uncertainties.

Even for well-characterized facilities, the determination of catalytic properties is affected by the noise present in the experimental data. The quantification of uncertainties in high-enthalpy experiments has previously been studied in the literature [1] [2] [3] [4]. In particular, in the previous work by Sanson et al. [5], the uncertainties on catalytic properties were evaluated by adopting a robust Bayesian inference framework in which the epistemic uncertainty of the reference probe calorimeter was also assessed. However, for the testing conditions presented in that work, the contribution to the measured heat flux of the molecu-

lar recombination is negligible. Therefore, the material catalytic property cannot be estimated precisely.

In the present work, the methodology developed by Sanson et al. is applied to the Mini-Max [6] testing strategy to better estimate the reference probe catalytic property. Adopting a different experimental approach can show better results in terms of the uncertainty of the catalytic property rebuilt. Based on this stochastic inference, we will assess whether accurate information on the catalytic properties of these thermal protection materials can be extracted from the experimental data.

The paper is structured as follows. In section 2, we recall the main features of the combined experimental and numerical methodologies developed at VKI to analyze the data obtained in the VKI Plasmatron facility to then, present the sources of experimental uncertainties involved in the process. In section 3, we reformulate the problem of determining the catalytic properties in a Bayesian framework. In Section 4, we apply this approach to new sets of experimental data presented additionally to the ones presented in [5].

2. Experimental and numerical methodologies

The present study uses sets of data measured during an experimental campaign documented in [6]. The first section briefly recalls the quantities measured experimentally for each testing condition and their associated uncertainties, whereas the following section introduces the numerical simulations performed to rebuild the quantities that cannot be directly measured. The last section introduces some uncertainty quantification terminology.

2.1. Experimental set-up

The logic behind the Mini-Max method is simple. Three heat flux measurements are taken on three different calorimeters under the same plasma conditions. Calorimeters being of different materials, those dedicated to Mini-Max application in air plasma are silver, copper and quartz. Differences in q_{cw} are consequence of different catalytic activities on the surface of each calorimeter.

Considering both silver and quartz as the high catalytic ($\gamma_{Ag} \approx 1$) and the low catalytic ($\gamma_{Qz} \approx 0$) standards, respectively, it is possible to define an enthalpy range inside which the testing conditions should be found. Thus, a minimum enthalpy h_{min} is given by the silver calorimeter and a maximum enthalpy h_{max} by the quartz calorimeter. An example is shown in Fig. 1. The intersection of this interval with the $h_e - \gamma$ relation obtained for copper defines a catalytic range for the plasma conditions at hand, with a maximum recombination coefficient γ_{max} given by h_{min} and a minimum recombination coefficient γ_{min} provided by h_{max}. The average value between both recombination coefficients will be considered as γ_{ref} for that particular test condition. Remark that Krassilchikoff similarly applied the Mini-Max with molybdenum instead of quartz [7].

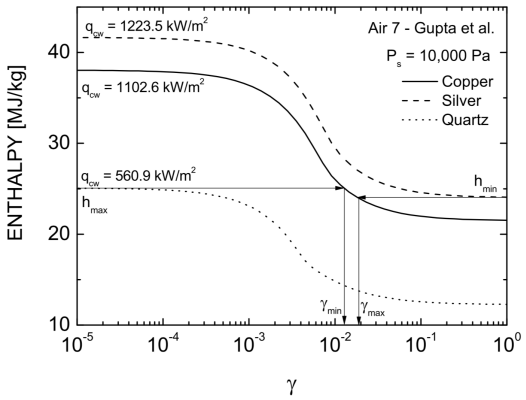

Figure 1: Illustration of Mini-Max method application. Credit: Viladegut REF

A dedicated testing campaign for Mini-Max methodology application was carried out in the Plasmatron [6] following the scheme shown in Fig. 2. The three calorimeters of Fig. 3 are inserted in ESA-Standard probes, located at 445 mm from the torch exit and aligned with the center of the plasma jet.

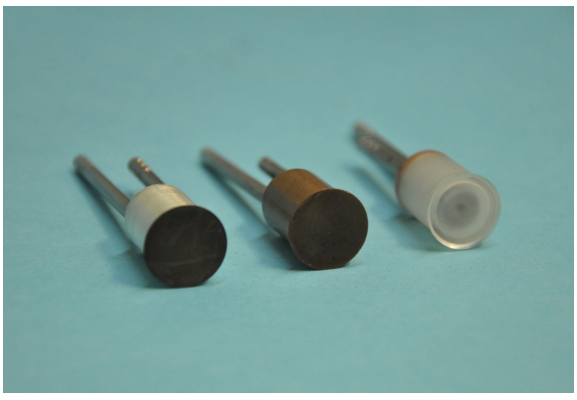

Figure 3: Calorimeters for Mini-Max methodology application: left - Ag, middle - Cu, right - SiO_2 -Quartz

Apart from the heat flux measurements with an es-

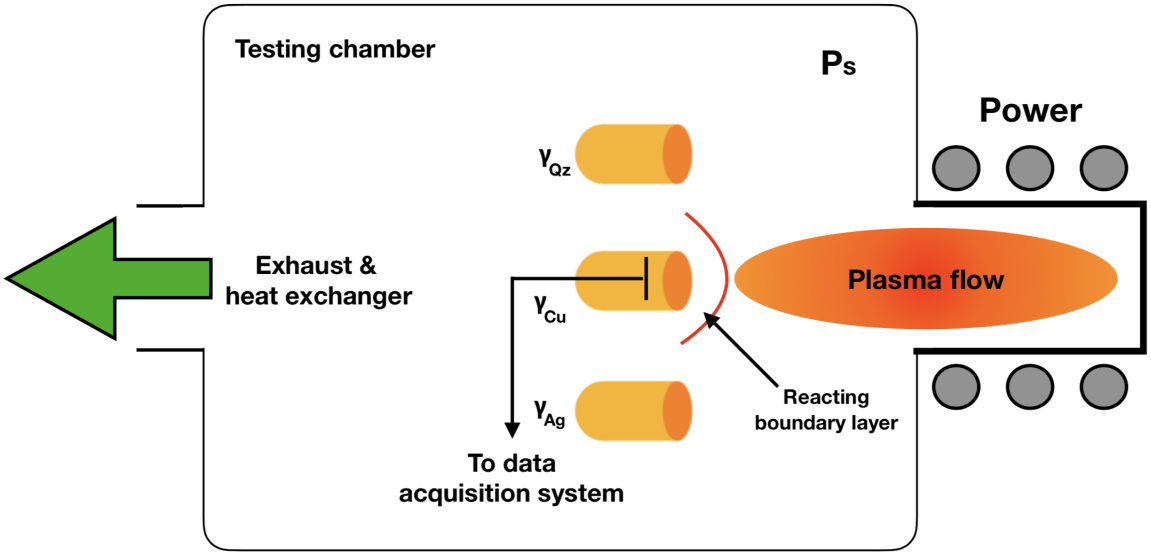

Figure 2: Plasmatron test configuration for γ_{ref} determination with the Mini-Max

timated uncertainty of ±10%, the dynamic pressure (featuring an uncertainty of ±6%) has been measured with a Pitot probe under the same configuration prior to Mini-Max application because only three samples can be introduced in the Plasmatron test chamber during the same run. The surface temperature of water-cooled probes T_{cw} is known by measuring the differential of temperature between the inlet and outlet water lines. The static pressure P_s of the test chamber is measured with a 2 Pa accuracy.

It is further assumed that the free stream flow is identical during the three independent experiments and that Local Thermodynamic Equilibrium (LTE) holds at the edge of the boundary layer.

2.2. *Numerical model*

The flow properties measured experimentally and explained in Sec. 2.1. are then used as input parameters for two numerical solvers developed at VKI that reconstruct the flow around a probe. The method provides a numerical solution of the chemically reacting boundary layer at the stagnation line, together with all the thermodynamic properties of the gas, from the outer edge to the wall. Although this procedure relies on intrusive measurement techniques and several physico-chemical models to determine the enthalpy at the boundary layer edge (h_e), it becomes a powerful tool for Plasmatron experiments that require additional insight on specific physical phenomena.

The first software intervening in the rebuilding process is CoolFluid for ICP simulations. This solver helps to define the framework of the problem to be solved around the probe by simulating the interaction between the electromagnetic field around the coil and the gas passing through, with the aim of reproducing the whole Plasmatron chamber. ICP simulations assume the test gas in LTE, which is reasonable away from both the torch exit and the probe [8]. The CFD simulations carried out with this solver use a Finite Volume Method (FVM) in a mesh with quadrilateral cells. All ICP computations performed in this work consider an 11-species air mixture, the transport coefficients of which are computed with the Mutation++ library [9], also developed at VKI. In the simulations, all the walls are cooled down to 350 K and an annular injection of the gas is imposed at the inlet. Static pressure is imposed at the outlet of the fluid domain, as required in subsonic flows.

The second numerical tool is the so-called Non-Equilibrium BOUndary LAyer (NEBOULA) solver developed by Barbante [10] at VKI. It assumes thermal equilibrium and chemical non-equilibrium to solve the finite thickness boundary layer equations at the stagnation line in front of the probe. These equations are solved with a 4th order Hermitian polyno-

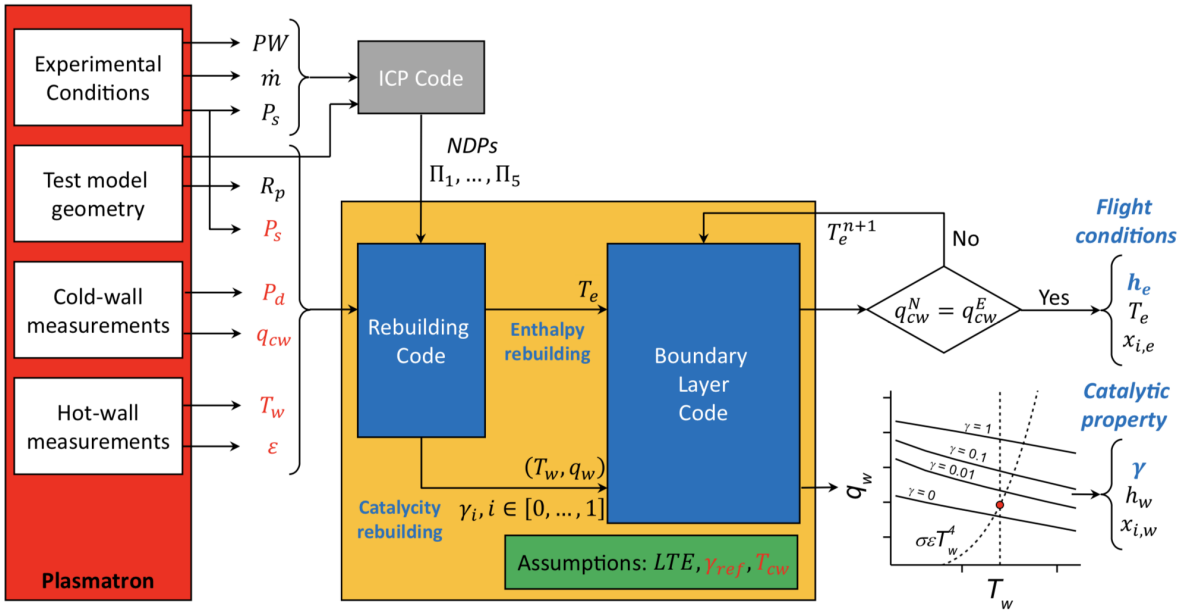

Figure 4: Overview of the enthalpy rebuilding and catalytic property determination. Credit: Sanson REF

mial discretization. NEBOULA interacts with PEGASE library [11] to compute the thermodynamic and the transport properties of the gas. In addition, different chemical models are available inside PEGASE to compute the reaction rates [12] [13] [14]. The Stefan-Maxwell equations are solved to model species diffusion [10] inside NEBOULA. The condition of LTE is imposed at the boundary layer edge for consistency with ICP simulations, while surface temperature T_w and γ are introduced as boundary conditions at the wall for the energy and the species equations, respectively. Despite catalytic NO formation was detected by Copeland et al. [15], only two catalytic recombination reactions are assumed relevant for an air mixture: $N+N \rightarrow N_2$ and $O+O \rightarrow O_2$. Catalysis is introduced through the diffusive flux at the wall.

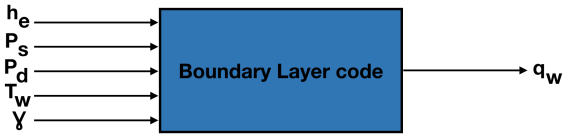

Figure 5: Flowchart of the BL solver with its main inputs

NEBOULA is called iteratively by a routine named CERBERE, in order to be used as a tool for Plasmatron data post-processing. The input variables of CERBERE being a combination of measured quantities in the Plasmatron and some hydrodynamic outputs from ICP simulations, it iterates with NEBOULA in order to reconstruct the stagnation line boundary layer in front of the probe and to provide a value of the recombination coefficient on TPS material samples. In the particular framework of the rebuilding method, the coupling between CERBERE and NEBOULA is commonly known as CERBOULA, and it can provide either an outer edge enthalpy he to characterize the plasma if wall catalysis is known, or a recombination coefficient γ on a reference material if h_e is given, but never both parameters at the same time.

Despite the fact that a large number of inputs are measured or unknown, the method is fully deterministic and provides no indication about the outputs uncertainty. A given estimation on the inputs uncertainties are given below:

Table 1: Experimental uncertainties estimated

Symbol	Variable	Uncertainty
$P_{d,meas}$	Dynamic pressure	6%
$P_{s,meas}$	Static pressure	0.3%
$q_{cw,meas}$	Heat flux	10%
$T_{cw,meas}$	Probe temperature	10%

2.3. Uncertainty characterization

The determination of the TPS catalytic property directly depends on experimental data, and intrinsically carries the uncertainty associated with actual measurements. Three categories of variables for the uncertainty quantification analysis are considered and explained hereafter:

- Measured quantities (MQ): The MQ are aleatory quantities that are assumed to be noisy versions of their true values: T_{cw}, q_{cw}, P_s, P_d. In this study, they are modeled as realization of a Gaussian distribution, meaning that they are assumed to be a value drawn out of a Gaussian distribution with mean the computational value coming from the numerical model.
- Quantities of interest (QoI): The QoI are the unknown quantities crucial to the application. In this study, the different probes catalytic properties denoted γ_{Ag}, γ_{Cu} and γ_{Qz}, along with the flow enthalpy h_e, are the QoIs.
- Nuisance parameters (NP): The NP are unknown quantities that must be estimated along with the QoIs in order to estimate the catalytic properties (T_{cw}, P_d, P_s).

3. Fully Bayesian approach

Bayes' rule applied as a ratio of probabilities is the foundation for the robust uncertainty estimation in this work. The joint uncertainty estimation of the three probes calorimeters γ_{Ag}, γ_{Cu} and γ_{Qz} and the boundary layer edge enthalpy h_e is performed by computing the posterior probability distribution as defined by Bayes:

$$P\left(\gamma_{Ag}, \gamma_{Cu}, \gamma_{Qz}, h_e \,|m\right) \tag{1}$$

where m are the different measurements described previously. This distribution carries all the necessary information for the uncertainty quantification analysis. It provides a robust estimate of the uncertainty through confidence intervals and the variance.

To compute it, the distribution is decomposed into a ratio of probabilities using Bayes rule (Eq. 2) that can be numerically evaluated:

$$\frac{P\left(m|\gamma_{Ag}, \gamma_{Cu}, \gamma_{Qz}, h_e, \omega_{nuis}\right) P\left(\gamma_{Ag}, \gamma_{Cu}, \gamma_{Qz}, h_e, \omega_{nuis}\right)}{P(m)} \tag{2}$$

The posterior distribution is numerically evaluated using a Markov Chain Monte Carlo (MCMC) algorithm described in [16]. Fig. 6 summarizes the rebuilding methodology from a Bayesian perspective. Note that, contrary to the deterministic strategy explained in Sec. 2.2, the QoIs are rebuilt all experiments simultaneously (P_s, P_d and h_e).

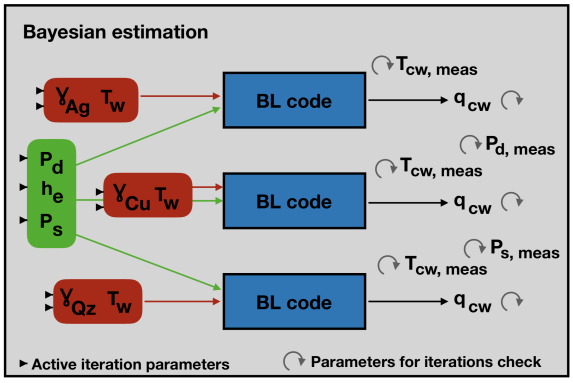

Figure 6: Flowchart of the Bayesian-based estimation of material catalytic properties

$P\left(\gamma_{Ag}, \gamma_{Cu}, \gamma_{Qz}, h_e \mid m\right)$ is the probability of observing the measured quantities knowing the QoIs. It measures the compatibility between the measurements and the value of unknown parameters, such as the catalytic property of the different calorimeters. The prior accounts for the knowledge of the unknown parameters before any experiment. In our case, as scarce prior information is available for ω_{nuis} and h_e, uniform priors are considered. As γ is defined on the interval [0;1], a beta distribution with parameters $\alpha = 1$ and $\beta = 1$ is chosen with a support of $[10^{-8}; 1]$.

4. Preliminary results

This section illustrates the preliminary results derived by Sanson from the application of the Bayesian framework to the problem of interest. The three calorimeter probes experiments were used to calibrate and accurately estimate copper probe catalycity quantities as they are widely used for reference catalytic property determination. As a first step, experiments in nitrogen were considered to estimate the catalytic property associated with nitrogen chemical reactions. As a second step, a two gamma model is considered using the catalytic property estimated from the nitrogen experiments as prior knowledge and a gamma parameter associated to the now present oxygen chemi-

cal reactions as a way of gaining more accuracy within the model.

4.1. Nitrogen experiments

Three different catalytic properties are assumed for each calorimeter subjected to a pure nitrogen flow. The reconstruction strategy traditionally followed for the deterministic computations is depicted in Fig. 7

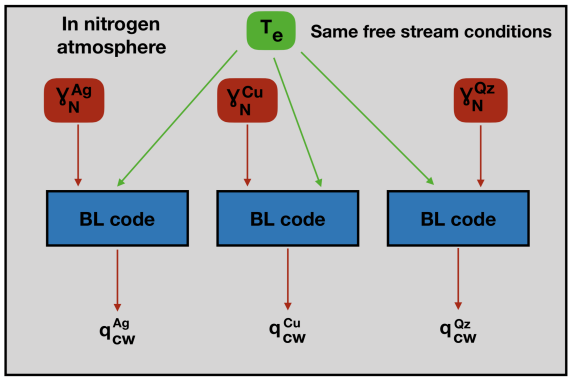

Figure 7: Reconstruction strategy

The key assumption made here is the fact that the free stream conditions are supposed to be the same for all three probes. Based on this approach, the Bayesian framework is built as described before.

The test cases under consideration for the nitrogen catalytic property determination are depicted in Table 2.

While the statistics obtained as a result for the three cases are shown on Table 3.

Regarding the probability distribution functions (PDFs) for the three different catalytic properties, the results for the different testing conditions showed:

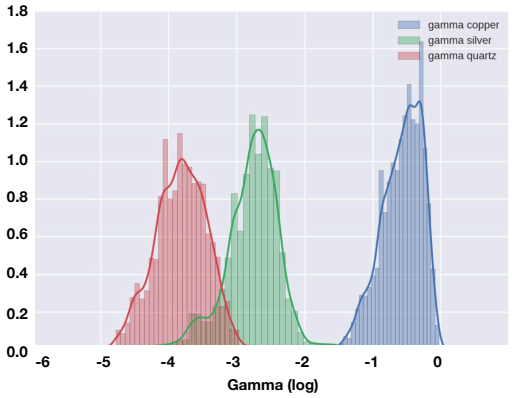

Figure 8: Gamma PDFs for test case 1b

As can be observed, in this test case with a purely nitrogen flow, the copper behaves as the fully catalytic probe which defeats the purpose of the methodology of estimating the reference probe catalytic properties (copper) by comparing it against a non-catalytic and fully catalytic materials (quartz and silver, respectively). One can argue that the method presents some limitations in terms of testing conditions valid for the copper catalytic parameter estimation. Choosing accordingly the experiments is a recommendation for having coherent and accurate results.

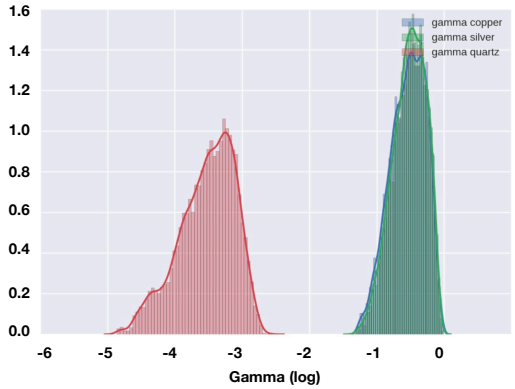

Figure 9: Gamma PDFs for test case 8b

In Fig. 9 a change in tendency can be appreciated where silver and copper behave the same way in terms of catalytic properties, being this the upper limiting case for the Mini-max method. By increasing the dynamic pressure and enthalpy the prediction capabilities of the method become more evident and more consistent results are obtained. Fig. 10 shows a better example of the potential of this method for the determination of copper catalycity which seems consistent with case 8b.

Table 2: Testing conditions for experiments in nitrogen atmosphere

Test case	P_{stat} $[Pa]$	P_{dyn} $[Pa]$	T_e	q_w^{Cu} $[kW/m^2]$	q_w^{Ag} $[kW/m^2]$	q_w^{Qz} $[kW/m^2]$	T_{wall} $[K]$
1b	5000	19.75	4915	309	209	150	350
8b	5000	84.89	6250	1717	1736	605	350
9b	5000	95.62	6630	2022	2110	778.3	350

Table 3: Statistics resulting from the case with nitrogen flow

Quantity	T_e $[K]$	γ_{Cu}	γ_{Ag}	γ_{Qz}
Mean 1b	4893	0.32	5.3e-3	2.1e-4
Std 1b	69	0.29	0.46	0.38
Mean 8b	6263	0.34	0.35	4.3e-4
Std 8b	44.3	0.25	0.24	0.41
Mean 9b	6586	0.27	0.35	8.4e-4
Std 9b	80	0.29	0.24	0.32

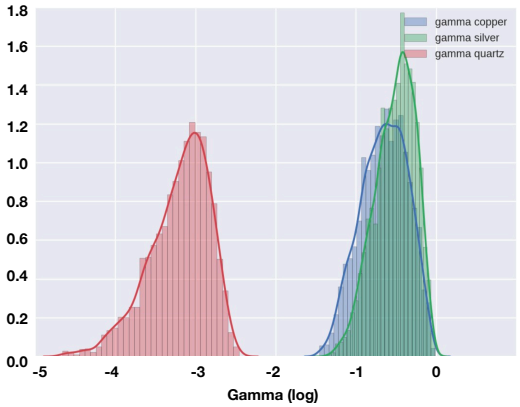

Figure 10: Gamma PDFs for test case 9b

Fig. 10 shows a better example of the potential of this method for the determination of copper catalycity which seems consistent with case 8b.

4.2. Air experiments

In the case of the experiments in an air atmosphere, the objective is two fold: i) to use the catalytic parameter estimated in the nitrogen experiments as a prior distribution to determine the catalycity associated to oxygen chemical reactions in what is known as a two gamma model and ii) to compare the results when the catalytic parameter for nitrogen reactions is assumed to be constant within the distribution obtained for the nitrogen experiments and when it is assumed to be unknown, using the previous distribution for nitrogen reactions as a prior, estimating the posterior along with the oxygen catalytic parameter in air flow. Fig. 11 depicts the logic behind the reconstruction strategy followed:

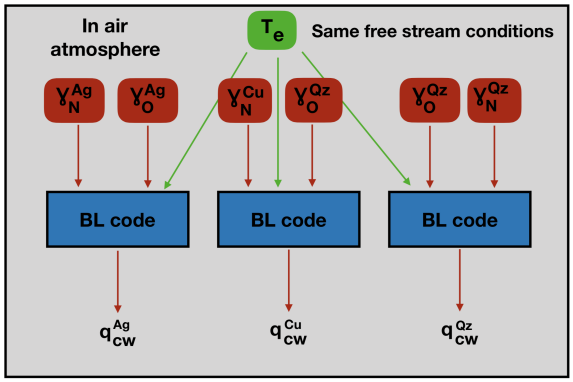

Figure 11: Reconstruction strategy for the two gamma model

These results can lead the way to the assumption that when oxygen and nitrogen are combined in the flow (conventional air mixture), the recombination at the wall for the different species are affected by the other species present: oxygen species recombination at the wall can affect the effective recombination of nitrogen species, making the gamma for nitrogen reactions estimated with a pure nitrogen flow not a realistic estimation. This is the way Bayesian inference tells us how to perform our experiments to extract useful and accurate information.

The experimental campaign taken into account for the air experiment is the equivalent of case 9b for nitrogen experiments and the data is detailed in Table 3.

The statistics obtained for the case where the gamma for nitrogen is assumed to be the one obtained for the pure nitrogen flow experiments are gathered in Table 4.

The results obtained for the three different gamma are depicted below in Fig. 12:

Table 4: Experimental conditions for air and nitrogen atmospheres

Test case	P_{stat} $[Pa]$	P_{dyn} $[Pa]$	T_e	q_w^{Cu} $[kW/m^2]$	q_w^{Ag} $[kW/m^2]$	q_w^{Qz} $[kW/m^2]$	T_{wall} $[K]$
9b (Air)	5000	177.18	6500	2003	2369	795	350
9b (N)	5000	95.62	6630	2022	2110	778.3	350

Table 5: Statistics resulting from the case with air flow

Quantity	T_e $[K]$	γ_{Cu}^N	γ_{Ag}^N	γ_{Qz}^N	γ_{Cu}^O	γ_{Ag}^O	γ_{Qz}^O
Mean	6518	0.21	0.35	7.0e-4	0.05	0.25	4.6e-3
Std	120	0.0	0.0	0.0	0.55	0.31	0.53

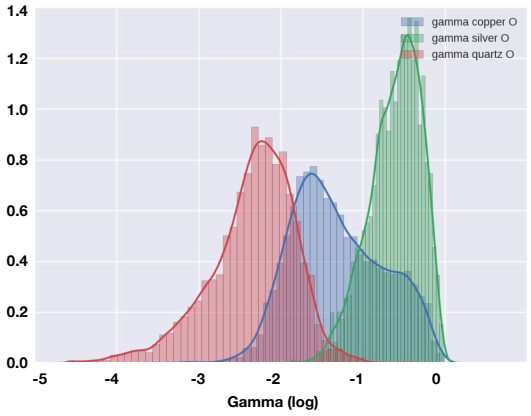

Figure 12: Gamma PDFs for test case 9b with air and previously determined nitrogen catalytic parameter distribution

By looking at the copper calorimeter catalytic parameter one can notice the decrease of accuracy for the oxygen chemical reactions at the wall. In this case, the results show that quartz is more catalytic for oxygen chemical reactions than in the case of just nitrogen flow. The testing conditions for this particular case leave the estimation of the copper catalytic parameter in the lower plateau of the correspondent S-curve, meaning that the range of catalytic parameter that complies with the conditions is wider than previously, therefore the loss of accuracy. While silver catalycity for oxygen does not differ much from the one for nitrogen (silver is equally catalytic for both according to the model adopted), the fact that quartz catalytic behavior moves to higher values means that the interval for copper catalycity is stretching, therefore *deforming* the shape of the PDF associated with this quantity and assigning very similar probabilities to a larger range of gammas. For the problem at hand, it is coherent with the experiments to have copper catalytic behavior in a wider interval when nitrogen recombination at the wall is prescribed from the previous experiments and assumed constant.

Looking now at the distributions obtained for the oxygen recombination parameter when the nitrogen one is assumed unknown:

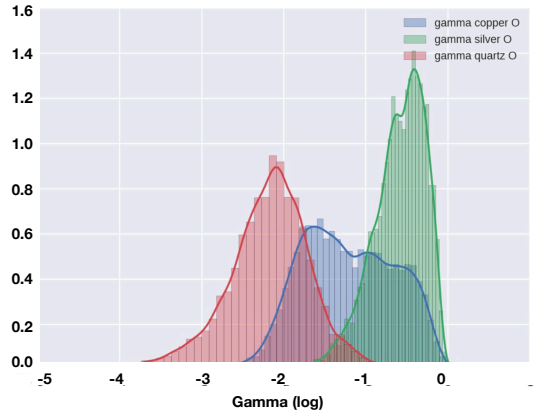

Figure 13: Gamma PDFs for test case 9b with air and nitrogen parameter unknown

The tendency described for the previous case, holds even more for the case of nitrogen catalycity unknown by making the quartz even more catalytic for oxygen reactions than previously seen. The catalytic behavior of quartz is influenced by the assumption of the nitrogen distribution (assumed constant or unknown), moving to higher values when the catalycity of nitrogen reactions is not assumed, leaving the determination of copper catalytic parameter in the flat part of the plateau for high catalycity values. The assumption of using the nitrogen case has a big impact on the results obtained, as seen when comparing both results.

The a posteriori distribution obtained for nitrogen in the air experiments can be seen below:

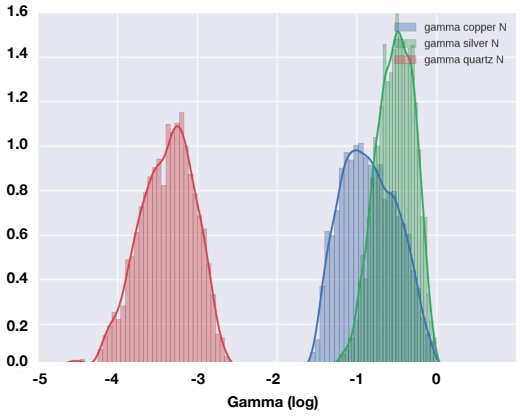

Figure 14: Nitrogen catalycity for air experiments

When compared to the previous results in pure nitrogen flow, the differences can be noted. In pure nitrogen flows the catalycity of nitrogen is overestimated. When considering air, the delicate interplay of the oxygen atoms occupying different active sites on the material surface makes the recombination of nitrogen atoms less likely, therefore decreasing their catalytic behavior.

5. Conclusions and remarks

In this study, a rigorous method for estimating the catalytic property of a material and the associated uncertainties is presented. By construction, the Bayesian approach is more adapted to cases where a limited number of experiments are available, moreover, we found that the Bayesian approach is also more flexible as it can naturally include epistemic variables such as the unknown reference calorimeter catalytic property uncertainty.

For the case of pure nitrogen flows, the strategy followed shows consistency for cases 8b and 9b, while for case 1b the methodology does not hold and the capability of predicting heat fluxes is lost in the sense that the a posteriori distribution for the heat fluxes obtained does not include the experimental point of consideration.

In a more accurate description of the phenomena by using a two gamma model, the assumption of assuming an a priori distribution for nitrogen recombination has a strong effect on the results observed and the determination of copper catalycity undergoes a loss of accuracy that renders the model not fit for the experimental conditions chosen.

A long-term objective will be to minimize the number of numerical and physical experiments to be performed in order to calibrate the physical model with a prescribed level of confidence while testing different physical assumptions along the way, gaining insight on the physics of the problem.

Acknowledgments

This work is partially funded by the European Commission's H2020 programme, through the UTOPIAE Marie Curie Innovative Training Network, H2020-MSCA-ITN-2016, Grant Agreement number 722734.

References

[1] T. M. Cheung, F. F. J. Schrijer, and G. Park, Nitrogen Catalytic Recombination on Copper Oxide in Tertiary Gas Mixtures, Journal of Spacecraft and Rockets, Vol. 53, No. 4 (2016), pp. 644-653.

[2] R. R. Upadhyay, K. Miki, O. A. Ezekoye, and J. Marschall, Uncertainty quantification of a graphite nitridation experiment using a Bayesian approach, Experimental Thermal and Fluid Science, vol.35, issue.8, pp.1588-1599, 2011

[3] A. Turchi, P. M. Congedo and T. E. Magin, Thermochemical ablation modeling forward uncertainty analysis—Part I: Numerical methods and effect of model parameters, International Journal of Thermal Sciences (2017)

[4] F. Sanson, N. Villedieu, F. Panerai, O. Chazot, P. M. Congedo and T. E. Magin, Quantification of uncertainty on the catalytic property of reusable thermal protection materials from high enthalpy experiments, Experimental Thermal and Fluid Science 82 (2017) 414-423

[5] F. Sanson, F. Panerai, T. E. Magin and P.M. Congedo, Robust reconstruction of the catalytic properties of thermal protection materials from sparse high-enthalpy facility experimental data, Under review

[6] A. Viladegut and O. Chazot, Deterministic modelling of copper catalysis for enthalpy determination in plasma facilities, Under review

[7] H. W. Krassilchikoff, Procedure for the determination of the cold copper catalycity, Project report 2006-18, von Karman Institute for Fluid Dynamics

[8] D. LeQuang, Spectroscopic measurements of sub- and supersonic plasma flows for the investigation of atmospheric re-entry shock layer radiation, Ph.D. thesis, von Karman Institute for Fluid Dynamics / Université Blaise Pascal (UBP) (2014)

[9] J.B. Scoggins and T.E. Magin, Development of mutation++: multicomponent thermodynamic and transport properties for ionized plasmas written in c++, 11th AIAA/ASME Joint Thermophysics and Heat Transfer Conference, American Institute of Aeronautics and Astronautics, AIAA 2014-2966, Atlanta, GA, 2014

[10] P.F. Barbante, Accurate and efficient modelling of high temperature nonequilibrium air flows, Ph.D. thesis, von Karman Institute for Fluid Dynamics / Université Libre de Bruxelles (2001)

[11] B. Bottin, D. P. V. Abeele, M. Carbonaro, G. Degree and G. S. R. Sarma, Thermodynamic and transport properties for inductively plasma modeling, Journal of Thermophysics and Heat Transfer 13 (3) (1999) 343-350

[12] C. Park, Nonequilibrium hypersonic aerothermodynamics, NASA Ames Research Center, New York John Wiley & Sons, 1989

[13] R. N. Gupta, J. M. Yos, R. A. Thompson and K.P. Lee, A review of reaction rates and thermodynamic and transport properties for an 11-species air model for chemical and thermal nonequilibrium calculations to 30000k, Nasa-rp-1232, NASA Langley Research Center, Hampton, VA, United States (1990)

[14] M. G. Dunn and S.-W. Kang, Theoretical and experimental studies of reentry plasmas, Nasa-cr-2232, State Univ. of New York; Buffalo, NY, United States, NASA, Washington, United States (April 1973)

[15] R. A. Copeland, J. B. Pallix and D. A. Stewart, Surface-catalyzed production of no from recombination of N and O atoms, Statistical Computing (2008) 18: 343373

[16] C. Andrieu and J. Thoms, A tutorial on adaptive MCMC, Springer Journal Statistics and Computing (2008) 18: 343373

Design of experiments to assess non-equilibrium nozzle flow phenomena in the VKI Longshot hypersonic tunnel

Zdeněk Ilich

Aeronautics and Aerospace Department, von Karman Institute for Fluid Dynamics, Belgium, zdenek.ilich@vki.ac.be

Supervisor: Olivier Chazot

Professor, Aeronautics and Aerospace Department, von Karman Institute for Fluid Dynamics, Belgium, chazot@vki.ac.be

University Supervisor: Herbert Olivier

Professor, Shock Wave Laboratory, RWTH Aachen University, Germany, olivier@swl.rwth-aachen.de

Abstract

This paper presents the design of experiments aiming to improve understanding of the nozzle flow in the VKI Longshot gun tunnel. The utilization of a test gas other than the commonly used nitrogen is proposed in order to find the origin of a free-stream Mach number lower than anticipated based on the nozzle geometry. The operation of the wind tunnel with a different test gas is reviewed and numerically simulated. This effort led to conducting the very first run with a monatomic test gas. The existing rebuilding methods for determination of free-stream conditions are modified for the new test gas. Preliminary results are presented. Despite a high uncertainty on the rebuilt free-stream Mach number, the results suggest that the lower Mach number occurs also for the monatomic gas. Proposals for next experiments which should allow drawing the final conclusions are given.

Keywords: Hypersonic, Longshot, test conditions, nozzle flow

Nomenclature

Symbols

A	area, m^2
C	Chapman-Rubesin factor, $C = \frac{\rho_w \mu_w}{\rho_\infty \mu_\infty}$
c_p	specific heat at constant pressure, J/(kg.K)
d	diameter, m
h	specific enthalpy, J/kg
$\bar{h}$	reduced enthalpy, $\bar{h} = h/(rT_{ref})$
K	hypersonic similarity parameter, $K = \mathrm{M}_\infty \frac{\mathrm{d}}{\mathrm{l}}$
l	length, m
M	Mach number
Nu	Nusselt number
p	pressure, Pa
$\dot{q}$	heat flux, W/m^2
r	specific gas constant, J/(kg.K)
R_N	nosetip radius, m
Re	Reynolds number
s	specific entropy, J/(kg.K)
T	temperature, K
u	velocity, m/s

Greek Symbols

δ	boundary-layer thickness
γ	specific heat ratio
ρ	density, kg/m^3
μ	dynamic viscosity, Pa.s
$\bar{\chi}$	viscous interaction parameter, $\bar{\chi} = \frac{\mathrm{M}_\infty^3 \sqrt{C}}{\sqrt{\mathrm{Re}_{x,\infty}}}$

Superscripts

*	critical quantities

Subscripts

t	total quantities
vib	relative to vibrational modes
$r-t$	relative to rot. and trans. modes
s	stag. condition outside boundary layer
w	at the wall
0	stagnation conditions in the reservoir
1	condition upstream a normal shock
2	condition downstream a normal shock
∞	free-stream value

1. Introduction

1.1. Background

Characterization of free-stream properties is an essential task for every wind-tunnel test. However, it may be very challenging. This is especially true for hypersonic facilities where relatively short test times may be associated with specific phenomena such as dense-gas effects, high temperatures, chemistry, or non-equilibrium effects. Due to limited measurement techniques which are available, all flow quantities of interest cannot be measured directly. Instead, rebuilding methods are required.

A rebuilding method takes a set of measured quantities, typically at the exit section of a nozzle and in its reservoir, and determines the rest of flow properties, characterizing the free-stream in the test section. The set of measured input quantities is not unique and can be selected to suit a particular facility or test purpose. Thus, two distinct rebuilding methods applied to the same facility may result in different accuracy on the rebuilt conditions and may also involve different assumptions about the nature of the flow.

Two methods for determining the free-stream test conditions in the VKI Longshot hypersonic wind tunnel (Fig. 3) are currently available. Hereafter, they will be referred to as *"nozzle method"* and *"free-stream method"*. The *nozzle method* is chronologically the first one. Unfortunately, its generality is reduced by required assumptions of adiabatic and isentropic nozzle flows. This significant drawback was a motivation for developing the new *free-stream method*.

Surprisingly, the comparison of both methods has shown that the Mach number issuing from the free-stream method is lower than from the other. Several different proofs for such a lower Mach number have been found during past years leading to good confidence in this conclusion [1]. Nevertheless, the physics responsible for such a behavior of the Longshot nozzle remains unknown[1].

More than forty years ago, a similar issue was experienced for Mach 14 contoured nozzle of the arc-heated AEDC Tunnel F. In order to explain the 25% drop in Mach number, Boudreau introduced a hypothesis about "melting" of the frozen vibrational energy

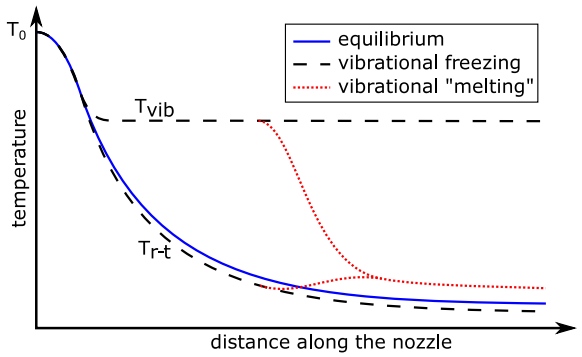

Figure 1: Evolution of temperature along a nozzle, redrawn from [3].

[2; 3]. Due to high temperatures reached in nozzle reservoirs of hypersonic wind tunnels[2], the vibrational mode of the test gas (nitrogen) is excited. Grossir [1] estimates that about 10% of the internal energy of nitrogen is stored in the vibrational mode at such temperatures. The high-temperature gas is then expanded through the nozzle. It can be shown that the finite relaxation time may cause the vibrational freezing. It is possible to numerically reproduce this phenomenon despite quite a large uncertainty on models for the relaxation rates. A 1D simulation of the Longshot nozzle predicts such a vibrational freezing to occur shortly downstream the throat [1]. Boudreau's hypothesis says that this frozen energy is relaxed ("melted") later in the nozzle expansion. Although the mechanism responsible for the melting has not been identified yet[3], its effects (corresponding to heating up a supersonic flow) can be predicted. An example of temperature evolution along a nozzle, where the vibrational melting takes place, is depicted in Fig. 1. The gas expands from the reservoir temperature T_0 and eventually reaches the final equilibrium state at the nozzle exit. However, the final equilibrium state in presence of the melting differs from one achieved in a fully-equilibrium expansion. The higher free-stream temperature means the higher speed of sound and thus the lower Mach number.

1.2. Objectives

Since no definitive conclusions have been drawn about Boudreau's hypothesis nor the Longshot non-

[1] Currently, two nozzles are available for the Longshot: a contoured nozzle designed for Mach 14 and a conical nozzle with adjustable throat diameter. The lower Mach number has been observed for both nozzles.

[2] High reservoir temperatures are required in order to avoid condensation in the test section. Typical reservoir temperature in the Longshot is about 2500 K.

[3] Boudreau attributed the melting to residual amounts of water vapor presented in the test gas.

equilibrium nozzle expansion, any related experimental data are very desired. The main idea of the present study is to utilize another test gas with vibrational behavior different than the commonly used diatomic nitrogen. Being monatomic, the noble gases represent the most attractive option as no vibrational modes can be excited. In short, if Boudreau's hypothesis is correct, the nozzle and the free-stream rebuilding methods should agree providing monatomic gas is used[4].

First, a selection of the suitable monatomic gas is discussed. The core of the present work is organized into two main sections: operation of the tunnel, and rebuilding of the flow properties. Finally, results from preliminary tests already carried out are presented.

2. Selection of test gas

The noble (or inert) gases are monatomic gases with very low chemical reactivity. Excluding the radioactive radon, there are five naturally occurring noble gases: helium, neon, argon, krypton, and xenon. Being within the same group of chemical elements, they all have similar properties. Their theoretical ratio of specific heats is 5/3. To select the suitable test gas for the Longshot tunnel, an essential requirement of condensation-free nozzle flows is considered.

The conical nozzle detailed in Section 3.2 has been selected for the present experiment as it has the universal geometry regardless Mach number or gas used. Knowing the nozzle geometry and thus the area ration A^*/A, the Mach number in the test section can be determined assuming calorically perfect gas[5]. The free-stream static pressure can be than roughly estimated assuming that the total free-stream pressure is equal to the reservoir pressure commonly achieved in the Longshot.

Saturation lines for the considered gases are plotted in Fig. 2. The supercooling effect is limited to at most 3 K for nitrogen. For sake of simplicity, it is assumed that condensation is initiated along the saturation lines. Therefore, one can easily read from Fig. 2 the limit temperature for the given static pressure. The corresponding total free-stream temperature is again considered to be equal to the reservoir temperature.

[4]It is assumed that the vibration melting is the only one responsible for the lower Mach number.

[5]The displacement thickness on the nozzle wall plays an important role on the area ratio as the boundary layers for hypersonic regimes are usually thick. For the preliminary assessment, the typical displacement thickness for nitrogen was used.

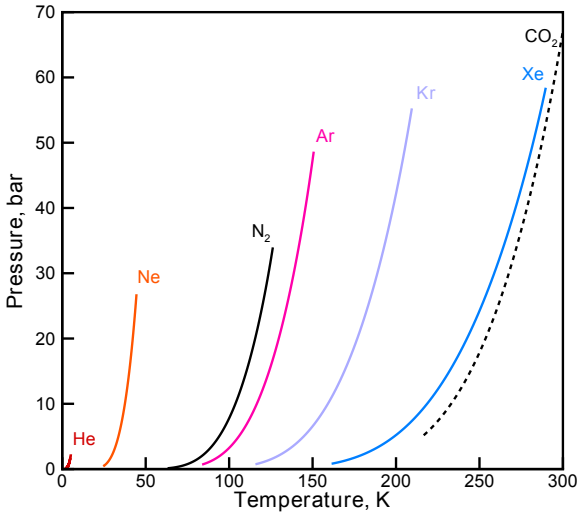

Figure 2: Saturation curves in terms of pressure and temperature.

Following the described approach, the minimal reservoir temperature required to ensure condensation-free flows can be estimated for every noble gas.

The results are summarized in Table 1. Helium seems to be the only noble gas which is below the maximal allowable temperature in the reservoir (about 3500 K). On the other hand, the ambient temperature is basically sufficient for helium. This explains the often use of helium for hypersonic facilities in the past since no extensive heating of the reservoir gas is required to achieve high Mach numbers [4].

Table 1: Minimal reservoir temperatures required to avoid flow condensation.

gas	γ	Mach	T_0(K)	
N_2:	1.4	14.7	2215	
CO_2:	1.3	10.6	2675	
He	1.66	37	330	$T_{0,max} \approx 3500$ K
Ne	1.66	37	6800	
Ar	1.66	37	17 973	

3. Operation of the wind tunnel

The final goal of this section is to define initial conditions for the tunnel which, first of all, would ensure the safe initial helium test without any damage of the facility and which would result in reasonable free-stream conditions. The initial conditions are the initial pressures in both driver and driven tubes, and the piston mass. From a safety point of view, the most important issues which must be avoided are the

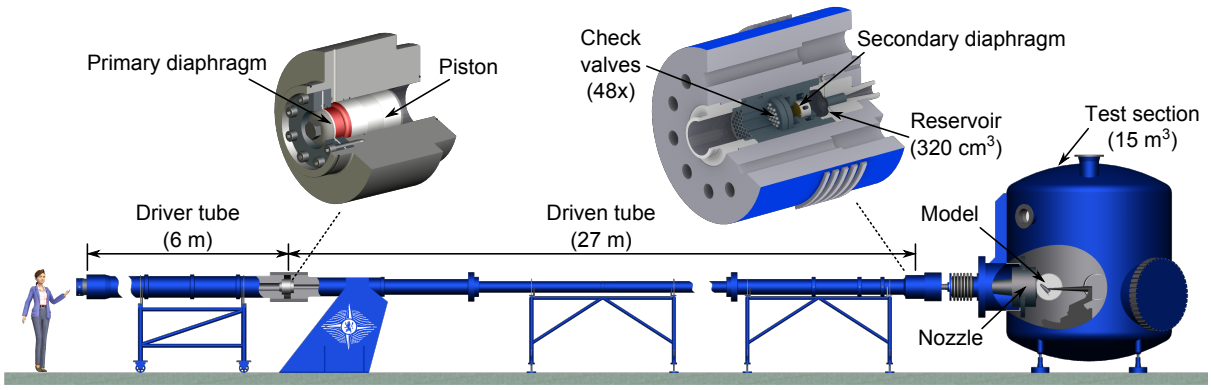

Figure 3: The VKI Longshot hypersonic gun tunnel.

impact of the piston against the check valves at the end of the driven tube and the development of excessive pressures and temperatures anywhere. The high temperatures, and thus also the large heat fluxes, are especially critical for the nozzle throat and for those parts of the check-valve system that have a low thermal inertia, like the check valves themselves or the secondary diaphragm[6].

In order to meet this point, the compression process of the tunnel has been simulated using the L1d code. The nozzle flow is then computed using the commercial software CFD++. If possible, the obtained results are compared with available data from two performed tests (run numbers #1791, #1792).

3.1. Compression process

The L1d is a quasi-one-dimensional Lagrangian solver developed by Jacobs (1999) from the University of Queensland (Australia) [5] and significantly customized at VKI during past years. The modeling of the compression process using the L1d solver is extensively detailed in [6; 7]. The behavior of nitrogen is described by the real Span & Wagner equation of state [8; 9; 10] and recently by the reference equation [11] implemented in the code through the look-up table approach. For the present case, modifications of the code have been made allowing it to handle different real gases for the driver and the driven tubes (nitrogen is still used as a driver gas). The state-of-the-art equation of state for helium [12], which is valid up to 1500 K, has been implemented. This equation is of a type which usually allows reasonable extrapolation to higher temperatures, nevertheless without guaranteed accuracy.

In order to retrieve the reliable peak reservoir pressure and temperature from the L1d computations, empirical loss coefficients must be applied at the end of the driven tube. This mimics the losses through the complex system of the check valves. It should be emphasized that the proper values of these loss coefficients are found based on available experiments. Therefore, it is not possible to set it correctly for the first helium run and the values for nitrogen must be used instead. After the initial run, these coefficients can be re-calibrated for helium[7].

The performed experiments have confirmed that helium can much easily pass through small orifices and obstacles. Therefore, the additional loss coefficients through the check valves have been set to zero. This provides a very good agreement on the peak reservoir pressure with the experimental data. However, the amount of gas which has left the reservoir through the throat before the peak pressure is reached is not negligible unlike for nitrogen. An extended geometry (with an appended dummy nozzle to mimic ventilating of the reservoir) must be used for helium. The peak pressure is then retrieved from pressure monitoring at a fixed location at the end of the reservoir rather than from the averaging method used for the closed geometry in [6; 7].

Several computations have been performed in order to define the initial conditions for the first helium test. Table 2 presents the reference computation using nitrogen and the final selected conditions for helium.

[6] Although the secondary diaphragm is not a critical component of the system, its excessive burning may lead to a higher pollution of the flow.

[7] If the closed computational domain along with the loss coefficient valid for nitrogen is used for helium, the computed reservoir conditions are $P_0 = 623$ bar and $T_0 = 1677$ K, i.e. both about 13% higher.

The latter provides reasonably low reservoir temperature and pressure. The corresponding total enthalpy is $h_0 \approx 7.8\,\mathrm{MJ/kg}$.

Table 2: L1d computations of the compression process.

gas	initial conditions driver p (bar)	driven p (bar)	piston mass (kg)
N_2	345	1.441	1.59
He	345	3.900	1.59
gas	**reservoir conditions** p (bar)	T (K)	Rebound (mm)
N_2	1350	2320.3	100.6
He	550	1478.8	750.1

The space-time diagrams resulting from the numerical simulations of these two tests are depicted in Fig. 4. The pressure for the selected helium test does not exceed values occurring for the standard nitrogen test. The much higher speed of sound for helium[8] leads to the remarkable change in the shock wave pattern between the piston and the end of the driven tube. The deceleration of the piston and the pressure increase before it are more gradual. The comparison of the piston acceleration is shown in Fig. 5 which also provides an idea of the involved forces (the piston mass is the same for both cases). The deceleration of the piston is almost an order of magnitude lower for the selected helium test than for the standard low Reynolds regime with nitrogen.

The discrete points (●, ●) in Fig. 4b represent characteristic events (shocks, piston passages,...) collected from the pressure measurements along the driven tube for two performed tests (#1791 and #1792). The agreement with the numerical prediction is excellent.

The distance between the maximal piston position and the check valves is more than seven times bigger than for the regular nitrogen test. This is regarded as a sufficient margin. The secondary diaphragm seems to withstand higher pressure as the pressure increase is more gradual than for nitrogen. However, it is ruptured about 3 ms earlier for the helium test (time measured with respect to the piston rebound). The computations have also shown that the check valves close only for a very brief time. This all leads to the very small useful test time (about 3 ms, see Section 5).

[8]Speed of sound for helium is 1019.1 m/s whereas for nitrogen only 353.1 m/s at 300 K.

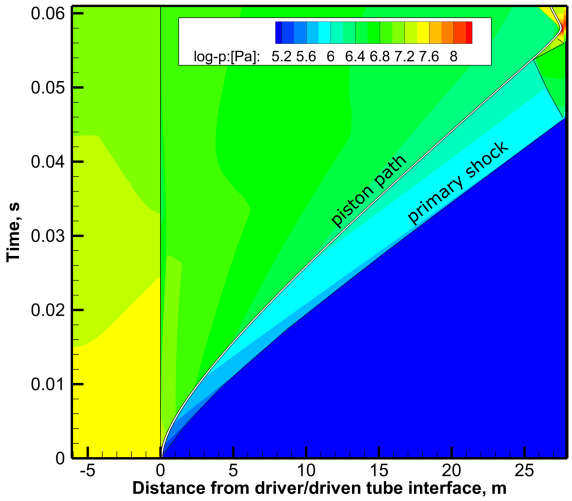

(a) Nitrogen - standard low Reynolds conditions.

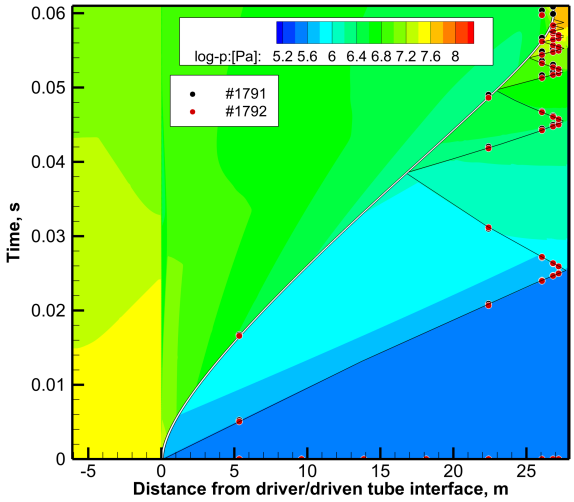

(b) Helium - selected conditions for the first run.

Figure 4: Space-time diagrams of the compression process with iso-pressure contours (log-scale) resulting from the L1d simulation. Symbols (●, ●) denote characteristic events measured experimentally along the driven tube.

3.2. *Nozzle flow*

The conical nozzle (6° half-angle) has been selected for the experiments. The length of the nozzle is 1.694 m as measured from the apex of the divergent. The corresponding nozzle exit radius is 0.178 m. The selected throat diameter for the first helium test is 5 mm. More details regarding the nozzle can be found in [13].

The 2D axisymmetric computation of the nozzle flow has been performed using the commercial software CFD++. This allows estimating the free-stream

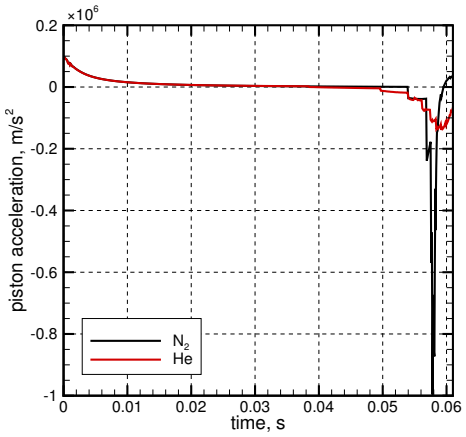

Figure 5: Piston acceleration.

flow properties and the heat fluxes experienced by the nozzle throat. The 2D structured mesh consisting of 156 975 quadrilateral cells has been used ensuring $y^+ < 0.5$ everywhere along the nozzle wall. In order to avoid the use of complex real gas equations of state, equivalent perfect gas conditions can be defined following the work of Culotta and Richards [14]. First, it is necessary to determine the gas enthalpy h_0 and entropy s_0 corresponding to the actual reservoir pressure and temperature using the real gas equations of state. The equivalent perfect gas reservoir conditions are determined as follows:

$$(T_0)_{\mathrm{PG}} = \frac{h_0}{\left(c_p\right)_{\mathrm{PG}}}, \tag{1}$$

$$(p_0)_{\mathrm{PG}} = p_{\mathrm{ref}}\ exp\left(\frac{s_0'}{r} - \frac{s_0}{r} + \frac{\left(c_p\right)_{\mathrm{PG}}}{r}\ ln\left(\frac{(T_0)_{\mathrm{PG}}}{T_{\mathrm{ref}}}\right)\right), \tag{2}$$

where s_0' is the perfect gas entropy at reference conditions (p_{ref} and T_{ref}) and the subscript PG refers to quantities determined using the calorically perfect gas relations. The equivalent reservoir conditions for both cases are listed in Table 3.

Table 3: Equivalent reservoir conditions.

gas	p (bar)	T (K)
N_2	1190	2770.49
He	573	1508.3

The *turbulent* computation using the SST $k-\omega$ model has been performed with a turbulent to laminar viscosity ratio $\frac{\mu_t}{\mu} = 2$ and a free-stream turbulence level of 5% in the reservoir. The nozzle wall is considered as isothermal with $T_w = 300\,\mathrm{K}$. Total enthalpy and Mach number contours are reported in Fig. 6. The boundary layer thickness in the exit plane is $\delta_{\mathrm{turb}} = 86.2\,\mathrm{mm}$ (based on 99% of the free-stream total enthalpy, Fig. 7), which is about 23 mm thicker than for the Low Reynolds regime using nitrogen reported in [13].

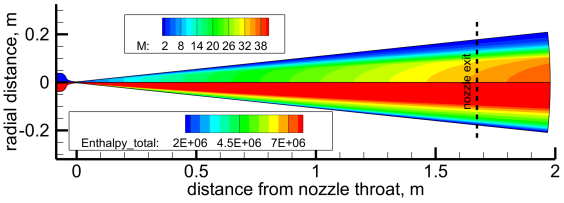

Figure 6: Conical nozzle flow using helium.

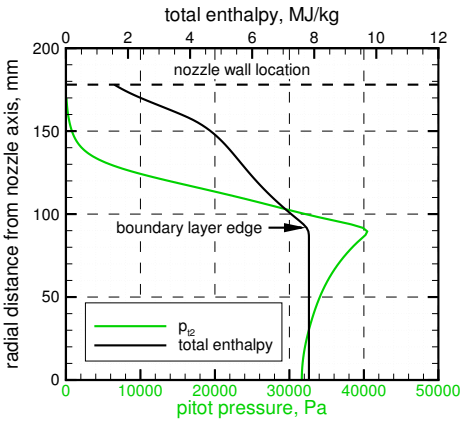

Figure 7: Total enthalpy and pitot pressure in the nozzle exit section.

The evolution of flow properties along the nozzle axis is shown in Fig. 8. The values corresponding to the exit plane are summarized in Table 4. The very low static temperature should still be sufficient to avoid condensation thanks to low static pressure. The saturation pressure for 4.18 K is about 0.64 bar.

The very low static pressure of about 18 Pa makes its accurate measurement harder and may lead to higher uncertainties. Although the numerical results for nitrogen exhibit rather low pressure as well (about 100 Pa), measured values are typically higher (usually above 250 Pa) as the numerical simulations predict higher Mach numbers than the rebuilt ones using the *free-stream method*. However, CFD computations of the static pressure probe reported in Section 4.2.2 shows that the wall-to-free-stream pressure ratio $\frac{p_w}{p_\infty}$ is bigger than for nitrogen and therefore the wall pres-

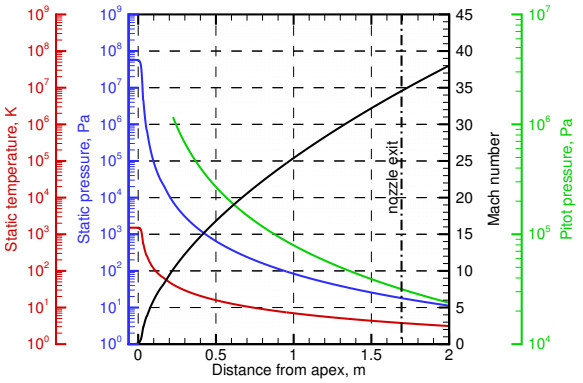

Figure 8: Evolution of flow quantities along the nozzle axis.

sure felt by sensors should be in reasonable range. The predicted value of the pitot pressure well fits the current instrumentation of the stagnation probe (piezo-resistive sensors Kulite XCQ-093-25PSI).

Table 4: Flow quantities at the exit plane of the conical nozzle using helium.

Mach number	34.55
static pressure	18.05 Pa
static temperature	3.78 K
velocity	3952.14 m/s
pitot pressure	31.66 kPa

The heat flux to the nozzle wall is reported in Fig. 11. The maximal wall heat flux occurs about 4 mm upstream the throat and is about 249 MW/m^2. This is about two times higher than for nitrogen.

It is important to note that above values correspond to the peak reservoir conditions. The flow quantities decay from these peak values in time. The test time is significantly shortened with respect to nitrogen. The test time[9] of helium run #1792 is about 7 ms which is only 35% of the typical test time for nitrogen ($\approx$ 20 ms).

4. Rebuilding of free-stream flow properties

The first part of the section briefly presents the existing rebuilding methods used in the Longshot along with their assumptions. Then, the methodology used to rebuild the free-stream properties for helium tests is introduced and discussed.

[9]The test time is limited by a closure of the jet at the nozzle axis. The useful test time is even shorter.

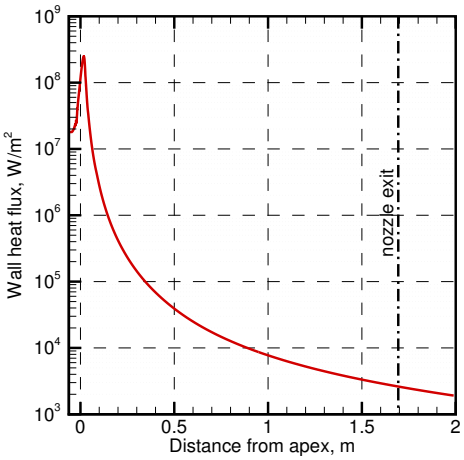

Figure 9: Wall heat flux along the nozzle.

4.1. Existing methods

An extensive overview of the methods currently used can be found in [1]. Only the main points important for the present content are pointed out here.

4.1.1. Nozzle method

Although this method is still available, it is not used as a primary tool to characterize the free-stream of the Longshot facility anymore. The method relies on measurements of three quantities: the stagnation point heat flux on a hemispherical probe $\dot{q}_w$ and the pitot pressure p_{t2} both measured in the test section, and the reservoir pressure P_0 monitored by a fast-response Kistler sensor. The main issue which must be overcome is that the reservoir pressure is not the same as the total pressure p_{t1} in the test section due to dense gas effects. Therefore, an iterative procedure is required. The first step is an estimation of the reservoir temperature T_0. Using the measured reservoir pressure P_0 and the real gas equation of state, it is possible to determine entropy and enthalpy of the reservoir gas. The nozzle flow is assumed to be adiabatic and isentropic allowing considering both entropy and enthalpy to be constant all along the nozzle. Corresponding equivalent perfect gas conditions p_{t1} and T_{t1} can be calculated using Eqs. 1 and 2. The Fay-Riddell equation [15] is used to infer the stagnation point heat flux which is then compared to the measured heat flux on the hemispherical probe. The iteration on T_0 is performed until both predicted and measured values of the stagnation point heat flux are equal. The perfect gas relation is then used to compute the Mach number from the total pressure ratio across the normal shock p_{t2}/p_{t1}.

The resulting Mach number usually agrees well with numerical computations of the nozzle flow as well as with the designed Mach number of the nozzle.

4.1.2. Free-stream method

Nowadays, this is the main procedure to determine the free-stream properties in the Longshot tunnel. It has been introduced by Grossir (2015) [1]. It benefits from the fact that all experimental inputs are acquired in the test section. No assumption about the nozzle flow nor the reservoir conditions is needed[10].

The thermal and transport properties are determined using the VKI *Mutation* library [16] where nitrogen is considered as a mixture of 5 species (N_2, N, N_2^+ , N^+, e^-) following the *thermally* perfect gas law. The method requires measurements of the stagnation point heat flux $\dot{q}_w$, the pitot pressure p_{t_2}, and the free-stream static pressure p_∞. First, two unknown free-stream quantities (the velocity u_∞, and the static temperature T_∞) are prescribed. They, together with the static pressure p_∞, represent a sufficient set to determine the total conditions behind the normal shock (p_{t2}, T_{t2}). Then, the Fay-Riddell equation is applied to find the corresponding stagnation point heat flux. The latter one along with the pitot pressure is compared to the measured values and the free-stream velocity and static temperature are iterated until the match is achieved.

This method has uncovered the lower Mach number issue in the Longshot facility. Several other proofs independent of the rebuilding method have been found: onset of flow condensation, shock angle, pressure distribution along a cone, and the spectrum of boundary-layer disturbances.

4.2. Simplified method for helium

Since there is no practical application so far, it is not planned to use helium as a standard test gas. For this reason, a simplified rebuilding method is proposed hereafter.

The methodology used to determine the free-stream flow properties for helium tests is based on the classical *free-stream method* described in Section 4.1.2. The main simplification raises from the fact that helium can be treated as the *calorically* perfect gas (vibrational modes cannot be excited). Therefore, the simple Rayleigh pitot formula and conservation of the total temperature across the normal shock can be used instead of solving the full Rankine-Hugoniot jump conditions[11].

The pressure measured by the static probe p_w is not, in fact, the free-stream static pressure p_∞ due to viscous effects along the probe. Therefore, the first step is to apply an estimation of the viscous correction p_w/p_∞ on the wall pressure p_w. The resulting static pressure p_∞ and the measured pitot pressure p_{t2} lead to the Mach number through the Rayleigh pitot formula. The stagnation point heat flux is obtained by integration of the wall temperature of the hemispherical probe T_w using the common semi-infinite slab model [17]. The total temperature behind the normal shock T_{t2} can be retrieved from a model replacing the Fay-Riddell equation (Section 4.2.1). Finally, the relations valid for calorically perfect gas are employed to determine all free-stream quantities of interest. The viscous correction p_w/p_∞ depending on free-stream conditions ($\bar{\chi}$, K) is then recomputed and used as the input for the next iteration until the match is obtained. This iteration is repeated for every time instant.

Despite the simplicity of the method, the models for the viscous correction and for the stagnation point heat flux must be defined.

4.2.1. Model for stagnation point heat flux

Starting from boundary layer equations for global continuity, species continuity, momentum, and energy, Fay and Riddell [15] have obtained a set of nonlinear ordinary differential equations for the stagnation point. The found self-similar solutions hold for chemically reacting viscous flows of air or nitrogen. This Fay-Riddell equation depending among others on the heat-transfer parameter $\mathrm{Nu}/\sqrt{\mathrm{Re}}$ relates the wall heat flux at the stagnation point to the free-stream total enthalpy. For the equilibrium boundary layers with Lewis number equal to one (acceptable for the Longshot case), the heat-transfer parameter depends only on the total variation of $\rho\mu$ across the boundary layer. The simple correlation $\mathrm{Nu}/\sqrt{\mathrm{Re}} = 0.67(\rho_s\mu_s/\rho_w\mu_w)^{0.4}$ has been established by fitting numerical data. The vicinity of the stagnation point of a hemisphere together with the corresponding nomenclature is depicted in Fig. 10.

The original formula does not hold for helium. Therefore, it is necessary to perform numerical simulations and determine new correlations. For this pur-

[10] Currently, it is assumed that the flow is in local equilibrium everywhere.

[11] The Rayleigh pitot formula gives reasonable results (within 2% on the Mach number) even for nitrogen where vibrational modes are clearly excited downstream the shock.

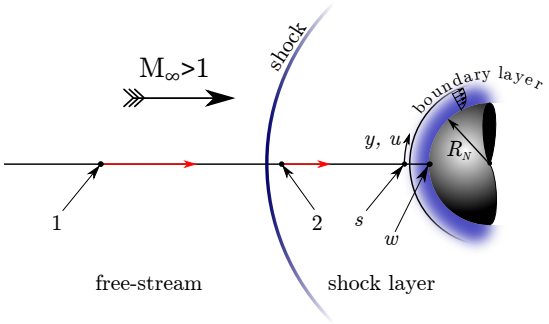

Figure 10: Nomenclature used in the Fay-Riddell equation.

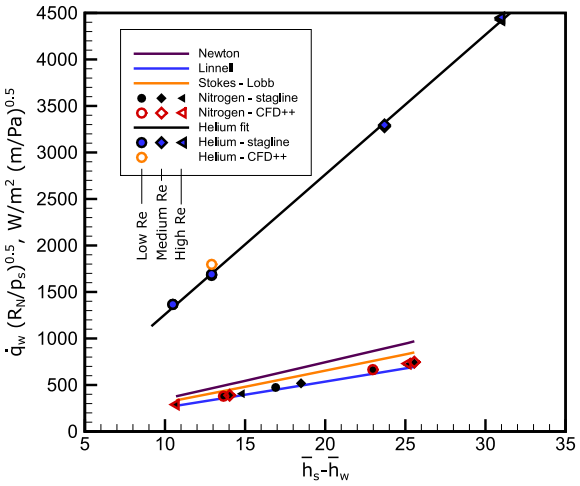

Figure 11: Reduced stagnation point heat flux as a function of reduced enthalpy difference.

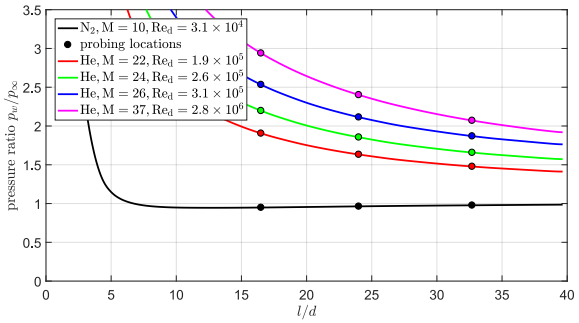

Figure 12: Viscous correction along the static probe.

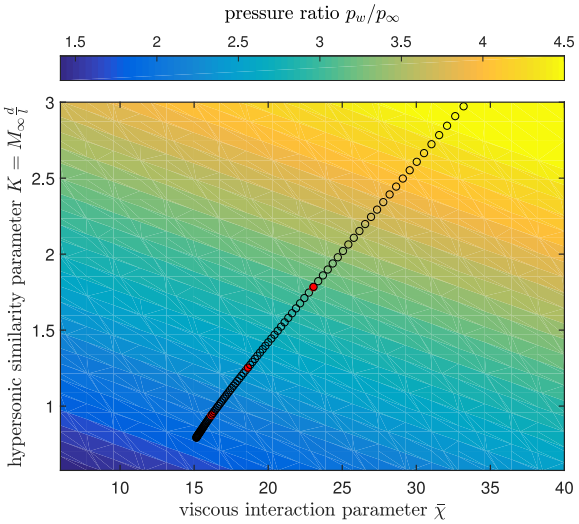

Figure 13: Correlation for the viscous correction of the static probe.

pose, the stagnation-line code has been used. It is a quasi-1D code enabling the determination of flow properties along the stagnation streamline of hypersonic (generally non-equilibrium) flows over spheres or cylinders. This solver developed by Munafò [18] can be coupled with the VKI *Mutation++* thermodynamic library [19; 16]. Results obtained using this numerical tool are presented in Fig. 11 (referred to as the "stagline") for eleven conditions covered the expected range of the enthalpy difference. Also, the numerical data for nitrogen as well as results given by the Fay-Riddell equation are plotted [20]. Due to limited applicability of helium, only a simple correlation of the form $\dot{q}_w \sqrt{R_N/p_{t2}} = c_1(T_{t2} - T_w) + c_0$ is determined by fitting the numerical data (black line in Fig. 11).

4.2.2. Viscous correction of static probe

The viscous correction p_w/p_∞ for the needle probe of Nagamatsu type must be determined in order to relate the measured pressure to the real free-stream static pressure. These corrections are found through numerical simulations using the commercial software CFD++.

Since the probe has been designed for nitrogen, its correction factor is very close to one and almost independent on the free-stream conditions providing nitrogen is used [1]. However, this is not the case for helium as can be appreciated in Fig. 12. A much more slender probe would be necessary. If the existing probe is needed to be used for helium, a relationship between the viscous correction and free-stream conditions must be inferred. It was found that, for limited ranges of appropriately chosen independent variables ($\bar{\chi}$ and K), the viscous correction can be represented by a plane. This is illustrated in Fig. 13 where an example of a particular distribution along the probe is plotted (empty black circles ○). The red dots (●) represent the positions of three sensors installed in the probe. This correlation allows the iterative process described in Section 4.2.

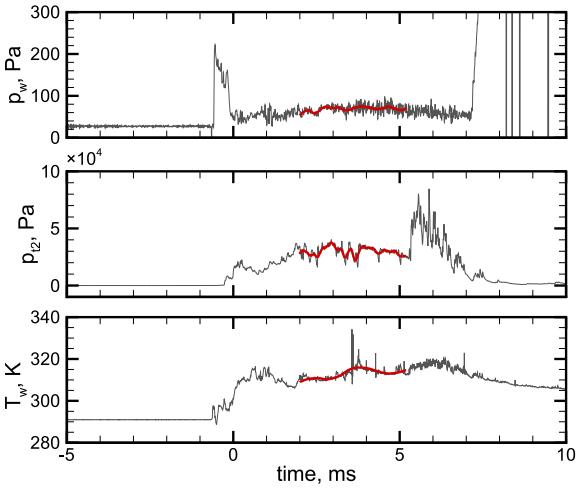

Figure 14: Experimental inputs to the rebuilding method.

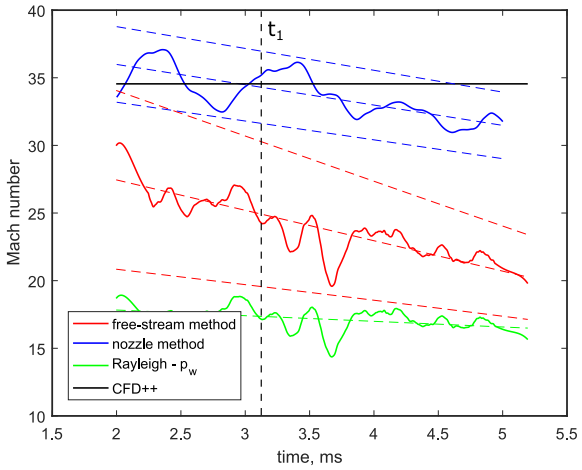

Figure 15: Rebuilt Mach number.

5. Helium test

Two tests with helium were performed as part of the present framework. This was the very first time when another gas than nitrogen or carbon dioxide was used in the Longshot tunnel[12]. The test section was instrumented with probes for full free-stream characterization only for the second test (#1792). As discussed in Section 3, rather moderate conditions were selected for these preliminary tests. Since the compression process had been predicted correctly (Fig. 4b), no damage to the facility occurred.

Figure 14 presents the measured quantities in the test section which are sufficient to rebuild the free-stream conditions (Section 4.2). The useful test time is limited by a closure of the jet at about 5 ms. The transient phenomena at the beginning last approximately 2 ms. Therefore, the useful test time is very short ($\approx$ 3 ms). The flow was quite unstable with pronounced fluctuations. This can be appreciated in Fig. 14 especially for the pitot pressure p_{t2}.

Following the main goal of the present study, attention is paid to the determination of the free-stream Mach number.

5.1. Mach number

Mach number for the preliminary helium test has been rebuilt using the *nozzle method* (Section 4.1.1) and the simplified *free-stream method* (Section 4.2). The results are depicted in Fig. 15.

[12] Accidentally, air has been used as well.

First of all, pronounced fluctuations can be noticed. The nozzle method agrees well with numerical prediction (CFD++) as usual. The Mach number inferred from the free-stream method is strongly influenced by the viscous correction of the static probe and is about 25% lower. For sake of completeness, Fig. 15 depicts also the Mach number corresponding to the wall pressure on the static probe (no viscous correction applied). The decay of the Mach number in time is usually explained by the decreasing Reynolds number and thus the thicker boundary layer on the nozzle wall which increases the effective area ratio A^*/A. However, the decay in Fig. 15 is very steep, especially for the free-stream method.

The dashed lines represent the mean values of the Mach number and their limiting positions when uncertainties on input quantities are considered. The input uncertainties are as follows: 20% on the pitot pressure p_{t2}, 9.5% on the wall pressure measured by the static probe p_w, and 8% on wall temperature of the hemispherical probe T_w. They include accuracy of the sensors, uncertainty resulting from their calibrations, and fluctuations of the acquired signals. The present uncertainties are generally larger than for nitrogen [1] mainly due to the pronounced fluctuations.

If the final uncertainty on the Mach number is taken into account, it is rather difficult to conclude based on Fig. 15 because the error bounds for the nozzle and the free-stream methods overlap.

The large uncertainty on the pitot pressure consists of the random fluctuations and the systematic error as the pitot pressure varies significantly in the radial direction. This can be clearly noticed in Fig. 7 presenting the numerical data of the nozzle flow (Sec-

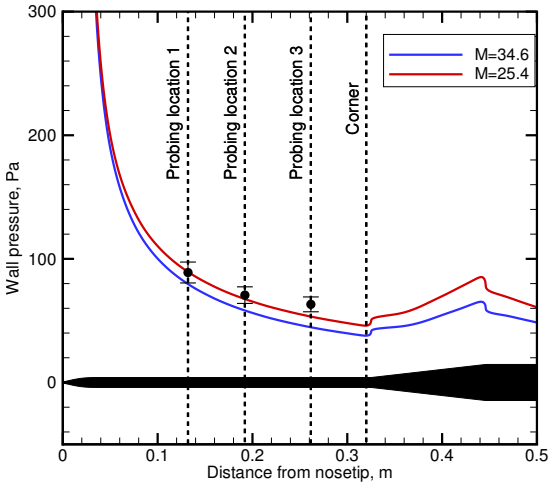

Figure 16: Pressure distribution along the static probe. Symbols (•) denote experimental data for time $t_1 = 3.128$ ms.

tion 3.2). Unfortunately, if the p_{t2} is biased, the nozzle and the free-stream methods go in different directions, i.e. if the measured p_{t2} is higher than the correct value, the rebuilt Mach number is higher and smaller than the correct one for the free-stream and the nozzle methods, respectively (and vice versa).

5.2. Additional results

As has been mentioned above, several independent phenomena proving the lower Mach number exist in the case of nitrogen. The acquired data for the helium test allows comparison of the shock angle and the pressure distribution (both regarding the static probe) against numerical predictions.

The comparison of a Schlieren picture at time $t_1 = 3.128$ ms with numerical contours of the density gradient is presented in Fig 17. The upper contours correspond to the nozzle method ($M_\infty = 34.6$) whereas the lower contours are computed for $M_\infty = 25.4$ as resulting from the free-stream method. Even though the Mach difference is almost 10, the shock angle differs only slightly. This is the well-known behavior of hypersonic flows as the Mach number approaches the limit $M_\infty \to \infty$. The Mach number seems to be somewhere between the nozzle and the free-stream methods. However, the Schlieren pictures cannot be treated as a definitive proof given fluctuations of the flow and uncertainties on the alignment of the probe with the flow.

Figure 16 compares the measured wall pressures along the static probe against the numerical simulations. The lower Mach number $M_\infty = 25.4$ is closer to the measurement. Nevertheless, the measurement from the last sensor is quite off. The reason is not yet clarified.

6. Conclusion

In order to assess the non-equilibrium phenomena of the nozzle expansion in the Longshot facility, the tunnel operation with monatomic test gas (helium) has been deeply investigated. The effort led to the definition of the initial conditions which ensured safety and reasonable free-stream conditions. The accuracy of predictions has been successfully confirmed by carrying out the very first test with another gas than commonly used nitrogen and carbon dioxide.

Modification of the rebuilding method to determine free-stream properties has been proposed to suit specifics of helium. The stagnation point heat flux models has been established replacing the Fay-Riddell equation. Due to the off-design operation of the static pressure probe, the model for its viscous correction had to be defined. The fact that viscous correction factor cannot be regarded as constant increases uncertainties on the rebuilt free-stream conditions.

The acquired data for the preliminary tests exhibits pronounced fluctuation of the flow. The free-stream Mach number has been computed by both nozzle and free-stream methods. Unfortunately, large uncertainties on the pitot pressure do not allow a final conclusion on the validation of Boudreau's hypothesis for the Longshot nozzle flow yet. The other phenomena (shock angles and pressure distribution along the static probe) do not clearly answer the question either. This is mainly due to the fact that hypersonic flows approaching very high Mach numbers become insensitive to it. However, the whole set of obtained results suggests that there is likely the lower Mach number issue even for monatomic helium.

For the planned following tests, the measurement of the pitot pressure should be improved using several pitot probes in the radial direction from the nozzle axes. The initial condition should be tuned to provide higher free-stream Reynolds numbers. Also, the measurement performed inside the nozzle should be preferred. This will moderate the Mach number and thus it should decrease the influence of the viscous corrections as well as slightly reduce insensitivity of the hypersonic flow to the Mach number. Such an experiment will also benefit with longer useful test time.

The conical nozzle can be instrumented by pressure and heat-flux sensors in several locations along its axis. Such a measurement will provide valuable information about the nozzle flow as well.

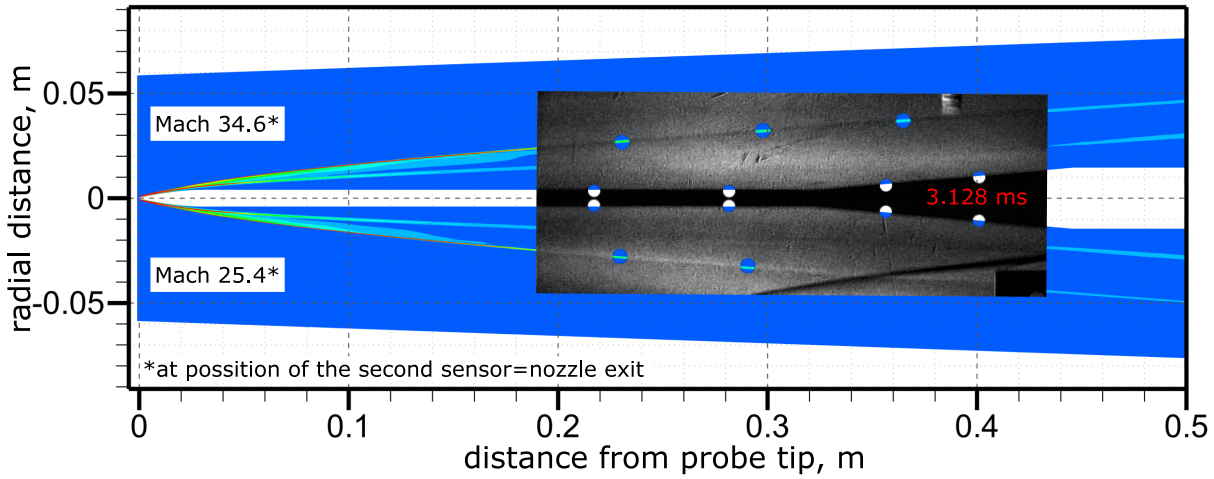

Figure 17: Comparison of Schlieren contours.

Acknowledgments

The author wishes to thank Dr. Grossir and Ing. Paris for their help in designing and conducting the helium tests.

References

[1] G. Grossir, Longshot hypersonic wind tunnel flow characterization and boundary layer stability investigations, Ph.D. thesis, von Karman Institute for Fluid Dynamics - Université Libre de Bruxelles (July 2015).

[2] A. H. Boudreau, Characterization of hypersonic wind tunnel flow fields for improved data accuracy, in: AGARD-CP-429, NATO, 1987.

[3] A. H. Boudreau, Characterization of flow fields in hypersonic ground test facilities, in: Methodology of hypersonic testing, VKI Lecture Series 1993-03, von Karman Institute for Fluid Dynamics, 1993.

[4] M. C. Fischer, D. V. Maddalon, L. M. Weinstein, R. D. Wagner, Jr, Boundary layer pitot and hot-wire surveys at Mach 20, AIAA Journal 9 (5) (1971) 826–834.

[5] P. A. Jacobs, Quasi-one-dimensional modeling of a free-piston shock tunnel, AIAA Journal 32 (1) (1994) 137–145.

[6] G. Grossir, Z. Ilich, O. Chazot, Modeling of the VKI Longshot gun tunnel compression process using a quasi-1D approach, in: 33rd AIAA Aerodynamic Measurement Technology and Ground Testing Conference, 2017 AIAA Aviation Forum, no. AIAA-2017-3985, 2017.

[7] G. Grossir, Z. Ilich, Modeling of the complete VKI Longshot compression process using a quasi-1D approach, Technical Note 4100, VKI CR 2017-05, von Karman Institute for Fluid Dynamics (2017).

[8] R. Span, W. Wagner, Equations of state for technical applications. I. Simultaneously optimized functional forms for nonpolar and polar fluids, International Journal of Thermophysics 24 (1) (2003) 1–39.

[9] R. Span, W. Wagner, Equations of state for technical applications. II. Results for nonpolar fluids, International Journal of Thermophysics 24 (1) (2003) 41–109.

[10] R. Span, W. Wagner, Equations of state for technical applications. III. Results for polar fluids, International Journal of Thermophysics 24 (1) (2003) 111–162.

[11] R. Span, E. W. Lemmon, R. T. Jacobsen, W. Wagner, A. Yokozeki, A reference equation of state for the thermodynamic properties of nitrogen for temperatures from 63.151 to 1000K and pressures to 2200MPa, Journal of Physical Chemistry 29 (6) (2000) 1361–1433.

[12] D. O. Ortiz Vega, A new wide range equation of state for helium-4, Ph.D. thesis, Texas A&M University (2013).

[13] G. Grossir, Flow characterization in existing Longshot nozzles, Technical Note 2400, VKI CR2016-17, von Karman Institute for Fluid Dynamics (2016).

[14] S. Culotta, B. E. Richards, Methods for determining conditions in real nitrogen expanding flows, Technical Note TN-58, von Karman Institute for Fluid Dynamics (February 1970).

[15] J. A. Fay, F. R. Riddell, Theory of stagnation point heat transfer in dissociated air, Journal of the Aeronautical Sciences 25 (2) (1958) 73–85.

[16] T. E. Magin, A model for inductive plasma wind tunnels, Ph.D. thesis, von Karman Institute for Fluid Dynamics - Université Libre de Bruxelles (June 2004).

[17] D. L. Schultz, T. V. Jones, Heat-transfer measurements in short-duration hypersonic facilities, in: AGARDograph No. 165, no. AGARD-AG-165, NATO, 1973.

[18] A. Munafò, Multi-scale models and computational methods for aerothermodynamics, Ph.D. thesis, von Karman Institute for Fluid Dynamics - École Centrale Paris (2014).

[19] J. B. Scoggins, T. E. Magin, Development of Mutation++: Multicomponent thermodynamic and transport properties for ionized plasmas written in C++, in: AIAA AVIATION Forum, no. AIAA 2014-2966, American Institute of Aeronautics and Astronautics, 2014.

[20] Z. Ilich, G. Grossir, O. Chazot, Evaluation of the stagnation point velocity gradient in low-enthalpy hypersonic flows, in: 33rd AIAA Aerodynamic Measurement Technology and Ground Testing Conference, 2017 AIAA Aviation Forum, to be published, 2017.

Experimental characterization and numerical modelling of space debris degradation during atmospheric re-entry

Francisco J. Torres Herrador

Aeronautics & Aerospace department, von Karman Institute for Fluid Dynamics, Belgium, fratorhe@vki.ac.be

Supervisor: Olivier Chazot

Head of the department, Aeronautics & Aerospace department, von Karman Institute for Fluid Dynamics, Belgium, chazot@vki.ac.be

Supervisor: Thierry Magin

Assistant Professor, Aeronautics & Aerospace department, von Karman Institute for Fluid Dynamics, Belgium, magin@vki.ac.be

University Supervisor: Julien Blondeau

Assistant Professor, Department of Mechanical Engineering, Vrije Universiteit Brussel, Belgium, julien.blondeau@vub.be

Keywords: space debris, demise, thermal degradation, high enthalpy flow, gas-surface interaction

First year doctoral summary

Space debris is predicted to increase drastically in the following decades [1]. This increase of debris can trigger the so-called Kessler syndrome: a cascade effect in which the debris impacts with satellites producing more debris, to ultimately destroy many useful satellites and hinder access to space [2]. It is important to tackle this issue before it becomes a real threat.

A cost-effective way to reduce space debris is to force its re-entry on Earth and full demise. During a re-entry, the high velocities of an in-orbit object will be transformed into heat. The high gas temperatures ($T \approx 10\,000\,\mathrm{K}$) will lead to the decomposition of the object [3, 4]. However, a complete decomposition may not be guaranteed. For example, a pressure vessel used for fuel pressurization on the Vega rocket of ESA of about 1 m in diameter was found in India in 2016. This debris can be an important threat if it was to fall in an inhabited area.

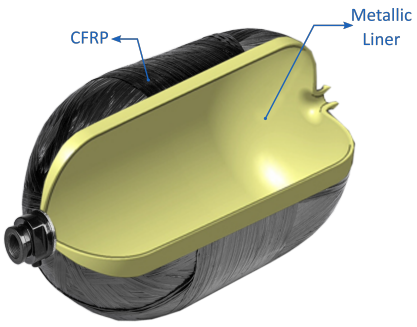

Figure 1: Pressure vessel. Adapted from SGL [6] Group and INOCOM [7]

These pressure vessels are made of a metallic liner, commonly titanium or aluminium, which is wrapped by carbon fibers [5] and impregnated with a polymeric (epoxy) resin (Fig. 1). The metal will provide impermeability in order to carry light gases (helium) while the resin will provide mechanical strength.

The purpose of this project is to develop new material decomposition models capable of predicting the demise of this particular type of space debris. The project is divided in four parts.

Firstly, a review of the existing literature is being carried out in order to understand the detailed physics of this problem and to familiarize with the material specific properties.

Secondly, an experimental characterization will be performed. This task is divided into two parts: detailed thermochemical analysis and global material response in high-temperature environments. The detailed analysis will be performed using thermal analysis techniques such as Thermogravimetric Analysis (TGA) and Differential Scanning Calorimetry (DSC) in order to retrieve physical parameters (Arrhenius coefficients, c_p, $h_{reaction}$, etc) that are needed to simulate the thermal decomposition of the material [8]. In the following, the reproduction of actual demising conditions with a scaled pressure vessel model will be performed using the VKI plasma wind tunnel Plasmatron [9].

The next step will consist in simulating the Plasmatron tests with the Porous media Analysis TOolbox (PATO) [10], which is a material degradation code using OpenFOAM libraries. New modules will be required including support for melting and vaporization of metals, or competitive reactions for degradation of the polymeric resin.

Finally, uncertainty quantification will be carried out in order to characterize the sources of error and to quantify the impact of the different experimental uncertainties in the simulations.

Acknowledgments

This research is supported by SB PhD fellowship 1S58718N of the Research Foundation Flanders (FWO).

The European Space Agency is acknowledged for their financial support of the experiments through *"Deorbitation "Design to Demise" Aerothermodynamic Aspects"* research Grant (ref: ESA-IPL-PLL-JLV-RFP-2016-113).

References

[1] *ESA's re-entry predictions.* URL: https://reentry.esoc.esa.int/index.html (visited on 02/19/2018).

[2] Heiner Klinkrad. *Space Debris: Models and Risk Analysis.* en. Springer Science & Business Media, Sept. 2006. ISBN: 978-3-540-37674-3.

[3] Ziniu Wu et al. "Space Debris Reentry Analysis Methods and Tools". In: *Chinese Journal of Aeronautics* 24.4 (Aug. 2011). ISSN: 1000-9361. DOI: 10.1016/S1000-9361(11)60046-0.

[4] Tobias Lips and Bent Fritsche. "A comparison of commonly used re-entry analysis tools". In: *Acta Astronautica.* Infinite Possibilities Global Realities, Selected Proceedings of the 55th International Astronautical Federation Congress, Vancouver, Canada, 4-8 October 2004 57.2 (July 2005). ISSN: 0094-5765. DOI: 10.1016/j.actaastro.2005.03.010.

[5] *New type of booster casing for ARIANE 6 successfully tested - MT Aerospace ENG.* URL: http://www.mt-aerospace.de/news-details-en/items/new-type-of-booster-casing-for-ariane-6-successfully-tested.html (visited on 02/19/2018).

[6] *SGL Group showcases innovative fiber materials and composites at China Composites Expo 2016 - SGL Carbon Newsroom.* URL: http://www.sglnewsroom.com/en/reports/report-detail-page.18561.php (visited on 02/20/2018).

[7] *INOCOM.* URL: http://www.inocom21.com/contents/product/product01.html?sm=2_1 (visited on 02/20/2018).

[8] Francisco Torres Herrador. *Experimental characterization and simulation of pyrolysis phenomenon: from carbon composite ablators to Pacific Islands plant biomass.* Technical report. von Karman Institute for Fluid Dynamics, 2017.

[9] Bernd Helber. "Material response characterization of low-density ablators in atmospheric entry plasmas". PhD thesis. Vrije Universiteit Brussel, 2016.

[10] J. Lachaud et al. "A generic local thermal equilibrium model for porous reactive materials submitted to high temperatures". In: *International Journal of Heat and Mass Transfer* 108, Part B (May 2017). DOI: 10.1016/j.ijheatmasstransfer.2016.11.067.

STABILITY AND TRANSITION IN HYPERSONIC FLOWS

Modeling transition to turbulence for hypersonic flows with metamodels of linear stability theory

Florian DANVIN

CEA-CESTA 15 avenue des Sablières, CS60001, 33116 Le Barp CEDEX, France and
Von Karman Institute Aeronautics and Aerospace Department, von Karman Institute for Fluid Dynamics, Belgium, danvin@vki.ac.be

CEA Supervisor: Marina OLAZABAL-LOUME

Senior research engineer, CEA-CESTA 15 avenue des Sablières, CS60001, 33116 Le Barp CEDEX, France, marina.olazabal@cea.fr

VKI Supervisors: Olivier CHAZOT and Fabio PINNA

Head of department and professor, Von Karman Institute Aeronautics and Aerospace Department, von Karman Institute for Fluid Dynamics, Belgium, chazot@vki.ac.be

Senior engineer, Von Karman Institute Aeronautics and Aerospace Department, von Karman Institute for Fluid Dynamics, Belgium, pinna@vki.ac.be

University Supervisor: Herman DECONINCK

Professor, Von Karman Institute Aeronautics and Aerospace Department, von Karman Institute for Fluid Dynamics, Belgium, deconinck@vki.ac.be

Abstract

Increasing the fidelity of transition prediction in RANS codes requires a more physical approach than empirical correlations. During a flight at hypersonic speeds in the continuous layer of the atmosphere, a boundary layer develops around the spacecraft's body. However the development of instabilities among the initially laminar boundary layer, may cause its transition to a turbulent state. At hypersonic regimes, a boundary layer transition is synonym of a rise in the wall heat fluxes and in the wall friction, demanding a thicker thermal protection shield in these areas to the detriment of the payload. This work demonstrates the performances of using a metamodel of LST (Linear Stability Theory) in forecasting the evolution of Mack's second mode, for compressible hypersonic flows around sharp cones at Mach 6. The metamodel is both fast and accurate, moreover its non-intrusivity makes it a convenient tool for coupling with a RANS (Reynolds Averaged Navier-Stokes) code.

Keywords: LST, metamodel, artificial neural network, active learning, hypersonics

Nomenclature

U: streamwise velocity component $[m.s^{-1}]$
V: normal to the flow velocity component $[m.s^{-1}]$
W: spanwise velocity component $[m.s^{-1}]$
P: static pressure $[Pa]$
R: density $[kg.m^{-3}]$
α: Non-dimensional streamwise wavenumber $[-]$
β: Non-dimensional spanwise wavenumber $[-]$
ω: Non-dimensional frequency $[-]$
A: perturbation amplitude $[-]$
N: N factor $[-]$
Tr: ratio of the adiabatic temperature over the wall temperature $[-]$
β_H: Hartree parameter
Re: Reynolds number based on Blasius length scale $[-]$
f: frequency $[Hz]$
ϵ: relative error $[\%]$

Subscripts
e: boundary layer edge value
∞: far field value
0: initial state value

r: real part
i: imaginary part
tr: value at transition point
w: value at the wall

Abreviations
LST: Linear Stability Theory
PSE: Parabolized Stability Theory
$RANS$: Reynolds Averaged Navier-Stokes
CFD: Computational Fluid Dynamics
$SSIFL$: Smart Sampling and Incremental Function Learning
NN: Neural Network
RBF: Radial Basis Functions
PL: Passive Learning
AL: Active Learning
N_{pts}: Number of points

1. Introduction

Since the first hypersonic flight in 1949 by the German $V-2$ rocket, the hypersonic field still carries many unknowns, and obstacles to tackle before considering routinely hypersonic flights. Both scientists and engineers are "facing the heat barrier" [1] problem whenever a spacecraft is submitted to an atmospheric reentry. In the continuous layer of the atmosphere, a boundary layer forms around the spacecraft and it can transition towards a turbulent state, causing both heat transfer and drag augmentation, further leading to surface deterioration. Though the phenomenon is not fully understood, several methods were proposed in order to predict transition on more or less sophisticated bodies.

Up to now, predicting boundary layer transition at hypersonic regimes in RANS computations can be tackled by several approaches. The modal theory is used for studying natural transition phenomenon, branching into the simple linear stability theory (LST) [2], BiGlobal stability theory [3], and the TriGlobal stability theory assuming the amplitude of the perturbations varies respectively in one, two, or three directions. The more degree of freedom is used to describe the perturbations, the more accuracy is achievable, and the more computational power is required. According to Juniper et al [4] the LST is limited to flows homogeneous in 2 directions, the BiGlobal is adequate to study flows homogeneous only along the span, whereas the TriGlobal doesn't rely on flow homogeneity assumption. Finally the PSE-3D is dedicated to flows depending strongly on 2 directions, and weakly on the last one, as in the investigation of curvature effect in the work of Lakebrink et al, who studied hypersonic flows past an elliptic cone [3].
However the modal stability theory may not be sufficient to justify a particular phenomenon, such as the blunt body paradox as described by Reshotko [5] and investigated by Paredes et al [6]. More appropriate ways of investigating other transition paths can use the transient growth theory as outlined by Reshotko [7]. However, both the modal and non modal theories are extensively used at a research level, they offer the ability of being applicable to any kind of geometry to the cost of being computationally expensive.
This is the reason why approaches based on empirical correlations emerged to predict transition onset for specific industrial applications. An example of correlation for hypersonic flows is the one provided by Pate [8], where he predicts the transition onset for sharp cones. These methods are often chosen for an eventual coupling with RANS codes. An example of such a methods is the $\gamma - Re_{\theta t}$ model of Menter and Langtry [9] [10] [11], which may be used for subsonic flows, but is not directly applicable to hypersonic ones, whereas some modifications around turbulence models sometimes correlated with the linear stability theory such as the modifications of the $k-\omega-\gamma$ model by Yang [12] demonstrate fair results for hypersonic conical flows.

Though linear stability theory computations can take several days, recent advances in computer hardware were accompanied with a surge of interest in metamodel establishment, as their use is way faster than the full theory, justifying the need to use a more physical approach to predict the transition position. The aim of this study is not to develop a new method to predict transition, but to reproduce the LST behaviour at a cheaper computational power enabling its application to complex geometries at an industrial level. One of the first to develop an LST metamodel was Fuller [13] in 1997 demonstrating the feasibility and performances of using a neural network to predict the growth rate in non reacting jet flows. A few years later, Crouch [14] developed a similar approach in order to predict Tollmien-Schlichting or crossflow induced transition in incompressible subsonic-transonic 3D swept-wing boundary layers. Crouch used a neural network for his metamodel and he stated that

he obtained firstly a method several hundred times faster than the actual LST calculations, but also robust enough to be incorporated in a CFD code. More recently, Rajnarayan [15] extended Crouch's method to supersonic compressible flows, combining kriging as a regression method and a database computed with CFD profiles. Rajnarayan metamodel's is also fast, robust, and it compares well with the LST growth rate predictions, but the error estimate provided by kriging on the growth rate predictions can lead to an N-factor error around 2, which is quite important. For this reason, this article follows the evolution of extending the metamodel of LST towards higher Mach numbers, i.e., at hypersonic regimes, by the development of an accurate and robust method.
This article describes the metamodel creation and its validation by firstly presenting the LST and the semi-empirical e^N method of van Ingen [16], or Smith and Gamberoni [17]. Secondly the regression method and the database development are presented, before discussing the first results obtained for conical flows at Mach 6.

2. Metamodel establishment

The metamodel theory is based on bounding a regression method to a database creating an approximator function $\tilde{f}$, of an oracle function $\hat{f}$. Therefore, the metamodel performances strongly depend on both the accuracy of the chosen regression method, and on the information conveyed by the database. The techniques used for each method are presented hereafter.

2.1. Linear Stability Theory (LST) and the e^N method

Considering the boundary layer as a complex oscillator, thus the transition to turbulence phenomenon is the response of this oscillator to exterior disturbances. Transition process can be viewed as freestream disturbances propagation into the boundary layer as steady or unsteady fluctuations of the basic state, i.e., the laminar flow field. These disturbances provide the initial conditions of amplitude, frequency or phase to the breakdown of a laminar flow [7].

A laminar flow variable q can be decomposed into a steady mean flow Q and an unsteady perturbation q' such as

$$q = Q + q' \tag{1}$$

with

$$Q(x, y, z) = (U, V, W, P, R, T) \tag{2}$$

and

$$q'(x, y, z, t) = (u', v', w', p', \rho', T') \tag{3}$$

These kind of perturbations are added to the velocity components (U, V, W), pressure P, temperature T, and density R. The resulting equations reduce to the *disturbance equations* after simplifications.

Before solving this problem several assumptions leading to the linear stability theory are made. Firstly the linearization is obtained by considering small perturbations with respect to the mean flow, i.e.

$$\frac{q'}{Q} << 1 \tag{4}$$

It stands for every perturbed variable. According to the previous assumption, terms arising from squares or by any multiplication of two disturbed quantities are neglected. Furthermore using the parallel flow assumption, each mean flow variable depends only on y. As a consequence the vertical mean velocity component is neglected $V = 0$. The last assumption is to consider a given perturbation q' to behave as a time-dependent wave propagating in x and z directions, in other words to consider modal perturbations,

$$q'(x, y, z, t) = \hat{q}(y) \exp\left[i(\alpha x + \beta z - \omega t)\right] + c.c. \tag{5}$$

where c.c. stands for complex conjugate.
The resulting disturbance equations form an eigenvalue problem, whose solutions are examined to determine if they grow (unstable disturbances), are constant (neutrally stable disturbances), or decay (stable disturbances). Usually perturbations are considered to grow either in space or in time, leading to either *the temporal theory* if perturbations are allowed to grow over time only (ω complex, α and β real), or *the spatial theory* for perturbations growing over space only (α, β complex and ω real)
As the LST doesn't predict the transition onset, the semi-empirical e^N method developed by Van Ingen (1956) and independently by Smith and Gamberoni (1956) is used. This criterion, widely used for industrial purposes, is the only one providing a physical approach of the transition phenomenon. This criterion provided by the following formula (6), links the amplification ratio given by the disturbance amplitude A at the transition position x_{tr} with the initial disturbance amplitude A_0 at the initial position x_0, where

perturbations start being unstable, with an exponentially integrated growth rate over the transition length $(x_{tr} - x_0)$.

$$\frac{A}{A_0} = \exp\left(\int_{x_0}^{x_{tr}} (-\alpha_i) dx\right) \approx e^N \tag{6}$$

This amplitude ratio is correlated with a particular facility, and strongly depends on the environment, indeed for noisy facilities corresponds an N at transition $N \approx 5$ and for a low disturbance environment such as flight $N \approx 9 - 10$.
As the e^N theory is used to predict the transition onset, the spatial approach is chosen. In this move, the LST problem is a generalized eigenvalue problem solved with VKI-VESTA toolkit using the pseudo-spectral Chebyshev collocation method (cfr [18], [19], [20]). Solutions are eigenvalues with their associated eigenfunctions. A last study consists in finding the most unstable / least stable eigenmode from the whole spectrum of solutions, in order to get the imaginary part of the mode of interest ($\Im(\alpha) = \alpha_i$ for the spatial theory, or $\Im(\omega) = \omega_i$ for the temporal one), which is the perturbation amplification rate.

2.2. Database generation

The database role is to describe as close as possible the oracle (LST), firstly being composed of meaningful parameters, and secondly by varying them in the desired range of interest for $\tilde{f}$ applications. The database is composed of thousands of linear stability computations performed on self similar profiles, rather than on CFD profiles for a matter of computational time. Thus led to link the approximator $\tilde{f}$ to the perturbations growth rate via six inputs found by Demange [21] given below,

$$\alpha = \tilde{f}(M_e, T_e, T_r, \beta_H, Re, f). \tag{7}$$

There are two general approaches of learning, the standard one is called passive learning. It means the database shape has been previously decided and is fixed throughout the problem evolution. The second one is called active learning. It consists in building the database interactively with the regression method thanks to a query algorithm. This aims at maximizing the database information accessible by the regression model. After a first passive learning (PL) approach database generation by Demange [21], an active learning (AL) strategy was chosen.

From the active learning strategy, two main methods can be distinguished according to Settles [22]. The first one consists in building up the database pointwisely maximizing some expected error reduction function, whereas the second method consists in building up an entire database maximizing the space covered in each dimension at each iteration.

For the LST metamodel purposes, the second active learning strategy is retained. The followed strategy comes from Pedergnana et al [23] and the detailed algorithm is called "Smart Sampling and Incremental Function Learning" (SSIFL). This method combines an iterative sampling method to a neural network until the metamodel reaches the desired fidelity and confidence levels. The sampling method prescribed (Halton sampling or LCVT sampling) aims at distributing uniformly the input parameters in the hyperspace.

Table 1 presents the chosen range of variation for each database input parameter. These database were computed with self similar profiles on a 7° half angle cone.

Table 1: Databases input range of fluctuations.

Parameter	Unit	Range PL	Range AL
Me	$[-]$	$5.5 - 6.5$	$5. - 5.6$
Te	$[K]$	$55 - 80$	$65 - 95$
Tr	$[-]$	$0.6 - 0.8$	$0.6 - 0.8$
β_H	[-]	0	0
Re	$[-]$	$1000 - 3000$	$1000 - 3000$
f	$[kHz]$	$100 - 800$	$100 - 800$
N_{pts}	$[-]$	$\approx 240,000$	$\approx 160,000$

2.3. Regression method

The construction of the $\tilde{f}$ function was performed with an artificial neural network, firstly for its ability to perform multidimensional regression, secondly for its modularity. These are the main reasons regardless of the obtained performances why the neural network use surged in the artificial intelligence field with applications ranging from data-clustering, image or speech recognition, regression etc...

A neural network can be composed of several layers as depicted in Fig 1. Each layer links an input vector p with a weight matrix W, a bias vector b and an activation function f so that the output vector a of a layer is given by:

$$a = f(W \cdot p + b) \tag{8}$$

Once the neural network architecture is parameterized, the metamodel has to be trained. The training step consists in teaching the previously computed

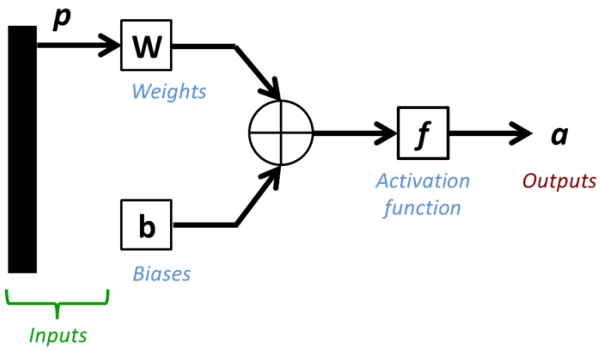

Figure 1: Artificial neural network principle, adapted from Hagan [24].

database to the metamodel. For a neural network, this step aims at finding the coefficients of the weight matrix and the bias vector, which best describe the function to be taught ($\bar{f}$). During this step the database is divided into two or three subsets. The first set, called the training set, is used to find the proper weights and biases coefficients. The second set, which sometimes also includes the third one is the validation set. It is used to measure the network generalization. Training usually stops, when the neural network stops improving its generalization. The last one, called the testing set is used to provide another measure of the network's performances. For this study Google's TensorFlow library [25] was used, alongside MATLAB's neural network toolbox. A parametric study on both the neural network shape and training methods motivated the use of a three layer neural network comprising sixty neurons in each hidden layer. Training was performed with the Adam optimizer algorithm from Kingma et al [26] for TensorFlow and the Levenberg-Marquardt algorithm from Moré [27] for MATLAB.

3. Results: passive learning vs active learning

The following sections are presenting comparisons of the metamodel with the LST predicted growth rate at first for a self-similar flow, and then for a CFD flow. Further comparisons between the metamodel using passive learning and the one using active learning are also displayed.
The estimation of the metamodel accuracy is firstly given by the relative growth rate peak error ϵ_P, i.e., the point where $-\alpha_i$ is maximum. Nevertheless, other measures of the prediction accuracy are needed to estimate independently the accuracy on the N-factor curve prediction ϵ_N and on the obtained enveloppe curve ϵ_{env}. The corresponding error formula are given below.

For a single frequency f_j, and denoting the mean function with $\bar{m}$:

$$\epsilon_P = \bar{m}(\epsilon_P(f_j), j = 1..M) = \bar{m}\left[\frac{|\, max(-\alpha_{I-NN}) - max(-\alpha_{I-LST})\,|}{max(-\alpha_{I-LST})}\right] \tag{9}$$

Considering only positive values of $-\alpha_I$, ϵ_N is given by:

$$\epsilon_N = \bar{m}(\epsilon_N(f_j), j = 1..M) = \bar{m}\left[\frac{|\int_x -\alpha_{I-NN}dx - \int_x -\alpha_{I-LST}dx\,|}{\int_x -\alpha_{I-LST}dx}\right] \tag{10}$$

and ϵ_{env} is computed with:

$$\epsilon_{env} = \frac{\int env_{NN} - \int env_{LST}}{\int env_{LST}} \tag{11}$$

3.1. Self-similar base flow

A first self similar flow past a 50 cm long 7° half angle cone was investigated. The freestream conditions correspond to a VKI-H3 facility configuration at Mach 6 given in Table 2. The post-shock conditions were computed using Taylor-Maccoll relations. The Table 3 displays the corresponding input range for each parameter of the metamodel.

The obtained predictions, plotted hereafter at two different frequencies in the figure 2, are in excellent agreement with the LST. A mean peak error ϵ_P of 0.88% is achieved for the metamodel using the passive learning approach, against 6.47% for the active learning counterpart. It can be noted from the figure 2 that the wave-shaped part of the growth rate is well reproduced. The corresponding ϵ_N error are respectively equal to 2.23% and 11.31%, leading to ϵ_{env} respectively of 0.6% and of 4.11%. Several remarks arising from the preceeding results can be made. Firstly the results obtained with the active learning approach for this test-case are less accurate than the one obtained with the passive learning one. Secondly the wave-shaped part of the growth rate is slightly shifted and

Table 2: Freestream conditions of the self similar example.

M_∞	$T_\infty\ [K]$	$P_\infty\ [Pa]$	$T_w\ [K]$
6	59.6	1317.4	300

Table 3: Self similar example input range of fluctuations.

Parameter	Unit	Value(s)
Me	$[-]$	5.3591
Te	$[K]$	72.5509
Tr	$[-]$	0.7149
β_H	[-]	0
Re	$[-]$	$961.6 - 3400$
f	$[kHz]$	$100 - 800$
N_{pts}	$[-]$	$1,200$

the peak error increase when the Reynolds number increase causes a rupture in the slope of the envelope curve past $x \approx 0.27cm$. Further investigation will be performed in order to cure this deficiency. According to Masutti [28], the N-factor of the VKI-H3 facility is N=4.8 for the LST, this is the reason why it is worth highlighting the first part of the enveloppe curve is well predicted by both metamodels.

3.2. CFD base flow

This other example is a CFD flow past a 25 cm and 7° half angle cone, at the same freestream conditions as the preceeding example. However this time, the input parameters of the metamodel are extracted from the CFD base flow. The LST was fed the corresponding CFD profiles. The corresponding input range for each parameter are given in Table 4.

The accuracy of the peak predictions stands at 12% for the passive learning metamodel, against a better 9.15% for the active learning one. The ϵ_N errors are actually closer from each other: 19.17% of discrepancy with the LST for the metamodel using the passive learning approach, against 20.09% for the active

Table 4: CFD example input range of fluctuations.

Parameter	Unit	Range
Me	$[-]$	$5.47 - 5.486$
Te	$[K]$	$69.53 - 59.89$
Tr	$[-]$	0.7104
β_H	[-]	0
Re	$[-]$	$1121 - 2525$
f	$[kHz]$	$375 - 750$
N_{pts}	$[-]$	$35,920$

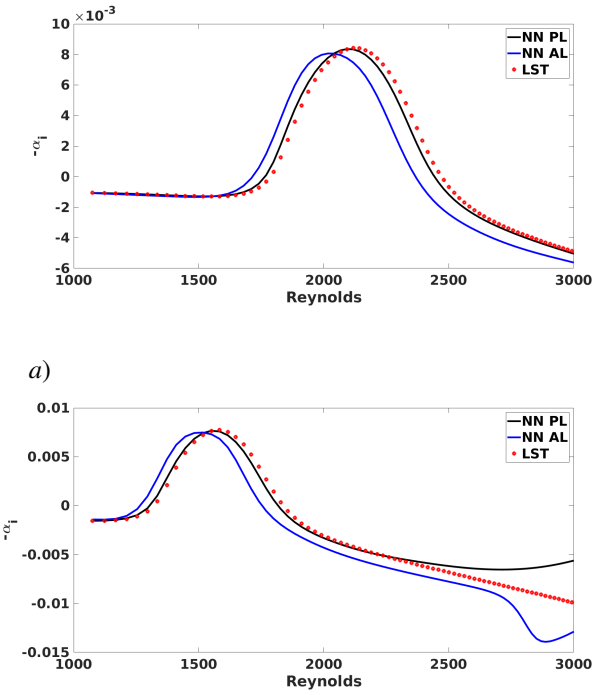

Figure 2: Growth rate comparison between the LST and the neural network outputs for self-similar profiles over a 7° half angle cone *a*) at a frequency of about 450 kHz *b*) and about 600 kHz vs Reynolds number

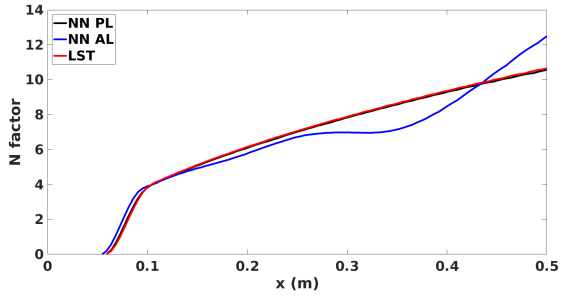

Figure 3: e^N envelope curves of the neural networks predicted vs LST growth rates for self-similar profiles over a 7° half angle cone against the abscissa x along the cone

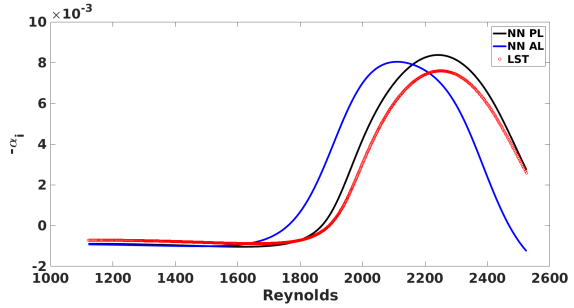

a)

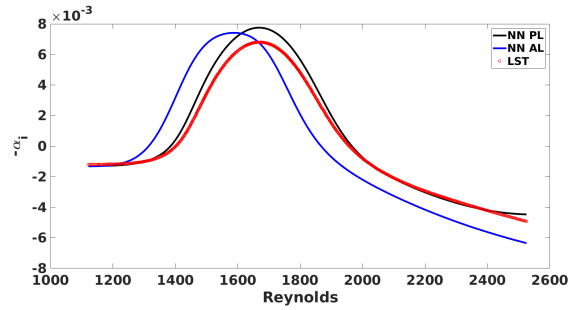

b)

Figure 4: Growth rate comparison between the LST and the neural network outputs for self-similar profiles over a 7° half angle cone *a*) at a frequency of about 450 kHz *b*) and about 660 kHz vs Reynolds number

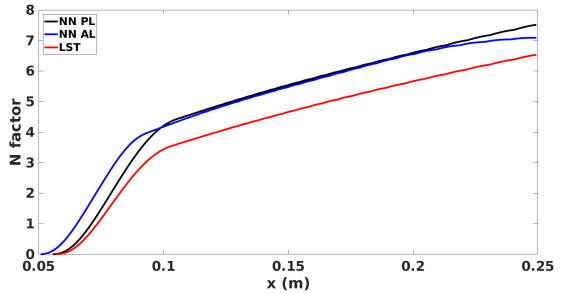

Figure 5: e^N envelope curves of the neural networks predicted vs LST growth rates for CFD profiles over a 7° half angle cone against the abscissa x along the cone

learning one. It can be noted once again the wave-shaped part of the growth rate is shifted, when the active learning database is used. This causes also an earlier start for the e^N enveloppe curve (cf figure 5). The author believes the shift in the growth rate curves, is due to a difference in pressure (p_e), when the two databases were computed. Furthermore, the results on the e^N achieved by each method remain close from each other, $\epsilon_{env} = 18.24\%$ for the metamodel using the passive learning approach, and 19.29% for the active learning one. However the reason why ϵ_{env} is higher in the active learning case is due to the premature rise of the enveloppe curve, otherwise it lies closer to the LST enveloppe curve.

In the whole, except from the $80,000$ point less used by this active learning generated database, the same degree of accuracy was achieved. Afterwards, the differences between a self-similar base flow and a CFD base flow lead to an acceptable error in the meta-model growth rate predictions.

4. Conclusions and perspectives

An LST metamodel has been developed using two different approaches regarding the database generation. The results presented in this article demonstrate the consistency of working with each of these approaches. However, attention may be drawn on the number of points used by the active learning strategy, which uses $80,000$ points less to provide at the same level of accuracy. Afterwards, another study not presented here exhibits better performances when considering also α_R as another output. To sum up, even if some improvements still need to be brought to the LST metamodel working with the active learning strategy, the obtained results are encouraging. Furthermore a performance benchmark on a wider variety of test cases is under development, alongside a database extension towards higher Mach numbers.

References

[1] T. A. Heppenheimer, Facing the heat barrier: a history of hypersonics, Vol. 4232, Government Printing Office, 2009.

[2] L. M. Mack, Boundary-layer linear stability theory, Tech. rep., CALIFORNIA INST OF TECHNOLOGY PASADENA JET PROPULSION LAB (1984).

[3] M. T. Lakebrink, P. Paredes, M. P. Borg, Toward robust prediction of crossflow-wave instability in hypersonic boundary layers, Computers & Fluids 144 (2017) 1–9.

[4] M. P. Juniper, A. Hanifi, V. Theofilis, Modal stability theorylecture notes from the flow-nordita summer school on advanced instability methods for complex flows, stockholm, sweden, 2013, Applied Mechanics Reviews 66 (2) (2014) 024804.
[5] R. E., Transient growth: A factor in bypass transition, Physics of Fluids 13 (5) (2001) 1067–1075.
[6] P. Paredes, M. M. Choudhari, F. Li, J. S. Jewell, R. L. Kimmel, E. C. Marineau, G. Grossir, Nosetip bluntness effects on transition at hypersonic speeds: experimental and numerical analysis under nato sto avt-240, in: 2018 AIAA Aerospace Sciences Meeting, 2018, p. 0057.
[7] E. Reshotko, Paths to transition in wall layers, AVT/VKI Lecture Series: Advances in Laminar-Turbulent Transition Modelling, von Karman Institute, Rhode-St.-Genese, Belgium (2008) 9–12.
[8] S. R. Pate, Dominance of radiated aerodynamic noise on boundary-layer transition in supersonic-hypersonic wind tunnels. theory and application, Tech. rep., ARNOLD ENGINEERING DEVELOPMENT CENTER ARNOLD AFB TN (1978).
[9] F. R. Menter, R. B. Langtry, S. Likki, Y. Suzen, P. Huang, S. Völker, A correlation-based transition model using local variables—part i: model formulation, Journal of turbomachinery 128 (3) (2006) 413–422.
[10] R. B. Langtry, F. Menter, S. Likki, Y. Suzen, P. Huang, S. Völker, A correlation-based transition model using local variables—part ii: test cases and industrial applications, Journal of Turbomachinery 128 (3) (2006) 423–434.
[11] R. B. Langtry, F. R. Menter, Correlation-based transition modeling for unstructured parallelized computational fluid dynamics codes, AIAA journal 47 (12) (2009) 2894–2906.
[12] M. Yang, W. a. o. Guangxing, Recalibration of the $k - \omega - \gamma$ transition model in units and application to transition prediction of blunt cones, in: 7th European Conference for Aeronautics and Space Sciences, EUCASS, 2017.
[13] R. Fuller, W. R. Saunders, U. Vandsburger, Neural network estimation of disturbance growth using a linear stability numerical model, AIAA Paper 559.
[14] J. Crouch, I. Crouch, L. Ng, Transition prediction for three-dimensional boundary layers in computational fluid dynamics applications, AIAA journal 40 (8) (2002) 1536–1541.
[15] D. Rajnarayan, P. Sturdza, Extensible rapid transition prediction for aircraft conceptual design using modal decomposition, AIAA Paper 231 (2013) 2013.
[16] J. van Ingen, A suggested semi-empirical method for the calculation of the boundary layer transition region (1956).
[17] A. Smith, N. Gamberoni, Transition, pressure gradient, and stability theory. report no. es. 26388, douglas aircraft co, Inc., El Segundo, CA.
[18] F. Pinna, Numerical study of stability flows from low to high mach number, Ph.D. thesis, Università Degli Studi Roma La Sapienza Facoltà di Ingegneria (2012).
[19] L. N. Trefethen, Spectral Methods in MATLAB, SIAM, 2000.
[20] C. Canuto, M. Y. Hussaini, A. Quarteroni, A. Thomas Jr, et al., Spectral methods in fluid dynamics, Springer Science & Business Media, 2012.
[21] S. Demange, Fast method for the prediction of the transition in the boundary layer for hypersonic flows (2016).
[22] B. Settles, Active learning literature survey, University of Wisconsin, Madison 52 (55-66) (2010) 11.
[23] M. Pedergnana, S. G. García, et al., Smart sampling and incremental function learning for very large high dimensional data, Neural Networks 78 (2016) 75–87.
[24] H. B. Demuth, M. H. Beale, O. De Jess, M. T. Hagan, Neural network design, Martin Hagan, 2014.
[25] M. Abadi, P. Barham, J. Chen, Z. Chen, A. Davis, J. Dean, M. Devin, S. Ghemawat, G. Irving, M. Isard, et al., Tensorflow: A system for large-scale machine learning., in: OSDI, Vol. 16, 2016, pp. 265–283.
[26] D. P. Kingma, J. Ba, Adam: A method for stochastic optimization, arXiv preprint arXiv:1412.6980.
[27] J. J. Moré, The levenberg-marquardt algorithm: implementation and theory, in: Numerical analysis, Springer, 1978, pp. 105–116.
[28] G. Grossir, D. Masutti, O. Chazot, Flow characterization and boundary layer transition studies in vki hypersonic facilities, in: 53rd AIAA Aerospace Sciences Meeting, 2015, p. 0578.

Nonlinear Parabolized Stability Analysis of Hypersonic Flows in Presence of Curvature Effects

Ludovico Zanus

Aeronautics and Aerospace Department, von Karman Institute for Fluid Dynamics, Belgium, ludovico.zanus@vki.ac.be

Supervisor: Fabio Pinna

Senior Research Engineer, Aeronautics and Aerospace Department, von Karman Institute for Fluid Dynamics, Belgium, fabio.pinna@vki.ac.be

Supervisor: Olivier Chazot

Professor and Head of the Aeronautics and Aerospace Department, von Karman Institute for Fluid Dynamics, Belgium, chazot@vki.ac.be

University Supervisor: Gérard Degrez

Professor and Head of the École Polytechnique de Bruxelles, Université Libre de Bruxelles, Belgium, gdegrez@ulb.ac.be

Abstract

Stability of hypersonic boundary layers over flat plates and cones is studied by means of Nonlinear Parabolized Stability Equations. Curvature effects on the second Mack mode stability of a Mach 6 flow over a straight cone at zero angle of attack are shown to be negligible. They modify all harmonic amplitudes in the same way and independently to each other.

Keywords: Transition, stability, PSE, curvature, hypersonic, boundary layer

1. Introduction

One of the main challenges of the future flight and space era concerns the development of supersonic and hypersonic speed cruise aircrafts for commercial transport purposes and reusable spaceplanes for access to and return from Low Earth Orbits. High Mach numbers characterize the flight operative conditions of such vehicles. A crucial aspect to take into account in the design phase of these machines is the phenomenon of laminar-to-turbulent boundary layer transition. It is well known that much higher levels of heat transfer and skin friction are experienced by bodies surrounded by turbulent flows compared to laminar ones[1]. Hence, being able to accurately estimate transition location is of paramount importance to reduce the design margins and eventually provide control measures[2]. Maintaining the flow laminar, for example, is highly desired for drag and thus fuel consumption reduction, or to reduce the amount of material used for the Thermal Protection Systems (TPS) for atmospheric re-entry missions. On the other hand, promoting turbulence can be useful to enhance air-fuel mixing at the intake of scramjet engines.

Transition prediction methods based on stability theories rather than empirical correlations offer the advantage of giving estimations based on the early stages of transition (see for a review[2]). Linear Stability Theory (LST) and Parabolized Stability Equations (PSE) are therefore valuable engineering tools. PSE can be considered as a superset of the more widely used LST equations[3]. Particularly, linear PSE (LPSE) can provide additional information, accounting also for nonparallel effects. Nonlinear methods such as NPSE allow to study also the advanced stages of the transition process, giving a full description of the phenomenon without requiring any additional correlation[4]. Literature studies showed that NPSE can provide details and reach accuracies which are comparable to DNS results[5; 6], with the advantage of requiring much less computational resources.

When applying stability and transition analysis to realistic vehicle configurations, curvature effects must be properly considered. Curvature can be due to surface geometries, but also to perturbation paths. Disturbances can indeed travel along curved lines, such as for example in the 3D boundary layers found in swept wings, rotating disks or yawed cones. In some of these cases, small differences in the metric coefficient have proved to be very important[7], giving appreciable differences in perturbation growth rates and N factors.

Even in the simple axisymmetric cone configuration, typical for hypersonic ground and flight tests, curvature can play a nonnegligible role. Transverse curvature and body divergence have been studied by Macaraeg et al.[8] in transonic flows and by Malik et al.[9] in hypersonic ones, by means of LST. It was found that transverse curvature can stabilize axisymmetric disturbances, while it can destabilize asymmetric ones, changing the most unstable perturbation of the first and second mode similarly to wall cooling[10].

In these works, mean flows and/or linear stability equations were modified in order to account for curvature effects. Because these are of the same order of nonparallel effect[9], ad hoc treatment were employed for local analysis, with lack of theory consistency. Nonparallel effects have shown to be mostly destabilizing, while convex surface curvatures are stabilizing. The dominance of one of these effects, however, remains problem dependent. Hence, as Malik et al.[11] explicitly pointed out, there is the need to simultaneously account both for nonparallel and curvature effects.

Simen et al.[12] were among the first to adopt a linear nonlocal theory in a curvilinear coordinate system, studying the two effects at the same time. They showed that in the aforementioned applications, curvature-modified LST analysis actually overestimates flow instabilities. More recent PSE codes allowed to perform nonlocal analysis on more complex problems, providing N-factor transition prediction and successful cross-validations against experiments. Examples of this are the LPSE studies of Perez et al.[13] on yawed cones and Li et al.[14] and Kocian et al.[15] on flared ones. Nonlinear PSE analysis were also conducted, as the works of Kuehl et al.[16], Kocian et al.[15] and Oliviero et al.[17] report. Adopting a curvilinear metric is showed to be crucial for some flow configurations. Beside body surface characteristics, it has to be included in order to correctly describe the paths followed by the perturbations and thus by the PSE marching algorithms.

In this work the stability of 2D hypersonic boundary layers in presence of curvature effects is studied by means of PSE. A new solver able to perform NPSE has been recently implemented in the framework of the VKI Extensible Stability and Transition Analysis (VESTA) toolkit[18]. The results hereafter presented serve as a a first verification of the algorithm and demonstrate its flexibility through the possibility to consider, with minor efforts, different flow assumptions and metric coordinates. Nonlinear mechanisms based on the resonance of a 2D primary wave with its higher harmonics are described on boundary layer flows over flat plates and straight circular cones. In the latter case, in addition to nonparallel and nonlinear effects, also the transverse curvature influence on flow stability is estimated.

2. Problem formulation

2.1. Governing equations

The Navier-Stokes equations in nondimensional invariant form, for a calorically perfect gas in absence of body forces are expressed in Eq. 1. Superscripts q^i denote vectorial contravariant variables, whereas subscripts q_i denote vectorial covariant variables (see Pinna and Groot[19]). Also, indexes following a comma denote spatial derivatives (e.g. $u^i_{,j} = \partial u^i / \partial x^j$). Details on the non-dimensionalization are given in §2.2.3.

$$\frac{\partial \rho}{\partial t} + (u^j \rho)_{,j} = 0 \,, \tag{1a}$$

$$\rho \frac{\partial u^i}{\partial t} + \rho u^j u^i_{,j} = -g^{ij} p_{,j} + \frac{1}{Re} \mathbb{T}^{ij}_{,j} \,, \tag{1b}$$

$$\begin{aligned} \rho c_p \Big(\frac{\partial T}{\partial t} + u^j T_{,j} \Big) = Ec \Big(\frac{\partial p}{\partial t} + u^j p_{,j} \Big) + \\ + \frac{1}{RePr} \left(\kappa g^{ij} T_{,i} \right)_{,j} + \frac{Ec}{Re} g_{ik} \mathbb{T}^{kj} u^i_{,j} \,, \end{aligned} \tag{1c}$$

where g^{ij} is the metric tensor, t the time, ρ the density, T the temperature, u^i the velocity component in different spatial directions, p the pressure, c_p the specific heat at constant pressure, κ the thermal conductivity and $\mathbb{T}$ the stress tensor defined as:

$$\mathbb{T}^{ij} = \lambda g^{ij} u^k_{,k} + \mu \Big(g^{jk} u^i_{,k} + g^{ik} u^j_{,k} \Big) \,, \tag{2}$$

where μ and λ are respectively the first and second viscosity coefficients. The system of governing equations is completed by the gas equation of state:

$$\gamma M^2 p = \rho T \,, \tag{3}$$

with γ the ratio of specific heats and M the Mach number. The other nondimensional numbers appearing in Eq. 1 are the Reynolds number Re based on the blasius length, the Eckert Ec and the Prandtl number Pr.

Generally, curvature effects associated with multiple directions are accounted for in the derivation of the current stability equations. When considering axisymmetric disturbances on straight cones at zero angle of attack, only the cone divergence and purely transverse curvature play a role. On the other hand, In more complex configurations, such the yawed cone described in § 4.2, also streamwise curvature becomes important. The metric tensor thus reads:

$$g^{ij} = \begin{bmatrix} (1 + x^2 K^1)^2 & 0 & 0 \\ 0 & 1 & 0 \\ 0 & 0 & (1 + x^2 K^2)^2 \end{bmatrix} \tag{4}$$

where K^i is the radius of curvature along direction x^i.[1]

Finally, in order to close the problem, proper modeling of the transport properties is required. For a calorically perfect gas, they are assumed to be dependent only on the temperature, through Sutherland's law:

$$\hat{\mu} = \hat{\mu}_{ref} \left(\frac{\hat{T}}{\hat{T}_{ref}} \right)^{\frac{3}{2}} \cdot \frac{\hat{T}_{ref} + \hat{S}}{\hat{T} + \hat{S}} \,, \tag{5}$$

Stokes' hypothesis ($\lambda = -\frac{2}{3}\mu$) and a constant Prandtl number ($\hat{\kappa} = \hat{cp}\hat{\mu}/Pr$) are assumed. If not otherwise specified, coefficients are fixed to the values proposed by White [20]:

$$\begin{aligned} \hat{\mu}_{ref} = 1.716 \cdot 10^{-5}\,\mathrm{kg\,m^{-1}\,s^{-1}} \quad &, \quad \hat{T}_{ref} = 273.15\,\mathrm{K} \\ \hat{S}_{\mu} = 110.6\,\mathrm{K} \quad &, \quad Pr = 0.7 \\ \hat{c}_p = 1004.5\,\mathrm{J\,kg^{-1}\,K^{-1}} \quad &, \quad \hat{R} = 287\,\mathrm{J\,kg^{-1}\,K^{-1}} \,. \end{aligned}$$

2.2. Parabolized Stability Equations

Parabolized Stability Equations are derived by following the classic approach adopted in perturbation theory. Every flow quantity q is decomposed into a mean part $\bar{q}$ (the laminar base flow) plus a perturbation q':

$$q(x^i, t) = \bar{q}(x^i) + q'(x^i, t) \,, \tag{6}$$

The total disturbance q' is assumed periodic in time and in the spanwise direction, and within the NPSE theory it is represented by the double Fourier series:

$$q'(x^1, x^2, x^3, t) = \sum_{n=-N_m}^{N_m} \sum_{m=-M_m}^{M_m} A^0_{(n,m)} \tilde{q}_{(n,m)}(x^1, x^2) \exp(i\,\Theta) + \; c.c. \tag{7}$$

where $c.c$ denotes the complex conjugate, and the argument of the exponential term is:

$$\Theta = i \left(\int_{x_0^1}^{x^1} \alpha_{(n,m)}(\xi) d\xi + m\beta_0 x^3 - n\,\omega_0\, t \right). \tag{8}$$

The couple of indexes (n, m) identifies the mode having as frequency and spanwise wavenumber respectively n and m times the frequency and spanwise wave number of the fundamental or primary mode (i.e. ω_0 and β_0). $A^0_{(n,m)}$ is the initial perturbation amplitude (see §2.2.4), while the streamwise wavenumber is defined by the phase-conditioned constraint:

$$\alpha_{(n,m)} = n\alpha_{r(1,0)} + i\,\alpha_{i(n,m)} \,. \tag{9}$$

Contrary to LST, the parallel flow assumption is not enforced within the PSE framework, meaning that the base flow and the perturbation shape functions $\tilde{q}_{(n,m)}$ depend not only on wall-normal direction, but also on the streamwise. The latter dependence though is considered "weak", in the sense that the flow variation over one disturbance wavelength is negligible [3]. This allows to drop second order derivatives along this direction.

By inserting the Eq. 6 into the Navier-Stokes equations, subtracting the equation satisfied by the base flow, substituting the NPSE ansatz (Eq. 7), and applying the aforementioned hypotheses, the NPSE equations are obtained.

Every single mode (n, m) has thus to satisfy the following equation written in matrix form:

$$\underline{\underline{L}}\,\underline{\tilde{q}} + \underline{\underline{M}}\,\underline{\tilde{q}}_{,1} + \alpha_{,1}\underline{\underline{Na}}\,\underline{\tilde{q}} \Big|_{(n,m)} = \underline{F}_{(n,m)} \,, \tag{10}$$

where $\tilde{q} = [\tilde{u}^1, \tilde{u}^2, \tilde{u}^3, \tilde{T}, \tilde{p}]$ is the vector of the perturbation variables, the $\underline{\underline{L}}$, $\underline{\underline{M}}$ and $\underline{\underline{Na}}$ matrices are functions of the mean flow quantities and the stability parameters, and $\underline{F}_{(n,m)}$ is the forcing vector for mode (n, m).

In order to solve the problem, a closure relation needs to be applied, thus assuring the weak streamwise dependence of every mode shape function. This can be obtained by a normalization through the following integral norm:

$$\int_{\Omega} \underline{\tilde{q}}^{\dagger}\,\underline{\tilde{q}}_{,1}\, dy \Big|_{(n,m)} = 0 \,, \tag{11}$$

[1] NB: the superscript 2 on x and K denotes here the normal to the wall coordinate, not an exponentiation.

where Ω indicates the domain in x^2. Different normalization conditions can be employed depending on the selected $\underline{\tilde{q}}$ components. Chang et al.[21] showed that the PSE results are basically independent on the chosen norm. In this work we chose to normalize by considering all five elements of the $\underline{\tilde{q}}$ vector.

2.2.1. Initial and boundary conditions

Eq. 10 and Eq. 11 constitute an initial boundary value problem. Hence, proper initial and boundary conditions are required both for the primary disturbance and the successively generated modes. Homogeneous boundary conditions are applied for the temperature and velocity components both at the wall and at the boundary layer edge. A compatibility condition is instead applied on the pressure disturbance by enforcing the x^2-momentum equation at the boundaries. An exception to this procedure is applied to the MFD, as explained in §2.2.2.

Initial conditions for the primary mode are obtained by performing a local LST calculation, thus in general:

$$\underline{\tilde{q}}_{(1,0)} = \underline{\tilde{q}}_{(1,0)_{LST}} \,, \quad \text{at } x^1 = {x^1}_0 \,. \tag{12}$$

Before marching the solution with the PSE equations, the eigenvalue is normalized by the maximum of the streamwise velocity component, in the incompressible case, and by the maximum of the temperature perturbation, in the compressible one. This assures the initial modes amplitude is uniquely defined by the $A^0_{(1,0)}$ quantity.

Higher harmonics and the MFD disturbance are initialized in a different way, since in these cases nonlinear effects cannot be neglected neither in the first simulation steps. Initial conditions for these modes are provided by imposing the following relations at $x^1 = {x^1}_0$:

$$\underline{\tilde{q}}_{(n,0)} = \underline{\tilde{q}}_{(1,0)} \,, \quad A^0_{(n,0)} = (A^0_{(1,0)})^n \,, \quad \alpha_{(n,0)} = n\alpha_{(1,0)} \tag{13}$$

This method provides a reasonable solution to the initialization problem, even if strong transients are expected.

2.2.2. Mean flow distortion treatment

The MFD represents a special mode. It is a stationary deformation of the boundary layer, directly related, among other things, to the change in the momentum and displacement thicknesses and the skin friction rise. The (0,0) mode function is purely real, it does not have a complex conjugate counterpart and its complex wavenumber is purely imaginary. There are no consistent suggestions in literature weather to impose also the imaginary part equal to zero or, on the contrary, to keep the exponential part contribution to the mode streamwise growth. In the current implementation the former approach was followed, as done by Hein [22]. Setting $\alpha_{(0,0)} = 0$ changes the nature of the equations to be fully parabolic, which created numerical convergence problems. For this reason, following the work of Hein [22], a new scaling of the wall-normal velocity perturbation was applied, i.e. $\tilde{u}^2_{(0,0)} \sim O(1/Re_0)$.

Moreover, for this variable, the usual freestream homogeneous Dirichlet boundary condition is substituted by a homogeneous Neumann, thus allowing the accommodation of the boundary layer growth.

2.2.3. Nondimensionalization and scaling considerations

Most variables are nondimensionalized with respect to their free stream values, denoted by the subscript e. Exceptions to this are the spatial coordinates, normalized with the Blasius length ℓ:

$$\ell_e = \sqrt{\frac{\mu_e \, \hat{x}^1}{U_e \, \rho_e}} \,, \tag{14}$$

the reference time scale ℓ/U_e and the reference pressure $\rho_e \, U_e^2$.

LST uses the local edge quantities at every $\hat{x}$ location as the reference, meaning that ℓ will slowly grow as the boundary layer develops. PSE however uses constant reference values for all $\hat{x}$ locations. These are obtained at a single $\hat{x}_0$ location, and are identified as: U_{e0}, μ_{e0}, ρ_{e0} and $\delta_{e0} = \ell_e(\hat{x}_0)$. The Reynolds number based on this reference Blasius length δ_{e0} thus identically:

$$Re_0 = \hat{x}^1_0/\delta_{e0} = x^1_0 \,. \tag{15}$$

The nondimensional frequency is defined as:

$$F = 2\,\pi\,\hat{f}\,\mu_{e0}/(U^2_{e0}\,\rho_{e0}) = \omega/Re_0 \,. \tag{16}$$

2.2.4. Measures of amplitudes

While in the linear case amplitudes are defined up to a constant, in the nonlinear problem this is no longer true. The choice of the initial modes amplitudes actually defines a specific nonlinear problem. NPSE results are usually displayed in terms of the evolution of the modes maximum amplitude value. For a generic quantity q', this is computed as:

$$({q_n}')_{max}(x^1) = r_n \, A^0_{(n,0)} \, |\tilde{q}_{(n,0)}(x^1)|_{max} \, \mathcal{A}_{(n,0)} \,, \tag{17}$$

where

$$\mathcal{A}_{(n,0)} = \exp\left(- \int_{x_0^1}^{x^1} \alpha_{i(n,0)}(\xi) d\xi \right), \qquad r_n = \begin{cases} 1 & \text{if } n = 0 \\ 2 & \text{if } n \neq 0 \end{cases}. \tag{18}$$

For comparison with experimental measures, sometimes amplitudes in terms of root-mean-square (RMS) values are presented as:

$$q'_{RMS} = C_n (q_n{}')_{max}, \quad \text{with} \quad C_n = \begin{cases} 1 & \text{if } n = 0 \\ 1/\sqrt{2} & \text{if } n \neq 0 \end{cases}. \tag{19}$$

3. Methodology

The tools used in this work to perform the stability computations have been developed within the VESTA toolkit[18]. The derivation of the PSE equations was done by means of VESTA's Automatic Derivation and Implementation Tools (AD&IT) written in Maxima and Matlab (see Pinna and Groot[19]). It consists of a computer algebra system, which allows to obtain stability equations for different stability theories, flow regimes and coordinate systems, in an automatic manner, avoiding errors associated with their manual derivation and implementation.

PSE constitute an initial boundary value problem, solvable by a marching technique. A first order backward Euler method is used to discretize the streamwise derivatives, while the wall-normal ones are approximated by a Chebyshev spectral collocation method based on Lagrangian polynomia defined on Gauss-Chebyshev-Lobatto points. Malik's mapping[23] is adopted to cluster points close to the wall and therefore a better resolution in the boundary layer. The same spectral method and mapping procedure are also used to perform the spatial LST calculations providing initial conditions for the PSE.

The nonlinear forcing terms were computed by means of FFT. Only quadratic nonlinearities are retained in this work. Perturbations in the physical space are retrieved by Eq. 7 and used to build the forcing term, looping until all $\alpha_{(n,0)}$ are converged. Each single mode forcing $\underline{F}_{(n,m)}$ is then computed from an FFT analysis with proper anti-aliasing precautions (see for details[24]).

If not otherwise specified, mean flows are calculated solving the self-similar boundary-layer equations, using the Mangler-Levy-Lees transformation for flows over straight cones.Transverse cone curvature is properly introduced when re-dimensionalizing the flow quantities. This approach adopted in VESTA has been shown to give negligible differences when self-similar profiles were compared to CFD solutions[25].

4. Results

In order to verify and prove the capability of the new implemented VESTA NPSE algorithm, four test cases are studied, as summarized in Table 1 (the subscript ∞ defining upstream flow conditions). Firstly, the nonlinear solver is used to reproduce the 2D resonance of a single disturbance in incompressible flow regime. A perturbation of frequency F, introduced in the boundary layer, leads to the appearance of its higher harmonics $2F$, $3F$, $4F$ ... and the $0F$ MFD mode, as result of the interaction between itself and the additional generated modes. Next, the correct derivation of stability equations in curvilinear coordinate system is checked by studying the crossflow instability of a yawed straight cone, by means of LST and LPSE. Results are compared against the solutions provided by the EPIC code [17], developed at Texas A&M University. Finally, NPSE with curvature terms are used to perform stability analysis of an axisymmetric 2nd Mack mode on a straight cone at zero angle of attack. Also in this case 2D resonance is investigated. It is important to point out that this does not represent a typical transition mechanisms that occurs in boundary layers. However, it is the easiest test to check weather fundamental aspects such for example the treatments of MFD distortion, initial conditions and nonlinear terms are correctly implemented in our solver.

4.1. Case 1 – Incompressible flow over a flat plate studied with NPSE

The first test case considered is the 2D resonance of a Tollmien-Schlichting (TS) wave in an incompressible boundary layer. This is a benchmark problem in literature, reproduced by numerous authors by means of PSE (Bertolotti[4], Chang et al.[28], Airiau[26], Hein[22] and Esfahanian[27]) and DNS (Bertolotti et al.[29] and Joslin et al[5]). A TS wave perturbation with a reduced frequency $F = 8.6 \cdot 10^{-5}$ and a RMS amplitude $u'_{RMS} = 0.0025$ is introduced into a Blasius flow at Reynolds number $Re = 400$. For the current simulations the Fourier series was truncated at the fifth harmonic (i.e. $N_m = 6$). Figure 1 shows

Table 1: Studied test cases

Case	Geometry	M_∞	T_∞ $[K]$	$\hat{f}$ $[kHz]$	PSE Analysis	Reference
1	Flat plate	$2.9 \cdot 10^{-3}$	-	$9.10 \cdot 10^{-4}$	Nonlinear	Bertolotti[4], Airiau[26], Hein[22]
2	Yawed straight cone	6	53.42	0	Linear with curvature	Esfahanian[27], Oliviero[17]
3	Axisym. straight cone	6	59.60	$5.59 \cdot 10^2$	Nonlinear	-
4	Axisym. straight cone	6	59.60	$5.59 \cdot 10^2$	Nonlinear with curvature	-

the maximum RMS amplitudes of the streamwise velocity component u'_{RMS}, of the primary mode (1,0) and the second harmonic (2,0), as a function of the Re number. Comparison against Esfahanian[27] highlights a good overall agreement, while results from Bertolotti[4] predict a slightly lower perturbation amplitude in the nonlinear regime. From the picture it is evident how the nonlinearity contributes to increase the amplitude of the primary wave, while the linear analysis would describe its decaying.

The amplitude evolution of all the modes considered in the simulation is collected in a logarithmic scale plot in Fig. 2. Airiau's[26] and Hein's[22] results are reproduced with good accuracy for all the harmonics. It is noteworthy to see that even if not very accurate initial conditions are provided for the higher modes, still the algorithm is able to retrieve, after a transient phase, the correct solutions. Discrepancies in the higher harmonics must be evaluated considering their amplification due to the logarithmic scale presentation of the results. Moreover, the disagreements shown are in the range of previously reported comparisons (see for example Hein[22]). Authors generally agree with the words of Airiau[26]:

> " [...] the generation of initial conditions and the resolution of the stationary mode (0,0) are the two delicate points of the weakly nonlinear theory treated by the PSE. The way to approach them is the main cause of discrepancies, which can sometimes occur while comparing PSE results from different authors [...]"

In Fig. 3 the RMS amplitude profiles of the streamwise velocity component for the MFD and the third harmonic at $Re \approx 800$ are displayed as examples and compared against Airiau[26]. Both curves perfectly superpose the reference values, as well as all the other modes here not reported. In Airiau[26] the special (0,0) mode is treated in a slightly different way

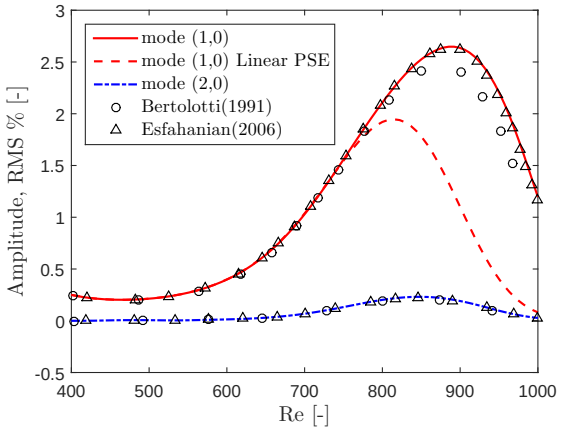

Figure 1: Evolution of the maximum RMS amplitude of the streamwise velocity component for the (1,0) and (2,0) modes: comparison against Bertolotti[4]. Case 1: TS wave, $F = 8.6 \cdot 10^{-5}$, $u'_{RMS} = 0.0025$ at $Re = 400$

compared to the current implementation. A non-zero imaginary part of the streamwise wavenumber is imposed (i.e. $\alpha_{i(0,0)} \neq 0$), splitting the mode growth between the shape function and the perturbation exponential part. Despite on this, both modeling correctly give as result the same profile shape.

Verification of the algorithm for stability analysis in the compressible regime can be found in Zanus[30]. The lack of literature results concerning 2D resonance problems against which to compare, and the bigger uncertainties related to the computations of thermodynamic and transport properties, result in more evident disagreements. Nevertheless, the main perturbations characteristic were correctly simulated. From these considerations and taking into account that the previously shown incompressible results were obtained by means of a compressible NPSE solver, the code can be considered verified.

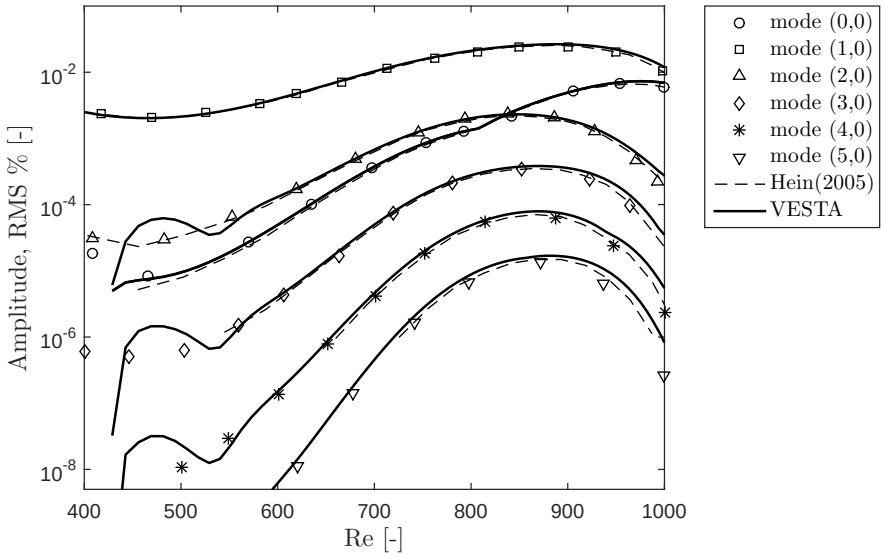

Figure 2: Evolution of the maximum RMS amplitude of the modes streamwise velocity component: comparison against Airiau[26] (symbols). Case 1: TS wave, $F = 8.6 \cdot 10^{-5}$, $u'_{RMS} = 0.0025$ at $Re = 400$

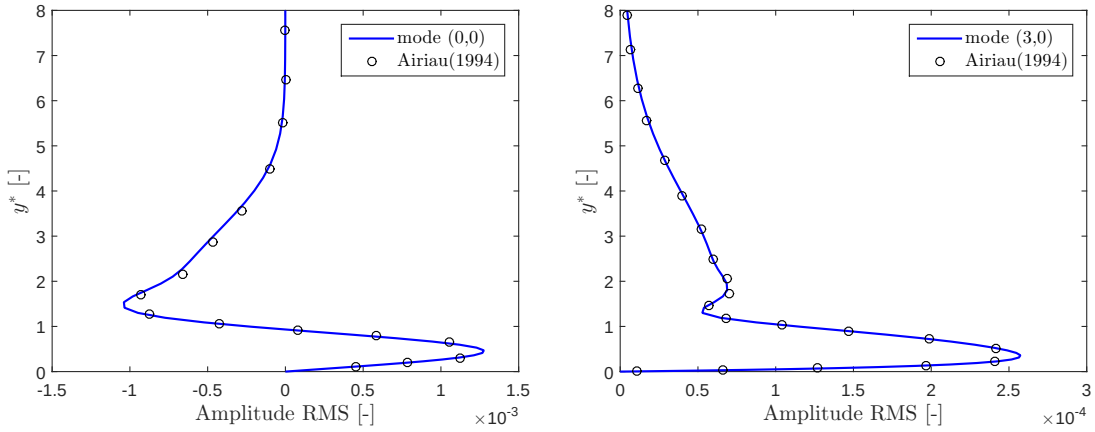

Figure 3: Streamwise velocity profiles of the MFD, and the third harmonic (3,0) at $Re = 800$: comparison against Airiau[26]. Case 1: TS wave, $F = 8.6 \cdot 10^{-5}$, $u'_{RMS} = 0.0025$ at $Re = 400$

4.2. Case 2 – Crossflow instabilities on a yawed cone studied with LPSE

Verification of the implementation in VESTA of the stability equations in a generalized curvilinear coordinate system is carried out by comparing against the LPSE solver developed by the Computational Stability and Transition Laboratory at Texas A&M University – EPIC [17].

The laminar mean-flow used for the comparison corresponds to a 7°-half-angle yawed straight cone, studied by Oliviero et al.[17]. The laminar mean flow, together with the LPSE and LST results, was kindly provided by A. Moyes. The upstream flow conditions are: $M_\infty = 6$, $T_\infty = 53.42\ K$, $P_\infty = 611.28\ Pa$, and the unit Reynolds number is $Re' = 10.09 \cdot 10^6\ [m^{-1}]$. The flow properties are computed following what was introduced in §2.1, yet with $Pr = 0.72$.

The perturbations are tracked along the crossflow vortex's path emerging from the generalized ρw inflection point.[17]

Fig. 4 shows the comparison of the LST and LPSE growth rate results against those obtained with EPIC. The LST results, with the inclusion of curvature terms, match perfectly, with a discrepancy of $\sim 0.1\%$. LPSE results show some discrepancies close to the growth rate peak, but they better approach each other while moving towards downstream locations. This happens both in Cartesian and curvilinear coordinates. A possible explanation for this discrepancy is the slightly different simplifying hypotheses assumed by the codes. In particular, in EPIC terms involving streamwise derivatives of the wall-normal velocity perturbation are retained. However, in VESTA these and all other terms of $O(1/Re_0^2)$ are dropped (see full development done by Pinna and Groot[19]). Moreover, numerical aspects, which have probably a link with the solution downstream wavy behavior, could also be a source of disagreement.

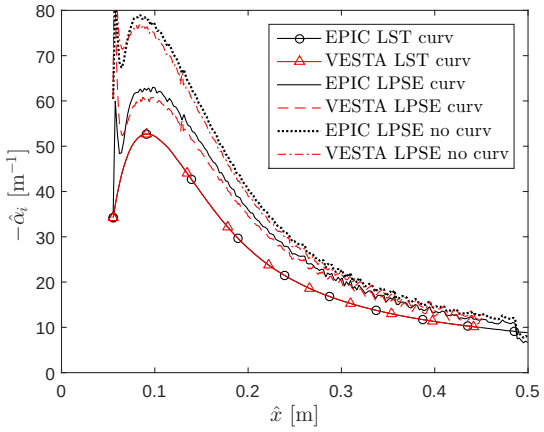

Figure 4: Dimensional growth rate as a function of the $\hat{x}$ coordinate along the vortex path, for the crossflow instability study on a yawed straight circular cone[17]. VESTA's LST and LPSE solver compared against EPIC

Despite the aforementioned and justified discrepancies in the PSE results, the implementation of the curvilinear coordinate system into VESTA's AD&IT can be considered successfully verified.

It is interesting to notice how neglecting curvature terms in the PSE analysis can lead to an appreciable overestimation of the crossflow instability. Considering curvature in the local analysis is not sufficient neither – nonparallel and curvature effects have to be simultaneously taken into account, since they have an influence on stability of the same order. In this particular case, nonlocal effects have a destabilizing role, while curvature stabilizes the disturbance, as the comparison between Cartesian and curvilinear PSE highlights.

4.3. Cases 3 & 4 – Hypersonic flow over an axisymmetric cone studied with NPSE with and without the curvature terms

In order to assess the influence of curvature terms in a nonlinear PSE analysis, a 7°-half-angle straight circular cone at zero angle of attack was considered. In this case only transverse curvature and body divergence effects can be eventually appreciated. The flow conditions are the typical ones found in the test section of the H3 hypersonic wind tunnel facility of the von Karman Institute: $M_\infty = 6$, $T_\infty = 59.6$ $[K]$, $P_\infty = 1317.4$ $[Pa]$, with a wall temperature of the tested model $T_w = 296.5$ $[K]$. The boundary layer edge values to compute the mean flow self-similar solution correspond to the post-shock values obtained from the Taylor-Maccoll equations for axisymmetric conical shocks. The primary mode investigated is the second Mack mode of frequency $\hat{f} = 5.59 \cdot 10^2$ $[kHz]$. An initial amplitude $A^0_{(1,0)} = 0.001$ was imposed at a Reynolds number $Re = 1078$. Six Fourier modes were considered in the computation. Figure 5 shows the maximum amplitude evolution of the temperature perturbation as result from the NPSE analysis in both Cartesian and curvilinear coordinate systems. As expected, curvature effects do not have an appreciable influence in this particular problem. The transverse curvature effects on axisymmetric modes is indeed weak [12], but it produces the major deviation from the solution in Cartesian coordinate in the correspondence of the amplitude peak. Moreover, nonlinearity and curvature seem to act in a decoupled manner, since the latter modifies perturbations amplitudes in the same way, regardless of the harmonic order.

5. Conclusion

This work investigated the stability of flows over flat plates and cones by means of Parabolized Stability Equations in Cartesian and curvilinear coordinates. Particularly, a new NPSE solver, recently developed in the framework of the VESTA toolkit, was presented and verified against results from the literature.

Good agreement was found in the incompressible NPSE results of a 2D resonance of a 2D Tollmien-Schlichting wave over a flat plate, in terms of both modes amplitudes and profile shapes.

Correct derivation of the stability equations in a curvilinear coordinate system in VESTA was proved

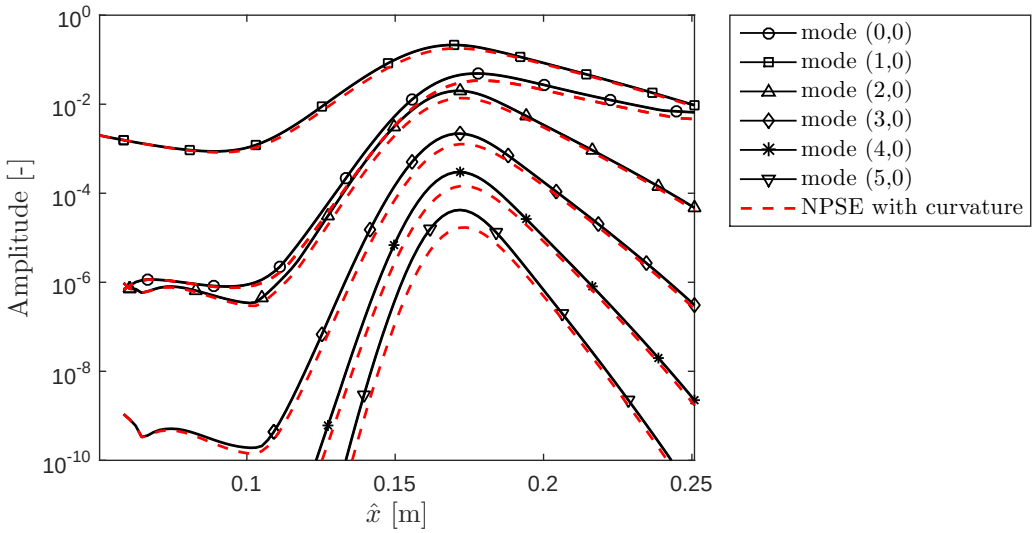

Figure 5: Evolution of the maximum amplitude of the modes temperature disturbances: NPSE comparison with and without curvature terms. Cases 3 & 4: 2nd Mack mode, $\hat{f} = 5.59 \cdot 10^2$ $[kHz]$, $A^0_{(1,0)} = 0.001$ at $Re = 1078$

by comparison against the results provided by EPIC. The linear PSE stability study of the hypersonic cross-flow instability on a yawed straight circular cone showed the importance of considering simultaneously both nonlocal and curvature effects. The PSE solution in Cartesian coordinates, in fact, overestimates the perturbation growth rates, while LST results including curvature underestimate it.

Finally, the NPSE in curvilinear coordinates were used to study the 2D resonance of an axisymmetric 2nd Mack mode on a straight circular cone at zero angle of attack. Transverse curvature and body divergence effects for this flow configuration were confirmed to give a negligible contribution to stability. In particular, curvature showed to slightly stabilize the flow, acting in the same way on each harmonic independently on the nonlinear effects.

Future work will concern the study of nonlinear interactions involving 3D perturbations, thus to be able to model more realistic natural transition mechanisms, such for example subharmonic breakdown, type H resonance or nonlinear secondary stability analysis. Moreover, extension to high Mach flows stability studies is planned. For this reason, high temperature gas effects involving equilibrium and nonequilibrium chemistry will be investigated.

Acknowledgments

This research is made possible thanks to the financial support provided by the Fonds de la Recherche Scientifique through their FRIA fellowship program. The author wants to thank Alexander J. Moyes for providing the base flow of the yawed straight cone problem, and for performing the related LPSE analysis with the EPIC code.

References

[1] H. L. Reed, R. Kimmel, S. Schneider, D. Arnal, Drag prediction and transition in hypersonic flow, AIAA Paper 97-1818.

[2] H. L. Reed, E. Perez, J. Kuehl, T. Kocian, N. Oliviero, Verification and validation issues in hypersonic stability and transition prediction, Journal of Spacecraft and Rockets 52 (1) (2014) 29–37.

[3] T. Herbert, F. P. Bertolotti, Stability analysis of nonparallel boundary layers, Bulletin of the American Physical Society 32 (1987) 2079.

[4] F. P. Bertolotti, Linear and nonlinear stability of boundary layers with streamwise varying properties, Phd thesis, The Ohio State University (1991).

[5] R. D. Joslin, C. L. Strett, C.-L. Chang, Spatial direct numerical simulation of boundary-layer transition mechanisms: Validation of pse theory, Theoretical and Computational Fluid Dynamics 4 (1993) 271.

[6] L. Jiang, C.-L. Chang, M. Choudhari, C. Liu, Cross-validation of dns and pse results for instability wave propagation in compressible boundary layers past curvilinear surfaces, in: AIAA (Ed.), 16th Computational Fluid Dynamics Conference, 2003.

[7] T. S. Haynes, H. L. Reed, Simulation of swept-wing vortices using nonlinear parabolized stability equations, Journal of Fluid Mechanics 405 (2000) 325–349.
[8] M. G. Macaraeg, Q. I. Daudpota, Numerical studies of transverse curvature effects on transonic flow stability, Physics of Fluids 4 (5) (1992) 975–983.
[9] M. R. Malik, R. E. Spall, On the stability of compressible flow past axisymmetric bodies, Journal of Fluid Mechanics 228 (1991) 443–463.
[10] N. P. Bitter, J. E. Shepherd, Stability of highly cooled hypervelocity boundary layers, J. Fluid Mech. 778 (2015) 586–620.
[11] M. R. Malik, P. Balakumar, Nonparallel stability of rotating disk flow using pse, in: Springer (Ed.), Instability, Transition, and Turbulence, Hussaini, M. Y. and Kumar, A. and Streett, C. L., 1992.
[12] M. Simen, U. Dallmann, Nonlocal vs. local instability of compressible flows including body metric, flow divergence and 3d-wave propagation, in: AIAA (Ed.), 24th Fluid Dynamics Conference, 1993.
[13] E. Perez, H. L. Reed, J. J. Kuehl, Instabilities on a hypersonic yawed straight cone, AIAA paper 2013-2879.
[14] F. Li, M. Choudhari, C.-L. Chang, J. White, Analysis of instabilities in non-axisymmetric hypersonic boundary layers over cones, in: AIAA (Ed.), 10th AIAA/ASME Joint Thermophysics and Heat Transfer Conference, 2010.
[15] S. Kocian, E. Perez, N. B. Oliviero, J. J. Kuehl, H. L. Reed, Hypersonic stability analysis of a flared cone, in: AIAA (Ed.), 51st Aerospace Sciences Meeting, 2013.
[16] J. J. Kuehl, E. Perez, H. L. Reed, Jokher: Npse simulations of hypersonic crossflow instability, in: AIAA (Ed.), 50th AIAA Aerosapce Science Meeting, 2012.
[17] N. B. Oliviero, T. S. Kocian, M. A. J., H. L. Reed, Epic: Npse analysis of hypersonic crossflow instability on yawed straight circular cone, in: AIAA (Ed.), 45th AIAA Fluid Dynamics Conference, 2015.
[18] F. Pinna, Numerical study of stability of flows from low to high mach number, Phd thesis, Von Karman Institute - Università degli Studi di Roma La Sapienza (2012).
[19] F. Pinna, K. Groot, Automatic derivation of stability equations in arbitrary coordinates and different flow regimes, in: AIAA (Ed.), 44th Fluid Dynamic Conference, 2014.
[20] F. M. White, Viscous Fluid Flow, McGraw-Hill, 2006.
[21] C.-L. Chang, M. R. Malik, G. Erlebacher, M. Y. Hussaini, Linear and nonlinear pse for compressible boundary layers, Icase report n. 93-70, NASA (1993).
[22] S. Hein, Nonlinear nonlocal transition analysis, Ph.D. thesis, DLR (2005).
[23] M. R. Malik, Numerical methods for hypersonic boundary layers, Journal of Computational Physics 86 (1990) 376–413.
[24] C. Canuto, A. Quarteroni, M. Hussaini, T. Zang, Spectral methods in fluid dynamics, 1987.
[25] F. Miró Miró, Numerical study of the stability of a hypersonic boundary layer in the presence of blowing, Research Master report 2015-28, von Karman Institute (May, 2015).
[26] C. Airiau, Stabilité linéaire et faiblement non linéaire d'une couche limite laminaire incompressible par un systèm d'équations parabolisé (pse), Phd thesis, École National Supérieure de l'Aéronautique et de l'Espace (1994).
[27] V. Esfahanian, S. Ghader, Numerical solution of parabolized stability equations using super-compact scheme, Journal of Aerospace Science and Technology 3 (2) (2006) 77–85.
[28] C. L. Chang, M. Malik, G. Erlebacher, M. Hussaini, Compressible stability of growing boundary layers using parabolized stability equations, AIAA Paper 91-1636.
[29] F. P. Bertolotti, T. Herbert, P. R. Spalart, Linear and nonlinear stability of the blasius boundary layers, Journal of Fluid Mechanics 242 (1992) 441–474.
[30] L. Zanus, F. Miró Miró, F. Pinna, Nonlinear parabolized stability analysis of hypersonic flows in presence of curvature effects, in: AIAA (Ed.), In pubblication.

Analysis of the stability of a flat plate high-speed boundary layer with discrete roughness

Iván Padilla Montero

Aeronautics and Aerospace Department, von Karman Institute for Fluid Dynamics, Belgium, ivan.padilla@vki.ac.be

Supervisor: Fabio Pinna

Senior Research Engineer, Aeronautics and Aerospace Department, von Karman Institute for Fluid Dynamics, Belgium, fabio.pinna@vki.ac.be

Supervisor: Olivier Chazot

Head of Department and Professor, Aeronautics and Aerospace Department, von Karman Institute for Fluid Dynamics, Belgium, olivier.chazot@vki.ac.be

University Supervisor: Gérard Degrez

Dean of the Faculty and Professor, Aero-Thermo-Mechanics Department, Université Libre de Bruxelles, Belgium, gdegrez@ulb.ac.be

Abstract

Two-dimensional linear stability theory is used to analyze the instability of the wake behind a cuboidal and a ramp-shaped roughness element mounted on top of a flat plate in a Mach 6 freestream. Spatial stability results are presented for a fixed frequency and streamwise location behind the elements, using base flows obtained from steady and laminar Navier-Stokes simulations.

Keywords: boundary layer, stability, transition, hypersonic, roughness

1. Introduction

Boundary layer transition from a laminar to a turbulent regime is one of the most important drivers in the design of hypersonic vehicles. Transition to turbulence in a high-speed boundary layer is typically associated with an increased skin friction, but also with an order of magnitude increase in the heat transfer at the surface of a body [1]. This behavior leads to challenging aerothermodynamic loads that can compromise the integrity of a mission if not properly accounted for. Despite being an active research topic for decades, the physical mechanisms governing hypersonic boundary layer transition are not well understood yet. Due to its complexity, the existing transition prediction tools for practical hypersonic applications still rely mainly on empirical correlations. This fact has important implications in the design process, involving the need for large safety factors that lead to oversizing of the thermal protection systems. In order to improve the transition prediction capabilities for the design of future high-speed applications, new methodologies involving a higher degree of flow physics for each particular case should be developed. The use of experimental-based correlations should be replaced by methods based on stability theory and transient growth considerations [2]. Nowadays, two-dimensional linear stability theory has become a computationally feasible tool for practical configurations which is able to provide accurate results in the first stages of the transition process [3].

Depending on their relative size with respect to the local boundary layer thickness, the presence of three-dimensional isolated roughness elements on the surface of a high-speed body can have an important impact in the transition process. Typical examples include damaged heat shield tiles, gap fillers and rivets, among many others. The perturbations generated by these elements can accelerate the growth of

incoming disturbances and introduce additional instability mechanisms in the boundary layer, eventually leading to a premature occurrence of transition. Although a physics-based prediction of roughness-induced transition is still not available nowadays, thorough experimental and numerical investigations have recently increased our knowledge, see for example [4; 5; 6; 7]. The flow structure in the wake behind isolated roughness elements is mainly characterized by strong counter-rotating vortices that persist a long distance downstream in the transitional wake. These vortices lift-up low-momentum fluid from the body surface and give rise to low-velocity streaks that are surrounded by regions of high wall-normal and spanwise shear. As a result, the flow field in the wall-normal (y) and spanwise (z) directions presents a strong inhomogeneity, and classical linear stability theory is no longer a valid technique for this problem. In order to obtain meaningful results, the amplitude functions considered in the stability analysis must be dependent on both y and z coordinates. This approach, in which the perturbations are inhomogeneous in two spatial directions but homogeneous in the third one and in time, is hereby referred to as two-dimensional linear stability theory, also known as BiGlobal stability theory, as introduced by Theofilis [8].

A significant amount of fundamental studies in roughness-induced transition involving the use of 2D linear instability theory have been carried out over the last years, both for supersonic and hypersonic flows and mostly for elements mounted on top of a flat plate. Groskopf et al. [4] performed temporal analyses of the instability of the wake behind isolated 3D cuboidal roughness elements in a Mach 4.8 boundary layer, and compared the results against direct numerical simulation (DNS), reporting a very good agreement in the disturbance amplitude shapes. Similar analyses were developed by De Tullio and coauthors [6] at Mach 2.5 and by Paredes [9] and De Tullio & Sandham [10] at Mach 6 for the same geometry, in both cases comparing DNS results against spatial BiGlobal stability theory and three-dimensional parabolized stability equations (PSE-3D). For the two cases investigated, the two-dimensional eigenfunctions obtained from the 2D stability computations and the growth rates extracted from the PSE-3D simulations were both found to be in close agreement with the DNS data. On the experimental side, Kegerise et al. [5] carried out measurements of the disturbance amplitudes behind a diamond element in a flat plate at Mach 3.5, and compared them against the spatial stability analyses of Choudhari and coworkers [11; 12] with satisfactory results, reinforcing the validity of the theory for such configurations. In all the cases analyzed, the dominant wake instability modes were found to be varicose (even) and sinuous (odd) deformations of the low-velocity streak that characterizes the wake flow structure. Nevertheless, whether the leading instability mode has an even or an odd nature appears to be case dependent. Moving to a more practical configuration, Theiss et al. [13; 14] performed 2D and PSE-3D linear stability computations in the wake behind different roughness geometries located on the heat shield of a reentry capsule in a Mach 5.9 freestream. The varicose wake mode was found to be the one undergoing a higher amplification, with the cylindrical roughness element being the most effective shape.

In this work, the instability of the wake behind a cuboidal and a ramp-shaped roughness element is investigated by means of two-dimensional linear stability theory. The elements are mounted on top of a flat plate inside a hypersonic freestream that matches the high Reynolds test conditions of the von Karman Institute H3 wind tunnel. Spatial stability calculations are performed in two different laminar base flow numerical solutions obtained by solving the compressible Navier-Stokes equations, one for each roughness geometry.

2. Governing equations

The governing equations considered in this analysis are the Navier-Stokes equations for a compressible Newtonian fluid. The primitive variables of the flow are denoted by density ρ, pressure p, temperature T and velocity components u_i, with $i = 1, 2, 3$. Considering a Cartesian reference frame, the system of equations can be written in conservation form as

$$\frac{\partial \rho}{\partial t} + \frac{\partial (\rho u_i)}{\partial x_i} = 0, \tag{1}$$

$$\frac{\partial (\rho u_i)}{\partial t} + \frac{\partial (\rho u_i u_j)}{\partial x_j} + \frac{\partial p}{\partial x_i} - \frac{\partial \tau_{ij}}{\partial x_j} = 0, \tag{2}$$

$$\frac{\partial (\rho E)}{\partial t} + \frac{\partial (\rho E u_i + p u_i)}{\partial x_i} + \frac{\partial q_i}{\partial x_i} - \frac{\partial (u_i \tau_{ij})}{\partial x_j} = 0, \tag{3}$$

where t is the time coordinate, x_i is the ith spatial coordinate and $E = e + u_i u_i/2$, with e being the specific internal energy of the fluid. The viscous stress tensor τ_{ij} is defined as

$$\tau_{ij} = \mu \left(\frac{\partial u_i}{\partial x_j} + \frac{\partial u_j}{\partial x_i} - \frac{2}{3} \frac{\partial u_k}{\partial x_k} \delta_{ij} \right), \tag{4}$$

where μ is the dynamic viscosity of the fluid and δ_{ij} is the Kronecker delta. The conductive heat flux vector q_i is modeled using Fourier's law of heat conduction, given by

$$q_i = -k\frac{\partial T}{\partial x_i}, \tag{5}$$

with k denoting the thermal conductivity of the fluid. Under the assumption of a calorically perfect gas, the system is closed by means of the perfect gas equation of state together with two additional thermodynamic relationships, respectively expressed as

$$p = \rho RT, \quad e = c_v T \quad \text{and} \quad c_v = \frac{R}{\gamma - 1}, \tag{6}$$

where R is the specific gas constant, c_v is the specific heat at constant volume and γ is the ratio of specific heats. Here, air is considered with the values $\gamma = 1.4$ and $R = 287.18$ J/(kg·K). Sutherland's law is used to model the variation of the dynamic viscosity with temperature, such that

$$\mu = \mu_{ref}\left(\frac{T}{T_{ref}}\right)^{3/2}\frac{T_{ref} + S_\mu}{T + S_\mu}, \tag{7}$$

where S_μ is the Sutherland temperature constant and μ_{ref} and T_{ref} are respectively the reference dynamic viscosity and static temperature. The same law is also assumed to take into account the variation of thermal conductivity with temperature, in this case with the parameters S_k and k_{ref}. The reference values considered for the dynamic viscosity and temperature are the same for all the cases presented in this study, namely $\mu_{ref} = 1.716 \times 10^{-5}$ kg/(m·s) and $T_{ref} = 273.15$ K. However, the values of S_μ, S_k and k_{ref} are specific to each particular case and can be found in Section 3.1. The resulting Prandtl number can then be directly obtained by $Pr = \mu c_p/k$, where c_p denotes the specific heat at a constant pressure. The flow similarity parameters that define the problem are γ and the freestream Reynolds, Mach and Prandtl numbers, respectively denoted by Re_∞, M_∞ and Pr_∞.

2.1. Formulation of the two-dimensional linear stability problem

According to classical linear stability theory, the vector of primitive flow variables $\mathbf{q} = [u, v, w, T, p]^T$ is split into a steady reference state $\bar{\mathbf{q}}$, also known as base flow, and a small unsteady perturbation field $\tilde{\mathbf{q}}$:

$$\mathbf{q} = \bar{\mathbf{q}} + \epsilon\tilde{\mathbf{q}}, \tag{8}$$

with $\epsilon \ll 1$. The base flow is assumed to be locally parallel in the streamwise (x) direction, so that $\bar{\mathbf{q}} = \bar{\mathbf{q}}(y, z)$ at a given x coordinate. As stated before, due to the high shear that characterizes the wake base flow in the wall-normal and spanwise directions, the amplitude of the perturbations is considered to be a function of both y and z. The ansatz of the modal perturbations for this case can be written as

$$\tilde{\mathbf{q}}(x, y, z, t) = \hat{\mathbf{q}}(y, z)\exp[i(\alpha x - \omega t)] + c.c., \tag{9}$$

where $\hat{\mathbf{q}}$ is the two-dimensional amplitude function, α is the wavenumber along the streamwise direction, ω is the angular frequency and $c.c.$ denotes the complex conjugate. In this work, the attention is focused on the spatial growth of the wake instabilities. In the spatial framework, ω is considered to be real and represents the angular frequency of the perturbations. On the contrary, α is complex, with the real part $\alpha_r = \Re\{\alpha\}$ being the streamwise wavenumber of $\tilde{\mathbf{q}}$ and the imaginary part $\alpha_i = \Im\{\alpha\}$ its spatial growth rate. With this definition, a positive value of α_i means a spatial decay of the amplitude function whereas a negative value implies spatial growth.

The equations governing the linear stability problem are obtained by substituting the splitting given by Eq. (8) together with the ansatz defined by Eq. (9) into the Navier-Stokes system, Eqs. (1) to (3), and then neglecting the resulting non-linear terms, which are of order $O(\epsilon^2)$. In the end, the resulting system of linear partial differential equations can be written in the following compact form

$$\mathbf{A}\hat{\mathbf{q}} = \alpha\mathbf{B}\hat{\mathbf{q}} + \alpha^2\mathbf{C}\hat{\mathbf{q}}, \tag{10}$$

where $\mathbf{A}$, $\mathbf{B}$ and $\mathbf{C}$ are complex and nonsymmetric differential matrix operators, whose specific structure for the current implementation used in this study can be found in the work of Groot [15]. The stability equations are made nondimensional using the freestream properties, denoted by the subscript ∞. The following dimensionless quantities are defined

$$t^* = \frac{tu_\infty}{l_\infty}, \quad x_i^* = \frac{x_i}{l_\infty}, \quad \rho^* = \frac{\rho}{\rho_\infty}, \quad u_i^* = \frac{u_i}{u_\infty}, \tag{11}$$

$$p^* = \frac{p}{\rho_\infty u_\infty^2}, \quad E^* = \frac{E}{u_\infty^2}, \quad T^* = \frac{T}{T_\infty}, \quad \mu^* = \frac{\mu}{\mu_\infty}, \tag{12}$$

where l_∞ is the local Blasius length scale at the streamwise location x where the stability analysis is performed, given by $l_\infty = \sqrt{\mu_\infty x/\rho_\infty u_\infty}$.

After discretization of Eq. (10), an algebraic generalized eigenvalue problem (GEVP) is obtained which is nonlinear in the eigenvalue α. The eigenvalue

problem is then linearized by means of the companion matrix method [16], which requires the definition of the following auxiliary vector: $\hat{\mathbf{q}}^+ = [\hat{u}, \hat{v}, \hat{w}, \hat{T}, \hat{p}, \alpha\hat{u}, \alpha\hat{v}, \alpha\hat{w}, \alpha\hat{T}, \alpha\hat{p}]^T$, so that the two-dimensional GEVP becomes

$$\mathcal{A}^+\hat{\mathbf{q}}^+ = \alpha\mathcal{B}^+\hat{\mathbf{q}}^+, \tag{13}$$

with

$$\mathcal{A}^+ = \begin{bmatrix} \mathcal{A} & -\mathcal{B} \\ \mathbf{0} & \mathbf{I} \end{bmatrix} \quad \text{and} \quad \mathcal{B}^+ = \begin{bmatrix} \mathbf{0} & C \\ \mathbf{I} & \mathbf{0} \end{bmatrix}, \tag{14}$$

in which $\mathcal{A}$, $\mathcal{B}$ and C denote the respective discrete matrix operators and $\mathbf{I}$ is the identity matrix. It is important to note that this linearization procedure duplicates the size of the system to be solved.

3. Numerical methodology

3.1. Computation of the laminar base flow

The roughness elements considered in this study are the three-dimensional sharp-edged geometries depicted in Fig. 1. The cuboidal geometry allows the design of a high-quality computational grid, making it ideal for fundamental studies and constituting a good case for validation purposes. On the other side, the ramp roughness element is based on a practical design developed by the Hypersonic Airbreathing Propulsion Branch (HAPB) at NASA Langley Research Center, who were exploring the possibility of using wall-mounted ramp fuel injectors in scramjet combustors [17]. Ramp injectors shed vortices and produce local flow separation which can enhance mixing and flame holding. This roughness shape has been previously tested at the von Karman Institute during a fundamental experimental campaign in roughness-induced transition by Tirtey [18], and is considered here with the purpose of obtaining numerical results that can later be compared against the experimental observations and provide additional understanding.

The geometrical configuration of the problem under investigation is represented in Fig. 2. The roughness elements are mounted on top of the flat plate surface at a given distance behind the leading edge and centered along the spanwise direction at $z = 0$ mm. Fig. 2 also shows the computational domain used to obtain the base flows for the stability analysis. As it can be observed, the domain is located inside the shock layer established between the surface and the shock wave induced at the flat plate leading edge. This approach has already been employed in similar studies by other

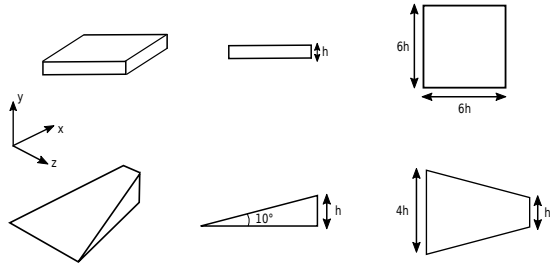

Figure 1: Roughness element geometries (not to scale).

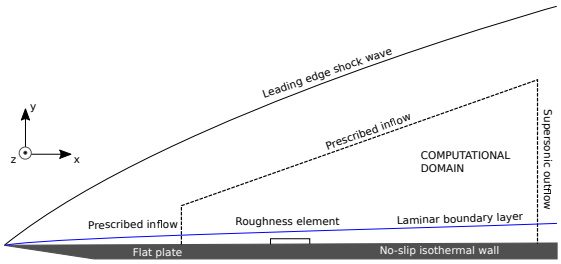

Figure 2: Representation of the geometrical configuration of the problem under study and the computational domain employed for the base flow calculations (not to scale). The same configuration is used for the ramp roughness element.

authors with successful results [6; 13]. Avoiding the leading edge induced shock wave helps to reduce the computational effort needed to obtain a converged numerical solution while adding flexibility to test different inflow conditions. On the other hand, it requires the imposition of adequate flow profiles at the inflow and top boundaries, which may come from another numerical solution of the Navier-Stokes equations or from a self-similar boundary layer computation. In all the cases presented in this work, a self-similar boundary layer profile is prescribed at the inflow boundaries of the domain. Additionally, the top boundary has a constant slope in order to avoid roughness-induced shock waves to impinge on it, which would complicate the treatment of boundary conditions at this boundary. The spanwise symmetry of the current geometrical configuration is also exploited by reducing the computational domain to solve only half of the flow field.

The dimensions of the computational domain used for each geometry are summarized in Table 1, which lists the streamwise coordinate and height of the inlet (x_{in}, y_{in}) and outlet (x_{out}, y_{out}) of the domain, as well as the spanwise size (z_∞), which is constant. Regarding the dimensions of the roughness elements, they are fully defined by the roughness height (h), which for the cuboidal element has a value of $h = 0.32$ mm

Table 1: Dimensions of the computational domain for each case. Units in millimeters.

	x_{in}	x_{out}	y_{in}	y_{out}	z_∞
Cuboid	20.28	67.59	1.26	9.60	6.31
Ramp	48.70	220.50	10	50	10

and for the ramp element of $h = 0.8$ mm. Finally, the streamwise location of the roughness element is defined by the streamwise coordinate of the leading edge of the roughness with respect to the flat plate leading edge, hereby denoted by x_r. In the current configuration, for the cuboid $x_r = 31$ mm whereas for the ramp $x_r = 55.46$ mm. In the case of the cuboidal element, the sizing of the problem has been carried out following the approach of De Tullio et al. [6], which consists in fixing the Reynolds number based on the displacement thickness at a reference streamwise position and assuming the roughness height to be equal to such displacement thickness. For the ramp geometry, the dimensions are obtained from the experimental campaign performed by Tirtey [18].

The freestream values considered for the numerical solution are summarized in Table 2. They correspond to the high-Reynolds test conditions of the von Karman Institute H3 hypersonic wind tunnel (see [18]). Because of the low freestream static temperature achieved, no high-temperature effects are expected in the flow field, and the assumption of a calorically perfect gas is a good approximation. Due to the short operating times of the wind tunnel, the flat plate wall is considered to be isothermal with a wall temperature of $T_w = 300$ K (room temperature). The Sutherland law parameters that are specific to each case are given in Table 3. For the cuboidal element, the parameters for the thermal conductivity law (S_k and k_{ref}) are calibrated to give a constant Prandtl number of 0.72. The numerical solution of the base flow is steady and laminar, and is carried out using the CFD package CFD++ on a block-structured grid consisting of hexahedral cells. The spatial discretization is based on a second-order upwind finite volume scheme which features a limited total variation diminishing (TVD) flux interpolation to minimize numerical oscillations in the vicinity of discontinuities. Concerning time integration, an implicit scheme (backward Euler) with multigrid acceleration and residual smoothing is employed to enhance convergence to the steady state as much as possible.

Regarding the boundary conditions, the primitive

Table 2: Freestream conditions used in the base flow computations.

M_∞	T_∞ [K]	p_∞ [Pa]	Re_∞/l [1/m]
6	60.98	1963.42	2.60×10^7

Table 3: Sutherland law parameters specific to each case.

	S_μ [K]	S_k [K]	k_{ref} [W/(m·K)]
Cuboid	110.4	110.4	2.40×10^{-2}
Ramp	111	194	2.41×10^{-2}

flow variables are prescribed at the inlet and the top boundaries of the domain with values that are obtained from a self-similar boundary layer computation. When no roughness is present, the flow field is constant along the spanwise direction and the problem becomes two-dimensional, so that the values to prescribe can be computed through a 2D simulation provided that the 3D domain boundaries are far enough for the influence of the element to be negligible. This is an additional advantage of using a subdomain with prescribed inflow data. At the center ($z = 0$ mm) and the far side ($z = z_\infty$) streamwise planes, symmetry conditions are specified, such that the actual problem would correspond to a spanwise array of discrete roughness elements. Lastly, at the wall and outlet boundaries the no-slip and supersonic outflow conditions are respectively applied. With respect to the initial conditions, the flow field is initialized with the freestream values in Table 2 and the system is integrated in time until a decrease of eight orders of magnitude in the residual norm is achieved.

The computational grids used to obtain the base flow solutions are generated using different meshing tools in each case. For the cuboidal roughness element, blockMesh is employed to obtain a perfectly orthogonal grid. In the case of the ramp geometry, ICEM CFD is used based on a block structure developed by Serino [19], who performed RANS simulations of the same geometrical configuration presented here in order to provide more insight into the experimental results of Tirtey [18]. In both cases, the grid is stretched towards the roughness in all directions as well as towards the flat plate wall to maintain a reasonable computational effort. Furthermore, the cell size transition between the different blocks is kept as smooth as possible. The resulting computational grids for the cuboidal and ramp elements respectively contain a total count of about 43 million and 73 million cells.

3.2. Solution of the generalized eigenvalue problem

The numerical solution of the stability problem given by Eq. (10) is performed using the von Karman Institute Extensible Stability & Transition Analysis (VESTA) toolkit, originally developed by Pinna [20; 21]. The particular structure of the matrices **A**, **B** and **C** for a given case is automatically derived and implemented in MATLAB by means of a tool based on the Maxima computer algebra system. The two-dimensional partial differential eigenvalue problem resulting from the linear stability formulation is assembled and discretized in MATLAB by means of a high-order finite difference scheme with uniform error developed by Hermanns & Hernández [22], also known as FD-q, as introduced by Paredes et al. [23]. Following the same philosophy as the Chebyshev collocation method, the idea behind the FD-q technique is to construct a finite difference scheme in a structured grid with a non-uniform point distribution, based on a piecewise Lagrange polynomial interpolation defined on a transformed domain $\xi, \eta \in [-1, 1]$, with ξ and η being respectively the spanwise and wall-normal transformed coordinates. For a given degree q of the interpolating polynomials, an optimal grid point distribution is computed which minimizes the interpolation error. In the limit of $q = N$, with $N + 1$ being the total number of grid points, the Chebyshev-Gauss-Lobatto point distribution is retrieved, making the FD-q discretization identical to the one provided by the Chebyshev collocation method. The advantage of this scheme lies upon the fact that by reducing the order of the discretization to $q << N$, a high degree of sparsity is introduced in the matrices that compose the discrete eigenvalue problem, which can then be exploited to provide a significant reduction of the computational cost at an acceptable decrease in accuracy.

In the majority of practical problems, the transformed grid does not coincide with the physical domain under study, and as a consequence adequate geometrical mappings have to be considered. In the computations presented in this work, the mapping originally introduced by Malik [24] is applied, which allows placing half of the grid points along a specific coordinate below a given location. In this way, the grid used for solving the stability problem can be clustered towards the boundary layer and the roughness centerline, which is the region containing the wake induced by the roughness element and as a result is where the strongest base flow gradients are encountered.

Before solving the stability problem, appropriate boundary conditions have to be imposed on the perturbation quantities to fully define the discrete GEVP. At the wall, the no-slip condition is enforced by setting the velocity perturbations to zero with a homogeneous Dirichlet condition. The same is also applied for the wall temperature disturbance, whereas the pressure fluctuation is determined by means of a compatibility condition satisfying the wall-normal momentum equation at the wall. In the wall-normal far-field boundary, the perturbations are forced to decay by imposing a Dirichlet boundary condition as well, with the exception of $\hat{p}$, which once again satisfies the compatibility condition. Regarding the spanwise boundaries, the symmetry of the problem is exploited once again in order to reduce the computational effort. In both the centerline and the spanwise far-field boundaries, symmetry or antisymmetry boundary conditions are specified. In the symmetric case, all the disturbances are set to zero except the spanwise velocity perturbation ($\hat{w}$), whose derivative normal to the boundary must be null. The latter is directly achieved through an homogeneous Neumann boundary condition. On the contrary, for the antisymmetric case the previous specifications are inverted, so that Neumann conditions are imposed for $\hat{u}$, $\hat{v}$, $\hat{T}$ and $\hat{p}$, and Dirichlet for $\hat{w}$.

The classical algorithm for solving generalized eigenvalue problems is the QZ method, which is able to compute the complete eigenvalue spectrum. Nevertheless, its high computational cost makes it feasible for the solution of small problems only. For the cases under consideration, the discrete matrices $\mathcal{A}^+$ and $\mathcal{B}^+$ reach a dimension of order $O(10^5)$, and therefore other options have to be assessed. For large-scale problems, the most common alternative is the implicitly restarted Arnoldi algorithm, which is an iterative method that only provides a given number of eigenvalues in the vicinity of a specific region. The solver built in VESTA toolkit makes use of the parallel implementation of the Arnoldi algorithm given by the (P)ARPACK library [25]. The Arnoldi iteration works optimally for extracting eigenvalues near the boundaries of the spectrum. However, in most of the interesting situations the focus is on the interior values that are closer to the origin. In order to modify the solution region, the so-called shift-invert transformation is applied, which transforms the problem into the following one

$$(\mathcal{A}^+ - \sigma\mathcal{B}^+)^{-1}\mathcal{B}^+\hat{\mathbf{q}}^+ = \nu\hat{\mathbf{q}}^+, \text{ with } \nu = \frac{1}{\alpha - \sigma}, \quad (15)$$

where σ is know as the shift-invert parameter, around which the eigenvalues are sought. The large matrix inversion involved in the solution process is based on

Table 4: Summary of the two different cases investigated.

Case	Re_h	h/δ_{99}	Inflow data
Cuboid	324	0.57	Self-similar solution
Ramp	419	0.68	Self-similar solution

a LU decomposition that is also performed in parallel by means of the Scalable Linear Algebra PACKage (ScaLAPACK) library [26]. A detailed description of the parallel solver, including the interfacing between the necessary libraries as well as different validation cases is provided by Naddei [27]. Additional validations of the two-dimensional stability solver for analyzing the stability of high-speed boundary layers developing over a smooth flat plate can be found in the study of Groot [15].

4. Results

Two different cases are analyzed in this work by means of linear stability theory, which are summarized in Table 4. The parameter Re_h is known as the roughness Reynolds number, and is defined as $Re_h = u_h h/\nu_h$, where u_h and ν_h are the local streamwise velocity and kinematic viscosity of the fluid evaluated at the streamwise location of the roughness element and at a height of $y = h$ in the corresponding clean flat plate boundary layer. Typical values reported in the literature above which transition starts to occur range around $Re_h \approx 300 - 500$ [13]. The value of h/δ_{99} describes the ratio between the roughness height and the local boundary layer thickness at the streamwise position of the roughness element, hereby denoted by δ_{99}. The value of δ_{99} is determined by means of the total enthalpy h_0 when $h_0/h_{0,\infty} = 0.995$, using once again the specific clean plate boundary layer profiles associated to each particular case. The inflow profiles prescribed in each calculation come from a self-similar solution of the compressible boundary layer equations, carried out with VESTA toolkit. Each self-similar profile is scaled according to the location of the domain inlet (x_{in}) given in Table 1.

In order to highlight the main physical features of the base flow, Figs. 3 and 4 depict the Mach number and streamwise velocity contours of the numerical solution obtained for both roughness geometries. Focusing on the streamwise flow structure, shown in the xy plane contour plots, it can be observed that the presence of the roughness elements introduces a displacement of the boundary layer upstream of the

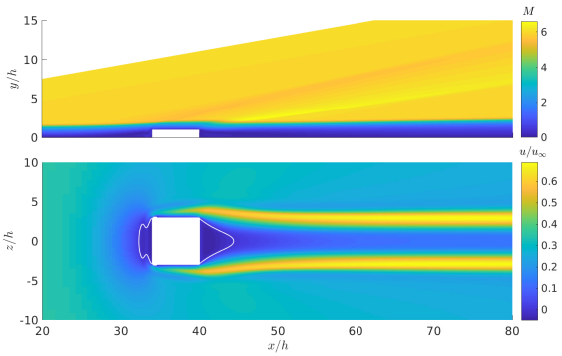

Figure 3: Base flow results obtained for the cuboidal roughness. (top) Mach number contours at the streamwise plane located at the roughness centerline ($z = 0$ mm), illustrating the roughness-induced shock and expansion waves. (bottom) Nondimensional streamwise velocity contours (u/u_∞) at a plane located at $y/h = 1/2$, showing the counter-rotating vortex pair generated by the roughness element. The white lines represent isolines of $u/u_\infty = 0$, delimiting regions of separated flow.

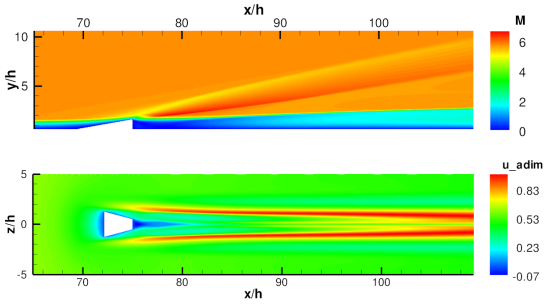

Figure 4: Base flow solution obtained for the ramp roughness. (top) Mach number contours at the streamwise plane located at the roughness centerline ($z = 0$ mm). (bottom) Nondimensional streamwise velocity contours (u/u_∞) at a plane located at $y/h = 1/2$.

leading edge, progressively inducing a set of compression waves that eventually merge into an oblique shock wave further downstream. As the flow reaches the trailing edge of the elements it turns and detaches, creating a region of separated flow immediately downstream and generating an expansion wave. Next, as the flow progressively reattaches further downstream, another fan of compression waves is induced and once again merges into an additional oblique shock. It is important to note that in the case of the cuboidal roughness, a region of separated flow is also encountered immediately upstream of the element due to the strong flow blockage imposed by the blunt geometry. The spanwise structure of the flow field is represented in the xz plane contour plots of Figs. 3 and 4 and in

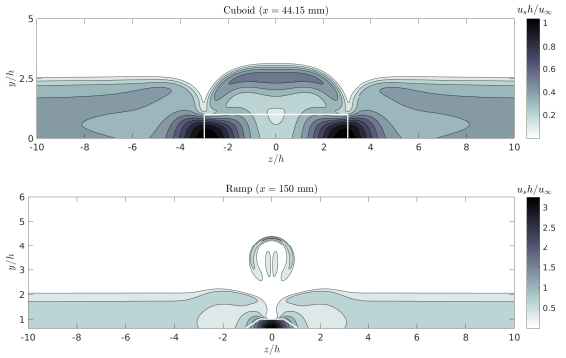

Figure 5: Contours of streamwise shear magnitude at a spanwise plane behind the cuboid (top) and the ramp (bottom) roughness geometries. The white solid lines represent a projection of the roughness elements.

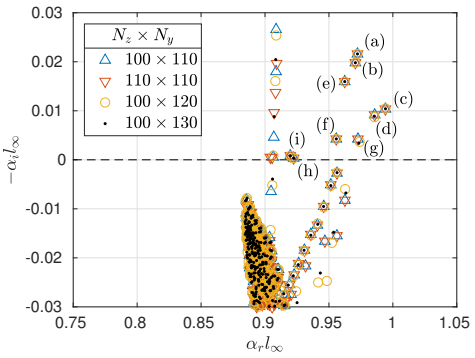

Figure 6: Spatial eigenvalue spectrum for the cuboidal roughness element. The letters in parenthesis label the different unstable discrete modes identified.

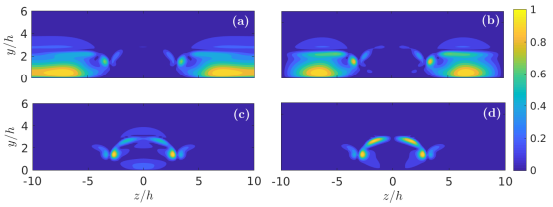

Figure 7: Contours of the normalized magnitude of the streamwise velocity eigenfunctions, $|\hat{u}|/max(|\hat{u}|)$, associated to modes (a) to (d) in Fig. 6. The eigenfunctions represented correspond to the case with 100×110 grid points.

Fig. 5, which shows contours of the streamwise shear magnitude, defined as

$$u_s = \sqrt{\left(\frac{\partial u}{\partial y}\right)^2 + \left(\frac{\partial u}{\partial z}\right)^2}, \tag{16}$$

on a spanwise (zy) plane located at a given distance x behind the roughness elements. In both cases, a pair of strong counter-rotating vortices can be identified, which form at the edges of the roughness due to a pressure gradient between the side and the top surfaces of the elements. These streamwise structures lift-up low-momentum fluid adjacent to the surface of the flat plate and give rise to a mushroom-shaped low-velocity streak [12], which is surrounded by regions of high streamwise shear and large shear gradients in the wall-normal and spanwise directions. Due to the side angle of the ramp geometry, narrowing the planform shape of the element towards the trailing edge, the counter-rotating vortex pair also presents a spanwise velocity component in the direction of the roughness centerline. This small lateral momentum makes the vortices come close to each other progressively along the wake, concentrating the vorticity in a smaller region and leading to a narrower but taller streak. This is in contrast with the results obtained in the case of a cuboidal roughness element, in which the vortices remain parallel to each other along the wake.

With respect to the spatial stability analysis, the calculations are performed at a different frequency and streamwise location for each geometry. On the one hand, the instability of the cuboidal roughness is examined at a nondimensional angular frequency of $\omega^* = \omega l_\infty / u_\infty = 0.88$ in a plane located at a streamwise distance of $x = 44.15$ mm. These values were chosen following the DNS results of De Tullio & Sandham [7] and the stability analysis of Paredes [9] on a similar problem, where this frequency is the one at which the highest disturbance growth rate is obtained and the plane is located at a distance where a significant linear development of the dominant instability modes has already been attained. On the other hand, the analysis in the wake induced by the ramp element is carried out at $\omega^* = 0.051$ and $x = 150$ mm, values that were chosen based on similar configurations found in the literature [12]. Regarding the discretization, the Chebyshev collocation method is employed for the cuboid case, whereas the ramp solution is discretized with an order of $q = 10$.

4.1. *Stability results for the cuboidal roughness element*

The results of the stability calculation for the cuboidal element are presented in Figs. 6 and 7, which respectively show the spatial spectrum and the two-dimensional streamwise velocity amplitude functions, also known as eigenfunctions, of some of the most unstable discrete modes obtained at the specified location and frequency. The number of eigenvalues re-

quested to the Arnoldi algorithm were 200, with a shift-invert parameter of $\sigma = 0.95$. Different grids were tested in order to check the convergence of the spectrum with respect to the number of grid points in both the spanwise (N_z) and the wall-normal (N_y) directions, providing at the same time a direct visualization of the location of continuous, discrete and spurious numerical modes. A discretized vertical continuous branch located at $\alpha_r l_\infty = \omega^*$ can be observed, which is a characteristic feature of the truncation of the stability domain [15]. According to Balakumar & Malik [28], the modes composing this branch represent entropy and vorticity waves. Although not shown in the picture, two additional horizontal continuous branches located in the real axis respectively at the right and left of the vertical branch can also be found in the spectrum. These branches are associated to the supersonic nature of the flow, and in this case represent acoustic waves. It has been checked that such branches can actually be retrieved when changing the shift of the transformed GEVP and/or solving for a larger number of eigenvalues. Several numerical spurious modes appear scattered along the imaginary axis at a nearly constant wavenumber of about $\alpha_r l_\infty = 0.91$, which do not show any grid convergence. Their unphysical nature has been further confirmed by looking at the associated amplitude functions. The discrete, and physically interesting, eigenvalues are located at the right of the continuous branch, spanning different dimensionless wavenumbers in the range approximately between 0.92 and 1. These modes are completely converged with respect to N_z, while convergence is close with respect N_y, specially for the unstable eigenvalues.

Nine unstable discrete modes are identified in Fig. 6, labeled with letters from (a) to (i), associated to the contour plots of the streamwise velocity amplitude functions in Fig. 7. For the particular frequency and streamwise position considered, the leading instability mode (a) is the Mack mode, which develops in the lateral boundary layer at the sides of the roughness element and spans the complete computational domain in the spanwise direction. The nature of this mode is not associated to the presence of the roughness and therefore it can also be retrieved both with a two-dimensional linear stability analysis considering a clean flat plate or by means of classical linear stability theory. The second dominant instability mode (b) also peaks at the sides of the element wake, with an antisymmetric shape function showing a similar amplitude distribution to that of the Mack mode. The same is true for modes (e) and (f). It is argued that modes (b), (e) and (f) are oblique perturbations of the same family as the Mack mode, with an increasing spanwise wavenumber β. Their diagonal-like distribution along the spectrum supports this argument. On the other side, modes (c) and (d) respectively correspond to the most unstable varicose (even) and sinuous (odd) deformations of the low-velocity streak, whose amplitude functions are maximum in the high-shear layer surrounding the mushroom-shaped structure. These are the most unstable perturbations developing in the wake behind the cuboidal roughness element, with the varicose mode showing a slightly higher growth rate in this case. The wake of the element also sustains the growth of two additional modes, denoted by (h) and (i), which have very small growth rates and their amplitude peaks are located at the interface between the streamwise vortices, the rising streak and the lateral boundary layer. It is worth noting that, as could be expected, the regions where the amplitude functions of the wake modes are higher mainly correspond to the areas with larger shear magnitude gradients. Finally, mode (g) is associated to the leading wake fluctuations (c) and (d). Similarly to perturbations (b), (e) and (f) in the case of the Mack mode, this mode is believed to correspond to an oblique ($\beta l_\infty > 0$) instability of the same family as the varicose and sinuous modes. In fact, all the modes located in the diagonal line at the right of the vertical continuous branch are oblique variations of the varicose and sinuous deformations, with increasing β when moving towards lower growth rates. Mode (g) is then the first oblique perturbation located in such diagonal branch.

The results obtained agree qualitatively well with the BiGlobal analysis of Paredes [9], performed at the same frequency and streamwise position on a DNS base flow with the same roughness geometry and size but at slightly different freestream conditions. In that study, the Mack mode is also the dominant instability mechanism, followed by the antisymmetric perturbation found in Fig. 7(b) and the varicose mode, although no sinuous instability is reported. On the same problem, Van den Eynde & Sandham [29] report that the varicose mode is linked to the development of the Mack mode and has a very similar nature, i.e. an acoustic mode that is trapped within the wake behind the roughness element and reflects back and forth between the wall and the sonic line of the low-velocity streak. An extended stability analysis for this case including the effects of the flat plate leading edge and wall temperature can be found in [30].

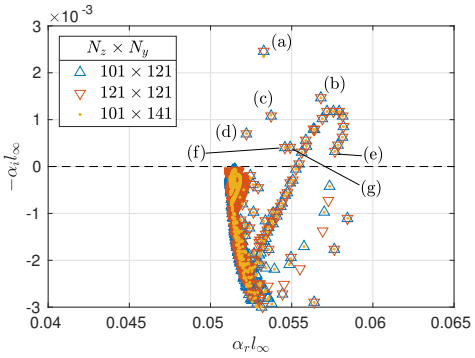

Figure 8: Spatial eigenvalue spectrum for the ramp roughness element. The letters in parenthesis label the different unstable discrete modes identified.

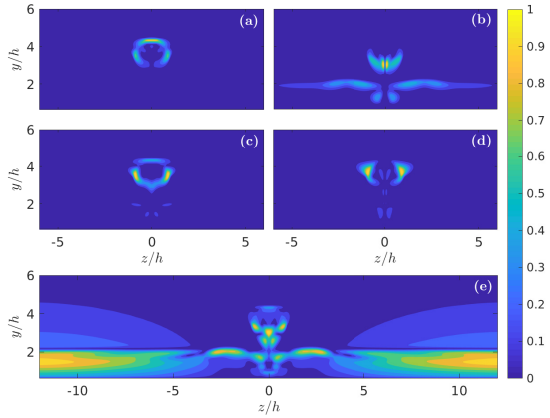

Figure 9: Contours of the normalized magnitude of the streamwise velocity eigenfunctions, $|\hat{u}|/max(|\hat{u}|)$, associated to modes (a) to (e) in Fig. 8. The eigenfunctions represented correspond to the case with 101×121 grid points.

4.2. Stability results for the ramp roughness element

In a similar way as the previous case, the stability results for the ramp roughness geometry are presented in Figs. 8 and 9. This time 300 eigenvalues were resolved with a shift of $\sigma = 0.055$. Once again, different grid resolutions were examined to check the convergence of the discrete modes. In this case, for the particular frequency and streamwise location considered, seven different unstable discrete modes can be identified, which are labeled with letters from (a) to (g). The leading instability perturbation (a) for this configuration is a varicose mode. This is evident from its symmetric (even) amplitude function growing in the region surrounding the low-velocity streak induced behind the roughness element. The corresponding maximum amplitude is located at the top of the mushroom-like structure, that is the region of the streak showing the highest shear magnitude. The next instability mode (b) corresponds to an antisymmetric deformation of the streak together with the adjacent lateral boundary layer, but as opposed to the previous mode, it features a maximum amplification inside the streak structure. Due to its odd eigenfunction with respect to the $z/h = 0$ symmetry plane, this perturbation belongs to the family of the so-called sinuous instability modes. The wake also sustains the growth of four additional disturbances, modes (c), (d), (f) and (g), which also show signatures of varicose and sinuous instabilities. A large discrete branch of modes is also retrieved, spanning a wide range of wavenumbers in a hook-like shape. When looking at the amplitude function of the first mode belonging to this branch (e), the amplitude signature of the Mack mode can be immediately recognized. It is an instability that is mainly developing in the lateral, undisturbed boundary layer, although due to the presence of the roughness its eigenfunction also shows amplitude peaks inside the wake region. The remaining modes from this discrete branch are simply oblique variations of the Mack mode which come out naturally from the two-dimensional eigenvalue problem since β is no longer a fixed parameter. It is interesting to observe that as β increases, the growth rate of the oblique mode reaches a maximum value and then decreases monotonically, eventually becoming stable. The nondimensional spanwise wavenumber for which this mode shows maximum growth is estimated to be $\beta l_\infty \approx 0.11$. It is well known from classical linear stability theory that for a smooth flat plate hypersonic boundary layer, the Mack mode has a maximum growth rate for $\beta l_\infty = 0$. This is in contrast with the results obtained here, and it is a matter for further investigation whether this behavior is due to the presence of the roughness element or a limitation of the computational setup in use, such as the spanwise size of the domain.

Additional stability calculations for this particular case are provided in [31], which include the effect of the flat plate leading edge.

5. Conclusions

The stability characteristics of the wake behind a cuboid and a ramp-shaped roughness element mounted on top of a flat plate inside a Mach 6 freestream have been investigated using two-dimensional linear stability theory. The base flows needed for the stability analysis were obtained by means of calorically perfect gas, laminar and steady

Navier-Stokes simulations employing a second-order finite volume scheme. The roughness elements induce a strong pair of counter-rotating vortices that give rise to a mushroom-shaped streak through the lift-up of low-momentum fluid from the surface of the flat plate. This structure is surrounded by regions of high streamwise shear and large shear gradients in the wall-normal and spanwise directions. Additionally, the ramp geometry induces a spanwise velocity component into the counter-rotating vortices that progressively makes them come closer to each other, concentrating the vorticity in a small region and increasing the lift-up of the streak.

The spatial stability spectrum and the associated two-dimensional amplitude functions were computed at a particular frequency and streamwise position for each geometry. In the case of the cuboidal roughness element, the Mack mode is the most unstable perturbation growing in the boundary layer, followed by varicose and sinuous fluctuations that develop in the region surrounding the low-velocity streak that characterizes the wake. When the ramp roughness configuration is considered, a varicose mode is the most unstable perturbation growing inside the wake behind the element, followed by sinuous deformations of the low-velocity streak. The Mack mode instability is also present in the ramp-induced flow field, associated with a large family of oblique modes that grow in the lateral, undisturbed boundary layer. A maximum in the growth rate for this family of modes is found for $\beta l_\infty > 0$. In both geometries, it is observed that the amplitude of the wake instabilities is higher in the regions where the base flow presents the strongest shear gradients.

Acknowledgments

This work is part of a project that has received funding from the European Union's Horizon 2020 research and innovation programme under the Marie Skłodowska-Curie grant agreement No 675008.

References

[1] E. R. van Driest, The problem of aerodynamic heating, Aeronautical Engineering Review (1956) 26–41.

[2] E. Reshotko, Transition issues for atmospheric entry, Journal of Spacecraft and Rockets 45 (2) (2008) 161–164.

[3] V. Theofilis, Global linear instability, Annu. Rev. Fluid Mech. 43 (2011) 319–352.

[4] G. Groskopf, M. J. Kloker, O. Marxen, Bi-global secondary stability theory for high-speed boundary-layer flows, in: Proceedings of the Summer Program 2008, Center for Turbulence Research, 2008.

[5] M. Kegerise, R. King, L. Owens, M. Choudhari, A. Norris, F. Li, C.-L. Chang, An experimental and numerical study of roughness-induced instabilities in a Mach 3.5 boundary layer, RTO-AVT-200/RSM-030 29, NATO (2012).

[6] N. D. Tullio, P. Paredes, N. D. Sandham, V. Theofilis, Laminar-turbulent transition induced by a discrete roughness element in a supersonic boundary layer, Journal of Fluid Mechanics 735 (2013) 613–646.

[7] N. D. Tullio, N. D. Sandham, Influence of boundary-layer disturbances on the instability of a roughness wake in a high-speed boundary layer, Journal of Fluid Mechanics 763 (2015) 136–165.

[8] V. Theofilis, Advances in global linear instability analysis of nonparallel and three-dimensional flows, Progress in Aerospace Sciences 39 (2003) 249–315.

[9] P. Paredes, Advances in global instability computations: from incompressible to hypersonic flow, Ph.D. thesis, Universidad Politécnica de Madrid (2014).

[10] N. D. Tullio, N. D. Sandham, Direct numerical simulations of roughness receptivity and transitional shock-wave/boundary-layer interactions, RTO-MP-AVT-200 22, NATO (2012).

[11] M. Choudhari, F. Li, M. Wu, C.-L. Chang, J. Edwards, M. Kegerise, R. King, Laminar-turbulent transition behind discrete roughness elements in a high-speed boundary layer, American Institute of Aeronautics and Astronautics.

[12] M. Choudhari, C. L. Chang, A. Norris, J. Edwards, Wake instabilities behind discrete roughness elements in high speed boundary layers, American Institute of Aeronautics and Astronautics.

[13] A. Theiss, S. Hein, Investigation on the wake flow instability behind isolated roughness elements on the forebody of a blunt generic re-entry capsule, EUCASS Proceedings Series 9 (2017) 451–480.

[14] A. Theiss, S. Hein, S. R. C. Ali, R. Radespiel, Wake flow instability studies behind discrete roughness elements on a generic re-entry capsule, 46th AIAA Fluid Dynamics Conference, 13-17 June 2016, Washington, DC.

[15] K. Groot, Derivation of and simulations with BiGlobal stability equations, Master's thesis, Technische Universiteit Delft (2013).

[16] T. Bridges, P. Morris, Differential eigenvalue problems in which the parameter appears nonlinearly, Journal of Computational Physics 55 (1984) 437–460.

[17] S. D. Stouffer, N. R. Baker, D. P. Capriotti, G. B. Northam, Effects of compression and expansion ramp fuel injector configurations on scramjet combustion and heat transfer, 31st AIAA Aerospace Sciences Meeting and Exhibit, 11-14 January 1993, Reno, Nevada.

[18] S. C. Tirtey, Characterization of a transitional hypersonic boundary layer in wind tunnel and flight conditions, Ph.D. thesis, Université Libre de Bruxelles and von Karman Institute for Fluid Dynamics (2009).

[19] G. Serino, Numerical prediction of transition in hypersonic flows, Tech. rep., von Karman Institute for Fluid Dynamics (2011).

[20] F. Pinna, Numerical study of stability of flows from low to high mach number, Ph.D. thesis, Universitá "La Sapienza" di Roma and von Karman Institute for Fluid Dynamics (2012).

[21] F. Pinna, VESTA toolkit: a software to compute transition and stability of boundary layers, 43rd Fluid Dynamics Conference, 24-27 June 2013, San Diego, California.

[22] M. Hermanns, J. A. Hernández, Stable high-order finite-difference methods based on non-uniform grid point distributions, Int. J. Numer. Meth. Fluids 56 (2008) 233–255.

[23] P. Paredes, M. Hermanns, S. Le Clainche, V. Theofilis, Order

10^4 speedup in global linear instability analysis using matrix formation, Comput. Methods Appl. Mech. Engrg. 253 (2013) 287–304.

[24] M. R. Malik, Numerical methods for hypersonic boundary layer stability, Journal of Computational Physics 86 (2) (1990) 376–413.

[25] K. J. Maschhoff, D. C. Sorensen, P_ARPACK: An efficient portable large scale eigenvalue package for distributed memory parallel architectures, Lecture Notes in Computer Science 1184 (1996) 478–486.

[26] L. S. Blackford, J. Choi, A. Cleary, E. D'Azevedo, J. Demmel, I. Dhillon, J. Dongarra, S. Hammarling, G. Henry, A. Petitet, K. Stanley, D. Walker, R. C. Whaley, ScaLAPACK Users' Guide, Society for Industrial and Applied Mathematics, 1997.

[27] F. Naddei, Parallel computation of global eigenmodes for space propulsion systems, Tech. rep., von Karman Institute for Fluid Dynamics (2016).

[28] P. Balakumar, M. R. Malik, Discrete modes and continuous spectra in supersonic boundary layers, Journal of Fluid Mechanics 239 (1992) 631–656.

[29] J. V. den Eynde, N. D. Sandham, Numerical investigation of roughness-induced transition at Mach 6 in the European ATLLAS-II programme, 8th European Symposium on Aerothermodynamics for Space Vehicles, 2-6 March 2006, Lisbon, Portugal.

[30] I. Padilla Montero, F. Pinna, BiGlobal stability analysis of the wake behind an isolated roughness element in hypersonic flow, 7th European Conference for Aeronautics and Aerospace Sciences (EUCASS), 3-6 July 2017, Milan, Italy.

[31] I. Padilla Montero, F. Pinna, Stability analysis of the boundary layer developing on a flat plate with discrete roughness elements in hypersonic flow, AIAA 2018-1079, 2018 AIAA Aerospace Sciences Meeting, AIAA SciTech Forum, 8-12 January 2018, Kissimmee, Florida.

Blowing and Chemical Non-Equilibrium Effects on Hypersonic Boundary-Layer Stability

Fernando Miró Miró

Aeronautics and Aerospace Department, von Karman Institute for Fluid Dynamics, Belgium, mymail@vki.ac.be

Supervisor: Fabio Pinna

Senior Research Engineer, Aeronautics and Aerospace Department, von Karman Institute for Fluid Dynamics, Belgium, fabio.pinna@vki.ac.be

Supervisor: Olivier Chazot

Head of Department, Aeronautics and Aerospace Department, von Karman Institute for Fluid Dynamics, Belgium, chazot@vki.ac.be

University Supervisor: Gérard Degrez

Professor, École Polytechnique de Bruxelles, Université Libre de Bruxelles, Belgium, gdegrez@ulb.ac.be

Abstract

The uncertainty in the prediction of the transition onset location in complex high-enthalpy re-entry environments remains a major cause for the vehicle's TPS oversizing. Two boundary-layer stability models accounting separately for wall blowing and chemical non-equilibrium effects are presented and used to study the early stages of transition. The modeling of the wall-normal velocity perturbation was seen to have a major impact on the stability of blown boundary layers. On the other hand, for reacting boundary layers, the thermochemical modeling of the perturbations was seen to be less significant than that of the base-flow quantities.

Keywords: Hypersonics, Boundary Layer, Transition, Stability, Wall blowing, Chemical Non-Equilibrium, Ablation

Nomenclature

Acronyms

ADIT	Automatic Derivation and Implementation Tool
CNE	Chemical Non-Equilibrium
CPG	Calorically Perfect Gas
DNS	Direct Numerical Simulations
LST	Linear Stability Theory
PSE	Parabolized Stability Equations
RK4	Runge-Kutta 4th order
TPS	Thermal Protection System

Roman Symbols

A	Perturbation amplitude [-]
B	Non-dimensional blowing mass-flow parameter [–]
$\mathbb{D}_{x^i}$	Spatial domain [–]
Da	Damköhler number [–]
$\mathcal{D}_s$	Diffusion coefficient of species s in the mixture [$m^2\ s^{-1}$]
$\mathscr{D}_{s\ell}$	Diffusion coefficient of species s in species ℓ [$m^2\ s^{-1}$]
Ec	Eckert number [–]
f_w	Self-similar non-dimensional Blasius velocity function at the wall [–]

g^{ij}	Metric tensor [–]
h	Mixture enthalpy per unit mass [J kg^{-1}]
$\mathcal{J}^j$	Energy diffusion flux [J m^{-2} s^{-1})]
J_s^j	Mass diffusion flux of species s [kg m^{-2} s^{-1}]
$\mathscr{M}$	Molar molecular mass [kg mol^{-1}]
N	N factor in the e^{N} method [-]
p	Pressure [Pa]
Pr	Prandtl number [–]
q	Flow variable
Re	Reynolds number [–]
Re_1	Unit Reynolds number [m^{-1}]
$\mathbb{S}$	Set of all species [–]
Sc	Schmidt number [–]
$\mathbb{T}^{ij}$	Viscous stress tensor [Pa]
T	Temperature [K]
t	Time [s]
u^j	Velocity components [m/s]
v_s^i	Species total velocity [m s^{-1}]
x^j	Spatial coordinates [m]
X_s	Species molar fraction [–]
Y_s	Species mass fraction [–]

Greek Symbols

α	Perturbation streamwise wavenumber [m^{-1}]
β	Perturbation spanwise wavenumber [m^{-1}]
η	Self-similar wall-normal variable [–]
ζ_s	Species thermal diffusion ratio [–]
κ	Frozen thermal conductivity [W K^{-1} m^{-1}]
μ	Dynamic viscosity [kg m^{-1} s^{-1}]
ρ	Density [kg/m^3]
τ_c	reference chemical time scale [s]
ξ	Streamwise coordinate in the computational domain [kg^2 s^{-2} m^{-2}]
ω	Perturbation frequency [s^{-1}]
$\dot{\omega}_s$	Species production rate [kg m^{-3} s^{-1}]
Ω_{Ms}^i	Species momentum source term [kg m^{-2} s^{-2}]

Sub- and superscripts

q'	Perturbation variable
$\overline{q}$	Base-flow variable
$\tilde{q}$	Perturbation amplitude variable
$\hat{q}$	Dimensional variable
q	Non-dimensional variable (not hatted)
q^j	Contravariant variable
q_j	Covariant variable
$q_{,j}$	Covariant derivative of a variable
q_e	Reference boundary-layer edge quantity (always dimensional)
q_M	Maximum value of a quantity
q_s	Species quantity
q_w	Wall quantity

1. Introduction

Space exploration likely poses the most ambitious endeavor in which human civilization has embarked itself. Getting to reach and colonize other worlds is not only challenging and inspiring, but also necessary. A critical part of all space missions is the atmospheric entry phase, where space vehicles must decelerate from their high approach speeds and effectively land. The excess kinetic energy is transformed into thermal energy through viscous dissipation. Shielding the payload from these high temperatures is essential for the mission's success, rendering crucial the design of the Thermal Protection System (TPS). In the past, designs have been non-optimal and overconservative in order to guarantee the mission's success, therefore penalizing the available payload. The lack of understanding of the dynamics behind laminar-to-turbulent transition plays a major role in this oversizing. Not being able to accurately predict the location of transition onset forces engineers to make the conservative fully-turbulent assumption. The highly fluctuating nature of turbulent flows leads to stronger energy mixing

than laminar flows, and therefore stronger gradients. These large energy gradients ultimately cause higher surface heat fluxes [1], up to 8 times higher than in a fully laminar regime [2].

In atmospheric entry missions, it is common to encounter situations where transition coexists and couples with other physical phenomena, such as the ablation of the TPS. Ablative TPS alleviate the vehicle's high heat fluxes through the pyrolysis of their polymeric matrix and subsequent fiber ablation [3]. The usage of such heat shields is often unavoidable, due to the large amount of energy that must be dissipated in high-speed entries such as those entering Mars [4; 5].

The presence of ablation affects boundary-layer transition through the modification of three of its key influencing parameters: altering the surface roughness due to the irregular burning of the TPS; changing the surface heat transfer due to the wall-flow chemical reactions; and outgassing pyrolysis and ablation subproducts into the boundary layer [6]. It is therefore of paramount importance to develop transition models including the aforementioned interactions.

Moreover, an improved understanding of laminar-to-turbulent transition will also allow to advance the development of hypersonic cruise vehicles. The issue at hand is not only the impact of transition on the heat flux, but also on the aerodynamic drag [7]. Turbulent flows also have stronger momentum mixing and gradients, ultimately leading to higher shear stresses at the wall. An increase in the drag coefficient of 15% (due to having a fully turbulent rather than a fully laminar regime in the boundary layer) of a single-stage-to-orbit mission can reduce the available payload to less than half [8].

Such environments feature very high temperatures, rendering calorically perfect gas (CPG) models inaccurate at describing the thermal processes. They therefore require multi-species frozen or chemically reacting models. The Damköhler number is of order one, meaning that the characteristic time scale of the chemical reactions has the same order of magnitude as the flow ($\tau_{flow} \sim \tau_c$). However, when the characteristic time scale of the flow is much smaller than that of the chemistry ($\tau_{flow} << \tau_c$) it is legitimate to assume the flow's chemical composition to be frozen. On the other hand, if the flow time scale were much larger than that of the chemistry ($\tau_{flow} >> \tau_c$), one may assume equilibrium chemistry [9].

Many authors have tackled the problem of modeling chemically reacting flows in the past. Malik [10; 11; 12; 13; 14] performed extensive studies in CPG and equilibrium conditions. Stuckert & Reed [15] extended the analysis to account for chemical non-equilibrium effects, and Hudson [16] extended it even further, modeling vibrational non-equilibrium with a two-temperature model. Other authors have continued and extended the stability analysis of non-equilibrium flows – Perraud & Arnal [17] performed LST studies in a wide range of flow regimes, including chemical non-equilibrium; Franko [18] investigated chemical and thermal non-equilibrium effects, showing that the viscosity model used has a dramatic effect on stability characteristics; Malik himself [19] and Johnson [20] used Parabolized Stability Equations (PSE), where non-parallel terms are not dropped; Marxen [21; 22] performed high-order accurate DNS studies of these flows; Lyttle [23] performed a sensitivity analysis on the thermodynamic and transport models; Klentzman & Tumin [24] studied viscous effects on receptivity and stability in a dissociating oxygen mixture; and Bitter & Shepherd [25] looked into the effect of thermal non-equilibrium on supersonic modes using a two-temperature model.

Ablation outgassing effects were extensively studied experimentally (see Schneider [26]) by looking at the effect of cold gas injection on the transition onset location. Analogous numerical studies of wall-blowing effects were carried out by Malik [10], Johnson [20] and Ghaffari [27]. However, they did not make any modeling of the wall-normal velocity perturbations, assuming them to be equal to zero.

This work presents two distinct stability models accounting respectively for chemical non-equilibrium and wall blowing effects. They were both developed in the framework of the VESTA toolkit [28; 29; 30]. The models are introduced in section 2, followed by a comment on the particularities of the methodology in section 3. They are then applied to a series of study cases in section 4 and finally some concluding remarks are made in section 5.

2. Governing equations

The system's equations are given in their non-dimensional and invariant form, such that they are valid in any coordinate system. Superscripts q^i denote vectorial contravariant variables, whereas subscripts q_i denote vectorial covariant variables (see Pinna & Groot [30]). Also, indices following a comma denote spatial derivatives (e.g. $u^i_{,j} = \partial u^i / \partial x^j$). The non-dimensionalization convention is given in table 1, where τ_c is the chemical time scale and $\ell_e = \sqrt{\rho_e \hat{x}^1 / (\mu_e u_e)}$ is the local Blasius length. Note the excess in notation of using the subindex e for the Blasius

length – it is by definition a function of the edge quantities. However, the redundant naming is kept for clarity. τ_c is the only reference quantity that is not defined at the boundary-layer edge. The reference chemical time scale is that associated to the fastest production or destruction of any species anywhere in the domain:

$$\tau_c = \min\left(\frac{\hat{\omega}_s}{\hat{\rho}_s}\right) \forall s \in \mathbb{S}\,,\; x^i \in \mathbb{D}_{x^i}\,, \tag{1}$$

where $\mathbb{S}$ is the set of all species, and $\mathbb{D}_{x^i}$ is the investigated spatial domain. All reference quantities, including τ_c, as well as universal constants such as $\mathscr{R}$ or $\hbar$, are spared from the hatted notation despite being obviously dimensional.

2.1. Linear Stability Theory

In order to study transition, the flow variables $q(x, y, z, t)$ are decomposed into a mean laminar steady term $\overline{q}(x, y, z)$ plus a perturbation $q'(x, y, z, t)$. Equations are then linearized by dropping higher-order perturbation terms $q'_1 \cdot q'_2 \approx 0$. A modal decomposition assumes perturbations to be periodic in the streamwise and spanwise directions and in time, letting the amplitude term depend solely on the wall-normal direction $\tilde{q} = \tilde{q}(y)$. Finally, the parallel flow assumption implies that $\overline{q} \approx \overline{q}(y)$. The flow variables are therefore ultimately decomposed into:

$$q(x, y, z, t) = \overline{q}(y) + \tilde{q}(y) \cdot \exp\left(i\ (\alpha x + \beta z - \omega t)\right) + \text{c.c.}\,, \tag{2}$$

where c.c. stands for complex conjugate, and α, β and ω are the complex perturbation wavenumbers and frequency.

These assumptions reduce the Navier-Stokes equations to a generalized eigenvalue problem [31], that can return either a complex α for fixed real β and ω, or a complex ω for fixed real α and β. The corresponding eigenfunctions represent the perturbation amplitude variables $\tilde{q}$.

LST, as well as any other stability theory, can be used in conjunction with the semiempirical e^N method to predict the location of transition onset. The idea of this method, developed by Smith and Gamberoni [32] and van Ingen [33], is to correlate the location of the transition onset with the linear growth of the most unstable modes' perturbation amplitude. The envelope of all N curves, computed by integrating the maximum amplification rate $-\alpha_{i,M}(x)$:

$$N = \ln(A/A_0) = \int_{x_0}^{x} -\alpha_{i,M}(\chi)\ \mathrm{d}\chi\,, \tag{3}$$

is then used to estimate the amplitude growth.

A complete review of LST and the e^N method, can be found in Arnal [34].

2.2. Blowing model

The wall-blown analyses are performed in environments with temperatures such that CPG assumptions still hold. The system can therefore be characterized with a mass-conservation equation (Eq. 4), three momentum-conservation equations (Eq. 5), and an energy-conservation equation (Eq. 6).

$$\frac{\partial \rho}{\partial t} + (u^j \rho)_{,j} = 0, \tag{4}$$

$$\rho \frac{\partial u^i}{\partial t} + \rho u^j u^i_{\ ,j} = -g^{ij} p_{,j} + \frac{1}{Re}\, \mathbb{T}^{ij}_{\ \ ,j}, \tag{5}$$

$$\rho \frac{\partial h}{\partial t} + \rho u^j h_{,j} = Ec\left(\frac{\partial p}{\partial t} + u^j p_{,j}\right) + \frac{1}{RePr}\left(\kappa g^{ij} T_{,i}\right)_{,j} + \frac{Ec}{Re}\, g_{ik} \mathbb{T}^{kj} u^i_{\ ,j}, \tag{6}$$

where g^{ij} is the metric tensor [35], h is the mixture enthalpy, κ is the thermal conductivity, and $\mathbb{T}^{ij}$ is the viscous stress tensor:

$$\mathbb{T}^{ij} = \lambda g^{ij} u^k_{\ ,k} + \mu\left(g^{jk} u^i_{\ ,k} + g^{ik} u^j_{\ ,k}\right). \tag{7}$$

Eqs. 4-6 are simplified applying the LST hypotheses introduced in section 2.1, reaching the CPG LST equations [28].

The study of wall-blowing configurations using LST leads to some mathematical inconsistencies, due to the combination of the parallel flow assumption and the continuity condition on the basic state quantities. A detailed explanation of this, together with the applicability limits of the theory can be found in Ref. [36].

Perturbation boundary conditions

Perturbation-amplitude boundary conditions in LST have to be defined such that the system remains a homogeneous problem. Namely, they must be relations between the different perturbation amplitude variables $\tilde{q}$. For impenetrable walls, all perturbations are imposed to be zero except for the pressure ($\tilde{u}^i(0) = \tilde{T}(0) = 0$, $\tilde{p}(0) \neq 0$). In the freestream, all perturbations should ideally be zero, but to account for the non-infinite size of the computational

Variable	Reference	Description
x^i	ℓ_e	spatial coordinates
t	ℓ_e/u_e	time
u^i	u_e	velocity components different spatial directions
T	T_e	translational-rotational temperature
p, p_s	$\rho_e\, u_e^2$	pressure
ρ, ρ_s	ρ_e	density
μ	μ_e	dynamic viscosity
λ	μ_e	second viscosity coefficient
κ	κ_e	frozen thermal conductivity
$\mathscr{M}$, $\mathscr{M}_s$	$\mathscr{M}_e$	molar mass
h, h_s	h_e	static enthalpy
$\mathscr{D}_s$,$\mathscr{D}_{s,\ell}$	$\mathscr{D}_e$	diffusion coefficient
$\dot{\omega}_s$	ρ_e/τ_c	species production rate

Table 1: Nondimensionalization convention used in VESTA.

domain (x^2_{max}), one of them is set free – the pressure ($\tilde{u}^i(x^2_{max}) = \tilde{T}(x^2_{max}) = 0$, $\tilde{p}(x^2_{max}) \neq 0$). The additional equations imposed in both boundaries to account for the two non-zero perturbation amplitudes come from the linearization and evaluation at $x^2 = 0$ and $x^2 = x^2_{max}$ of the wall-normal momentum conservation equation [37].

When studying the stability of wall-blown boundary layers, many authors have used the same set of boundary conditions [10; 20; 27]. However, the assumption of an evenly blowing wall, that corresponds to zero wall-normal velocity perturbation, seems irrealistic. An additional boundary condition is therefore needed to account for this additional non-zero variable $\tilde{u}^2(0)$. Three different possibilities are explored:

- The homogeneous condition used by Malik [10], Johnson [20] and Ghaffari [27]: $\tilde{u}^2(0) = 0$.
- The porous condition developed by Gaponov [38] and Fedorov [39], where the velocity perturbation is related to the pressure's $\tilde{u}^2(0) = K \cdot \tilde{p}(0)$, through an admittance that is function of the porous properties $K = K(r, h, n)$.
- An ablation-mimicking condition developed by the authors [36; 40].

Further details of the aforementioned boundary conditions can be found in [36].

The influence of the wall boundary model is analyzed for a variety of different flow conditions, looking into how they affect the stability of flows with different Mach numbers and wall temperature ratios.

2.3. Chemical Non-Equilibrium model

In order to characterize a chemical non-equilibrium (CNE) flowfield, one needs a mass-conservation equation for every species (Eq. 8), three momentum-conservation equations (Eq. 9), and an energy-conservation equation (Eq. 10).

$$\frac{\partial \rho_s}{\partial t} + (u^j \rho_s)_{,j} = -\frac{1}{ReSc}\, J^j_{s,j} + Da\, \dot{\omega}_s, \tag{8}$$

$$\rho \frac{\partial u^i}{\partial t} + \rho u^j u^i_{,j} = -g^{ij} p_{,j} + \frac{1}{Re}\, \mathbb{T}^{ij}_{,j}, \tag{9}$$

$$\begin{aligned} \rho \frac{\partial h}{\partial t} + \rho u^j h_{,j} = Ec\left(\frac{\partial p}{\partial t} + u^j p_{,j}\right) + \frac{1}{RePr}\left(\kappa g^{ij} T_{,i}\right)_{,j} \\ - \frac{1}{ReSc}\, \mathcal{J}^j_{,j} + \frac{Ec}{Re}\, g_{ik} \mathbb{T}^{kj} u^i_{,j}, \end{aligned} \tag{10}$$

where J^j_s are the diffusion mass fluxes of each species, $\mathcal{J}^j$ are the diffusion energy fluxes, $\dot{\omega}_s$ are the species source terms, and Re, Sc, Pr, Ec and Da are all reference non-dimensional parameters:

$$Re = \frac{\rho_e\, u_e\, \ell_e}{\mu_e} \quad , \quad Sc = \frac{\mu_e}{\rho_e\, \mathscr{D}_e} \quad , \quad Pr = \frac{\mu_e\, h_e}{\kappa_e\, T_e}$$
$$Ec = \frac{u_e^2}{h_e} \quad , \quad Da = \frac{\ell_e}{u_e\, \tau_c}\,.$$

Note that this definition of the reference Prandtl number differs from the classic definition expressed in

terms of the heat capacity at constant pressure. However, the two definitions coincide for CPG flows where $h_e = c_{pe} \cdot T_e$.

There exist several models for the mass and energy diffusion fluxes (J_s^j & $\mathcal{J}^j$). The simplest comes from assuming a constant Schmidt number throughout the domain $Sc = \hat{\mu}/(\hat{\rho}\hat{\mathcal{D}}_s)$. The mass diffusion flux thus equals:

$$J_s^j = -g^{ij}\rho\,\mathcal{D}_s X_{s,j} = -g^{ij}\mu\left(\frac{\rho_s}{\rho}\frac{\mathscr{M}}{\mathscr{M}_s}\right)_{,j}, \tag{11}$$

where $\mathcal{D}_s$ is the diffusion coefficient of species s within the mixture, X_s is the molar fraction of species s, $\mathscr{M}_s$ is the molar mass of species s and $\mathscr{M}$ is the mixture molar mass. Note that this expression does not include the Schmidt number, since it was already premultiplying the mass diffusion flux in Eq. 8.

Assuming a constant Schmidt number is equivalent to assuming that all species diffuse with the same diffusion coefficient. More elaborate diffusion theories, such as that arising from Stefan-Maxwell's equations can model the diffusion of every species within every other species. Retaining both thermo and barodiffusion terms, the diffusion mass fluxes are:

$$J_s^i = -\sum_{\ell=1}^{N_s} g^{ij}\rho_s\mathscr{D}_{s\ell}\left(X_{\ell,j} + \frac{X_\ell}{p}p_{,j} + \frac{\zeta_\ell}{T}T_{,j}\right), \tag{12}$$

where $\mathscr{D}_{s\ell}$ is the diffusion coefficient of the species pair $s-\ell$ and ζ_ℓ is the thermal diffusion ratio of species ℓ.

Having established the mass diffusion fluxes, the energy diffusion fluxes can be easily obtained from the species enthalpies:

$$\mathcal{J}^j = \sum_{s=1}^{N_s} h_s J_s^j. \tag{13}$$

The present work focuses on the constant-Schmidt-number diffusion model. It is certainly a less accurate model than Stefan-Maxwell's, but it has the advantage of condensing all diffusion effects in one sole parameter. Therefore, by varying it, one is capable of easily analyzing the effect of diffusion on the laminar flowfield and stability [41].

Again, Eqs. 8-10 are simplified applying the LST hypotheses introduced in section 2.1, reaching the CNE LST equations.

Perturbation boundary conditions

The perturbation boundary conditions for the CNE model are those of an impenetrable wall ($\tilde{u}^i(0) = 0$), with a thermal inertia presumed to be large enough to assume the temperature perturbations on it to be zero $\tilde{T}(0) = 0$. Species partial density perturbations at the wall do not necessarily need to be zero, requiring additional relations to account for them. Stuckert [15], Hudson [16] and Mortensen [42] used a non-catalytic wall boundary condition. However, the usage of this boundary condition led to the appearance of spurious oscillations in the perturbation eigenfunctions, which were documented by Stuckert [15] and to very ill-conditioned matrices [43]. To avoid this, the species momentum conservation equation in the wall-normal direction at the wall is linearized and used as a compatibility condition:

$$\rho_s\frac{\partial v_s^i}{\partial t} + \rho v_s^j v_{s,j}^i = -g^{ij}p_{s,j} + \frac{1}{Re}\mathbb{T}_{s,j}^{ij} + \Omega_{Ms}^i, \tag{14}$$

where p_s is the species partial pressure, Ω_{Ms}^i is the species momentum source term, responsible for the exchange of momentum between species, and v_s^i is the species total velocity, equal to the mixture velocity plus the species diffusion velocity. Two additional simplifications are imposed on this equation – the **contribution to the momentum of each species** of its diffusion as well as its exchange of momentum with other species is neglected making:

$$v_s^i \approx u^i \qquad , \qquad \Omega_{Ms}^i \approx 0\,. \tag{15}$$

The species momentum is therefore assumed to be driven by the mixture velocity. The physical interpretation, is that the momentum gain or loss due to the species diffusion velocity is equivalent to the momentum being exchanged with other species. These simplifications imposed on the boundary equations do not introduce additional physical limitations to the model, since they are already intrinsic to the mixture-momentum model used for the flow equations.

The perturbation boundary conditions in the freestream are obtained from assuming that the perturbations damp and become zero in an infinitely far wall-normal location. However, to account for the non-infinite size of the computational domain, one of the perturbation variables is allowed to not necessarily be zero. The wall-normal velocity perturbation at the top limit of the domain is obtained by imposing mixture continuity:

$$\frac{\partial\rho}{\partial t} + (\rho\,u^i)_{,i} = 0\,. \tag{16}$$

The aforementioned boundary conditions must obviously be linearized and simplified according to the expressions introduced in §2.1. One therefore has that in the freestream $\tilde{u}^1(x^2_{max}) = \tilde{u}^3(x^2_{max}) = \tilde{\rho}_s(x^2_{max}) = \tilde{T}(x^2_{max}) = 0$ and $\tilde{u}^2(x^2_{max}) \neq 0$. This set of freestream boundary conditions has been extensively used in the literature [15; 16; 17; 18; 19; 44].

Thermodynamic and transport models

The stability solvers are generated avoiding any assumption on the specific thermodynamic and transport models to be used. It is left to the user to impose them through the inputted laminar flow-field quantities.

For the cases presented in this work, air was modeled as a mixture of five ideal gas species: N, O, NO, N_2 and O_2, accounting for three dissociation and two exchange reactions. The species internal energy due to the different energy modes is obtained from their partition functions, neglecting the rotational energy of monoatomic species, assuming diatomic molecules to behave like rigid rotors and harmonic oscillators, and assuming a Boltzmann population of the electronic energy states. With these energy contributions one can obtain the species enthalpies, and with them the mixture enthalpy.

The dynamic viscosity is obtained from Blottner's curves for each species [45] and then applying Wilke's mixing rule [46]. The mixture thermal conductivity $\hat{\kappa}$ is retrieved by applying Wilke's mixing rule on the species conductivities, obtained using Eucken's relation [47].

The species source terms for a set of chemical reactions are obtained from applying the law of mass action, with the equilibrium constants being obtained from the jump in Gibbs free energy due to each reaction.

For a detailed description of the models, constants and parameters used, see Ref. [41].

3. Methodology

3.1. Automatic Derivation and Implementation Tool

In order to develop the required stability solvers, VESTA's Automatic Derivation and Implementation Tool (ADIT) [30] is extended and used. The ADIT is a collection of functions in Maxima and Matlab that effectively pass from the Navier-Stokes equations to functions building the necessary system matrices for stability analyses.

The derivation tool operates symbolically with the system's equations for a variety of flow assumptions, and coordinate systems, applying the necessary hypotheses corresponding to the different stability theories. It currently allows for solvers to be generated for incompressible, compressible, Local-Thermodynamic-Equilibrium (LTE), CEel, CNE and TCNE flow assumptions. It also features a range of coordinates systems (3D-cartesian, polar-cylindrical, spherical and six ortho-curvilinear systems), and three stability theories (LST, PSE and BiG).

Once the stability equations are derived, the implementation tool translates the symbolical expressions into a script to be used to build the system's matrices with the required boundary conditions. This implementation tool has been extended in such a way that it is completely transparent to the set of equations and variables that it receives from the derivation tool.

VESTA's ADIT also includes a module handling the analytical derivation of the expressions modeling the thermodynamic and transport properties with respect to the independent state variables – $\partial\overline{\mu}/\partial\overline{T}$, $\partial\overline{h}/\partial\overline{\rho}_s$, $\partial^2\overline{\kappa}/\partial\overline{\rho}_s\partial\overline{T}$, etc. Once derived, they are automatically implemented into scripts that can be then used to compute the necessary base-flow quantities for the stability analysis. These derivatives are needed due to the particular nature of the stability equations. More information on this can be found in Ref. [41].

3.2. Laminar basic state

Stability analyses are performed on a laminar basic state solution, which provides the $\overline{q}$ variables present in the stability equations. All cases presented in this work were obtained from solving the boundary-layer equations [48].

For the cold blowing cases, the basic states were obtained using VESTA's built-in RK4 self-similar boundary-layer solver. In order to respect the self-similarity conditions, the blowing introduced at the wall must scale with the inverse of the Reynolds number based on the Blasius length:

$$\overline{u}^2_w = -\frac{f_w}{\sqrt{2}\,Re\,\overline{\rho}_w}\,, \tag{17}$$

where f_w is the value of the Blasius function at the wall [48].

A non-dimensional blowing mass-flow parameter B is introduced, corresponding to a non-dimensionalization of the blown mass flow with the

mass flow going through the boundary layer:

$$B = \frac{\hat{\overline{\rho}}_w \, \hat{\overline{u}}_w^2}{\rho_e \, u_e} = \overline{\rho}_w \, \overline{u}_w^2 = -\frac{f_w}{\sqrt{2Re}} \, . \tag{18}$$

This parameter scales different blowing rates and gases with respect to their freestream conditions. For instance, denser pyrolysis gases will disturb more the incoming flow. Denser must not be confused with heavier (higher molecular weight), since Stalmach et al. [49] reported that lighter blowing gases have a stronger destabilizing effect.

For the CNE analyses, frozen base flow computations are carried out with the DEKAF boundary layer solver. It uses a pseudo-spectral method, using Chebyshev polynomials on a set of Chebyshev-Gauss-Lobatto [50] points to solve the self-similar system. The computational domain is mapped using Malik's mapping [14], in order to have a point clustering closer to the wall. The clustering is done such that half of the points lie below $\eta = 6$, where:

$$\mathrm{d}\eta = \frac{u_e}{\sqrt{2\xi}} \hat{\rho} \, \mathrm{d}\hat{x}^2 \qquad , \qquad \mathrm{d}\xi = \rho_e \, \mu_e \, u_e \, \mathrm{d}\hat{x}^1 \, .$$

The frozen solution is then marched in the ξ-direction using a 6th-order backward finite-difference method. The chemical source terms during this marching are non-zero, thus leading to the desired boundary-layer base flow in chemical non-equilibrium.

4. Results

The verification of the aforementioned models can be found in Refs. [36; 40; 43; 41]. They are then used to analyze a series of cases of interest, to better understand both the blowing and the chemistry effects on the early development of instabilities in a boundary layer.

4.1. Blowing effects

Analyses of wall-blown flat plates are performed in cold conditions, with a free-stream temperature of $T_e = 70\,\mathrm{K}$, and a pressure of $p_e = 4000\,\mathrm{Pa}$. The Reynolds number is fixed to $Re = 2000$ throughout the study. CPG conditions are assumed, therefore imposing constant Prandtl number $Pr = 0.7$, specific heat ratio $\gamma = 1.4$ and specific heat at constant pressure $\hat{c}_p = 1004.5\,\mathrm{J/kg \cdot K}$. The dynamic viscosity is obtained from Sutherland's law with $\hat{\mu}_{ref} = 1.716 \cdot 10^{-5}\,\mathrm{kg/(m \cdot s)}$, $\hat{S}_\mu = 110.6\,\mathrm{K}$ & $\hat{T}_{ref} = 273.15\,\mathrm{K}$. The investigation is carried out fixing the spanwise wavenumber β to zero, since, in the range of considered Mach numbers, second-mode two-dimensional perturbations are well-known to be the most unstable [34].

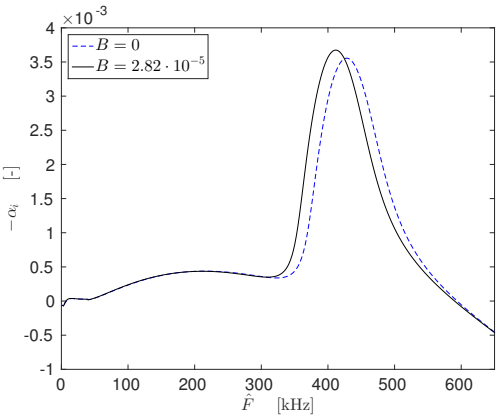

Figure 1: Effect of the blowing parameter B on the perturbation growth rate $-\alpha_i$ using a homogeneous boundary condition. The flow conditions are $M_e = 6$, $T_w/T_{adiab} = 1$, $p_e = 4000\,\mathrm{Pa}$, $T_e = 70\,\mathrm{K}$, and $Re = 2000$.

Figure 1 shows the well-known destabilizing effect of wall-blowing on the boundary layer by looking at the perturbation's spatial growth rate ($-\alpha_i$). The blown boundary layer is larger, and therefore there is also a decrease in the frequency of this most unstable perturbation. No wall boundary condition was used here on the wall-normal velocity perturbation, meaning that $\tilde{u}^2(0) = 0$ also for the blowing case. The difference between the two curves is not very large, meaning that, in absence of a wall-normal velocity perturbation model, this mild blowing appears to not have a large effect on stability.

Using the porous boundary condition, a preliminary analysis on the effect of porosity n, defined as the surface fraction occupied by pores, shows in Fig. 2 its limited role on stability. A higher porosity, for constant r, effectively means that there is a higher pore concentration on the surface. It is therefore expectable to have a stronger stabilizing/destabilizing effect of the porous layer with a higher porosity. The porosity will be hereafter fixed to $n = 0.8$.

The other two porous parameters, pore radius r and porous-layer height h, affect stability in a more complex and non-trivial fashion. Fig. 3 shows the maximum amplification rate (a) and the frequency for which this maximum is achieved (b), as a function of the pore radius and the porous-layer height. Fig. 3 (b)

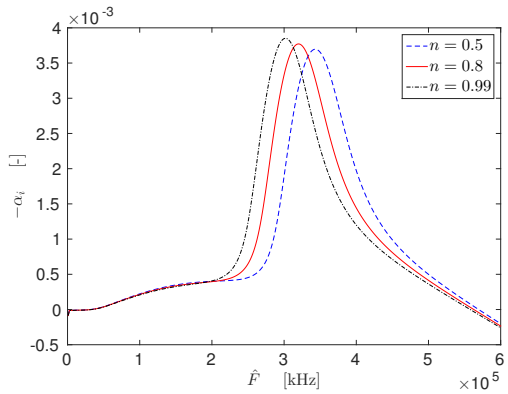

Figure 2: Effect of the surface porosity n on the perturbation growth rate $-\alpha_i$. The flow conditions are $M_e = 6$, $T_w/T_{adiab} = 1$, $p_e = 4000\,\text{Pa}$, $T_e = 70\,\text{K}$, $B = 2.82 \cdot 10^{-5}$ and $Re = 2000$, and the porous layer has $\hat{r} = \hat{h} = 0.1\,\text{mm}$.

shows that both parameters, when increased, move the most unstable mode towards lower frequencies. The maximum amplification rate (Fig. 3 (a)) shows a non trivial behavior – its minimum corresponds to high values of $\hat{h}$ and values of $\hat{r}$ around 0.1 mm, whereas its maximum corresponds to high values of $\hat{r}$ and values of $\hat{h}$ around 1 mm.

Performing the same analysis of Fig. 3 for several Mach numbers and wall temperature ratios, one can build maps of porous amplification/damping, such as that in Fig. 4. One can use them to predict what porous configurations will damp or amplify perturbations under different flow regimes. It is remarkable to see such a strong dependency of these regions on the flow regime. This suggests that a single porous configuration may not be suitable to damp perturbations (and therefore delay transition) for all flow regimes.

Figure 5 shows a comparison of the different boundary conditions. It is here where one can see the dramatic effect that the wall-normal velocity perturbation modeling has on the flow stability results. The two curves with a homogeneous boundary condition appear to be significantly close. This shows that, in absence of wall-normal velocity perturbation modeling, the analyzed blowing has very little effect on the boundary layer's stability. The usage of different porous layers is seen to have the importance stressed in the previous paragraphs. Depending on the values of $\hat{r}$ and $\hat{h}$ the porous layer can range from having a strongly destabilizing effect ($\hat{r} = \hat{h} = 0.81\,\text{mm}$), passing through a slightly destabilizing effect ($\hat{r} = \hat{h} = 0.13\,\text{mm}$), up to a strongly stabilizing effect ($\hat{r} = 0.13\,\text{mm}$ and $\hat{h} = 0.81\,\text{mm}$). The ablation-mimicking condition is the one predicting the most unstable boundary layer and the one moving the most unstable mode to the lowest frequencies. One of the most interesting results of this comparison, is that the porous condition, when the pores become very large, predicts the same behavior as the ablation-mimicking. In other words, having a very large pore, is equivalent to having a surface that is blowing continuously. This is reasonable from a physical perspective, but it is remarkable to observe this when comparing such different models: one coming from an acoustic condition, and another from a mass conservation approach. These facts clearly show that the outgassing from an ablative boundary layer cannot be experimentally mimicked with an arbitrary pore setup, but their size needs to be carefully considered.

4.2. Chemistry effects

Chemistry effects are studied by analyzing a Mach 10 flow over an adiabatic non-catalytic flat plate. The freestream air mixture is 22% O_2 and 78% N_2 in mass. The free-stream temperature is $T_e = 600\,\text{K}$, and the unit Reynolds number is $Re_1 = 6.6 \cdot 10^6\,\text{m}^{-1}$. This could correspond to fast reentry trajectories with a strong bow shock. The result is that the adiabatic wall temperature in frozen conditions (Fig. 6 b) reaches more than 8500 K – close to the limit after which ionization should start to be considered [9]. The mass fraction profiles in Fig. 6 c) demonstrate the high chemical activity taking place in the boundary layer. This chemical activity subsequently introduces a reduction in the adiabatic wall temperature, as well as a shrinking of the boundary layer.

Figure 7 shows the comparison of the growth rates of the highly reacting test case. Four distinct curves are included in this plot. The first corresponds to neglecting all chemical activity (frozen flow). As anticipated from the base-flow profiles, assuming frozen chemistry is a major simplification for this particular case. The reduction in the adiabatic wall temperature caused by the chemical activity, appears to enhance the propagation of instabilities. The associated shrinking of the boundary layer also causes the most unstable perturbations to have larger frequencies.

The other three curves were obtained from the chemically reacting flowfield showed in Fig. 6. However, the difference between them is the thermodynamic modeling of the perturbations. The third curve corresponds to assuming frozen perturbations, meaning that the perturbations of the species source terms are neglected: $\dot{\omega}_s' = 0$. This simplification causes only a slight overshooting of the instabilities' growth rates,

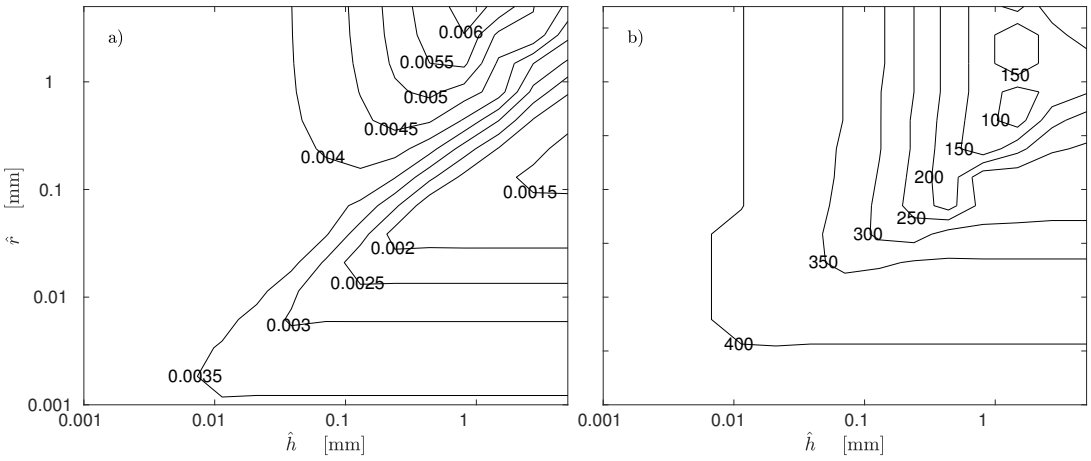

Figure 3: Effect of the pore radius $\hat{r}$ and the porous-layer height $\hat{h}$ on the perturbation non-dimensional maximum amplification rate $-\alpha_{i,M}$ (a) and the frequency for which this maximum is achieved $\hat{F}|_{\alpha_{i,M}}$ in kHz (b). The flow conditions are $M_e = 6$, $T_w/T_{adiab} = 1$, $p_e = 4000\,\text{Pa}$, $T_e = 70\,\text{K}$, $B = 2.82 \cdot 10^{-5}$ and $Re = 2000$, and the porosity is $n = 0.8$.

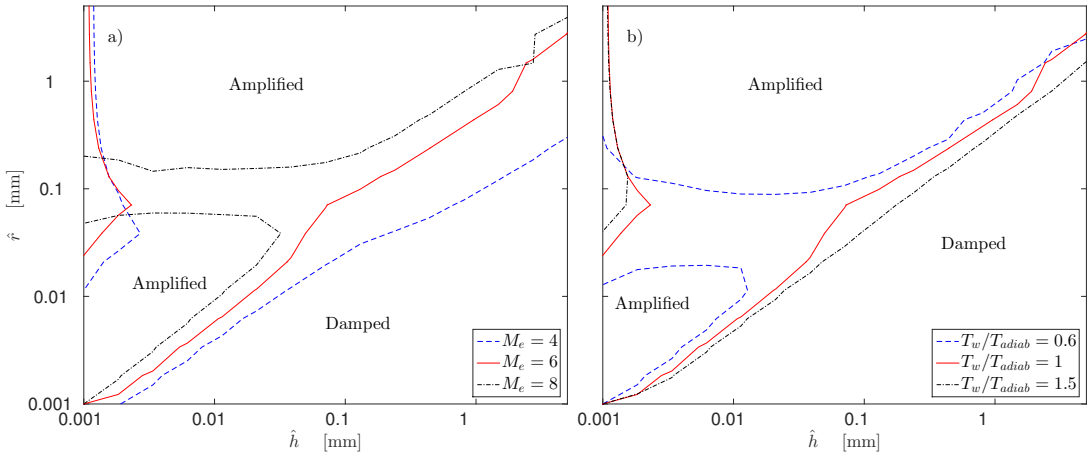

Figure 4: Zones of porous-layer damping and amplification for different Mach numbers (a) and wall temperature ratios (b) on the porous-conditions map. The fixed flow conditions are $T_w/T_{adiab} = 1$ for (a), $M_e = 6$ for (b), and $p_e = 4000\,\text{Pa}$, $T_e = 70\,\text{K}$, $B = 2.82 \cdot 10^{-5}$ and $Re = 2000$ for both. The porosity is $n = 0.8$.

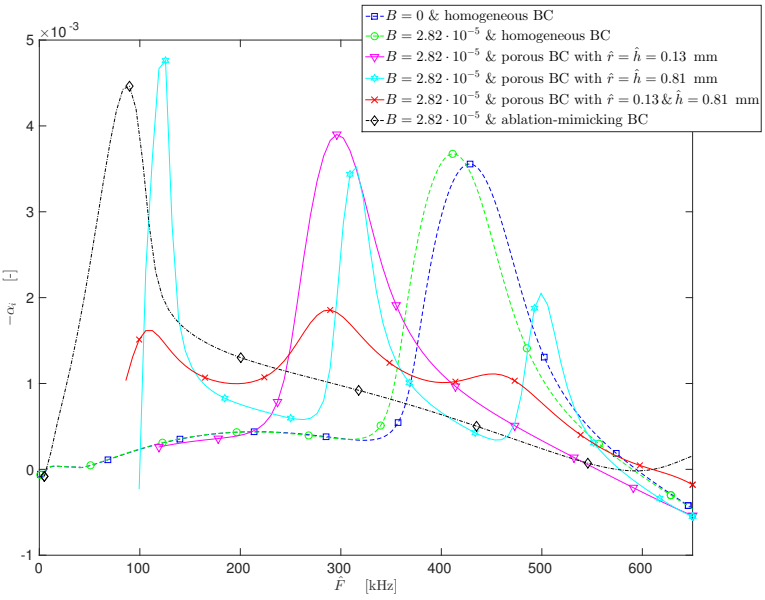

Figure 5: Comparison of the different boundary conditions. The flow conditions are $M_e = 6$, $T_w/T_{adiab} = 1$, $p_e = 4000\,\text{Pa}$, $T_e = 70\,\text{K}$ and $Re = 2000$.

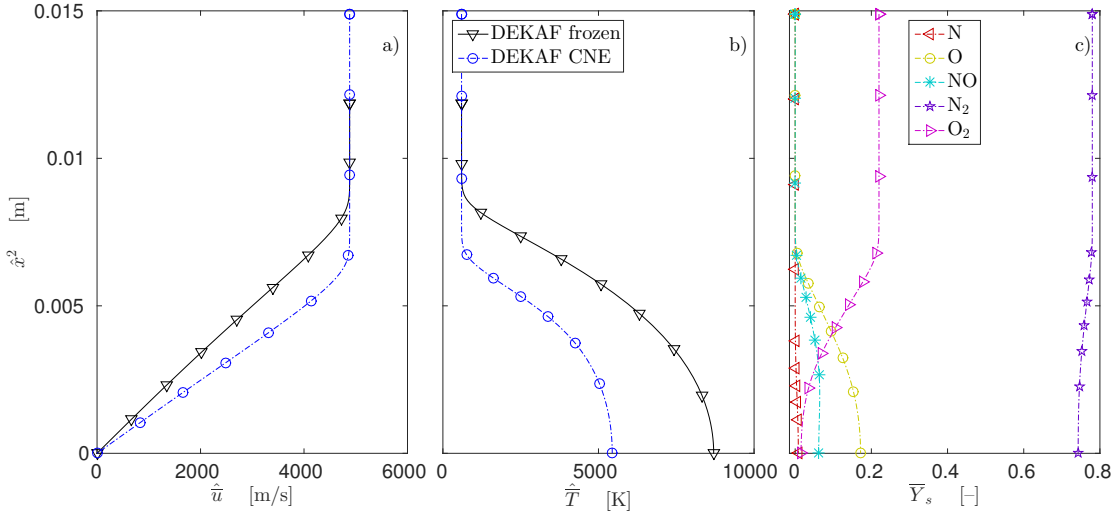

Figure 6: Boundary-layer base-flow profiles for the highly reacting test case. Adiabatic non-catalytic flat plate with $M_e = 10$, $Y_{O_2\,e} = 0.22$, $Y_{N_2\,e} = 0.78$, $Re_1 = 6.6 \cdot 10^6\,\text{m}^{-1}$, $T_e = 600\,\text{K}$ and $\hat{x}^1 = 0.6\,\text{m}$.

hinting that the perturbations' timescale must be significantly smaller than that of the chemistry. This result is in agreement with Bitter and Shepherd's [25] observations for flows in thermal non-equilibrium.

The final curve introduces an even further simplification on the perturbation terms, by neglecting also the perturbations of the diffusion fluxes $J_s^{i\prime} = 0$. This essentially renders all stability equations coming from the species-conservation (Eq. 8) identical to the linearized mixture continuity equation. This implies that:

$$\rho_s' = \overline{Y}_s \rho' \,,$$

thus requiring a single mass stability equation to account for the mixture density perturbation ρ' rather than one for every species.

This assumption introduces an almost inappreciable overshooting of the growth rates. It is remarkable to obtain such a close stability behavior having introduced such a radical simplification. Especially in a highly reacting test case like this one, where the composition of the air mixture changes greatly throughout the boundary layer (Fig. 6 c)). These results demonstrate once again the importance of having accurate, well-resolved base flows.

5. Conclusions

LST models were developed to study the effects of surface outgassing and air chemistry on the early development of instabilities in a hypersonic flat-plate boundary layer.

Three different models for the wall-normal velocity perturbation were analyzed and compared for one same blowing configuration. For a blowing that was predicted to introduce very little destabilization according to the homogeneous $\tilde{u}^2(0) = 0$ model, large differences were observed depending on the modeling used for the wall-normal velocity perturbation boundary condition. The ablation-mimicking continuously-blowing boundary condition showed the same behavior as the porous for very large pore sizes, suggesting that it could correspond to the limit for infinitely large pores.

A thorough parametric study performed on the porosity parameters revealed significantly different damping/amplification introduced by the porous surface depending on the flow conditions. This suggests that one same porous configuration may have very different effects on the transition location for different flow conditions. One should therefore be very careful when extrapolating trends observed in ground test facilities to flight.

Chemistry effects where analyzed by looking at a Mach 10 flow at 600 K, over an adiabatic flat plate. The large temperatures reached inside the boundary layer produced highly varying mixture compositions, and proved to make a substantial difference in the stability of the flow. The wall-cooling introduced by the dissociation reactions was seen to destabilize the flow and increase the frequency of the most-unstable perturbations.

Different perturbation models were investigated, i.e. different thermodynamic assumptions were made in the derivation of the stability equations, whilst working with a unique base flow. Assuming frozen perturbations introduced only a slight overshoot in the perturbation growth rates. This result suggests that the chemical activity itself reduces the growth of instabilities. However, in adiabatic wall conditions, the associated wall-cooling affecting the mean-flow quantities overly out-weighs this stabilization. Neglecting also the perturbations of the diffusion fluxes leads to a minor discrepancy from the full non-equilibrium multi-species perturbation model. These results highlight the importance of having an accurate, well-resolved base-flow when performing stability analyses. Moreover, it also suggests that simpler thermodynamic models can be used in the stability equations, hardly penalizing the observed stability characteristics. Further work should quantify the effect of these simplifications in the ultimate transition-location prediction, through the semi-empirical e^N method.

Acknowledgments

This work has been made possible thanks to the financial support of the Belgian *Fonds National de la Recherche Scientifique*, through the FRIA fellowships (*Fonds pour la formation à la Recherche dans l'Industrie et l'Agriculture*).

References

[1] F. P. Incropera, D. P. DeWitt, T. L. Bergman, A. S. Lavine, Fundamentals of Heat and Mass Transfer, John Wiley & sons, 2006.

[2] E. R. V. Driest, Investigation of laminar boundary layer in compressible fluids using the crocco method, Tech. Rep. TN 2597, NACA/North American Aviation Inc., Washington (January 1952).

[3] F. S. Milos, Y. K. Chen, Ablation, thermal response, and chemistry program for analysis of thermal protection systems, Journal of Spacecraft and Rockets 50 (1).

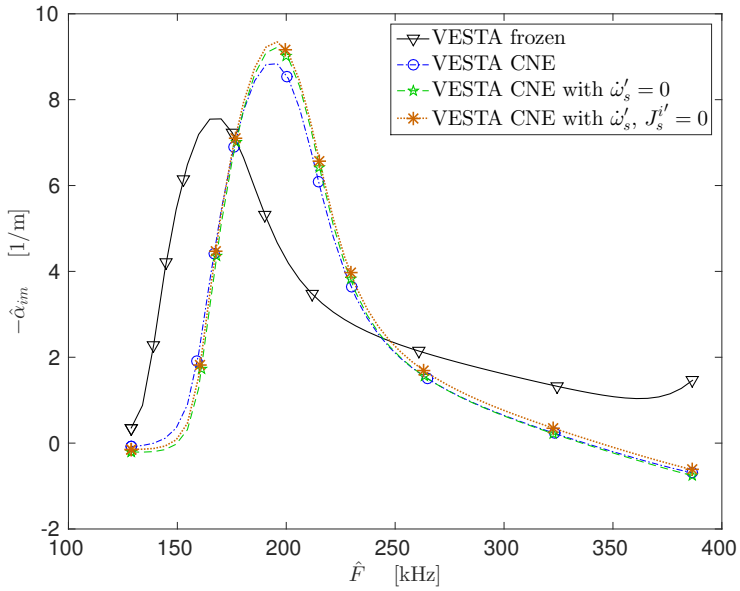

Figure 7: Growth rate of the most unstable mode for the highly reacting test case and for different perturbation models. Adiabatic non-catalytic flat plate with $M_e = 10$, $Y_{O_2\,e} = 0.22$, $Y_{N_2\,e} = 0.78$, $Re_1 = 6.6 \cdot 10^6\,\mathrm{m}^{-1}$, $T_e = 600\,\mathrm{K}$ at $\hat{x} = 0.6\,\mathrm{m}$.

[4] J. M. Bouilly, F. Bonnefond, L. Dariol, P. Jullien, F. Leleu, Ablative thermal protection systems for entry in mars atmosphere. a presentation of materials solutions and testing capabilities, 4th International Planetary Probe Workshop, Pasadena California.

[5] E. Venkatapathy, C. E. Szalai, B. Laub, H. H. Hwang, J. L. Conley, J. Arnold, . Co-authors, Thermal protection system technologies for enabling future sample return missions, NASA, White Paper to the NRC Decadal Primitive Bodies Sub-Panel, Washington DC.

[6] G. Duffa, Ablative Thermal Protection System Modeling, AIAA Education Series, 2013.

[7] H. L. Reed, R. Kimmel, S. Schneider, D. Arnal, Drag prediction and transition in hypersonic flow, AIAA Paper 97-1818.

[8] A. H. Whitehead Jr., Nasp aerodynamics, in: AIAA First National Aero-Space Plane Conference, American Institute of Aeronautics and Astronautics, Dayton, Ohio, 1989.

[9] J. D. Anderson Jr., Hypersonic and High Temperature Gas Dynamics, Second Edition, American Institute of Aeronautics and Astronautics, Blacksburg, Virginia, 2006.

[10] M. R. Malik, Prediction and control of transition in supersonic and hypersonic boundary layer, AIAA Journal 27 (11) (1989) 1487–1493.

[11] M. R. Malik, Stability theory for chemically reacting flows, in: D. Arnal, R. Michel (Eds.), Laminar-Turbulent Transition, IUTAM Symposium Tolouse/France, 1989, pp. 251–260.

[12] M. R. Malik, Stability theory for chemically reacting flows, in: D. Arnal, R. Michel (Eds.), IUTAM Symp. "Laminar-Turbulent Transition", Springer Verlag, Toulouse, 1990.

[13] M. R. Malik, Transition in hypersonic boundary layers, in: T. Cebeci (Ed.), Numerical and Physical Aspects of Aerodynamic Flows IV, Springer Verlag, 1990.

[14] M. R. Malik, Numerical methods for hypersonic boundary layers, Journal of Computational Physics 86.

[15] G. K. Stuckert, H. L. Reed, Linear disturbances in hypersonic, chemically reacting viscous flows, AIAA Journal 32 (7).

[16] M. Hudson, N. Chokani, G. Chandler, Linear stability of hypersonic flow in thermochemical nonequilibrium, AIAA Journal 35 (6) (1997) 958–964.

[17] J. Perraud, D. Arnal, L. Dussillois, F. Thivet, Studies of laminar-turbulent transition in hypersonic boundary layers at onera, in: Proceedings of the Third European Symposium on Aerothermodynamics for Space Vehicles, European space Agency, ESTEC, The Netherlands, 1998.

[18] K. J. Franko, R. W. MacCormack, S. K. Lele, Effects of chemistry modeling on hypersonic boundary layer linear stability prediction, AIAA Paper 2010-4601.

[19] M. R. Malik, Hypersonic flight and transition data analysis using parabolized stability equations with chemistry effects, Journal of Spacecraft and Rockets 40 (2003) 332–344.

[20] H. B. Johnson, J. E. Gronvall, G. V. Chandler, Reacting hypersonic boundary layer stability with blowing and suction, 47th AIAA Aerospace Sciences meeting.

[21] O. Marxen, T. Magin, G. Iaccarino, E. S. G. Shaqfeh, A high-order numerical method to study hypersonic boundary-layer instability including high-temperature gas effects, Physics of Fluids 23 (8).

[22] O. Marxen, T. Magin, E. S. G. Shaqfeh, G. Iaccarino, A method for the direct numerical simulation of hypersonic boundary-layer instability with finite-rate chemistry, Journal of Computational Physics 255.

[23] I. J. Lyttle, H. L. Reed, Sensitivity of second-mode linear stability to constitutive models within hypersonic flow, in: 43rd AIAA Aerospace Sciences Meeting and Exhibit, Reno, Nevada, 2005.

[24] J. Klentzman, A. Tumin, Stability and receptivity of high speed boundary layers in oxygen, in: 43rd Fluid Dynamics Conference, San Diego CA, 2013.

[25] N. P. Bitter, J. E. Shepherd, Stability of highly cooled hypervelocity boundary layers, J. Fluid Mech. 778 (2015) 586–620.
[26] S. P. Schneider, Hypersonic boundary-layer transition with ablation and blowing, Journal of Spacecraft and Rockets 47 (2010) 225–237.
[27] S. Ghaffari, O. Marxen, G. Iaccarino, E. S. G. Shaqfeh, Numerical simulations of hypersonic boundary-layer instability with wall blowing, 48th AIAA Aerospace Sciences Meeting.
[28] F. Pinna, Numerical study of stability flows from low to high mach number, Ph.D. thesis, von Kármán Institute for Fluid Dynamics and Universitá "La Sapienza" di Roma (2012).
[29] F. Pinna, Vesta toolkit: a software to compute transition and stability of boundary layers, 43rd AIAA Fluid Dynamics Conference, San Diego, California.
[30] F. Pinna, K. Groot, Automatic derivation of stability equations in arbitrary coordinates and for different flow regimes, 44th AIAA Fluid Dynamics Conference, Atlanta.
[31] L. Mack, Boundary layer stability theory. report 900-277 rev. a, Jet Propulsion Laboratory, Pasadena, CA 22.
[32] A. M. O. Smith, N. Gamberoni, Transition, pressure gradient and stability theory, Tech. Rep. ES 26388, Douglas Aircraft Co., El Segundo, California (1956).
[33] J. L. van Ingen, A suggested semi-empirical method for the calculation of the boundary layer transition region, Tech. Rep. VTH-74, Univ. of Delft. Dept. Aerospace Engineering, Delft, the Netherlands (1956).
[34] D. Arnal, Boundary layer transition: Predictions based on linear theory, Tech. Rep. 793, AGARD, VKI, Brussels (1993).
[35] R. Aris, Vectors, Tensors and the Basic Equations of Fluid Mechanics, Dover - Prentice Hall, 1962.
[36] F. Pinna, F. Miró Miró, Numerical modeling of continuous blowing surface in hypersonic boundary layers, Journal of Aerospace Engineering.
[37] L. M. Mack, Boundary-layer linear stability theory, Tech. Rep. 709, AGARD (1984).
[38] S. A. Gaponov, N. M. Terekhova, Controlling supersonic boundary layer stability by means of distributed mass transfer through a porous wall, Fluid Dynamics 48 (6) (2012) 761–772.
[39] A. V. Fedorov, N. Malmuth, Stabilization of hypersonic boundary layers by porous coatings, AIAA Journal 39 (4) (2001) 605–610.
[40] F. Miró Miró, Numerical study of the stability of a hypersonic boundary layer in the presence of blowing, Tech. Rep. 2015-28, von Karman Institute for Fluid Dynamics, Rhode-Saint-Genèse, Belgium (2015).
[41] F. Miró Miró, F. Pinna, E. Beyak, P. Barbante, H. Reed, Diffusion and chemical non-equilibrium effects on hypersonic boundary-layer stability, 48th AIAA Fluid Dynamics Conference, Orlando, FL.
[42] C. Mortensen, Effect of thermochemical nonequilibrium on hypersonic boundary-layer instability in the presence of surface ablation or isolated two-dimensional roughness, Ph.D. thesis, University of California Los Angeles (2015).
[43] F. Miró Miró, F. Pinna, Linear stability analysis of a hypersonic boundary layer in equilibrium and non-equilibrium, 47th AIAA Fluid Dynamics Conference, Denver, CO.
[44] C. H. Mortensen, X. Zhong, Real gas and surface ablation effects on hypersonic boundary layer instability over a blunt cone, 43rd Fluid Dynamics Conference, American Institute of Aeronautics and Astronautics.
[45] F. G. Blottner, M. Johnson, M. Ellis, Chemically reacting viscous flow program for multi-component gas mixtures, Research Report SC-RR-70-754, Sandia Laboratories, Albuquerque, New Mexico (1971).
[46] C. Wilke, A viscosity equation for gas mixtures, The Journal of Chemical Physics 18 (4).
[47] A. Eucken, Über das Wärmeleitvermögen, die spezifische Wärme und die innere Reibung der Gase (in German), Physik. Zeitschrift XIV.
[48] T. Cebeci, J. Cousteix, Modelling and Computation of Boundary Layer Flows, Springer, 1999.
[49] C. J. Stalmach, J. J. B. Jr., T. C. Pope, A study of the boundary layer transition on outgassing cones in hypersonic flow, Tech. Rep. NASA CR-1908, Vought Aeronautics Company/NASA Langley Research Center, Washington D.C. (December 1971).
[50] L. N. Trefethen, Spectral Methods in MATLAB, SIAM, 2000.

Analysis of the mean flow unsteadiness impact on the near wall flow region

Jorge Saavedra

Aeronautics and Aerospace Department, saavedra@purdue.edu

Supervisor: Olivier Chazot

Head of Department and Professor, Aeronautics and Aerospace Department, von Karman Institute for Fluid Dynamics, Belgium, chazot@vki.ac.be

Guillermo Paniagua

Professor, Mechanical Engineering, Purdue University, US, gpaniagua@purdue.edu

Abstract

Unsteady effects impact the aerothermal performance of aerospace and turbomachinery hardware. The characterization of the thermal boundary layer under periodic fluctuations is vital to improve the performance of compact power plant units. The present investigation analyzes the flow over a flat plate and boundary layer detachment submitted to periodic mean flow oscillations, allowing the development of more efficient methods to apply flow control under non-temporally uniform inlet conditions.

Keywords: Boundary layer, transient flow, flow separation

1. Introduction

Many vital components of axial turbomachinery are exposed to pulsating flow conditions dictated by the engine operating regime, which may severely affect the performance incurring on endurance detriments[1]. Traditionally, the performance of such devices is characterized based on steady state experimental evaluations. However, in the quest towards performance improvement, researchers have found that the transient response of the turbomachinery and its associated elements is one of the main areas that still demands more understanding. As an example, Binder et al. [1] analyzed the influence of the stator wakes on the rotor performance through series of laser-2-focus velocimetry measurements, revealing that the wake impingement on the rotor blades modifies the flow turning across the rotor, generating overturning on the wake region. Similar conclusions were withdrawn by Arndt [2] on a multistage low pressure turbine. The interaction of the periodic stator wakes with the rotor result in strong amplitude modulations of the flow velocity and turbulent intensity, altering the secondary flows through the rotor and modifying the radial distribution of the flow turning. Numerically, Giles [3] looked into the propagation and reflection of the shocks generated on the stator trailing edge across the rotor row, which induce large variations on the rotor lift performance. Chaluvadi et al. [4] analyzed the wake and stator passage vortices influence on the rotor behavior through smoke flow visualizations and hotwire measurements, describing the influence of the incoming perturbations on the rotor secondary flows and its final contribution on the rotor performance loss.

The effect of the incoming wakes on the heat flux along the rotor blade was highlighted thanks to the comparison of the forward and reverse rotation experiments [5]. Completely different trends and magnitudes of heat flux take place in the rear suction side of the blade because of the presence of the stator wakes. Similarly, the comparison of the rotation results with cascade experimental data, further supports the strong influence of the upcoming wakes and its relevant role

[1]This work will be presented during the ASME 2018 Turbo Expo, Turbomachinery Technical Conference & Exposition, Oslo, Norway, Jun. 11-15, 2018 (Paper No. GT2018-75128 & GT2018-76896).

in the boundary layer transition.

As new combustion methodologies are proposed for advanced aircraft propulsion, like pulse detonation or rotating detonation combustors [6], new turbomachinery is developed [7; 8]. Their response under pulsating conditions becomes a primary need for future technology integration. In this sense, Sousa et al. [9] performed a detailed characterization of the unsteadiness experienced across internal flow passages exposed to variable inlet flow conditions. The interaction of such flow structures with the exhaust propulsive elements results of extreme interest in order to guarantee an optimum energy usage during the entire flight envelope [10].

In addition, the uprising use of UAVs and the breakthrough of the distributed thrust is promoting the design of ultra-compact and versatile gas turbine engines [11; 12]. The cruise operation of such power plants at high altitudes is limited because of the small Reynolds number through the low pressure turbine stages. At reduced Reynolds numbers <100000 (based on blade axial cord) the rear part of the blade suction can suffer flow separation, which dramatically lowers the stage efficiency [13]. Due to the flow separation, the flow capacity of the low pressure turbine stage is significantly reduced while the viscous loses are boosted [14]. This inferior performance prevents its operation at higher altitudes and reduces the overall airframe range.

In order to explore the boundary layer response to periodic flow perturbations we should first look into the boundary layer development phenomena. The boundary layer establishment was previously documented in theoretical and analytical studies of various degrees of complexity only for laminar flow conditions or very particular applications. Several authors proposed analytical solutions of the unsteady boundary layer settlement. Stewartson [15; 16] focused on the impulsive start of motion of semi-infinite flat plates. In addition, Moore [17] performed a dimensionless analysis of the establishment of the flow over a flat plate set into motion with a time-dependent velocity. Considering a quasi-steady approach, the response of the boundary layer is driven by the diffusion across the near wall flow. Analytically, Wen and Huang [18] demonstrated the prime influence of the acceleration rate on the boundary layer development.

Regarding the boundary layer response to continuous flow fluctuations, Lighthill performed analytical studies on the laminar boundary layer reaction to mean flow variations, pointing out the main differences between subsonic and supersonic mean flow regimes [19; 20]. In this analysis, the onset of separation was also assessed as a function of the dynamic pressure distribution along the surface. The interaction between the main stream and the boundary layer was treated mathematically by perturbing pure parallel flow neglecting the viscous forces. Including the energy equation in the analysis, the effect of random free stream conditions and wall temperature distributions allowed the investigation of the heat transfer rate across laminar incompressible boundary layers [21].

The fundamentals of periodic free stream fluctuations on laminar flow on circular pipes were explored by Uchida [22]. Disseminating the influence of the dynamic pressure gradients travelling along the pipe on the wall fluxes. Correspondingly, Mizushina et al. [23] experimentally looked at the instantaneous profiles of velocity and turbulence intensity for pulsating flow inside of tubes. Based on their empirical research two main flow regimes were distinguished, for low frequency perturbations the turbulence levels remained at a nominal values but the mean flow conditions suffered high variations. On the contrary, for higher oscillation frequencies, the mean flow quantities seemed to tend to an average value while the turbulence properties suffered strong variations. Towards a better understanding of the nature of pulsating flow in a pipe, Shemer et al. [24] conducted an extensive analysis on turbulent and laminar pulsating flows at identical frequencies and Reynolds numbers for small amplitude perturbations. They found that the radial distribution on the flow velocity amplitude and phase were strongly dependent of the flow regime, whether laminar or turbulent. The turbulent cases depicted a slower response than the laminar flow at some radial locations due to the influence of the eddy viscosity.

Regarding the consequences of free stream fluctuations on the wall heat flux, Moschandreou and Zamir [25] originally disclosed the strong dependence of the heat flux rate on the Prandtl number and the mean flow pulsating frequency. Furthermore, the relative size of the thermal boundary layer to the momentum one has a strong influence on the heat flux settlement, as also discussed by Saavedra et al [26].

The presence of unsteady flow conditions on adverse pressure gradient regions will affect the behavior of the flow separated regions and its reaction to any flow control approach. In this regard, Schobeiri et al. [27] provided experimental data describing the evolution of inception and separated flow region as a consequence of unsteady mean flow conditions, where the wake passing had a strong influence on the recirculation bubble, modulating its extension. In a similar

way, Wissink [28] numerically investigated the effect of incoming wakes on a low pressure turbine cascade with DNS simulations. Where also the influence of the incoming flow disturbances on the separated flow region was highlighted.

In this paper, a numerical research analyzing the dynamic response of the aerothermal boundary layer and flow separated regions is presented. In this sense, the effect of free stream fluctuations on the wall fluxes and recirculated flow for turbulent flow are explored. Through URANS and LES simulations, we looked into the dynamic response of two different domains, a flat plate and a wall mounted hump, to mean flow periodic excitations or sudden flow accelerations, which revealed the strong dependence of the thermal boundary layer and recirculation bubble on the mean flow velocity variations.

2. Methodology

The numerical investigations for the aerothermal boundary layer response were carried out in a 2D geometry. The domain, Fig. 1, was meshed following a blocking strategy with ANSYS ICEM . In order to guarantee a proper geometrical discretization, a grid sensitivity study was accomplished following the approach outlined by Celik et al. [29]. For this purpose, the axial flow velocity just outside of the boundary layer and the boundary layer height were acquired for all the different grids. A summary of the different mesh properties is presented in the Table 1.

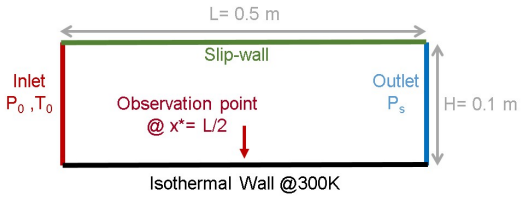

Figure 1: Numerical domain for flow acceleration research

The results for the mesh of forty thousand cells show a relative uncertainty around 0.25% and a convergence indicator below 0.006. The grid convergence indicator (GCI) is a parameter that quantifies the concurrence of the fine grid. Selecting a target value of 0.006 the confluence of the discretization level to the finest accuracy is guaranteed. Therefore, that grid resolution was selected for the rest of the numerical analysis. To enhance correct near wall flow prediction the y+ was maintained below 0.5 along the entire plate. Similarly, the grid expansion ratio was fixed at 1.15, ensuring sufficient wall resolution. To resolve quantitatively the transient aerodynamic structures and the wall fluxes evolutions Unsteady Reynolds Averaged Navier-Stokes Simulations were performed with ANSYS Fluent .

The time step and inner iterations used for the simulations were selected based on a benchmark analysis keeping a minimum frequency resolution of 40 kHz. As a result, the time step was initially set to $5x10^{-7}$s with up to 16 inner iterations for internal time step convergence. A minimum of 20000 time steps were evaluated per period on the periodic flow perturbation analysis. The static pressure level was fixed in the outlet boundary condition at 100 kPa, modeling the discharge of the flow to a constant pressure environment. The inlet of the domain was modeled as an inlet pressure boundary condition where the total temperature was kept constant at 500K. The inlet flow variations were imposed following total pressure transient profiles, P0(t). The turbulence intensity was fixed to a 2.5% level with a viscosity ratio of 10. The top wall of the domain was modeled as an adiabatic inviscid wall, while the plate was simulated as a smooth viscous isothermal surface at 300K. The wall fluxes and both momentum and thermal boundary layer were monitored at x/L = 0.5 (x*). For this numerical research the turbulence closure was achieved through the use of the Langtry-Menter 4 equation Transitional SST model [30]. The transition was numerically enhanced in the leading edge of the plate through the addition of a source term 0.5 mm downstream of the inlet to trip the transition. However, following this procedure, the turbulent to laminar re-laminarization effects on the thermal boundary layer response are taken into account. The working fluid was air, modeled as an ideal gas using the Sutherland law to include the effect of the temperature on the molecular fluid viscosity. Second order upwind schemes were adopted for the flow

Table 1: Grid convergence analysis

Cells $x10^3$	xv (m/s)	δ (mm)	Cell Size (m)	A. ratio $r = h_c/f_f$
5	168.27	6.981	0.00360	1.41
10	166.25	7.067	0.00255	1.41
20	165.25	7.115	0.00180	1.41
40	164.38	7.219	0.00127	1.41
80	164.12	7.223	0.00090	1.41
160	164.02	7.224	0.00063	1.41

and turbulent kinetic energy. The unsteady convergence of the simulations for all the excitation frequencies was ensured prior to the data acquisition based on the methodology outlined by Clark and Grover [31]. Which evaluates the phase, amplitude, mean value and the cross correlation for each single cycle.

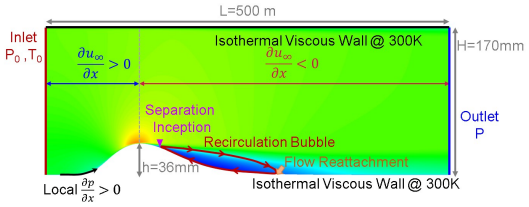

Figure 2: 2D domain for numerical analysis of flow separation dynamics

Looking into the phenomena driving the flow separation and reattachment under transient inlet flow conditions, a wall mounted hump was designed making use of Bezier curves in order to guarantee the continuity of the curvature. The domain design was suited to perform like the rear suction side of a low pressure blade, where massive flow separation can occur at low Reynolds conditions, while at high Reynolds number ($Re > 200000$) the flow is fully attached. Where the Reynolds number is based on a 100mm cord length (Lref).

$$Re = \rho u L_{ref} / \mu \tag{1}$$

Figure 2 presents the numerical domain used for the flow separation analysis. The upper and lower walls of the domain were modeled as an isothermal viscous surface at 300K. The static pressure level was imposed by a pressure outlet boundary condition, whereas the total pressure and temperature were dictated by the inlet pressure boundary condition. Proper geometrical discretization was ensured through a mesh sensitivity analysis. In order to enhance correct near wall flow prediction, the y+ was kept below 0.5 along the walls for all the proposed meshes.

Vogel and Eaton's combined heat transfer and aerodynamic measurements, [31], were used to verify the validity of the proposed 2D URANS methodology. They documented the heat flux distribution downstream of a backward-facing step and its coupled nature with the fluid dynamic structures. Fig. 3 a) represents the numerical domain, which mimics Vogel and Eatons test section. Free stream velocity and total temperature were set in the inlet of the domain, 2.5 m upstream of the backward facing step. The static

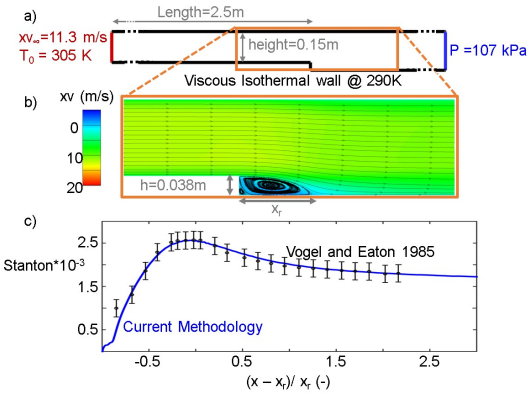

Figure 3: Validation of the numerical methodology

pressure was set in the outlet of the domain, a couple of meters downstream of the step. The upper and lower walls were modeled as viscous isothermal surfaces at 290 K. Fig. 3 b) depicts the axial velocity contour on the backward facing step region, where a separated flow region of about 3 times the step height is displayed.

Figure 3 c) shows the comparison of the Stanton number ($Stanton = htc/(c_p xv)$) for the numerical and experimental results. The agreement between both is notable along the recirculated region and the posterior reattached portion. There is only a small disagreement in the first measured location, which could be related to 3D flow phenomena not captured with the 2D numerical domain.

In addition to the 2D URANS simulations, LES simulations were carried out to verify the performance of the URANS models resolving the transient flow dynamics of the ongoing study. For this purpose, we selected the Smagorinsky Lilly subgrid scale model [32; 33]. Fig. 4 depicts the numerical domain for the LES evaluation. The lateral walls were set as periodic translational boundary conditions. The static pressure was fixed in the outlet of the domain, while the total temperature and the temporal evolution of the total pressure were imposed in the inlet. Both bottom and upper surfaces were modeled as viscous isothermal walls. The width of the domain was limited to 46 mm to reduce the numerical burden of the simulation. The geometrical discretization followed the guidelines established by Chapman, Choi and Moin [34; 35], where Δz_w+ was set to 20, Δx_w+ was fixed at 40 and at least 30 points per boundary layer thickness were discretized in the normal direction. The total cell count is 260 nodes in the normal direction, 900 elements in the axial direction and 125 across the width

of the domain, with a grid of 29.25 million cells.

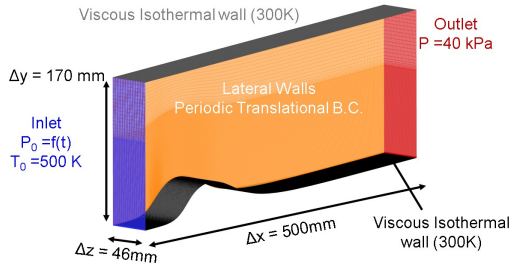

Figure 4: LES numerical domain

3. Sudden flow acceleration

3.1. Aerothermal boundary layer sudden reaction

The sudden flow acceleration was set imposing a smoother step rise profile on the inlet total pressure P_0. The use of this sort of rising profile is preferred since it guarantees the continuity of the input signal. The initial pressure level $P_0(t < 0)$ was equal to 100.1 kPa. The overall pressure rise had a duration of 10 ms and the final level was $P_0(t > 0.01)$ =106 kPa. Based on the total to static pressure ratio the flow velocity in the domain accelerates from 16.5 m/s up to 128.8 m/s. For comparison purposes, some steady state simulations were evaluated along the total pressure rise. At those simulations, the total pressure level at the inlet is maintained constant. Once the case reached convergence the local wall fluxes and mean flow conditions were recorded.

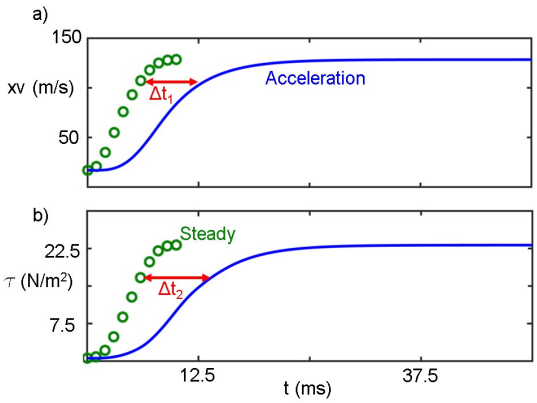

Figure 5: a) Free stream axial velocity evolution; b) Wall shear stress evolution: during a sudden flow acceleration

Figure 5 depicts the comparison of free stream velocity a) and wall shear stress b) at the observation location, x = L/2. Looking at the axial velocity comparison between the transient evolution and the steady evaluations there seems to be a delay on the mean flow settlement Δt_1. For the same values of inlet total pressure, the axial velocity found during the transient evaluation appear to happen at a later phase. In a similar manner, for the wall shear stress, the delay is even larger. The results suggest that there is an additional delay related with the viscous propagation effects across the boundary layer. ($\Delta t_2 = \Delta t_1$ + viscous propagation effects.)

The temporal delay Δt_1, is due to the characteristics propagation and can be approximated based on the speed of sound and the flow velocity upstream and downstream of the compression and expansion wave fronts. By shifting the steady point evaluations with the time required for the characteristics to establish the mean flow conditions, a better representation is obtained. The transient profile values are then compared with steady evaluations for the same free stream conditions, as depicted in Fig. 6 a) for the free stream velocity.

Figure 6 b) represents the skin friction coefficient compared with the steady evaluations. Two different trends are observed during the flow acceleration. At first, the transient evaluation overshoots the steady skin friction values. Under this circumstance, Fig. 7 a) depicts the boundary layer for both steady and transient run at half of the pressure rise. During the initial phase of the acceleration the inertia of the fluid close to the wall stretches the boundary layer. For the same axial velocity, a strained boundary layer with shorter height leads to higher skin friction values.

Laminar and turbulent boundary layer skin friction correlations are also included in Fig. 6 b) for comparison purposes. Due to the inertia of the flow in the first phase of the acceleration the skin friction slightly overshoots the turbulent prediction. However, during the latter phases of the flow stimulation, the transient evaluation undergoes the prediction for turbulent flow without reaching laminar boundary layer character. This phenomena is a consequence of the turbulence settlement delay. In the steady evaluations the turbulence inside of the boundary layer has been completely established. During the acceleration, the boundary layer is continuously evolving and it suffers some temporal shifting due to the diffusion delay. This phenomenon can also be recognized in the momentum boundary layer profile in Fig. 7 b).

Figure 6 c) represents the heat flux rate during the flow acceleration compared with the steady conditions. Laminar and turbulent boundary layer heat

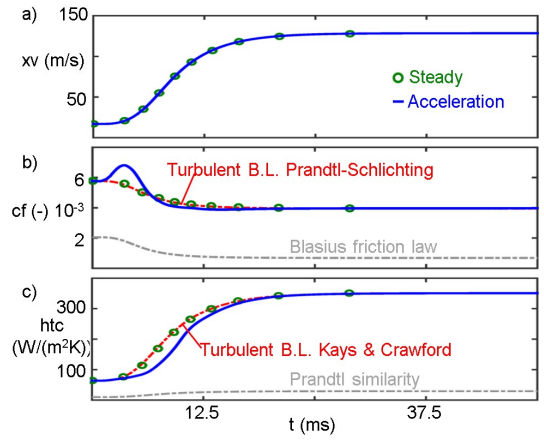

Figure 6: : a) Free stream axial velocity b) Skin friction coefficient c) Heat flux: evolution during a flow acceleration after characteristics delay correction

transfer coefficients derived from Nusselt correlations are also included in the figure. The wall heat fluxes during the transient evolution depict smaller values than the ones acquired in the independent steady evaluations, which are in agreement with the ones predicted for turbulent flow. Those smaller heat transfer values are the symptoms of thermal distribution delay across the near wall flow. In this sense, Fig. 8 represents the thermal boundary layer profiles for both transient and steady evaluations during three different phases of the flow acceleration.

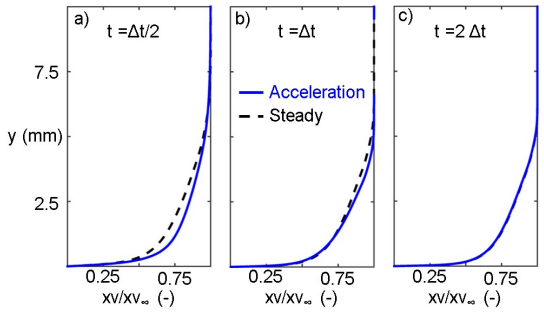

Figure 7: Momentum boundary layer profile at different acceleration phases for both steady and transient evaluation

The first set of thermal boundary layer profiles at half of the total pressure rise, ($t = \Delta t/2$), show similar thicknesses but different slopes near the wall. During the transient evaluation, the boundary layer profiles have not been adjusted yet to the new Reynolds conditions. Therefore, the slope at the wall is still lagging behind, adjusting from a thicker boundary layer. By the end of the pressure rise (t=Δt), this lag is further augmented and the slope near the wall during the unsteady evaluation is much smaller than the one found in the steady state condition. This could also be perceived in Fig. 6 b), where the difference between the steady and the transient evaluation reaches its maxima at t=10ms. Afterwards, the differences between the transient and steady profiles are gradually mitigated.

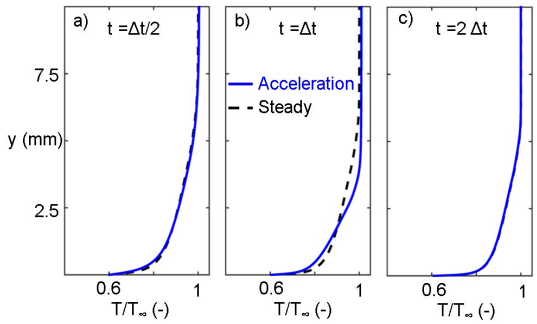

Figure 8: Thermal boundary layer profile at different acceleration phases for both steady and transient evaluation

3.2. *Separated flow region reaction to sudden flow start up*

The behavior of the separated flow region after a sudden flow startup was modeled to determine its effect on the performance of the recirculation bubble. The sudden flow discharge was set imposing a SmootherStep rise profile on the inlet total pressure. The initial pressure level $P_0(t < 0)$ was equal to 65 kPa. The overall pressure rise required 50 ms and the pressure was boosted up to $P_0(t > 0.05s) = 65.516$ kPa. Based on the dynamic pressure increment, the mean flow through the domain accelerates from stagnant conditions up to 47.61 m/s. The passage is initialized at room temperature, 300 K, just before the sudden flow is discharged at 500 K. During the flow start-up, the Reynolds number rises up to 80000. For comparison purposes, several steady state simulations were carried along the total pressure rise. For those evaluations, the inlet total pressure is maintained constant till convergence is achieved.

Figure 9 a) represents the axial velocity at x = 0.25m during the sudden flow release compared to the steady state simulations. The steady state simulations are represented at the time of the inlet total pressure conditions they correspond to. There is a noticeable time shift between the steady results and the actual conditions in the center of the domain during the transient. This temporal delay is a consequence of

the mean flow establishment. The temporal shift can be corrected based on the characteristic speeds and the particular axial location. Using this approach, the steady results in the Fig. 9 b,c,d,e and f are shifted in time to match the free stream conditions of the transient evolution.

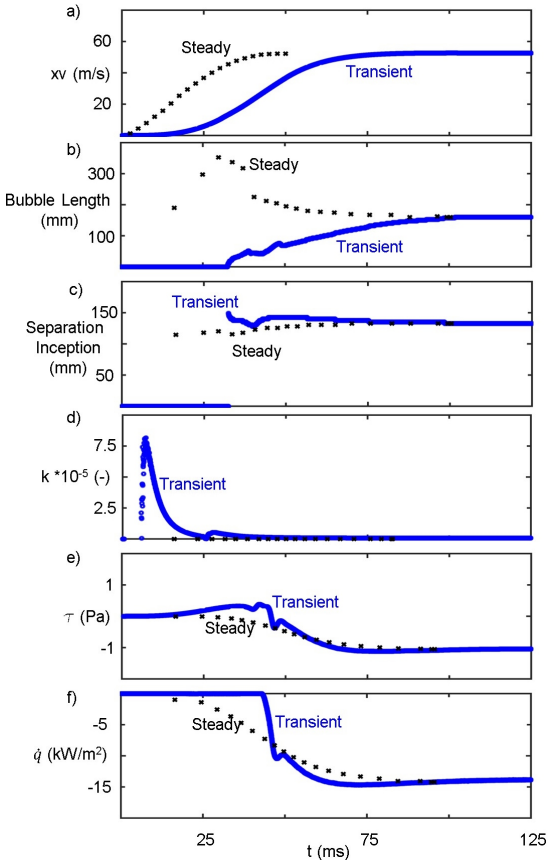

Figure 9: Free stream, wall fluxes and separated region evolution during the sudden flow acceleration

Figure 9 b) depicts the evolution of the bubble length during the sudden flow start up compared to the steady state results. Likewise, Fig. 9 c) represents the separation inception location. For the first instances of the acceleration, where the flow velocity is smaller and consequently the Reynolds number the lowest, the steady simulations depict early boundary separation and the longest separated flow region. Although, for the transient flow acceleration during the first 30 ms there is no separation at all. In a similar way, as opposed to the steady results the inception starts further downstream and then gradually moves upstream. This is because of the mean flow evolution effect on the near wall flow region. During the first instances of the sudden flow discharge there is a strong acceleration that energizes the near wall region, preventing the flow separation. As the acceleration dilutes, near the end of the total pressure rise, the scarcity of flow momentum in the boundary layer, together with the adverse pressure gradient triggers the flow separation and the bubble starts to grow up. Fig. 7 d) represents the evolution of the acceleration parameter (k) right at the summit of the hump.

$$k = \mu/(\rho x v_\infty{}^2) du/dx \tag{2}$$

This parameter provides a notion of the flow acceleration and it is commonly used to determine the likelihood of flow relaminarization [36; 37] . For the first part of the acceleration ($t < 30ms$) the acceleration parameter is above 10^{-7}, denoting that during this period, the mean flow conditions are driving the narrowing of the boundary layer and preventing the flow separation. Once the flow approaches its final free stream velocity and the acceleration vanishes, the boundary layer smoothly recovers its status and becomes more prone to separation.

Figure 9 e) and f) represent the axial wall shear stress evolution and the heat flux footprint at the center of the domain. Because of the differences on the recirculation bubble size, the wall shear stress on the transient evolution stays positive till t = 40 ms while the steady results depict always negative values. In terms of heat flux, due to the initialization of the domain at room temperature, the heat flux during the initial phase of the acceleration is zero. Once the sudden discharged flow reaches the observation location through convection at $t = 45ms$ there is a sudden increase on the heat flux magnitude. Afterwards due to the smaller size of the bubble during the transient evaluation the heat flux level is higher. The smaller the bubble, the fewer isolation is provided between the wall and the warmer core flow. This analysis proves how the dynamic pressure gradients; particularly the mean flow accelerations, have a strong influence modulating the flow separation, being able to abate the separation at the lowest Reynolds numbers ($Re < 50000$) through the stimulation of the flow momentum inside of the boundary layer.

4. Periodic flow perturbation

4.1. Aerothermal boundary layer dynamic response

For the analysis of the boundary layer response to periodic perturbations we used the same numerical domain displayed in Fig. 1. The inlet total pressure followed a pure sinusoidal profile with a mean

level of 105 kPa and an absolute amplitude of 4 kPa, ($P_0 \in [101 - 109kPa]$), leading to a mean Reynolds level of 1.5×10^6. To analyze the phenomena at low and moderate pulsating flow regimes, the following frequencies were explored: 5, 10, 20, 50,100 and 1000 Hz. For comparison purposes 80 steady evaluations where performed at various total pressures along the period. Instead of referring to the various frequencies analyzed it results more convenient to use the non-dimensional Strouhal number of the domain. The Strouhal number if the domain is obtained dividing the frequency of excitation is by the frequency response of the domain:

$$St_{domain} = f_{excitation}/f_{domain} \tag{3}$$

The frequency response of the domain is defined as the time that the fastest characteristic takes to travel from the inlet to the outlet of the domain:

$$f_{domain} = L_{domain}/(c + xv) \tag{4}$$

Using the massflow averaged velocity over an entire period the frequency response of the domain is approximately 1100 Hz. Each one of the excitation frequencies is translated into a Strouhal number (St_{domain}), as presented in Table 2.

Table 2: Range of Strouhal numbers analyzed

Excitation Frequency	St_{domain}
5	0.0045
10	0.009
20	0.018
50	0.045
100	0.091
1000	0.909

Figure 10 a) represents the free stream axial flow velocity at x=L/2 for all the Strouhal numbers under analysis compared to the steady state cases. For low Strouhal numbers the results are similar to the steady state cases. However, as the Strouhal number gests closer to one, the deviation from the steady state increases. Fig. 10 b) represents the static pressure in the same location for the steady evaluations, and for three different Strouhal numbers, 0.009, 0.091 and 0.909. For low Strouhal numbers the acoustic and convective characteristics can travel along the domain multiple times before new changes are applied in the inlet. Consequently, the flow can smoothly adjust to the new inlet conditions. However, for Strouhal numbers closer to unity, there is not enough time for the characteristics to commute across the domain and an average value is settled. In terms of static pressure, for the low Strouhal numbers there are moderate pressure and expansion waves travelling across the domain to establish the new flow conditions. On the other hand, for larger Strouhal numbers, the strength of these waves is increased, revealing that for actuation frequencies similar to the frequency response of the domain, the plate suffers the passage of strong pressure and expansion waves that rapidly accelerate and decelerate the flow. Fig. 10 c) represents the skin friction evolution for the same set of Strouhal numbers. Laminar and turbulent boundary layer skin friction correlations are also included in the representation. For low Strouhal numbers (0.009), during the final total pressure rise ($0 < t/p < 0.25$) the skin friction clearly undershoots the prediction for turbulent flow, reaching values of almost laminar boundary layer conditions. On the contrary, for the latest total pressure decay ($0.5 < t/p < 0.75$), the skin friction exceeds the predicted turbulent boundary layer. However, for moderate or closer to unity Strouhal numbers, the deviations from the turbulent boundary layer prediction are much smaller and the value oscillates around the steady state simulations data. Nonetheless, the larger Strouhal number result underpredicts and overshoots the skin friction predicted for turbulent boundary layer on the flow acceleration and deceleration.

Figure 10 d) depicts the heat transfer coefficient evolution over the entire actuation period. It also includes the heat transfer coefficient predictions from turbulent and laminar Nusselt correlations. For low Strouhal numbers the amplitude variations perceived on the heat flux are similar to the ones predicted for turbulent boundary layers, and on the same order of magnitude that the steady state evaluations. Although, there exists a phase lag associated with the settlement of the mean flow conditions and the diffusion of the information across the thermal boundary layer. For larger Strouhal numbers, the amplitude of the variations on the heat transfer coefficient are mitigated. The heat transfer coefficient on larger actuation frequencies tends to a mean level, which is always above the laminar boundary predictions but also in disagreement with the turbulent prediction, displaying lower values during the flow acceleration and larger during the flow deceleration. Table 3 and Table 4 summarize the mean level and amplitude of the fluctuations. As the Strouhal number increases the mean level of the axial flow velocity, wall shear stress and heat transfer coefficient ascents. However, the amplitude of the

variations of such quantities is reduced. Once the actuation frequency approaches the frequency response of the domain, the variables tend to a period averaged value.

Table 3: Mean value

St_{domain}	$\overline{xv}$ (m/s)	$\overline{\tau_x}$ (N/m^2)	$\overline{htc}$ $(W/(Km^2))$
Steady	111.7	20.54	329.26
0.0045	111.5	18.19	322.2
0.008	112.1	18.49	323.5
0.018	113.2	18.97	326.2
0.045	115.4	19.76	330.6
0.091	116.5	20.04	332.5
0.909	116.9	20.05	331.5

Table 4: Maximum amplitude of the oscillations

St_{domain}	Δxv (m/s)	$\Delta\tau$ (N/m^2)	Δhtc $(W/(Km^2))$
Steady	51.1	14.68	143.3
0.0045	48.7	9.88	124
0.008	46.3	8.98	109.1
0.018	40.9	7.31	83.8
0.045	27	4.49	41
0.091	15.9	2.87	24.7
0.909	9.7	3.21	9.4

In terms of heat transfer, for the larger Strouhal numbers the deviations from the turbulent prediction could be a consequence of the boundary layer nature. In a similar way, based on the sudden flow acceleration analysis, we could expect that the fastest fluctuations will display higher skin friction coefficients since the inlet flow conditions changes happen at much faster rates. However, based on the results shown in Fig. 10 c) we observe the contrary. For the highest frequencies, the amplitude of the skin friction coefficient is minimized; with values at least one order of magnitude smaller than the ones found for the slowest fluctuating rates. Based on the static pressure evolution depicted in Fig. 10 b), for the lower Strouhal number the domain gradually adjusts to the new inlet boundary conditions. Although, for larger Strouhal numbers there are relatively strong pressure waves that travel across the domain to adjust the flow to the inlet changes. The presence of such strong positive and negative pressure gradient leads to sudden free stream flow decelerations and accelerations. The strength or rate of acceleration is quantified by the acceleration parameter (K).

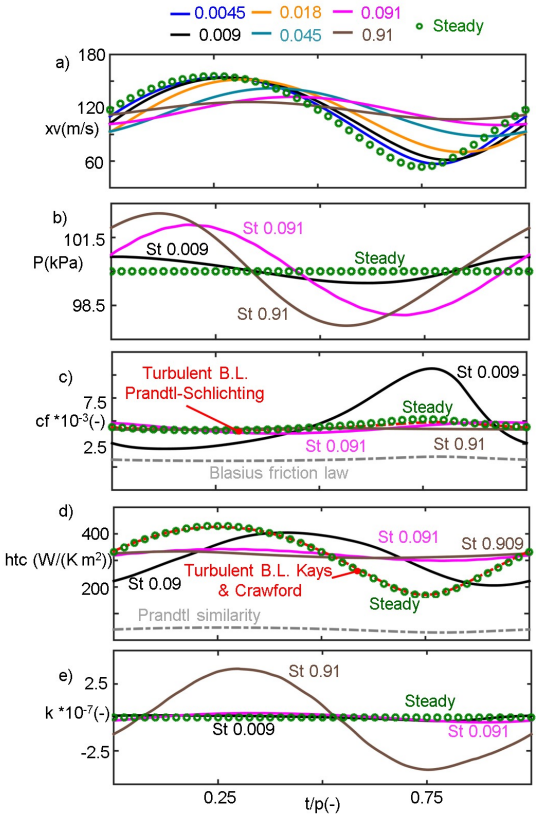

Figure 10: Flow and wall fluxes response to periodic excitaions at x/L = 0.5: a) Axial free stream velocity, b)Static pressure, c)Skin friction coefficient, d) Heat transfer coefficient, e) Acceleration parameter

Following the acceleration parameter formulation (eq. 2), for small fluctuating frequencies the acceleration along the plate results negligible with values around 10^{-15}, Fig. 10 e). However, as the frequency increases the acceleration parameter reaches higher values getting closer to the threshold of flow relaminarization, which is set by most authors in the range of $3x10^{-6} to 3.5x10^{-6}$ [38]. For the analyzed frequencies, the maximum acceleration parameter found at mid cord was $4x10^{-7}$, which is not enough to cause relaminarization but could have a significant influence on the wall fluxes by means of turbulence mitigation.

4.2. Flow acceleration effect on boundary layer

Figure 11 represents the effect of a strong acceleration on the wall shear stress and heat transfer coefficient over a flat plate. For this analysis, the upper wall

of the domain was contoured and modeled as a smooth no slip wall to impose a negative pressure gradient on the flow. Fig. 11 a) represents the achieved acceleration parameter through the imposed pressure gradient. Fig. 11 b) and c) represent the skin friction coefficient and the heat flux respectively. The predictions for turbulent and laminar boundary layer correlations for flat plates are also included for comparison purposes. Natural transition onset takes place at about x = 200mm and at approximately x = 280 mm the boundary layer is fully turbulent. Right after that point, the flow starts to be accelerated. As the acceleration parameter exceeds $1x10^{-7}$ (x=350mm) the skin friction coefficient and heat transfer coefficient deviate from the turbulent prediction. Eventually, once the acceleration parameter reaches the threshold of $3x10^{-6}$ the boundary layer suffers relaminarization and the skin friction coefficient achieves almost laminar boundary layer values. In a similar way, the heat flux also experiences a decay because of the flow relaminarization. The reverse transition is the consequence of the turbulence mitigation due to the flow acceleration, which freezes the eddies breakup and dumps the turbulence dissemination. Once the acceleration is completed, the near wall flow rapidly recovers its turbulent nature and the skin friction coefficient exhibits again similar values to the turbulent prediction. This analysis represents the effect of a static pressure gradient over the flat plate. Translating this analogy onto dynamic pressure gradients across the flat plate, a dynamic negative pressure gradient will foment the same near wall behavior. However, in this case rather than being localized at a given axial location, it will follow the motion of the pressure waves, rendering the flow nature along the entire domain. By means of the local flow acceleration, the dynamic pressure gradients alter the essence of the boundary layer and its turbulent status.

In order to verify the accuracy of the numerical model resolving the near wall flow and predicting the flow relaminarization, the experimental analysis performed by Bader et al. [39] on the flat plate boundary layer in accelerated flow were numerically replicated. Fig. 12 a) represents the numerical discretization of the experimental test section of Graz University. The boundary conditions are: xv_∞ = 4.824m/s, T = 318 K, Ps = 97.7 kPa and Tu = 5.45%.

Figure 12 b) represents the velocity magnitude contour in the modeled test section. The presence of separated flow regions at the end of the flat plate and below the test article require the performance of an URANS simulation to guarantee the convergence of the simulation. Fig. 12 c) compares the skin friction coefficient

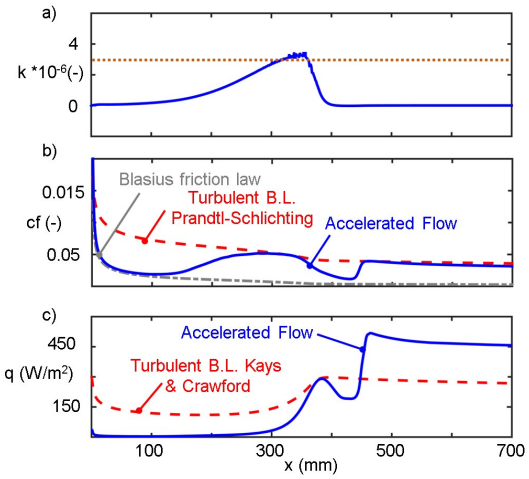

Figure 11: Acceleration parameter effect on the aero-thermal boundary layer: a) Acceleration parameter, b) Skin friction, c) Heat flux

retrieved with the current numerical set-up against the experimental results of Bader et al.; including laminar and turbulent boundary layer skin friction correlations. Overall, there is an excellent agreement between the numerical and the experimental results. The only discrepancy takes place on the transition tripping, where the numerical results overshoot the experimental findings, due to the differences on the tripping approaches. However, in terms of capturing the boundary layer relaminarization the comparison of the results is satisfactory.

4.3. Mean flow oscillations effect on the wall fluxes

Figure 13, top, represents the momentum boundary layer profiles for all the frequencies and the steady evaluations at different time steps along the period. Looking at the velocity profiles at t/p = 3/4 there is shrinkage of the boundary layer as a consequence on the flow inertia after the sudden flow acceleration driven by the pressure rise. The boundary layer stretching is maximum for the low Strouhal numbers where the velocity variations amplitudes are larger. As the excitation frequency increases, the velocity fluctuations are reduced, and the boundary layer suffers less contraction. On the other hand, at t/p = 1/4 the boundary layer has its maximum thickness, associated with the slowest flow velocity condition and a decelerated trend. The profiles of larger Strouhal number do not seem to depart much from the steady boundary layer results and preserve a constant boundary layer thickness because of the averaging of the in-

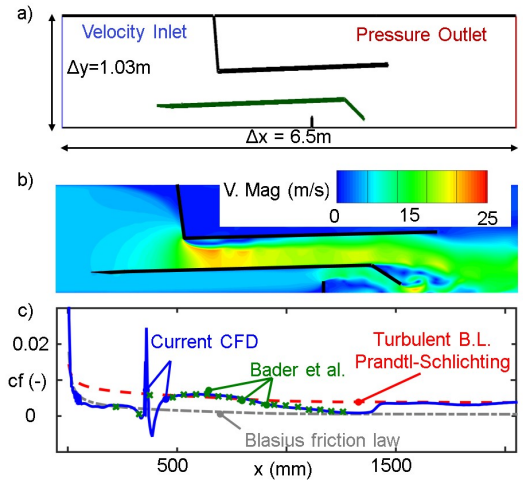

Figure 12: a) Numerical domain for validation b) Velocity magnitude contour on the modeled test section c) Skin friction coefficient over test article

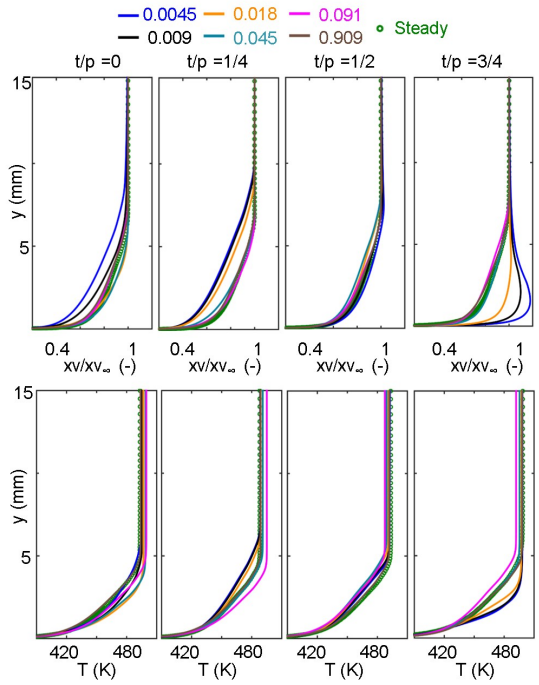

Figure 13: : Momentum and thermal boundnary layer profiles during the excitation period, for 5,10,20,50,100 Hz and steady conditions

let flow conditions.

Figure 13, bottom, represents the thermal boundary layer profile for all the Strouhal numbers under scrutiny. For the lower excitation frequencies, the thermal boundary layer thickness suffers notable variations as a consequence of the mean flow acceleration and deceleration, dictating the span of the heat transfer coefficient amplitude. It is remarkable how even displaying much thinner thermal boundary layers, like the ones at t/p = 3/4 the near wall region does not completely adjust to these conditions because of the diffusion delay. Consequently, the heat transfer coefficient during these phases does not overshoot the turbulent boundary prediction or the steady state result. Hence, the thermal diffusion delay prevents the near wall flow to generate much higher heat flux rates than the steady turbulent evaluations. On the other hand, for the higher excitation frequencies, although displaying similar boundary layer thickness to the ones exhibited in the steady state evaluations, their wall flux rates do not follow the same trend. This is the consequence of the flow acceleration and deceleration modulating the boundary layer nature. At the time where the steady evaluations reflect their higher heat transfer coefficient, the larger Strouhal numbers experienced the stronger acceleration parameter, mitigating the turbulence and reducing the wall flux rates.

4.4. *Flow separation performance under fluctuating inlet conditions*

For the analysis of the flow separation performance under fluctuating inlet conditions the hump domain was used. The inlet total pressure evolution followed a sinusoidal profile with a mean level of 71.3 kPa and an amplitude of 2.4 kPa, ($P_0 \in [70.1 - 72.5kPa]$). The total temperature at the inlet of the domain was fixed at 500 K, with a minimum flow velocity of 20.24 m/s and a maximum of 100.1 m/s. Based on the flow temperature and its velocity, the Reynolds number during this inlet fluctuation spanned from 36000 up to 180000. The flow separation was explored at frequencies of 10, 20, 50, 100, 200, 400 and 1000 Hz. In addition, several steady state simulations were evaluated with various inlet flow conditions along the period.

Figure 14 a) represents the mean flow axial velocity for all the analyzed frequencies together with the steady evaluations at $x = 0.25m$. As the excitation frequency approaches the domain frequency response, determined by the time that the characteristics take to travel across the domain ($f_{domain} = L/c$), the amplitude of the free stream velocity is reduced. For low frequencies, 10 Hz, the peak-to-peak variations in the velocity are very similar to the ones present

in the steady cases. However, as the frequency rises, since the domain does not have time to react to the inlet changes, the amplitude variations are limited. For high fluctuation rates, the free stream velocity tends to an average status. Although the mean level of the free stream velocity along the period keeps increasing as the excitation frequency intensifies. In this regard, Fig. 14 b) represents the acceleration parameter at the hump summit. For the slower frequencies, the acceleration parameter displays its larger magnitude, over $1.5 * 10^{-6}$. Once the frequency increases, the acceleration parameter is reduced due to the minimization of the flow velocity fluctuations. However, after the frequency exceeds 100 Hz the acceleration raises again. Although suffering small velocity fluctuations the changes at those frequencies happen so fast that flow acceleration is build up again.

For frequencies above 100 Hz the variations on the axial velocity profile are minimal, while for small frequencies, 10, 20 and 50 Hz the profiles suffer more distortion. In fact the 10 Hz profiles seem to follow closely the evolution dictated by the steady evaluations at the various inlet total pressure conditions. Fig. 14 c) and d) represent the bubble length and the separation onset respectively. It is remarkable how regardless of the fluctuation frequency, or even for the steady evaluations the separation inception remains locked in the same region for the wide range of Reynolds number explored, near x = 140mm. In terms of bubble length, the 10 Hz case follows along some parts of the period the steady simulation evolution due to its similitude on the flow velocity. However, as the acceleration parameter peaks (at $t/p = 0.8$) the bubble length is suddenly reduced. Reflecting again the strong influence of the mean flow temporal evolution on the separation onset.

For higher actuation frequencies, the amplitude of the bubble length variations is lessened due to the smaller velocity changes. At the highest analyzed frequencies, 200, 400 and 1000 Hz the bubble size variations are minimal and mainly driven by the dynamic flow acceleration. In particular, for the 200 Hz case the bubble length is locked at 125mm. In terms of heat transfer rates, the Fig. 14 e) depicts the heat flux evolution at the center of the domain. The magnitude of the heat flux level is reduced when the frequency increases because of the smaller bubble sizes.

An additional URANS simulation was performed to compare the results to an LES simulation with the same inlet properties. The purpose of this comparison is to verify the accuracy of the selected turbulence model resolving the dynamic performance of the flow-

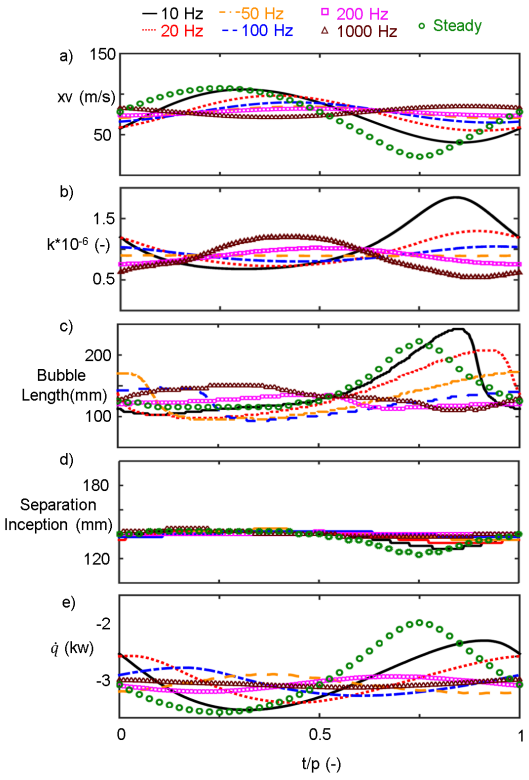

Figure 14: Mean flow, separated region and wall fluxes evolution at various excitation frequencies for a complete inlet fluctuation period

separated region. The fluctuation on the Reynolds number ranged 47000 up to 82000 to reduce the computational effort. Driven by a total pressure oscillation, between 40.3 and 40.9 kPa, with a static pressure level of 40 kPa. As a consequence, the mean flow velocity oscillates between 40 and 80 m/s. The LES results are the phase locked average results of 14 cycles of the solution after convergence is ensured. This procedure is required to achieve an average solution comparable to Reynolds Averaged Navier-Stokes simulations. Fig. 15 a) represents the energy spectra of three different points in the domain. The first one is at the hump summit axial location and 4 cm above its peak. The second one is at the same height at x = 270 mm. While the third one is at x = 270 mm and y = 40 mm. For all the points there is a peak corresponding to the inlet fluctuation frequency 25Hz. Points 1 and 2 follow the Kolmogorov -5/3 power law energy decay. While the energy distribution at Point 3 is quite altered by the separated flow.

Figure 15 b) represents the axial flow velocity contour at 75% percent of the period for the 11th cy-

cle. Displaying the flow separation present in the latter deceleration phase of the flow. In the bottom, there is a representation of various Q-criterion isosurfaces, providing an illustration of the vortical structures present in the flow.

Figure 16 represents the evaluation of the phase locked average LES results and the 2D URANS prediction with the transitional SST turbulence model. Fig. 16 a) depicts the development of the bubble length throughout the period. The size of the separated region on the 2D URANS is over-predicting the LES results, as was already discussed in steady evaluations by Biswas et al. [40]. However, the evolution of the bubble length along the period, following the inlet total pressure fluctuations, is identical in both numerical approaches. Where only a constant offset along the period is present between the URANS and LES results, which demonstrates the capability of the 2D URANS simulations on predicting the dynamics of the separated flow region under transient mean flow conditions. In this way, Fig. 16 b) represents the separation inception for the LES and URANS simulations. Displaying a perfect agreement between both numerical schemes with less than 5mm of discrepancy between them.

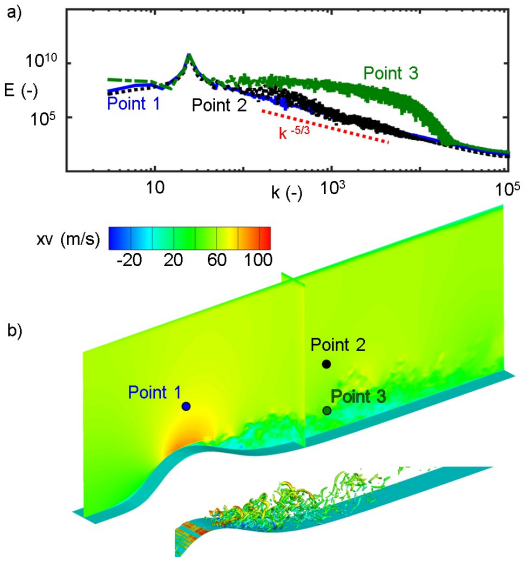

Figure 15: Energy spectra on the domain at 3 given points, b) Axial velocity contour at t/p = 0.75 with q-criterion display

Additionally, Fig. 16 c) represents the heat transfer coefficient evolution at x=0.25. Both cases follow similar evolutions with variations in the magnitude driven by the differences on the recirculated flow region size.

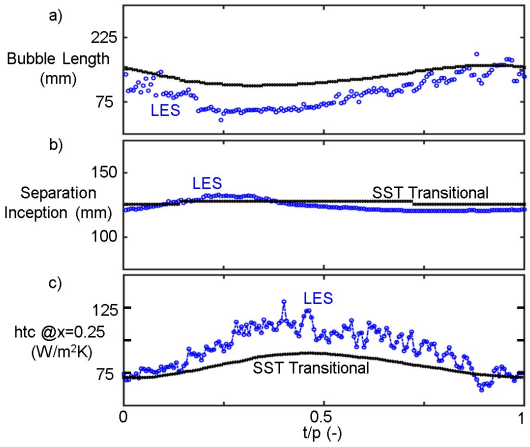

Figure 16: Large Eddy Simulation vs 2D SST Transitional results, a) bubble length, b) separation inception, c) heat transfer coefficient at x=0.25m during the periodic oscillation

5. Conclusion

In this analysis, the effect of a sudden flow acceleration and periodic flow perturbation on the heat flux, wall shear stress and separated flow regions were numerically explored through URANS and LES simulations. After sudden flow acceleration, the boundary layer suffers first an inertia delay that intensifies the wall shear stresses, exceeding the turbulent predictions. This is followed by a delay on the final wall shear stress establishment, which abates the shear for the latter phases of the acceleration. In terms of heat flux, the transient growth and adaptation of the boundary layer infers lower heat flux rates than the ones expected for turbulent boundary layer conditions. Based on the sudden flow discharge analysis it was proven that for similar Reynolds conditions, the presence of flow acceleration energizes the near wall flow preventing the flow separation. On the contrary, in case of mean flow deceleration, the boundary layer is more prone to detach and the length of the separated region increases.

The temporal lag of the heat flux and the wall shear stress on the flat plate is the consequence of the propagation delay across the boundary layer height. The mean flow quantities are transfered convectivelly (T) and acoustically (P) along the domain. However, the propagation of the information across the the boundary layer happens in a diffusive manner. The diffusion transmissivity is much slower than the convective one and consequently there exists a perceptible delay on the reaction of the wall fluxes.

When the boundary layer is under periodic flow

perturbations there are two distinct behaviors depending on the actuation to response rate of the domain. For lower Strouhal numbers there are large fluctuations on the wall heat fluxes. The skin friction coefficient greatly exceeds the turbulent prediction due to the flow inertia right after the acceleration, while the turbulent delay during the flow decelerations drives smaller friction values. In terms of heat flux, due to the slower thermal diffusion across the boundary layer, the heat transfer rates do never exceed the turbulent heat transfer predictions for the analyzed amplitudes and frequencies. Although, the maximum and minimum heat transfer peaks have a phase lag with respect to the mean flow conditions because of the thermal diffusion delay. In the case of large Strouhal numbers, the amplitude of the heat flux and wall shear stress variations are mitigated. For excitation frequencies similar to the domain frequency response, the flow approaches an average condition due to its inability to fully adapt to the inlet flow changes.

Similarly, the strong influence of the mean flow temporal evolution on the separation onset was remarked based on sinusoidal inlet total pressure profiles at various frequencies. Once the excitation rates approach the domain frequency response, the mean flow quantities tend to an average condition due to the lack of ability to adapt to them. However, the boundary layer flow will perceive the influence of the pressure and expansion waves propagating across the domain, modulating its reaction on the exposure to adverse pressure gradients. Interestingly, for a wide range of Reynolds number ($40000 < Re < 180000$), the separation inception happens in the same axial location.

The mean levels of heat transfer and shear stress keep rising as the excitation frequency increases following a logarithmic rate. In terms of periodic inlet fluctuations, the mean flow quantities strongly modulate the boundary layer status for low Strouhal numbers, although its consequences are not completely reflected in the wall fluxes due to the diffusion delay across the boundary layer height. In addition, for larger actuation frequencies, the mean flow sudden variations are able to modify the nature of the boundary layer mitigating or enhancing the wall fluxes rate for accelerations or decelerations respectively.

Acknowledgement

This material is based upon work supported by the Air Force Office of Scientific Research, Air Force Material Command, USAF under Award No. FA9550-16-1-0120. This work will be presented during the ASME 2018 Turbo Expo, Turbomachinery Technical Conference & Exposition, Oslo, Norway, Jun. 11-15, 2018 (Paper No. GT2018-75128 & GT2018-76896).

Table 5: Nomenclature

c	Speed of sound	m/s
cf	Skin friction	-
k	Accel. parameter	-
htc	Heat transfer coef.	$W/(m^2K)$
LES	Large Eddy Sim.	-
x	Axial distance	m
y	Normal distance	m
P	Pressure	Pa
Re	Reynolds number	-
T	Temperature	K
μ	Dynamic viscosity	$kg/(ms)$
τ	Wall Shear Stress	Pa
ρ	Density	kg/m^3
δ	B. L. thickness	mm
δ^*	B. L. disp. thickness	mm
Pr	Prandtl number	-
xv	Axial velocity	m/s
St	Strouhal number	-
Tu%	Turbulence Intensity	-
q	Heat flux rate	W/m^2
f	Frequency	Hz
	SUBSCRIPTS	
0	Stagnant	
c	Coarse	
∞	Free stream	
f	Fine	
i	Inlet	
r	Reattachment	
o	Outlet	
exc	Excitation	
th	Thermal	
ref	Reference	
dyn	Dynamic	
	SUPERSCRIPTS	
+	Wall units	
	Observation point	

References

[1] A. Binder, W. Forster, H. Kruse, H. Rogge, An experimental investigation into the effect of wakes on the unsteady turbine rotor flow, Journal of Engineering for Gas Turbines and Power 107 (2) (1985) 458–465.

[2] N. Arndt, Blade row interaction in a multistage low-pressure turbine, ASME 1991 International Gas Turbine and Aeroengine Congress and Exposition 1 (1) (1991) 115–125.
[3] M. B. Giles, Calculation of unsteady wake/rotor interaction, Journal of Propulsion and Power 4 (4) (1988) 356–362.
[4] V. P. Chaluvadi, A. Kalfas, M. Banieghbal, H. Hodson, J. Denton, Blade-row interaction in a high-pressure turbine, Journal of Propulsion and Power 17 (4) (2001) 892–901.
[5] R. W. Moss, R. W. Ainsworth, T. Garside, Effects of rotation on blade surface heat transfer: An experimental investigation, in: ASME 1997 International Gas Turbine and Aeroengine Congress, American Society of Mechanical Engineers, 1997, pp. V003T09A034–V003T09A034.
[6] J. Braun, B. H. Saracoglu, G. Paniagua, Unsteady performance of rotating detonation engines with different exhaust nozzles, Journal of Propulsion and Power (2016) 121–130.
[7] G. Paniagua, M. Iorio, N. Vinha, J. Sousa, Design and analysis of pioneering high supersonic axial turbines, International Journal of Mechanical Sciences 89 (2014) 65–77.
[8] A. Grönman, T. Turunen-Saaresti, A. Jaatinen, J. Backman, Numerical modelling of a supersonic axial turbine stator, Journal of Thermal Science 19 (3) (2010) 211–217.
[9] J. Sousa, G. Paniagua, J. Saavedra, Aerodynamic response of internal passages to pulsating inlet supersonic conditions, Computers & Fluids 149 (2017) 31–40.
[10] A. T. Hasan, Characteristics of overexpanded nozzle flows in imposed oscillating condition, International Journal of Heat and Fluid Flow 46 (2014) 70–83.
[11] J. P. Bons, R. Sondergaard, R. B. Rivir, The fluid dynamics of lpt blade separation control using pulsed jets, in: ASME Turbo Expo 2001, ASME, 2001, pp. V003T01A064–V003T01A064.
[12] C. Goldberg, D. Nalianda, P. Pilidis, D. MacManus, J. Felder, Installed performance assessment of a boundary layer ingesting distributed propulsion system at design point, in: 52nd AIAA/SAE/ASEE JPC, 2016, p. 4800.
[13] O. Sharma, Impact of reynolds number on low pressure turbine performance, NASA TR 1998 (1998) 65–70.
[14] H. S. Hura, J. Joseph, D. E. Halstead, Reynolds number effects in a low pressure turbine, in: ASME Turbo Expo 2012, ASME, 2012, pp. 1121–1130.
[15] K. t. Stewartson, On the impulsive motion of a flat plate in a viscous fluid, The Quarterly Journal of Mechanics and Applied Mathematics 4 (2) (1951) 182–198.
[16] K. Stewartson, The theory of unsteady laminar boundary layers, in: Advances in Applied Mechanics, Vol. 6, Elsevier, 1960, pp. 1–37.
[17] F. K. Moore, Unsteady laminar boundary-layer flow, Tech. rep., NATIONAL AERONAUTICS AND SPACE ADMINISTRATION WASHINGTON DC (1951).
[18] H.-S. Huang, W.-J. Yang, Unsteady compressible laminar boundary-layer flow over a flat plate., AIAA Journal 7 (1) (1969) 100–105.
[19] M. Lighthill, On boundary layers and upstream influence. i. a comparison between subsonic and supersonic flows, Proc. R. Soc. Lond. A 217 (1130) (1953) 344–357.
[20] M. Lighthill, On boundary layers and upstream influence ii. supersonic flows without separation, Proc. R. Soc. Lond. A 217 (1131) (1953) 478–507.
[21] M. Lighthill, Contributions to the theory of heat transfer through a laminar boundary layer, Proc. R. Soc. Lond. A 202 (1070) (1950) 359–377.
[22] S. Uchida, The pulsating viscous flow superposed on the steady laminar motion of incompressible fluid in a circular pipe, Zeitschrift für angewandte Mathematik und Physik ZAMP 7 (5) (1956) 403–422.
[23] T. MIZUSHINA, T. MARUYAMA, Y. SHIOZAKI, Pulsating turbulent flow in a tube, Journal of Chemical Engineering of Japan 6 (6) (1974) 487–494.
[24] L. Shemer, I. Wygnanski, E. Kit, Pulsating flow in a pipe, Journal of Fluid Mechanics 153 (1985) 313–337.
[25] T. Moschandreou, M. Zamir, Heat transfer in a tube with pulsating flow and constant heat flux, International journal of heat and mass transfer 40 (10) (1997) 2461–2466.
[26] J. Saavedra, S. Lavagnoli, G. Paniagua, Implications of boundary layer establishment on convective heat transfer experiments, in: 53rd AIAA Aerospace Sciences Meeting, 2015, p. 0258.
[27] M. T. Schobeiri, B. Öztürk, D. E. Ashpis, On the physics of flow separation along a low pressure turbine blade under unsteady flow conditions, Journal of fluids engineering 127 (3) (2005) 503–513.
[28] J. Wissink, Dns of separating, low reynolds number flow in a turbine cascade with incoming wakes, International Journal of Heat and Fluid Flow 24 (4) (2003) 626–635.
[29] I. B. Celik, U. Ghia, P. J. Roache, et al., Procedure for estimation and reporting of uncertainty due to discretization in {CFD} applications, Journal of fluids {Engineering-Transactions} of the {ASME} 130 (7).
[30] F. Menter, R. Langtry, S. Völker, Transition modelling for general purpose cfd codes, Flow, turbulence and combustion 77 (1-4) (2006) 277–303.
[31] J. Vogel, J. Eaton, Combined heat transfer and fluid dynamic measurements downstream of a backward-facing step, Journal of heat transfer 107 (4) (1985) 922–929.
[32] M. Germano, U. Piomelli, P. Moin, W. H. Cabot, A dynamic subgrid-scale eddy viscosity model, Physics of Fluids A: Fluid Dynamics 3 (7) (1991) 1760–1765.
[33] D. K. Lilly, A proposed modification of the germano subgrid-scale closure method, Physics of Fluids A: Fluid Dynamics 4 (3) (1992) 633–635.
[34] H. Choi, P. Moin, Grid-point requirements for large eddy simulation: Chapmans estimates revisited, Physics of fluids 24 (1) (2012) 011702.
[35] D. R. Chapman, Computational aerodynamics development and outlook, AIAA journal 17 (12) (1979) 1293–1313.
[36] B. E. Launder, W. P. Jones, On the prediction of laminarisation, HM Stationery Office, 1969.
[37] P. R. Spalart, Numerical simulation of boundary layers. part 3: Turbulence and relaminarization in sink flows, Journal of Fluid Mechanics.
[38] R. Narasimha, K. Sreenivasan, Relaminarization in highly accelerated turbulent boundary layers, Journal of Fluid Mechanics 61 (3) (1973) 417–447.
[39] P. Bader, M. Pschernig, W. Sanz, J. Woisetschläger, F. Heitmeir, W. Meile, G. Brenn, Flat-plate boundary layers in accelerated flow, in: ASME Turbo Expo 2016, American Society of Mechanical Engineers, 2016, pp. V02BT38A003–V02BT38A003.
[40] G. Biswas, M. Breuer, F. Durst, Backward-facing step flows for various expansion ratios at low and moderate reynolds numbers, Journal of fluids engineering 126 (3) (2004) 362–374.

MULTISCALE AND MULTIPHASE FLOW PROBLEMS

CFD Analysis of the Erosion of a Light Gas Stratification by Means of a Hot Air Jet in the MiniPanda Facility

Andrea Attavino

Environmental and Applied Fluid Dynamics Department , von Karman Institute for Fluid Dynamics, Belgium, andrea.attavino@vki.ac.be

Supervisor: Philippe Planquart

Research Manager, Environmental and Applied Fluid Dynamics Department, von Karman Institute for Fluid Dynamics, Belgium, philippe.planquart@vki.ac.be

University Supervisor: Alessandro Parente

Associate Professor, Aero-Thermo-Mechanics Department, Universite Libre de Bruxelles, Belgium, alessandro.parente@ulb.ac.be

Abstract

Following the Fukushima-Daichii accident many countries decided to strengthen the security systems of their nuclear power plant in order to increase the capabilities of managing sever nuclear accidents. To achieve this goal detailed analysis of postulated design and beyond-design-basis accidents is essential. However, the only tools available for the analysis of these complex scenarios are Advanced Lumped Parameters (LP) and Computational Fluid Dynamics (CFD) codes. At present, the validation of these codes is the most limiting factor in their application. In this work the validation procedure of a CFD solver built in the numerical environment of OpenFOAM is presented. Numerical simulations of the erosion of a light gas stratification by means of a hot air jet have been performed, and results of the simulations were analysed and confronted with experimental results obtained by Rittherath et al. in the MiniPanda facility [1]. Two different scenarios have been considered, each characterized by a different value of the mass flow rate of the jet used to erode the stratification. The buoyancy modified $k-\epsilon$ and $k-\omega$ SST turbulence models have been compared, including the analysis of the effect of the buoyancy modification. Moreover a mesh convergence study has been carried out.

Keywords: Light gas diffusion, Thermal Hydraulics, Turbulence Modelling,

1. Introduction

During a severe nuclear accident a huge amount of hydrogen can be generated by different sources in a Light Water Reactor (LWR) core. Leakage of hydrogen from the core to the containment building can lead to the formation of a combustible mixture. In case of ignition the deflagration of the combustible mixture could severely damage and in the worst case breach the reactor containment building leading to dispersion of radioactive material in the environment.

There are many phenomena governing the behaviour of containment in case of a severe accident, including gas (hydrogen, air and steam) mixing, steam condensation, turbulent transport, wall heat transfer, etc. These phenomena are driven by the leakage of gases form the reactor. The leakage can happen in three different regimes: high momentum release (jet), buoyant low momentum injection (plume) and a transient regime in which the injection starts as a jet and turn into a pure plume after a certain distance [2].

Due to the simultaneous presence of all the phenomena mentioned above, the analysis of the thermal hydraulics behaviour of the containment during a severe nuclear accident is really complex. For this reason, advanced Lumped Parameters (LP) and Computational Fluid Dynamics (CFD) codes are fundamental tools for the analysis of LWR behaviour during postulated design and beyond-design-basis accidents.

In nuclear safety, the reliability of the analysis made with a computational tool is of prime importance. At present, the validation of codes is the major limiting

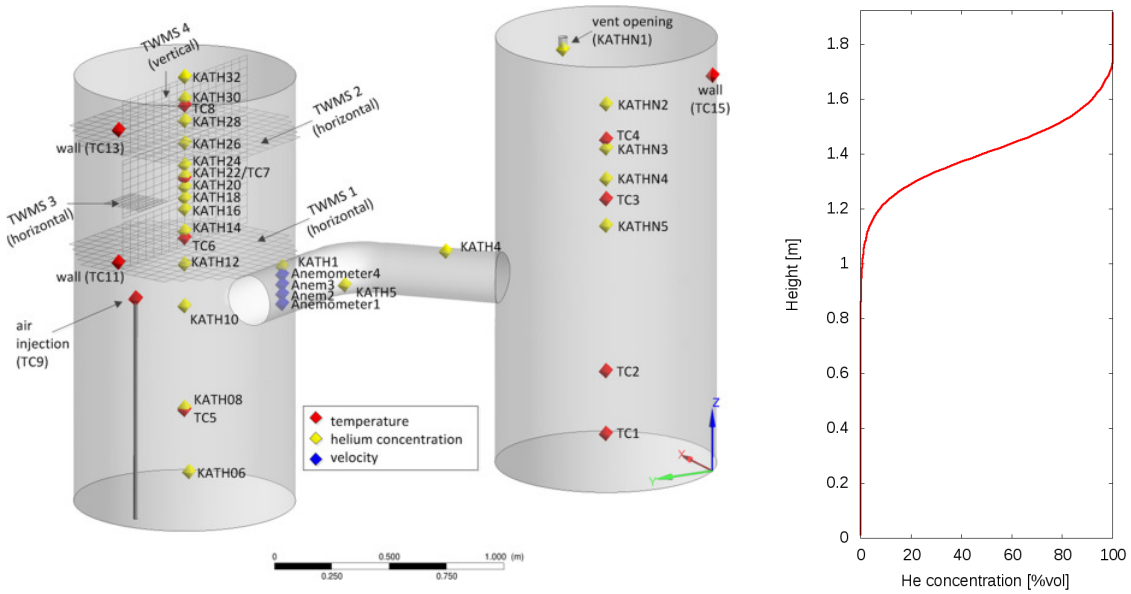

Figure 1: Instrumentation of the MiniPanda facility from [4] (a) and initial helium concentration profile (b)

factor in their application. The main issue for the validation of computational codes is the lack of adequate experimental data with the required temporal and spatial resolutions. Therefore, in the past years many experimental project have been carried out, in order to create a large database for the validation of CFD codes [3].

The validation of a CFD code is a long procedure, and the effect of the different phenomena that are involved in a nuclear accident have to be analysed in an isolated way. The aim of this work is to develop and validate a solver in the OpenFOAM simulation environment for predicting the erosion of a light gas stratification by comparing the simulation's results with experimental data. The work includes the study of the effect of buoyancy in turbulence modelling, as well as, the influence of temporal discretization and mesh refinement.

2. MiniPanda Experiments

As a reference, the experiments performed in the MiniPanda facility in ETH Zürich [1] has been used, because the spatial and temporal resolution of the measurements performed are suitable for the validation of a CFD code, and the reduced dimension of the facility results in a low computational cost of the simulations, allowing to study a larger numbers of parameters.

The MiniPanda Facility as shown in Fig.1a is composed of two cylindrical compartments connected with a bended interconnecting pipe. Both compartments have a diameter of 1 m and a height of 2 m. The experiments have been conducted using helium as a replacement for hydrogen. The gas injection is located in the first compartment while the venting, used to keep the pressure constant during the tests, is located in the second one. The facility is equipped with 45 katharometer for measuring helium concentration, the majority of which are arranged along 4 vertical lines.

The test chosen for this study is the erosion of a helium stratification layer by means of a hot air jet. First, helium is injected in the facility in order to obtain a sharp concentration profile in the upper section of the first compartment, as shown in Fig.1b. Then, a jet of hot air at 85 $^{\circ}C$ is used to erode the stratification. The evolution of the helium concentration profile and temperature are recorded for 3000 s.

3. Governing equations

Due to the large difference in the density of air and helium, it is not possible to use the Boussinesq

approximation for the buoyancy force in the Navier-Stokes equation. For this reason the solver uses the Favre averaged equations closed with the perfect gas law. The transport equation for mass (ρ), momentum ($\vec{U}$) and enthalpy (h) of the gaseous mixture are the following:

$$\frac{\partial \rho}{\partial t} + \nabla \cdot (\rho \vec{U}) = 0. \tag{1}$$

$$\frac{\partial \left(\rho \vec{U}\right)}{\partial t} + \nabla \cdot \left(\rho \vec{U} \vec{U}\right) = \nabla P + \nabla \cdot \left[(\mu + \mu_t) \nabla \vec{U}\right] + \rho \vec{g}. \tag{2}$$

$$\frac{\partial (\rho h)}{\partial t} + \nabla \cdot \left(\rho \vec{U} h\right) = \nabla \cdot \left[\left(\alpha + \frac{\mu_t}{Pr_t}\right) \nabla h\right] + \vec{q}_{diff} + \rho \vec{U} \cdot \vec{g}. \tag{3}$$

$$p = \rho R T. \tag{4}$$

Where μ, α and Pr_t are respectively the viscosity, the thermal diffusivity and the turbulent Prandtl Number of the mixture. μ_t represents the eddy viscosity which is derived form the modeling of turbulence.

In order to obtain a CFD model that can be used for large scale facilities the turbulence is resolved using the URANS approach. In the current model the URANS equations are closed with the $k - \epsilon$ [5] and the $k - \omega$ SST model [6].

3.1. Species transport equation

To compute the concentration of the different gases in the atmosphere of the facility, a transport equation for $N - 1$ specie's mass fraction Y_i is solved, where N is the total number of species in the system. In the transport equations the diffusion process is modelled using the 2nd Fick's Law:

$$\frac{\partial (\rho Y_i)}{\partial t} + \nabla \cdot \left(\rho \vec{U} Y_i\right) = + \nabla \cdot \left[\left(\rho D_i + \frac{\mu_t}{S c_t}\right) \nabla Y_i\right] + \dot{\omega}_i. \tag{5}$$

The laminar diffusion coefficient D_i for the specie i is calculated as a weighted average based on the molar fraction of each other specie j and the respective binary diffusion coefficient D_{ij}:

$$D_i = \frac{1 - X_i}{\sum_{j \neq i} \frac{X_j}{D_{ij}}}. \tag{6}$$

Where X_i is the molar fraction of the $i - th$ specie and D_{ij} is the binary diffusion coefficient for the couple of species i and j. The binary diffusion coefficients are computed using the Fuller-Schetter-Giddings model:

$$D_{ij} = \frac{A T^{1.75} \left(\frac{1}{W_i} + \frac{1}{W_i}\right)^{0.5}}{p \left(D v_i^{0.33} + D v_j^{0.33}\right)^2}. \tag{7}$$

Where W_i is the molecular weight of the specie i and Dv_i are empirical coefficients calculated form the molecular composition of the specie as shown in [7].

Similarly to the transport equation of energy the turbulent diffusion is considered to be proportional to the eddy viscosity μ_t. The turbulent Schmidt number $S c_t$, which represents the proportionality between the eddy viscosity and the turbulent molecular diffusivity, has been set to a constant value of 0.7 [8].

Due to the simultaneous presence of mass diffusion and heat transfer it is important to consider the Lewis number, which is the ratio between the thermal diffusivity of the mixture and the molecular diffusivity of the species:

$$Le = \frac{\alpha}{\rho D_i}. \tag{8}$$

Most commonly the Lewis number is considered to be 1. When this approximation is done, it is possible to neglect the mass diffusion contribution in the energy equation $\vec{q}_{diff}$. However, for small molecules like hydrogen and helium the mass diffusivity is larger than the thermal diffusivity of the mixture, resulting in a small Lewis number [9]. Therefore the flux $\vec{q}_{diff}$ has to be introduced in the energy equation:

$$\vec{q}_{diff} = -\nabla \left(\sum_{i=1}^{N} \frac{h_i}{\rho C p} \vec{J}_i \right). \tag{9}$$

3.2. Buoyancy correction on the turbulence model

As Kelm et al. [4] proposed, the interaction between the light gas stratification and the jet is characterized by the interaction Froude number, which is the ratio between the inertial forces of the jet and the buoyant forces of the stratified layer:

$$Fr_i = \frac{U_i}{\sqrt{g d_i (\rho_0 - \rho_i)/\rho_0}}. \tag{10}$$

Where U_i, d_i and ρ_i are the velocity, the diameter and the density of the jet at the interface with the helium stratification, ρ_0 the ambient density and g the gravitational acceleration ($9.8m/s$). Three cases are possible: when Fr_i is lower than 1 the jet is driven by the buoyancy force and is stopped at the interface with the stratification. In this case, the mixing of the gas is dominated by the molecular diffusion process. When Fr_i is greater than 1, the jet is driven by inertial forces (momentum), and it is able to penetrate through the stratified layer, causing a fast mixing of the gases and a faster erosion of the stratification. An interaction Froude number around 1 indicates that inertial and buoyant forces have equivalent importance, resulting in a turbulence aided erosion process.

Another nondimensional number that can be used to characterize the interaction between the jet and the helium stratification is the mass Peclet number, that correlates the diffusive dilution to convective erosion of a stratified layer:

$$Pe_m = \frac{U_0 d_0}{D_i}. \tag{11}$$

As in the case of the Fr_i, when the mass Peclet number increases the mixing process becomes dominated by advection instead of molecular diffusion.

The two cases considered in this study have respectively and interaction Froude number of 0.7 and 1.3, while the respective mass Peclet numbers are 530 and 990, meaning that buoyancy forces have a strong influence on the erosion process. For this reason, it is essential to consider the effect of buoyancy in the turbulence models.

In the derivation of standard $k-\epsilon$ and $k-\omega$ SST models the buoyancy is usually neglected, leading in a simplification of the model. However, when there are strong gradients of density in the flow the buoyancy force has a strong influence on the turbulence, therefore, it is necessary to include in the kinetic energy equation the following source term:

$$P_{bk} = \frac{\overline{\rho' u_j'}}{\overline{\rho}} \left(\frac{\partial \overline{p}}{\partial x_j} + \overline{\rho} g_j \right) \approx \overline{\rho' u_j'} g_j. \tag{12}$$

Where u_j' and ρ' are the velocity and the density fluctuations. This term can be directly linked to the components of the Reynold's stresses tensor $\overline{u_i' u_j'}$ and the gradient of density $\partial\rho/\partial x_i$. In the case considered the density gradient is parallel to the jet and the Eqn. 12 can be simplified as follows.

$$P_{bk} = -\frac{\mu_t}{\sigma_c \overline{\rho}} \nabla \overline{\rho} \cdot \vec{g}. \tag{13}$$

Where σ_c is a constant of the model and in this case has been set to 1. Adding this therm also in the ϵ and ω equations does not affect the calculated value of eddy viscosity μ_t, however, it makes the system of equations more stable.

4. Numerical setup

The equations showed in the previous chapter are solved using a solver built in the numerical environment of OpenFOAM. The finite volume method is used for the spatial discretization of the domain and the computational grid has been generated through the builtin mesher of OpenFOAM, SnappyHexMesh. The whole domain has been considered, without adding any additional boundary, such as symmetry planes or cyclic boundaries. The injection line has been modelled as a cylinder with adiabatic walls and with an inlet on the upper surface. As shown in Fig.2 the mesh is predominantly hexahedral and it is more refined near the walls and above the hot air injection. Different meshes have been tested with number of cells varying between 300'000 and 700'000.

Due to the large dimension of the domain it was not possible to have a fine refinement of the mesh on the walls in order to obtain a y^+ lower than 1, therefore wall function had to be used in the turbulence model.

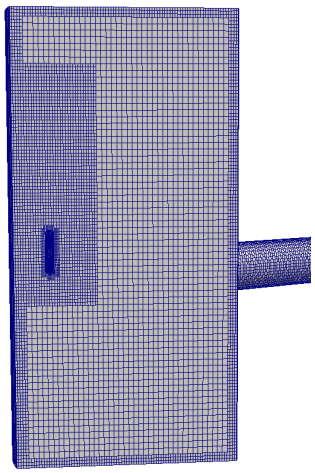

Figure 2: Computational grid for the MiniPanda erosion test.

The simulation has been initialized with the measured atmospheric conditions (~ 20°C and 1 bar). The vertical helium concentration profile in the first compartment has been set as the one provided in the experimental database. The other variables have been initialized considering that the atmosphere in the facility at the beginning of the test is at rest ($\vec{U}, k, \omega = 0$).

Table 1: Boundary conditions for the numerical simulations.

	Boundary conditions
Walls	Fixed temperature T = 25° C, fixed velocity $\vec{U} = \vec{0}$, wall functions.
Inlet	Fixed mass flow rate $\dot{m} = 0.68 g/s$, fixed temperature T = 85° C, low turbulence ($k = 10^{-6}$, $\omega = 1$), air mass fraction Y_{Air} = 1.
Outlet	Free stream, fixed pressure p = 1 bar.

The walls of the MiniPanda facility are made of PVC-U, a material characterized by an high thermal capacity. For this reason the walls have been considered to be at a constant temperature of 25° C for the entire simulation. The venting in the second compartment has been considered to be open on the atmosphere and therefore, the pressure at this boundary has been set constant and equal to 1 *bar*. The boundary conditions for the simulations have been resumed in Tab. 1.

All the variables have been discretized using a second order upwind numerical scheme, while the time discretization is of first order.

Table 2: Properties of the components of the mixture.

	$\mu\ [Pa \cdot s]$	Pr	Pr_t
Air	$1.72 \cdot 10^{-5}$	0.71	0.85
Helium	$1.98 \cdot 10^{-5}$	0.65	0.85

The thermal diffusivity is calculated from the Prandtl number of the mixture: $\alpha = \mu/Pr$, and all the properties of the gaseous mixture are calculated as weighted averages of the properties of each specie:

$$\mu = \sum_{i=1}^{N} X_i \mu_i \tag{14}$$

Where μ_i is the viscosity of the i-th component of the mixture The properties of the single components are reported in Tab. 2.

4.1. Time discretization

The time step Δt of the simulation is adaptively calculated based on the Courant number Co as follows:

$$\Delta t = Co \cdot min\left(\frac{\Delta x_i}{U_i}\right). \tag{15}$$

Where Δx_i is the dimension in the i direction of the cell and the U_i is the velocity in the same cell and direction. The value of $\Delta x_i / U_i$ used to calculate the time step is the lowest one found in the computational domain.

To solve efficiently the system of equations (1)-(3) it is necessary to write an additional equation for the pressure. In case the momentum and the pressure equations are not solved simultaneously the system becomes stiff and a small time step is required to obtain a solution. The stability criteria for the system mentioned above is: $Co \leq 1$.

In OpenFOAM it is possible to couple the equations through the PIMPLE algorithm. The algorithm consist in a loop where every equation is decoupled from the other and solved sequentially. The loop is repeated a fixed number of times. In this way it is possible to introduce under relaxation factors and the system becomes stable for a wide range of Courant numbers ≥ 1. However, by fixing the number of iterations of the algorithm and increasing the Courant number the time accuracy of the simulations reduces as it is shown in Fig. 3.

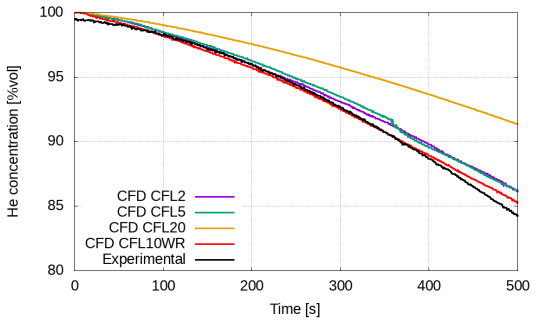

Figure 3: Influence of time discretization on the Helium concentration in a fixed point of the computational domain.

The purple (CFL2), green (CFL5) and orange (CFL20) curves represents the helium concentration in the upper part of the first compartment, obtained with simulations in which the Courant number was changed and the number of iterations of the PIMPLE

algorithm is kept constant and equal to 3. The curves corresponds respectively to Courant numbers of 2, 5 and 20, while the black curve is constructed form the experimental data in the same location. As it can be seen the accuracy of the simulation is progressively reduced as the time step is increased, and the relative error, after 500 s of physical time, increases from 2.3%, for the case with the smallest time step, to 8.5% for the case with the biggest time step.

This loss of accuracy happens because the number of iterations of the PIMPLE algorithm is kept constant, and when the Courant number is increased convergence of the solution within a time step is not achieved.

However within the loop of the PIMPLE algorithm it is possible to set a convergence criteria for each variable. The red curve (CFL10WR) in Fig. 3 shows the results of a simulation in which the Co number is fixed to 10 but the number of iteration of the PIMPLE loop is not fixed, and the equations are sequentially solved until the residuals of all the variables are reduced to 10^{-3}. With this method the number of iterations within a time step is , for most of the simulation, between 3 and 6 and the relative error is reduced to 1.3%.

5. Results

The validation procedure has been carried out by comparing the Helium concentration profile, in different positions of the computational domain, obtained with the numerical simulations, against the experimental data.

5.1. Mesh convergence

The first step in the validation procedure has been the testing of different meshes. The aim has been to compare the influence of an uniform refinement of the numerical grid with a localised refinement. Fig. 4 shows the helium concentration profiles in the centre line of the first compartment, where the hot air injection is located, at a fixed time $t = 300s$. The profiles are obtained by performing numerical simulations using different computational grids. The details of the different meshes are reported in Tab. 3.

The first two meshes have a uniform size of the cells in the whole domain, except from area near the walls, the injection point and the venting. The simulations done with both those grids fail to predict the evolution of the helium concentration profile. Moreover, in the case of the refined mesh the increase of the number of

Table 3: Characteristic of the meshes used in the study.

	N° cells	Δt [s]	CPU time [h]
Coarse Mesh	307765	$1.3 \cdot 10^{-2}$	640
Fine Mesh	665677	$7 \cdot 10^{-3}$	4515
PR	410015	$1.3 \cdot 10^{-2}$	1152
IP	578266	$1.3 \cdot 10^{-2}$	2572

cells and the decrease of the time step, leads to a great increase in the computational cost of the simulation.

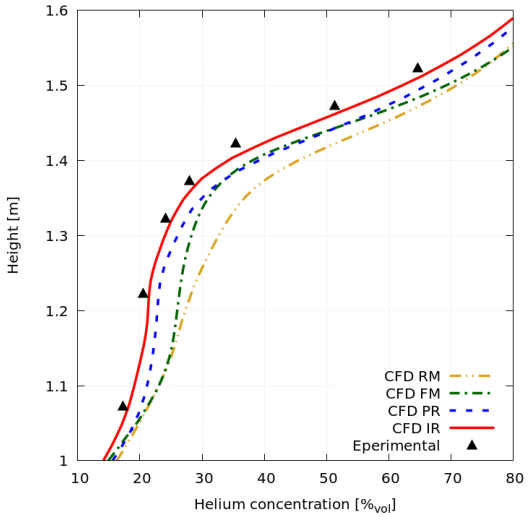

Figure 4: Effect of mesh refinement on the Helium concentration profile in the centre line of the first compartment.

The last 2 computational grids have been constructed form the original mesh, by sequentially refining the piping (PR) and the area above above the injection point (IR).

When the stratification is dissolved, helium is transported through the piping. However, when helium reaches the second compartment, due to its low density, buoyancy forces push it upward and force air to recirculate through the pipe to the first compartment, creating a stratified reverse flow, as shown in Fig. 5a . The simulation done with the original mesh failed to predict the stratification of the flow in the pipe (Fig. 5b), while by refining the computational grid in the pipe, the accuracy of the computation is increased, and the computational cost of the simulation is increased by a factor of 1.8.

In the last step the mesh has been refined in the area

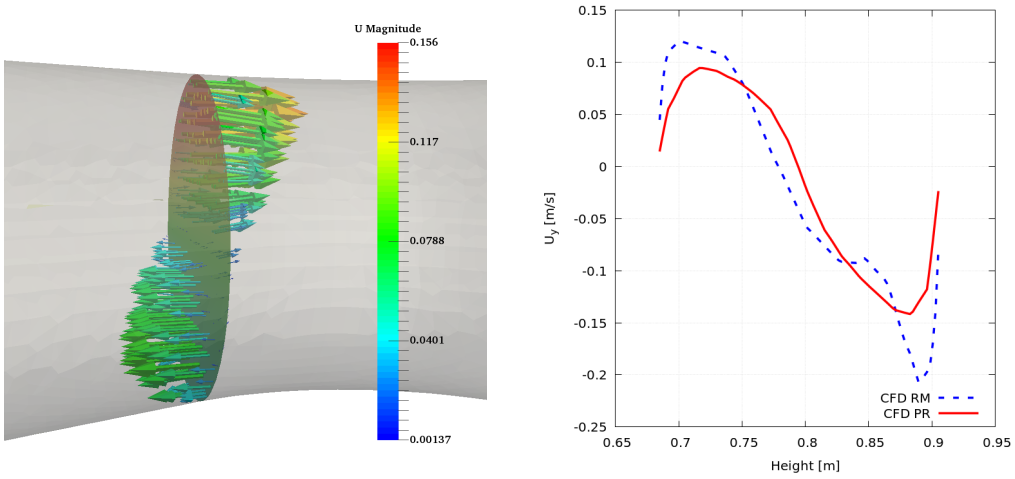

(a) (b)

Figure 5: Stratified reverse flow in the interconnecting pipe of the MiniPanda Facility (a) and vertical profile of the normal component of the velocity computed with two different meshes (b)

around the injection of the hot air, since the eroding jet is the most important feature of the flow field. The improvement of the mesh in this area leads to a better prediction of the entrainment of air in the jet, resulting in an accurate calculation of the shape of the jet and of the interaction with the stratified layer.

5.2. *Influence of the buoyancy*

The first case simulated is characterized by a Fr_i of 0.7 and a Pe_m of 530, meaning that the jet is driven by buoyancy forces.

In Fig. 6 are reported the results of simulations performed using different turbulence models. The lines shows the helium concentration profile at the centre line of the first compartment ate the time $t = 300s$. Both the standard $k - \epsilon$ model and the one including buoyancy modification fails to predict the interaction between the jet and the stratification.

The reason is that the $k-\epsilon$ overestimates the spreading on the jet [10], resulting in an higher diameter of the jet at the interaction with the stratification. As of Eqn. 11 and Eqn. 10, if the diameter d_0, is increased both the mass Peclet and the interaction Froude numbers increase, leading to a faster mixing of the gas and acceleration in the process of erosion of the stratification. For this reason the simulated helium concentration is higher than the experimental one in the area below the interaction of the jet and the stratification ($1.5m$) and lower in the area above.

Using the $k - \omega$ SST turbulence model, the spreading of the jet is well predicted resulting in a correct

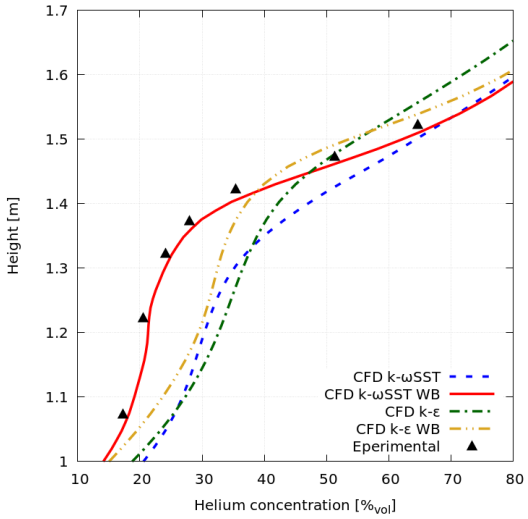

Figure 6: Helium concentration profile obtained with different turbulence models: $k - \omega SST$ (blue dashed line), $k - \omega$ SST with buoyancy correction (red line), $k - \epsilon$ (green dashed line), $k - \epsilon$ with buoyancy correction (yellow dashed line).

prediction of the interaction Froude number. However, the mixing rate is over estimated if the buoyancy force is not included in the turbulence model. The reason can be explained by looking at Fig. 7. The velocity profile, above the injection point, is directly influenced by the density profile (which is proportional

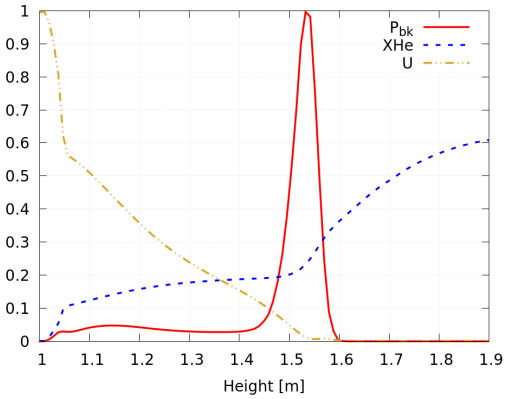

Figure 7: Non dimensional profile of velocity (blue dashed line), Helium concentration (yellow dashed line) and absolute value of turbulence production/destruction (red line), above the hot air injection point.

to the helium concentration), and the jet is stopped exactly where it comes in contact with the helium cloud. The deceleration of the jet leads also to the decrease of turbulence in the interaction area, resulting in a slowdown of the mixing process. The red curve in Fig. 7 is the absolute value of the source term Pb_k. The value is negative since the density gradient is in the same direction as the velocity, and it has its minimum in the interaction layer. The inclusion of this term in the turbulence equations, leads to a correct estimation of the eddy viscosity and of the turbulent diffusivity $D_t = \mu_t / Sc_t$. As a consequence the helium concentration profile is correctly predicted.

5.3. Influence of the flow rate on the erosion of the stratification

A second test case has been considered, where the mass flow rate of hot air has been increased to $1.51 g/s$. For this case the injection Froude number is $Fr_i = 1.3$ and the mass Peclet number is $Pe_m = 990$. Fig. 8 shows the calculated helium concentration profile at the centre line of the fist compartment at the time $t = 150 s$.

Compared to the first case the mixing process is faster and it is mostly driven by the inertial forces of the jet. For this reason not including the buoyancy forces in the turbulence model results in a lower error, although, it is still necessary to include it for an accurate prediction of the concentration profile.

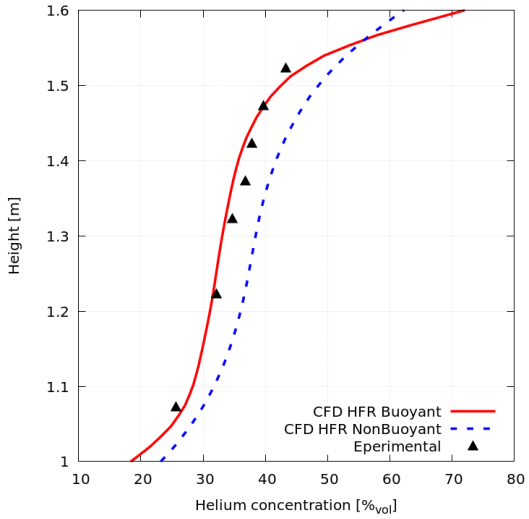

Figure 8: Influence of the buoyancy production/destruction on the Helium concentration profile in the centerline of the first compartment.

6. Conclusions and future work

The aim of this work has been to develop and validate CFD code for the erosion of light gas stratification in a closed atmosphere. The correct setting of the algorithm for the coupling of the equations is essential to obtain a accurate solution of the transient problem.

The mesh convergence study showed the importance of locally refining the mesh in the area of the domain where the main features of the flows are located.

In the end we showed the influence of buoyancy forces in turbulence models and demonstrated that it is really important to consider the effect of the density gradients in the cases where the flow is mostly driven by buoyancy.

The next step in the development of a simulation environment that can be used for the analysis of sever nuclear accidents, is the inclusion of steam and water in the mixture. This will lead to an increase in the complexity of the system because a liquid phase will have to be simulated and a proper model for the evaporation/condensation of the water will be required.

Acknowledgments

The development and validation of the CFD model for light gas transport and mixing have been sponsored by BelV (Belgium) and carried on at the von Karman Institute for Fluid Dynamics.

Special thanks to Dr. Ritterath and the Laboratory of Nuclear Energy Systems at Federal Institute of Technology Zrich (ETHZ), for providing the experimental database.

References

[1] M. Ritterath, Instrumentation and mixing experiments on safety relevant gas flows in containments of nuclear reactors, Ph.D. thesis, ETH Zurich Switzerland (2012).

[2] G. Yadigaroglu, M. Andreani, J. Dreier, P. Coddington, Trends and needs in experimentation and numerical simulation for LWR safety., Nuclear Engineering and Design 221 (2003) 205223.

[3] S.Gupta, E.Schmidt, B.von Laufenberg, M.Freitag, G.Poss, F.Funke, G.Weberc, THAI test facility for experimental research on hydrogen and fission product behaviour in light water reactor containments, Nuclear Engineering and Design 294 (2015) 183–201.

[4] S. Kelm, M. Ritterath, H.M. Prasser, H.J. Allelein., Application of the MiniPanda test case 'erosion of a stratified layer by a vertical jet' for CFD validation, Nuclear Engineering and Design 299 (2016) 124–135.

[5] B.E.Launder, D.B.Spalding, "the numerical computation of turbulent flows.

[6] F. R. Menter, Two-equation eddy-viscosity turbulence models for engineering applications", AIAA Journal, AIAA Journal 32 (8) (1993) 1598–1605.

[7] E.N. Fuller, P.D. Schettler, J.C. Giddings, New method for prediction of binary gas-phase diffusion coefficients, Industrial Engineering and Chemistry 58 (5) (1966) 1827.

[8] Y. Tominaga, T. Stathopoulos, Turbulent Schmidt numbers for CFD analysis with various types of flowfield, Atmospheric Environment 41.

[9] A.W. Cook, Enthalpy diffusion in multicomponent flows, Physics of Fluids 21.

[10] S.B. Pope, An explanation of the turbulent round-jet/plane-jet anomaly, AIAA Journal 16.

Development of wake meandering detection algorithms and their application to large eddy simulations of a wind turbine

Nicolas Coudou

Environmental and Applied Fluid Dynamics Department, von Karman Institute for Fluid Dynamics, Belgium, nicolas.coudou@vki.ac.be

Fluids-Machines unit, Université de Mons, Belgium

Institute of mechanics, materials and civil engineering, Université catholique de Louvain, Belgium

Supervisor: Jeroen van Beeck

Professor, Environmental and Applied Fluid Dynamics Department, von Karman Institute for Fluid Dynamics, Belgium, vanbeeck@vki.ac.be

University Supervisor: Laurent Bricteux

Professor, Fluids-Machines unit, Université de Mons, Belgium, Laurent.BRICTEUX@umons.ac.be

University Supervisor: Philippe Chatelain

Professor, Institute of mechanics, materials and civil engineering, Université catholique de Louvain, Belgium, philippe.chatelain@uclouvain.be

Abstract

We investigate several algorithms to perform run-time tracking of a wake centerline during large eddy simulations of an isolated wind turbine subject to a uniform and a turbulent inflow. The simulations are performed using a vortex-particle mesh method with the blades modeled using immersed lifting lines. The most robust algorithm is then applied to a 3×5 wind farm.

Keywords: LES, Vortex Particles-Mesh method, Wake meandering, Wake tracking, Wind turbine

1. Introduction

Wind turbine wake meandering is a critical issue in wind farms as this oscillatory motion of the wakes increases fatigue loads on downstream machines and impacts their power production. The first step to study this phenomenon is to detect the wake centerline. Several methods are used in the literature, usually to detect the position of the wake for turbines in yaw [1; 2; 3; 4]. In this work, we compare several techniques based on linear/angular impulse, velocity/momentum deficit and available power in the flow for run-time tracking of the wake centerline during large eddy simulations of the NREL offshore 5-MW baseline wind turbine subject to a uniform inflow and to a synthetic turbulent inflow. The simulations are performed with a state-of-the-art Vortex Particle-Mesh (VPM) method combined with immersed lifting lines [5; 6; 7]. The most robust technique is then deployed inside a fourth-order finite differences [8] code to track the wakes of the machines at wind farm scale.

2. Methodology

2.1. The Vortex Particle-Mesh method

The Vortex Particle-Mesh method [5; 6; 7] relies on the discretization of the velocity ($\mathbf{u}$)-vorticity ($\boldsymbol{\omega} = \nabla \times \mathbf{u}$) formulation of the Navier-Stokes equations in a Lagragian form. For an incompressible flow, it gives

$$\frac{D\boldsymbol{\omega}}{Dt} = (\boldsymbol{\omega} \cdot \nabla)\,\mathbf{u} + \nu \nabla^2 \boldsymbol{\omega}, \tag{1}$$

$$\nabla \cdot \mathbf{u} = 0, \tag{2}$$

where $\frac{D}{Dt} = \frac{\partial}{\partial t} + \mathbf{u} \cdot \nabla$ denotes the Lagrangian derivative and ν is the kinematic viscosity.

Vortex particle methods [5; 6; 7; 9] discretize the vorticity field with particles, characterized by a position $\mathbf{x}_p$, a volume V_p and a strength $\alpha_p = \int_{V_p} \boldsymbol{\omega} d\mathbf{x} \approx \boldsymbol{\omega}_p V_p$. Particles are advected by the flow field and their strength is modified to account for vortex stretching and diffusion

$$\frac{d\mathbf{x}_p}{dt} = \mathbf{u}\left(\mathbf{x}_p\right), \tag{3}$$

$$\frac{d\boldsymbol{\alpha}_p}{dt} = \int_{V_p} \left((\boldsymbol{\omega}\cdot\nabla)\,\mathbf{u} + \nu\nabla^2\boldsymbol{\omega}\right) d\mathbf{x} \tag{4}$$

$$\simeq \left((\boldsymbol{\omega}\cdot\nabla)\,\mathbf{u} + \nu\nabla^2\boldsymbol{\omega}\right)_p V_p. \tag{5}$$

The velocity field $\mathbf{u}$, which is needed for the above particles evolution equations, can be recovered from the vorticity through an Helmholtz decomposition $\mathbf{u} = \mathbf{U}_\infty + \mathbf{u}_\omega$ and the Poisson equation

$$\nabla^2\mathbf{u}_\omega = -\nabla\times\boldsymbol{\omega}. \tag{6}$$

The use of a mesh along with the particles in the VPM method offers several advantages. The mesh enables the treatment of the Lagrangian distortion through the periodic regularization onto the grid of the particles set (remeshing) [9]. In addition, the mesh handles the computationally intensive tasks : the evaluation of differential operators and the use of fast Poisson solvers for the computation of velocity, which allow the combination of unbounded directions and inlet/outlet boundaries. Both discretizations communicate through high order interpolation.

Since the flow passing a wind turbine is a complex turbulent flow at high Reynolds number, it quite naturally imposes the use of a Large Eddy Simulation (LES) approach. Our LES vorticity-velocity equations are then

$$\frac{D\boldsymbol{\omega}}{Dt} = (\boldsymbol{\omega}\cdot\nabla)\,\mathbf{u} + \nu\nabla^2\boldsymbol{\omega} + \nabla\cdot\mathbf{T}^M \tag{7}$$

where $\mathbf{T}^M$ is the subgrid-scale stress model. In this work, we use the Regularized Variational Multiscale (RVM) model [10] which is designed as an eddy viscosity model acting only on the small scales

$$\mathbf{T}^M = \nu_{SGS}\left(\nabla\boldsymbol{\omega}^s + \nabla^T\boldsymbol{\omega}^s\right) \tag{8}$$

where $\boldsymbol{\omega}^s$ represents the small-scales part of the vorticity field. The eddy viscosity $\nu_{SGS} = C_r^{(n)}\Delta^2\,(2S:S)^{1/2}$ is evaluated using the complete velocity field: the strain rate tensor is thus given by $S = 1/2(\nabla\mathbf{u} + \nabla^T\mathbf{u})$. The LES cutoff Δ is taken equal to the mesh size h. The small scale vorticity field is computed by removing a low pass filtered vorticity field $\bar{\boldsymbol{\omega}}^{(n)}$

$$\boldsymbol{\omega}^s = \boldsymbol{\omega} - \bar{\boldsymbol{\omega}}^{(n)} \tag{9}$$

itself obtained by the iterated application of a discrete filter in physical space (n = 1 in the present work). We refer to [11] for a more detailed exposition of the subgrid-scale model.

The use of this hybrid discretization offers several advantages. The particles are used solely for the advection, thereby avoiding dispersion errors and waiving classical time stability constraints (CFL number). They also exploit the compactness of vorticity support while the mesh handles the computationally intensive tasks, leading to high computational gains for external flow simulations [7].

Concerning the spatial and temporal discretization, a fourth order finite difference scheme is used to carry out the differential operators and a third-order low-storage Runge-Kutta scheme is used for the time integration.

2.2. Blades modeling through immersed lifting lines

The generation of vorticity along the rotor blades is accounted for through immersed lifting lines. Under the assumption of slender blades, we can approximate a blade as a concentrated bound vortex going through the quarter-chord line, and treat the flow around the airfoil in a section as essentially two-dimensional. For a steady flow, the lift per unit span $\mathbf{L}$ and the bound circulation $\boldsymbol{\Gamma}(r,t)$ are then related by the Kutta-Joukowski theorem

$$\mathbf{L} = \rho\mathbf{V}_{rel}\times\boldsymbol{\Gamma} \tag{10}$$

where ρ is the air density and $\mathbf{V}_{rel} = \mathbf{u} - \mathbf{u}_{blade}$ is the velocity relative to the blade. We note that the application of such a relationship in unsteady flow conditions means that our approach makes a quasi-steady assumption about the generation of lift and circulation around the airfoil. Since the lift can also be obtained from the relative velocity and the airfoil lift and drag coefficients C_L and C_D, the bound circulation $\boldsymbol{\Gamma}(r,t)$ can be computed as well as the shed vortex sheet from the solenoidal property of $\boldsymbol{\omega}$ (Fig. 1). The particle discretization of this bound vortex and our particle-mesh toolset then enable the interpolation of the velocity field onto these particles and the geometric construction of the shed vorticity with Lagrangian tracers a la

vortex lattice method, accounting for time and space variations of the circulation $\mathbf{\Gamma}(r,t)$ (Fig. 1). This treatment is fully Lagrangian and allows large time steps unconstrained by the blade tip speed, unlike an actuator line technique [6].

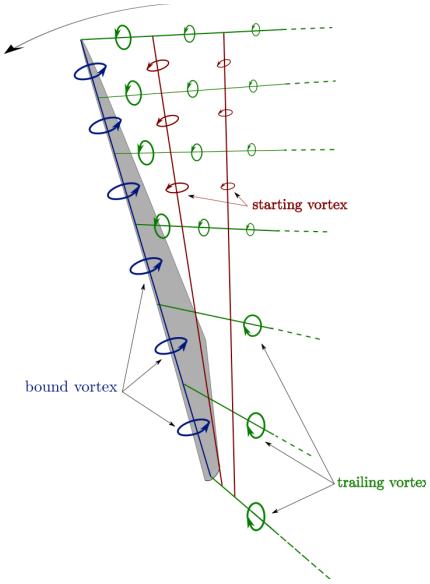

Figure 1: Immersed lifting line : blade vorticity sources modeled through a lifting line approach [6].

2.3. Turbulent inflow

A turbulent velocity field $\mathbf{u}'$ is synthesized through Mann's algorithm [12]. In order to carry the turbulence into the domain through the inflow plane, this turbulent velocity field is translated into a set of vorticity particles, as required for the Lagrangian method used. Note that due to the unbounded conditions in the $y-$ and $z-$directions, this initially periodic velocity field is made compact through a smooth clipping along its edges.

2.4. Wake centerline diagnostics

The proposed diagnostics take advantage of the specific signatures of a wind turbine wake, namely its vortical structures, the deficits of mass flow, momentum, and available power in the flow. The first investigated technique relies on the moments of vorticity in a cross-flow plane, i.e. the densities of linear and angular impulse, along and about $\mathbf{e}_x$, i_x and l_x

$$i_x = \frac{1}{2}\left(\mathbf{x}\times\boldsymbol{\omega}\right)\cdot\mathbf{e}_x\,,\ l_x = \frac{1}{3}\left(\mathbf{x}\times\left(\mathbf{x}\times\boldsymbol{\omega}\right)\right)\cdot\mathbf{e}_x. \quad (11)$$

One can also use the analogy with the displacement and momentum thicknesses of a boundary layer [13] and exploit the densities of the deficits of velocity/momentum in a cross-flow plane in the wake

$$s_1 = U_\infty - u_x\,,\ s_2 = \left(U_\infty - u_x\right)u_x. \quad (12)$$

From one of these densities $q = i_x, l_x, s_1, s_2$, the centroid of the wake can be obtained in every plane normal to the streamwise direction by computing the first moment of the density q [4]

$$y_c = \frac{\int y\,q dS}{\int q dS}\,,\ z_c = \frac{\int z\,q dS}{\int q dS}. \quad (13)$$

Given the deficit of available energy in the wake of a wind turbine, we also tested a diagnostic based on the available power density in the wake. The principle of this method is to compute the power inside several disks of a diameter equal to the rotor diameter D and located in a cross-flow plane; these disks being shifted in $y-$ and $z-$direction. The wake center corresponds to the center of the disk with the minimum available power [3]. Practically, this method consists in locating the minimum of the 2D convolution

$$\begin{aligned}\left(y_c, z_c\right) &= \operatorname{argmin}\left(p\left(y,z\right) * f_s\left(y,z\right)\right)\\ &= \operatorname{argmin}\left(\int_{-\infty}^{\infty}\int_{-\infty}^{\infty} p\left(\tau_1,\tau_2\right)\right.\\ &\qquad\left.\cdot\, f_s\left(y-\tau_1, z-\tau_2\right)d\tau_1 d\tau_2\right)\end{aligned} \quad (14)$$

between the available power density $p(y,z) = \frac{1}{2}u_x|\mathbf{u}|^2$ and a masking function f_s set to minus unity inside the rotor disk and to zero outside of it

$$f_s(y,z) = \begin{cases} -1 \text{ if } y^2+z^2 < \left(\frac{D}{2}\right)^2, \\ 0 \text{ otherwise.}\end{cases} \quad (15)$$

Since VPM relies on a structured mesh, the convolutions are performed efficiently in wavespace using Fast Fourier Transforms.

Due to the good quality of the results obtained with this last method, the convolution was also performed using the densities of velocity/momentum deficit (Eq. 12) in the wake.

Finally, the influence of the mask was investigated by replacing the discontinuous masking function by a continuous one

$$f_g(y,z) = A\exp\left(-\left(\frac{\left(y-\mu_y\right)^2}{2\sigma_y^2} + \frac{\left(z-\mu_z\right)^2}{2\sigma_z^2}\right)\right) \quad (16)$$

with $A = -1$, $\mu_y = \mu_z = 0$, and $\sigma_y = \sigma_z = D/4$.

In order to obtain the wake centerline, these techniques are applied in each cross-flow plane (depending on the mesh resolution) in the wake of the machine.

3. Computational setup

The LES computations are performed for the NREL offshore 5-MW baseline wind turbine [14] operating at its optimum tip-speed ratio $TSR = 7.55$. Only the blades of the wind turbine are modeled using immersed lifting lines. The spatial resolution is such that 32 points are used to model each blade. The computational domain initially extends over $14D \times 4D \times 4D$ ($L_x \times L_y \times L_z$); the domain is unbounded in $y-$ and $z-$directions. Based on the spatial resolution of the blades, it leads to an initial grid with approximately 59 millions nodes. The wind turbine rotor is located $3D$ after the inlet and is subject to a uniform and a turbulent wind. The inflow velocity is $U_\infty = 9$ ms^{-1} in the $x-$direction and the turbulence intensity $TI = u'/U_\infty = 0\%$ and $TI = 10\%$. The turbulent field is synthesized through Mann's algorithm and fills a $26D \times 4D \times 4D$ box.

The simulations were performed on the Tier-1 supercomputer with 512 processors in less than a half-day, what shows the efficiency of the computational method. The wake centreline diagnostics were started after one convective time $t^* = L_x/U_\infty$.

4. Results

The diagnostics presented in Section 2.4 are first applied to the wake of an isolated wind turbine subject to a uniform and a turbulent inflow, and then to the wakes of a 3×5 wind farm subject to a turbulent inflow.

4.1. Isolated wind turbine

4.1.1. Uniform inflow

Figure 2 a,c,e,g,i shows snapshots of diagnostic quantities with the wake center superimposed in a cross-flow slice located at $x/D = 5$ and Fig. 2 b,d,f,h,j shows snapshots of dimensionless velocity fields in a horizontal slice located at hub height on which the wake centerline is superimposed. As expected for a uniform inflow ($TI = 0\%$), all the techniques provide a wake centerline that remains close to the rotational axis of the rotor, except for that based on the angular impulse. The techniques based on the linear and angular impulse produce clearly a noisier signal compare to the other techniques. The diagnostic based on the convolution between the available power and a circular mask leads to some oscillations in the near wake because it does not account for the presence of the hub jet within the wake.

4.1.2. Turbulent inflow

The techniques applied in Section 4.1.1 are now applied to a turbulent inflow ($TI = 10\%$). Figure 3 a,c,e,g,i shows snapshots of diagnostic quantities with the wake center superimposed in a cross-flow plane located at $x/D = 5$ and Fig. 3 b,d,f,h,j shows snapshots of dimensionless velocity fields in a horizontal slice located at hub height on which the wake centerline is superimposed. As it can be observed, only the techniques based on the velocity/momentum deficit and on the convolution between the available power and a circular mask are robust enough once the inflow is turbulent; the other techniques are too sensitive to the ambient turbulence.

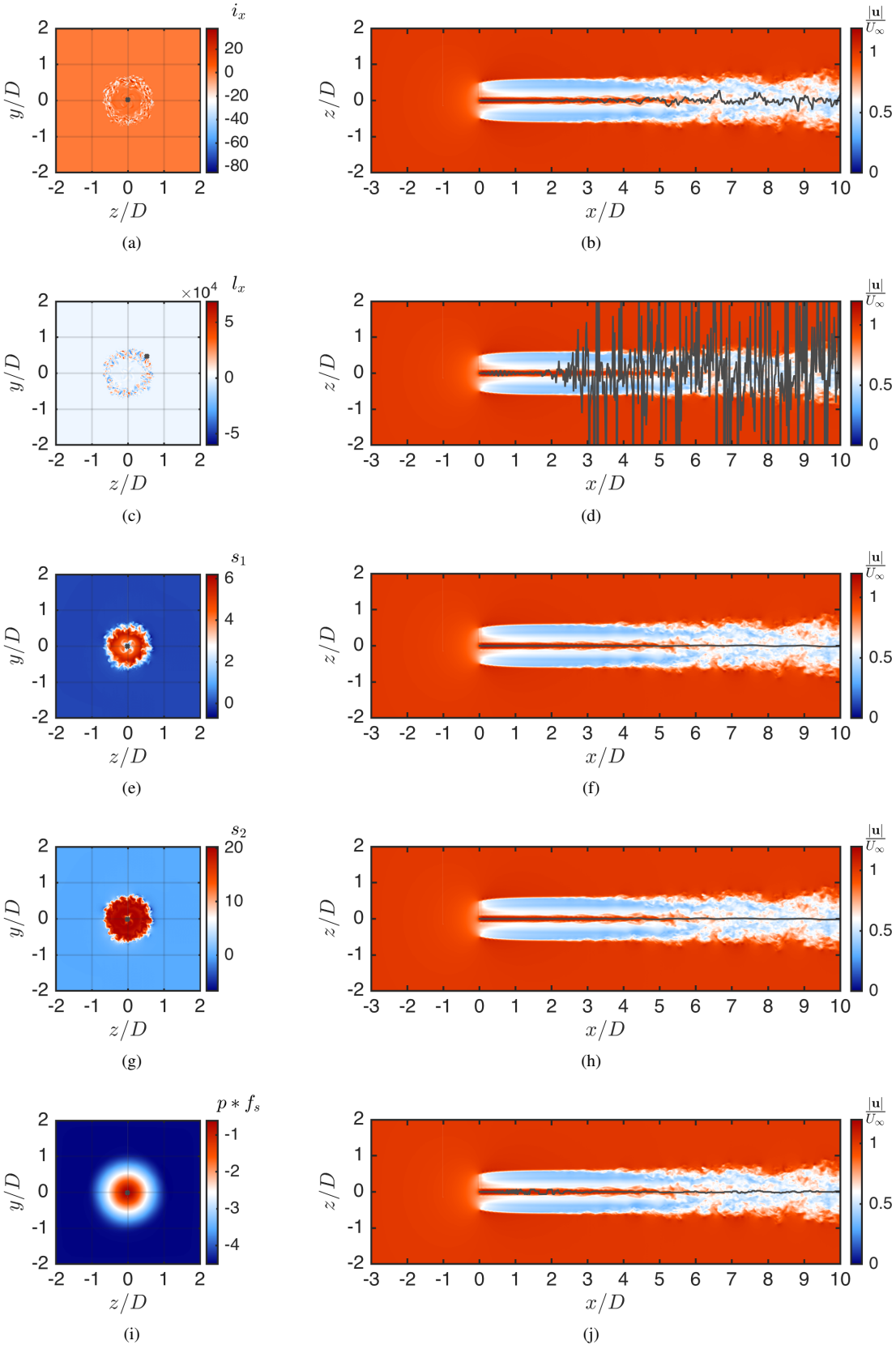

Figure 2: *Left*: Wake center position superimposed on snapshots, in a cross-flow slice located at $x/D = 5$, of the densities of linear impulse (a), angular impulse (c), velocity deficit (e), momentum deficit (g), and on the convolution between a circular mask of a diameter D and the density of available power (i). *Right* : Snapshots, in a horizontal slice located at hub height, of dimensionless velocity magnitude on which is superimposed the wake centerline obtained with the diagnostic based on the linear impulse (b), angular impulse (d), displacement deficit (f), momentum deficit (h), and convolution between a circular mask of a diameter D and the density of available power (j). Uniform inflow with $TI = 0\%$.

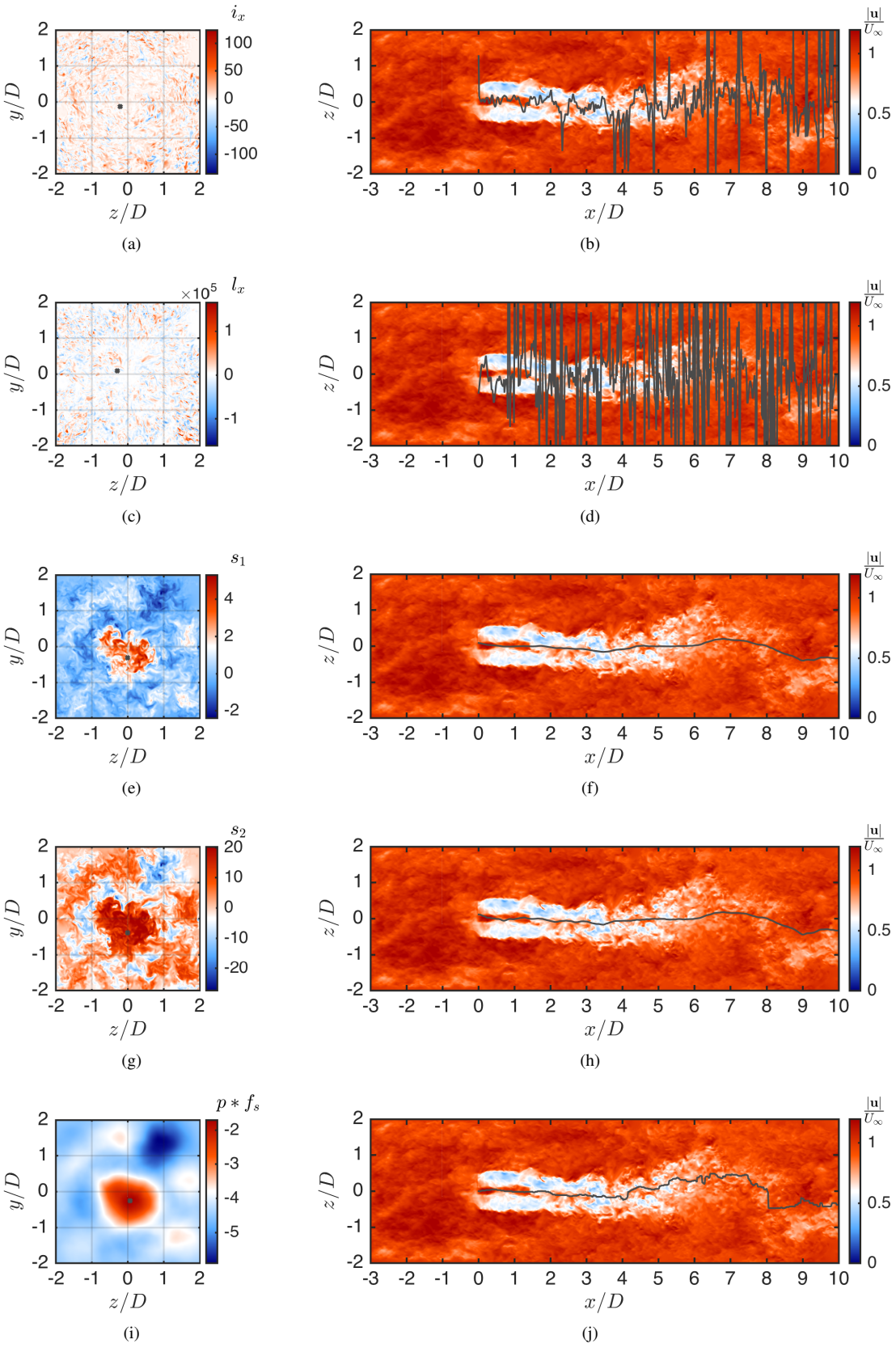

Figure 3: *Left*: Wake center position superimposed on snapshots, in a cross-flow slice located at $x/D = 5$, of the densities of linear impulse (a), angular impulse (c), velocity deficit (e), momentum deficit (g), and on the convolution between a circular mask of a diameter D and the density of available power (i). *Right* : Snapshots, in a horizontal plane located at hub height, of dimensionless velocity magnitude on which is superimposed the wake centerline obtained with the diagnostic based on the linear impulse (b), angular impulse (d), displacement deficit (f), momentum deficit (h), and convolution between a circular mask of a diameter D and the density of available power (j). Turbulent inflow with $TI = 10\%$.

It also appears that the wake centerlines obtained through Eq. 13 applied to the velocity/momentum deficit seem to be "smoothed" in comparizon with the one obtain from the convolution between the circular mask and the available power in the flow; they therefore follow less properly the wake motion. This encourages to try to apply the convolution method with the velocity/momentum deficit densities instead of the available power density. Figure 4 shows the result of these convolutions. The wake centerlines appear now to follow more properly the wake motion than with the application of Eq. 13. Figure 5 shows that the change from the available power density to the velocity/momentum deficit densities in the convolution method does not have a significant impact on the wake centerline localization.

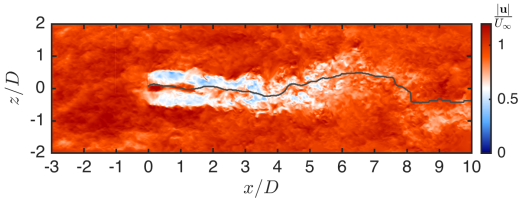

(a)

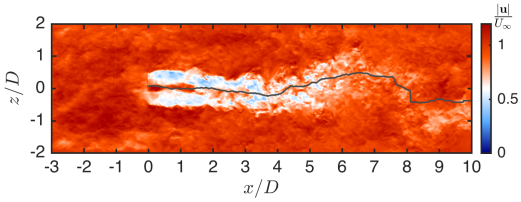

(b)

Figure 4: Snapshots, in a horizontal plane located at hub height, of dimensionless velocity magnitude on which is superimposed the wake centerline obtained with the method based on the convolution between a circular mask of a diameter D and the densities of velocity deficit (a) and momentum deficit (b). Turbulent inflow with $TI = 10\%$.

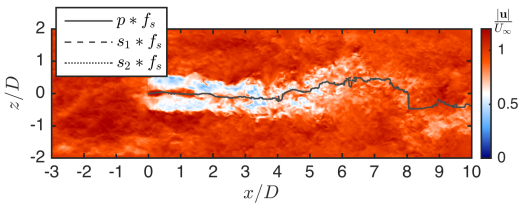

Figure 5: Snapshot, in a horizontal plane located at hub height, of the dimensionless velocity magnitude on which is superimposed the wake centerline obtained with the method based on the convolution between a circular mask of a diameter D and the densities of power, velocity deficit and momentum deficit. Turbulent inflow with $TI = 10\%$.

It is also interesting to investigate the influence of the mask used for the convolution. This is done by replacing the discontinuous masking function (Eq. 15) by a continuous one (Eq. 16). As it can be observed on Fig. 6, the mask has a larger influence than the field density on the wake centerline localization.

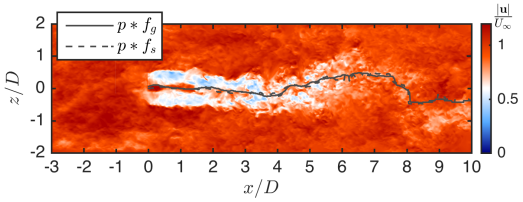

(a)

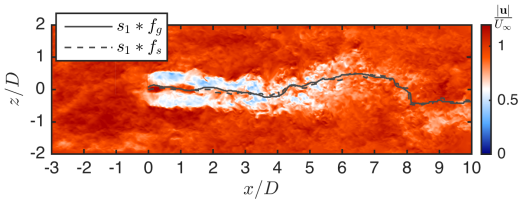

(b)

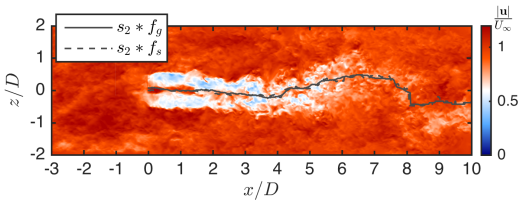

(c)

Figure 6: Snapshots, in a horizontal plane located at hub height, of dimensionless velocity magnitude on which is superimposed the wake centerline obtained with the method based on the convolution between a circular/gaussian mask of a diameter D and the densities of power (a), velocity deficit (b) and momentum deficit (c). Turbulent inflow with $TI = 10\%$.

4.2. Wind farm

Some of these techniques are currently deployed by a colleague [M. Moens, UCL] within a wind farm simulation tool based on fourth-order finite differences and actuator disks [8]. Figure 7 shows preliminary results obtained in a snapshot of velocity field for a 15-machine wind farm.

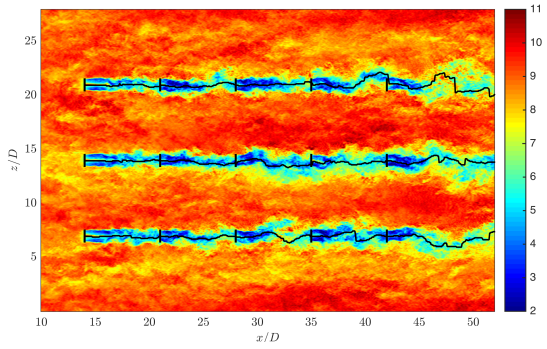

Figure 7: Snapshot, in a horizontal slice located at hub height, of the velocity magnitude on which are superimposed the wake centerlines obtained with the method based on the convolution with the available power inside the wind farm [M. Moens, UCL]. The units are in [m s^{-1}].

5. Conclusions and perspectives

The Vortex Particle-Mesh method used in this work allows the accurate capture of wake dynamics with minimal spurious dispersion and diffusion, what makes it an efficient tool to investigate the meandering of wind turbine wake. Several run-time, computationally-efficient wake tracking techniques were therefore implemented inside this tool to track the wake centerline of an isolated wind turbine subject to a uniform ($TI = 0\%$) and a turbulent inflow ($TI = 10\%$). The results show the robustness of the technique exploiting the convolution. Additional investigations for this method highlight that the influence of the field density used in the convolution is weaker than the influence of the mask shape. It was therefore decided to select the method based on the convolution between the available power density and a gaussian mask to study the wake positions inside a wind farm. Indeed, the available power is a quantity of high interest concerning the power production of wind turbines and the gaussian mask is a good candidate for further improvements of the technique.

In that context, we note that it could be interesting to implement the method in such a way to have an adaptation of $\sigma_{y,z}$ of the masking function as a function of space and time. We hope to obtain a growing evolution of the $\sigma_{y,z}$ equivalent to the one of the wake. This method will then be implemented and tested on long-time large-scale simulations of a isolated wind turbine and on a wind farm for the characterization of the wake meandering phenomenon and for the development and assessment of real-time wake models.

The perspectives of this work are many; we identify two main ones: (1) the tuning and validation of operational wake models [15] and (2) a support to wake-detection for the development of turbine and farm-level control schemes.

Acknowledgments

Nicolas Coudou is funded by the *Fonds pour la Formation à la Recherche dans l'Industrie et dans l'Agriculture (FRIA)*, Belgium. The simulations used computational resources made available on the Tier-1 supercomputer of the Federation Wallonie-Bruxelles, infrastructure funded by the Walloon Region under the Grant Agreement No. 1117545

6. References

References

[1] F. Bingöl, J. Mann, G. C. Larsen, Light detection and ranging measurements of wake dynamics part I: one-dimensional scanning, Wind Energy 13 (1) (2010) 51–61.

[2] S. Aubrun, T. F. Tchouaké, G. España, G. Larsen, J. Mann, F. Bingöl, Progress in Turbulence and Wind Energy IV: Proceedings of the iTi Conference in Turbulence 2010, Springer Berlin Heidelberg, Berlin, Heidelberg, 2012.

[3] L. Vollmer, G. Steinfeld, D. Heinemann, M. Kühn, Estimating the wake deflection downstream of a wind turbine in different atmospheric stabilities: an LES study, Wind Energy Science 1 (2) (2016) 129–141.

[4] M. F. Howland, J. Bossuyt, L. A. Martínez-Tossas, J. Meyers, C. Meneveau, Wake structure in actuator disk models of wind turbines in yaw under uniform inflow conditions, Journal of Renewable and Sustainable Energy 8 (4) (2016) 043301. doi:10.1063/1.4955091.

[5] P. Chatelain, A. Curioni, M. Bergdorf, D. Rossinelli, W. Andreoni, P. Koumoutsakos, Billion vortex particle direct numerical simulations of aircraft wakes 197 (13) (2008) 1296–1304.

[6] P. Chatelain, S. Backaert, G. Winckelmans, S. Kern, Large eddy simulation of wind turbine wakes, in: W. Rodi (Ed.), Proceedings of The 9th International Symposium on Engineering Turbulence Modelling and Measurements (ETMM-9), June 6–8, 2012, Thessaloniki, Greece, Vol. 91 of Flow, Turbulence and Combustion, ERCOFTAC, Springer, 2013, pp. 587–605. doi:10.1007/s10494-013-9474-8.

[7] S. Backaert, P. Chatelain, G. Winckelmans, Vortex particle-mesh with immersed lifting lines for aerospace and wind engineering, in: J. H. Walther (Ed.), Symposium on Particle Methods in Fluid Dynamics, October 15-17 2012, DTU Copenhagen, Vol. 18 of Procedia IUTAM, IUTAM, 2015, pp. 1–7. doi:10.1016/j.piutam.2015.11.001.

[8] M. Moens, M. Duponcheel, G. Winckelmans, P. Chatelain, Les of wind farm response to transient scenarios using a high fidelity actuator disk model, Journal of Physics: Conference Series 753 (2016) 032053.

[9] G. Winckelmans, Vortex methods, in: E. Stein, R. De Borst, T. J. Hughes (Eds.), Encyclopedia of Computational Mechanics, Vol. 3, John Wiley and Sons, 2004.

[10] H. Jeanmart, G. Winckelmans, Investigation of eddy-viscosity models modified using discrete filters: A simplified "regularized variational multiscale model" and an "enhanced field model" 19 (5) (2007) 055110. doi:10.1063/1.2728935.

[11] R. Cocle, L. Bricteux, G. Winckelmans, Scale dependence and asymptotic very high reynolds number spectral behavior of multiscale subgrid models 21 (8) (2009) 085101. doi:10.1063/1.3194302.

[12] J. Mann, Wind field simulation, Probabilistic Engineering Mechanics 13 (4) (1998) 269–282.
URL http://www.sciencedirect.com/science/article/pii/S0266892097000362

[13] S. Pope, Turbulent Flows, Cambridge University Press, 2000.
URL https://books.google.be/books?id=HZsTw9SMx-0C

[14] J. Jonkman, S. Butterfield, W. Musial, G. Scott, Definition of a 5-mw reference wind turbine for offshore system development, Tech. Rep. NREL/TP-500-38060, National Renewable Energy Laboratory (NREL) (February 2009).

[15] Y. Marichal, I. De Visscher, P. Chatelain, G. Winckelmans, Towards physics-based operational modeling of the unsteady wind turbine response to atmospheric and wake-induced turbulence, Journal of Physics: Conference Series 854 (1) (2017) 012030.
URL http://stacks.iop.org/1742-6596/854/i=1/a=012030

Analytical and experimental investigation of icing phenomena on wind turbine blades

Adriana Enache

Environmental and Applied Fluid Dynamics Department, von Karman Institute for Fluid Dynamics, Belgium, adriana.enache@vki.ac.be

Supervisor: Jeroen van Beeck

Professor, Environmental and Applied Fluid Dynamics Department, von Karman Institute for Fluid Dynamics, Belgium, vanbeeck @vki.ac.be

Co-Supervisor: Philippe Planquart

Research Engineer, Environmental and Applied Fluid Dynamics Department, von Karman Institute for Fluid Dynamics, Belgium, philippe.planquart @vki.ac.be

University Supervisor: Herman Deconinck

Professor, Aero-Thermo-Mechanics Department, Université libre de Bruxelles, Belgium, hdeconink@ulb.ac.be

Abstract

Operating wind turbines in icing conditions is the biggest challenge of wind energy production in cold climate regions. For a wide range of low temperatures, the supercooled water droplets present in the atmosphere freeze at impact with the turbine blades. Depending on the atmospheric conditions, these form rime or glaze ice accretion profiles, which degrade the aerodynamic blade properties and lower the energy production. Furthermore, the ice accretion generates unbalanced forces acting on the rotor and important safety hazards due to ice shedding.

In order to limit these negative effects, ice mitigation systems are used. These techniques imply high additional costs and have several drawbacks, being sometimes inefficient or decreasing the wind turbine capacity.

This project proposes an experimental and analytical research of the most typical icing phenomena, in order to investigate the drawbacks of widely used electro-thermal de-icing systems. For this mitigation technique, the applied heat transfer induces a phase change at the blade-ice interface. Under the action of wind generated dynamical forces, two phenomena are possible: the ice can slide and refreeze backward on the blade profile - creating the run-back ice phenomena, or it can detach from the substrate - producing ice shedding.

To obtain a complete understanding of which parameters trigger each phenomenon, a series of experimental campaigns will be conducted in the VKI icing wind tunnel (CWT-1) facility.

First, the effects of different ice accretion regimes over the wind turbine blade aerodynamic performances will be studied. Second, resistive elements will be applied to a simplified configuration and, by using laser illuminated flow visualizations, the phase change and the liquid layer evolution and properties that influence the run-back ice phenomenon will be studied. As a third step, a three component force balance will be used to determine the critical parameters that produce the ice shedding. These benchmark cases will improve the development of an analytical model which will be used to design an optimized de-icing system.

The last experimental campaign will consist in testing the optimized de-icing technique in a real wind turbine blade configuration.

The final aim of this research project is to generate an easy to use analytical tool to improve the electro-thermal de-icing systems design, increasing their efficiency. Furthermore, the acquired experimental data could provide validation for already existing CFD codes.

Keywords: wind turbine, run-back ice, ice shedding, electro-thermal de-icing systems, heat transfer, phase change

Experimental study of different cavitating regimes through an orifice

Claudia Esposito

Environmental and Applied Fluid Dynamics Department, von Karman Institute for Fluid Dynamics, Belgium, claudia.esposito@vki.ac.be

Supervisor: Jean-Marie Buchlin

Professor, Environmental and Applied Fluid Dynamics Department, von Karman Institute for Fluid Dynamics, Belgium, buchlin@vki.ac.be

University Supervisor: Johan Steelant

Associate Professor, Department of Mechanical Engineering, KU Leuven - ESA-ESTEC, Johan.Steelant@esa.int

University Co-Supervisor: Maria Rosaria Vetrano

Associate Professor, Department of Mechanical Engineering, KU Leuven, rosaria.vetrano@kuleuven.be

Abstract

This paper presents the last experiments on a cavitating orifice in water. The framework of these experiments is a study about the effect of fluid properties on the performances of hydraulic systems once cavitation has occurred. Specifically, this comparison will concern isothermal and cryogenic fluids. The experimental campaign in isothermal environment is discussed here. Mass flow rates and steady pressure measurements have been used to describe the hydraulic curve of the orifice. High-speed imaging has allowed to characterize the cavitation evolution. Finally, the void fraction during cavitation has been measured with the three pressure probes technique.

Keywords: cavitation, orifice, void fraction,

1. Introduction

1.1. Background

Hydrodynamic cavitation can be faced in several industrial applications where the flow undergoes sudden pressure drops, e.g. valves, pumps and orifices. Cavitation occurrence in hydraulic machinery leads to loss of performance, structural vibrations, noise and damages. That is why, these subsystems must be properly designed to avoid critical alterations in the proper operation of the whole hydraulic system.

For this purpose, orifices are widely used in literature to induce cavitation and to study its effects. In fact, they are practical and effective thanks to their simple geometry and the very high velocities which can be reached at the section called *vena contracta*.

An useful guide to predict cavitation intensity in valves and orifices is provided by Tullis [1]. He derived from his experimental database some scaling laws to take pressure effects and size scale effects into account. Hydraulic performances of orifices during different flow regimes transitions are discussed in [2].

The effects of cavitation on microscale are adressed in the works by Mishra [3] and Cioncolini [4]. Their results suggest the presence of strong scale effects. Concretely, these differences with macroscale orifices concern, first, the transition from incipient cavitation to choking. In micro-orifices this transition is much faster. Moreover, supercavitation immediately follows the onset of choking and it results in a thick cavity submerged by the liquid. On the contrary, on macroscale, supercavitation takes place for further reductions in the pressure drop and it appears as a liquid jet surrounded by a vapor cavity.

The mechanism of cavitation instability due to the bubble growth and collapse has been examined in [5], [6] and [7]. Cyclic shedding of cavitation structures has been observed by means of pressure measurements and high speed imaging.

De Giorgi et al. [7] also studied the thermal effects on cavitation. They observed that the transition

from two different cavitation behaviours was affected by temperature. In addition, cavitation intensity was stronger at higher temperatures. To take these thermal effects into account becomes really important for cryogenic fluids which are used as propellants in liquid rocket engines. Indeed, their physical and thermal properties suggest a meaningful difference in the nature of cavitation respect to the isothermal fluids, e.g. water, see for example [8],[9].

The effect of this thermal properties on macroscopic performances of the hydraulic systems is still object of reasearch. Pinho [10] tested the performances of an orifice with both water and liquid nitrogen as working fluids. Based on his experimental results, he concluded that hydraulic similarity exists between different fluids at single phase condition. Unfortunately, the two-phase cavitating regime has not been investigated experimentally.

That is why, now the concern is to experimentally verify this hydraulic similitude between isothermal and thermosensitive fluids in two-phase conditions. From the theoretical point of view similar testing conditions for orifices with both fluids can be ensured by keeping the same thickness and the same β ratio, which is defined as the ratio between the orifice diameter and the test-section diameter.

1.2. Objectives

As a part of this research activity which aims at looking for a similarity between isothermal and thermosensitive cavitation, the current work focuses on the characterization of cavitating orifices in water. Three different orifice geometries are considered and their hydraulic performances are compared. The hydraulic behaviour of the orifices has been analyzed from the fully liquid conditions up to super-cavitation. Synchronized time-resolved pressure measurements and flow visualizations have been performed to characterize the different cavitating stages. In addition, the void fraction has been measured by using the three pressure sensors technique [11]. It was validated with a known void fraction content in the work by Yenigun [12].

2. Experimental set-up and procedure

The experimental campaign with water has been carried out with three orifice geometries, see Fig. 1. The first one is a cylindrical sharp-edged thick orifice with $\beta = 0.17$ and thickness $s/d = 1.2$, asd shown in Fig. 1.a. This orifice has been made in steel to guarantee a better precision in the manufacture. It is in geometrical similarity with the one which will be used later on for the experiments with the cryogenic fluid, namely liquid nitrogen. The other two geometries are divergent orifices in Plexiglas. One is classified as thick and it has $\beta = 0.15$. The other one is thin with $\beta = 0.30$.



Figure 1: Orifice configurations: a) cylindrical thick orifice; b)thick divergent orifice; c)thin divergent orifice

The aim of this test campaign was to characterize cavitation through the three orifices in terms of hydraulic curve, frequency analysis, void fraction and flow topology. Fig. 2 illustrates the experimental setup. Water is stored in a 750 l tank which feeds the system in a closed loop. This tank is provided with an electrical resistance to heat the water. The maximum operating pressure is limited to 5 bar to prevent any damage to the test section built in Plexiglas. The back pressure is adjusted either slightly by a valve located downstream of the test section, or by the vacuum pump which is connected to the top of the reservoir. A minimum back pressure of 0.2 bar abs can be achieved. A smaller reservoir is located just after the pump to calm the water flow before entering the test section. The test section has an inner diameter (D) of 4 cm. The mass flow rate is measured by an electromagnetic flowmeter placed upstream the test section. The static pressure upstream of the orifice and the pressure drop across the orifice are measured by two Valydines (0.25% full-scale accuracy). The upstream pressure is measured 7D upstream the orifice and the downstream pressure is measured 16D downstream the orifice. The test-section is also instrumented with three unsteady pressure transducers (XTL-M Kulites 0.1% full-scale accuracy). They are positioned downstream of the orifice at 4.8D, 6.4D and 7.9D, respectively. The spacing of 6 cm between consecutive transducers and the acquisition frequency of 100 kHz have been set according to the previous calculations for the three pressure probes technique validation [12].

Visualizations are performed at two different locations of the test section. Immediately downstream of the orifice, a High Speed Camera recorded 5349 im-

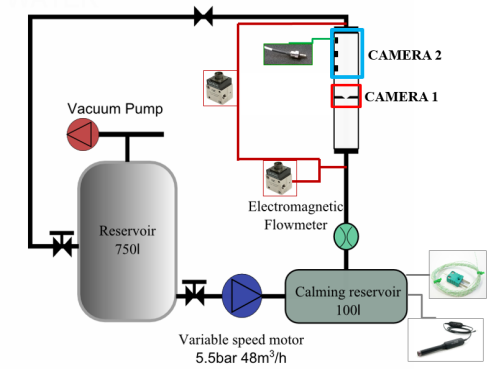

Figure 2: Schematic of the water loop facility

ages at 14035 frames per second. Images at 1000 Hz have been acquired with a high-resolution camera at the location of the three pressure transducers, which is 4D downstream the orifice. The two cameras are synchronized between them as well as with the pressure measurements. Temperature is measured in the calming reservoir by means of a thermocouple type K. The dissolved amount of oxygen in the water is measured as well. For this purpose a Vernier Optical DO probe is mounted in the calming reservoir too. The test water has been deaerated before each test. Water is let circulating at the minimum speed in vacuum conditions for at least four hours. By doing so, the oxygen is liberated and removed through the vacuum pump. The dissolved oxygen concentration is expressed as a percentage of the maximum amount of oxygen that water can hold at a given temperature, specifically as written in Eq. 1.

$$\%saturation = \left(\frac{actualDOreadingmg/L}{saturatedDOreadingmg/L}\right) \cdot 100 \tag{1}$$

Fig. 3 depicts the reduction of this percentage during eight hours. The cavitation tests start when the measured dissolved oxygen content is below the 10% of the saturated dissolved oxygen at the testing temperature. During the tests, this value changes of only 2.5%. For each orifice, an average of thirty testing conditions have been recorded. Different flow rates have been tested by varying the upstream pressure. The downstream pressure was set either at ambient or at two different vacuum conditions, i.e. 0.2 bar abs and 0.5 bar abs, in order to cover the whole range from fully liquid up to the super cavitation regime.

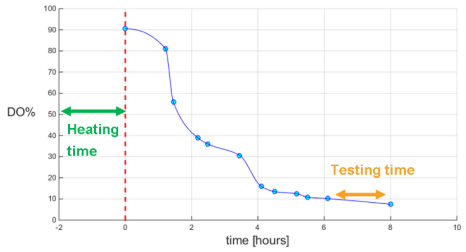

Figure 3: Evolution with time of the dissolved oxygen content

3. Hydraulic characterization of the orifice

The first measurements to characterize the flow through the orifices concern the mass flow rate and the pressure drop.

3.1. Single-phase flow

The characteristics of the flow through the orifice have been extracted first in single-phase conditions. Two parameters are considered at this purpose: the discharge coefficient C_d and the flow coefficient K_V. The discharge coefficient is the ratio between the actual flow rate and the ideal one predicted with Bernoulli equation, see Eq. 2. Thus, C_d takes the viscous effects into account in computing the discharge of the orifice.

$$Q = C_d \cdot Q_{ideal} = C_d \cdot A \cdot \sqrt{\frac{2 \cdot \Delta P}{\rho \cdot (\frac{1}{\beta^4} - 1)}} \tag{2}$$

Fig. 4 illustrates the measured discharge coefficient against the Reynolds number in fully liquid conditions. The C_d increase with the Reynolds number is a feature already observed in literature, see for example [13] and [14]. Lichtarowicz [14] observed that an asymptotic value is reached when the flow is fully turbulent. Orifice geometry strongly affects the way this asymptotic value is reached. The variation in the C_d obtained within these tests witnesses a non-fully developed turbulent flow.

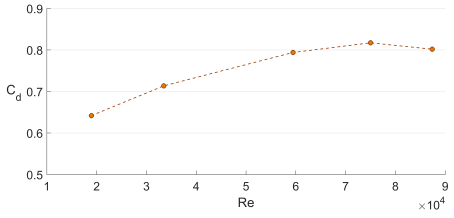

Figure 4: Discharge coefficient against the Reynolds number

The other parameter which describes the hydraulic performances of an orifice is the flow coefficient (K_V). It is defined as the volumetric flow of water which passes through a restriction with a pressure drop of 1 bar. The experimental K_V has been computed. The comparison with the values obtained from both Chisholm's [15] and Idelchik's [16] correlations is depicted in Table 1. Here, Cases from 1 to 3 stand for the cylindrical orifice, the thick divergent orifice and the thin divergent orifice, respectively. Experimental values are really close to the theoretical ones. The higher discrepancy is found for the thick divergent orifice with a percentage error of the 15% respect to Chisholm's correlation. On the contrary, a maximum difference of the 3% between the experimental K_V and those derived from both Idelchik's and Chisholm's correlations is measured for the other two orifices (Case 1 and Case 3).

Table 1: K_V values for the three orifice geometries

	Case 1	Case 2	Case 3
Experiments	1.45±0.07	1.05±0.04	4.43±0.13
Chisholm	1.57	1.24	4.55
Idelchik	1.49	1.19	4.33

3.2. Cavitation inception

A practical way to include cavitation in the design process and to characterize its extent is provided by the *Cavitation number*,σ. It is a dimensionless parameter given by the ratio of the pressure which provokes cavitation and the actual pressure of the system. Different definitions exist in literature. They depend on the particular flow to study: external jets, flows around bodies or through valves or orifices. The definition we are going to use is the one in Eq. 3 proposed by [17] and also used by [18].

$$\sigma = \frac{P_{dw} - P_{sat}}{\Delta P} \tag{3}$$

In Eq. 3 P_{dw} is the pressure downstream the orifice, ΔP is the pressure drop through it and, finally, P_{sat} is the saturation pressure of the fluid, that is the pressure threshold which induces this phase change. Fig. 5 shows the value of P_{sat} for water at different temperatures. Above this pressure, water is in its liquid phase, below it becomes vapor.

Cavitation inception indicates the boundary between a non-cavitating and a cavitating flow. The way

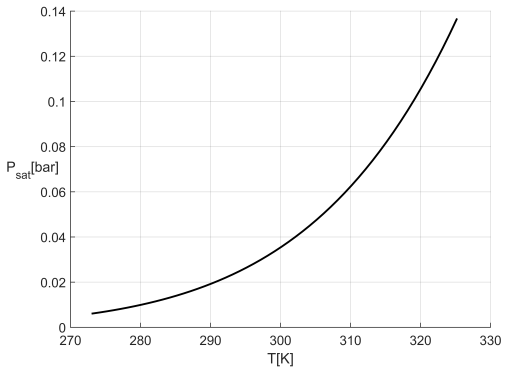

Figure 5: Saturation curve for water

to define this transition is still matter of discussion. Tullis [18] determines the starting of cavitation just on the basis of acoustic measurements, stating that cavitation is not observable yet at this stage. On the contrary, both Yan et al. [2] and Mishra et al. [3] define the inception as the intermittent appearance of the first tiny bubbles. In both cases, cavitation inception has been observed to occur with a downstream pressure higher than the saturation pressure. Within this work cavitation inception has been first identified by looking at the unsteady pressure measurements collected downstream the orifice. As an example, Fig. 6 shows the evolution of these fluctuations due to the reduction of the cavitation number which has been computed according to Eq. 3.

Up to $\sigma = 1.08$ the pressure signals are almost flat in time. Fluctuations within the signal start appearing at $\sigma = 0.77$. This value has been considered the cavitation inception number for that testing campaign. At that condition, high speed images recorded immediately downstream the orifice show the intermittent occurrence of tiny bubbles.

Cavitation inception is believed to be strongly affected by the gaseous cavitation, which is the diffusion of dissolved gases into the available nuclei in the liquid [19], [2]. As noticed in the works by Gustavsson [20] and Arndt [21], dissolved gas made easier the bubble growth by lowering the pressure threshold to be overcome. This means that cavitation in degassed water starts at higher pressure drop respect to tap water. Fig. 7 depicts the cavitation inception number as a function of the amount of dissolved oxygen in the testing water. Four different cases are considered. As expected, cavitation inception number (σ_{in}) is larger for higher oxygen content. No appreciable difference can be noticed between the two lower cases (5% and

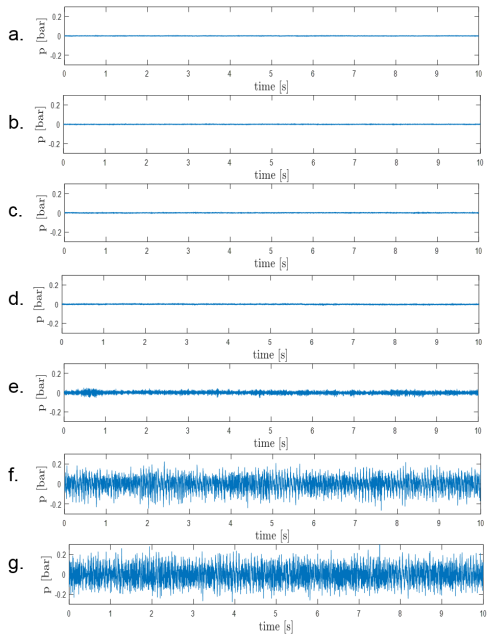

Figure 6: Pressure fluctuations recorded 7.9D downstream the orifice: a) $\sigma = 6.23$, b) $\sigma = 2.41$, c) $\sigma = 1.58$, d) $\sigma = 1.08$, e) $\sigma = 0.77$, f) $\sigma = 0.62$, g) $\sigma = 0.56$

10%), suggesting the idea that below the 10% the water behaviour keeps unchanged.

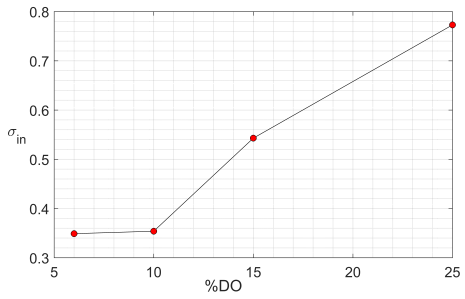

Figure 7: Cavitation inception number against the dissolved oxygen content in water

3.3. *Choking and super-cavitation*

Further reductions in the cavitation number make cavitation to be stronger. The cavity size increases progressively. It becomes large enough to stabilize the flow rate around a certain value even for further increases in the pressure drop. This condition is called choked flow. Fig. 8 illustrates a comparison between the measured flow characteristics and the theoretical curves with a 2 bar abs pressure upstream of the orifice. The linear part of the curve is drawn according to Eq. 2. As for the choked flow rate, two further parameters have to be introduced. One is the liquid critical pressure ratio factor, F_F , which is defined in Eq. 4. It takes into account the fact that liquid vaporizes at a pressure lower than the saturation one because of thermodynamic non-equilibrium effects.

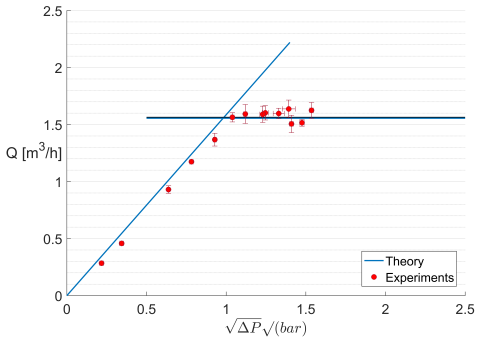

Figure 8: Hydraulic curve for the cylindrical orifice ($\beta = 0.17$) with $P_{up} = 2$ bar

$$F_F = 0.96 - 0.28 \cdot \sqrt{\frac{P_{sat}}{P_{cri}}} \tag{4}$$

where P_{cri} is the critical pressure of the liquid. In the case of water P_{cri} is 220.64 bar [**?**]. The other parameter is the liquid pressure recovery factor F_L which was introduced by Baumann [22]. It is defined as the ratio between the overall pressure drop through an orifice and the drop between the static pressure at the inlet and the static pressure at the vena contracta, Eq. 5. The pressure at the vena contracta can be calculated by combining Bernoulli equation and the continuity equation between the sections upstream the orifice and the section at the vena contracta. Once F_L has been computed, the maximum allowable pressure drop ΔP_{max} can be retrieved from Eq. 6. Finally, Eq. 7 gives the maximum flow rate which can be obtained.

$$F_L = \sqrt{\frac{P_{up} - P_{dw}}{P_{up} - P_{vc}}} \tag{5}$$

$$\Delta P_{max} = F_L^2 \cdot (P_{up} - F_F \cdot P_{sat}) \tag{6}$$

$$Q_{max} = \frac{C_d \cdot A_1}{\sqrt{\frac{1}{\sigma_a^2} - 1}} \cdot \sqrt{\frac{2 \cdot \Delta P_{max}}{\rho}} \tag{7}$$

Even after the flow becomes choked, a further regime transformation takes place. This transition is called super-cavitation and it is documented in Fig. 9.

A submerged liquid jet becomes visible at the center of the test section while a thick vapor cavity surrounds it. On the walls of the test section a film of water is falling down due to the finite length of the super-cavitating region. This condition has already been observed by Yan[2]. An attempt to simulate a super-cavitating flow has been carried out by [23]. In their work the computational domain was too short and the cavity was periodically collapsing. On the contrary, during the experiments the water jet surrounded by vapor was stable enough.

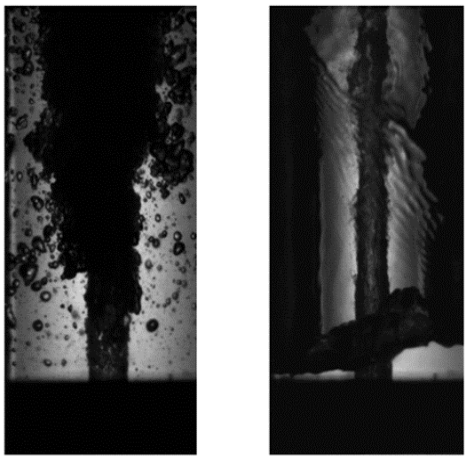

Figure 9: Instantaneous images recorded at $\Delta P = 1.94$ (left) and $\Delta P = 2.18$ (right)

Once super-cavitation has been reached in the current testing campaign, the upstream pressure has been progressively decreased to bring the flow back to fully liquid. Fig. 10 illustrates the results obtained. The purple rounds correspond to the data acquired when going from fully liquid regime to the super-cavitation one. The blue squares are the data acquired when going back from super-cavitation to fully liquid. A hysteresis effect can be noticed. In fact, the water jet surrounded by vapor is still present at such low discharges as 1 m^3/h. As also observed by [3] for micro-orifices, the occurrence of super-cavitation reduces the available area for the liquid to flow. High local dynamic heads are caused and they make the fluid more resistant to the transition back to fully liquid.

3.4. Non-dimensional hydraulic curve

A non-dimensional representation for the hydraulic curve of the orifice has been considered to compare different working conditions among them. Indeed,

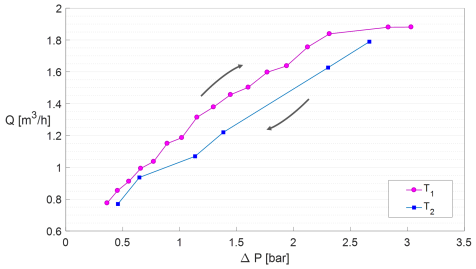

Figure 10: Flow characteristics hysteresis

during a test campaign, the upstream pressure has been increased to characterize a single orifice from the fully liquid condition up to the super-cavitation. Different upstream pressures correspond to different hydraulic curves. Specifically, what is changing is the choked flow rate and the choked pressure drop. So, to obtain a unique curve Q vs. $\sqrt{\Delta P}$, it is suggested to divide them by Q_{chok} and ΔP_{chok} respectively.

As an example, Fig. 11 shows the non-dimensional theoretical hydraulic curve together with the experimental points for the cylindrical orifice with $\beta = 0.17$. Four different testing campaign are plotted on the same graph. They differ in terms of dissolved oxygen concentration and in terms of pressure downstream of the orifice. Test 1 corresponds to the measurements taken with atmospheric pressure downstream the orifice and $DO = 25\%$ of the saturation value. Tests from 2 to 4 have been carried out by progressively reducing the downstream pressure. In particular, a downstream pressure of 0.1 bar abs was kept for the Test 4. It can be noticed that lowering the downstream pressure the value of $\widehat{Q}$ becomes lower respect to the non-dimensional theoretical one. Indeed, a lower downstream pressure enhances the formation of vapor which leads to lower flow rates. Fig. 12 illustrates what is happening in terms of the flow topology immediately downstream the orifice. Both images stand for $\widehat{\Delta P} = 1.13$. The image on the left has been recorded with a downstream pressure of 0.8 bar abs. The vapor size is almost disappeared at a distance of 3 cm downstream the orifice. On the other hand, the vapor extends further for the same $\widehat{\Delta P}$ but with a lower downstream pressure, namely $P_{dw} = 0.1$ bar abs.

Finally, it is worth to mention that under cavitating conditions the discharge coefficient is no longer function of the Reynolds number but it only depends on the cavitation intensity [17],[13]. Fig. 13 shows the theoretical relation provided by [17] and written in Eq. 8. As cavitation starts occurring, all the experimental C_d

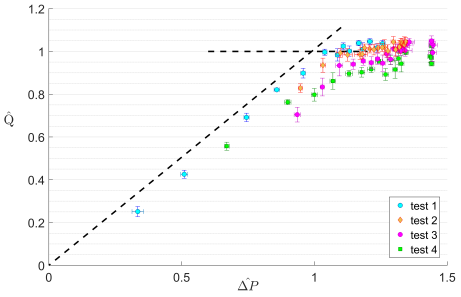

Figure 11: Non dimensional hydraulic curve for cylindrical orifice ($\beta = 0.17$)

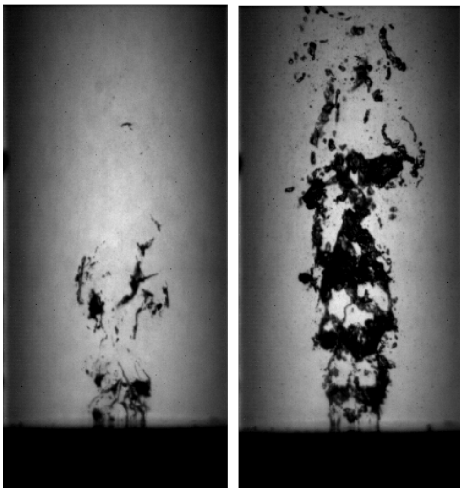

Figure 12: Flow topology downstream the orifice at $\widehat{\Delta P} = 1.13$: $P_{dw} = 0.8$ bar abs (left); $P_{dw} = 0.1$ bar abs(right)

collapse on this curve.

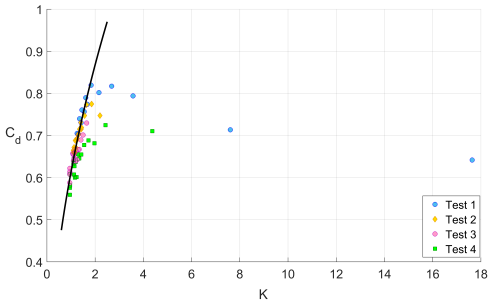

Figure 13: Discharge coefficient vs the cavitation number

$$C_d = \sigma_c \cdot \sqrt{K} = \sigma_c \cdot \sqrt{\frac{P_{up} - P_{sat}}{\Delta P}} \tag{8}$$

4. Void fraction measurements

The technique of the three pressure transducers [10] has been applied to measure the void fraction. This technique is based on the fact that the pressure waves propagate with the same amplitude through the pipe. The pressure signal recorded by the sensors is used to build a transfer function in the frequency domain. This function is directly linked to the speed of sound.

The three pressure sensors are installed equidistantly, with a distance of 6 cm between consecutive transducers. By doing so, the transfer function reduces itself to a cosine signal. An example of the transfer function (H) computed from the unsteady pressure measurements is depicted in Fig. 14. The first minimum of this function is directly linked to the confined speed of sound of the flow. Then, the properties of the test-section material are considered to compute the speed of sound confined to the Plexiglas test-section environment. Eq. 9 [24] is used at this purpose. Fig. 15 illustrates this theoretical relation, Eq. 9, together with the experimental values collected in such a way to cover a wide range of speeds of sound

$$c_{conf} = c_{free} \cdot \sqrt{1 + \frac{D}{e \cdot E} \cdot (1 - \nu^2) \cdot c_{free}^2 \cdot \rho} \tag{9}$$

The void fraction is finally computed by using Eq. 10 .

$$c_{free} = \left(\frac{(1 - \alpha + \alpha \cdot \frac{\rho_L}{\rho_G})}{c_L^2/(1-\alpha)} + \frac{\alpha/c_G^2}{\left(\alpha + (1-\alpha) \cdot \frac{\rho_L}{\rho_G}\right)} \right)^{0.5} \tag{10}$$

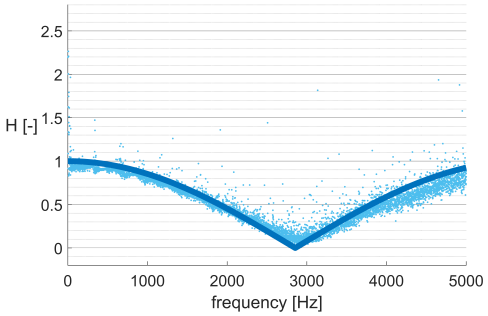

Figure 14: Transfer function from the three pressure sensors in the frequency domain

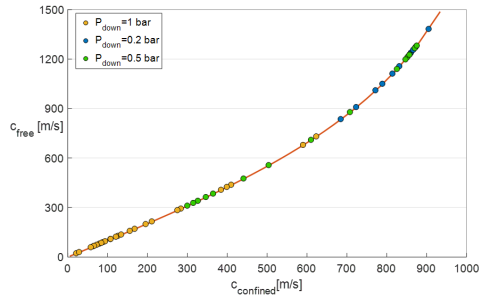

Figure 15: Free speed of sound against the speed of sound confined to the Plexiglas test-section

Fig. 16 illustrates some results in terms of void fraction as a function of the cavitation parameter σ. The images on the bottom of Fig. 16 are those recorded in the upper part of the test section for the cylindrical thick orifice. They show the flow topology at three different flow conditions, namely $\sigma = 0.77$, $\sigma = 0.09$; and $\sigma = 0.03$. The σ values higher than 0.77 correspond to a fully liquid flow. In this range, a correct speed of sound couldnt be calculated. In fact, this technique would require an acquisition frequency higher than 100 kHz to capture such high speeds of sounds as those in a fully liquid flow (around 1500 m/s in water)[12]. At $\sigma = 0.77$, cavitation is barely visible at the exit of the orifice but the flow appears completely liquid in the region of the transducers (Fig. 16.a). However, a constant whistling can be heard at this condition and a free speed of sound of 1381 m/s has been computed. It corresponds to a void fraction of $3.8 \cdot 10^{-7}$. Fig. 16.b shows the case of $\sigma = 0.09$. The vapor phase appears well dispersed in the liquid, which satisfies the homogeneous two-phase flow assumption. The void fraction is estimated at 0.0003. Finally, the highest value of void fraction (i.e. 0.0013), has been measured at $\sigma = 0.03$. From this point, the flow starts choking and the cavitation cloud extends itself farther and farther from the orifice. In fact, the front of this cavitation cloud starts appearing in the frame as we can see on Fig. 16.c. Reducing the cavitation parameter, super-cavitation appears. In this regime the three pressure probes technique is no longer applicable.

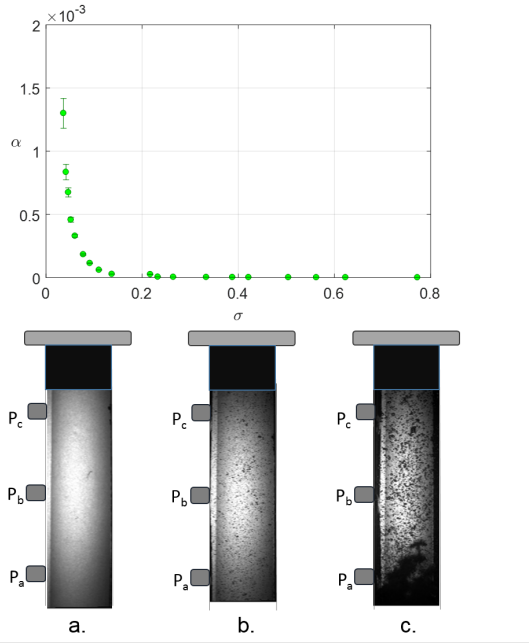

Figure 16: Void fraction vs cavitation number(top); Flow visualization at a)$\sigma = 0.77$; b)$\sigma = 0.09$; c)$\sigma = 0.03$ (bottom)

5. Conclusion

This work was devoted to create a test bench in water to characterize a cavitating flow. Three different orifice geometries have been analyzed, two divergent orifices, thin and thick, respectively, and a thick cylindrical orifice. The hydraulic behavior of these orifices has been observed from the fully liquid to the super-cavitation. Flow visualizations have helped to investigate some peculiarities of the orifice macroscopic behavior, such as the flow hysteresis in the transition from super-cavitation to fully liquid. The impact of the dissolved oxygen in water has been questioned as well. Special attention has been given to the void fraction, which has been estimated by means of time-resolved pressure measurements. These results have been linked to the cavitation parameter in order to correlate the cavitation intensity to the void fraction.

Acknowledgments

This research is supported by the ESA's Networking/Partnering Initiative (NPI).

References

[1] J. P. Tullis, Cavitation guide for control valves, Tech. rep., Nuclear Regulatory Commission, Washington, DC (United States). Div. of Engineering; Tullis Engineering Consultants, Logan, UT (United States) (1993).

[2] Y. Yan, R. Thorpe, Flow regime transitions due to cavitation in the flow through an orifice, International journal of multiphase flow 16 (6) (1990) 1023–1045.

[3] C. Mishra, Y. Peles, Cavitation in flow through a micro-orifice inside a silicon microchannel, Physics of fluids 17 (1) (2005) 013601.

[4] A. Cioncolini, F. Scenini, J. Duff, M. Szolcek, M. Curioni, Choked cavitation in micro-orifices: an experimental study, Experimental Thermal and Fluid Science 74 (2016) 49–57.

[5] K. Sato, Y. Saito, Unstable cavitation behavior in a circular-cylindrical orifice flow, JSME International Journal Series B Fluids and Thermal Engineering 45 (3) (2002) 638–645.

[6] S. Nishimura, O. Takakuwa, H. Soyama, Similarity law on shedding frequency of cavitation cloud induced by a cavitating jet, Journal of Fluid Science and Technology 7 (3) (2012) 405–420.

[7] M. De Giorgi, A. Ficarella, M. Tarantino, Evaluating cavitation regimes in an internal orifice at different temperatures using frequency analysis and visualization, International Journal of Heat and Fluid Flow 39 (2013) 160–172.

[8] M. Billet, D. Weir, Thermodynamic effects on developed cavitation, Journal of Fluids Engineering (1975) 507.

[9] A. Hosangadi, V. Ahuja, Numerical study of cavitation in cryogenic fluids, Transactions of the ASME-I-Journal of Fluids Engineering 127 (2) (2005) 267–281.

[10] J. Pinho, J.-M. Buchlin, S. Chabane, B. Haut, Experimental investigation of cavitation in a safety relief valve using water: extension to cryogenic fluids.

[11] D. Margolis, F. Brown, Measurement of the propagation of long-wavelength disturbances through turbulent flow in tubes, Journal of Fluids Engineering 98 (1) (1976) 70–78.

[12] O. Yenigun, Experimental characterization of teo-phase flows under cavitation conditions, Rm, von Karman Institute for Fluid Dynamics (2017).

[13] F. Payri, V. Bermudez, R. Payri, F. Salvador, The influence of cavitation on the internal flow and the spray characteristics in diesel injection nozzles, Fuel 83 (4-5) (2004) 419–431.

[14] A. Lichtarowicz, R. Duggins, E. Markland, Discharge coefficients for incompressible non-cavitating flow through long orifices, Journal of mechanical engineering science 7 (2) (1965) 210–219.

[15] G. Kojasoy, F. Landis, P. Kwame-Mensah, C. Chang, Two-phase pressure drop in multiple thick-and thin-orifice plates, Experimental thermal and fluid science 15 (4) (1997) 347–358.

[16] I. Idelchik, Handbook of hydraulic resistance. aec-tr-6630, Atomic Energy Commission.

[17] W. Nurick, Orifice cavitation and its effect on spray mixing, Journal of fluids engineering 98 (4) (1976) 681–687.

[18] J. P. Tullis, Cavitation guide for control valves, Tech. rep., Nuclear Regulatory Commission, Washington, DC (United States). Div. of Engineering; Tullis Engineering Consultants, Logan, UT (United States) (1993).

[19] C. E. Brennen, Cavitation and bubble dynamics, Cambridge University Press, 2013.

[20] J. Gustavsson, K. Denning, C. Segal, Experimental study of cryogenic cavitation using fluoroketone, in: 46th AIAA Aerospace Sciences Meeting and Exhibit, 2008, p. 576.

[21] R. E. Arndt, A. P. Keller, Water quality effects on cavitation inception in a trailing vortex, Journal of fluids engineering 114 (3) (1992) 430–438.

[22] H. D. Baumann, The introduction of a critical flow factor for valve sizing, ISA Transactions 2 (2).

[23] J. Kozák, P. Rudolf, D. Štefan, M. Hudec, M. Gríger, Analysis of pressure pulsations of cavitating flow in converging-diverging nozzle, in: 6th IAHR International Meeting of the Workgroup on Cavitation and Dynamic Problems in Hydraulic Machinery and Systems, 2015.

[24] J. Lighthill, M. Lighthill, Waves in fluids, Cambridge university press, 2001.

Scaled model of the pollutant dispersion driven by a condensed-phase explosion in an urban environment

Charline Fouchier

Environmental and applied fluid dynamics, von Karman Institute for Fluid Dynamics, Belgium, charline.fouchier@vki.ac.be

Supervisors: Jean-Marie Buchlin[1], Delphine Laboureur[2]

[1]*Professor and Head of Department,Environmental and applied fluid dynamics, von Karman Institute for Fluid Dynamics, Belgium, buchlin@vki.ac.be*

[2]*Research Engineer, Environmental and applied fluid dynamics, von Karman Institute for Fluid Dynamics, Belgium, delphine.laboureur@vki.ac.be*

University Supervisor: Alessandro Parente

Professor, Aero-Thermo-Mechanical Department, Université Libre de Bruxelles, Belgium, alparent@ulb.ac.be

Abstract

The propagation of a blast induced by a condensed-phase explosion and the atmospheric dispersion in a complex environment are well documented in the literature. However, it is possible to observe a lack of knowledge about the dispersion due to an explosion, which represents a source of pollutant fast and short in time. The global objective of the present research is to investigate the pollutant dispersion driven by a condensed-phase explosion in an urban environment. Two condensed-phase explosives have been selected and characterized to reproduce the explosive source. The explosion leading to the dispersion of solid particles is experimentally simulated in free field under a controlled urban atmospheric boundary layer. The pollutant dispersion and the overpressures caused by the explosion are measured through a fast response optical measurement technique and fast response pressure sensors. The main challenge of the study is the adaptation of the existing measurement technique of dispersion to fast phenomena visualizations.

Keywords: Blast Wave, Detonation, Dispersion, Pressure measurements, PIV, Safety

1. Introduction

Explosion, whether accidental or not, is a major concern in the security and safety fields. Examples of tragedies caused by explosions along with dangerous chemical dispersion are numerous. Improvement of security and safety is driven by a better understanding of the phenomenon. An explosion generates a pressure wave, called blast wave. If a pollutant is released together with the explosion, both the dispersion of the pollutant and the blast wave will be affected. To predict the pollutant dispersion after an explosion in a complex environment, it is necessary to understand the propagation of the blast wave and its effect on the plume dispersion.

Numerical models have been developed in attempt to simulate the plume dispersion after an explosion. A model based on the Large Eddy simulations (LES) approach has been used to simulate the Oslo bombing in 2011 [1]. The dispersion and deposition of particles following the detonation have been calculated using both an Eulerian and a Lagrangian model, based on the spherical particle sizes smaller than 20 μm with a high density (1000kg.m-3), assuming a no particle-particle interaction. To couple the cloud dynamics and chemical transformations, the numerical model called ADORA has been recently developed by N. Moussa et al. [2]. This model provides the time evolution of toxic emissions and their dispersion in the atmosphere after a fire or an explosion by solving the conservation of mass, momentum, energy and species equations in

an integral formulation.

To ensure an accurate and reliable prediction of the plume dispersion after an explosion, it is necessary to couple the modeling with strong empirical data. The rapid dispersion of inert spherical steel particles [3] [4], glass bubbles [5] or liquid [6] after a detonation has been investigated using a high speed camera coupled with pressure sensors. The dispersion turned out to depend on the pollutant characteristics (solid or liquid) and the geometry of the explosive charge. The particle image velocimetry technique (PIV) has been applied to obtain the velocity field of the metallic particles after the detonation [7].

However, the existing studies focus on the near-field effects of the explosion, few milliseconds after the detonation. An effort still has to be made to improve the experimental data base on the dispersion of the plume under an atmospheric boundary layer (ABL). Moreover, explosions in laboratory scale with controlled atmospheric conditions are not familiar. This knowledge is essential to develop accurate tools in order to simulate the dispersion after an explosion inside a complex environment.

The global objective of the present research is the investigation of pollutant dispersion driven by a condensed-phase explosion in an urban environment. Two explosives, used as the pollutant source, are first characterized. The present paper summarizes the experimental set-up used and the characteristics of the explosives in free field. A condensed phase explosion surrounded by a pollutant (solid particles) is then experimentally simulated in free-field under an urban ABL through a scale of 1:200. Flows visualizations and large scale particle image velocimetry (LS-PIV) are conducted to investigate the displacement of the plume and the velocity and concentration fields of the dispersion.

2. Materials and Methods

This chapter describes the experimental set-ups used for the investigation of the dispersion and the blast wave propagation in free field.

2.1. Dispersion

Experiments have been performed inside the subsonic wind tunnel L1-b at the von Karman Institute. It is 2 m high, 3 m wide and 15 m long with a roughened floor to allow the growth of a turbulent boundary layer similar in nature to the lower part of the neutral atmospheric boundary layer. The test section ceiling is flexible and continuously adjustable to achieve control of the longitudinal pressure gradient. Flow velocity can be varied between 2 and 50 m/s. An urban atmospheric boundary layer is developed inside the wind tunnel through plastic cups fixed on the floor. The dimensions of the roughness elements have been defined by B. Conan [8] to obtain an atmospheric boundary layer typical to an urban environment at a 1:200 reduced scaled. Tests are conducted on a 2.8 m diameter circular wood table. Figure 1 left illustrates the test table inside the wind tunnel.

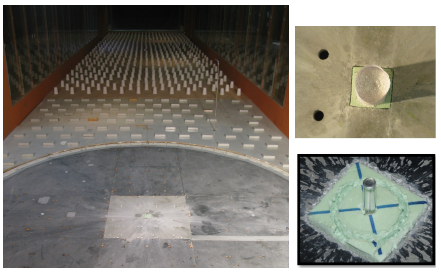

Figure 1: Left: Experimental wood test table, 2.8 m diameter, inside a wind tunnel. The roughness elements create turbulences to develop an urban boundary layer at a 1:200 reduced scale. Right bottom: Solid foam support with a RP83 detonator. A groove has been performed to place properly the paper cylinder around the explosive. Right top: Paper cylinder filled with talc powder

The dispersion is simulated using two diameters talc powder, distributed by Imerys. The talc is an inert powder that will not react after the explosion. The first powder, called JetFine 1, or light powder, has a diameter of 1 μm and a density of 0.15 g/cm^3. The second powder, called Mistron 200, or heavy powder has a diameter of 7.8 μm and a density of 0.42 g/cm^3. The Table 1 summarizes the characteristics of the powders used. The two talc powders have different response time and are expected to be affected by the explosion in a different way. The powder is maintained around the explosive by a paper cylinder. A circular groove is performed on the solid foam support to maintain the cylinder and assure that the talc is homogeneously distributed around the explosive. Figures 1 right show the detonator inside the talc powder kept by a paper cylinder and the groove inside the support.

Name	Diameter	Density	Response Time
Heavy Powder	7.8 μm	0.42 g/cm^3	0.51 ms
Light Powder	1 μm	0.15 g/cm^3	0.0084 ms

Table 1: Characteristics of the talc powders used

The dispersion of the solid particles is investigated through Flow Visualization (FV) and Large Scale Par-

ticle Image Velocimetry (LS-PIV) [9]. A Phantom V7.1 high speed camera (HSC) is used to acquire the images of the dispersion. The camera is set on the side of the wind tunnel to have a front view of the dispersion or on the top to obtain a top view. For the flow visualization, the flow is illuminated with powerful spots and acquired at 10869 Hz with an exposure of 60 μs to observe the global evolution of the dispersion. For the LS-PIV acquisition, the flow is illuminated by a 10 W continuous laser sheet, produced by an optical set-up coupling divergent, convergent and cylindrical lenses and acquires at 2000 Hz with an exposure of 500 μs.. Three wind speeds are investigated: 0 m/s, 3 m/s and 5 m/s.

2.2. Blast

The setup has been designed to conduct non-destructive studies of 3 dimensional free field air blast propagation. For each test, the explosive is placed at the center of the circular test table. A metal plate of 55 x 55 cm replaces the wood in the middle of the table to protect it against the explosion.

The effects of the explosive source are studied through the use of two exploding-bridge-wire (EBW) detonators (RP80-EBW and RP83-EBW, distributed by RISI [10]). The explosives are metal cylinders of 7 mm diameter and 21 mm and 40 mm length, respectively for the RP80-EBW and RP83-EBW. They are filled with 0.08 g of Pentaerythritol tetranitrate PETN as initiating explosive and 0.123 g or 1.031 g of cyclotrimethylenetrinitramine RDX as output explosive, (*cf.* Table 2).

Explosive	Distributor	Composition
RP-80 EBW detonator	RISI	0.08 g PETN
		0.123 g RDX
RP-83 EBW detonator	RISI	0.08 g PETN
		1.031 g RDX

Table 2: Characteristics of explosives used (EBW: exploding-bridge-wire)

The explosive charges are stored in an aluminum cup with a plastic molded head. Detonators are set inside a solid foam block of 5 x 5 cm in the center of the test table, standing out from a given height (*i.e.* 9 mm for the RP80-EBW, 22.5 mm for the RP83-EBW) to have only the secondary explosive (RDX) outside of the support. From past experiments, these heights correspond to the optimal position for an hemispherical blast. The foam support is destroyed by the explosion and has to be changed after each test. The detonators are activated using a FM150 firing module and a FD201 firing system.

The TNT equivalent of the detonators used can be estimated using their composition, by summing the TNT mass equivalent of the two components (*i.e.* RDX and PETN), themselves evaluated from past experiments (*i.e.* 1.3 for the RDX and 1.27 for the PETN). The energy theoretically released by the explosives has been obtained using the energy of a TNT explosion (4686 J/g [11]) and the TNT equivalent mass. The Table 3 gathers the obtained values.

Explosive	TNT eq		
RP-80 EBW detonator	1.29	0.261 g	1.22 kJ
RP-83 EBW detonator	1.3	1.44 g	6.74 kJ

Table 3: TNT equivalent estimated of explosives used (EBW: exploding-bridge-wire): TNT equivalent, mass equivalent of TNT and energy released

The test table is perforated with 1 cm diameter holes to mount sensors flush to the surface. Ten flush mounted sensors are used to record the blast: seven piezoresistive transducers (five PCB 116 and two Kistler 603B) and three piezoelectric transducers (two Kistler 4043A5, one Kistler 4043A2). Each sensor is statically and dynamically calibrated with its measurement chain (amplifier and cables). The characteristics of sensors and amplifiers used are summarized in Table 4 and Table 5. The resonance frequencies are provided by the supplier. The rise times have been estimated from measurements of pressure steps inside a shock tube. The pressure variations of all sensors are recorded with a sample frequency of 8 MHz, using a NI PXIe 7962R system with an acquisition module NI-5751. The sample size is equal to 40.10^6 points per channel, which represents 5 seconds of acquisition.

The sensors are maintained by elastics to disconnect them from the test table. This system, shown in Figure 2, has been designed and tested to reduce the effect of the table vibrations on the blast measurement.

3. Results

3.1. Characteristics of the explosives

This section is dedicated to the characterization of the explosives. The symmetry and repeatability of each explosive are investigated through free field tests.

Name	Type	Range bars	Resonance kHz	Rise Time
PCB 106	Piezo-electric	0 - 3.45	> 100	4 μs
Kistler 603 B	Piezo-resistive	0 - 200	> 400	2 μs
Kistler 4043A2	Piezo-resistive	0 - 5	> 30	14 μs
Kistler 4043A5	Piezo-resistive	0 - 5	> 80	10 μs

Table 4: Sensor characteristics

Sensor	Amplifier	Low pass filter frequency
PCB 106	Kistler 5011	200 kHz
Kistler 603 B (1)	Kistler 5007	330 kHz
Kistler 603 B (2)	Kistler 5001	180 kHz
Kistler 4043A2	VKI	200 kHz
Kistler 4043A5	VKI	200 kHz

Table 5: Amplifier characteristics

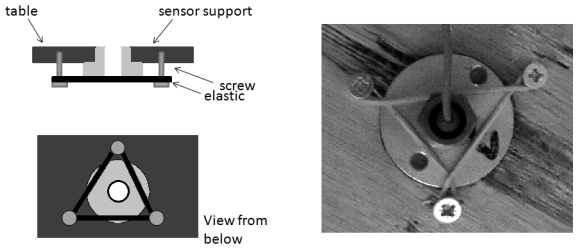

Figure 2: Two types of sensor fixations tested

Three tests with detonators are conducted in free field to investigate the repeatability of the explosion. Figure 3 depicts the variation regarding the distance of the pressure peaks and the positive impulses of blasts generated by the two types of explosives. The standard deviation, based on 3 tests, is also added. The blast characteristics decrease exponentially regarding the studied distance, from more than 1200 mbar close to the explosion to lower than 200 mbar at 1.2 m for the RP83-EBW detonator.

Figure 4 presents the pressure signal of blasts obtained from RP83 detonators free field tests at 1225 mm from the explosion. As the RP80 detonator presents similar results, it is not presented here. The signals from the RP83 detonators have been superposed by taking as the initial time the impulse of the firing system. A small difference of overpressure peaks can be observed. It is due to the response of the

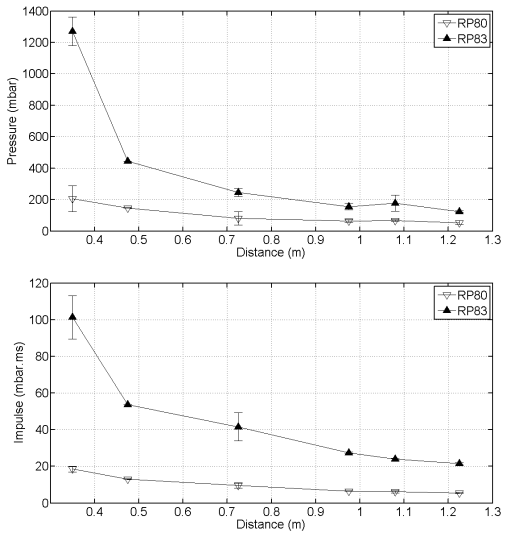

Figure 3: Variation of the overpressure peak and the impulse of blasts generated by a pyrotechnic device, a detonator RP80 and a detonator RP83

sensor itself. Nonetheless, the shapes of the blasts after the pressure peak are similar, highlighting the fact that the study of the positive impulse is more reliable than the study of the overpressure peak as it depends less on the response time of the sensors.

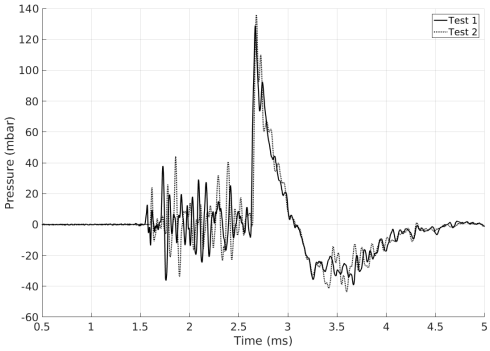

Figure 4: Repeatability of explosions of RP83 detonators - signal from a Kislter 4043A2 at 1225 mm from the explosion - 200 kHz low-pass filtered

The explosion geometry has been measured using four pressure sensors at 725 mm from the center of the explosion and at different angles. Polar plots of one explosion of each type of explosive are proposed in Figure 5. The characteristics (positive impulse and overpressure peak) of blasts recorded by the sensors equidistant to the explosion are given. To highlight the symmetry of each explosion, a mean value has been

added and corresponds to the average of the characteristics obtained in the four directions. A good circularity of detonator explosions is observed, with an average variation of 5 % from the average.

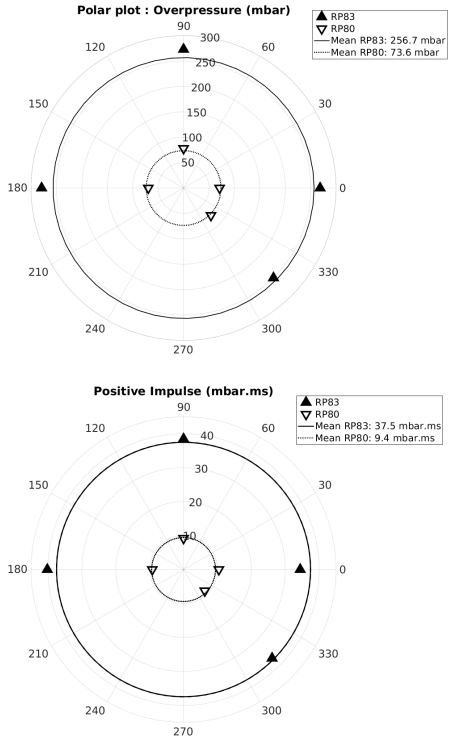

Figure 5: Polar plot: symetry of the explosion at 725mm from the explosion

3.2. Experimental TNT equivalent

The TNT equivalent is used to characterize the blast produced by an explosion. This chapter describes the investigation on the TNT equivalent of the two explosives used.

The variation of the positive impulse regarding the distance, scaled using the theoretical TNT equivalent estimated for each explosive (Table 2) is proposed in Figure 6 (top figure). Reference curves for hemispherical TNT explosions at the ground from Kinney and Graham [12] and GEMO [13] are included. It appears that the experimental points do not fit the reference curves. The actual TNT equivalents of the explosives are not equal to the theoretical ones. An experimental TNT equivalent can be estimated by curve fitting the experimental results to the reference curves [13]. Figure 6 (figure bottom) represents the variation of the impulse regarding the distance scaled with the new equivalents obtained.

The estimated TNT mass equivalents, the actual values and the difference between the two are gathered in the Table 6. The same amount of energy is lost, suggesting that this energy is absorbed by the plastic deformation of the metal cylinder of the detonator and the ground. The absorption of energy by the casing of the explosion has been often observed in the litterature, such as [14], as well as the ground effect [11][12]. The results presented here point once again the importance of conducting tests to characterize the explosive studied and its support.

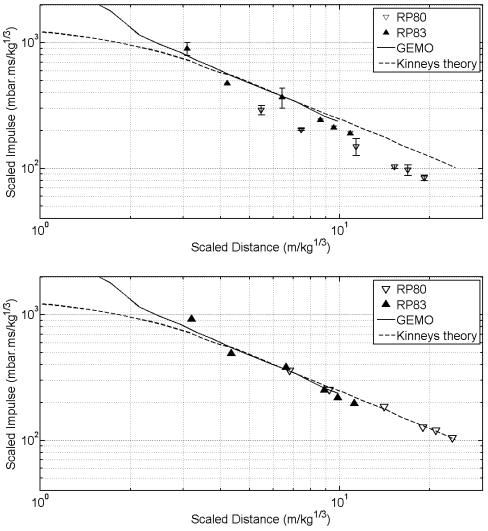

Figure 6: Variation of the positive impulses regarding the distance (scaled by the theoretical TNT equivalent (top) and experimental TNT equivalent (bottom)

Explosive	Theoretical TNT eq.	Experimental TNT eq.	Difference	
			mass	energy
RP80	0.261 g	0.136 g	-0.125 g	0.59 kJ
RP83	1.44 g	1.31 g	-0.13 g	0.61 kJ

Table 6: Theoretical and Experimental TNT mass equivalent

The previous estimations are based on the supposition that the TNT mass equivalent is constant with the distance and the characteristics chosen (impulse or overpressure). However, as discussed in the introduction, it is known that this assumption is not always valid. The experimental TNT equivalent given previously is actually an averaged TNT equivalent based on the impulse. The variations of the TNT equivalent regarding the distance and the characteristic studied are proposed in the Table 7 for the RP83 detonator. The TNT mass equivalent varies randomly regarding the distance. This variation might be due to the un-

certainties in the blast analysis (*i.e.* the reading of the start and end of the blast for the positive impulse and the reading of the peak of overpressure of the overpressure). This observation can be made for the two explosives: the blasts produced are similar to the one produced by a TNT explosion. On the other hand, the values of the averaged TNT mass equivalents from the overpressure and the impulse data are close to each other. As a consequence, the choice of characteristics for the value of TNT mass equivalent is not important in the study case: the resulting TNT mass equivalent will be the same whether the overpressure peak or the positive impulse is analyzed. These results allows us to conclude that, in the present study, the estimation of a constant TNT mass equivalent regarding the distance and the characteristic used is consistent.

Distance (mm)	EqTNT impulse	EqTNT pressure
350	2.07 g	1.40 g
475	1.06 g	0.80 g
725	1.38 g	1.15 g
975	1.15 g	1.15 g
1079.8	1.06 g	2.00 g
1225	1.09 g	1.40 g
Average :	**1.31 g**	**1.32 g**

Table 7: TNT mass equivalent variation with the distance based on the overpressure pics and the positive impulse (RP83)

Energy is absorbed by the plastic deformation of the casing of the detonators and the ground. These results shows the importance of conducting tests to characterize an explosive and not only use the estimation of the TNT equivalent of each explosive compound. Moreover, the blast driven by the explosion of a RP80-EBW and RP83-EBW can be compared to a blast from a TNT explosion. A constant TNT mass equivalent is then relevant to characterize the explosives studied.

4. Results: Pollutant dispersion

4.1. Repeatability of tests

The blast wave generated by a detonation is typical of each explosive. Tests have been conducted without and with talc around the detonators to investigate the effect of the powder on the pressure wave. Figure 7 gives the blast pressure signals obtained with a RP80 detonator, measured at 350 mm from the center of the explosion without powder around the explosive, with the light powder and with the heavy powder. An equal volume of powder (67 cm^3) is used, which represents 10 g for the light powder and 28 g for the heavy powder. It has been estimated that 28 g of heavy powder was reducing the total energy of the detonation by 70 %; while 10 g of light powder reduces the energy by 30 %.

As the powder affects the blast characteristics, the homogeneity of the distribution of the powder around the explosive before the explosion can be investigated using the pressure sensors: if the powder is equally distributed, the blast propagation should be hemispherical, as it is without powder. Figure 8 gives an example of a case where the powder was not well distributed around the explosion. The four pressure signals, C3, C6, C7, and C2 generated by a RP83 detonator, have been measured at 750 mm around the explosive. These blasts are not equal, highlighting a non hemispherical propagation of the blast. The geometry of the explosion is controlled systematically in this way to assure the repeatability between tests.

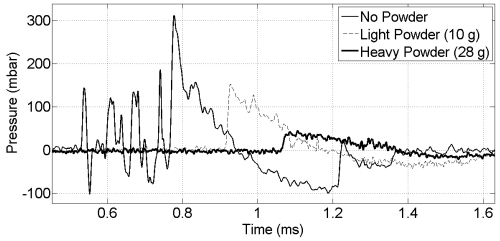

Figure 7: Effect of the talc powder on the blast wave generated by the explosion of a RP80, signal at 350 mm from the explosion, 200 kHz filtered

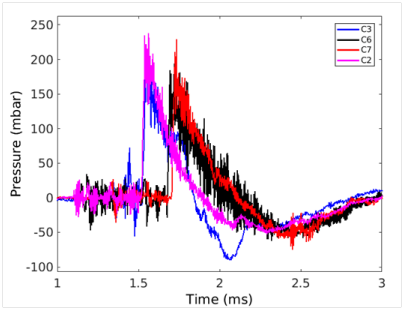

Figure 8: RP83 detonator pressure signals at 750 mm around the explosion, 200 kHz filtered, example of powder not well distributed around the explosive

4.2. *Flow visualization*

The two talc powders (light and heavy) and the two detonators (RP80 and RP83) have been tested inside the wind tunnel under three wind speeds (0 m/s, 3 m/s and 5 m/s). To investigate the dispersion through flow visualization, a code has been written, using the functions of Matlab [15] to obtain the contour of the cloud for each images. Figure 9 shows the images resulting from the post-processing, step by step. Image A is the initial image. Image B is the image where the background has been removed and the contrast increased to make the processing easier. Image C is the image binarized by a threshold of 0.15. This threshold has been chosen arbitrarily and represent the best value to obtain a contour, taking into account the luminosity of the images and the variation of powder concentration regarding the time. Image D is the contour obtained, after a smoothing of the border to remove the solid projectiles that should not be taken into account and applying the edge detection function from Matlab.

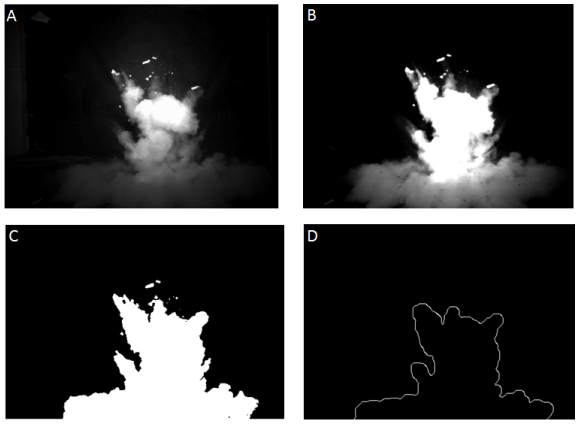

Figure 9: Post-processing of the flow visualization images to obtain the contour of the cloud. A: initial image. B: Background removed and contrast increased. C: Binarization by threshold (0.15) and crop of the image. D: Border smoothing and edge detection

The contour analysis allows to have fast visual comparison between different cases, to investigate the spacial position of the dispersion through the barycenter of the contour and to obtain the variation of the dispersion area regarding the time. The spacial position of the cloud (horizontal and vertical position of the barycenter of the contour) has been investigated for the dispersion of 28 g of heavy powder talc by a RP80 detonator under no wind, a wind of 3 m/s and 5 m/s. Figure 10 gives the variation of the horizontal and vertical position of the barycenter regarding the time. It can be noticed that the horizontal dispersion is approximatly equal for the two wind conditions until 100 ms. After this time, the clouds have a constant propagation and reach 85 % of the wind speed. The vertical propagation under 3 m/s wind is faster than the other dispersions. For the three cases, the vertical dispersion reach a speed of 0.5 m/s.

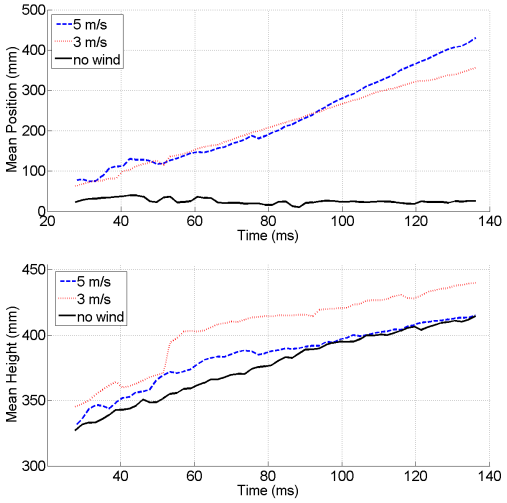

Figure 10: Post-processing of the dispersion of 28 g of heavy powder under no wind, 3 m/s wind and 5 m/s wind. Top: barycenter horizontal position. Bottom: barycenter vertical position

Figure 11 gives the variation of the plume area regarding the time of a dispersion driven by a RP80 detonator under no wind for 10 g and 28 g of heavy powder. As it could be foreseen, the area is larger for a cloud containing more powder.

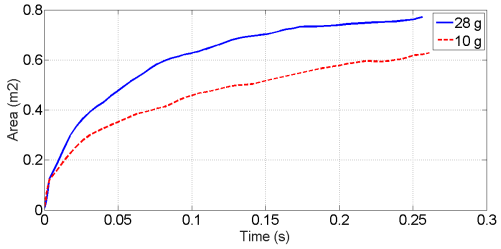

Figure 11: Variation of the area of the RP80 detonator dispersion of 10 g and 28 g of heavy powder under no wind.

4.3. *Velocity fields*

Large-scale particle image velocimetry (LS-PIV) analysis has been conducted using PIVLab [16] with Matlab [15]. The minimum size of window chosen is 8 pixels, with a displacement of 50 %. A LS-PIV

frame taken 19 ms after the explosion is given in Figure 12. The LASER light comes from the left of the plume and is absorbed by it. As a consequence, the right part of the cloud cannot be analyzed.

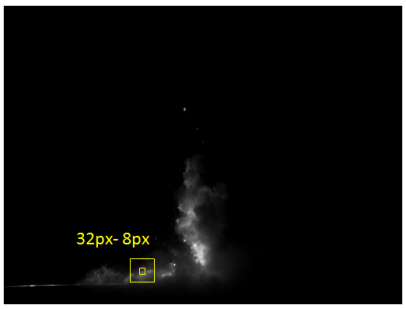

Figure 12: Dispersion of 10g of heavy powder with a RP80 detonator under a 5 m/s urban ABL (19 ms after the explosion) LS-PIV frame

Figure 13 gives the results of the LS-PIV analysis on the dispersion of a RP80 detonator surrounded by 10 g of heavy powder under a wind 5 m/s. Several periods of the dispersion are studied: 1.5 ms, 4 ms, 16 ms and 62 ms after the explosion. The velocity vectors and the velocity magnitude field are given. At 4 ms after the explosion, the particles are propagating away from the center of the explosion, creating a hemispherical dispersion. Propagation speeds of up than 60 m/s can be observed. After 16 ms, the wind impacts the dispersion. The propagation against the wind is slowed down with turbulences and the plume continues to rise up. After 62 ms, the particles are following the wind.

5. Conclusion and perspectives

The dispersion by explosive under an atmospheric boundary layer is investigated inside a subsonic wind tunnel.

The first phase of the research is to gain a solid technical knowledge about blast propagation in an urban environment at laboratory scale. This paper presents gram-scale experimental investigations on blast wave measurement using two types of detonators: RP80-EBW and RP83-EBW. A methodology to study the characteristics of a blast has been applied. It has been showed that the theoretical TNT equivalent differs from the experimental one because of the plastic deformation of the set-up. However, it appeared that the positive impulse and the overpressure have a similar variation regarding the distance than a TNT

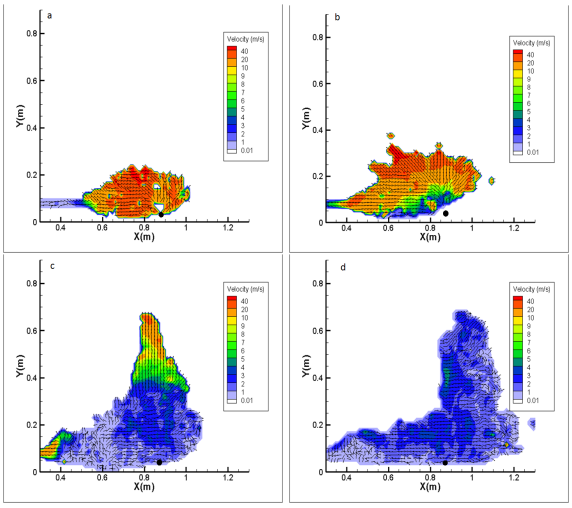

Figure 13: LS-PIV analysis of the dispersion of 10 g of heavy powder with a RP80 detonator at 1.5 ms (a), 4 ms (b), 16 ms (c) and 62 ms (d) after the explosion under an urban ABL of 5 m/s (black circle: centre of the explosion)

explosion, once scaled by the appropriate TNT mass equivalent .

Once the explosives have been characterized, talc powder has been added around the explosive to simulate the dispersion. The analysis of the blast generated by the explosion highlights the effect of the particles around the explosive on the energy released by the detonation: an increase of the powder mass decreases the energy. As a consequence, the homogeneity of the powder around the explosive is controlled by the investigation of the blast propagation. Flow visualizations and large scale PIV have been performed to investigate the dispersion.

Future works will be conducted to have a parametric analysis of the effect of the diameter of the powder, the detonator used and the speed of the wind applied. Then, the dispersion inside urban environments will be investigated.

Acknowledgments

This work has been conducted in the context of collaboration with the Direction des applications militaires (DAM) of the Centre d'Etudes de Gramat (CEG), from the Commissariat à l'énergie atomique et aux énergies alternatives (CEA).

References

[1] E. Wingstedt, H. Fossum, B. Reif, Simulation of bomb residue deposition following the oslo bombing, July 22 2011, FFI Rapport 2012/01836, ISBN 978-82-464-2176-6.

[2] N. Moussa, V. Devarakonda, Prediction of toxic emissions from chemical fire and explosion, Fire safety science-proceedings of the eleventh international symposium. pp. 1457-1468. DOI:10.308/IAFSS.FSS.11-1457.

[3] F. Zhang, D. Frost, P. Thibault, S. Murray, Explosive dispersal of solid particles, Shock Waves, January 2001, Volume 10, Issue 6, pp 431-443.

[4] D. Frost, C. Ornthanalai, Z. Zarei, V. Tanguay, F. Zhang, Particle momentum effects from the detonation of heterogeneous explosives, Journal of applied physics 101, 113529 (2007). DOI:10.1063/1.2743912.

[5] C. Sturtzer, Etude des mécanismes de dispersion par choc et des régimes de combustions de nuages de particules d′aluminium, ISAE-ENSMA-Poitier, 2014.

[6] L. Li, X. Ren, X. Lu, X. Yan, On the characteristics of liquid explosive dispersing flow, World academy of science, engineering and technology 70 2010, pp 606-610.

[7] C. Jenkins, R. Ripley, C. Wu, Y. Horie, K. Powers, W. Wilson, Explosively driven particle fields imaged using a high speed framing camera and particle image velocimetry, Internation journal of multiphase flow, Volume 51, May 2013, pp 73-86.

[8] B. Conan, Wind resource accessment in complex terrain by wind tunnel modelling, Ph.D. thesis, Université d′Orléans, 2012.

[9] I. Fujita, M. Muste, A. Kruger, Large-scale particle image velocimetry for flow analysis in hydraulic engineering application, Journal of hydraulic research, 1998, 36:3, 397-414, DOI:10.1080/00221689809498626.

[10] Risi, data base - risi - subsidiary of reynolds industries incorporated.

[11] S. mannan. lees loss prevention in the process industries, volume 2 2012, fourth edition.

[12] Explosive shocks in air, Second Edition., s.l. : Spring Science Business Media New York, 1985., ¢.

[13] Groupe d′étude des Modes Opératoires, Détermination des équivalents tnt par effet de souffle des explosifs, november 2013 edition.

[14] P. Cooper, Comments on tnt equivalence, 20th international pyrotechnics seminar, colorado springs, colorado july 24-29, 1994.

[15] C. Thompson, L. Shure, Image Processing Toolbox: For Use with MATLAB;[user's Guide], MathWorks, 1995.

[16] W. Thielicke, E. Stamhuis, Pivlab towards user-friendly, affordable and accurate digital particle image velocimetry in matlab, Journal of Open Research Software, 2: e30, DOI: http://dx.doi.org/10.5334/jors.bl.

Multiphase Flow Modeling for CBRN Applications

Yoshiyuki Nishio

Environmental and applied fluid dynamics department, von Karman Institute for Fluid Dynamics, Belgium, yoshiyuki.nishio@vki.ac.be

Supervisor: Jeroen van Beeck

Professor, Environmental and applied fluid dynamics department, von Karman Institute for Fluid Dynamics, Belgium, vanbeeck@vki.ac.be

University Supervisor: Bart Janssens ; Karim Limam

Assoc. Professor, Royal Military Academy (RMA) - Renaissancelaan 30 - 1000 Brussels, Belgium, bart.janssens@rmi.ac.be ;
Professor, Université de La Rochelle (ULR): Technoforum - 23 avenue Albert Einstein - BP 33060 - 17031 La Rochelle, France, klimam01@univ-lr.fr

Abstract

A DNS model for fluids laden with small particles was developed in the thesis of Janssens, B. [1].
The resulting model uses a finite element method for both the fluid and the dispersed phase.
In the context of a chemical, biological, radiological and nuclear (CBRN) application for the Belgian Defense, the current work is proposed to adapt this model to predict the dispersion of particles in the atmosphere. The first step is to design a one-phase model and to represent correctly a thermally neutral atmospheric boundary layer (ABL). Thus, the turbulence is predominantly generated mechanically due to wind shear.
Therefore, a neutral pressure-driven (i.e. constant pressure gradient) boundary layer with symmetry condition at the top, periodicity in the stream-/span-wise directions and impermeability in combination with Schumanns [2] wall-stress boundary conditions at the bottom is considered. For the latter, the wall-stress is being related to the wall parallel velocity components at the first grid points using [3; 2]:

$$\tau_{1,2} = -\left[\frac{\kappa}{\ln(y_1/y_0)}\right]^2 \left(\bar{u}_1^2 + \bar{u}_2^2\right)^{0.5} \bar{u}_{1,2} \tag{1}$$

with κ the von Karman constant, y_0 the surface roughness, y_1 the vertical location of the first grid point and $\bar{u}$ the local average (the filtering being omitted for this work) in directions parallel to the wall [4].
This methodology was developed for a finite difference method in [4] and is adapted to finite element method in current work. The adaptation in finite element code is not trivial but could be beneficial when using tetrahedral meshes (allowing automatic meshing). Indeed, in finite element, the type of element has less impact on the accuracy of the results and can improve its accuracy by use of higher order polynomials [5].
The results are validated by comparing with the work of Goit, J.P. [4].

Keywords: CFD, Multiphase Flow, ABL, Turbulent Flow, LES, Finite Element Method (FEM).

References

[1] B. Janssens, Numerical modeling and experimental investigation of fine particle coagulation and dispersion in dilute flows, Ph.D. thesis, Université de La Rochelle (2014).
[2] U. Schumann, Subgrid scale model for finite difference simulations of turbulent flows in plane channels and annuli, Journal of computational physics 18 (4) (1975) 376–404.
[3] E. Bou-Zeid, C. Meneveau, M. Parlange, A scale-dependent lagrangian dynamic model for large eddy simulation of complex turbulent flows, Physics of fluids 17 (2) (2005) 025105.
[4] J. P. Goit, Optimal control of energy extraction in large-eddy simulation of windfarms, Ph.D. thesis (2015).
[5] T. Hughes, T. Tezduyar, Finite element methods for first-order hyperbolic systems with particular emphasis on the compressible euler equations, Computer Methods in Applied Mechanics and Engineering 45 (1984) 217–284.

Offshore wind wave interaction: a new roughness parameterization

Sara Porchetta

Environmental & Applied Fluid Dynamics Department, von Karman Institute for Fluid Dynamics, Belgium, sara.porchetta@vki.ac.be

Supervisor: Jeroen van Beeck

Professor, Environmental & Applied Fluid Dynamics Department, von Karman Institute for Fluid Dynamics, Belgium, vanbeeck@vki.ac.be

University Supervisor: Nicole van Lipzig

Professor, Department of Earth and Environmental Sciences, KULeuven, Belgium, nicole.vanlipzig@kuleuven.be

Abstract

Due to the dynamic characteristics of the sea state, the roughness parameterization should include parameters responsible for it in order to respond to this dynamic behavior. From the investigation of offshore wind wave measurements of the ASIT mast it is shown that the relative propagation direction between the wind and the waves have a major influence on the roughness parameterization and a new law is proposed which includes this phenomena.

Keywords: wind wave interaction, roughness parameterization, ASIT measurement mast

1. Introduction

During the last few years there has been an increased interest in wind turbines. It has been proposed as an ideal alternative for non-clean emission gas producing sources of energy, and a good candidate to meet the rising energy demands. Moreover, there is more and more interest in offshore wind turbines because of their societal benefits and their higher wind extraction possibilities compared to onshore turbines. The last ten years the European offshore capacity increased by 11 GW [1]. Moreover, by 2020 20% of the total energy should be renewable, in order to reach this target the estimated installed wind energy capacity is 40 GW [2]. However, due to the high cost of offshore wind turbines, it is important to have accurate wind and turbulence profiles. Such accurate profiles will help estimate the energy production, the dynamic loads, the wind turbine wakes and thus the allocation of new wind farms.

In order to obtain high fidelity wind and turbulence profiles, the wind wave interaction offshore should be fully understood. This can help improve numerical forecasting models who predict the velocity. Hence, it is important to have offshore measurement data available, this to improve our understanding of the wind wave interaction. The wind wave interaction is located within the Marine Atmospheric Boundary Layer (MABL), which is the lowest part of the atmosphere directly influenced by the sea surface. Compared to the Atmospheric Boundary Layer (ABL) on land, the MABL differs because of a changing sea surface and the diurnal character present on land is absent. Because of the reduced wind drag offshore higher wind speeds are present together with lower turbulence intensities [3; 4]. Through the years this has been investigated thoroughly. A well described phenomenom is the difference in momentum transfer between ABL and MABL. The momentum transfer between the sea surface and the atmosphere consist out of complex interactions shown in Fig. 1.

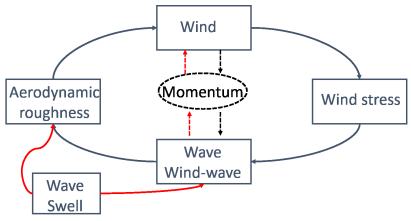

Figure 1: Wind wave interactions [5].

An important factor in correctly estimating the momentum transfer is the total shear stress. The total shear stress, τ_{tot}, and thus the momentum transfer, offshore is dependent on the turbulent shear stress, τ_{turb}, the wave induced shear stress, τ_{wave}, and the viscous shear stress τ_{visc} (Eq. 1) [6].

$$\tau_{tot}(z) = \tau_{turb}(z) + \tau_{wave}(z) + \tau_{visc}(z) \tag{1}$$

The viscous shear stress is assumed to be negligible as it is only important in the viscous sublayer, which is considered of inconsequential height. The wave shear stress, however, is considerable in the MABL and decreases with height. As can be seen on Fig. 1, momentum transfer can go two ways; from the wind to the wave and vice versa. The sign of the wave shear stress is strongly dependent on the wave age, which most often is defined as in Eq. 2. In this equation U_{10} is the wind speed at 10m and c_p is the wave phase speed. When $\chi < 1.2$, the wind is dominant and the waves present are called wind waves or young waves, however when $\chi > 1.2$, the wave speed is dominant over the wind speed and we speak about swell waves or old waves [7]. This can also be written in function of the friction velocity, u_*, shown in Eq. 3 where $\chi < 20$ corresponds with young waves and $\chi > 20$ with old waves [8].

$$\chi = \frac{c_p}{U_{10}} \tag{2}$$

$$\chi = \frac{c_p}{u_*} \tag{3}$$

For wind waves, the wave shear stress is positive. As such there is a downward momentum flux, and the aerodynamic roughness (z_0) increases. On the other hand, for swell waves, the aerodynamic roughness decreases up to a point that the wave shear stress can become negative. This can cause the total shear stress to become negative which results in a upward momentum flux, because of which momentum is transported from the sea surface to the atmosphere [9; 10].

The most commonly used offshore aerodynamical roughness parameterization, in order to have the correct momentum transfer from the sea to the atmosphere, is the Charnock relation (Eq. 4). Where α is the Charnock parameter depending on the sea state and assumed to be constant and g is the gravitational constant [11].

$$z_0 = \alpha \frac{u_*^2}{g} \tag{4}$$

Later [12] suggested that the Charnock parameter should include an explicit relation containing information of the sea surface characteristics. As such, it included the wave steepness H_s/L, where H_s is the significant wave height and L the wave length. For deep water waves, where the depth of the sea (h) is bigger than half the wave length, the wave speed is related to the wave length by Eq. 5 while for shallow regions it is equal to Eq. 6. The modified roughness parameterization is shown in Eq. 7, where A is a constant.

$$c_p = \sqrt{\frac{gL}{2\pi}} \tag{5}$$

$$c_p = \sqrt{gh} \tag{6}$$

$$\frac{z_0}{H_s} = A\left(\frac{u_*}{c_p}\right)^2 \tag{7}$$

A more general roughness parameterization was found by [13] and is shown in Eq. 8.

$$\frac{z_0}{H_s} = A\left(\frac{u_*}{c_p}\right)^B \tag{8}$$

However, by not estimating the roughness relation on one data set but multiple ones [8] found Eq. 9 to be a correct roughness parameterization.

$$\frac{z_0}{H_s} = 3.35\left(\frac{u_*}{c_p}\right)^{3.4} \tag{9}$$

An alternative proposal came from [14], which found the parameterization shown in Eq. 10 and was based on field and laboratory data sets.

$$\frac{z_0}{H_s} = 1200\left(\frac{H_s}{L}\right)^{4.5} \tag{10}$$

The latest parametrization of [15] is based on LES simulations where the angle, θ, between the wind speed at 10m and the wave propagation direction is taken into account, this is shown in Eq. 11. However, the aerodynamic roughness should be limited at low inverse wave ages.

$$\frac{z_0}{H_s} = A\left(\frac{u_*}{c_p}\right)^{3.4cos(0.94\theta)} \tag{11}$$

All these parametrizations, except [15], do not include the effect of the angle between wind and waves. One can expect that this effect, however, is significant. In this paper we will investigate this effect of

the angle between wind and waves and try and find a better roughness parametrization. For this we will use offshore ASIT mast data, which measured atmospheric and oceanographic parameters from 2003 to 2012. Later this parameterization can be implemented in coupled atmosphere-ocean-wave models in order to improve the wind forecasting offshore.

2. ASIT test site and instrumentation

The Air-Sea Interaction Tower (ASIT) is located 3.2 km south of Martha's Vineyard in the Atlantic Ocean (Fig. 2, point C) and is part of the CBLAST measurement campaign. At the location of the ASIT tower the water is around 15 m deep. Measurements are continuously available between 2003 up to 2012. Wind coming from a direction between 140° and 250° is fetch unlimited, because it is not influenced by the land in the north and to shallow water to the east and west. Moreover, directions between 0° and 150° are affected by flow distortions by the tower itself [16], resulting in wind shadow distortions.

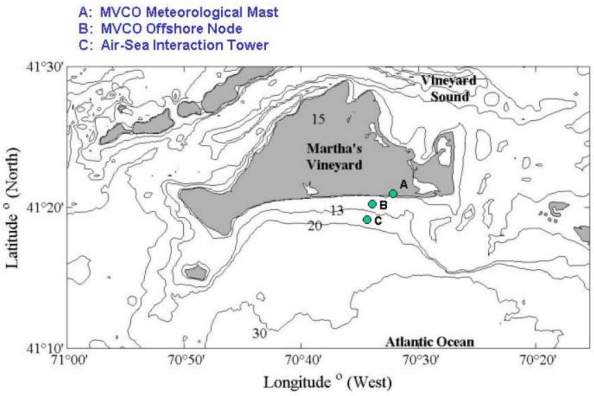

Figure 2: Location of the ASIT tower indicated by a red triangle [16].

The instrumentation of the ASIT tower is shown on Fig. 3. In this paper where the wind wave interaction is investigated measurements from the R3-sonic anemometer (Fig. 3, point C) are used. These measurements are taken at 18 m above sea level with a measuring frequency of 20 Hz. This results in measurements of eddy correlation fluxes of momentum and virtual heat averaged over 20 minutes. Slow response measurements of air temperature, pressure and relative humidity are measured with a vaisala RH/T sensor. The oceanic variables are obtained from the subsurface node (Fig. 2, point B) located 1.5 km south of Martha's Vineyard and is 12m deep. Wave characteristics such as wave height and propagation direction are measured.

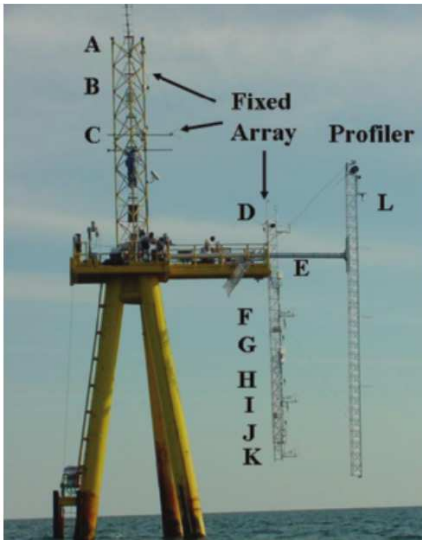

Figure 3: ASIT instrumentation [16].

Even though the oceanographic data and the atmospheric data are non co-located we assume that the distance of 1.7 km and a water depth difference of 3 m are small enough to assume the same oceanographic features. Furthermore, if the slow response atmospheric measurements (wind speed, wind direction, temperature ...) are compared between the meteorologic mast (Fig. 2, point A) and the ASIT tower (Fig. 2, point C) no significant differences are noticed. For these reasons we assume that the ASIT measurements can be combined with the subsurface node to investigate the wave induced velocity changes.

3. Analysis of ASIT data

From the years 2003 to 2012 the measurements of 2005, 2009 and 2012 were excluded because they did not contain all the necessary information in order to do the following analysis. This results in an analysis of 63 944 measurement points. Investigation of the dominant wind and wave direction (Fig. 4 & Fig. 5) shows that the main wind direction is coming from the South-West, not taking into account the mast shadow directions. Furthermore, the waves are mostly coming from the South which corresponds to the fetch unlimited area South of Martha's Vineyard while no waves are coming from the fetch limited North side.

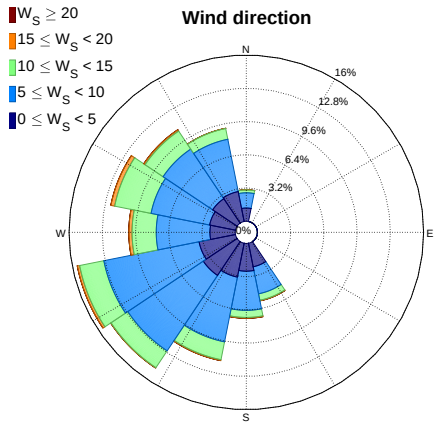

Figure 4: Wind rose excluding the wind shadow zones of the mast.

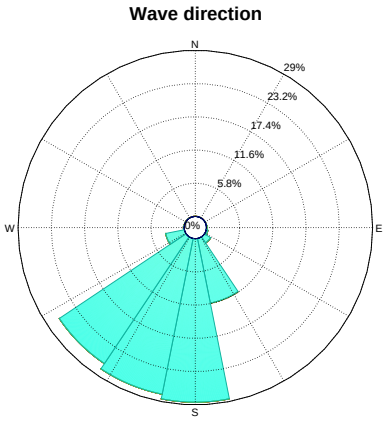

Figure 5: Wave rose.

Wind wave direction alignment occurs most of the time (Fig. 6), which means that a wind wave equilibrium is present. In these cases the wave field is fully developed and in equilibrium with the wind field. However, as can be seen from Fig. 6 alignment is not always the case. Less frequent the wave and wind direction are opposed to each other, for this site it is the case when the wind is blowing from land (Fig. 7) while the waves (Fig. 8) are coming from their fetch unlimited area in the South. The reverse, where wind is blowing from the sea and waves are coming from the land does not occur. Moreover, wind wave equilibrium often occurs at higher wind speeds than opposed wind wave direction (Fig. 9). The waves traveling opposed to the wind direction with a lower wind speed are mostly remotely generated swell moving towards the measurement tower.

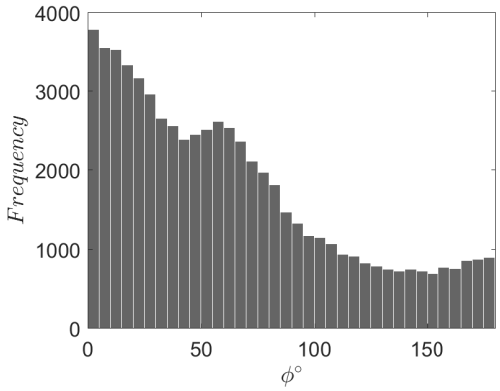

Figure 6: Frequency histogram of the angle between the wind and the wave propagation direction.

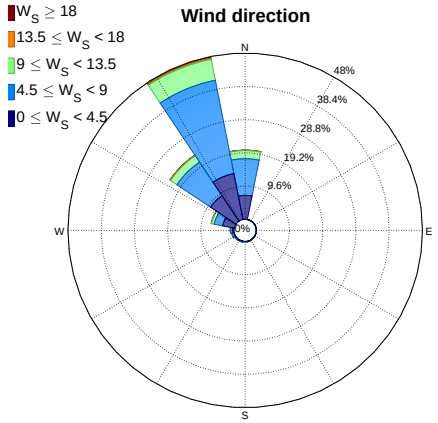

Figure 7: Wind rose excluding the wind shadow zones of the mast for opposed wind waves directions.

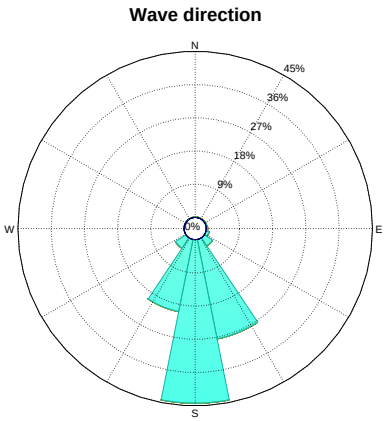

Figure 8: Wave rose for opposed wind waves directions.

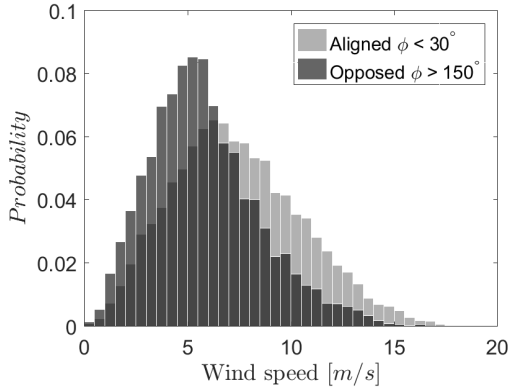

Figure 9: Wind speed probability for aligned wind wave direction (20 370 points) and opposed wind wave direction (4 852 points).

In order to validate the ASIT measurements against the roughness parameterization of [8], we processed the data following [8]. The friction velocity (Eq. 12) can be calculated based on the measured alongwind, $< w'u' >$, and crosswind, $< w'v' >$, momentum flux components which are averaged over 20min intervals.

$$u_*^2 = \left[(- < w'u' >)^2 + (- < w'v' >)^2\right]^{0.5} \tag{12}$$

The roughness, z_0, is calculated from the logarithmic wind profile assumption shown in Eq. 13, where κ is the von Karman constant, U_{zN} is the neutral wind speed and U_0 is the surface drift speed. The latter is small and assumed to be zero.

$$\frac{1}{\kappa} log \frac{z}{z_0} = \frac{U_{zN} - U_0}{u_*} \tag{13}$$

The neutral wind speed is calculated based on Eq.14, where U_z is the wind speed at 18 m above sea level and ψ_u is the integrated stability function according to [17].

$$U_{zN} = U_z + \frac{u_*}{\kappa} \psi_u \left(\frac{z}{L}\right) \tag{14}$$

In order to find the integrated stability function, the stability of the atmosphere should be classified in stable and unstable atmospheric conditions. This distinction is made based on the Obukhov length (Eq. 15), where θ_v is the virtual potential temperature and $< w'\theta_v' >$ is the virtual potential temperature flux. The latter is directly available from the measurements averaged over 20 min intervals while the former is calculated based on the Clasius-Clapeyron relation, the relative humidity and the pressure.

$$L = -\frac{u_*^3 \theta_v}{g\kappa < w'\theta_v' >} \tag{15}$$

The classification of the atmosphere in the different stability classes is shown in Tab. 1 [18].

Table 1: Stability classification

Stability class	Range of L	Frequency
Very Stable	$0 \leq L < 200$	23 300
Stable	$200 \leq L < 1000$	3 856
Near-Neutral	$1000 \leq \|L\|$	481
Unstable	$-1000 < L \leq -200$	4 593
Very Unstable	$-200 < 0 \leq -200$	25 730

For stable conditions (L > 0) the integrated stability function is equal to Eq. 16, while for unstable conditions (L < 0) it is equal to Eq. 17 together with Eq. 18.

$$\psi = -5\frac{z}{L} \tag{16}$$

$$\psi = 2ln\left(\frac{1+x}{2}\right) + ln\left(\frac{1+x^2}{2}\right) - 2tan^{-1}x + \frac{\pi}{2} \tag{17}$$

$$x = \left[1 - 16\left(\frac{z}{L}\right)\right]^{\frac{1}{4}} \tag{18}$$

The dimensionless roughness, z_0/H_s, is plotted against the inverse wave age parameter u_*/c_p for 63 944 measurement points of the ASIT data and this is compared to [8]. Wind generated waves are better represented by [8] law while there is much more scatter for swell waves. This indicates that for swell waves there are more parameters defining the roughness parameter apart from the wave speed and the wave height. As the study of [15] on LES simulation suggested, the swell waves influence the roughness based on their propagation direction relative to the wind direction. [15] indeed proposed a new roughness parameterization (Eq. 11) including the angle between the wind and the wave direction. However, no formulation is given for A and it has not been tested on offshore measurement data.

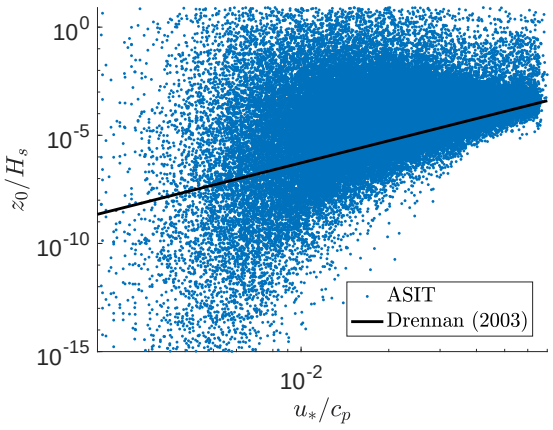

Figure 10: Dimensional roughness z_0/H_s against the inverse wave age parameter u_*/c_p

4. New parameterization

In order to find a new parametrization of the roughness taking into account the angle (ϕ) between the wind and the wave direction, the dimensionless roughenss, z_0/H_s, is plotted against the inverse wave age parameter u_*/c_p for six different alignments (Fig. 11). The number of measured points for each of these alignments is shown in Tab. 2.

Table 2: Number of measurement points

$\phi°$	# measurements points
0° - 30°	20 790
30° - 60°	15 643
60° - 90°	12 541
90° - 120°	6 584
120° - 150°	4 590
150° - 180°	4 912

In general swell waves have a lower roughness compared to wind generated waves, this due to the reduced shear stress. However, this is only valid for swell waves aligned with the wind direction. The roughness increases gradually with increasing misalignment between the wave direction and the wind direction. This increased roughness appears to be most present when the waves are propagating against the wind pressure gradient. Starting from the parameterization of [8] a new parameterization is proposed where the angle between the wind and wave direction is taken into account. Because both the inclination and the intersection with the vertical axes changes for the different alignments, ϕ should be included in the constant term and in the exponent (Eq. 19).

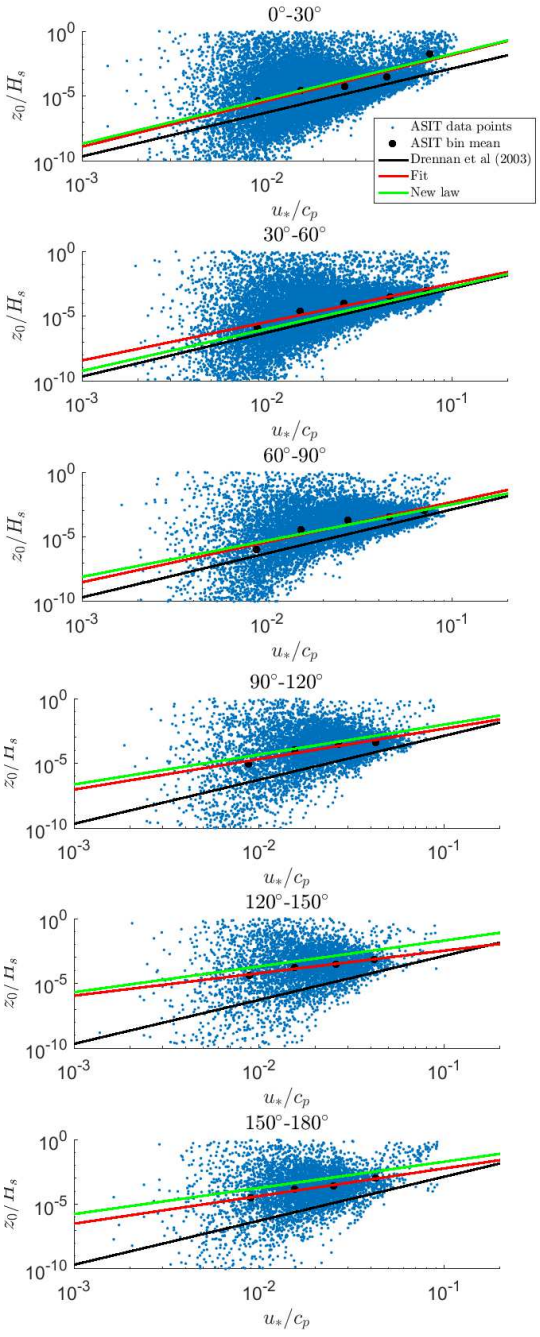

Figure 11: Dimensionless roughenss measurement points, z_0/H_s, plotted against the inverse wave age parameter u_*/c_p for six different alignments. Black dots are the bin means of the measurement point and the red line is the fit through them, while the black line is the law proposed by [8]. The green line is the new proposed roughness parameterization.

$$\frac{z_0}{H_s} = A(\phi)\left(\frac{u_*}{c_p}\right)^{B(\phi)} \tag{19}$$

In order to find the relation of the constant term and the exponent in function of the the angle between the wind and wave direction, this latter is plotted against the coefficients of the fitted curve (Fig. 11, red curve) obtained by the bin mean average values. Using this method a general formulation can be found for $A(\phi)$ and $B(\phi)$. The result are shown in Fig. 13 and Fig. 12 for respectively the constant term and the exponent.

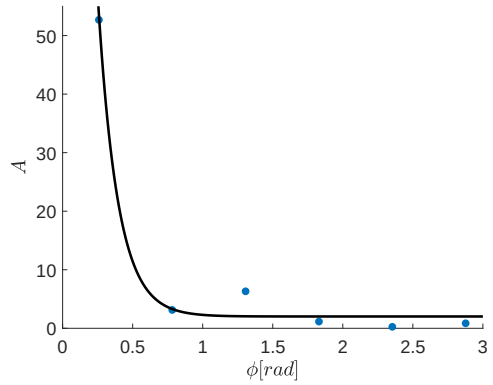

Figure 12: Constant term of the new parameterization in function of ϕ, for the measured values (blue dots) and the proposed fit (R^2 = 0.989).

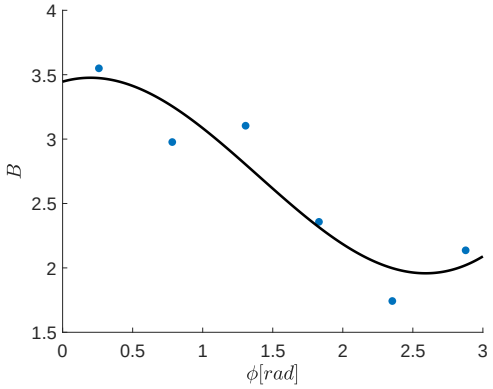

Figure 13: Exponent of the new parameterization in function of ϕ, for the measured values (blue dots) and the proposed fit (R^2 = 0.89).

For the constant term an exponential function is proposed (Eq. 20), while a sum of two sine is proposed for the exponent (Eq. 22). The new parameterization taking into account the direction between the wind and the wave is shown in Eq. 24.

$$A(\phi) = a_1 e^{(a_2\phi)} + a_3 \tag{20}$$

$$\begin{cases} a_1 = 321.3 \\ a_2 = 7.061 \\ a_3 = 2.017 \end{cases} \tag{21}$$

$$B(\phi) = b_1 sin(b_2\phi + b_3) + b_4 sin(b_5\phi + b_6) \tag{22}$$

$$\begin{cases} b_1 = 72.76 \\ b_2 = 0.01492 \\ b_3 = 0.016552 \\ b_4 = 2.422 \\ b_5 = 0.848 \\ b_6 = 1.959 \end{cases} \tag{23}$$

$$\frac{z_0}{H_s} = \left[a_1 e^{(a_2\phi)} + a_3\right]\left(\frac{u_*}{c_p}\right)^{\left[b_1 sin(b_2\phi+b_3)+b_4 sin(b_5\phi+b_6)\right]} \tag{24}$$

As can be seen from Fig. 11 (blue curve) this new parameterization is wel describing the behavior of the swell waves influenced by the changing roughness due to the alignment between the wind and the wave direction. However, this relation is based on one measurement location and should be verified if it is valid for other location as well.

5. Conclusions

Investigating the roughness parameterization for offshore conditions, shows us that the roughness of swell waves is strongly dependent on the relative direction between the wind and the wave propagation. Swell waves aligned with the wind result in a lower roughness compared to swell waves opposed to the wind. This phenomenon is not included in the most recent roughness parameterization, moreover up to now it is only observed by LES simulations. In this paper we showed that the changing roughness due to different alignments between wind and wave direction is present for the offshore measurement of the ASIT tower. Based on these measurement a new roughness parameterization is proposed which described the measurement data well. However, validation with other measurement data should be necessary in order to propose this new parameterization as general one.

Acknowledgments

This research was funded by FWO-SB.

References

[1] A. Ho, A. Mbistrova, The European offshore wind industry: Key trends ans statistics 2016, Tech. rep., Wind Europe (2017).
[2] A. Arapogianni, J. Moccia, Wind in our Sails: The coming of Europe's offshore wind energy industry, Tech. rep., European Wind Energy Association (2011).
[3] F. Ardhuin, B. Chapron and F. Collard, Observation of swell dissipation across oceans, Geophys. Res. Lett. 36 (2009) 1–5.
[4] R. Stull, An intoduction to boundary layer meteorology, Springer Netherlands, 1988.
[5] A. Al Sam, Wind-wave interaction effects on offshore wind energy, Ph.D. thesis, Lund University (2016).
[6] O. Phillips, Dynamics of the Upper Ocean. 2d ed., Cambridge University Press, 1977.
[7] M.A. Donelan, The dependence of the aerodynamic drag coefficient on wave parameters, Amer. Meteor. Soc. (1982) 381–387.
[8] W.M. Drennan, H.C. Graber, D. Hauser and C. Quentin, On the wave age dependence of wind stress over pure wind seas, J. Geophys. Res. 108 (2003) 8062.
[9] M. Cathelain, Development of a deterministic numerical model for the study of the coupling between an atmospheric flow and a sea state., Ph.D. thesis, l'Universite Bretagne Loire (2017).
[10] P.P. Sullivan, J.C. McWilliams and C.-H. Moeng, Simulation of turbulent flow over idealized water waves, J. Fluid. Mech. 404 (2000) 47–85.
[11] H. Charnock, Wind stress on a water surface, Quart. J. Roy. Meteor. Soc. 81 (1955) 639–640.
[12] S.A. Hsu, A Dynamic Roughness equation and Its Application to Wind Stress Determination at the Air-Sea Interface, J. Phys. Oceanogr. 4 (1973) 116–120.
[13] M. Donelan, The sea: the air-sea interaction, Wiley and Sons, 1990.
[14] P.K. Taylor and M.J. Yelland, The dependence of sea surface roughness on the height and steepness of the waves, J. Phys. Oceanogr. 31 (2001) 572–590.
[15] E. Patton, B. Kosovic, J. D. P. Sullivan, L. Mahrt, M. Zagar, L. Gulstad, Final techincal report: impacts of stratification and non-equilibrium winds and waves on hub-height winds, Tech. rep., National Center for Atmospheric Research (2015).
[16] J., Edson, Crawford, T., Crescenti, J., Farrar, T., Frew, N., Gerbi, G., Helmis, C., Hristov, T., Khelif, D., Jessup, A., Jonsson, H., Li, M., Mahrt, L., McGilles, W., Plueddemann, A., Shen, L., Skyllingstad, E., Stanton, T., Sullivan, P., Sun, J., Trowbridge, J., Vickers, D., Wang, S., Wang, Q., Weller, R., Wilkin, J., Williams III, A.J., Yue, D.K.P., and Zappa, C , The coupled boundary layers and air-sea transfer experiment in low winds, Bull. Amer. Meteoril. Soc. 88(3) (2007) 341–356.
[17] R.J. Barthelmie, The effects of atmospheric stability on coastal wind climated, Meteorol. Appl. 6 (1999) 39–47.
[18] A.J.M van Wijk, A.C.M. Beljaars, A.A.M. Holtslag and W.C. Turkenburg, Evalutaion of stability corrections in wind speed profiles over the North Sea, Journal of Wind Engineering and Industrial Aerodynamics 33.

Experimental characterization of a solid-liquid mixture flowing in circular pipes

Maria Teresa Scelzo

Environmental and Applied Fluid Dynamics Department, von Karman Institute for Fluid Dynamics, Belgium, mariateresa.scelzo@vki.ac.be

Supervisor: Jean-Marie Buchlin

Professor, Environmental and Applied Fluid Dynamics Department, von Karman Institute for Fluid Dynamics, Belgium, buchlin@vki.ac.be

Co-Supervisor: Laura Peveroni

Research Engineer, Environmental and Applied Fluid Dynamics Department, von Karman Institute for Fluid Dynamics, Belgium, peveroni@vki.ac.be

University Supervisor: Herman Deconinck

Professor, Areo-Thermo-Mechanics Departement, Université Libre de Bruxelles, Belgium, deconinck@ulb.ac.be

Abstract

This work presents the experimental study of an isothermal slurry − liquid carrier with dispersed solid particles − flowing in circular pipelines. A mixture of $HFE7200$ and sucrose crystals at ambient temperature flows in a horizontal, vertical and oblique pipe as well as in two vertical bends. Pressure losses are evaluated for fully liquid state and for slurry with the solid mass fraction (ϕ) up to 40%; the flow velocity between $0.4m/s$ and $0.9m/s$, resulting in a fully turbulent flow.
The data analysis shows different behaviours depending on the geometrical configuration: pressure drop rises by increasing the flow rate and the solid mass fraction in the oblique and horizontal section. In the vertical pipe the presence of particles does not affect the wall friction coefficient, resulting in unchanged losses with respect to the liquid state. In the vertical 90° bend the presence of particles seems to reduce the vortex region after the fitting, resulting in a lower coefficient with respect to the fully liquid state.
The paper gives an overview about the experimental results suggesting design-oriented correlations and models for each test section.

Keywords: two-phase flow, slurry, pressure drops, circular pipelines

1. Introduction

The experimental campaign described in this paper is part of a project in development at von Karman Institute for Fluid Dynamics, intended to characterize *slush* flows as a propellant for future launcher engines. Nowadays, cryogenic liquids are widely used as fuel in rocket engines due to the high specific impulse they provide. However, the use of liquid propellants still leads to problems of sloshing, large storage volume requirements and short holding time due to their physical properties and highly thermo-sensitive nature. One promising way to reduce these problems is to use slush instead of pure liquid as fuel **?**. Slush is a solid-liquid mixture which possesses density and specific enthalpy higher than the liquid state. Recent studies conducted at the SART dipartement at DLR have shown a potential improvement on the Gross Payload of about 20% if slush replaces the liquid propellant **?**.

However, the presence of solid particles in the liquid suspension changes the flow and the thermal properties: the rheological behaviour becomes non-Newtonian for high particle concentration and, due to the heat transfer, the solid fraction partially melts changing slush properties in a currently unpredictable

process. This implies that the standard correlations for the liquid flow in tubes are no longer valid. Thus, the optimization of the slush transport through circular pipelines requires the characterization of the slush thermal and fluid dynamics, along with their modelling by means of numerical simulations.

In a first approximation, neglecting the thermal effects and phase change, a slush flow can be regarded as a slurry flow, i.e. an isothermal two-phase flow at room temperature involving a carrier liquid and dispersed solid particles **?**.

This paper describes the experimental study of an isothermal slurry in flow similarity with slush hydrogen – the current target for space propulsion applications. An extensive literature survey on the hydraulic behavior of slurry flows in circular pipelines, presented in Section 2, supported the preparation of the experiments in the VKI Predict facility (Section 3) and the analysis of the data (Section 4).

2. Literature Survey

Due to the large range of applications in which slurries are involved, such as hydro-transportation or energy plants cooling, many studies are already available concerning slurries flowing in horizontal circular pipes, in which the carrier and the dispersed phases are made of different materials (water-sand or water-glass spheres).

The straightforward method to evaluate the pressure losses for slurry flows is to consider the solid – liquid mixture as a uniform fluid with enhanced density. Therefore, the pressure drop can be evaluated by mean of Eq. 1:

$$\Delta P_m = \frac{1}{2}\lambda \rho_m U^2 \frac{L}{D}, \tag{1}$$

where ΔP_m is the pressure loss for concentrated slurry, λ the friction coefficient, ρ_m the mixture density, U the mean slurry velocity, D the pipe diameter, L the axial length of the section. The mixture density is formulated in Eq. 2 as an average of the liquid and solid densities weighted on the solid volume concentration α.

$$\rho_m = (1-\alpha)\rho_l + \alpha\rho_s \tag{2}$$

Consequently, the pressure drop increases with the mass flow rate Q and α, as shown in Figure 1 , where ΔP_m are plotted in function of of the mixture Reynolds number, calculated as in Eq. 3 (**?**):

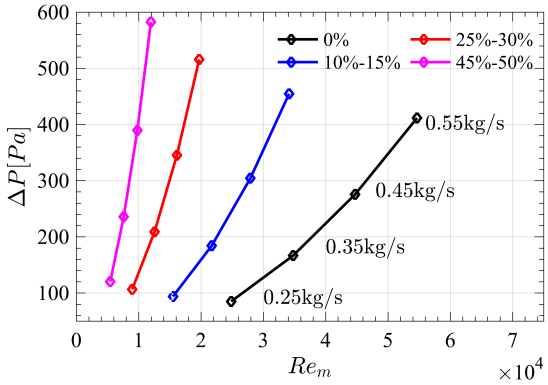

Figure 1: Expected ΔP versus Re_m in function of α (different colours lines) according to Eq.1.

$$Re_m = \frac{\rho_m U D}{\mu_m} \tag{3}$$

The simplicity of Eq. 1 implies that the phenomenon of flow regime transition occurring in liquid conveying of solids in pipes are not taken into account. These regimes have been identified by Durand and Condiolis **?** and they are reported in Figure 2. When the flow speed is low, particles deposit on the bottom wall of the pipe in a moving bed (3). As the flow speed increases, turbulence is sufficient to lift more solid and all the particles move in an asymmetric pattern, referred to as heterogeneous flow regime (2). If the particle size decreases ($10-20\mu m$) or the velocity further increases, the solid phase follows the liquid showing a homogeneous distribution (1). As shown in Figure 2, the pressure drop depends upon the exhibited flow pattern.

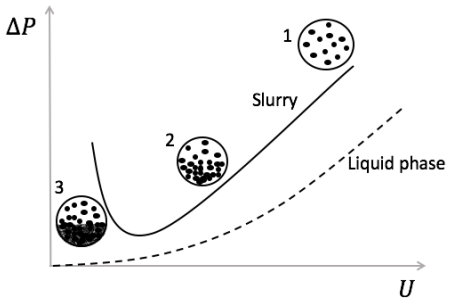

Figure 2: Slurry ΔP for different flow regime, w.r.t. the liquid state; (1) homogeneous flow regime, (2) heterogeneous flow regime, (3) moving bed.

Moreover, transitional velocities are identified between these patterns: in particular, the so−called critical velocity, corresponding to the minimum pressure drop, separates the moving bed configuration and the heterogeneous flow **?**. Purely empirical correlations to predict friction losses depending on the exhibited pattern are found in literature. Zandi and Gavotos **?**, based on experiments conducted with water slurries, proposed to express the rise of the pressure drops with respect to the fully liquid state in function of different parameters, as in Eq.s 4 − 5:

$$\frac{\Delta P_m - \Delta P_l}{\Delta P_l} = \alpha K \Psi^m \tag{4}$$

$$\Psi = \frac{U^2 C_d / 1 - 2}{Dg(\beta - 1)} \tag{5}$$

where C_d is the particle drag coefficient, β the density ratio equal to ρ_s/ρ_l.

Some years later, based on 594 experimental points with different water slurries, several pipe diameters and particle size distributions, Turian **?** proposed to correlate, instead, the pressure coefficient of the mixture. In this work, the relative importance of the different parameters involved, such as the minor effect of the particle size and the dramatic influence of the pipe diameter, are detailed. Moreover, several empirical coefficients are given for the different flow regimes investigated.

Despite the large numbers of correlations found in literature, none of them is yet comprehensive of the flow regime transition without relying on empirical parameters. Moreover, they all imply the knowledge of the slip velocity between the two phases, information that is not always known either experimentally or theoretically. An extensive compendium of the different correlations for pressure drops of slurries in horizontal pipes is given by Miadema **?**.

Concerning the slurry flow in vertical circular pipes, Newitt **?** conducted tests for water slurry of fine particles, discovering that ΔP_m is well described by correlation given in Eq. 6:

$$\frac{\Delta P_m - \Delta P_l}{\Delta P_l} = \alpha \frac{(gD)^{0.5}}{U} \frac{D}{d} \beta^2 \tag{6}$$

However, in the same paper, for slurries of large particles ($d = 0.5 - 0.7mm$), the pressure drops are rather identical or lower than the pure liquid. The same conclusion is drawn in **?**, based on experiments in a $150mm$ diameter pipe with particles ranging from $0.12mm$ to $1.84mm$. The authors attributed the lack of contribution to the total friction pressure drop of the solid phase to the absence of particles in the boundary layer adjacent to the pipe wall; instead, the particles travel in a core distribution in the center of the pipe.
On the other hand, when the pipe is inclined from the horizontal position of an angle $0° < \gamma < 90°$, Worster and Danny **?** indicated that the friction losses decrease, regardless the direction of the flow, as in the following equation:

$$\Delta P_{oblique} = \Delta P_l + (\Delta P_{horizontal} - \Delta P_l) cos\gamma. \tag{7}$$

In this frame, more attention has been given to upward slurry flows in oblique sections, due to their large applicability in conveying solid patterns in long overland pipelines. For example, Kao and Howang **?** showed different results and modified the correlations in Eq. 7 for upward flows, finding out the critical velocity below which the solid starts to slide back contributing to particle accumulation and pipe blockage.

As for what concerns the bends, a reference study is the work of Turian **?** that used the theory suggested by Crane **?** for fully liquid turbulent flows. According to this approach, similarly to the straight sections, the pressure drop is proportional to U and ρ through a term K (Eq. 8) that is in turn function of the Re_D (λ) and the bend geometry N (Eq. 9).

$$\Delta P = \frac{1}{2} \rho U^2 K \tag{8}$$

$$K = \frac{L_{equivalent}}{D} \lambda = N\lambda \tag{9}$$

For fully liquid flow in standard bends, $N = 16$ for $45°$ and $N = 32$ for $90°$ **?**. In **?**, the coefficient K does not depend on solid mass fraction, that varied during the experiments up to 33%. This detailed study focused only on standard bends laying in the horizontal plane. On the other hand, Toda **?** reported that vertical bends (elbows placed in the vertical plane) behave differently because of the effect of gravity. Whilst he proposed an empirical correlation for the horizontal bends, he did not further investigate on the vertical ones. Later, Ayukawa **?** observed that also the direction of the flow upstream and downstream the fitting plays a role, identifying as responsible the relative velocity of particles and fluid.
The main conclusion of this literature survey summary resides in the clear dependence of the physical behaviour on the case study geometry and flow field. Therefore, the need for accurately designing the pipeline in the framework of space propulsion, drives

the research towards purposely designed test benches, as the one used in this work.

3. Experimental facility and working fluid

In order to establish the flow similarity, a future upgraded version of the Ariane 6 LH2 feedline with slush hydrogen was taken as target scenario. A substitute non-cryogenic slurry at ambient temperature has been chosen to match fully turbulent Re, density ratio $\beta = 1.12$ and expected pressure drop ($200 - 1600 Pa/m$). The substitute mixture is 3M Novec Engineering Fluid $HFE7200$ and sucrose crystals with an equivalent diameter d between $0.2 - 1.2 mm$ (properties in Table 1).

The VKI Predict experimental facility, reported schematically in Figure 3, is in open loop configuration to avoid undesired accumulation of solid particles in the pump or in the returning circuit, resulting in a change of solid mass concentration during the test. The upstream feeding tank is kept closed and connected to the facility by means of a valve. A stirrer equipped with electrical engine is activated to mix the slurry before and during the experiments to facilitate the mixture to flow out, towards the test section. This latter, consisting of plexiglass cylindrical pipes of diameter (D) of $22 mm$, scales down the main components of a real fuel feeding line for launcher engines: an oblique, horizontal and vertical section, connected by means of one 45° and one 90° vertical bend. All the sections are instrumented with differential pressure transducers with measurement range $\pm 860 Pa$. The sensors are placed at a distance $L = 500 mm$ from each other in the straight section and about $3D$ upstream and downstream the bends. The mass flow rate and the slurry concentration are measured by means of a Coriolis based flow meter. A capacitance densimeter, appositely studied for the chosen solid-liquid mixture, has been designed **?** in collaboration with Waseda University . The working principle of the probe is based on the linear change of the mixture dielectric constant with increasing concentration. The electric field generated by two opposite electrodes changes accordingly, resulting in a different value of capacitance. During this experimental campaign, the probe has been calibrated in different known conditions and compared during the experiments with the flowmeter. Moreover, it played a fundamental role when the highly concentrated slurry did not allow the use of the Coriolis flow meter to assess the solid content of the mixture.

Table 1: Properties of the liquid and solid phase.

	ρ	μ	d
	$[kg/m^3]$	[Pa · s]	[mm]
HFE7200 @ 25C	1430	0.00058	-
Sucrose Crystals	1590	-	0.2 - 1.2

At the beginning of the test, the flow regulation valve is opened to allow the slurry passing through the test sections for about $60 s$. The mixture is collected in the buffer tank, also equipped with an electrical stirrer, is lifted up to fill again the feeding reservoir in order to start a new test.

The test matrix foresaw a flow velocity between $0.4 - 0.9 m/s$ and a solid mass fraction up to 45%, being 50% the target solid content in the real slush application.

4. Experimental results

4.1. Pure liquid flow

Before operating the facility with concentrated slurry, fully liquid tests were performed within a Re_l range $Re_l = [1 - 5] \cdot 10^4$. For the straight sections the theoretical pressure drop is evaluated by means of the Darcy-Weisbach equation:

$$\Delta P = \frac{1}{2} \rho U^2 \lambda \frac{L}{D}, \tag{10}$$

in which the friction coefficient λ is calculated with the Blasius approximation of the Darcy friction factor for smooth pipes, $\lambda = 0.316 Re_l^{-0.25}$. The comparison between the experimental results the theoretical prediction is reported in Figure 4. Despite the overall quadratic trend is respected, the divergence between the experiments and the theory increases at high Reynolds number when the entrance length of the test sections is not long enough to establish a fully developed flow. Moreover, as the entrance length of the three straight test sections differ from each other, the experimental points distribute differently.

For what concerns the two bends, theoretical values of pressure drops are given by Crane **?**. The coefficient N for the 90° elbow, with curvature radius of 2, is taken equal to 12 **?**. As the value is not given for the corresponding 45° elbow, N_{45} has been considered 0.5 $\cdot N_{90}$, retracing the relationship between the same two angles for standard elbows, presented in **?**. From a first comparison in Figure 5, the described correlation is not suitable for Predict experimental data for the

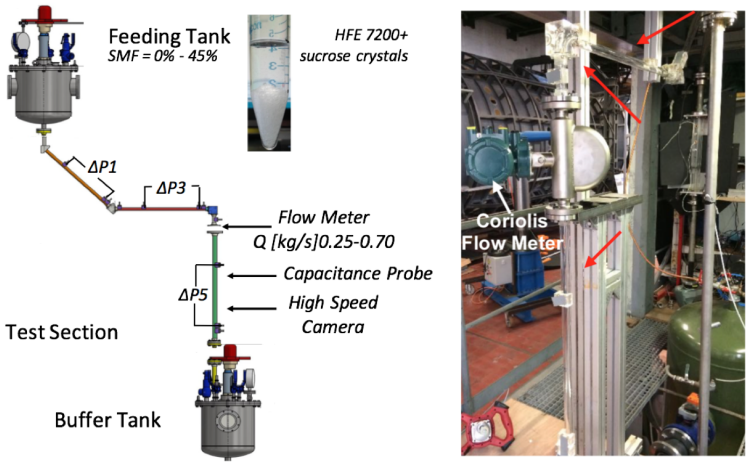

Figure 3: (left) Sketch of the VKI Predict Facility and picture of a mixture sample; (right) photo of the facility

45° bend. This is probably due to the not complete development of the flow upstream the bend and to the too close position of the pressure tap downstream of the fitting.

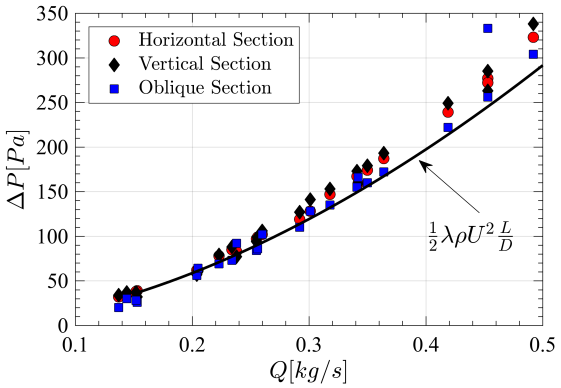

Figure 4: Experimental ΔP versus Q for fully liquid tests in the straight sections (symbols). Comparison with the Darcy-Weisbach equation (continuous line).

4.2. *Slurry in the horizontal section*

As a general consideration, the pressure losses in a concentrated turbulent slurry flow increase because of two components: an inertial contribution, due to the increasing mixture density, and a viscous term, that affects the friction coefficient because of the particles-wall interaction.

For the mixture used in this work, HFE7200 with sucrose particles, the inertial contribution is always

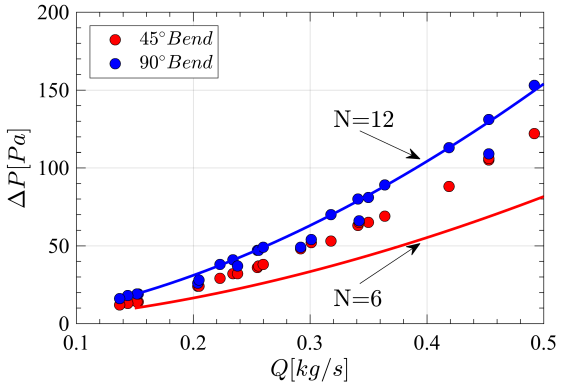

Figure 5: Experimental ΔP versus Q for fully liquid tests in the straight sections (symbols). Comparison with the Crane theory (continuous lines).

negligible being the density ratio β close to the unity. On the other hand, the viscous effect is visible in the transition experienced by the mixture between the flow regimes – from heterogeneous flow regime to moving bed. In Figure 6a the pressure losses are plotted versus the measured mixture mass flow rate, for different solid mass fractions. Two groups of data are identified: the points at low ϕ and the ones at high ϕ, that exhibit higher friction losses for all the flow rates. The transition is located at about $\phi = 15\%$: in this range, for higher velocities, the behaviour follows the hypothesis of heterogeneous flow regime. As the slurry velocity decreases and the concentration increases, the flow enters in the moving bed regime,

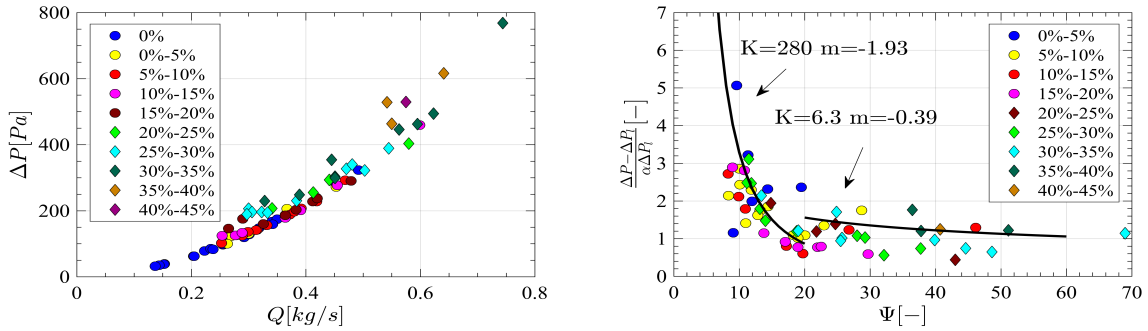

(a) (b)

Figure 6: Horizontal section: (a) Experimental ΔP versus Q in function of ϕ (different markers colour) ; (b) Comparison with Zandi correlation (Eq. 4)**?**.

with higher viscous effect at the wall. The presence of this transition has been investigated optically by means of high speed visualisations as detailed in **?**. Moreover, the results for this section are used to validate a two fluid model in OpenFoam described in **?**. The results have been compared with the correlation given by Zandi and Gavatos **?** in Figure 6b. The empirical values of K and m are the ones proposed by the authors and outline two different behaviours of the pressure drops depending on the flow regime. The calculation of the drag coefficient needed to compute the experimental Ψ requires the knowledge of the slip velocity between the carrier and the particles. As this is an unknown parameter, has been retrieved iteratively to match the Zandi correlation, resulting in $C_d = 1$, i.e. a particle Reynolds number of 100. The main outcome is an empirical correlation, shown in Figure 7, that predicts the friction coefficient for the two flow regimes, without relying on empirical coefficients depending on the exhibited flow pattern **?**.

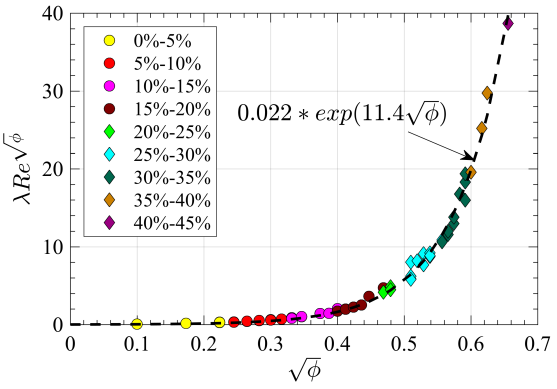

Figure 7: Horizontal pipe: experimental friction coefficient in function of ϕ (symbols) together with the exponential fit (dashed line)

4.3. Slurry in the oblique section

Figure 8a shows the experimental data obtained for the 45° inclined test section. Concentrated slurries, at different solid mass content, exhibit higher pressure losses than the tests with pure HFE for different mass flow rate. However, the gradual enhancement of the mixture density is not visible in the pressure drop. Additionally, according to the theory presented in **?**, the downward inclined section presents lower pressure drops than the horizontal one, depending on the concentration, as expressed in the formula:

$$\Delta P_{oblique} - \Delta P_l = cos\gamma(\Delta P_{horizontal} - \Delta P_l) \qquad (11)$$

The comparison is done in Figure 8b, that depicts the difference between the slurry and the liquid state pressure drops in comparison with the prediction. In average, the experimental pressure coefficient is higher than expected, especially at low concentrations. This discrepancy is believed to be due to a swirl motion observed in the pipe during the experiments. The oblique section is placed in the Predict facility right after the upstream feeding tank. In order to keep the mixture homogeneous and to avoid settling in the reservoir, a stirrer is activated before and during the test at variable rotational speed. This motion is at the origin of the swirling of the flow and it is mostly felt when the solid fraction is low. Increasing the solid concentration of the flow, an higher uniformity is reached and the effect of the swirl is less important.

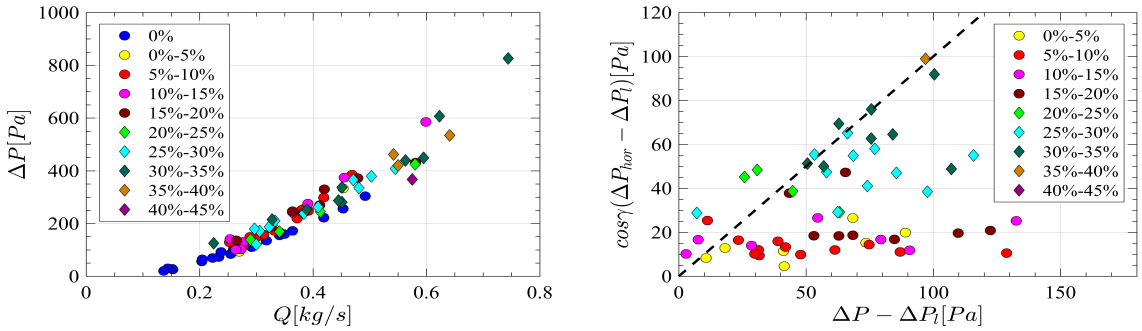

(a) (b)

Figure 8: Oblique section: (a) experimental ΔP versus Q in function of ϕ (different markers colour); (b) comparison between experimental and predicted rise of ΔP **?**.

4.4. Slurry through the bends segments

Figure 9a and Figure 10a show the experimental results for the bends. While for the of 45° bend there is a clear enhancement of the losses when increasing the concentration, for the one at 90° the interpretation of the data is not straightforward. In fact, in this section, the cloud of point is aligned on the typical quadratic trend in function of the mass flow rate without differentiating among the solid mass content states. Therefore, the data are organised according to the approach proposed by Crane **?** and adopted by Turian **?** for slurries.

Figure 9b and Figure 10b show the experimental N factor calculated as in Eq. 12:

$$N = \frac{\Delta P}{\lambda U^2 \rho} \tag{12}$$

The trend for 45° (Figure 9b) recalls the results found in **?**: the factor N is a constant of Re_{ml} calculated as in Eq. 13.

$$Re_{ml} = \frac{\rho_m U D}{\mu_l} \tag{13}$$

As no reference values are given for this geometry in literature, no further comparison was performed. The evolution of the N coefficient for 90° is in agreement with the literature results, i.e maintaining a constant behaviour regardless the solid fraction. However, the N coefficient of the slurry is lower than the one measured during the fully liquid test, at the same Re_{ml}. The interpretation of this outcome is found in the flow topology downstream the bend: when the liquid flow from a straight section changes its direction due to the presence of a bend, there is an adverse pressure gradient generated from the curvature. Therefore there is a decrease in velocity close to the convex wall, and the opposite occurs towards the outer side of the pipe. This gives rise to a secondary motion superposed on the primary flow. This secondary motion is expected to appear as a pair of counter-rotating vortices, which are called Dean vortices **?**. The literature does no offer a detailed explanation of the interaction between this secondary flow and the slurry, but from the current data analysis, the presence of particles seems to decrease the losses of the bend. Eventually, the solid particles could destroy the secondary structures at the bend outlet, resulting in a better quality of the flow.

4.5. Slurry in vertical the section

For the vertical pipe, the results are presented in Figure 11. The signal measured by the differential pressure transducer is evaluated net of the hydrostatic contribution, two order of magnitude higher than the losses, by experimentally nulling the effect of gravity. The results show a comparable pressure loss between the slurry at different concentrations and the pure liquid. This outcome is similar to the case described in **?** and **?**. The literature and the evidence of the video taken with the high speed camera during this experimental campaign **?** suggest that a core distribution of particles is formed in the vertical pipe, reason for which only the inertial contribution has an effect. Being the latter negligible in our case, the appreciable differences in the measured values of pressure drops are within the uncertainty of the experiments, resulting in slurry pressure coefficients comparable to the one in fully liquid conditions.

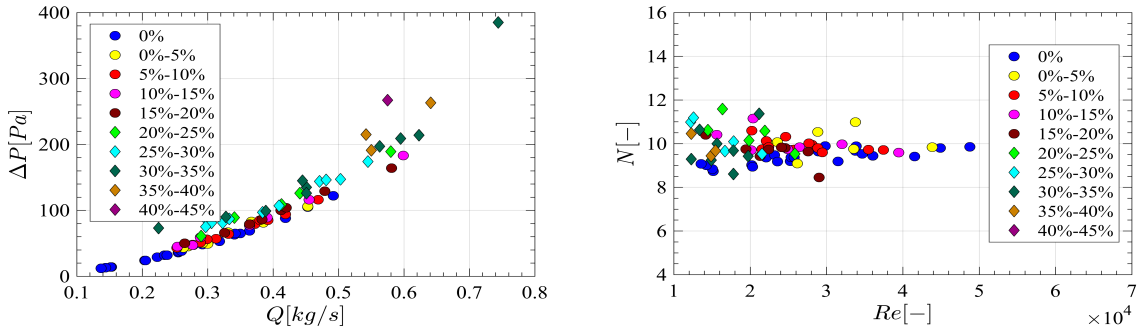

(a) (b)

Figure 9: 45°bend: (a) experimental ΔP versus Q in function of ϕ (different markers colour); (b) experimental N coefficient (Eq. 12), **?**.

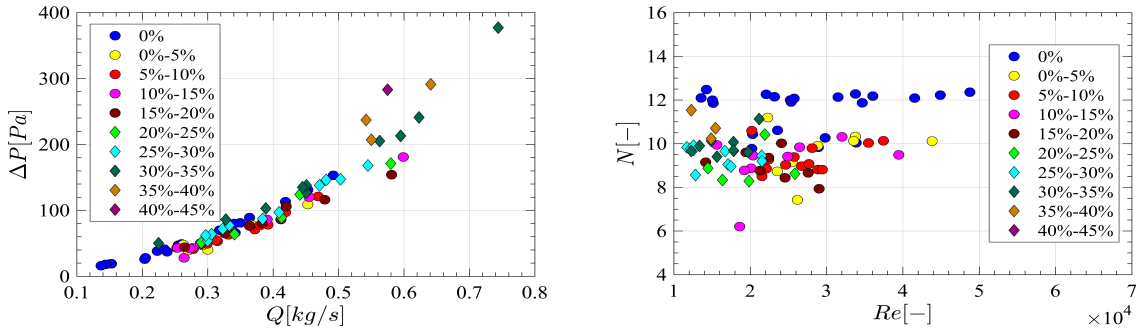

(a) (b)

Figure 10: 90°bend: (a) experimental ΔP versus Q in function of ϕ (different markers colour); (b) experimental N coefficient (Eq. 12) **?**.

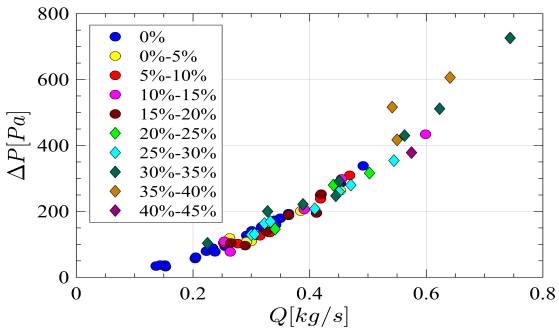

Figure 11: Experimental ΔP versus Q in function of ϕ (different markers colour) for the vertical segment.

5. Conclusions

An extensive experimental campaign took place in the Predict VKI facility to characterize the hydraulic behavior of a highly concentrated solid-liquid mixture in circular pipelines, with solid mass content up to 45% and mass flow rate between $0.2 - 0.7 kg/s$. In the framework of the characterization of cryogenic slush for space application, an isothermal mixture has been chosen in flow similarity with slush hydrogen. In the same framework, the facility scaled down the main components of a real launcher fuel feeding line. An experimental procedure was tested to treat solid liquid mixture in a open loop facility in turbulent flow conditions. Most importantly, knowledge was gained about the flow patterns and the pressure drop of such a flow in straight horizontal, inclined and vertical sections as well as in two vertical bends. The data analysis revealed a number of evidences to orient the modelling of this phenomenon and to drive an accurate design of slurry transport systems.

For the horizontal test section, the data show the expected behaviour, with an increased loss as the solid mass content increases and the flow regime transients from homogeneous to heterogenous. The main outcome is an empirical correlation, shown in Figure 7, that predicts the friction coefficient **?**.

As for the bends, we recommend to employ the model suggested by Crane **?**, with the values found experimentally during this test campaign and reported in Table 2. The oblique pipe followed a non conventional behaviour. The presence of a swirl motion in the pipe increased the losses, especially at the lowest solid mass fractions. However, the presence of the stirrer in the upstream feeding tank could not be avoided to conduct the experiments. Moreover, a similar stirring system is envisaged in the real new slush architecture to permit the fuel to flow in the feeding line, avoiding settling and aggregation at the tank wall. This is why this phenomenon should be taken into account in the design of the pipeline.

Concerning the vertical pipe, some past models tend to overestimate the pressure losses. In fact, in this configuration, the solid particles do not increase the losses because of their core distribution across the pipe diameter.

6. Acknowledgement

This experimental campaign was performed in the framework of the ESA-TRP Predict project.

Table 2: N values found experimentally for bends.

N	***45***	***90***
Liquid	10	12
Slurry	10	8

Notation

Symbols

d	particle diameter	m
D	pipe diameter	m
f	pressure coefficient	$-$
L	test section length	m
U	slurry velocity	m/s
Q	slurry mass flow rate	kg/s
Re	Reynolds number	$-$
ΔP	distribuited pressure drops	Pa
μ	dynamic viscosity	$Pa \cdot s$
ρ	density	kg/m^3
α	solid volume fraction	$-$
ϕ	solid mass fraction	$-$

Subscripts

l	properties of the liquid phase
m	properties of the mixture
s	properties of the solid phase

References

A. Friedlander, R. Zubrin, T. L. Hardy, Benefits of slush hydrogen for space missions, Cryogenics 52 (7-9) (2012) 428–440.

E. Dumont, S. Stappert, T. Ecker, J. Wilken, S. Karl, S. Krummen, M. Sippel, Evaluation of future ariane reusable vtol booster stages.

C. T. Crowe, Multiphase handbook, Taylor & Francis, Gloucestershire, 2005.

R. Durand, E. Condolios, Experimental investigation of the transport of solids in pipes, Deuxieme Journée de lhydraulique, Societé Hydrotechnique de France.

R. Turian, F.-L. Hsu, T.-W. Ma, Estimation of the critical velocity in pipeline flow of slurries, Powder Technology 51 (1) (1987) 35–47.

I. Zandi, G. Govatos, Heterogeneous flow of solids in pipelines, Journal of the Hydraulics Division 93 (3) (1967) 145–159.

R. M. Turian, T.-F. Yuan, Flow of slurries in pipelines, AIChE Journal 23 (3) (1977) 232–243.

S. A. Miedema, An overview of theories describing head losses in slurry transport: A tribute to some of the early researchers, in: ASME 2013 32nd International Conference on Ocean, Offshore and Arctic Engineering, American Society of Mechanical Engineers, 2013.

D. Newitt, J. Richardson, Hydraulic conveying of solids in vertical pipes, Transaction of the institution of chemical engines 39 (1961) 93–100.
V. Matoušek, Pipe-wall friction in vertical sand-slurry flows, Particulate Science and Technology 27 (5) (2009) 456–468.
R. Worster, D. Denny, Hydraulic transport of solid material in pipes, Proceedings of the Institution of Mechanical Engineers 169 (1) (1955) 563–586.
D. Kao, L. Hwang, Critical slope for slurry pipelines, in: P Hydrotransport 6 Conference of the British Hydromechanical Research Association, Cranfield, England, 1979.
R. Turian, T. Ma, F. Hsu, D.-J. Sung, G. Plackmann, et al., Flow of concentrated non-newtonian slurries: 2. friction losses in bends, fittings, valves and venturi meters, International Journal of Multiphase Flow 24 (2) (1998) 243–270.
Crane, Flow of fluids: through valves, fittings, and pipe, 1977.
M. Toda, N. Komori, S. Saito, S. Maeda, Hydraulic conveying of solids through pipe bends, Journal of Chemical Engineering of Japan 5 (1) (1972) 4–13.
K. Ayukawa, Pressure drop in the hydraulic conveyance of solid materials through a bend in a vertical plane, Bulletin of JSME 12 (54) (1969) 1388–1396.
S. Eneren Aksoy, Slurry characterization with captive and optical probes (2017).
M. T. Scelzo, L. Peveroni, J. Wilken, J.-M. Buchlin, J. Persson, Densified propellants for future launch vehicles: Experimental characterization of an isothermal slurry in circular pipelines in flow similarity with slush hydrogen, Space Propulsion Conference, Seville.
M. T. Scelzo, L. Peveroni, J.-M. Buchlin, Experimental and numerical study of slurry flows in horizontal pipes, Journal of Multiphase flow, in submission.
I. E. Idelchik, E. Fried, Handbook of hydraulic resistance, Hemisphere Publishing, New York, NY, 1986.

Modeling turbulent polydispersed multiphase flows in stirring tank reactors

PhD Candidate: Maxim Van Cappellen

Environmental and Applied Fluid Dynamics department, von Karman Institute for Fluid Dynamics, Belgium, maxim.van.cappellen@vki.ac.be

Supervisor: Jean-Marie Buchlin

Head of the department, Environmental and Applied Fluid Dynamics, von Karman Institute for Fluid Dynamics, Belgium, buchlin@vki.ac.be

University Promoter: Rosaria Vetrano

Associate Professor, Faculty of Engineering Science, Katholieke Universiteit Leuven, Belgium, rosaria.vetrano@kuleuven.be

University Co-promoter: Pierre Proulx

Professor, Department of Chemical and Biotechnology Engineering, Sherbrooke University, Canada, Pierre.Proulx@USherbrooke.ca

Abstract

Turbulent solid-liquid flows are frequently encountered in the pharmaceutical, food, (bio-)chemical and process industries. The desired turbulent flow conditions are created by mixing equipment such as continuous stirring tank reactors (CSTR) and fluidized beds. The objective of mixing is to increase the homogeneity of a solution, which will favor secondary phenomena such as mass transfer, chemical reactions and/or product growth mechanisms. Despite the simple concept of mixing devices, their designed and operating conditions have to be carefully evaluated in order to obtain cost efficient and high quality yields. Conventionally, new mixing applications are design by using engineering correlations to scale-up laboratory-scaled experiments. However, after scaling the impact of process specific phenomena can significantly deviate from small scale results, possibly leading to complete process breakdown [1]. As a result, optimization of solids-liquid systems is often expensive and time consuming. In order to overcome the inherent limitations of the classical design approach, considerable efforts are being made to develop numerical tools for simulating multiphase flows to aid in the design of industrial-scale mixing equipment [2]. Current multiphase state-of-the-art models can be categorized based on their applicability in different particle-laden flow regimes, defined by the combination of the particle Stokes number St_p and particle volume fraction α_p [3]. This is summarized in fig. 1. There are however some mayor drawback with these multiphase models. First of all, in industrial particle-laden flows the flow regime is not a priory known and can vary in space and time, which makes model selection a difficult task. Secondly, the Lagrangian solvers, which are theoretically applicable over a wide range of flow regimes, suffer from statistical noise in highly coupled flows and are computational expensive which limits the total number of particles in the domain. Lastly, are wide particle-size distributions too expensive to simulate using current modeling techniques. In the last decade a new type of Eulerian models has emerged, namely the quadrature-base moment methods (QBMM) [6]. These family of models have the mathematical capability to simulate the evolution of a particulate phase with a multivariate distribution of properties. In most recent studies, such multivariate QBMMs have been successfully developed and tested for mono-dispersed particles with a variable velocity-distribution [7, 8]. Which means that they can be used for high Stokes flows and can be applied in regimes where until recently only Lagrangian solvers could be

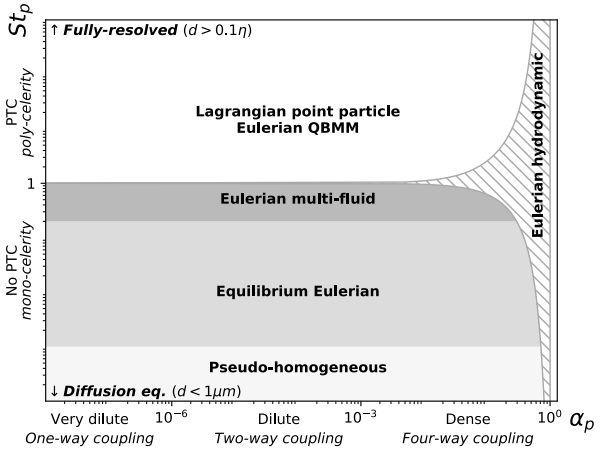

Figure 1: Modeling approaches for turbulent multiphase flow based on particle Stokes number St_p and particle volume fraction α_p. [3–5]

used. The general aim of this project is to develop a predictive Eulerian multiphase solver applicable for particle-laden flows with a wide size- and velocity-distribution. The starting point of this model will be a QBMM which will be extended for a particulate phase with a multi-modal size-distribution. The model will be developed in different steps where in each step the coupling complexity is increased (from one to four-way coupling). During each step extensive code and solution verification will be performed against existing solvers and analytic solutions. In the final phase of this project, the solver will be validated against experimental data.

Keywords: Multiphase flow modeling, quadrature based moment methods, multivariate population balance, liquid-solid suspension, particle-laden flow, poly-celerity

References

[1] Edward Paul, Victor Atiemo-obeng, and Suzanne Kresta. *Handbook of Industrial Mixing science and practice*. John Wiley & Sons, 2004. ISBN: 3175723993.

[2] Antonio Buffo and Daniele L. Marchisio. "Modeling and simulation of turbulent polydisperse gas-liquid systems via the generalized population balance equation". In: *Reviews in Chemical Engineering* 30.1 (2014). ISSN: 01678299. DOI: 10.1515/revce-2013-0015.

[3] S. Balachandar. "A scaling analysis for point-particle approaches to turbulent multiphase flows". In: *International Journal of Multiphase Flow* 35.9 (2009). ISSN: 03019322.

[4] F. Laurent et al. "A hierarchy of Eulerian models for trajectory crossing in particle-laden turbulent flows over a wide range of Stokes numbers". In: *Proceedings of the Summer Program 2012 - Center for Turbulence Research* (2012).

[5] Daniele L. Marchisio and Rodney O. Fox. *Computational Models for Polydisperse Particulate and Multiphase Systems Providing*. Cambridge Series in Chemical Engineering, 2013. ISBN: 9780521858489.

[6] R. O. Fox, F. Laurent, and M. Massot. "Numerical simulation of spray coalescence in an Eulerian framework: Direct quadrature method of moments and multi-fluid method". In: *Journal of Computational Physics* 227.6 (2008). ISSN: 00219991.

[7] Aymeric Vié et al. "On the Anisotropic Gaussian velocity closure for inertial- particle laden flows To cite this version : HAL Id : hal-00912319 On the Anisotropic Gaussian velocity closure for inertial- particle laden flows". In: *Communications in Computational Physics* 17 (2015). ISSN: 19917120.

[8] C. Yuan and R.O. Fox. "Conditional quadrature method of moments for kinetic equations". In: *Journal of Computational Physics* 230.22 (2011). ISSN: 00219991.

Turbulent heat transfer at different Prandtl number fluids in natural convection boundary layer on a vertical plate

Agustín Villa Ortiz

Environmental and Applied Fluid Dynamics Department, von Karman Institute for Fluid Dynamics, Belgium, villaortiz@vki.ac.be

Supervisor: Jean Marie Buchlin

Head of Department, Environmental and Applied Fluid Dynamics Department, von Karman Institute for Fluid Dynamics, Belgium, buchlin@vki.ac.be

University Supervisor: Tony Arts

Professor, Institute of Mechanics, Materials and Civil Engineering, Université Catholique de Louvain, Belgium, arts@vki.ac.be

Abstract

In the context of the Generation IV of nuclear power reactors, liquid metals (whose Prandtl number $Pr \ll 1$) are proposed as coolant agents. The thermal design of such reactors depends on the proper thermo-hydraulic characterization. However, the actual Reynolds Averaged thermal turbulence models have problems to reproduce accurately the thermal field of this sort of fluids, especially in natural convection flows. Therefore, the effect of Pr number on heat transfer needs to be further analyzed to improve this modeling.

In the roadmap of this PhD, the Large Eddy Simulations of a turbulent natural convection boundary layer of low Prandtl numbers is proposed to assess the existing turbulence modeling for such kind of flows. Before these simulations, the development of the appropriate environment, i.e. numerical configuration, boundary and initial conditions definition, is mandatory to ensure the quality of the results. Therefore, the scope of the present document is the characterization of a natural convection boundary layer at a $Pr = 0.71$ through Large Eddy Simulations, where a controlled transition is proposed to promote into a turbulent regime. Six different transition configurations are proposed in this document. They are compared with an experimental database and between themselves. Different flow properties, such as the Nusselt number along the boundary layer and the non-dimensional velocity and temperature are compared against experimental and numerical data. Time series analysis is also considered for a better understanding of the different flow regimes: laminar, transitional and turbulent. The introduction of a perturbation technique allows an earlier transition, useful to approach the simulations to the experimental dataset. Different configurations (perturbed field and perturbation frequency) of this method are analyzed.

Keywords: turbulence, heat transfer, natural convection, low Prandtl number, boundary layer, LES, turbulence modelling, OpenFOAM

1. Introduction

1.1. Context of the project

The MYRRHA reactor (**M**ulti-purpose h**Y**brid **R**esearch **R**eactor for **H**igh-tech **A**pplications) is a fast reactor under design in Belgium by SCKCEN, which can operate in critical and subcritical modes [1]. It contains a proton accelerator of 600 MeV, a spallation target and a multiplying medium with MOX fuel, cooled by a eutectic of lead and bismuth.

In normal operating conditions, MYRRHA works in forced convection. The liquid metal transports the produced heat in the core to the external heat exchangers. During the maintenance of the reactor, the pump system is shut down, and there is still heat production. The heat exchangers, which are operative, remove this heat, creating then a natural convection loop. During the design phase of MYRRHA natural convection plays an important role, where its behavior must be taken into account for the structural design.

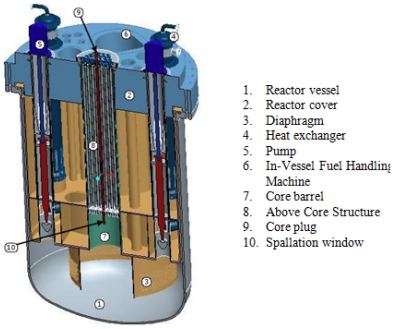

Figure 1: MYRRHA reactor cross section.

1.2. Natural convection

Natural convection flows are driven by buoyancy forces. These forces are originated by the gravitational acceleration and density variations (due to changes in the temperature field), and both momentum and thermal fields are coupled. The Prandtl number Pr relates the diffusion of the momentum and thermal fields. It is expressed as:

$$Pr = \frac{\nu}{\alpha} \tag{1}$$

where ν is the kinematic viscosity and α is the thermal diffusivity.

The influence of the Prandtl number in natural convection flows is evident when the thickness of momentum and thermal boundary layers δ_U and δ_T are compared. Both of them develop when a wall is heated, as shown in fig. 2. Figure 2a presents the case of a high Prandtl number fluid. As it is observed, the kinematic viscosity is larger than the thermal diffusivity, being the momentum boundary layer thicker than the thermal one. There is a balance between viscous and buoyancy forces near the wall, but out of the thermal boundary layer, where there is no buoyancy effect, the viscous forces are balanced with the inertial ones. Since the thermal boundary layer is thinner than the momentum one, the viscosity-inertia balance is present in most part of the momentum boundary layer.

At low Prandtl number, shown in fig. 2b, the thermal diffusivity is larger than the kinematic viscosity. It results in a thicker thermal boundary layer in comparison with the previous case. The viscous forces are only significant near the wall, and their influence decreases after the peak of velocity. The buoyancy forces are then balanced with the inertial forces up to the end of the boundary layer. Out of the thermal boundary layer, since there are no buoyancy forces to produce motion, there is no velocity. This is why

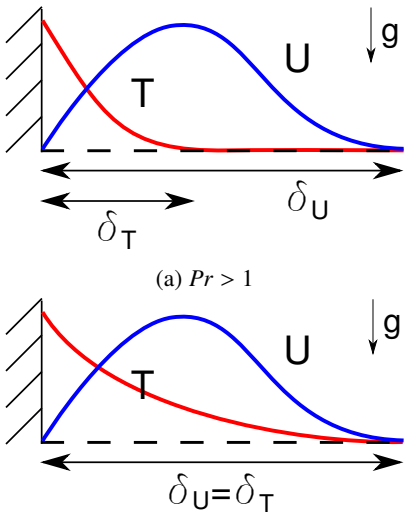

(a) $Pr > 1$

(b) $Pr < 1$

Figure 2: Velocity and temperature boundary layers in natural convection.

the momentum and thermal boundary layers have the same thickness.

A natural convection flow can be characterized by different dimensionless numbers. The Grashof number relates the buoyancy and viscous forces. At big values it is observed that turbulence features appear in the flow. This is the reason why the Grashof number has the same role as the Reynolds number in forced convection flows. Its expression is:

$$Gr_L = \frac{g\beta\Delta T L^3}{\nu^2} \tag{2}$$

where g is the gravity acceleration, β the thermal expansion coefficient, ΔT the representative difference of temperature of the flow, and L a characteristic length.

The combination of the Grashof and Prandtl number leads to the Rayleigh number, which relates buoyancy and thermal forces. It is the analogous dimensionless number in natural convection of the Peclet number.

$$Ra_L = Gr_L \cdot Pr = \frac{g\beta\Delta T L^3}{\nu\alpha} \tag{3}$$

The Nusselt number defines the ratio between the convective and the conductive heat flux in the wall. It is usually expressed as:

$$Nu_L = \frac{(\partial T/\partial y|_w)\, L}{T_w - T_0} = \frac{hL}{k} \tag{4}$$

where h is the convective heat transfer coefficient, and k the thermal conductivity of the fluid.

1.3. State of the art of natural convection simulation

In the literature several numerical simulations of turbulent natural convection boundary layers (TNBL) are found, specially inside the Reynolds Averaged Navier Stokes simulations (RANS) context. In 1986, To [2] developed two buoyant low Reynolds turbulence models: a $k-\varepsilon$ and an algebraic stress model. The obtained results predict well the mean flow quantities. A posterior comparison between different turbulence models was performed in 1989 by Henkes [3]. Different low Reynolds $k-\varepsilon$ models are compared with the standard $k-\varepsilon$ model and an algebraic model. Henkes sentenced that accurate simulations require the use of low Reynolds modifications in the $k-\varepsilon$. Further investigations were done by Peeters and Henkes under the same flow configuration [4]. They indicated that the $k-\varepsilon$ assumptions are not capable to describe the different turbulent structures due to the isotropic nature of this model. The turbulent diffusion is predicted correctly if a Reynolds Stress Model (RMS) is used, but a differential model is needed to predict in detail the turbulence structures.

The increase of computing power has allowed to perform in since the last decade Large Eddy Simulations (LES) and Direct Numerical Simulations (DNS) for natural convection cases. In 2005, Yan [3] used LES to study the dynamics of a TNBL and the associated convective heat transfer at $Pr = 0.71$, with the Smagorinsky sub-grid scale turbulence model. A space-developing technique was used, where the whole boundary layer is simulated. Simulations in 2D and 3D were performed, and two different wall functions were compared. There is a good agreement with the experimental data of Tsuji [4]. The flow transition is well captured. The comparison of the wall functions shows that in the 2D computation, both wall functions give similar results. However, in the case of the 3D simulation, all turbulence characteristics are included, and differences about 15% were found between both wall functions.

A natural boundary layer over a cylinder was studied by Barhaghi [5] in 2006. Similarities were found between this cylindrical surface and the flat plate of Tsuji [4] using Large Eddy Simulations. Barhaghi estimated the region y^+ where the linear law of the wall is hold.

Later in 2009, Zoinal [6] performed DNS in a vertical boundary layer for $Pr = 0.71$ and 6. A time-developing technique was considered, where a correlation is used in order to express the flow as if the space-developing was used. This technique offers the advantage that a lower computational effort is needed, since the boundary layer can be studied by using a shorter computational domain. In both Prandtl number cases, the transition to turbulence was observed at the same Grashof number Gr_δ. A good agreement with the experimental data of Tsuji [4] was found. Discrepancies in the turbulent heat fluxes are present, and a lack of accuracy is indicated by the author due to the use of the Boussinesq approximation for buoyant flows.

Similar discrepancies were found by Abramov [7] during his DNS in a TNBL, but the explanation was the absence of convective entrainment, since the time-developing technique does not allow a good estimation of the inflow from the far field. A comparison with experiments showed an agreement between the performed simulations and the experimental data for $Pr = 0.71$.

Recently, Nakao [8] have performed *LES* of a TNBL at $Pr = 0.71$. The transition from laminar to turbulence regime was observed to change in function of the mesh resolution. In one case, they needed to introduce velocity perturbations to produce the transition. Nevertheless, a good agreement between numerical simulations and the experiments of Tsuji [4] was shown.

1.4. Objectives

The simulation of the thermo-hydraulics of MYRRHA needs the use of proper models that can deal with the present fluid and flow conditions. It has been shown that the usual turbulence models cannot handle the simulation of flows when low Prandtl numbers fluids are present [9]. This is why in the last years a great effort has been done to improve the existing turbulence models. Several European projects, such as within FP7, THINS, SESAME or MYRTE have been created in order to face this problematic. High fidelity simulations performed in these project frameworks, such as DNS and LES, provide relevant information to improve the different model. Nevertheless, most of this effort is focused in forced convection flows, not in natural convection ones.

The objective of this PhD project is the contribution to the state of the art of thermal turbulence modeling at low Prandtl numbers in natural convection flows. The understanding of the physics beyond these phenomena is required. LES will be performed to study the Prandtl number effect in natural convection, and to test the available turbulence models. In the future,

these models will be used in the design phase of the MYRRHA reactor.

1.5. Summary

In the current paper, an introduction to LES simulations, the used modeling in the performed simulations and the fundamental knowledge of time correlation during this document is presented in section 2. The investigated test cases and their results are explained in section 3. A summary with conclusions and the future work is detailed in section 4.

2. Methodology

2.1. LES equations

Large Eddy Simulations are characterized by resolution of large turbulent motions and the modeling of the smaller ones. Continuity, momentum and energy equations are filtered in space. The filtered Navier Stokes equations for incompressible flows using the Boussinesq approximation are then expressed as:

$$\sum_j \frac{\partial \overline{U_j}}{\partial x_j} = 0 \tag{5a}$$

$$\frac{\partial \overline{U_i}}{\partial t} + \sum_j \frac{\partial \left(\overline{U_i}\,\overline{U_j}\right)}{\partial x_j} = -\frac{1}{\rho}\frac{\partial \overline{p}}{\partial x_i} + \sum_j \frac{\partial}{\partial x_j}\left(\nu \frac{\partial \overline{U_i}}{\partial x_j} - \tau_{ij}\right) + g_i(1-\beta(\overline{T}-T_0)) \tag{5b}$$

$$\frac{\partial \overline{T}}{\partial t} + \sum_j \frac{\partial \left(\overline{U_j}\,\overline{T}\right)}{\partial x_j} = \sum_j \frac{\partial}{\partial x_j}\left(\alpha \frac{\partial \overline{T}}{\partial x_j} - \pi_j\right) \tag{5c}$$

where the filter operator is represented as $\overline{\ }$. τ_{ij} denotes the sub-grid stresses, appearing after the filtering process. π_j appears as well, due to the filtering, taking into account the sub-grid heat fluxes. The term containing the gravity acceleration g_i and the thermal expansion coefficient introduces the buoyancy forces in the momentum equation.

Several sub-grid scale models are available to model the sub-grid scale stress. A common way is to express it as a stress:

$$-\tau_{ij} = 2C\Delta^2 \overline{|S|S}_{ij} \tag{6}$$

where C is a constant provided by the sub-grid model, Δ is the size of the filter, and $\overline{S}$ is the symmetric part of the tensor of the velocity gradient $\overline{S}_{ij} = 1/2\left(\partial \overline{U_i}/\partial x_j + \partial \overline{U_j}/\partial x_i\right)$.

If an analogy between the momentum exchange and the energy exchange is applied, then a sub-grid thermal diffusivity α_{sgs} is defined, and is used to model the sub-grid heat flux as:

$$-\pi_j = \alpha_{sgs}\frac{\partial \overline{T}}{\partial x_j} \tag{7}$$

and the definition of a sub-grid Prandtl number indicates the ratio between the turbulent momemtum and energy exchanges as $Pr_{sgs} = \nu_{sgs}/\alpha_{sgs}$. The use of a sub-grid Prandtl number of $0.4 - 0.5$ is very common in literature.

2.2. Transition to turbulence

A flow becomes turbulent when complex flow patterns appear, due to perturbations given by the initial conditions, boundary conditions and material properties. Every laminar flow will, eventually, become turbulent when the perturbations in the system grow. This fact is evidenced in experiments, and also during numerical simulations. In the first case, small variations in the imposed boundary conditions, the roughness of the surfaces, or inserted elements are the responsible of transition to turbulence. However, in the case of numerical simulations, the origin of perturbations is numerical. It means that, eventually, the flow will become turbulent, due to the numerical schemes, the proposed boundary conditions, or just because of the domain discretization. This transition to turbulence is more artificial, and the numerical reproduction of experiments would be affected for this uncertainty.

The use of transitions methods allows to provoke turbulence in a desired region, and not as a response to the erros introduced by the simulation setup. In this paper, the introduction of a vibration in the wall is proposed, whose objective is to excite the natural frequency of the Tollmien-Schlichting (TS) waves of the boundary layer. This technique has been used in the past in forced convection flows, such as Sayadi [10], but the principles are the same for natural convection flows. This natural frequency can be obtained through a Fourier analysis in the boundary layer, or by linear stability analysis.

The transition technique proposed by Sayadi was set on the momentum field, since a forced convection flow was considered. In natural convection, buoyancy forces due to temperature gradients are considered. It allows to suppose that the same transition technique could be applied to the energy field (in this case, the temperature field).

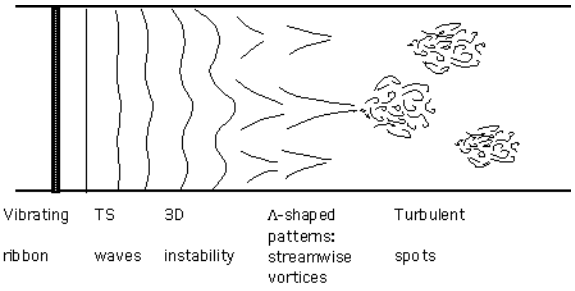

Figure 3: Transition to turbulence over a flat plate, University of Colorado Denver

3. Results

The simulation of a Turbulent Natural Boundary Layer (TNBL) at $Pr = 0.71$ is shown in this section. The setup and validation of the numerical code is done by comparing with the experimental data of Tsuji [4]. The computational domain is shown in fig. 4. A constant temperature T_h has been imposed at the heated wall, where a no slip condition has been considered for velocity. The boundary below the wall is a symmetry plane, forcing the fluid to flow parallel to the wall. The bottom plane consist in a slip patch, forbidding the entrance of flow through. In both cases, adiabatic conditions are imposed. The upper plane is considered as the outlet. A zero gradient is specified for all the fields, and the entrance of fluid is not allowed through this patch. Hence, all the mass flow that leaves the domain is recirculated with a constant temperature T_c. The spanwise sides are defined as periodic patches.

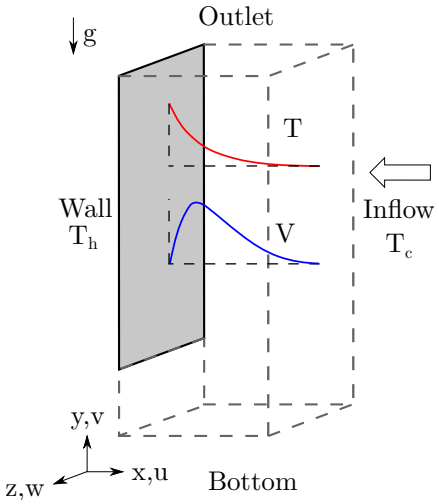

Figure 4: Computational domain of the TNBL.

Three characteristic parameters are computed to scale the results:

$$u_b = (g\beta\Delta T\nu)^{1/3} \tag{8a}$$

$$t_b = (g\beta\Delta T)^{-2/3}\,\nu^{1/3} \tag{8b}$$

$$l_b = (g\beta\Delta T)^{-1/3}\,\nu^{2/3} \tag{8c}$$

The baseline simulation's parameters are given in table 1, where the different lengths are normalized with l_b. The length L_y of the symmetry plane below the wall is 20% of the length of the wall.

The time averaged results of the cases are compared against the experimental data of Tsuji [4]. The velocity and temperature are normalized with u_τ and T_τ, defined at the wall as:

$$u_\tau = \frac{\tau_w}{\rho} \tag{9a}$$

$$T_\tau = \frac{q_w}{\rho c_p u_\tau} \tag{9b}$$

As sub-grid models, the WALE sub-grid model and a sub-grid Prandtl number of $Pr_{sgs} = 0.5$ have been used to model the sub-grid kinematic viscosity and thermal diffusivity, respectively.

3.1. Flow analysis

Once the TNBL simulation reached the steady state, a time and spatial averaging have been performed. The mean flow has been obtained and compared with the reference experimental data. The Nusselt number along the TNBL is shown in fig. 5.

The transition from laminar to turbulent regime is very clear. It takes place in the range $2 \cdot 10^{10} < Ra < 5 \cdot 10^{10}$. There, a steep change of the Nusselt number is observed, therefore an increase of the temperature gradient in the wall. This step indicates the heat transfer enhancement due to the turbulence regime. However, this heat transfer improvement never reaches the levels obtained during the experiments. Furthermore, the numerical transition appears very late if compared with the experimental one. An order of magnitude in Ra is observed between the numerical and experimental transitions.

Velocity and temperature profiles at two Grashof numbers, $1.52 \cdot 10^8$ and $1.8 \cdot 10^{11}$ ($Ra = 10^8$ and $1.3 \cdot 10^{11}$), have been compared with the experiments of Tsuji [4]. They represent the laminar and turbulent regions. The velocity boundary layers of fig. 7 are characterized by three regions: an inner one at low x^+, a maximum velocity zone at moderate x^+, and an outer one where the velocity decays after the peak.

Case	L_x^*	H	L_y^*	L	L_z^*	W	N_x	N_y	N_z	x_1^*	Gr	Pr	Ra
TNBL	3920	3.92	7430	7.43	930	0.93	100	512	128	0.076	$4.1 \cdot 10^{11}$	0.71	$2.9 \cdot 10^{11}$

Table 1: Information of TNBL case: dimensions of the boundary layer L_i^*, number of cells on i-direction N_i, first grid point distance x_1^*, and maximum Grashof, Prandtl and Rayleigh numbers for the simulations at $Pr = 0.71$. $H = L_x^* L_b$, $L = L_y^* L_b$ and $W = L_z^* L_b$ corresponds to the physical mesh dimensions.

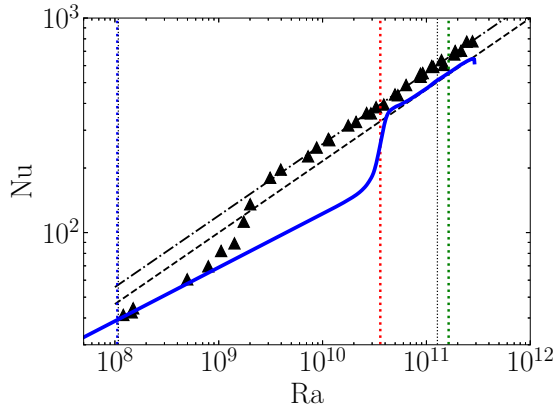

Figure 5: Nusselt number against Rayleigh number for the TNBL (blue line) against the experimental data (▲) of Tsuji [4]. Vertical colored lines indicate the Rayleigh number location where the time series analysis was performed. Black point lines indicate the location of the extracted profiles.

Turbulence in the outer sub-layer increases the thickness of the boundary layer at high Grashof numbers. The enhanced diffusion increases and propagates momentum far from the wall. In the case of velocity in fig. 7a, the laminar velocity profile is well predicted. However, for the turbulent regime in fig. 7b, the simulations captures the profile trend, but slightly underestimate the velocity magnitude and the boundary layer thickness. A perfect agreement in the inner region is noticed.

Since velocity and temperature are coupled, a good prediction in the laminar region and a deviated one in the turbulent zone are expected for temperature in fig. 8. Temperature profiles have three regions: an inner region at low x^+, a logarithmic region at moderate x^+, and finally a constant temperature region, which is already the free-stream temperature. The laminar temperature profile of fig. 8a is well captured by the simulations. However, as it is for momentum, the turbulent profile does not reproduce properly the experimental results, as shown in fig. 8b. An increased diffusion by turbulence is needed to improve the temperature prediction. This lack of heat transfer was also noticed previously when studying the Nusselt number in fig. 5.

The understanding of the flow in the laminar, transition and turbulent regions is needed. If the transition mechanisms are known, they could be used to improve the flow predictions. Several probes have been set in different locations (laminar, transitional and turbulent regions) on the boundary layer to perform a time series analysis. They track the velocity and temperature at the same wall distance (normalwise direction) and three different height (streamwise direction). Some probes at the spanwise direction is also set to study the domain size effect, and to provide a more accurate time analysis. Detailed information about them is indicated in table 2. Velocity and temperature have been acquired at a sampling frequency of $f = 500\ Hz$ during 131 s, giving an amount of $\sim$ 65000 sampled points.

Probe	x_b	y_b	Gr	Ra	N_z	f_s
1	10	530	1.5^8	1.1^8	32	500
2	10	3700	5.1^{10}	3.6^{10}	32	500
3	10	6131	2.3^{11}	1.6^{11}	32	500

Table 2: Probes information to perform the time and space analysis of the transition. Coordinates correspond to $x_b = x/L_b$ and $y_b = y/L_b$. The N_z probes where spaced regularly in the spanwise direction Z. The sampling frequency is specified as f_s.

At the given three locations, the power spectrum density of the velocity and temperature signals is computed. They are shown in figs. 9 to 11. A similar behavior is found between the velocity and temperature spectra. In the laminar region fig. 9a, the maximum power spectrum is reached at a frequency of 0.156 Hz. After that, an abrupt decay on the power at higher frequencies is observed. The most energetic frequencies are the lower ones.

When going in the transition region, a huge difference appears. The power spectra density increases

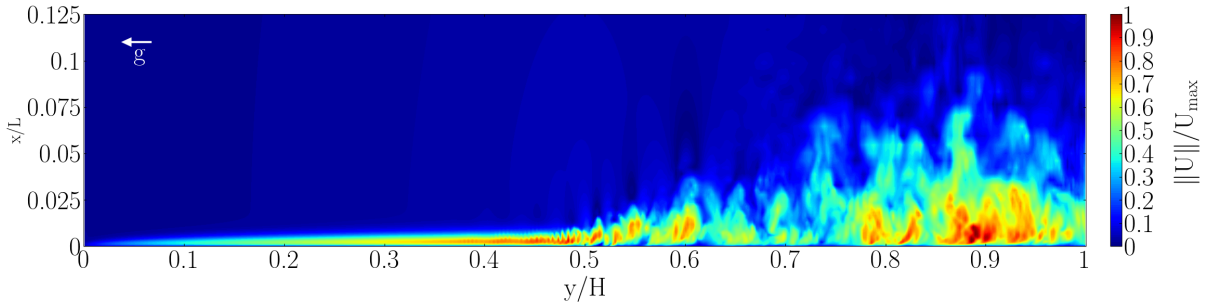

(a) Velocity

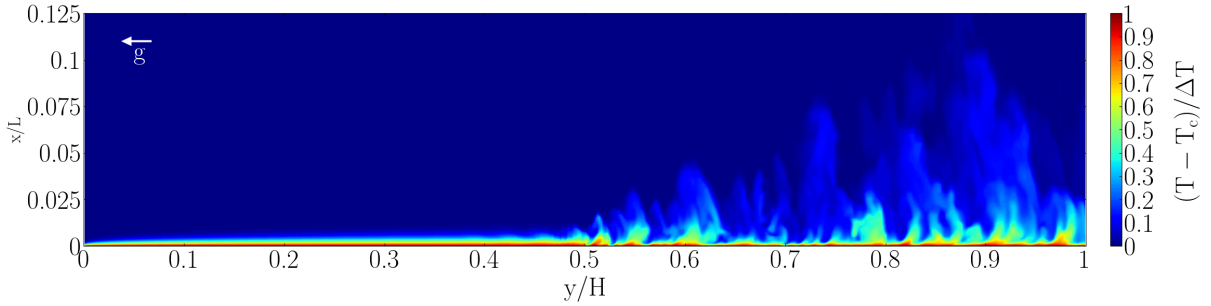

(b) Temperature

Figure 6: Instantaneous flow field of the TNBL case

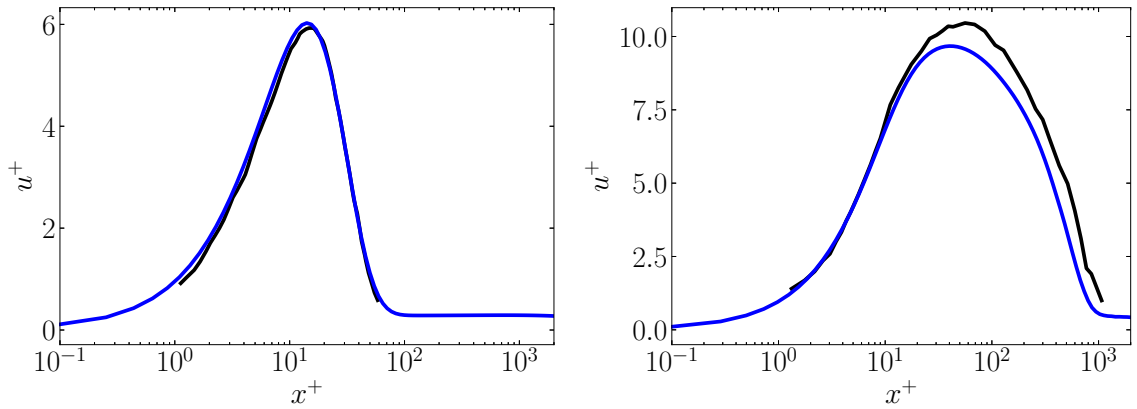

(a) $Gr = 1.52 \cdot 10^8$

(b) $Gr = 1.8 \cdot 10^{11}$

Figure 7: Non dimensional velocity profiles u^+ for the TNBL (blue line) against the experimental data (black line) of Tsuji [4], at two different Grashof numbers.

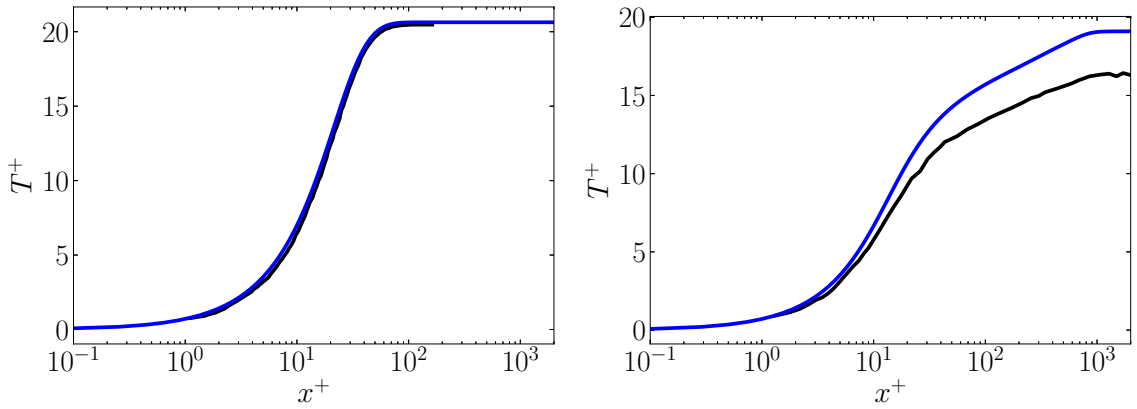

(a) $Gr = 1.52 \cdot 10^8$ (b) $Gr = 1.8 \cdot 10^{11}$

Figure 8: Non dimensional temperature profiles T^+ for the TNBL (blue line) against the experimental data (black line) of Tsuji [4], at two different Grashof numbers.

in several orders of magnitude when the flow promotes to transition. Low frequencies are still the energetic ones, but some peaks appear in the range $1.25 < f < 1.55\ Hz$. These frequencies are considered as the one that induces transition through velocity and temperature oscillations.

When the flow is already turbulent, there is not a predominant frequency that keeps the turbulence in the flow. Low and high frequencies oscillations cohabit by means of the energy transport between the small and big scales of motion. One can see that the energy decay appear much more later than in the laminar region.

Autocorrelation can be used too to detect the transition to turbulence. The autocorrelation of a variable φ indicates if its values are related at different times or locations. When the time autocorrelation of a variable is studied with a time interval τ, its coefficient is:

$$\rho_\varphi(\tau) = \frac{\langle \varphi(t-\tau)\,\varphi(t)\rangle}{\left(\langle \varphi(t-\tau)^2\rangle\langle \varphi(t)^2\rangle\right)^{1/2}} \tag{10}$$

The obtained time autocorrelations for the previous time signals are shown in figs. 12 to 14. However, the differences when Grashof increases are clear. When the flow is still laminar, one can see that the signal is quasi-periodic. Peaks with high autocorrelation value in fig. 12 indicate that the flow is periodic, there are no random oscillations that disturb the flow.

When the flow goes to transition, the autocorrelation changes as shown in fig. 13. The velocity autocorrelation goes to zero, and the signal periodicity decreases. However, a symmetric signal is found in the temperature autocorrelation, decreasing the correlation when the separation time increases. In both cases there is more noise when one compares with the laminar autocorrelation. It means that inside the flow, random fluctuations due to turbulence appear, decreasing the autocorrelation. A high frequency is also observed, since the separation time between two consecutive peaks is shorter than in laminar conditions.

Once the flow becomes turbulent, the autocorrelation functions are the ones of fig. 14. In this case, the autocorrelation goes immediately to values very close to zero, meaning that the signal is random.

As a conclusion, the transition to turbulence is observed in the autocorrelation function in the reduction of its value, and the loss of periodicity.

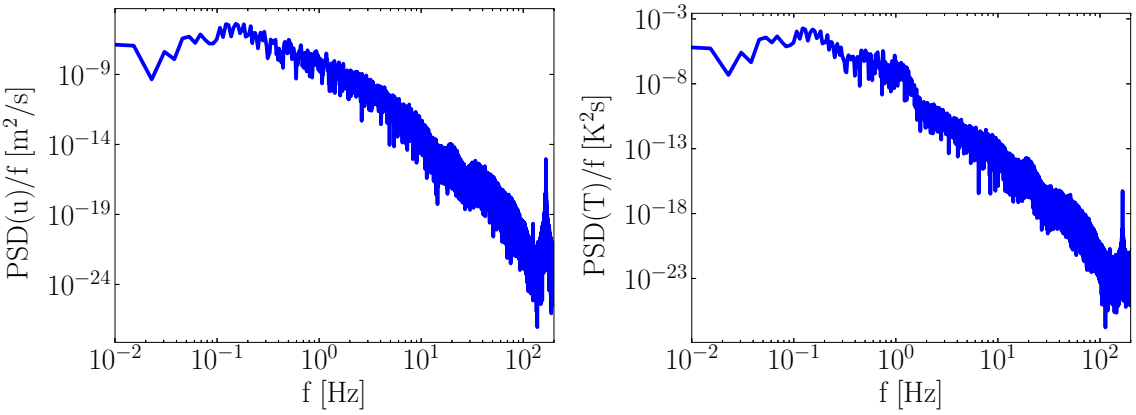

(a) Velocity PSD

(b) Temperature PSD

Figure 9: Power spectral density of the TNBL at $Pr = 0.71$, $Gr = 1.5 \cdot 10^8$.

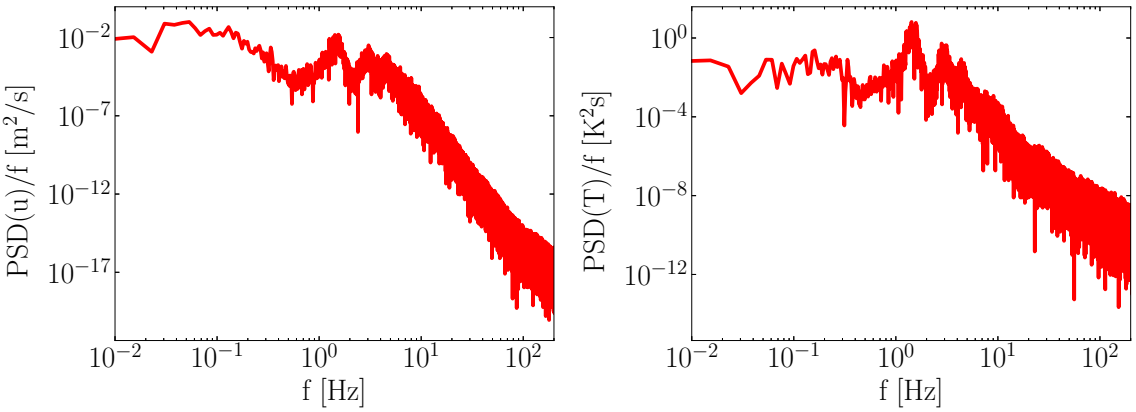

(a) Velocity PSD

(b) Temperature PSD

Figure 10: Power spectra of the TNBL at $Pr = 0.71$, at $Gr = 5 \cdot 10^{10}$.

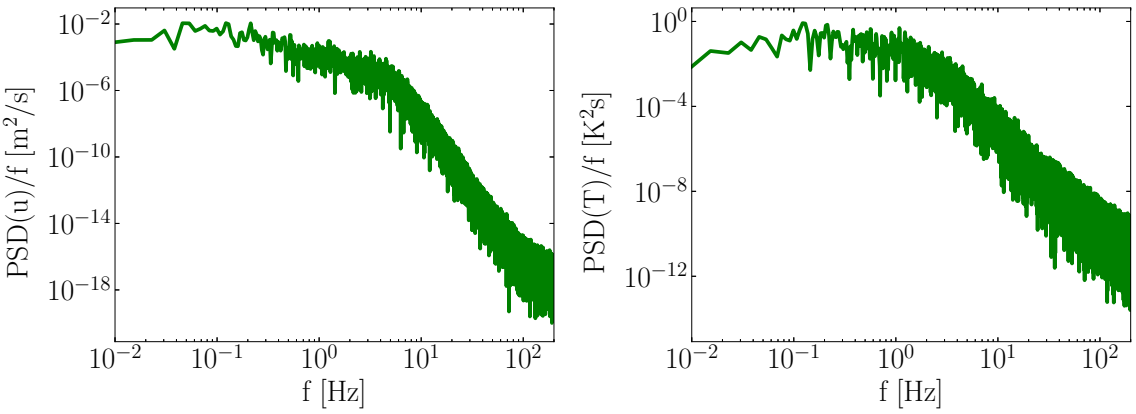

(a) Velocity PSD

(b) Temperature PSD

Figure 11: Power spectra of the TNBL at $Pr = 0.71$, at $Gr = 2.3 \cdot 10^{11}$.

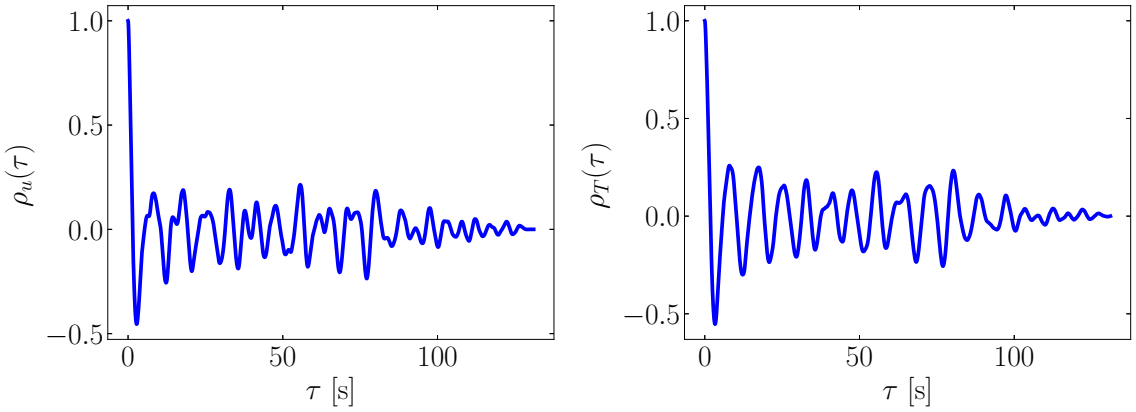

(a) Velocity time correlation

(b) Temperature time correlation

Figure 12: Time correlation of the TNBL at $Pr = 0.71$, at $Gr = 1.5 \cdot 10^8$.

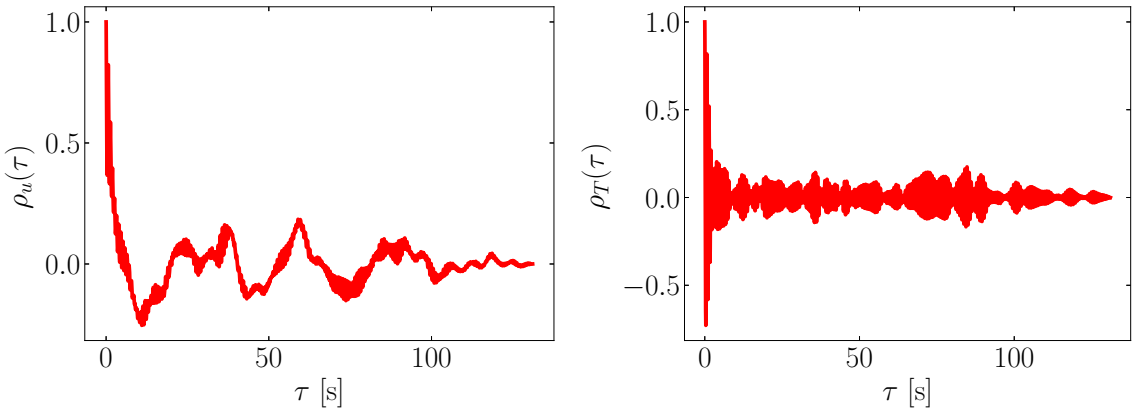

(a) Velocity time correlation

(b) Temperature time correlation

Figure 13: Time correlation of the TNBL at $Pr = 0.71$, at $Gr5 \cdot 10^{10}$.

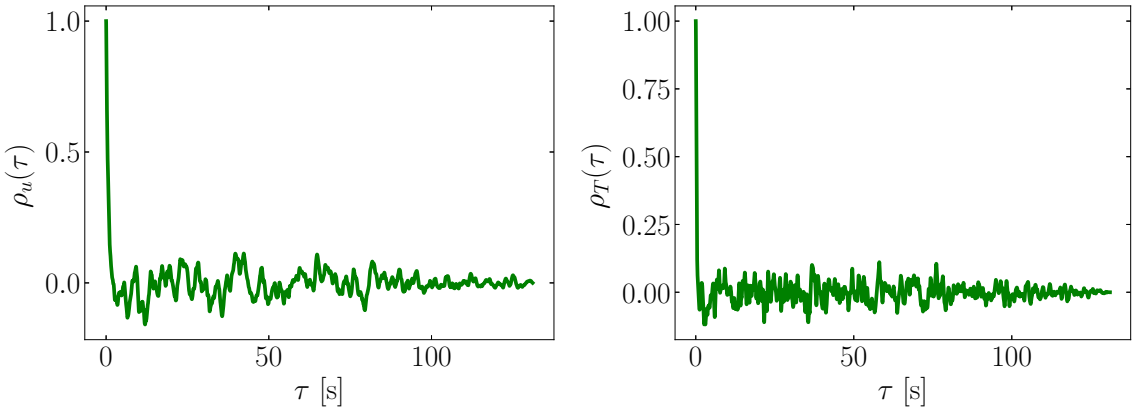

(a) Velocity time correlation

(b) Temperature time correlation

Figure 14: Time correlation of the TNBL at $Pr = 0.71$, at $Gr = 2.3 \cdot 10^{11}$.

3.2. Perturbation technique introduction

The time series analysis of the previous LES showed that, in the transition region, there is a dominant frequency range. The most energetic frequencies are located there and they promote transition in the considered system. This last assumption implies that transition takes place when this frequency is excited in the system, amplifying the flow fluctuations. If an artificial velocity or temperature perturbation is applied in the wall, where one of the strongest frequencies is used, transition should occur after the perturbation location.

Three different pertubation frequencies have been tested in the previous TNBL simulation. Also, they have been included in both velocity and temperature fields (one per simulation). The details of the simulated test cases are indicated in table 3.

The Nusselt number computed in these simulations is shown in fig. 15, and compared with the Tsuji [4] experiments and with the previous simulation, where no perturbation is applied. The inserted fluctuations in the wall introduce transition much earlier, as one can see comparing any perturbed case against the TNBL case. The transition point appears at different Rayleigh values in function of the selected perturbation frequency, and the perturbed field, as it is observed in table 3. At low frequencies, the flow transitions earlier. Taking a look at the same perturbation frequency, transition appears sooner when it is applied in the velocity field. However, the transition in those cases is less steep than in any PertT case.

It is found that no matter which frequency or perturbed field, all the simulations converge at the same heat transfer prediction than the LES without this perturbation method. That means that at a given point, the turbulent flow goes back to the equilibrium, already altered by the perturbation technique. The gap between simulations and experiments in the Nusselt number is kept when the flow turns turbulent. It is possible to fit the Nusselt number for all the simulations with the correlations

$$Nu_{lam} = 0.387 Ra^{1/4} \tag{11}$$

$$Nu_{turb} = 0.1 Ra^{1/3} \tag{12}$$

Figure 18 shows the velocity profiles at two different Grashof numbers, in laminar and turbulent regions. A good agreement is found between all of them with the experimental database. Slight overestimations are found in $Gr = 1.8 \cdot 10^{11}$ in fig. 18b, in the maximum velocity and the outer sublayer profile. As

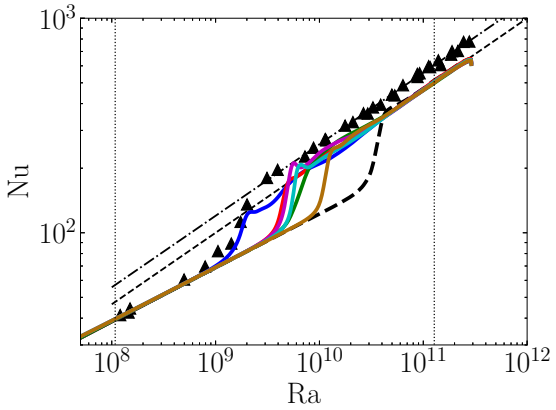

Figure 15: Nusselt number against Rayleigh number for PertU1 (blue), PertU2 (red), PertU3 (green), PertT1 (magenta), PertT2(cyan) and PertT3 (caramel) against the experimental data (▲) of Tsuji [4], and the TNBL case (dash). Black point lines indicate the location of the extracted profiles.

in fig. 7b, the turbulent diffusion increases the thickness of the momentum boundary layer. Comparing with the TNBL case, the perturbed cases predict more accurately the experimental profile.

The temperature comparison between simulations and experiments is shown in fig. 19. As for velocity, the temperature profile in the laminar region in fig. 19a, no differences are observed between al the simulations and experiments. However, in the logarithmic region and the free-stream value for the turbulent profile of fig. 19b, one can see that TNBL is closer to the experiments, while the perturbed cases follow it closely. The inner sublayer is well characterized in all the simulations.

Regarding the turbulent fluctuations of velocity and temperature at $Gr = 1.8 \cdot 10^{11}$, fig. 20 shows the RMS of the vertical velocity component and temperature. In general, all the cases reproduces the velocity fluctuations, though slightly overpredicting the reference data. PertT1 provides the closest approximation to the experiments, and PertU2 provides the farther one. The temperature RMS in fig. 20b does not show huge differences between the perturbed cases and TNBL, except for the maximum reached fluctuation value. All the simulations overpredict the temperature fluctuations. The maximum temperature fluctuation is reached at $x^+ = 20$ in both experiments and simulations.

In addition, the Reynolds stress $\langle u'v' \rangle^+$ of fig. 21 is slightly under-predicted in all the simulations, no mat-

Case	Gr	A	f [Hz]	Turbulence transition	Recover point [Ra]
pertU1	10^7	10%	1.31935	$10^9 < Ra < 2 \cdot 10^9$	$4 \cdot 10^{10}$
pertU2	10^7	10%	1.42578	$3 \cdot 10^9 < Ra < 5 \cdot 10^9$	$2 \cdot 10^{10}$
pertU3	10^7	10%	1.59445	$4 \cdot 10^9 < Ra < 10^{10}$	$4.6 \cdot 10^{10}$
pertT1	10^7	50%	1.31935	$3 \cdot 10^9 < Ra < 7 \cdot 10^9$	$2.8 \cdot 10^{10}$
pertT2	10^7	50%	1.42578	$4 \cdot 10^9 < Ra < 8 \cdot 10^9$	$8.2 \cdot 10^9$
pertT3	10^7	50%	1.59445	$8 \cdot 10^9 < Ra < 1.6 \cdot 10^{10}$	$4 \cdot 10^{10}$

Table 3: Proposed test cases where the perturbation method is applied. The perturbation is located in the point Gr, and the amplitude A is the fraction of the laminar velocity at that given Gr for pertUX, and the temperature difference $T_h - T_c$ for pertTX. The applied frequency on each case is f. The transition region is indicated in function of the Rayleigh number.

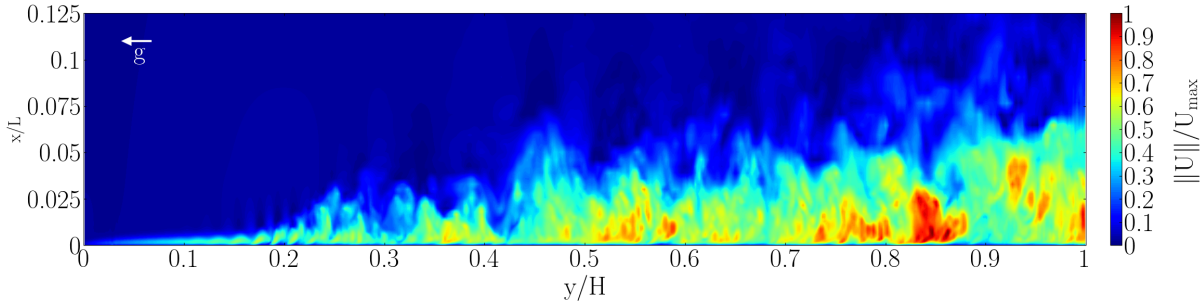

(a) PertU1

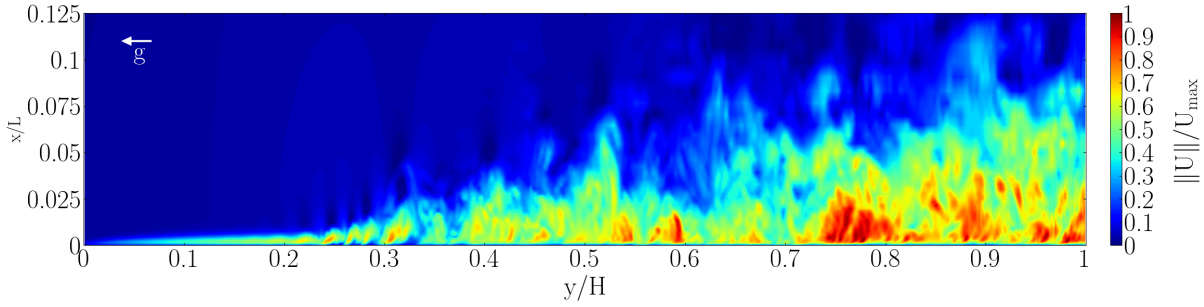

(b) PertT1

Figure 16: Instantaneous velocity field for PertU1 and PertT1

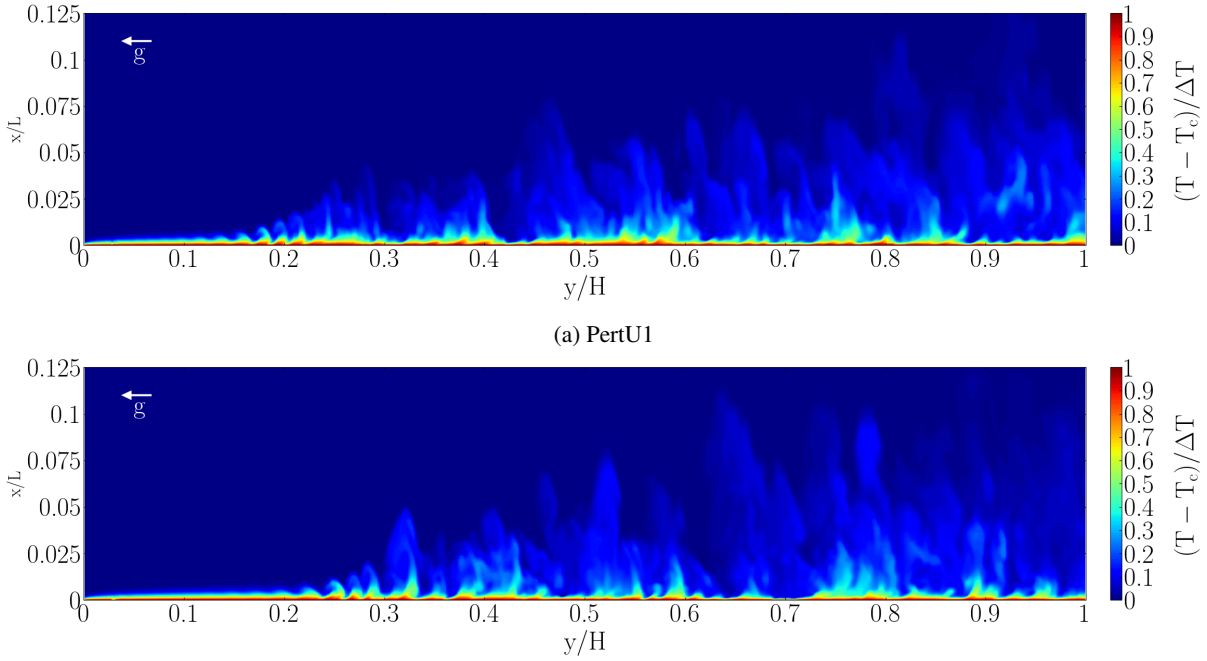

(a) PertU1

(b) PertT1

Figure 17: Instantaneous temperature field for PertU1 and PertT1

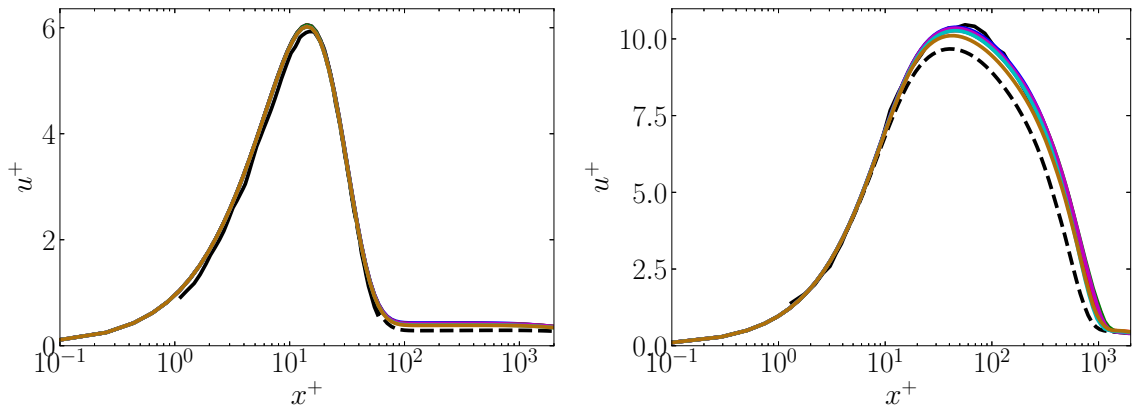

(a) $Gr = 1.52 \cdot 10^8$

(b) $Gr = 1.8 \cdot 10^{11}$

Figure 18: Non dimensional velocity profiles u^+ for PertU1 (blue), PertU2 (red), PertU3 (green), PertT1 (magenta), PertT2 (cyan) and PertT3 (caramel) against the experimental data (black line) of Tsuji [4] and the TNBL case (dash line), at two different Grashof numbers.

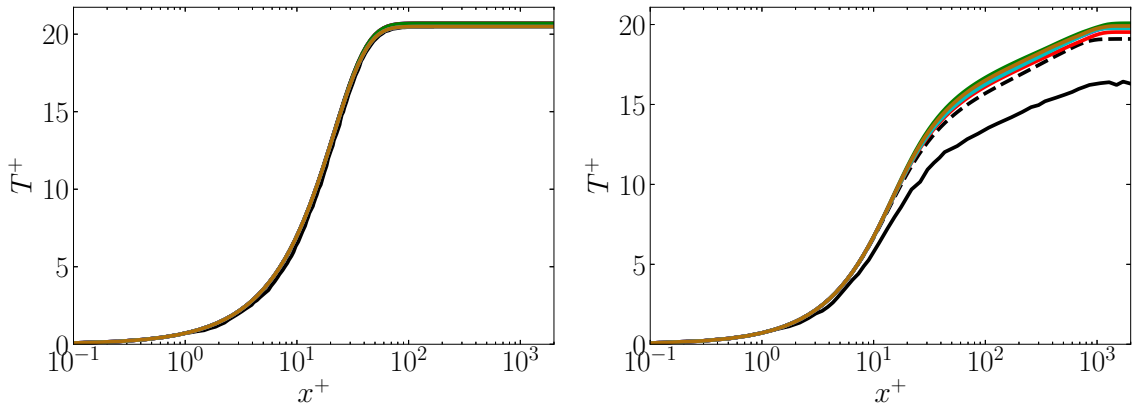

(a) $Gr = 1.52 \cdot 10^8$ (b) $Gr = 1.8 \cdot 10^{11}$

Figure 19: Non dimensional temperature profiles T^+ for PertU1 (blue), PertU2 (red), PertU3 (green), PertT1 (magenta), PertT2 (cyan) and PertT3 (caramel) against the experimental data (black line) of Tsuji [4] and the TNBL case (dash line), at two different Grashof numbers.

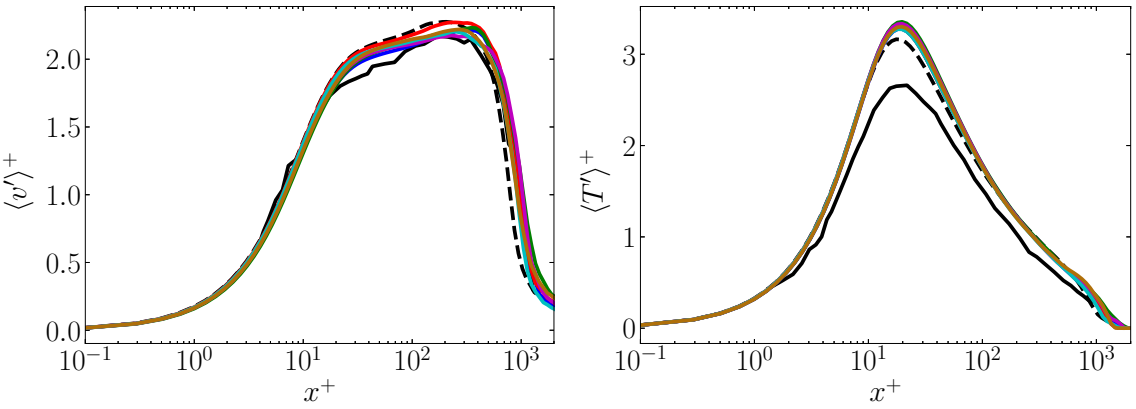

(a) Velocity RMS (b) Temperature RMS

Figure 20: Non dimensional resolved RMS profiles for velocity and temperature for PertU1 (blue), PertU2 (red), PertU3 (green), PertT1 (magenta), PertT2 (cyan) and PertT3 (caramel) against the experimental data (black line) of Tsuji [4] and the TNBL case (dash line), at $Gr = 1.8 \cdot 10^{11}$, $Pr = 0.71$.

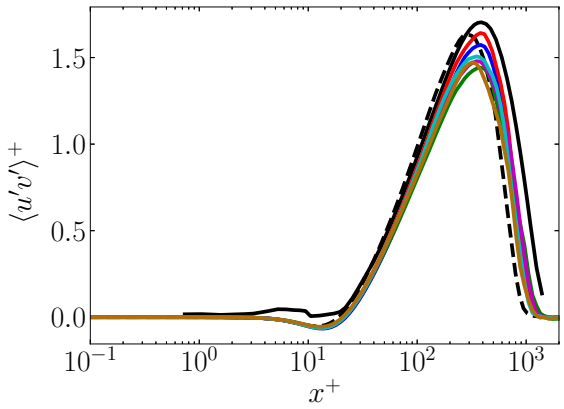

Figure 21: Resolved Reynolds stress for the LES with velocity perturbation: PertU1 (blue), PertU2 (red), PertU3 (green), PertT1 (magenta), PertT2 (cyan) and PertT3 (caramel) against the experimental data (black line) of Tsuji [4], at $Gr = 1.8 \cdot 10^{11}$, $Pr = 0.71$.

ter what frequency is used, or which flow field is perturbed. PertU2 gets a good approximation in this case, following the trend of the stress. It presents the highest Reynolds stress, followed by by PertU3. When the temperature perturbation is applied, the Reynolds stress is lower than in case of velocity fluctuations. This fluctuation is a good indicator of turbulence, and it has been used to assess the characteristics of the boundary layer in literature. In the inner sub-layer region, one can see some negative values of the stress, whereas in experiments, a positive value is found. This phenomenon has been observed in LES and DNS in the past by Abramov [7] and Nakao [8].

Finally, the resolved turbulent heat fluxes of fig. 22 are shown in fig. 22. Figure 22a shows the normalwise turbulent heat flux $\langle u'T' \rangle^+$, whose prediction is slightly overestimated by PertU1 and PertT1, PertT2 and PertT3. In all the cases, the prediction at low x^+ is underestimated. PertU2 and PertU3 values are closer to the experiments, reproducing accuratelly the maximum heat flux value and the outer layer region. In the streamwise heat flux $\langle v'T' \rangle^+$ of fig. 22b the same behavior is found. The use of the perturbation technique in the velocity field reduces the error comparing with the TNBL case. When the perturbation is applied on the temperature field, the differences with the original LES are not significant.

From these simulations, one can conclude that the transition is promoted thanks to the controlled transition technique. When perturbing the velocity, earlier transitions are found, however a bigger length is required to reach the equilibrium in the turbulence production. Temperature fluctuations have the opposite behavior in these points. No extreme differences are found when comparing mean and second order statistics once the flow becomes turbulent.

4. Conclusions and future work

A Large Eddy Simulation of a turbulent natural convection boundary layer with $Pr = 0.71$ has been performed, and the signal analysis of velocity and temperature provided information about the mechanisms of transition to turbulence. An increase of high frequency fluctuations is observed, related with the chaotic nature of turbulence. During the transition, a range of frequencies have a high power spectrum density, showing the natural frequency if the natural boundary layer.

If these frequencies are introduced in the flow as velocity or temperature fluctuations on a small portion of the heated wall, the flow reaches the turbulence regime earlier. Three different frequencies have been tested, and the obtained results show that the higher the frequency is, the better is the approach for velocity and temperature profiles in the turbulent region. However, the transition occurs later than in the case of a lower frequency is used. Also, one can see that globally, when the velocity field is perturbed, the heat transfer, and the rest of mean and second order statistics are better reproduced than if the temperature field was excited.

As future work, the presented methodology will be applied at two low Prandtl numbers, 0.2 and 0.025. A signal analysis to study the promotion to turbulence and the study of the mean and turbulent statistics will be performed on them, in order to observe the effect of the Prandtl number in this given flow configuration.

References

[1] MYRRHA Project `http://myrrha.sckcen.be/`.
[2] W. To, J. Humphrey, Numerical simulation of buoyant, turbulent flow-i. free convection along a heated, vertical, flat plate, International journal of heat and mass transfer 29 (4) (1986) 573–592.
[3] Z. Yan, E. Nilsson, Large eddy simulation of natural convection along a vertical isothermal surface, Heat and Mass Transfer 41 (11) (2005) 1004–1013.
[4] T. Tsuji, Y. Nagano, Characteristics of a turbulent natural convection boundary layer along a vertical flat plate, International Journal of Heat and Mass Transfer 31 (8) (1988) 1723–1734.
[5] D. G. Barhaghi, L. Davidson, R. Karlsson, Large-eddy simulation of natural convection boundary layer on a vertical cylinder, International journal of heat and fluid flow 27 (5) (2006) 811–820.

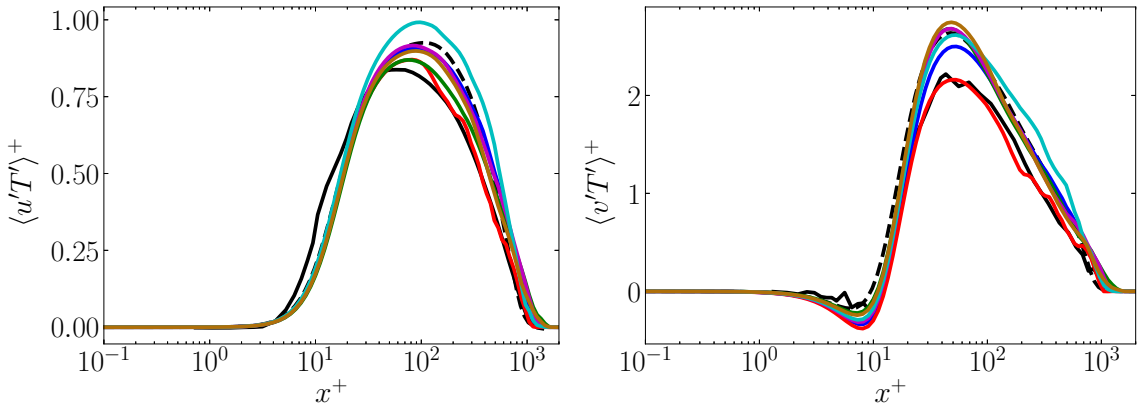

(a) Normal wise heat flux

(b) Stream wise heat flux

Figure 22: Dimensionless resolved heat fluxes for PertU1 (blue), PertU2 (red), PertU3 (green), PertT1 (magenta), PertT2 (cyan) and PertT3 (caramel) against the experimental data (black line) of Tsuji [4] and the TNBL case (dash line), at $Gr = 1.8 \cdot 10^{11}$, $Pr = 0.71$.

[6] M. Z. Abedin, T. Tsuji, Y. Hattori, Direct numerical simulation for a time-developing natural-convection boundary layer along a vertical flat plate, International Journal of Heat and Mass Transfer 52 (19) (2009) 4525–4534.

[7] A. G. Abramov, E. M. Smirnov, V. D. Goryachev, Temporal direct numerical simulation of transitional natural-convection boundary layer under conditions of considerable external turbulence effects, Fluid Dynamics Research 46 (4) (2014) 041408.

[8] K. Nakao, Y. Hattori, H. Suto, Numerical investigation of a spatially developing turbulent natural convection boundary layer along a vertical heated plate, International Journal of Heat and Fluid Flow.

[9] OECD Nuclear Energy Agency. Nuclear Science Committee, Handbook on Lead-bismuth Eutectic Alloy and Lead Properties, Materials Compatibility, Thermal-hydraulics and Technologies, OECD Nuclear Energy Agency, 2007.

[10] T. Sayadi, C. Hamman, P. Moin, Direct numerical simulation of h-type and k-type transition to turbulence, Center for Turbulence Research Annual Research Briefs (2011) 109–121.

NOISE AND AEROACOUSTICS

Leakage characterization through structural vibration analysis

Bouanati Nicolas

Chpolansky S.A.S, Marcoussis, 91460, France, bouanati.nicolas@vki.ac.be

Supervisor: Schram Christophe

Associate Professor,Environmental and Applied Fluid Dynamics Department, von Karman Institute for Fluid Dynamics, Belgium, christophe.schram@vki.ac.be

University Supervisor: Pezerat Charles

Professor, Mechanical and Acoustics Engineering, Le Mans University, France, charles.pezerat@univ-lemans.fr

Abstract

Internal leakage detection is an important research field for maintenance and safety in industrial plans. The understanding of links between the leakage topology and the generated vibrations in the pipes due to pressure fluctuations could improve the leak quantification techniques. The potential of FAT for leakage detection and quantification is assessed.

Keywords: Valve, leakage rate, acoustic emission, force analysis technique

1. Introduction

Fluid leakages (gas, liquid or biphasic) in industrial plans may be the origins of important material and money losses and represent safety risks as they can lead to explosions or environmental contaminations. Distinction is maid between external and internal leakages depending if the fluid leaks outside of the pipping system or remains inside. Internal leakages have several causes, including damaged seats or plugs or due to impurities in the flow leading to incomplete valve closing (Sharif, 1998 [1]; Yan, 2015 [2]).

The first problem in valve maintenance is to detect if a valve is leaking and, if possible, to determine the resulting mass flow rate in order to choose if the valve has to be fixed or replaced. Because a visual inspection necessitates the dismounting of the valve, which means stopping one part of the plan, and the classical techniques of external leakage detection are ineffective (Geiger, 2006 [3]; Murvay, 2012 [4]), some techniques have been developed in this field mainly based on the analysis of the structural vibrations of the valve and surrounding pipes (Thompson and Zolkiewsky, 1997 [5]; Kaewwaewnoi, 2005 [6]; Dickey, 1978 [7]). Vibrations generated in the structure by the leak have three origins:

- turbulent: the turbulence of the confined jet produced by the leak generates pressure fluctuations;
- acoustic: the turbulence generates acoustic pressure variations resonating and exciting the structure;
- cavitation: for incompressible fluids, cavitation may appear leading to strong and very localized pressure variation.

Different authors have worked on valve leakage detection and quantification focusing on the mass flow rate determination. The approach has been experimented in a large frequency range, from low frequencies where the first acoustic modes appear in the pipe, i.e. a few dozens of Hz [5], to very high frequencies like Acoustic Emission (EA), i.e. from 100 kHz to a few MHz (Yan, 2015 [2]; Kaewwaewnoi, 2005 [6]).

Detection techniques at low frequencies are easier to realize because of the recording and post processing systems. Nevertheless, the noise present in industrial plans make these techniques ineffective in real conditions. On the other side, the AE techniques are mainly empirical, like it is the case for the VPAC and Clam-

pOn systems by example. This is due to the misunderstanding of the origin of the vibrations for such high frequencies.

2. Thesis objectives

This work has two main objectives: the first one is the understanding and the modelling of the different relations existing between the leak configuration (fluid, temperature, pressures, leak geometry, etc.) and the vibrations generated in the structure. The second objective is to assess the potential of the Force Analysis Technique (FAT) for the determination of the pressure that the leak applies to the structure (Pezerat, 1996 [8]; Lecoq, 2013 [9]).

Experimental data are needed for this work. A test bench with the necessary equipment in order to observe and measure different characteristics of the flow has to be designed. This thesis is limited to the study of air leakages at ambient temperature and for a maximum pressure of 14 bar. The leaks will be made of a drilled diaphragm placed in a 2 inches diameter duct. The equipment has to insure the control and measurement of the inlet and outlet pressure and the measurement of the mass flow rate and the temperatures. Moreover, four different test sections will be realized in order to perform PIV, HW, wall pressure fluctuations and wall vibrations measurements.

The FAT is used for the determination of the forces exciting a structure. The technique is based on the discretization of the movement equations of the structure and the the measure of deformation at different locations with accelerometers. This could allow the determination of some characteristics of the pressure field exciting the structure that are directly linked with the leak configuration and allow the determination the mass flow rate. The aim is to find the disposition of the sensors and the frequency in which some characteristics of the wall pressure field strongly related to the mass flow rate could be measured by the FAT, if this is possible.

3. State of the art

3.1. Leak detection background

Valve leakage detection using AE measurements started at the end of 70's with Dickey and al. [7]. Nakamaura and Terada proposed in 1985 [10] an investigation about the link between AE RMS and the mass flow rate Q. The two variables are in good agreement following the authors and is still investigated by Lee and al. in 2003 [11] or Prateepasen in 2011 [12] by example.

The first work aiming to model the jet noise is due to Lighthill in 1952 [13]; this model links the jet noise power to the different characteristics of the jet and is summerised in Eq. 1.

$$\Pi_{jet} = K\rho\left(\frac{v^8}{c^5}\right)d^2 \tag{1}$$

With K a function of the fluid variables, c the speed of sound, ρ its density, v the velocity at the jet outlet and d its diameter. In 2010 [14], Kaewwaewnoi proposed a model linking the RMS of the AE to different leak variables affecting the generated flow taking in account the quadrupolar noise, typical of the turbulence. Meland proposed an equivalent model in 2010 [15] taking also in account the dipolar sources relative to the wall pressure fluctuations and leading to Eq. 2:

$$AE^2_{RMS} = \frac{(C_1P_1 + C_2)P_1^3}{c^5\rho D^{14}}\left(\frac{Q_v}{c_v}\right)^8\left(\frac{S}{\Delta P}\right)^4 \tag{2}$$

Where C_1 and C_2 are function of the fluid variables, D the valve size, c_v its valve coefficient, P_1 the inlet pressure, ΔP the pressure difference across the leak and S the fluid specific weight.

The pipes also present vibrations at low frequencies. Different authors investigated the possibility to diagnosis a leakage using low frequency vibrations which shown promising results. Nevertheless, the application of those methods in an industrial environment did not succeed because of the background noise, typically less than 20 kHz. Thompson and Zolkiewsky investigated, in 1997 [5], the possibility of leak detection at low frequency by studying experimentally leakages with different gas and leak configurations. The conclusion is that the vibration spectrum features peaks at frequencies defined by:

$$f_{peak} = C\frac{c}{d} \tag{3}$$

Where c is the speed of sound in the fluid and d is the internal diameter of the pipe.

Most of the time, the post processing of the AE signals is a comparison with signals recorded in known conditions. As it shown by Meland in 2012 [15], except a few analytical models as the one presented previously, all the detection methods make use of reference signals like it is the case for the VPAC and ClampOn systems by example. This limits their field of application and lead to wrong conclusions if some parameters are erroneous.

3.2. Wall pressure and vibration

The space-time spectrum of the pressure fluctuations can be experimentally investigated by different methods discussed by Bull in 1996 [5]. A first one uses an array of pressure sensors. The distances between the sensors and the dimensions of the pressure holes are function of the wavelength of the pressure perturbations. This method is used by Durant and al. in 2000 [16] for the study of an enclosed jet in a circular duct. Pressure sensors were placed axially and circumferentially in order to determine the spectrum and the correlation length of the turbulent structures in both directions. The authors also took advantage of the coherence of the acoustic contribution to discard the turbulent one.

A second method takes advantage of the natural filtering behavior of a structure in the wave-number domain. Each vibration mode filters the wave-numbers associated to its deformation. Lecoq, in 2013 [9], uses the fourth order low-pass filtering properties of a flat plate in order to measure the acoustic contribution (low wave-number) of the wall pressure field of a turbulent boundary layer. The FAT, introduced by Pezerat in 1996 [8], allows Lecoq to determine the pressure field applied to the plate. He also uses methods developed from the FAT like the FWFAT (Filtered Windowed) and the CFAT (Corrected).

The FAT methods are based on the discretization of the movement equation of the investigated structure. The application of a FAT technique in the case of a pipe will necessitate the development of such an equation for a thick pipe and its discretization. The formulation of the response of thin cylindrical structures to an internal pressure field has been developed by Frymoyer in 1967 [17] and extended by Walter in 1980 [18]. These lasts seem to give a good starting point for the needed equations.

3.3. Acoustic wall pressure field

As it has been said earlier, different authors have worked on the analysis and measurement of wall pressure fluctuations inside ducts or in other configurations. The analysis of the acoustic field inside a duct (and in any reflective environment in general) is not trivial due to the presence of acoustic modes inside the pipe. System identification techniques based on multiple microphones measurements permit to reduce the complexity of intricate flow-acoustic coupling phenomena to acoustic two-ports as presented by Lavrentjev and Åbom in 1996 [19] or more recently by Sack and al. in 2014 [20] with the acoustic multi-ports. These methods are based on the modal decomposition of the acoustic field and are valid till the number of cut-on modes is limited, the maximum being around 10 modes.

At higher frequencies, the number of modes is too high and would need too many pressure sensors, two microphones being necessary for each mode. Baxter and Morfey proposed an investigation in a methodology for high frequency modal decomposition in 1983 and presented experimental results in 1985 [21; 22]. The methodology remains similar in some points at the multi-ports technique but the results are given in terms of modal energy density.

4. Test bench

The test bench that will be realized will take place in the VKI using the 40 bars air supply. The specifications are detailed hereafter. The approach used for the dimensioning of the different equipment and measurement tools is explained and the design of the test bench is finally presented.

4.1. Specifications

The test bench has to allow observation and measurements of leakage flows with air at ambient temperature in a 2 inches'duct with 2 mm wall thickness. The maximum pressure difference at the leak will be 13 bar (14 bar at the inlet and the atmospheric pressure at the outlet). Calibrated leak geometries will be made from holed diaphragms. Different geometries will be investigated with equivalent diameters going from 0.25 to 4 mm.

The different measurements the will be realized are:

- HW measurements at the inlet and outlet of the leak in order to obtain information about the mean velocity and turbulence at frequencies reaching a few dozen kHz. This will allow us to validate the turbulence spectrum models used by the leak detection method. Measurements have to be done at different axial positions to describe the all leak flow;

- PIV measurements around the leak in order to understand the flow topology, the flow inside the leakage will not be observed. Inlet and outlet transparent sections are necessary with all the classical tools for PIV measurements and particle injection. A light insulation also has to be realized;

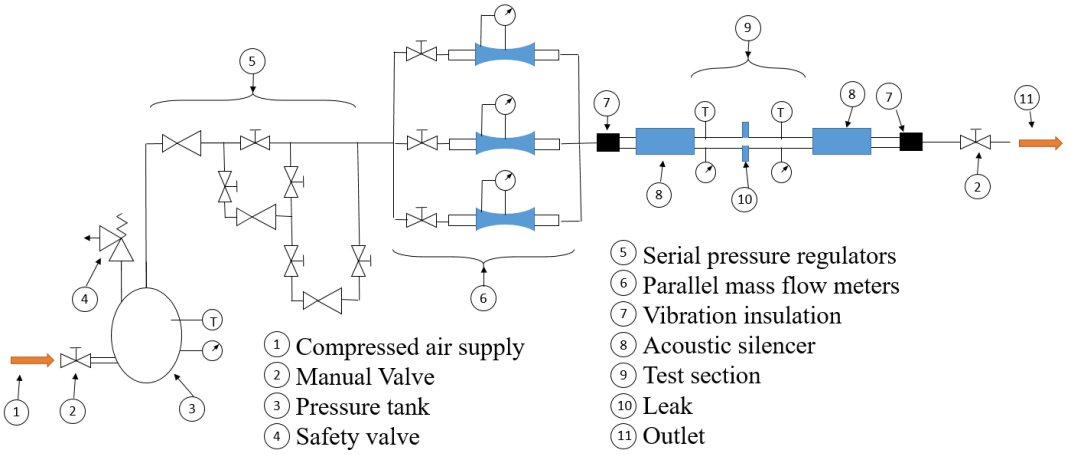

Figure 1: functionnal scheme of the set-up featuring equipement for the establishment and control of the feak flow.

- Pressure measurements in order to quantify the pressure wall fluctuations and able to make the distinction between the turbulent and the acoustic contribution. Microphone arrays will be installed localized axially and azimuthally in order to characterize the exciting pressure field in terms of space-time distribution in both directions. An acoustic insulation is needed on both sides of the test section in order to avoid external noise contamination and internal noise reflections;

- Wall vibration measurements at the inlet and outlet of the leak. Different tools will be used according to the frequency of interest (accelerometers, AE sensors,). 2 inches steel ducts with wall thickness of 5 mm will be employed. The system will be hanged with flexible supports and linked to the air supply with flexible tubes in order to avoid contamination by external vibrations.

Because the requirements for the different measurements are not compatibles, the test bench will feature four different test sections that will be installed on the rest of the set-up for each new measurement. The holed diaphragm will be rotatable, in order to be able to take measurements in different azimuthal positions.

The rest of the set-up comprises all the necessary equipment for the generation and the control of the leak flow: control of the pressure and measurement of the mass flow rate, pressure and temperature on both side of the leak. The flow conditions will have to be constant, dynamic behavior will not be investigated.

4.2. Flow parameters evaluation

A schematic of the test bench is proposed at Fig. 1 featuring the equipment necessary to the establishment and the control of the flow conditions. The test sections will take place between the mechanic and acoustic insulations.

The sizing of the equipment has been done by evaluating the flow parameters for the different leakage dimensions and pressure differences. The theory and empirical models have been used at low pressure drops (while the Mach number in the leak is less than 0.5) and the thermodynamic laws at high pressure drops, the objective being to determine the working range of the different equipment. The work of Idel'cik in 1969 [23] about pressure losses has been used for incompressible and lowly compressible flows. The results are presented in Fig. 2 where the mass flow rate is given in function of the pressure difference across the leak for different circular hole diameters d. The iso-Mach and iso-Reynolds within the leak are also presented: the iso-Mach curve permit to see the limit of the model which, according Idel'cik, is Mach 0.7. The iso-Reynolds give us the minimum pressure difference that has to be realized in order to observe laminar leaks, i.e. Reynolds inferior to 2000. It can be observed that the sensitivity of the pressure control system has to be a few kPa in order to control laminar leaks and the mass flowmeter has to be able to measure minimum mass flows around 0.5 Nl/min.

The maximum mass flow rate will be reached for the maximum pressure drop (14 bar at the inlet) and leak diameter, i.e. 4 mm. The flow will be sonic in the leak and will lead to a maximum mass flow rate of

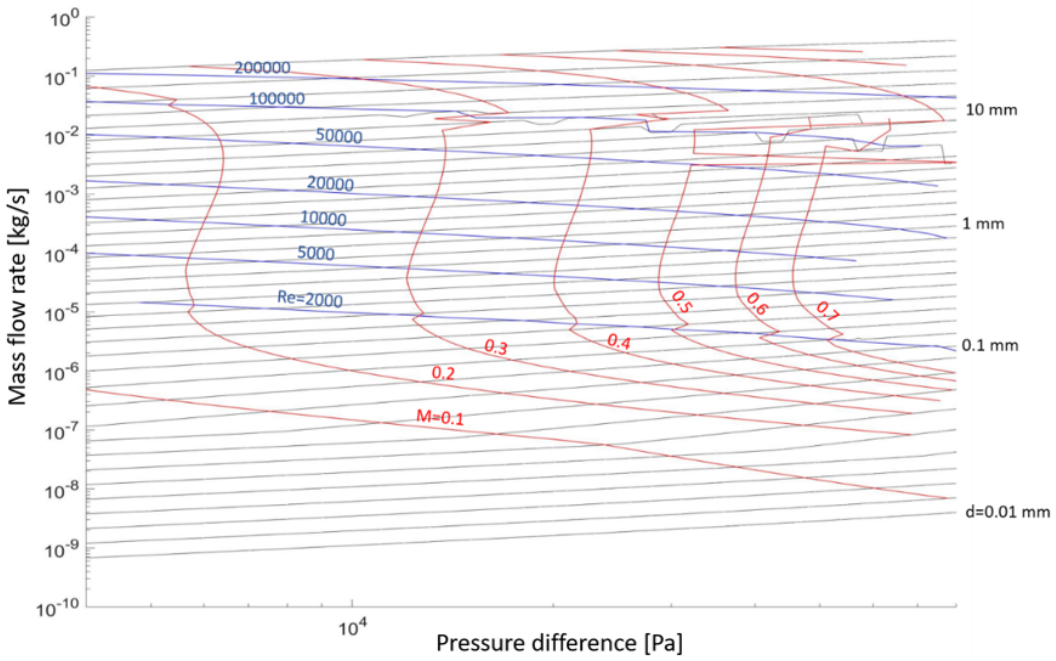

Figure 2: evaluation of the mass flow rate in function of the pressure difference across the leak for different leak diameters d.

approximatively 3,000 Nl/min.

4.3. Set-up design

The purpose of the tank present on Fig. 1 is to damp the air supply variations in order to maintain constant conditions at the leak, the maximum mass flow rate of the air supply being superior to the estimated maximum leak flow rate. A 500 liters horizontal tank with a maximum pressure of 16 bar has been selected, allowing 2 bar of pressure losses between the tank and the leak in order to reach the 14 bar figuring in the specifications. This should be respected because, even for 4 mm diameters holes, the sonic conditions will involve low velocities in the rest of the pipe system.

The pressure regulation system is composed of three manual pressure regulators installed in series with by-pass pipes. Three different pressure regulators featuring different pressure ranges and sensitivities are needed because of the large regulation range (0.01 to 13 relative bar). The manual control has been preferred to an electronical one because of the eventuality that the PID controller could become instable for some investigated flow conditions.

Then take place the mass flowmeter system composed of three different thermic mass flowmeters. Once again, the wide range of mass flows, from 0.5 to 3,000 Nl/min, involve the use of three different tools. Thermal mass flowmeters have been selected because this technology features the best turndown ratio of 100, so only three ones were needed. The selected tools insure a minimum precision of 3% over the all range from 0.5 to 3,000 Nl/min.

The manual valve at the outlet of the system allows us to modify the outlet pressure at the leak, giving one more dimension to our experimental possibilities. Finally, the silencers presented on Fig. 1 will be designed by ourselves due to the difficulty to find industrial silencers corresponding to our expectations. The work done for the design is presented hereafter.

5. Acoustic insulation

In order to insure a good quality and the repeatability of the acoustic measurements, it is needed to avoid external noise contamination, especially at low frequencies, and to limit the effect of the system on the leak noise. This mean that the inlet and outlet should be anechoic and act as infinite straight ducts. It is difficult to find an industrial acoustic system reaching our requirements because of the imposed dimensions of the system, the necessity to resist to 14 bar internal pressure and the behavior for both noise attenuation and anechoicity has to be known, moreover at high frequencies.

For this reason, it has been decided that the acoustic insulation system would be designed by ourselves. Among the different type of silencers, it has been decided to investigate dissipative silencers, an example is presented at Fig. 3. These silencers are composed of an expansion chamber, the wall of the chamber is covered of absorptive foam maintained and protected by a perforated screen.

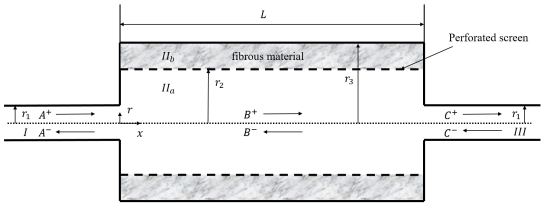

Figure 3: Geometry of dissipative silencers. The different geometry parameters and the different acoustic modes are presented.

The evaluation of the acoustic performances of the considered silencer designs will be done thanks to an analytical model and confronted with numerical simulations. The selected silencers will then be realized and their performances determined thanks to the acoustic equipment designed for the test bench. The analytical model used is based on modal matching techniques (relevant at low frequencies) and details can be find in the work of Selamet in 2004 [24] or the one of Denia in 2007 [25] by example.

The analytical model is explained hereafter and preliminary results are presented and discussed in the last section.

5.1. Analytical model

The analytical model used is based on modal matching techniques which involve the decomposition of the acoustic field in its different modes. Of course, only a finite number of modes can be used and the approach becomes invalid when the investigated frequency increases. The method is done in two step:

- first, the shape functions of the different acoustic modes used for the computation are determined. The shape functions are known in the case of rigid circular pipes but needs to be determined for the expansion chamber. It is important to notate that only axisymmetric modes are envisaged in this work;
- then, a system is written based on the conservation laws of pressure and velocity at each domain interface, junctions I-II and II-III on Fig. 3. The components A^+ and C^- are the boundary conditions of the system and have to be imposed. The system is finally inverted giving the amplitude of the different modal components of the acoustic field in the all system.

A generic solution of the function shapes $\psi(r)$ of the acoustic modes in the expansion chamber is given by a combination of Bessel functions of first and second kind as:

$$\psi_{B,n,P}(r) = \begin{cases} \psi_{II_a,n,P}(r) = C_1 J_0(k_{r,B,n} r) + C_2 Y_0(k_{r,B,n} r), \\ \qquad 0 \leq r \leq r_2, \\ \psi_{II_b,n,P}(r) = C_3 J_0(\tilde{k}_{r,B,n} r) + C_4 Y_0(\tilde{k}_{r,B,n} r), \\ \qquad r_2 \leq r \leq r_3 \end{cases} \tag{4}$$

Where J_0 and Y_0 are respectively the zero order first and second kind Besell functions and $k_{r,B,n}$ and $\tilde{k}_{r,B,n}$ are respectively the radial wave numbers of the nth mode in the empty and porous regions of the expansion chamber. C_1, C_2, C_3 and C_4 are constant that have to be determined as well as $\tilde{k}_{r,B,n}$.

$\psi_{B,n,P}(r)$ being defined up to a scale factor, C_1 can be set as 1 and C_2 as to be 0 for $\psi_{B,n,P}(r)$ to be finite at $r = 0$, only three unknowns remain. The different unknowns are determined by taking in account the continuity of the axial wave number between region II_a and II_b, the 0 velocity boundary condition at r_3 and by modeling the pressure difference across the perforated screen. Finally, a characteristic equation is written from the different previous considerations and solved by the Newton algorithm applied in the complex domain. This has to be done at each frequency of interest for every mode.

The Newton method needs an initial solution close to the real solution of the problem. In order to solve the problem in an efficient way, the solution is computed for one frequency with the solution of the previous computed frequency as initial solution. The initial solution for the first frequency at which the solution is computed is the solution for an empty circular duct of radius r_3. Then, the flow resistivity of the acoustic material and the thickness of the perforated screen are iteratively increased till the solution for the actual expansion chamber is determined.

The acoustic pressure field can then be written, for region I by example, as:

$$P_A(r, x) = \sum_{n=0}^{N} \left(A_n^+ e^{-jk_{x,A,n}x} + A_n^- e^{jk_{x,A,n}x} \right) \psi_{A,n}(r) \tag{5}$$

where A_n^+ and A_n^- are respectively the amplitudes of nth mode right-going and left-going waves and N is

the number of considered modes. A system is written based on the conservation of the pressure (Eq. 6) and the velocity (Eq. 7) of the acoustic field at the different interfaces. The interfaces are divided in N different centered circular areas in order to obtain a number of equations equal to the number of unknowns. For interface *II-III*, by example, this leads to:

$$\sum_{n=0}^{N} (C_n^+ + C_n^-) \int_0^{r_{m,P}} \psi_{C,n}(r)dr = \sum_{n=0}^{N} \left(B_n^+ e^{-jk_{x,B,n}L} + B_n^- e^{jk_{x,B,n}L} \right) \int_0^{r_{m,P}} \psi_{B,n,P}(r)dr \quad (6)$$

and

$$\sum_{n=0}^{N} k_{x,B,n} \left(B_n^+ e^{-jk_{x,B,n}L} - B_n^- e^{jk_{x,B,n}L} \right) \int_0^{r_{m,u}} \psi_{B,n,u_x}(r)dr = \begin{cases} \sum_{n=0}^{N} (C_n^+ - C_n^-) \int_0^{r_{m,u}} \psi_{C,n}(r)dr, \\ 0 \le r_{m,u} \le r_1, \\ \sum_{n=0}^{N} (C_n^+ - C_n^-) \int_0^{r_1} \psi_{C,n}(r)dr, \\ r_1 \le r_{m,u} \le r_3 \end{cases} \quad (7)$$

Where L is the expansion chamber length and $r_{m,P}$ and $r_{m,u}$ are the diameters of the different areas that compose the interfaces and are defined by:

$$r_{m,P} = \frac{m}{N+1} r_1 \,, \; m = 1, ..., N+1; \quad (8)$$

and

$$r_{m,u} = \frac{m}{N+1} r_3 \,, \; m = 1, ..., N+1. \quad (9)$$

The unknowns, in this case the amplitudes A_n^-, B_n^-, B_n^+ and C_n^+, are so determined and the performances of the silencer evaluated.

5.2. Results and discussion

Some possible silencer investigated are presented at Fig. 4. These configurations feature sections with chamber radii increasing gradually in order to limit the area ratio between two successive sections and reduce the global reflection coefficient of the silencer.

We consider first the reference configuration with one single expansion chamber, shown in Fig. 3. The radii r_1 and r_2 are 0.02015 m, the external radius r_3 is 0.07015 cm, the screen is 0.001 m thick and perforated at 10% porosity with 0.001 m diameter holes, the flow resistivity of the porous material is 20,000 Rayls/m.

Fig. 5 presents the reflection and transmission performance for different silencer lengths. Here, the transmission performances are represented by the TL coefficient, which is the ratio between the incoming acoustic power A^+ and the outgoing one C^+. the reflection performances are represented by the IRC, which is the ratio between the incoming acoustic power A^+ and the outgoing one A^-. The effect of the silencer length is as expected: the transmission loss increases with the length over the whole frequency range. The transmission loss reduces above 2 kHz, but it remains possible to reach TL of 40 dB at 15 kHz.

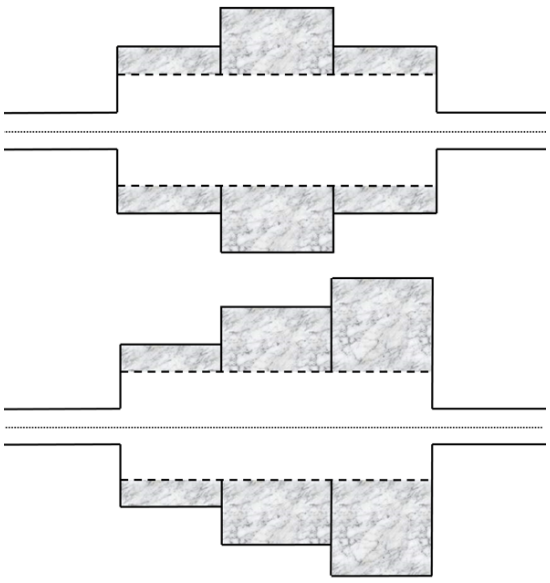

Figure 4: Examples of configurations investigatedwith gradually varying expansion chambern radius to decrease the sound reflection across discontinuities.

The IRC features oscillations that appears when the length of the expansion chamber decreases. Actually, the asymptotical limit of the IRC for an infinitely long silencer correspond to the IRC of the junction *I-II* only as it is represented on Fig 6-1. Moreover, the contraction Fig. 6-2 are much more reflective, so the following reasoning can be held to explain the preliminary partial results: as most of the amplitude of the wave that is transmitted through the expansion chamber inlet is reflected by the contraction at its outlet, both waves can interfere constructively or destructively depending of the frequency. If acoustic material is present, the reflected waves at the outlet are dissipated explained the asymptotical limit of results Fig. 5.

The next results concern different configurations composed of 3 different silencer sections. The different sections are all 0.3333 m long, so the complete

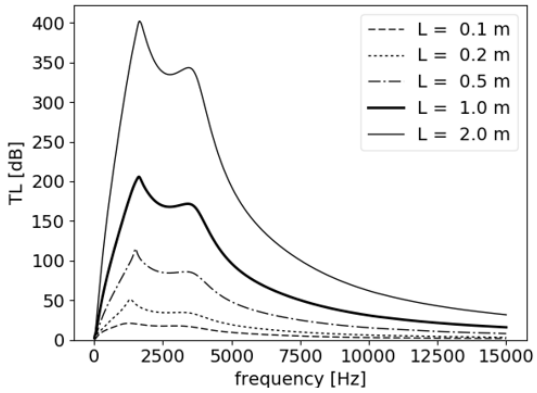

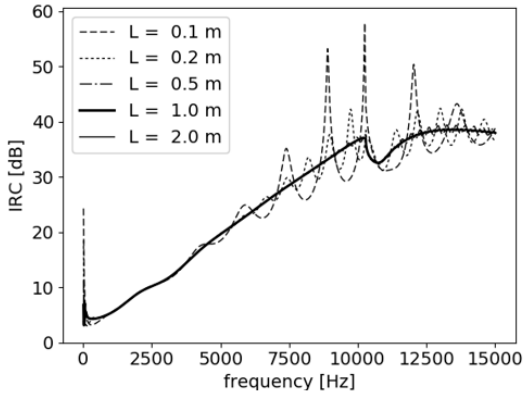

Figure 5: Evolution of the TL(left) and IRC(right) for the reference configuration silencer with different lengths.

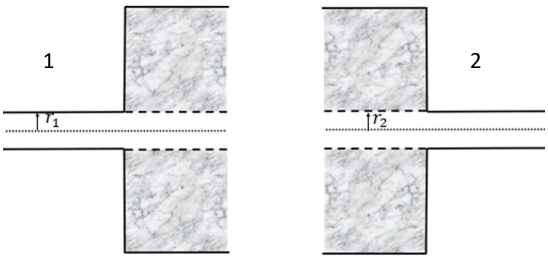

Figure 6: Scheme of the different configurations.

silencer is 1 m length, the inlet, outlet and perforated screen radius are always 0.02015 m, the expansion chamber radius is 0.07015 m and the central section *II* has the same parameters as the reference configuration, that is why the configuration 1 as the same behavior as the reference configuration and is represented by the thicker line on the results presented at Fig. 7. Table 5.2 presents the different tested configurations and gives the parameters used for sections *I* and *III*. The purpose is to observe if the increase or decrease of the different parameters has an effect on the IRC and TL of the silencer.

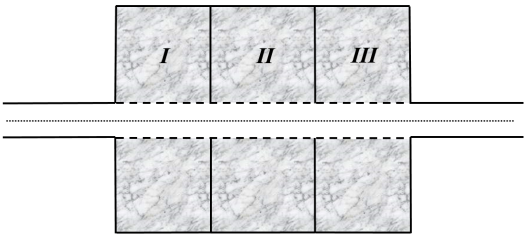

Figure 7: Scheme of the different configurations.

Conf.	*I*				*II*			
	R	*tw*	*dh*	ϕ	*R*	*tw*	*dh*	ϕ
1	20	1	1	10	20	1	1	10
2	10	1	1	10	50	1	1	10
3	50	1	1	10	10	1	1	10
4	20	1	1	5	20	1	1	20
5	20	1	1	20	20	1	1	5
6	20	2	1	10	20	0.5	1	10
7	20	0.5	1	10	20	2	1	10
8	20	1	0.5	10	20	1	2	10
9	20	1	2	10	20	1	0.5	10

Table 1: Tested configurations for the 3 sections silencers. The central section II as the same parameters as the reference configuration. The units of the different parameters are: flow resistivity (*R*) in Rayls/mm, wall thickness (*tw*) and hole diameters (*dh*) in mm and the porosity (ϕ) in %.

Only the results concerning the effect of varying the porosity of the perforated screen are presented on Fig. 8. Nevertheless, they are representative of what is observed for the other cases. It can be observed that the effect of varying any of the presented parameters along the different sections of the silencer always have a negative effect on the TL: the limit at high frequencies does not seem to change and the maximum, that is located in the 1-4 kHz range, always decreases. However, it seems that, in order to optimize the transmission losses within the silencer, it is well suited to keep constant the configuration along the silencer. It can be finally observed that oscillations of the TL appear between 5 and 9 kHz for some configurations.

Concerning the IRC, we can observe more oscillations in any configuration different of the reference one with constant parameters along the all silencer. This is due to the fact that the second reflection will not be located at the expansion-outlet junction but at

the junction between sections I and II, which mean that the transmission losses encountered by this second reflected wave will be inferior than the ones of the reference case. The second and higher orders reflections will be higher leading to more interactions between them and an oscillating IRC.

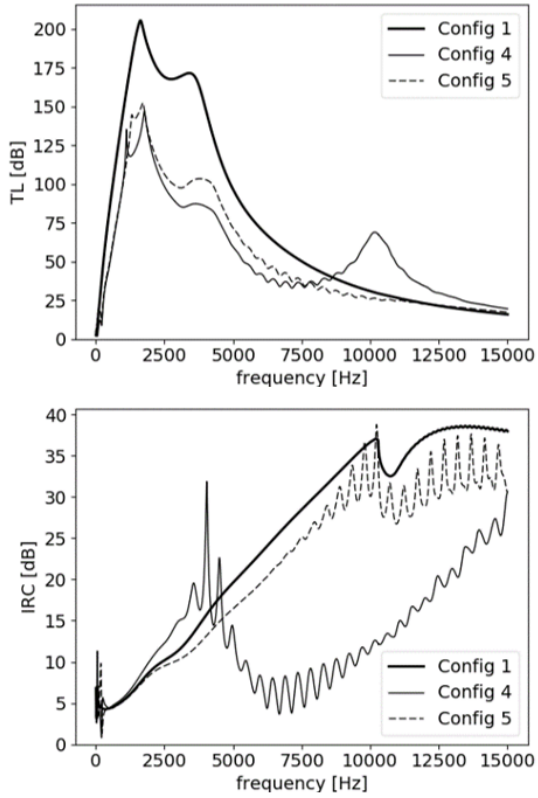

Figure 8: Evolution of the TL(left) and IRC(right) for different 3 sections silencers with varying perforated screen porosities. The different configurations are detailed in Table 1, the reference silencer with constant parameters all along is represented by the thick line.

Except for the case of varying flow resistivity, all the results present a minimum around 7 kHz for one of the tested configuration. The origin of this behavior will be further investigated, as it could lead to configurations with optimized IRC. However, this type of configuration does not seem to improve particularly the reflective properties as it was expected.

The last results concern the investigation of the high frequency acoustic performances. The results presented earlier are all done by computing only the power of the plane-wave mode, which is the only mode at low frequencies. However, the cut-off frequency of the first radial mode in a 4.03 cm diameter pipe is 10.3 kHz which means that this contribution has to be took in account for the evaluation of the acoustic performances. This has been done for the reference silencer of 1 m length and the results are presented on Fig. 9 and compare the results obtained by taking in account with the plane wave mode.

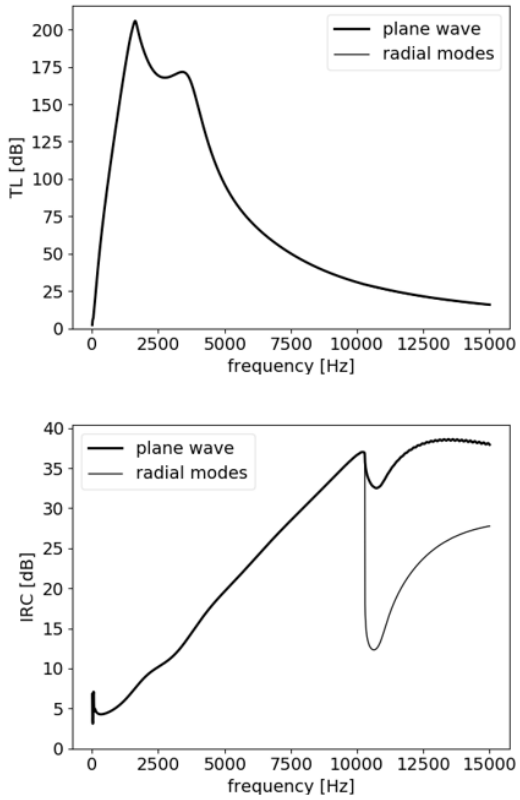

Figure 9: Comparison of the computed acoustic performances of the refeence silencer by taking in acount only the plane wave mode or the the plane wave and first radial modes.

The contribution of the first radial mode is negligible in what concerns the acoustic transmission performances. On the other side, the contribution of the first radial mode on the reflected sound is clear and even dominates the contribution of the plane wave mode. This seems to indicate that the transmissive performances can be evaluated by taking in account only the plane wave mode even at high frequencies, which is not the case for the reflective performances.

6. Conclusions

A test bench has been designed in order to study the fluid-structure interaction of an air leakage through a

valve. The test bench features all the equipment necessary to the generation and the control of the flow, acoustic and vibratory insulations and four different test sections in order to realize PIV, HW, wall pressure fluctuation and vibration measurements.

The acoustic silencers have to insure good reflective and absorptive performances over a wide frequency range to insure the repeatability of the acoustic measurements. An analytical model based on modal matching has been implemented and numerical simulations will be done to validate the results. Experimental multi-ports method will be used in order to determine the real acoustic performances of the silencers that will be realized.

Acknowledgments

I owe sincere gratitude to Professor Christophe Schram with whom most of my work has been conducted. Many thanks also goes to Nicolas Van de Wier, Julien Christophe and all the Acoustics department of the VKI for all the good moments and their precious help. I would also like to thank all colleagues at the Chpolansky S.A.S. for the nice atmosphere contribution. Finally, I am in debt to my family and to all my friends for their support.

References

[1] M. A. Sharif, R. I. Grosvenor, Internal valve leakage detection using an acoustic emission measurement system, Transactions of the Institute of Measurement and Control 20 (5) (1998) 233–242.

[2] J. Yan, Y. Heng-hu, Y. Hong, Z. Feng, L. Zhen, W. Ping, Y. Yan, Nondestructive detection of valves using acoustic emission technique, Advances in Materials Science and Engineering 2015.

[3] G. Geiger, D. Vogt, R. Tetzner, State-of-the-art in leak detection and localization, Oil Gas European Magazine 32 (4) (2006) 193.

[4] P.-S. Murvay, I. Silea, A survey on gas leak detection and localization techniques, Journal of Loss Prevention in the Process Industries 25 (6) (2012) 966–973.

[5] G. Thompson, G. Zolkiewski, An experimental investigation into the detection of internal leakage of gases through valves by vibration analysis, Proceedings of the Institution of Mechanical Engineers, Part E: Journal of Process Mechanical Engineering 211 (3) (1997) 195–207.

[6] W. Kaewwaewnoi, A. Prateepasen, P. Kaewtrakulpong, Measurement of valve leakage rate using acoustic emission, in: Proceedings of the International Conference on Electrical Engineering/Electronics, Computer, Telecommunications, and Information Technology (ECTI05), 2005, pp. 597–600.

[7] J. Dickey, J. Dimmick, P. Moore, Acoustic measurement of valve leakage rates, Materials Evaluation 36 (1) (1978) 67–77.

[8] C. Pezerat, Méthode d'identification des efforts appliqués sur une structure vibrante, par résolution et régularisation du problème inverse, Ph.D. thesis, INSA de Lyon (1996).

[9] D. Lecoq, Identification par problème inverse vibratoire des bas nombres d'onde de pressions pariétales turbulentes., Ph.D. thesis, LAUM-Le Mans (72) (2013).

[10] T. Nakamura, M. Terada, Development of leak monitoring system for pressurizer valves, Progress in Nuclear Energy 15 (1985) 175–179.

[11] J. Lee, M. Lee, J. T. Kim, J. S. Kim, V. Luk, Condition monitoring of a check valve for nuclear power plants by means of acoustic emission technique, in: Proceedings of the 17th International Conference on Structural Mechanics in Reactor Technology, 2003.

[12] A. Prateepasen, W. Kaewwaewnoi, P. Kaewtrakulpong, Smart portable noninvasive instrument for detection of internal air leakage of a valve using acoustic emission signals, Measurement 44 (2) (2011) 378–384.

[13] M. J. Lighthill, On sound generated aerodynamically i. general theory, in: Proc. R. Soc. Lond. A, Vol. 211, The Royal Society, 1952, pp. 564–587.

[14] W. Kaewwaewnoi, A. Prateepasen, P. Kaewtrakulpong, Investigation of the relationship between internal fluid leakage through a valve and the acoustic emission generated from the leakage, Measurement 43 (2) (2010) 274–282.

[15] E. Meland, N. Thornhill, E. Lunde, M. Rasmussen, Quantification of valve leakage rates, AIChE Journal 58 (4) (2012) 1181–1193.

[16] C. Durant, G. Robert, P. Filippi, P.-O. Mattei, Vibroacoustic response of a thin cylindrical shell excited by a turbulent internal flow: comparison between numerical prediction and experimentation, Journal of sound and vibration 229 (5) (2000) 1115–1155.

[17] E. M. Frymoyer, Vibration and wave propagation in cylindrical shells., Tech. rep., PENNSYLVANIA STATE UNIV UNIVERSITY PARK ORDNANCE RESEARCH LAB (1967).

[18] J. L. Walter, Coincidence of higher-order modes-a mechanism of the excitation of cylindrical shell vibrations via internal sound.

[19] J. Lavrentjev, M. Åbom, Characterization of fluid machines as acoustic multi-port sources, Journal of Sound and Vibration 197 (1) (1996) 1–16.

[20] S. Sack, M. Åbom, C. F. Schram, K. Kucukcoskun, Generation and scattering of acoustic modes in ducts with flow, in: 20th AIAA/CEAS aeroacoustics conference, 2014, p. 3115.

[21] S. Baxter, C. Morfey, Modal power distribution in ducts at high frequencies, AIAA Journal 21 (1) (1983) 74–80.

[22] C. Morfey, S. Baxter, Experimental investigation of modal power distribution in a duct at high frequency, AIAA journal 23 (2) (1985) 172–176.

[23] I. Idel'Cik, Memento des pertes de charge, Collection de la Direction des Etudes et Recherches d'Electricite de France, Paris: Eyrolles, 1969.

[24] A. Selamet, M. Xu, I.-J. Lee, N. Huff, Analytical approach for sound attenuation in perforated dissipative silencers, The Journal of the Acoustical Society of America 115 (5) (2004) 2091–2099.

[25] F. Denia, A. Selamet, F. Fuenmayor, R. Kirby, Acoustic attenuation performance of perforated dissipative mufflers with empty inlet/outlet extensions, Journal of Sound and Vibration 302 (4-5) (2007) 1000–1017.

Towards quieter fans: Investigation of installation effects and noise mitigation strategies

Dominique Joachim

Aeronautics and Aerospace Department, von Karman Institute for Fluid Dynamics, Belgium, joachim.dominique@vki.ac.be

Supervisor: Schram Christophe

Associate Professor, Aeronautics and Aerospace Department, von Karman Institute for Fluid Dynamics, Belgium, christophe.schram@vki.ac.be

Abstract

. The reduction of the noise generated by industrial fans that is imposed by ever increasing regulations requires an improved understanding of aeroacoustic mechanisms, in particular of the interactions taking place between the components of HVAC systems or household appliances. Indeed, while the noise produced by an isolated blower is usually characterized under ideal inflow conditions with uniform inlet profile and low turbulence intensity, such conditions are in practice rarely met in the full system, due to product compactness and integration constraints. This leads to extraneous noise generation that can compromise the acoustic performance of the equipment, and thereby increase its development time and cost. The influence of non-ideal installation on fan acoustic performance is called the installation effects and constitutes the purpose of the research presented below.

. This project aims at investigating qualitatively and quantitatively the complex relationships between the quality of the flow ingested by a low-speed air-moving and its noise production, in order to elaborate better design guidelines and devise innovative noise mitigation strategies. This will be achieved by combining advanced experimental diagnostics, numerical simulations and theoretical models.

. On the experimental side, extensive campaigns coupling multi-port acoustic measurements with aerodynamic hot-wire measurements will be conducted. By using the multi-ports methodology, it is possible to remove the scattering effects due to the reflection of noise generated by the blower on the duct terminations that would contaminate the microphones measurements otherwise. This technique, implementing arrays of loudspeakers and microphones, is used to discriminate between aerodynamic and acoustic effects and therefore allows to investigate the aerodynamic installation effects alone.

. To correlate the experimental flow measurements with the specific sound power production of the fan, two different approaches will be followed. The first one relies on evolutionary computation based on gene expression programming permitting to identify from a purely mathematical viewpoint the main influential flow parameters responsible for the installation effects. The knowledge thereby created should pave the way towards new optimization possibilities, by relating flow features and noise emissions without having to rely on a resolution of the equations of fluid mechanics. The second approach is physics-based, and relies upon simplified semi-analytical models (e.g. linearized airfoil theory) in order to gain a physical understanding of the critical parameters. Crucially, it will also permit to validate assumptions made on the predominance of presumed sound generation mechanisms. It is expected that a novel understanding of installation effects should emerge from the comparison of the outcomes of both approaches.

. The knowledge gained in this project will be used to: i) propose guidelines about the integration of multiple components in a system, and ii) suggest the most promising noise mitigation strategies, based on flow and/or acoustic control.

Investigation of turbulence-surface interaction noise mechanisms and their reduction using porous materials

Riccardo Zamponi

Environmental and Applied Fluid Dynamics Department, von Karman Institute for Fluid Dynamics, Belgium, riccardo.zamponi@vki.ac.be

Supervisor: Christophe Schram

Associate Professor, Aeronautics and Aerospace Department / Environmental and Applied Fluid Dynamics Department, von Karman Institute for Fluid Dynamics, Belgium, christophe.schram@vki.ac.be

Advisor: Nicolas Van de Wyer

Research Engineer, Environmental and Applied Fluid Dynamics Department, von Karman Institute for Fluid Dynamics, Belgium, vandewye@vki.ac.be

University Supervisor: Fulvio Scarano

Full Professor, Aerospace Engineering, TU Delft, Netherlands, F.Scarano@tudelft.nl

Abstract

The investigation of the noise generation mechanisms involved in the interaction of an airfoil with incoming turbulence represents a core topic for a great variety of application fields. These include airframe noise, aeronautical propulsion devices, wind turbines and HVAC systems for automotive and construction. From the physical point of view, part of the noise generated in this way radiates to the far field as a consequence of the rapid changes of the inertia of vortical patterns due to the presence of the airfoil. This phenomenon is maximum in the vicinity of a singular point of its surface, such as a corner or an edge. The sharper the edge, the louder the sound. This is the essence of turbulence impingement noise. For the applications above mentioned, the turbulence itself is not an intrinsic feature of the airfoil and must be often considered as un unavoidable effect of the installation. Therefore, acting directly on the airfoils to make them less sensitive to it in terms of acoustic response can be a promising strategy.

The objectives of the PhD are to improve the understanding of the phenomenon of turbulence-impingement noise and to evaluate the effectiveness of the use of porous materials as noise mitigation technique for these kinds of application. Concerning the first one, the study of the distortion that is experienced by turbulence in the immediate vicinity of the airfoil surface is instrumental for the modeling of the problem. In this regard, Rapid Distortion Theory (RDT) provides a turbulence energy spectra model for the prediction of the noise generated that is in accordance with experimental data. For the second objective, the implementation of porous material as part of the structure of the airfoil represents a novel technique able to reduce the variation of the inertia of the vortical patterns through viscous effects within the pores. Despite several studies have been conducted on the topic, it is still necessary to develop more comprehensive models for the influence of the porous material parameters.

These two aspects will be investigated experimentally. In this framework, a rod-airfoil configuration mounted in the anechoic chamber of VKI will be considered. The flow around the airfoil will be characterized by means of advanced flow diagnostics, such as Particle Image Velocimetry (PIV), hot-wire anemometry and wall pressure fluctuations and the aeroacoustic sources generated on the surface of the airfoil will be localized and quantified with acoustic beamforming techniques. Particularly, an improved version of the Generalized Inverse Beamforming (GIBF) has been developed and implemented at VKI. This code has been successfully validated by processing an experimental benchmark dataset corresponding to a small-scale open-jet facility for the characterization of the self-noise of an airfoil immersed in the flow. In order to perform a comparison with a standard airfoil, a porous NACA 0024 has been designed and manufactured. It consists of three different layers: a hard-plastic case with a porosity of 80% has the function to contain melamine foam and to ensure the profile shape, while a metallic cloth is aimed at covering the airfoil and granting a proper surface roughness. A solid centerplane is placed to prevent an unwanted air flow between suction and pressure surface. Before proceeding with the measurements, the porous model will be characterized in order to determine the physical parameters of the material.

SmartAnswer - Flow and acoustic control of low-speed cooling fans

PhD Candidate: Alessandro Zarri

Environmental and Applied Fluid Dynamics Department, von Karman Institute for Fluid Dynamics, Belgium, alessandro.zarri@vki.ac.be

Advisor: Julien Christophe

Research Engineer, Environmental and Applied Fluid Dynamics Department, von Karman Institute for Fluid Dynamics, Belgium, julien.christophe@vki.ac.be

Supervisor: Christophe Schram

Professor, Environmental and Applied Fluid Dynamics Department, von Karman Institute for Fluid Dynamics, Belgium, christophe.schram@vki.ac.be

University Supervisor: Michel Roger

Professor, Fluid Mechanics and Acoustic Laboratory, École Centrale de Lyon, France, michel.roger@ec-lyon.fr

Abstract

The noise pollution is nowadays considered as a relevant issue, not only from the private companies, but also because of the strict rules imposed by the International European Community. The SmartAnswer consortium has been thought to deal with unwanted noise generated in several application fields, such as the aeronautic, automotive, wind turbine and HVAC sectors. Within this framework, the automotive low-speed cooling fans represent a key problem about the overall emitted noise for both passengers and pedestrians. In particular, concerning electrical cars, the customers will have to likely recharge them at night in their garages. Since the engine needs to be cooled down during this phase too, it is appropriate that the fans work quietly. Different acoustical sources are involved on the fan itself, such as the leading edge, trailing edge and tip clearance noise, or are due to either non-uniformity of the upstream flow or to interactions between the rotor wake and the downstream support struts. The corresponding emitted sound has then both tonal and broadband components. The purpose of this PhD program is to mitigate the radiated noise acting directly on the acoustical sources or by employing acoustic absorption techniques to alterate their propagation. About the last ones, investigations at the VKI have been carried out exploiting micro perforated anisotropic metallic sheets as liners. They showed to be a promising technology to solve this task. If one wants to directly mitigate the acoustic sources though, trailing and leading edge serrations for example, have been studied at the École Centrale de Lyon and might be applied to this problem as well.

Nevertheless, before choosing which material and technology is more suitable, an experimental campaign will be carried out in the VKI anechoic chamber ALCOVES in order to isolate, localize and generally, better understand the acoustic sources on a real cooling unit. This mock-up, composed by the fan, the shroud and the heat exchanger, will be furnished by the French company Valeo. From the experimentally identified source mechanisms, a numerical analysis will be carried out in parallel. As an initial step, the turbulent flow coming from the heat exchanger and impinging on the fan blades, as well as the flow surrounding the fan blades will be modelled through a CFD simulation technique. This flow simulation of the fan will provide the necessary inputs to the VKI in-house developed code BATMAN, based on Amiets theory, which is able to calculate the sound pressure levels emitted by the model in the far-field. The developed methodology will be validated with experimental measurements. The proposed method is based on a fast prediction techniques employing RANS simulations which are less expensive in terms of time and computational cost. If necessary, detailed and more accurate flow simulations as LES may be used to complement and support the development of the computational tool. The fast prediction developed method will allow testing several fan configurations with a fast turn-over and possibly apply optimization techniques such as genetic algorithms and artificial neural networks. This will be exploited to develop a tool capable of taking into account several parameters, like the new materials addition or the geometrical modifications, to compare the aerodynamic and acoustic performances for different fan configurations.

AERO-THERMAL INVESTIGATIONS IN TURBOMACHINERY

On the Dynamic Response of Constant Temperature Hot Wire Anemometers (CTHWA)

Elissavet Boufidi

Turbomachinery and Propulsion Department, von Karman Institute for Fluid Dynamics, Belgium, boufidi@vki.ac.be

Supervisor: Fabrizio Fontaneto

Assistant Professor, Turbomachinery and Propulsion Department, von Karman Institute for Fluid Dynamics, Belgium, fontaneto@vki.ac.be

University Supervisor: Tony Arts

Professor, Head of Department, Turbomachinery and Propulsion Department, von Karman Institute for Fluid Dynamics, Belgium
iMMC, Université Catholique de Louvain, Belgium, arts@vki.ac.be

Abstract

The dynamic reponse of Constant Temperature Hot Wire Anemometers is investigated using a numerical model and experimental square wave tests' results. The focus is placed on heat conduction effects, non-linear effects in the presence of large fluctuations and differences between the response to velocity fluctuations and electronic testing.

Keywords: hot wire anemometry, dynamic response, turbulence measurement

1. Introduction

A rigorous characterization of flow turbulence (i.e. turbulence intensity, time and length scales, spectrum) is needed to better understand loss mechanisms and heat transfer phenomena in complex turbomachinery flows. Moreover, the increasing use of CFD, as both a design and an investigation tool, requires reliable experimental data for validation of turbulence models and input of boundary conditions (which normally include turbulence kinetic energy and length scales at the inlet of the computational domain). It is therefore evident, that the reliable measurement of turbulence parameters is critical for the reliable and cost-effective design of turbomachinery components.

The experimental characterization of turbulence requires demanding measurements with high temporal and spatial resolution. This requirement is even more important at high speed flows where higher frequencies are typically present. Constant Temperature Hot-Wire Anemometry (CTHWA) is one of the most popular techniques for measuring velocity fluctuations and, therefore, turbulence quantities, thanks to its high frequency response (up to 50 kHz) and high spatial resolution (wire diameters up to 5 μm) [1]. A CTHWA is composed of a hot wire probe and an electronic control unit, which consists of a Wheatstone bridge (the hot wire is part of the active leg of the bridge) and a feedback loop which adjusts the current in order to keep the temperature of the wire constant. The dynamic response of the system is, therefore, defined by the properties of the wire and the electronics.

The most popular method to test the frequency response of a CTHWA is the "square-wave" test. It consists in injecting a pulsating current in the circuit and monitoring the output voltage response in an oscilloscope. The system is then tuned in order to obtain an optimal response, resembling to a second order system. A square wave testing unit is implemented in most commercial anemometers. According to Freymuth [2], the cut-off frequency of the system f_c, defined as the frequency at which the amplitude is attenuated by -3 dB, can be determined as:

$$f_c = \frac{1}{1.3 t_w} \tag{1}$$

where t_w is defined as the time when the amplitude is decreased at 3% of the peak value. This criterion

is valid for a system optimized in order to achieve the highest cut-off frequency with maximally flat frequency response. It is suggested that the tuning of the system is performed for the highest velocity expected in the measurements, since operation at higher velocities can lead to instabilities and self-oscillations.

Despite being easy to perform, the square wave test is not a very reliable way to determine the dynamic response. Optimal adjustment is not easy to achieve by monitoring the time response, thus Eq. (1) should be used only as an approximation of the cut-off frequency. Moreover, assuming a flat response up to the cut-off frequency can lead to over- or underestimation of the turbulent energy. As the dynamic response of the CTHWA depends on the flow conditions, it is clear that Eq. (1) is valid only for the velocity at which the tuning was performed. In order to overcome these problems, Weiss et al. [3] proposed to compute the complete transfer function of the system by the Fourier transform of the time response to the square wave voltage. The transfer function was used in the post-processing to correct the amplitude of the turbulent spectra.

In theory, the dynamic response of a CTHWA should be directly tested by imposing a known flow disturbance on the wire. In practice, it is difficult to create a velocity fluctuation of adequately high known frequency and amplitude and this led to the popularity of the square wave test. Nevertheless, there is disagreement in the literature on whether the square wave test is really equivalent to the imposition of a velocity perturbation on the wire. The equivalence of electronic testing to direct experimental testing is supported by theoretical investigations, like the work of Freymuth [4], who was the first to propose it, and Weiss et al. [3] who reconfirmed Freymuth's result. The few attempts to validate the square wave test by direct testing with flow perturbations produced contradicting results. Khoo et al. [5] compared voltage-perturbation testing to velocity-perturbation testing using a chopped rotating disc and reported a cut-off frequency of almost one order of magnitude lower for the latter, suggesting that the square wave test leads to significant overestimation of the cut-off frequency. Hutchins et al. [6] proposed a direct method to test the temporal resolution of CTHWA using the capabilities of the Princeton Superpipe to produce pipe flows with the same Reynolds number and turbulent energy in different frequency ranges. Assuming Reynolds similarity and scaling the spectra, they attributed differences at the high frequency range to limited frequency response. They concluded that the square wave test correctly estimated the dynamic behaviour for the two of the three anemometers tested. Li [7] conducted a numerical investigation of the response of a CTHWA under different types of perturbations. More specifically, he compared the response to a velocity impulse to the response when step voltage perturbations are introduced at the wheatstone bridge and at the offset voltage of the amplifier. The point of the voltage perturbations' injection seems to affect the response, with the response to offset voltage perturbations being closer to the one obtained by a velocity impulse.

The present work attempts to contribute to the investigation of this issue by using the experimental results of square wave tests applied to different hot wires combined with a numerical analysis. The non-linear model proposed by Freymuth [2] and used by Weiss et al. [8] is employed, in order to examine the effects of non-linearity at flows with high-frequency, large-amplitude fluctuations. Freymuth [2] developed the non-linear theory for CTHWA and demonstrated that for a well tuned system and small fluctuations their behaviour can be sufficiently described by a third-order linear equation. Thereafter, most investigations have focused on the linear theory and most experimental investigations neglect non-linear effects even for large fluctuations (see for example [9]). Freymuth [10] demonstrated that non-linear effects become important when the amplitude or the frequency of the fluctuations increase. Fluctuations as large as 50% of the mean velocity fall in the linear regime when their frequency is lower than 10% of the cut-off frequency of the anemometer. The non-linearity has a small effect on the intensity of the fluctuation but affects significantly odd moments like the skewness. Weiss et al. [8] verified Freymuth's [10] analytical results by solving numerically the system of non-linear equations and comparing with experimental results by electronic testing for three different anemometers. This non-linear behaviour has been investigated for Constanst Current Anemometry (CCA) by Comte-Bellot & Schon [11] and for Constant Voltage Anemometry (CVA) by Berson et al. [12]. Berson et al. [12] applied a post-processing algorithm to correct for non-linearities by inversely solving the differential equations characterizing the CVA's response. No similar method is available for CCA or CTA in the author's knowledge.

The model of Freymuth [2] and Weiss et al. [8] is modified to include the heat conduction from the wire to the prongs, which leads to a non-uniform temperature distribution along the wire. This allows to also investigate the attenuation of fluctuations due to

thermal transient effects. This attenuation occurs at frequencies lower than the cut-off frequency of the system, since the time constant of thermal effects is longer compared to the time constant of the system. This means that even for an optimally adjusted anemometer, the response is not flat up to the cut-off frequency. Freymuth [13], Morris & Foss [14] and Li [15], among others, have investigated this phenomenon. The attenuation starts at a frequency f_1, which according to Freymuth [13] can be estimated as:

$$f_1 = \frac{40 D_w}{2\pi l^2} \tag{2}$$

where D_w is the thermal diffusivity of the wire material and l is the wire length. As the frequency increases, the attenuation reaches a plateau. The value of the final attenuation factor is a function of the Biot number of the wire, which can be estimated by [13]:

$$Bi = \frac{l}{d}\left(\frac{k_f}{k_w} Nu\right)^{1/2} \tag{3}$$

The Biot number is a function of the wire aspect ratio l/d, the Nusselt number and the ratio of the thermal conductivities of fluid and wire.

The conduction losses to the wire supports, and consequently the attenuation, clearly decrease for wire materials of low conductivity, for high Nusselt numbers and for large length-to-diameter ratios. It should be noted, however, that large wire lengths decrease the spatial resolution of hot-wires, since fluctuations smaller than the wire are averaged over the wire length, a phenomenon called spatial filtering. Therefore, while it would be convenient to increase the wire length in order to achieve large l/d ratios without decreasing the diameter (and thus making the wire more fragile), this comes at the expense of spatial resolution. In their well-known study, Ligrani & Bradshaw [16] suggested that for accurate measurements of turbulence in the viscous sublayer of a turbulent boundary layer, the length should be 20 times larger than the viscous length scale and the length-to-diameter ratio larger than 200. While the criterion of $l/d > 200$ has since been often used as a rule of thumb to avoid conduction effects, the limit value should depend on the flow conditions and the wire material, as expressed by Eq. (3). In this context, Hultmark et al. [17] proposed a new criterion for negligible attenuation due to heat conduction which takes into account the aforementioned parameters.

Considering the above,it is clear that the optimal design for a hot wire probe, in terms of temporal and spatial resolution, depends on the flow conditions expected. Therefore, in the present work the effect of some design parameters will be investigated as well.

2. Model and methodology

2.1. Equations of the dynamic response model

A CTHWA system is composed by a hot-wire probe and an electronic unit. A schematic of a simplified circuit is presented in Figure 1. The hot wire probe is connected at the bottom left leg of the wheatstone bridge, with R_w the resistance of the wire and r_L the resistance of the prongs, stem and cable. The resistance R_{dec} is adjustable and it is used to set the desired overheat ratio. The resistance R_w is maintained constant by the feedback amplifier, which adjusts the current to compensate for resistance fluctuations.

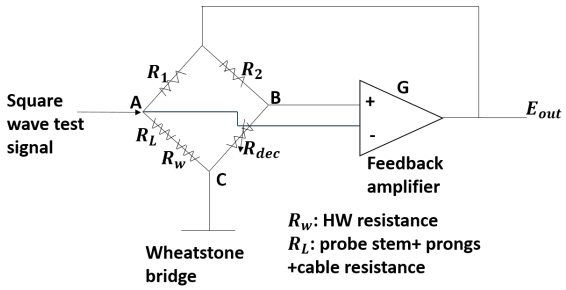

Figure 1: Simplified circuit of a CTWHA

As mentioned before, the model of Freymuth [2] and Weiss et al. [8] is used to simulate the dynamic behaviour of a CTHWA system. Three equations are needed: an equation for the wheatstone bridge, one for the feedback amplifier and one for the wire.

The equation representing the behaviour of the wheatstone bridge is the following:

$$\delta = \frac{R_1(R^* - R_w)}{(R_1 + R^* + r_L)(R_1 + R_w + r_L)} E + M_B \frac{dE}{dt} + \frac{R_1(R_w + r_L)}{R_1 + R_w + r_L} \frac{E_t}{R_t} \tag{4}$$

where δ is the voltage difference at the bridge diagonal ($\delta = V_B - V_A$, see Fig. (1)), R^* is the value of the operating wire resistance for a balanced bridge (the set value), E is the bridge output voltage and M_B a time constant. The last term in Eq. (4) is present only in the case of electronic testing, when a square wave voltage perturbation is injected at point A of the bridge. E_t is the square wave voltage and R_t is the resistance placed

in series of the square wave voltage generator. During flow measurements this term is set to 0.

The equation simulating the behaviour of the amplifier is a second order linear equation:

$$M^{''}\frac{d^2E}{dt} + M^{'}\frac{dE}{dt} + E = G\delta + E_b \tag{5}$$

where $M^{''}$ and $M^{'}$ are the first and second order time constants of the amplifier and G is the gain. E_B is the offset voltage of the amplifier which can be adjusted to ensure a stable operation.

The wire equation has been modified to take into account the heat conduction losses and a non-dimensional calibration law for the convective heat transfer ($Nu = f(Re)$ instead of $E = f(U)$). The equation can be expressed as follows:

$$m_w c_w \frac{\vartheta T_w}{\vartheta t} = \frac{E^2 R_w}{(R_1 + r_L + Rw)^2} - Nu\pi l_w k_f (T_w - \eta T_0) - k_w A_c \frac{\vartheta^2 T_w}{\vartheta x^2} \tag{6}$$

The LHS expresses the heat accumulation in the wire, and at the RHS the first term expresses the Joule heating, the second term the convection losses, and the last term the conduction losses.

2.2. Numerical solution

When the conduction loss term is neglected, Eq. (4), (5) and (6) consist a system of ODEs, which can be solved with a numerical method, e.g. Runge-Kutta. In order to take into account thermal transient effects, the unsteady temperature distribution along the wire must be taken into account. But when the heat conduction is considered, Eq. (6) is a PDE. In order to solve the system, the methodology proposed by Morris & Foss [14] is followed, where the wire is discretized in $n-1$ elements along its length, as can be seen in Fig. 2. A node is placed at the center of its element and at the two edges of the wire.

By discretizing the second order spatial derivative with a central difference, the wire equation is written for each node as follows:

$$m_{w,i} c_w \frac{dT_{w,i}}{dt} = \frac{E^2 R_{w,i}}{(R_1 + r_L + R_{w,i})^2} - Nu\pi l_{w,i} k_f (T_{w,i} - \eta T_0) - k_{w,i} A_{c,i} \frac{T_{w,i+1} - 2T_{w,i} + T_{w,i-1}}{dx} \tag{7}$$

In this way, the PDE is transformed into an ODE for each node, so the system is now a system of n+2

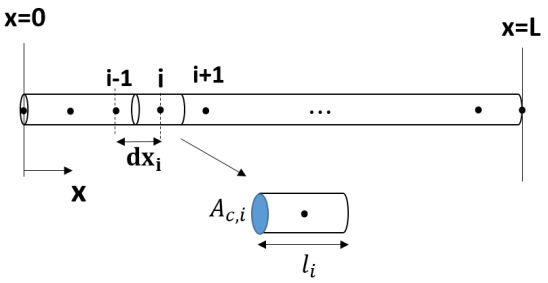

Figure 2: Wire discretization

ODEs (where n is the number of nodes) and it can be solved using the ode45 function of Matlab, which implements a Runge-Kutta method.

The wire temperature that the circuit "feels" at each time is the spatial average of the temperature along the wire length:

$$T_w = \frac{1}{L}\int_0^L T_w(x)dx \tag{8}$$

The wire resistance R_w corresponding to this temperature is the input at Eq. (4) and (5):

$$R_w = R_{ref}(1 + a_w(T_w - T_{ref}) \tag{9}$$

where a_w is the temperature coefficient of resistance of the wire material and R_{ref} the wire resistance at a reference temperature T_{ref}.

In Fig. (2) the case of an unplated wire is presented, but Eq. (7) can also be applied to plated wires. In this case, the conductivity of the plating material and the corresponding diameter should be considered for the nodes in the plated length.

The wire is discretized in 101 nodes, and a time step of $10^{-7}s$ is used. The boundary condition at the edge of the wire is $T_{w,0} = T_{w,L} = T_{flow}$, assuming that the prongs remain at the temperature of the flow. This assumption is based on the fact that the mass of the prongs is much larger compared to the mass of the wire.

2.3. Experimental method

The model is used in addition to experimental data obtained by a Dantec Streamline anemometer and a tungsten wire with 9 μm diameter and $1mm$ length, with an operating wire temperature of $455K$. The measurements were carried out at an open-jet facility. The nozzle is connected to the pressure supply through a heater, which is used to vary the flow temperature. The head of the HW probe was placed inside

the potential core of the jet. The total temperature and total pressure inside the nozzle are measured by means of a thermocouple and a validyne transducer.

The static calibration methodology proposed by Cukurel et al. [18] was followed in this study. This method consists in the use of an effective wire temperature and of empirical correlations to eliminate the dependency of the calibration on total temperature and Mach number of the flow respectively, which allows establishing a unique Nu-Re calibration curve. The procedure will not be described here, as more details can be found in [18]. The calibration curve obtained for this hot-wire is presented in Fig. 3.

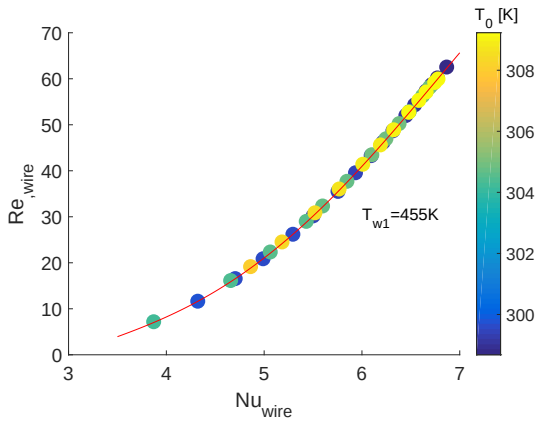

Figure 3: Calibration curve

With the wire in the core of the jet subject to a constant flow of $M = 0.25$, the square wave test is performed, using the function implemented in the anemometer. The output voltage is acquired for $1s$ with a sampling frequency of $1.25MHz$. The response to the square wave voltage is superimposed to the response to flow fluctuations, therefore phase averaging is performed to obtain a clean signal. In Fig. (4) the output voltage before and after phase averaging is presented.

In order to obtain the frequency response, the fourier transform of the time response is performed and then it is non-dimensionalized by its value at a low frequency, since the magnitude of the input signal is not known. The frequency used for non-dimensionalization should be low enough to be considered unaffected by the cut-off of the system but also by the attenuation due to heat conduction, so that the amplitude of the response is equal to 1. The frequency response computed by this method is presented in Fig. (5). The cut-off frequency, computed as the frequency where the amplitude has attenuated by $-3dB$, is shown

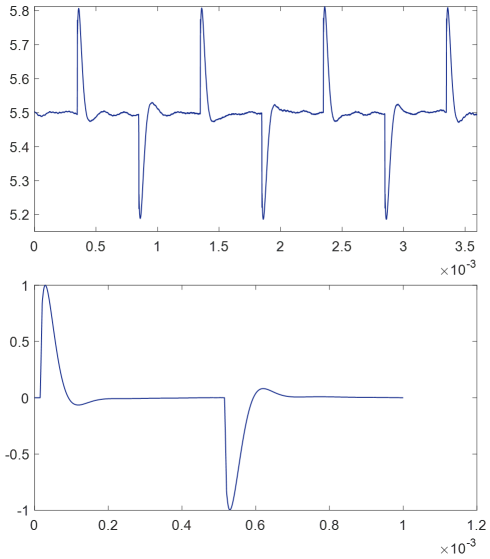

Figure 4: Experimental response to square wave voltage: Raw signal(upper) and phase-averaged signal (lower)

to be $9.6kHz$. Nevertheless, it can be seen that the amplitude is not completely flat up to the cut-off frequency. There is a small amplification which indicates that the system is slightly underdamped.

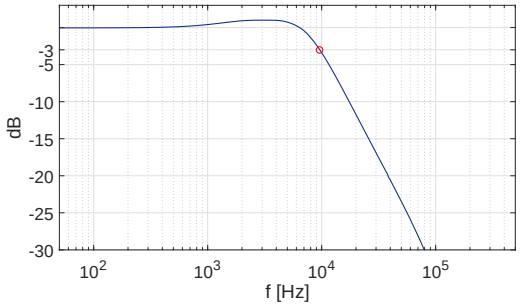

Figure 5: Experimental frequency response to square wave voltage

2.4. *Estimation of the model parameters*

The model parameters should be adjusted in order to represent correctly the electronic circuit and the hot wire used. Since a commercial anemometer system is used in this study, some parameters from Eq. (4) and (5) are not known and should be estimated. The resistances R_1 and R_2 of the bridge are known, the resistances R_w and r_L depend on the hot wire probe used and the resistance R_{dec} is adjusted accordingly, to fix the desired overheat ratio. The unknown parameters are therefore M_B, E_b, G, $M^{''}$ and $M^{'}$.

Weiss et al.[8] encountered the same problem and proposed to compute these parameters assuming an optimally adjusted anemometer and specifying the cut-off frequency of the system using the experimental result. This methodology will not be followed here for two reasons: firstly, as can be seen in Section 3, the response obtained from the experimental square wave test is not optimal but slightly underdamped. Moreover, the methodology of Weiss et al. [8] assumes a constant amplifier gain G and adjusts the parameters M_B, E_b. On the other hand, the Streamline system allows three modifications during the square wave test: the gain and filter of the feedback amplifier and the compensation for the cable inductance. The gain of the amplifier is therefore adjustable, and the filter setting f_{limit} is used to set the amplifier bandwidth limit. The compensation for the cable inductance is achieved by varying a set of capacitors or by varying the inductance of a set of coils placed in the bottom right leg of the bridge. No adjustment is available for the bridge voltage E_b.

The time constant M_B is used to take into account the high frequency effects of reactive elements in the bridge. According to Freymuth [2], if the cable inductance λ_c and an inductance λ_L in series with the resistance R_{dec} are considered, M_B can be computed as:

$$M_B = \frac{\lambda_L/R_2 - \lambda_c/R_1}{(n+1)^2} \tag{10}$$

where n is the bridge ratio. Since the compensation is not perfect, a finite small value is selected, $M_B = 10^{-10}$. Since the same cable is assumed for all simulations, the value of M_B will be kept constant.

The offset value voltage E_b is assumed to be constant as well, as no adjustment is provided by the anemometer. As the parameter E_b increases the damping of the system, Perry & Morrison [19], suggested that when its adjustment is not available, a high value should be used to ensure the stability of the system at different conditions. Therefore, a constant value of $E_b = 5V$ is used.

Finally, since the parameters G, M'' and M' can not be known, they are adjusted in order to better match the response to the experimental square wave test.

3. Results

3.1. Comparison with experimental data

In this section, the model is used to simulate the experimental case presented in section 2.3, with a square wave voltage $E_t(t)$ as forcing function. The Nu number value in Eq. (6) is computed by the $Nu - Re$ calibration, as explained in section 2.3. The circuit parameters used are the following:

- $M_B = 10^{-10}$;
- $E_b = 5V$;
- $G = 230$;
- $M' = 1.6 \cdot 10^{-5}$
- $M' = 10^{-11}$

In Figure 6 the comparison of the model with the experimental response is presented. It can be seen that while the model predicts correctly the cut-off frequency at $9.6kHz$ and features as well a small amplification, its overall response is different. The most prominent difference is the attenuation slope at high frequencies. The experimental signal features a less steep slope. It has to be noted that the same behavior has been noticed by Weiss et al. [8]: from the three anemometers that they tested, the Streamline featured the highest divergence from the model. This indicates that more research should be done to address this issue. Nevertheless, even if the model can not be used at the moment to accurately predict the dynamic behaviour of the CTHWA in question, it can still be used to investigate the phenomena of interest, as will be demonstrated in the following sections.

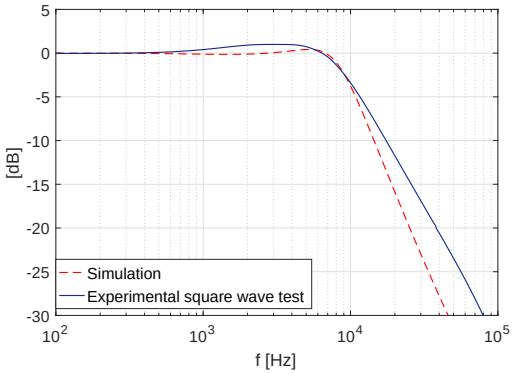

Figure 6: Frequency response to square wave test: comparison between experiment and model

3.2. Square wave test vs velocity perturbations

While the square wave test is the most popular method to test the dynamic response of a CTHWA, there is disagreement in literature on whether it is

equivalent to the imposition of a flow perturbation, which is the case during measurements. To test the response to a flow perturbation, the last term in Eq. 4 is set to 0 and $Nu(t)$ in Eq. 6 is the forcing function. More specifically, an impulse perturbation of 10% the mean Reynolds value is imposed, and using the calibration law Nu is computed as $Nu(t) = f(Re(t))$.

The comparison between the response to the impulse in Reynolds and the square wave test is given in Figure 7 for the frequency domain and in Figure 8 for the time domain. The frequency response matches well for the two cases, with differences appearing at a frequency significantly higher than the cut-off. In the time domain, we can see that the response to the square-wave does not decay to 0 but instead stabilizes in a slightly higher value. This is typical behaviour for the square wave test, as mentioned also by Li [7], who notes that oscilloscopes with ac coupling that remove the dc voltage are usually used to monitor the square wave test response.

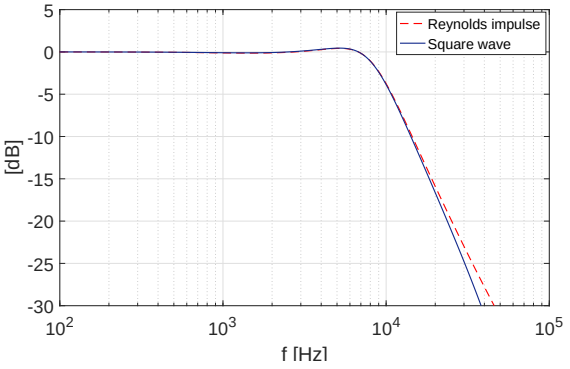

Figure 7: Frequency response to square wave test and to Reynolds perturbation

The results demonstrate that the square wave test simulates considerably well the response to a flow perturbation and the inverse transfer function could be used to correct the amplitude of turbulence spectra (as e.g. in Weiss et al. [3]), since differences occur for frequencies higher than the cut-off. These results do not agree with the results of Li [7], who observed bigger differences, especially when the square wave was injected in the bridge diagonal. He thus suggested to inject the square wave voltage at the offset of the last stage amplifier. In our case, the square wave generator used is implemented in the commercial anemometer unit and injects the voltage at the bridge diagonal. Therefore, this was the only case simulated.

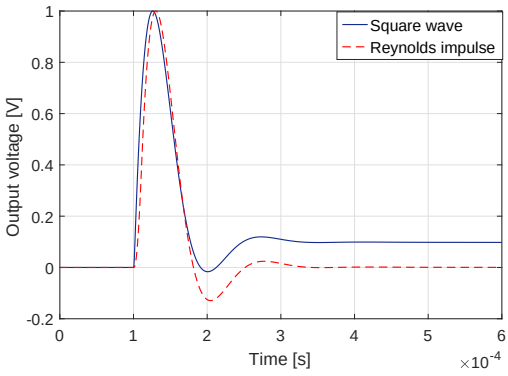

Figure 8: Time response to square wave test and to Reynolds perturbation

3.3. *Heat conduction effects*

Heat conduction to the wire prongs results in a non-uniform temperature distribution along the wire and to amplitude attenuation. The mean wire temperature profile for the case presented in the previous sections, when the wire is exposed to a uniform flow of $M = 0.25$, is presented in Figure 9. The resulting spatially averaged wire temperature is $T_w = 450K$, which is 5 degrees lower than the wire temperature obtained by the experimental static calibration at section 2.3. This is considered an indication that the assumption taken for the prongs' temperature may not be valid and should be further investigated.

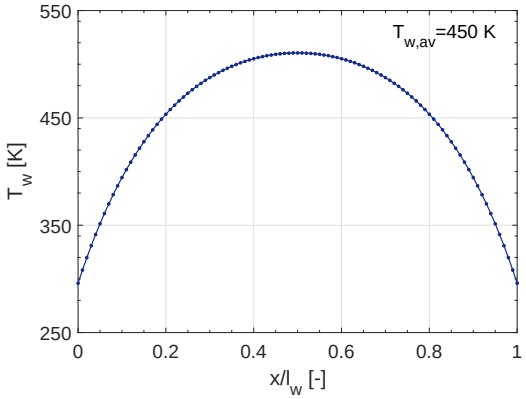

Figure 9: Wire temperature profile

The wire aspect ratio in this case is $l/d = 111$, so lower than 200 which is assumed to be the limit value for negligible attenuation by some researchers (see section 1). Indeed, if we zoom in the low frequency part of Figure 7 (presented at Figure 10), we

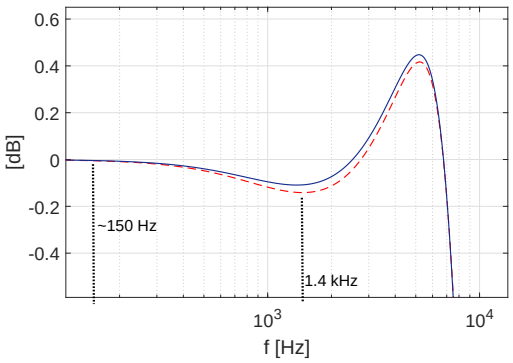

Figure 10: Amplitude attenuation due to heat conduction

can see that amplitude attenuation starts at a frequency of $f_l = 150Hz$ and extends up to a frequency of at least $1.4kHz$. This attenuation is present at both plots. The attenuation seems to be slightly stronger for the square wave test, but this difference can be considered negligible, therefore the square wave test could be used with an acceptable accuracy to estimate the attenuation effect. Li [7] arrived to the same conclusion.

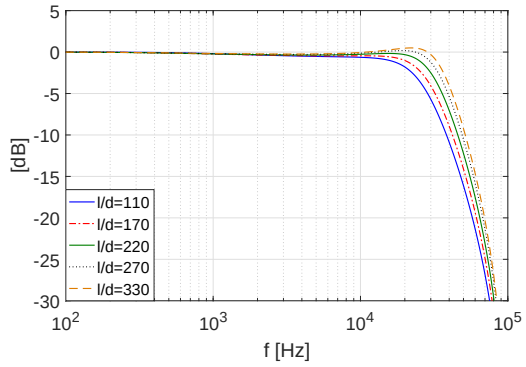

Figure 11: Length to diameter ratio's effect on the amplitude transfer function

For frequencies higher than $1.4kHz$, the amplification due to the system's dynamics does not allow to observe when the attenuation would reach the plateau. In order to focus on this phenomenon, the model's amplifier parameters are adjusted in order to move the system's cut-off to higher frequencies:

- $G = 1000$;
- $M^{'} = 5 \cdot 10^{-5}$
- $M^{'} = 10^{-12}$

and the wire's length is varied in order to examine the length to diameter ratio's effect. The results are presented in Figure 11, where it can be seen that the cut-off has moved to much higher frequencies with the new parameters. The effect of l/d on the wire temperature profile is presented in Figure 12. It can be seen that the profile becomes flatter with increasing l/d values, which is due to the fact that the convection effect becomes more important than the conduction effect.

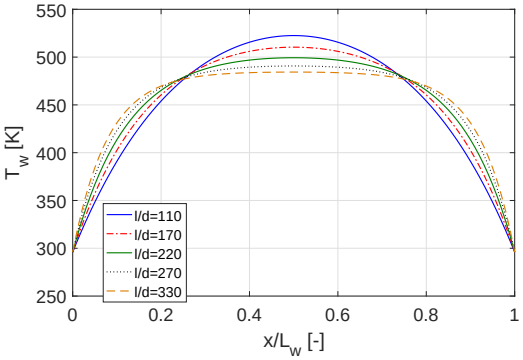

Figure 12: Length to diameter ratio's effect on wire temperature profile

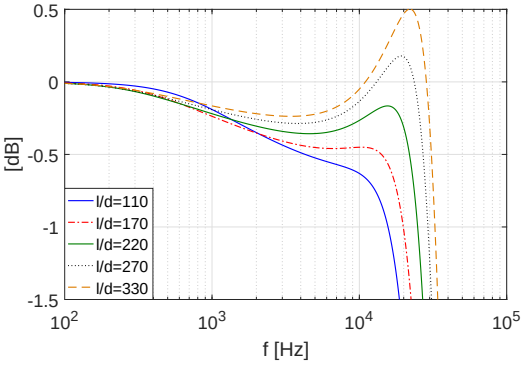

Figure 13: Length to diameter ratio's effect on the amplitude attenuation due to heat conduction

Focusing on the low-frequency part of the amplitude spectrum, given in Figure 13, it can be seen that the l/d has a strong effect on the attenuation. There is also an effect on the system dynamics: with increasing l/d (increasing l in this case) the convection term, which is the forcing function, gets a higher value and the system becomes underdamped. Nevertheless, this effect is present at high frequencies and should not affect the attenuation. As expected, the final attenuation value decreases with increasing l/d values. Thus, high

l/d ratios should be used in order to minimize this error. This can be achieved either by increasing the wire length at the expense of spatial resolution, or by decreasing the diameter compromising the mechanical strength. The optimal design should be decided depending on the requirements of each application. Finally, it can be observed by Figure 13 that the attenuation is present for a wide range of l/d, even for the highest value of 330. This indicates the importance of applying a correction.

3.4. Non-linearity

The non-linear behaviour of CTHWAs can be neglected under the small-fluctuations assumption, but it should be taken into account for large fluctuations at high frequency. This behaviour is investigated here by giving a synthetic Reynolds number signal as input to the model and attempting to reconstruct the signal by applying the static calibration law to the output voltage. The input signal is a sinusoid, as presented in Figure 14, whose period and amplitude are varied. Three different amplitudes are tested, corresponding to input turbulence intensity levels of 3.8%, 7% and 10.5%, as well as six different frequencies ranging from $500Hz$ to $8kHz$.

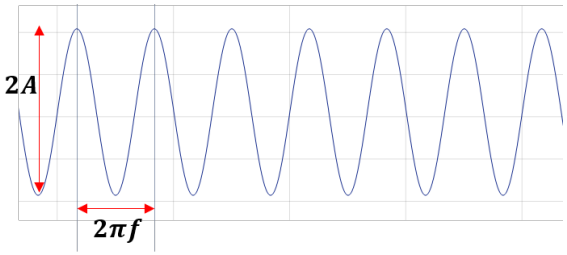

Figure 14: Reynolds number input

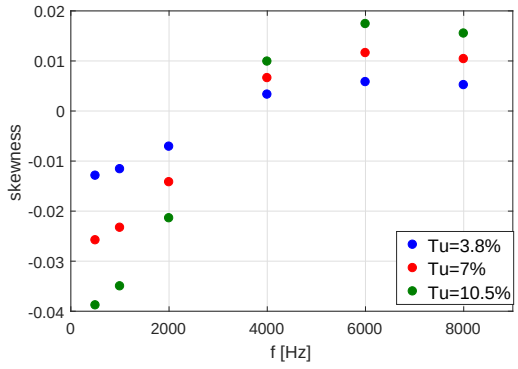

Figure 15: Output skewness

The results are presented in Figures 15 and 16. The skewness is indeed affected by the non-linearity, with the values ranging from negative in lower frequencies to positive in higher frequencies. The effect is stronger with increasing turbulence intensity levels, as expected. It has to be noted that the results agree with the results of Weiss et al. in [8]. The turbulence intensity computed by the reconstructed output signal is presented in Figure 16. The turbulence intensity features significant attenuation as the frequency increases. This should be interpreted by looking at the amplitude spectrum in Figure 17. It can be seen that attenuation is present for all the input frequency range, therefore the attenuation of the turbulence intensity is mainly due to the system damping and should not be attributed to the non-linearity. Nevertheless, the cut-off frequency ($-3dB$ attenuation) is at 7 kHz. This indicates the possible error from assuming a flat frequency response up to the cut-off frequency and underlines the need for correction methods.

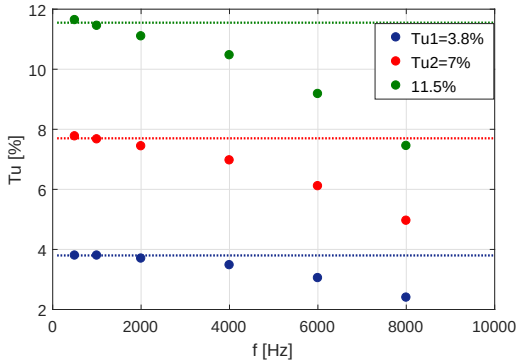

Figure 16: Output turbulence intensity

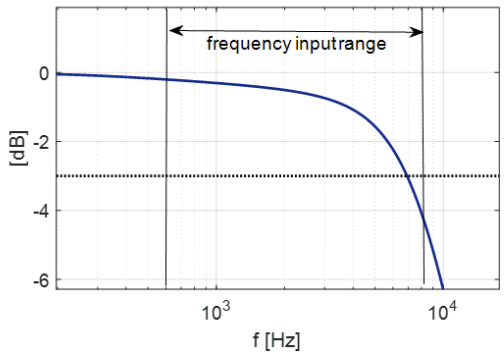

Figure 17: Amplitude spectrum for the input frequency range

4. Conclusions

The present work uses a non-linear model to simulate the dynamic response of a CTHWA, taking into account also heat conduction effects. The comparison with an experimental square wave test reveals a rather poor agreement between the model and the experiment for the anemometer used, especially at high frequencies. Therefore, further work will be dedicated to this issue. In the meantime, the model is used for more general investigations of the behaviour of a CTHWA.

The possible errors in turbulence measurements stemming from the dynamic response of the CTHWA are identified as follows:

- Attenuation due to heat conduction
- Amplification or damping due to system dynamics
- Non-linearity errors

For small fluctuations, the first two could be corrected by applying a transfer function to the measured spectrum. For large fluctuations, the effect of non-linearity can have a significant effect on the skewness which can not be corrected by a transfer function. A correction method exists for Constant-Voltage-Anemometry (Berson et al. [12]) but not for CTHWA.

Subjecting the model to both a square wave voltage and a Reynolds impulse, it is observed that the response to the square wave simulates well the response to the impulse, until a very high frequency. This indicates that the square wave test is representative of a velocity impulse in this case, which is contradictory to the results of Li [7].

The amplitude attenuation due to heat conduction can begin at a frequency as low as $150Hz$, and therefore affect almost all the useful range for turbulence measurements, and it can be present even for large length to diameter ratios. This attenuation is also present at the response to the square wave, which indicates that the square wave could be used as a transfer function to correct for the attenuation when its effect is not negligible.

Acknowledgments

The support of the Fonds de la Recherche Scientifique-FNRS, through the award of a FRIA doctoral grant, is greatly acknowledged. The contribution of Mattia Cottes in the implementation of the model in matlab has to be acknowledged as well.

References

[1] H. H. Bruun, Hot-Wire Anemometry: Principles and Signal Analysis, Oxford University Press, 1995.

[2] P. Freymuth, Frequency Response and Electronic Testing of Constant-Temperature Hot-Wire Anemometers, Journal of Physics E: Scientific Instruments 10 (1977) 705–710.

[3] J. Weiss, H. Knauss, S. Wagner, Method for the Determination of Frequency Response and Signal to Noise Ratio for Constant-Temperature Hot-Wire Anemometers, Review of Scientific Instruments 72 (3) (2001) 1904–1909.

[4] P. Freymuth, Feedback Control Theory for ConstantTemperature Hot Wire Anemometers, Review of Scientific Instruments 38 (5) (1967) 677–681.

[5] B. C. Khoo, Y. T. Chew, C. P. Lim, The Dynamic Response of a Hot-Wire Anemometer: III. Voltage-Perturbation Versus Velocity-Perturbation Testing For Near-Wall Hot-Wire/Film Probes, Measurement Science and Technology 10 (1999) 152–169.

[6] N. Hutchins, J. P. Monty, M. Hultmark, A. J. Smits, A Direct Measure of the Frequency Response of Hot-Wire Anemometers: Temporal Resolution in Wall-Bounded Turbulence, Experiments in Fluids.

[7] J. D. Li, Dynamic Response of Constant Temperature Hot Wire Systems Under Various Perturbations, Measurement Science and Technology 17 (2006) 2665–2675.

[8] J. Weiss, A. Berson, G. Comte-Bellot, Investigation of Non-Linear Effects in Constant Temperature Anemometers, Measurement Science and Technology 24 (2013) 08532.

[9] A. Berson, P. Blanc-Benon, G. Comte-Bellot, On the Use of Hot-Wire Anemometry in Pulsating Flows. A Comment on 'A Critical Review on Advanced Velocity Measurement Techniques in Pulsating Flows', Measurement Science and Technology 21 (2010) 128001.

[10] P. Freymuth, Further Investigation of the Nonlinear Theory for Constant-Temperature Hot-Wire Anemometers, Journal of Physics E: Scientific Instruments 10 (1977) 710–713.

[11] G. Comte-Bellot, J. P. Schon, Harmoniques Creés Par Excitation Parametrique Dans les Anemometres Á Fil Chaud Á Intensité Constante, International Journal of Heat and Mass Transfer 12 (12) (1969) 1661–1677.

[12] A. Berson, P. Blanc-Benon, G. Comte-Bellot, A Strategy to Eliminate All Nonlinear Effects in Constant-Voltage Hot-Wire Anemometry, Review of Scientific Instruments 80 (2009) 045102.

[13] P. Freymuth, Engineering Estimation of Heat Conduction Loss in Constant Temperature Thermal Sensors, TSI Quarterly 4 (1979) 3–6.

[14] S. C. Morris, J. F. Foss, Transient Thermal Response of a Hot-Wire Anemometer, Measurement Science and Technology 14 (2003) 251–259.

[15] J. D. Li, Dynamic Response of Constant Temperature Hot-Wire System in Turbulence Velocity Measurements, Measurement Science and Technology 15 (2004) 1835–1847.

[16] Ligrani P. M. and Bradshaw P., Spatial Resolution and Measurement of Turbulence in the Viscous Sublayer Using Subminiature Hot-Wire Probes, Experiments 5 (1987) 407–417.

[17] M. Hultmark, A. Ashok, A. J. Smits, A New Criterion for End-Conduction Effects in Hot-Wire Anemometry, Measurement Science and Technology 22 (2011) 055401.

[18] B.Cukurel, S. Acarer, T. Arts, A Novel Perpesctive to High-Speed Cross-Hot-Wire Calibration Methodology, Experiments in Fluids 53 (4) (2012) 1073–1085.

[19] A. E. Perry, G. L. Morisson, A Study of the Constant-

Temperature Hot-Wire Anemometer, Journal of Fluid Mechanics 47 (3) (1971) 577–599.

Influence of gas-to-wall temperature on bypass transition

Tânia Sofia Cação Ferreira

Turbomachinery and Propulsion Department, von Karman Institute for Fluid Dynamics, Belgium, tania.sofia.cacao.ferreira@vki.ac.be

Supervisor and promotor: Tony Arts

Professor and Head, Turbomachinery and Propulsion Department, von Karman Institute for Fluid Dynamics, Belgium, arts@vki.ac.be
Professor, Institute of Mechanics, Materials and Civil Engineering, Université Catholique de Louvain, Belgium, tony.arts@uclouvain.be

Co-promotor: Vincent Legat

Professor and Head, Applied Mechanics and Mathematics, Université Catholique de Louvain, Belgium, vincent.legat@uclouvain.be

Abstract

The need to improve heat transfer predictions in turbomachinery is met by an investigation of the thermal effects on bypass transition on a highly loaded turbine guide vane. Heat flux measurements are conducted in the von Karman Institute (VKI) Isentropic Compression Tube (CT-2) facility where the gas-to-wall temperature ratio is varied from 1.14 to 1.51 by changing the inlet gas temperature. Four test cases are presented for different exit Mach numbers (0.52 and 0.86) and freestream turbulence intensities (0.8% and 5.3%) while the isentropic exit chord Reynolds number is maintained at 10^6. The experimental results are accompanied by heat transfer predictions from a boundary layer code.

Keywords: thermal effects, boundary layer transition, heat transfer measurements, high pressure turbines

1. Introduction

A major source of uncertainty and losses in fluid dynamics is due to transition, the inception of turbulence, with rising shear stresses and heat flux rates. The high complexity of laminar to turbulent boundary layer transition on a turbine airfoil surface is difficult to characterize, due to the flow topology (wall bounded, unsteady, 3D) and non-linear interactions between flow variables [1]. A deeper understanding of this fundamental issue is therefore needed to improve performance predictability and efficiency of gas turbines, leading to safer and greener aviation.

Nowadays, several models attempt to predict transition on non film-cooled high-pressure (HP) turbine blades (helicopter engines, second HP rotor of large civil engines, etc). Yet, sufficiently detailed, accurate and representative experimental data are unfortunately scarce for their validation.

Furthermore, the assumption of a constant turbulent Prandtl number (Pr_t) is commonly applied to transition and turbulence RANS modelling to compute the turbulent heat fluxes. Notwithstanding, limited experimental results indicate that under distinct pressure gradients the thermal boundary layer behaves differently than the momentum one [2] and also that different Pr_t values are obtained near the wall [3]; their value is far from the commonly used one in such models ($Pr_t \approx 0.9$). In addition, results of RANS simulations using two distinct well-known models, $\gamma - Re_\theta$ [4] and $\kappa-\kappa_l-\omega$ [5], indicate contradictory behaviours of the thermal boundary layer transition onset when changing the freestream temperature [6].

Considering the highly varying pressure gradients in gas turbines as well as the role of the turbine inlet temperature and the machine compression ratio in their efficiency, an accurate heat transfer prediction becomes crucial.

Therefore, this research project aims at increasing the knowledge on transition physics by means of an experimental and numerical study on the thermal effects. The experimental effort is conducted in VKI's Isentropic Compression Tube (CT-2) facility on a linear HP turbine cascade. Thermal effects are addressed

by varying gas-to-wall temperature ratio and turbulence intensity, Mach and Reynolds numbers can be also independently varied. Lastly, a boundary layer code is used for heat transfer predictions.

2. Experimental campaign

2.1. Facility

Tests are performed in the CT-2 facility (Fig. 1) in the "Jacques Chauvin" laboratory of the VKI. The facility is based on an isentropic compression which allows simulating the working conditions of a real engine in terms of temperature ratio and exit isentropic Mach and Reynolds numbers for a short duration of about 0.5 second. The gas temperature, the exit Mach and Reynolds numbers can be set independently by adjusting the overall pressure level and the pressure ratio across the test section. In the present study, the exit Mach number is set by adjusting the opening area of a sonic throat placed at the exit of the test section. This device allows maintaining the operating conditions constant during the complete test duration despite the finite volume of the discharge reservoir.

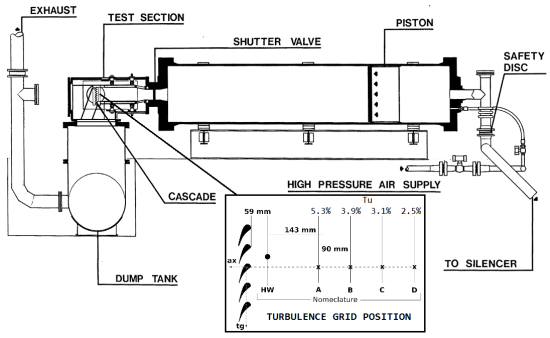

Figure 1: Illustration of CT-2 facility [7] and turbulence levels [8].

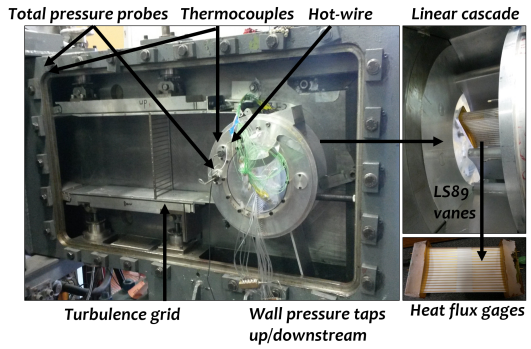

Figure 2: Photograph of the test section, cascade and central blade.

2.2. Instrumentation

The test section (Fig. 2) contains a five-blade linear cascade of a well-known geometry (LS89) which has been used for several test campaigns in the past [7; 8]. The flow is directed to the cascade through a 230x100 mm^2 channel coinciding with the leading edge of the upper and bottom blades. The central blade is used for the heat transfer measurements.

A turbulence grid made of horizontal cylindrical bars (3 mm diameter, 12 mm pitch) is placed in discrete streamwise positions upstream the test section to vary the freestream turbulence levels, as in Fig. 1.

2.2.1. Pressure sensors

Total pressure in the compression tube is measured by a Validyne® variable reluctance differential transducer while National Instruments® semiconductor differential transducers are used for total and static pressure in the test section and static pressure in the dump tank. Pitot probes are installed upstream the cascade and inside the tube while wall tapings are drilled up- and downstream of the cascade for inlet and exit static pressure measurements. The exit static pressure distribution is measured by a Scanivalve® miniature pressure scanner and covers two pitches. The taps are located at 43% axial chord downstream of the trailing edge plane.

2.2.2. Thermocouple

The upstream total gas temperature is measured by a 25 μm type K thermocouple placed half an axial chord upstream of the cascade.

2.2.3. Thin films

Constant current thin film thermometry is used for wall temperature and heat transfer measurements. Forty-five platinum thin films (~10 μm of thickness) are painted around the central blade of the cascade. This airfoil is made of Macor® glass ceramic, a good thermal and electric insulator. Further information about the manufacturing characteristics of the thin films are described by Ligrani et al [9]. The temperature measurements are based on the following linear relation between resistance and temperature:

$$R = R_0[1 + \alpha_R(T - T_0)] \quad (1)$$

where R_0 is the thin film resistance at a temperature T_0 and α_R is the temperature coefficient of resistance. The resistance values are obtained from the measured voltage signals by applying the Ohm's law.

2.2.4. Analog circuits

Heat flux in a semi-infinite substrate can be simulated using electric analog circuits where the Fourier law and the unsteady heat conduction equation are respectively analogous to the Ohm's law and to the transmission line circuit equation. This will result in a heat flux given by the following equation [10]:

$$\dot{q}_w = \frac{V_{out}}{V_0} \frac{\sqrt{\rho c k}}{\alpha_R} \frac{A}{\beta}^* \tag{2}$$

where V_{out} is the thin film Wheatstone bridge voltage, V_0 is the thin film voltage, $\sqrt{\rho c k}$ is the substrate thermal product, α_R is the thin film temperature coefficient of resistance and A/β^* is the analog circuit calibration coefficient. A more detailed analysis of the above-mentioned procedure is reported in [11; 12].

2.2.5. Data acquisition

The signal from the analog circuits is amplified and low-pass filtered at 12 kHz. All the voltage signals (except from the Scanivalve® scanner which possesses a specific hardware and software) are recorded by an acquisition system at a sampling frequency of 50 kHz for a total duration of 1 second.

2.3. Uncertainty analysis

The analysis of the uncertainties associated to the present experimental campaign uses the error propagation theory and its results are evaluated within a confidence interval of 95% [13]. Uncertainties for the quantities of interest are reported in Table 1.

Uncertainty [%]	T_g/T_w	$M_{s,2}$	$Re_{s,2}$	h
	1.4	1.5	4.0	8.0

Table 1: Uncertainties within a 95% confidence interval.

3. Experimental results - high Mach number

A fully subsonic Mach number distribution is selected for a shock-free flow. As seen in the previous work [14], a shock would render a very short transition region, hindering the focus on the thermal effects.

In addiction to the gas-to-wall temperature ratio, the freestream turbulence intensity is also considered. Experiments are performed with the natural intensity of the facility (0.8%) and the maximum available value provided by a turbulence generator (5.3%) [8]. The latter freestream turbulence level is achieved by means of a passive grid placed 202 mm upstream the cascade.

The exit isentropic Mach and Reynolds number are constant for every test. The Reynolds number is based on the chord and outlet velocity and is around 10^6.

3.1. Heat transfer coefficient

The thermal boundary layer evolution on the vane suction side can be illustrated by its heat transfer coefficient distribution, here defined as:

$$h = \frac{\dot{q}_w}{T_g - T_{w,initial}} \tag{3}$$

The stagnation region is characterized by high heat flux due to elevated heating impinging on a still developing thin laminar boundary layer. Because of its nature, it acts as an insulating layer and the heat transfer decreases. A further variation in heat transfer would be due to the presence of film cooling, separation bubbles, shocks or transition (which can be also triggered by the former factors). In this investigation, a change in heat transfer is expected to be due to bypass transition considering the flow nature and the model geometry: relatively high natural wind tunnel turbulence intensity (0.8%), subsonic Mach numbers (< 1), high Reynolds number (10^6) and curved (convex) surface.

The heat transfer coefficient evolution at low and high freestream turbulence intensity is presented for three gas-to-wall temperature ratios in Fig. 3 and 4. The time-averaged values are calculated for a short time interval at the start of the test, where the adopted data processing technique is the most sensitive and a uniform temperature thermal boundary condition is best verified. The isentropic Mach number distribution along the blade suction side obtained from RANS simulations [6] is also shown in each figure.

Both test cases show no clear indication of an effect of gas-to-wall temperature ratio on the onset of transition. Transition begins at the same position for the three temperature ratios: in Fig. 3 ($Tu_\infty = 0.8\%$) it starts around $s = 57.1$ mm and in Fig. 4 ($Tu_\infty = 5.3\%$) at $s = 50.3$ mm.

Comparing the two cases, a minor difference can be seen in the exit Mach number. However small, it translates in a slightly different pressure gradient distribution. The peak pressure for Fig. 3 ($M_{s,2} = 0.86$) is shortly after the peak for Fig. 4 ($M_{s,2} = 0.83$). Therefore, the earlier transition onset is secondarily due to a very small difference in the pressure gradients and mostly due to the increase of turbulence intensity. Nevertheless, the effect of increasing the turbulence

levels is clearly present in the stagnation region, where considerably higher ($\approx 33\%$) heat transfer coefficients are obtained for approximately the same temperature ratios.

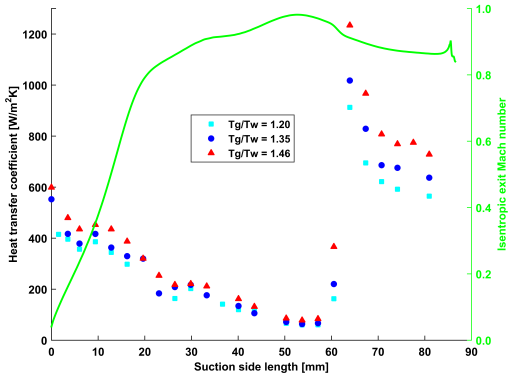

Figure 3: Heat transfer coefficient distribution at T_g/T_w = [1.20, 1.35, 1.46], $Tu_\infty = 0.8\%$, $M_{s,2} = 0.86$ and $Re_{s,2} = 0.98 \cdot 10^6$.

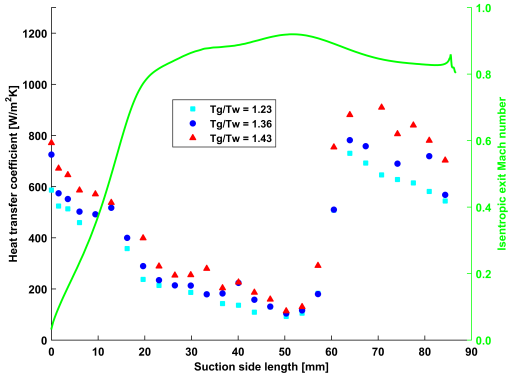

Figure 4: Heat transfer coefficient distribution at T_g/T_w = [1.23, 1.36, 1.43], $Tu_\infty = 5.3\%$, $M_{s,2} = 0.83$ and $Re_{s,2} = 0.96 \cdot 10^6$.

3.2. Skewness

Skewness allows the representation of the transition evolution since it is a measure of the degree of asymmetry of the probability distribution of data (Fig. 5).

A normal distribution, mirror-shaped around the mean value, has, therefore, a null skewness and symmetrical data have skewness close to zero. Hence, a null skewness corresponds to a fully laminar, to a 50% transitional or to a fully turbulent state. In between, two peaks are present at the start (mainly laminar signal with some turbulent fluctuations) and towards the

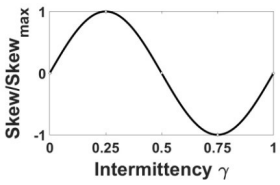

Figure 5: Expected trend of skewness versus intermittency.

end of transition (almost fully turbulent signal with remaining laminar zones). A relation between the skewness and the intermittency can be accordingly established, as shown in Fig. 5.

Looking into the differences due to the increase of the freestream turbulence level, the skewness for the lowest gas-to-wall temperature ratio tests is shown in Fig. 6. Even though, from time-averaged values in Fig. 4 (high turbulence case), transition starts at $s = 50.3$ mm, the skewness indicates that the boundary layer is already disturbed since $s = 40$ mm.

As for the low turbulence case, the skewness is accordingly with the heat transfer distribution is Fig. 3.

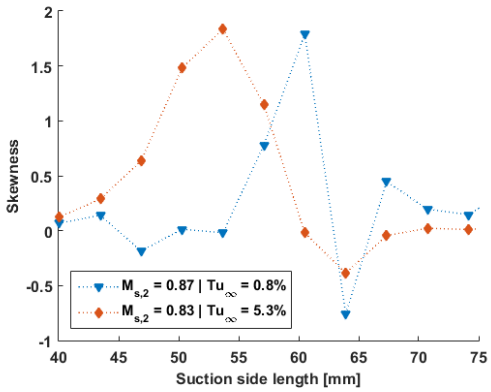

Figure 6: Skewness distribution for the low turbulence intensity case ($T_g/T_w = 1.20$, $Tu_\infty = 0.8\%$, $M_{s,2} = 0.86$ and $Re_{s,2} = 0.98 \cdot 10^6$) and for the high ($T_g/T_w = 1.23$, $Tu_\infty = 0.8\%$, $M_{s,2} = 0.83$ and $Re_{s,2} = 0.96 \cdot 10^6$).

3.3. Acceleration parameter

The acceleration parameter is computed using the software TEXSTAN [15] and is defined as follows:

$$K = \frac{\nu}{u_\infty^2} \frac{du_\infty}{ds} \tag{4}$$

where ν is the kinematic viscosity, u_∞ is the local freestream velocity and du_∞/dx is the local freestream streamwise velocity derivative.

The comparison of this parameter for the two Mach number distributions ($M_{s,2} = 0.87$ and $M_{s,2} = 0.83$) is displayed in Fig. 7 for a deeper insight on the origin of the skewness results. In fact, the change in the pressure gradient distribution (from Fig. 3 to 4) results in a slight advance of the peak velocity before diffusion but it is too small to account alone for the earlier transition onset. It is more likely that adding the higher turbulence intensity to the almost null pressure gradient just before $s = 40$ mm (the start of instability) was enough to destabilize the boundary layer. However, the subsequent acceleration region suppresses the development of transition and maintains the heat transfer coefficient decrease (Fig. 4) until diffusion is reached.

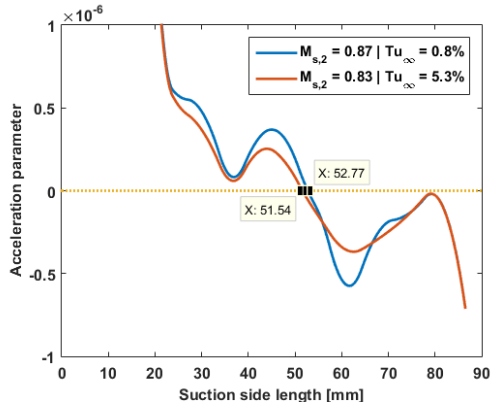

Figure 7: Acceleration parameter distribution for the low turbulence intensity case ($T_g/T_w = [1.20, 1.46]$, $M_{s,2} = 0.86$, $Tu_\infty = 0.8\%$ and $Re_{s,2} = 0.98 \cdot 10^6$) and for the high ($T_g/T_w = [1.23, 1.43]$, $M_{s,2} = 0.83$, $Tu_\infty = 5.3\%$ and $Re_{s,2} = 0.96 \cdot 10^6$).

4. Experimental results - low Mach number

An isentropic Mach number distribution as uniform as possible is aimed at since the previous results show a predominant effect of the pressure gradients. Rubini [6] suggests an exit Mach number of 0.6 based on numerical simulations. The present experimental results are for a Mach number of 0.52-0.54.

4.1. Heat transfer coefficient

Heat transfer measurements and Mach number computations are displayed in Fig. 8 and 9. The isentropic Mach number distribution is characterized by adverse pressure gradients starting as soon as $s = 24$ mm which are only interrupted by an null pressure gradient for $s = 40 - 50$ mm.

In Fig. 8 ($Tu_\infty = 0.8\%$), transition starts after the velocity plateau. The tests at lower temperature ratios show the first turbulent fluctuations at $s = 53.4$ mm whereas the test at the highest temperature ratio remains laminar until $s = 57.1$ mm. These results indicate that the increase of the gas temperature in some way delays the development of transition.

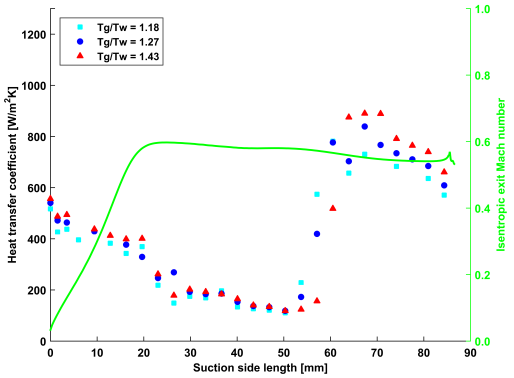

Figure 8: Heat transfer coefficient distribution at $T_g/T_w = [1.23, 1.35, 1.46]$, $Tu_\infty = 0.8\%$, $M_{s,2} = 0.54$ and $Re_{s,2} = 0.96 \cdot 10^6$.

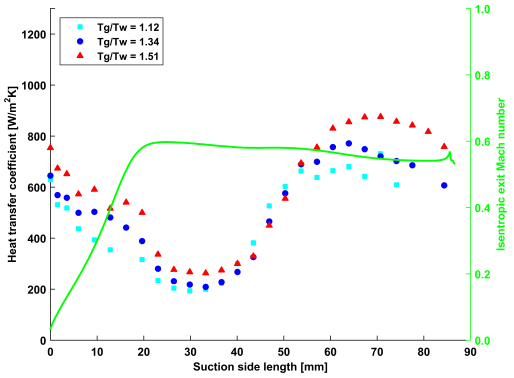

Figure 9: Heat transfer coefficient distribution at $T_g/T_w = [1.14, 1.34, 1.51]$, $Tu_\infty = 5.3\%$, $M_{s,2} = 0.52$ and $Re_{s,2} = 0.94 \cdot 10^6$.

On the other hand, in Fig. 9 ($Tu_\infty = 5.3\%$), an effect of temperature is seen on the transition length but not on the onset. Transition onset is at $s = 29.8$ mm for the three temperature ratios, but their transition evolution is different. Higher temperature ratios reach the peak in heat flux further downstream on the vane suction side. This indicates that transition length is longer at higher gas temperatures for these flow conditions.

Regarding the increase of freestream turbulence intensity from Fig. 8 to Fig. 9, transition is moving

upstream 28% the suction side length for an increase of 4.5% of turbulence intensity. Nevertheless, the advance in transition is still linked to the pressure gradients since, in both test cases, transition starts along with a distinct velocity diffusion. In fact, the thermal effect on transition is most likely perceivable in the present cases due to the milder pressure gradients than the high Mach number case in Section 3.

4.2. *Statistical moments*

The root-mean-square of the low turbulence case is presented in Fig. 10. As in the time-resolved signal, the onset of transition is later for the highest temperature ratio, as well as the end of transition.

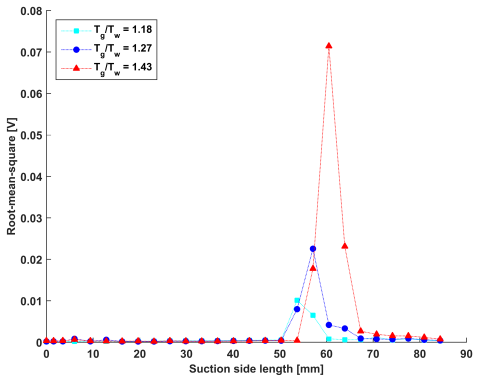

Figure 10: Root-mean-square distribution at $T_g/T_w = [1.18, 1.27, 1.43]$, $Tu_\infty = 0.8\%$, $M_{s,2} = 0.54$ and $Re_{s,2} = 0.96 \cdot 10^6$.

The third statistical moment, the skewness, is used to represent the results for the high turbulence case in Fig. 11. The increase of transition length with the temperature ratio is clear. The lower values of skewness between the middle and the end of transition, the most turbulent region, are likely due to high frequency fluctuations which cannot be captured by the limited frequency response of the analog circuits.

However, this case indicates no effect of temperature on onset of transition. Therefore, a doubt remains for the low turbulence case: if there is indeed an effect on the onset or if transition is triggered as in the lower temperature ratio cases but with lower turbulence spot production and/or growth. As for the higher Mach number cases, no difference on the transition onset or length is observed due to higher adverse pressure gradients which dictate a shorter transition. A potential small effect of temperature is thus not measurable.

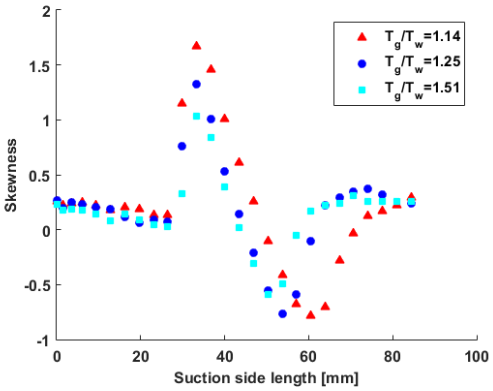

Figure 11: Skewness distribution at $T_g/T_w = [1.14, 1.34, 1.51]$, $Tu_\infty = 5.3\%$, $M_{s,2} = 0.52$ and $Re_{s,2} = 0.94 \cdot 10^6$.

5. Analysis of temperature effect

On a turbulent boundary layer, a heat transfer dependence on the thermal effects is shown in [16], where the Nusselt number increases with the gas-to-wall temperature ratio. An analytical analysis related this effect to the variation of density and transport proprieties with the temperature across the boundary layer. For the laminar boundary layer, however, the effect of temperature ratio is found to be smaller, as seen in the present experiments.

Regarding the transition region, the effect of wall heating has been shown to destabilize the boundary layer by Schlichtling [17], Liepmann and Fila [18] and van Driest and Blumer's [19]. Moreover, buoyancy effects also indicate that cold flow over a hot wall would be an unstable configuration. Therefore, in our experiments, the boundary layer should be thermally stable.

The boundary layer stability is expected to be enhanced by increasing the near-wall negative velocity curvature [20]:

$$\left(\frac{\partial^2 u}{\partial y^2}\right)_w = \frac{1}{\mu_w}\left[\frac{dp}{dx} - \frac{d\mu}{dT}\left(\frac{\partial T}{\partial y}\right)_w\left(\frac{\partial u}{\partial y}\right)_w\right] \tag{5}$$

Therefore, the increase of the gas temperature will result in the augmentation of the viscosity and temperature gradient which, adding to the same streamwise pressure and spanwise velocity gradient gives a more negative curvature and thus a more stable boundary layer. The presence of a dependence on the pressure gradient could explain the dissimilar thermal effects at distinct Mach number distributions.

On the other hand, optimal growth theory for compressible boundary layers found wall cooling to be

destabilizing at M=0.5 [21]. Moreover, in experiments by Costantini et al [16], a small decrease of T_w/T_{aw} considerably lowered the turbulent spots production (roughness induced-transition, very low turbulence). However, in the present case, the RMS indicates that the turbulent spot production is increasing with the gas temperature. Thus, the temperature effect is most likely upon the growth of turbulent spots.

6. Analysis of turbulence intensity effect

The augmentation of turbulence intensity altered the heat transfer levels as well as their sensitivity to the gas-to-wall temperature ratio, depending on the boundary layer state.

Starting from the stagnation laminar region, it can be clearly observed that the heat transfer coefficient is increasing with the turbulence intensity. Adding to this, a bigger heat transfer dependence on the gas-to-wall temperature is also evident, particularly for the complete laminar boundary layer.

Oppositely, slightly lower heat transfer levels are obtained for the turbulent boundary layer. The same effect is observed in results from Arts et al [7] for $Re_{s,2} = 2 \cdot 10^6$ and $M_{s,2} = 0.92$. Also, results from Wang et al [21], for turbulence intensities from 0.2 to 18% show decreasing heat transfer coefficient values in the turbulent region. Nevertheless, these results might be due to a slightly distinct transition onset and evolution due to the turbulence intensity effect itself.

Attention must be given also to the turbulent length scales, changing due to the presence of the grid, which are found to have an influence on the heat transfer.

7. Boundary layer code - TEXSTAN

The purpose of using a boundary layer code (BLC) is to compare the heat transfer coefficient values for the laminar and turbulent regions and to check the pertinence of the implemented transition models. TEXSTAN [15] is selected since it has been validated against several tests cases, including the present one [7]. This software was developed to solve the convective transport of heat, momentum and mass transfer of distinct flow geometries by using a finite difference technique to resolve the 2D parabolic boundary layer equations.

The present initial conditions are estimated at 0.5 mm from the stagnation point by creating 2D flow profiles (velocity, temperature/stagnation enthalpy) from the Falkner-Skan equation for the 2D stagnation point solution.

Velocity and wall static temperature distribution on the suction side of the vane are given as boundary conditions. The inlet total pressure and total temperature, along with the velocity distribution, allow the computation of the static pressure and temperature distribution. The inlet flow velocity and turbulence intensity give the initial value of the turbulence kinetic energy.

TEXSTAN turbulence modelling uses the mean field closure through a choice of the Prandtl mixing length model or one/two equation models. Since the calibration of one/two equation models is not the present concern of this paper, Abu-Ghannam and Shaw (AG-S) mixing length transition model with a constant turbulent Prandtl number set to 0.9 is used for the transition/turbulence modelling.

The outcome of these simulations was very satisfying with respect to the laminar and turbulent heat transfer coefficient values. However, the downside in using the boundary layer code is not being able to proceed computations after flow separation.

The first result is a validation of the laminar region (measurements [7], fully laminar computations [6] and BLC results) shown in Fig. 12. Measurements and computations are perfectly matching until $s = 60$ mm where the BCL stops due to the prediction of a local separation region. This is due to the adverse pressure gradient acting continuously since $s = 55$ mm.

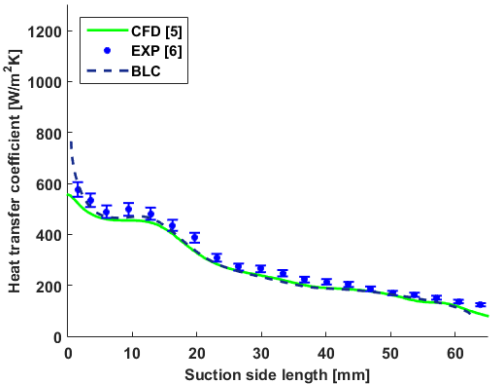

Figure 12: Experimental data [7], TEXSTAN results (AG-S mixing length) and laminar simulation of $T_g/T_w = 1.37$, $Tu_\infty = 0.8\%$, $M_{s,2} = 0.84$ and $Re_{s,2} = 1.14 \cdot 10^6$.

There is a slight under-prediction for the stagnation region and the beginning of the laminar region (s/c <20%) which is due to the modelling itself, not able to account for the enhancement in the laminar heat transfer with the increase of turbulence intensity [22]. This difference is also higher with the increase of gas temperature, as can be seen for the following test cases

(Fig. 13 and 15).

On Figure 13 (higher freestream turbulence), the boundary layer simulation stops just after the transition model is triggered due to the presence of a shock as predicted in [14]. The comparison with the measured isentropic Mach number and the measured heat transfer coefficient distribution indicates a destabilization of the boundary layer (increase of heat transfer coefficient) starting from s=40 mm due to a prior velocity plateau. A subsequent favorable pressure gradient delays the development of transition, which is anyway rapidly completed once the shock is reached at $s = 60$ mm. The BLC is unable to display neither phenomena: AG-S transition criterion is not achieved by $s = 40$ mm, so the small disturbance in the boundary layer is not appreciable and since the mathematical formulation of the model does not allow reverse flow, the code stops at the shock position.

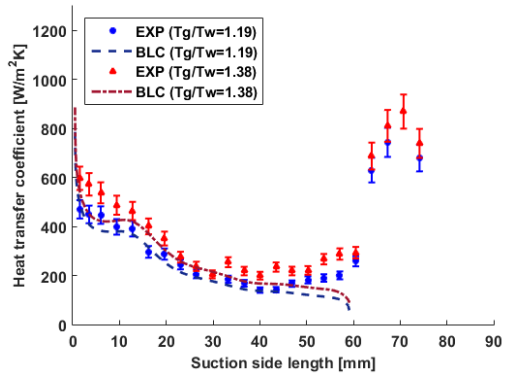

Figure 13: Experimental data and TEXSTAN results (AG-S mixing length) at $T_g/T_w = [1.19, 1.39]$, $Tu_\infty = 5.3\%$, $M_{s,2} = 0.93$ and $Re_{s,2} = 1.04 \cdot 10^6$ [14].

The simulation of the low exit Mach number and turbulence intensity case predicts a later transition onset (more than 10 mm) with respect to the experiments (Fig. 14). To have a better insight on the turbulent heat transfer levels, an abrupt mixing length transition model (AT) was used instead of the Abu-Ghannam and Shaws (AG-S), since it allows to trigger transition instantaneously at a selected geometrical position. This model was formulated for flows over rough surfaces or in presence of a boundary layer trip. In this mode, the flow starts laminar and, once the transition momentum Reynolds number defined by the user is reached, the boundary layer state switches to turbulent by adding the computed eddy viscosity to the molecular viscosity. The transition momentum Reynolds number is simply obtained by performing a laminar BLC simulation and analyzing its momentum Reynolds number evolution along the vane length and the start of transition shown in the experimental results.

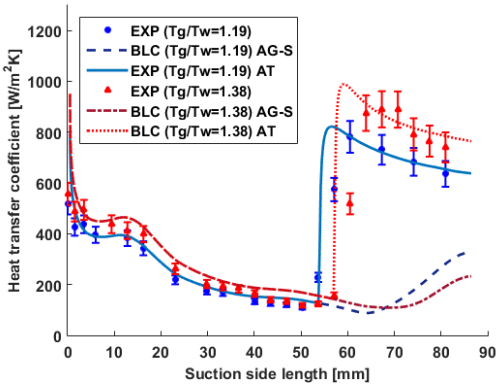

Figure 14: Experimental data and TEXSTAN results (AG-S and abrupt transition mixing length) at $T_g/T_w = [1.18, 1.43]$, $Tu_\infty = 0.8\%$, $M_{s,2} = 0.54$ and $Re_{s,2} = 0.96 \cdot 10^6$.

The experimental and numerical results for both transition models are presented in Fig. 14. Although the evolution of transition does not reflect that of the experiments, the computed turbulent levels are found to be in good agreement with the experimental data.

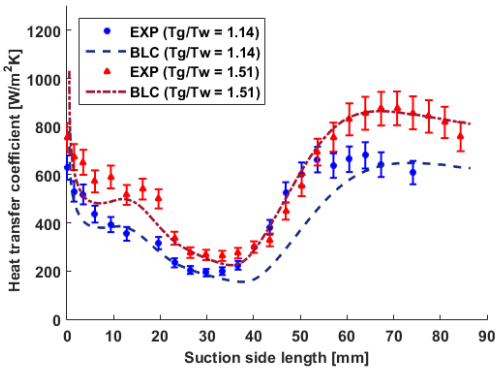

Figure 15: Experimental data and TEXSTAN results (AG-S mixing length) at $T_g/T_w = [1.14, 1.51]$, $Tu_\infty = 5.3\%$, $M_{s,2} = 0.52$ and $Re_{s,2} = 0.94 \cdot 10^6$.

Lastly, the results for the highest turbulence intensity are presented in Fig. 15. As in Fig. 13, there is an underprediction of the heat transfer values for the stagnation and laminar regions, which is due to the higher turbulence levels. The prediction of the transition onset and evolution is, surprisingly, quite accurate for the highest temperature ratio, as well as of the tur-

bulent heat transfer coefficient values. The simulation of the lowest temperature ratio test shows a later transition onset, which does not correspond at all to the measured data. Even though the transition criterion is not built to take the gas-to-wall temperature ratio into account, the BLC code still yields the correct turbulent heat transfer coefficient values.

The need to include the effects of freestream turbulence intensity in the laminar boundary layer modelling has been also pointed out by Cutrone et al [23] from their analysis of six bypass transition models.

8. Conclusion

Experimental results of the investigation of thermal effects on bypass transition are presented for a turbomachinery application.

Apart from test cases with marked pressure gradients, a clear effect of the gas-to-wall temperature ratio (1.14-1.51) is shown on the transition length through measurements of the wall heat flux. These results were obtained at a relatively high level of freestream turbulence intensity (0.8%), with mild pressure gradients ($M_{s,2} = 0.52$) and high Reynolds number ($1 \cdot 10^6$). Further research is necessary to make a sure statement on the physical effect behind the phenomenon.

In addiction, similar flow conditions at low turbulence intensity (0.8%) point towards a delay on the transition onset due to the increase of the temperature ratio. However, this case ought to be deeper investigated for a definitive confirmation of the occurrence of bypass transition.

Heat transfer predictions using a boundary layer code are in good agreement with the measurements for the turbulent boundary layer, even when transition is artificially triggered. As for the laminar heat transfer, the increase of freestream turbulence intensity results in underpredicted heat transfer values for the stagnation region since the mixing length model does not have high turbulence leading edge effects incorporated. One or two equation models should therefore be used in future calculations.

Acknowledgments

The dedicated work of Nikolaus Vasilokopoulos in the experimental campaign and data post-processing is thankfully acknowledged as well as the Mach number predictions from Riccardo Rubini and the help and advice in the lab from Mr. Pierre Londers. The support for the TEXSTAN software from Prof. Mike Crawford is also thankfully appreciated.

Greek symbols

α_R	temperature coefficient of resistance	K^{-1}
κ	kinetic energy	m^2/s^2
μ	dynamic viscosity	kg/ms
ν	kinematic viscosity	m^2/s
ρ	density	kg/m^3
ω	specific turbulence dissipation	s^-1

Roman symbols

A/β^*	analogue circuits coefficient	$s^{-0.5}$
c	specific heat	J/KgK
h	heat transfer coefficient	W/m^2K
K	acceleration parameter	–
k	thermal conductivity	W/kgK
M	Mach number	–
P	pressure	Pa
Pr	Prandtl number	–
$\dot{q}$	heat flux	W/m^2
R	resistance	Ω
Re	Reynolds number	–
s	suction side length	mm
T	temperature	K
u	axial velocity component	m/s

Subscripts

0	total or reference quantity
1	upstream the cascade
2	downstream the cascade
g	referred to the gas
initial	value referred to the start of a test
l	laminar
s	isentropic quantity
t	turbulent
w	referred to the wall
∞	referred to the freestream

Acronyms

AG-S	Abu-Ghannam and Shaw correlation
AT	abrupt transition
BLC	boundary layer code
CT-2	Isentropic Compression Tube
HP	high-pressure (turbine)
VKI	von Karman Institute for Fluid Dynamics

References

[1] R. E. Mayle, The role of laminar-turbulent transition in gas turbine engines, Journal of Turbomachinery 113 (4) (1991) 509–536.

[2] O. P. Sharma, Momentum and thermal boundary layers on turbine airfoil suction surfaces, AIAA (Paper 87-1918).

[3] W. M. Kays, Turbulent prandtl number – where are we?, Journal of Heat Transfer 116 (2) (1994) 284–295.

[4] R. B. Langtry, F. R. Menter, Correlation-based transition modeling for unstructured parallelized computational fluid dynamics codes, AIAA Journal 47 (12) (2009) 2894–2906.

[5] D. K. Walters, D. Cokljat, A three-equation eddy-viscosity model for reynolds-averaged navier-stokes simulations of transitional flow, Journal of Fluids Engineering 130 (12) (2008) 121401–121401–14.

[6] R. Rubini, Numerical study of the effect of the gas to wall temperature ratio on the bypass transition, PR 2017-21, von Karman Institute for Fluid Dynamics (2017).

[7] T. Arts, M. Lambertderouvroit, A. W. Rutherford, Aero-thermal investigation of a highly loaded transonic linear turbine guide vane cascade. A test case for inviscid and viscous flow computations, Journal of Turbomachinery 114 (1) (1992) 147–154.

[8] F. Fontaneto, Aero-thermal performance of a film-cooled high pressure turbine blade/vane: a test case for numerical codes validation, Ph.D. thesis, von Karman Institute for Fluid Dynamics/Universitá degli Studi di Bergamo, Rhode-Saint-Genèse, Belgium (2014).

[9] P. M. Ligrani, C. Camci, M. S. Grady, Thin film heat transfer gage construction and measurement details, Internal Note 72, von Karman Institute for Fluid Dynamics, Rhode-Saint-Genèse, Belgium (1982).

[10] C. Camci, Experimental and theoretical study of film cooling on a gas turbine blade, Phd thesis, Katholieke Universiteit Leuven, Rhode-Saint-Genèse, Belgium (1985).

[11] D. L. Schultz, T. Jones, Heat-transfer measurements in short-duration hypersonic facilities., Advisory Group for Aerospace Research and Development AGARDograph 165.

[12] M. Oldfield, T. Jones, D. Schultz, On-line computer for transient turbine cascade instrumentation, IEEE Transactions on Aerospace and Electronic Systems (5) (1978) 738–749.

[13] R. J. Moffat, Describing the uncertainties in experimental results, Experimental Thermal and Fluid Science 1 (1) (1988) 3–17.

[14] T. S. Cação Ferreira, T. Arts, Influence of gas-to-wall temperature on bypass transition, in: ASME Turbomachinery Technical Conference & Exposition, ASME International Gas Turbine Institute, Charlotte, North Carolina, 2017.

[15] M. E. Crawford, TEXSTAN (1996).
URL `http://www.texstan.com/`

[16] A. D. Fitt, C. J. P. Forth, B. A. Robertson, T. V. Jones, Temperature ratio effects in compressible turbulent boundary layers, International Journal of Heat and Mass Transfer 29 (1) (1986) 159–164.

[17] H. Schlichting, K. Gersten, Boundary Layer Theory, 8th Edition, Springer, 2000.

[18] H. W. Liepmann, G. H. Fila, Investigation of effects of surface temperature and single roughness elements on boundary-layer transition, Technical Note 1196, NACA (1947).

[19] E. R. van Driest, C. B. Blumer, Boundary layer transition: Freestream turbulence and pressure gradient effects, AIAA Journal 1 (6) (1963) 1303–1306.

[20] F. M. White, Viscous fluid flow, Vol. 3.

[21] H. P. Wang, R. J. Goldstein, S. J. Olson, Effect of high free-stream turbulence with large length scale on blade heat/mass transfer, Journal of Turbomachinery 121 (2) (1999) 217–224.

[22] L. Daniels, W. Browne, Calculation of heat transfer rates to gas turbine blades, International Journal of Heat and Mass Transfer 24 (5) (1981) 871–879.

[23] L. Cutrone, P. De Palma, G. Pascazio, M. Napolitano, An evaluation of bypass transition models for turbomachinery flows, International Journal of Heat and Fluid Flow 28 (1) (2007) 161–177.

On the Time-Resolved Flow Field Downstream of a Turbine Stage Mounting Optimized Rotor Tip Geometries

PhD Candidate: Bogdan Cezar Cernat

Turbomachinery and Propulsion Department, von Karman Institute for Fluid Dynamics, Belgium, cernat@vki.ac.be

Supervisor: Sergio Lavagnoli

Assistant Professor, Turbomachinery and Propulsion Department, von Karman Institute for Fluid Dynamics, Belgium, lavagnoli@vki.ac.be

University Promoter: Tony Arts

Professor, Universite catholique de Louvain / von Karman Institute for Fluid Dynamics, Belgium, arts@vki.ac.be

Abstract

This paper addresses the investigation of the highly unsteady, three-dimensional HP turbine rotor outlet flows in a short-duration rotating test-rig. The rainbow rotor setup, allowing the simultaneous test of different optimized tips, is described, together with the time-resolved measurement and processing techniques employed for the investigation of the total pressure field downstream of the stage.

Keywords: HP Turbine, Tip Flows, Aerothermal, Measurements, Pressure, Heat Transfer, Rainbow Rotor

1. Introduction

Modern research in gas turbine aero-engines aims at maximizing the propulsion efficiency and components lifetime while reducing fuel consumption, polluting emissions and overhaul expenses. This performance-driven design implies ever-increasing aerothermal and mechanical loads on the system components. [1].

Despite the remarkable research efforts dedicated to the improvement of the "hot gas path", the overall system efficiency is still dramatically affected by the unsteady flow phenomena which characterize the engine aerodynamic and thermal field. This research paper focuses on the time-dependent total pressure field at the outlet of a HP turbine stage mounting a variety of optimized blade tip profiles. A critical analysis on the effect of each profile on the outflow aerodynamics is proposed, with particular focus on the tip leakage phenomenon. Noteworthy research works agree on attributing about one third of the total stage losses [2] to these by-pass streams, mainly promoted by the time varying blade tip loading [3] and representing a significant entropy source within the flow path [4]. Moreover, as reported in [5], the periodic disruption of the endwall boundary layer and high velocities associated to the leakage stream markedly contribute to an increase in heat transfer rates towards both the rotating airfoil and the stationary casing. Both the performance and lifetime of unshrouded rotor configurations rely therefore on a thorough understanding of the tip region aero-thermodynamics, as even a 10 K increase in blade metal temperature can reduce by 50% the lifespan of the component [6].

Numerical and experimental studies focusing on the overtip flow physics [7] confirm the inherent time-dependent nature of the leakage phenomenon [8], which results to be heavily modulated by blade row interactions. On flat tip configurations, a separation bubble gradually develops from the pressure towards the suction side, effectively reducing the leakage mass flow by establishing a vena contracta effect. A heat transfer peak is generally detected at the flow reattachment location, strongly dependent on the blade thickness-to-gap ratio and on the local flow parameters (Mach and Reynolds numbers). A vortical structure, commonly known as tip leakage vortex, is then generated by the ejection of the spilled fluid in the main stream, accompanied by entropy-generating mixing phenomena.

Alternative tip designs were proposed throughout the years to mitigate the amount of fluid spilled through the tip clearance while limiting the inherent thermal stresses on the rotating and stationary parts [9]. Rimmed solutions, as squealer profiles, aim at amplifying the vena contracta effect while guiding the leakage stream along the blade camberline. A delayed discharge of the by-pass fluid into the main stream is generally promoted. However, despite exhibiting overall superior thermal performance [10], an increased appearance of hot spots is registered in these geometries [11].
As an alternative to squealer solutions, contoured tip profiles are specifically designed to promote the acceleration of the leakage flow up to chocking conditions [12], thus decoupling the amount of spilled fluid from the blade tip loading [13]. Despite the great potential of shape design for tip flows manipulation, very scarce information is available in the open literature on the gap flow physics of alternative tip configurations. Furthermore, the optimization methods and numerical models employed for their design necessitate validation through experimental data collected at engine representative conditions.
Various experimental investigations devoted to the study of the unsteady overtip heat transfer and pressure fields have been performed in linear cascades [14]. Nevertheless, the importance of stator-rotor interactions [15; 16; 17] and rotor-casing relative motion [18] on the unsteady turbine flow physics has been extensively assessed. A lack of reliable experimental data at engine relevant conditions still prevents from a thorough validation of the multiple numerical studies on this topic.
An engine-representative replication of the aerothermal boundary conditions is thus of fundamental importance to characterize the HP stage flow physics and test new blade tip designs. Nevertheless, establishing such a high degree of engine similarity in a laboratory environment considerably increases the complexity of the experimental hardware and challenge the measurement accuracy. Advanced measurement techniques must be adopted in combination with appropriate processing strategies to accurately evaluate the time-resolved flows of distinct tip designs.
The present work pursues a detailed aerothermal characterization of a series of high-performance blade tips operated at scaled engine conditions in the HP turbine test rig of von Karman Institute. Relevant Reynolds and Mach numbers, as well as the gas-to-wall temperature ratios, are achieved. Furthermore the rotating nature of the one-stage rig allows to properly reproduce turbine flows interactions in terms of vane wakes, secondary flows and rotation effects. A rainbow rotor configuration is adopted in order to perform the simultaneous aerothermal testing of the different geometries arranged in distinct sectors. Time-averaged and time-resolved measurements are performed in order to characterize the aerothermodynamics of each sector, allowing a quantitative comparison of the blades performance.
For the current work, a contoured blade tip [19], resulting from a Bezier surface-based parametrization, and a squealer-like geometry, characterized by an optimized pattern of rims and cavities, are compared against a classical squealer design. The two non-conventional blade shapes were designed by a previous optimization effort targeting the maximization of the rotor efficiency and the thermal loads reduction [11].The experimental data are used to explore the effect of the blade tip geometry on the HP stage outlet flow.

2. High Performance Rotor Tips

The high-performance tip profiles tested during this experimental campaign were designed by employing an optimization procedure [11] aimed at the simultaneous increase of rotor aerodynamic efficiency and minimization of tip thermal loads. Steady-state Reynolds-Averaged Navier-Stokes (RANS) simulations were adopted in order to evaluate the performance of each profile. A multi-block unstructured meshing strategy was chosen to grid the computational domain, consisting of a single blade passage of the HP stage, and engine-scaled boundary conditions were imposed.
A parametrization strategy employing 48 control-points Bezier surface mapped onto the blade top surface allowed to create smoothly contoured tip shapes. The resulting carved tip profiles, particularly suited for transonic rotors operating at tight clearances, permitted a substantial limitation of the tip heat transfer by controlling the acceleration of the leakage streams beyond sonic conditions [20]. A second strategy employed a topology optimization, with the tip surface parametrized into a series of block, to enable the design of high-performance rimmed geometries [21]. The best tip designs in terms of rotor efficiency were chosen for the combined experimental-numerical characterization.
Three tip designs are analyzed in this paper, visualized in Fig. 1 from left to right: a conventional

squealer geometry (IN01D), a multi-cavity squealer-like tip (AC06D) and a contoured profile (AC07T). The schematic in Fig. 2 provides a detail of the tip cross-sections along the rotor axial chord.

The AC06D geometry features discontinuous lateral rims, as presented on the left hand side of Fig. 2. The suction side rim presents two cuts extending for about 10% of the rotor axial chord on the rotor leading edge and trailing edge regions. The pressure side wall opens only in the last 30% of the rotor axial chord. An island closed rim is present in the middle of the squealer cavity. The AC07T profile is a three-dimensional contoured surface characterized by a maximum tip gap variation of 3% of the rotor blade span (right-hand side of Fig. 2). According to the original design philosophy, the carved tip does not present any sharp corners. In the front part of the profile, the shaped surface imitates a squealer-like configuration. Considering a stream-wise section of the gap, the tip profile presents in the aft part of the rotor a rounded pressure side knife-edge followed by a progressive opening of the tip channel. The squealer-type profiles are tested at a nominal clearance value of 1.38% of the blade span, while the carved tip geometry operates at a nominal gap of 0.85% of the blade span.

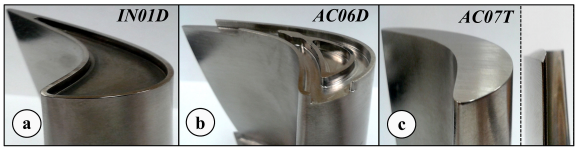

Figure 1: Investigated tip geometries: (a) single squealer, (b) optimized squealer, (c) contoured profile

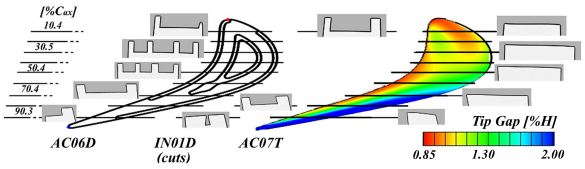

Figure 2: Evolution of the tip profiles along the blade

3. Experimental test rig

The aerothermal characterization of the high performance tips was carried out in the short-duration rotating turbine test rig of von Karman Institute [22]. The test rig (Fig. 3) operates on the principle of a compression tube and allows testing a high-pressure turbine stage at a larger scale while preserving the actual engine Mach and Reynolds numbers [23]. For this particular campaign the test section consists of a high-subsonic uncooled stage, counting 34 vanes and 48 rotor blades. The rotating nature of the cascade ensures the correct reproduction of stator-rotor interactions and rotation effects, of primary importance for the establishment of relevant tip flow phenomena. Representative gas-to-wall temperature ratios (1.5-1.6) are replicated thanks to the transient testing strategy, generating engine-relevant thermal fields and heat-transfer distributions in the HP stage.

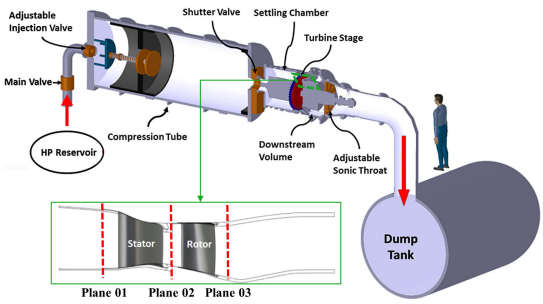

Figure 3: CT-3 Short Duration HP Turbine Test Rig

4. Operating conditions

One single flow regime, representative of engine cruise conditions, was considered for the present test campaign (Table 1). The rotor was operated at a thermodynamic speed of 281, engine-scaled thermodynamic flow conditions were respected and the nominal stage pressure ratio was set to 2.2. Endwall pressure taps, together with mid-span reference pressure and temperature probes, served to monitor the turbine operation throughout the test. Inlet radial profiles of total temperature, total pressure and turbulence intensity measured half axial chord upstream of the NGV leading edge plane (Plane 01) are presented in Fig. 4. These distributions, plotted in the form of experimental points complemented by fitting curves, served as boundary conditions for the related numerical studies.

All the plots are normalized by their mid-span values reported in Table 1.

Table 1: Test Rig Operational Specifications

Parameter	Mean	Repeatability	Units
P_{01}	$1040 \cdot 10^5$	±1.5%	mbar
T_{01}	$436.3 \cdot 10^5$	±4%	mbar
$P_{01}/P_{s3,h}$	$2.196 \cdot 10^5$	±0.5%	mbar
$P_{01}/P_{s3,t}$	$2.222 \cdot 10^5$	±0.8%	mbar
Re_{out,C_x}	$2.76 \cdot 10^5$	-	
$Mach_{r,out}$	0.78	-	
N	5925	±0.3%	rpm

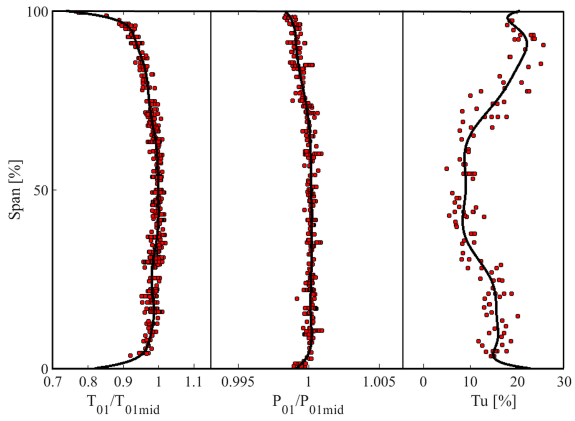

Figure 4: Inlet flow conditions

5. Rainbow rotor setup

The diverse high-performance tip profiles are tested simultaneously in order to minimize the test-to-test discrepancies caused by any variability in the rig operating conditions. A "rainbow rotor" setup is adopted (Fig. 5), arranging the 48 rotor airfoils in seven different sectors on the HP rotor. Each sector consists of 6 to 7 blades of equal tip seal geometry in order to assure flow periodicity. Five high-performance squealer-like and one contoured tip profile are investigated, with five sectors running at a nominal clearance of 1.38% of the blade span and the remaining two at a "tight" value of 0.85%. The present paper focuses on the analysis of two high performance geometries (AC06D / AC07T) compared to the baseline squealer profile (IN01D).

The rainbow rotor strategy, besides drastically reducing the costs of the campaign, is highly time efficient and assures a consistent and precise performance comparison between the optimized blade tip seals. The multiple clearance effect is investigated by coupling the time-resolved aerothermal flow information with time-accurate casing-to-tip distance measurements [24].

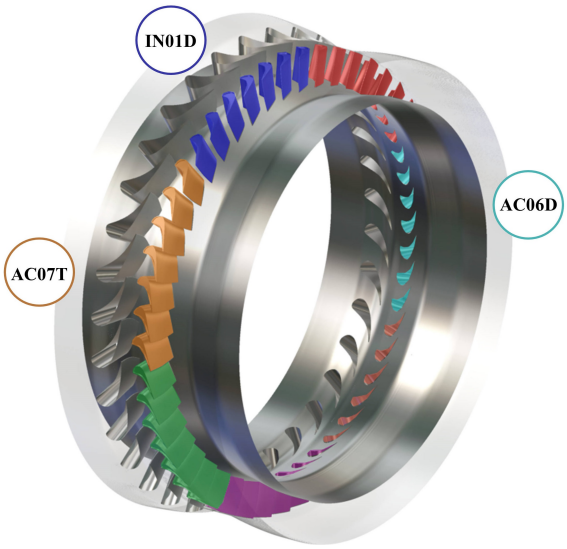

Figure 5: Rainbow Rotor Setup

6. Measurement Setup

The main objective of the experimental test campaign is the quantitative evaluation of the flow aero-thermodynamics related to each of the seven sectors. An accurate aerothermal comparison of the different blade seals requires reliable, time-resolved information on the pressure and temperature fields. Fast response instrumentation is needed to correctly detect the blade-to-blade flow variations at frequencies in the order of 5 kHz. Time-averaged aerothermal measurements are used for the characterization of the overall turbine stage characteristics (i.e. boundary conditions, average casing pressure distribution, thermal fields).
The flow information is complemented with real time monitoring of the blade passage event and tip clearance size. Proximity sensors ([24]) provide the gap time-resolved measurement at three different positions around the annulus and five axial stations

on the rotor chord.
The rainbow rotor approach allows to detect sector-to-sector differences in total pressure with an accuracy 0.02% of P01 (0.1 mbar).

6.1. Stage Outlet Flow Field

The measurement plane at the outlet of the turbine stage lies half axial chord downstream of the rotor blades trailing edge. The time-average flow field is characterized by means of a slow-response four-head Kiel pitot rake, two pneumatic five-hole probes and a thermocouple rake, periodically displaced in radial direction to retrieve the quasi-steady outflow profiles. Fast-response single-hole pressure probes are employed in virtual-three-hole mode for the characterization of the time-varying flow angle, Mach number and static/total pressure.



Figure 6: Outlet Plane Aerothermal Probes

This paper presents the time-resolved measurements performed by two double-head Kulite sensor rakes are employed for the characterization of the outlet total pressure distribution. The fast-response sensors (XCQ-062 25A, 1.7 mm external diameter), directly exposed to the flow, are covered by a thin elastomer that assures a good protection and negligible influence on the frequency response (Fig.6). The probes are displaced in both raidal and pitchwise direction, ultimately providing a measurement matrix which covers one entire vane passage and allows to entirely resolve the HP stage spatial periodicity (Fig.7). The number of measurement locations is chosen in order to allow an appropriate spatial resolution of the outlet flow, generally affected by large unsteady interaction effects which produce significant radial and circumferential gradients.

6.2. Signal Acquisition

In the case under investigation, the outlet flow field is affected by a combination of low and high frequency flow oscillations. The analog pressure signals

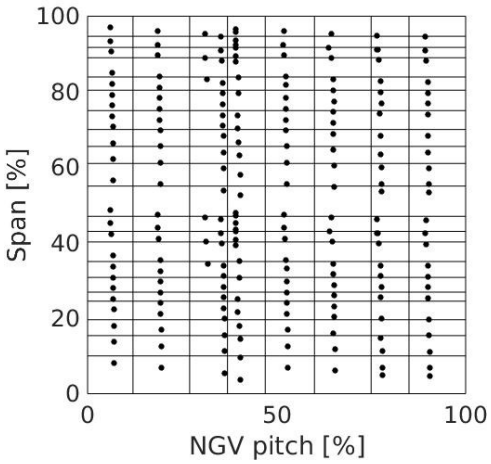

Figure 7: P03 Measurement Matrix

are therefore split in two components to allow the resolution of fluctuations at both the time scale of the blowdown test (0.5 s) and of the blade passing events (200 s).
A 500 Hz low pass filter is adopted for the low frequency signal, which is then sampled at 10 kHz for 10 seconds at 16-bit resolution. The high-bandwidth signal is conditioned through an analog band-pass filter allowing the information transfer in the range between 60 Hz and 200 kHz. The AC component is further amplified by a factor of 10 before being sampled on a 16-bit data acquisition system at 1 MHz for 3 seconds. With such sampling frequency, 210 measurement points per blade passage are taken. This is equivalent to a spatial sampling of 0.25 mm over the rotor tip area. The static gain and the frequency response of the entire measurement chain was calibrated from 0 Hz to 1 MHz to generate the de-boosting functions used for the signal data reduction.

6.3. Data reduction

The deterministic and random fluctuations characterizing the outlet flow unsteadiness are isolated by applying an ensemble averaging procedure [25]. While the random component is due to turbulent and revolution-to-revolution flow phenomena, the deterministic component is strictly periodic with the blade passage event. In order to account for the flow periodicity imposed by the rainbow rotor configuration, the phase-locked averaging is operated over a complete disc revolution.

The PLA of a typical unsteady static pressure signal is presented on the top of Fig.8. The raw unsteady data are averaged over 23 rotor revolutions corresponding

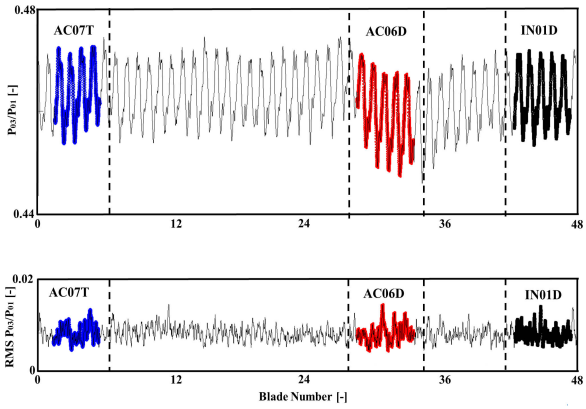

Figure 8: Data reduction technique: PLA applied to tmie-resolved P03 signal

to a time window of 250 ms. The unsteadiness uncorrelated with the blade period is quantified by the root-mean-square (RMS) of the raw signal against the time-resolved PLA, calculated with a 95% confidence interval. A sector-bounded analysis is further performed on the phase-locked data by pitch averaging the information related to each single sector. The instantaneous rotor angular position is measured by optical shaft encoders, ensuring an accuracy of 0.25% of a rotor pitch at a rotational speed of 5900 rpm. In order to exclude all sector-to-sector flow interactions and ensure the highest flow periodicity between rotor channels, the outer passages of each sector are removed from the averaging procedure. Thus, the sector average is performed considering five blade passages at each revolution, corresponding to 23 x 5 = 115 blade periods.

7. Results

7.1. Time-Average Total Pressure

A sector-bounded analysis of the time-resolved pressure distributions collected in Plane 03 is performed, allowing the characterization of each tested profile. The pitchwise-averaged time-average radial profiles of total pressure are presented in Fig. 9 as normalized by the inlet total pressure value. These distributions highlight a similar trend in the simple squealer (IN01D) and carved (AC07T) tip up to 70% of the airfoil span. In the same height interval, the high-performance rimmed profile (AC06D) shows a slightly lower average value, with an offset amounting to 0.3% of P_{01} (3 mbar).

At 70% of the span the three profiles show a discontinuity in the pressure distribution, which may be attributed to the upper passage vortex. In the tip region the two squealer tips present first an important pressure drop of 10-15 mbar around 87% of the blade height, followed by a maximum around 95%. This effect denotes the position of the tip leakage vortex and appears slightly attenuated in the carved geometry.

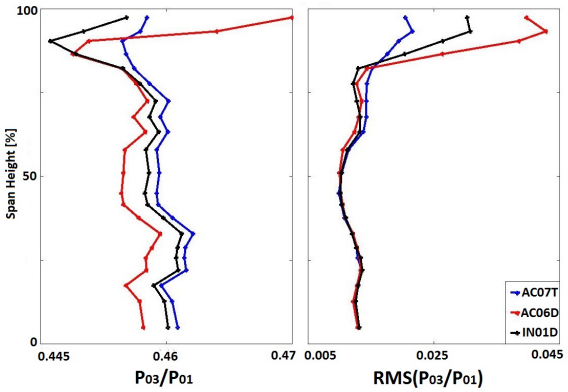

Figure 9: Radial Profiles of Normalized P_{03} (left) and RMS(P_{03}) (right)

The random unsteadiness related to the P_{03} signal is presented on the right side of Fig. 9. The first 70% of the blade height is characterized by a low value of RMS for the three different sectors, showing no dependency of the random flow fluctuations on the tip geometry. In the tip region, on the other hand, higher RMS intensity peaks are shown by the rimmed tips at 90% f the span, where the tip leakage vortex is located. In particular, tip AC06D presents the highest average unsteadiness in this area, probably due to the open rim tip geometry. The time-mean total pressure contours are presented in the absolute frame of reference in Fig. 10, normalized by the average total pressure at the stage inlet. The radial gradients observed in this kind of plot are to be ascribed to both stator- and rotor-related flow structures. With respect to this, a generally lower pressure level can be observed in the tip area, where vortical structures related to the tip leakage phenomenon are present. In the case of AC06D, important pressure peaks are registered in the upper endwall proximity, probably due to the rim apertures at the leading and trailing edge of the blade. A general lower pressure level is, on the other hand, registered in the first 70% of the span, denoting a larger general expansion operated on the fluid by this profile with respect to the others.

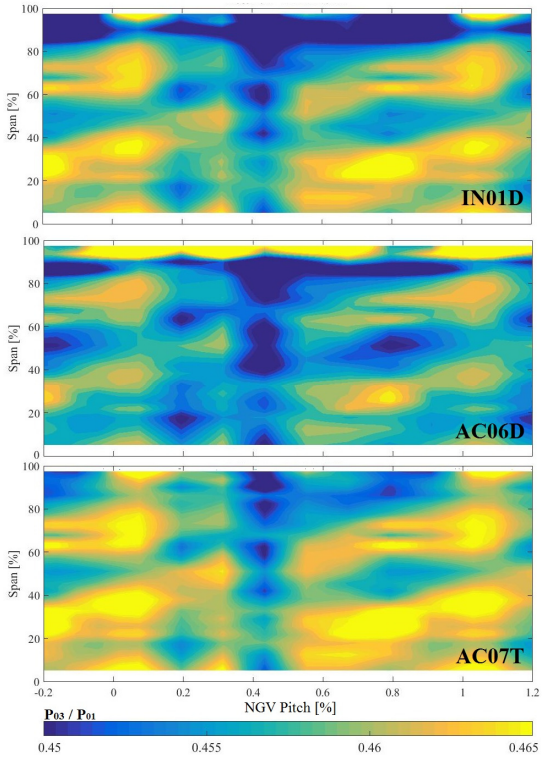

Figure 10: Time Averaged Total Pressure Contours

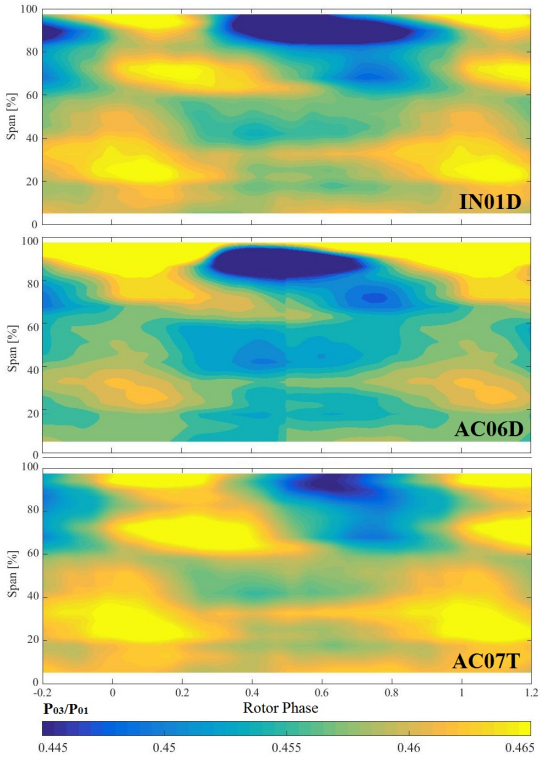

Figure 11: Time Resolved Total Pressure Contours

Only NGV-related structures, as vane wakes and secondary flows, contribute to the time-mean pitchwise gradients in this contour.

7.2. Time-Resolved Total Pressure

In Fig. 11, the time-resolved total pressure distributions are presented as a function of the rotor blade passage. Large pressure fluctuations are detected in the near-tip area, indicating the presence of tip-leakage and upper-passage vortices. Tip AC06D is characterized by higher gradients in this zone, while the carved geometry (AC07T) seems to be the least affected by flow fluctuations in the upper endwall proximity. This effect resulted already clear from the pitchwise averaged pressure distributions, and may be explained also by the lower clearance value of this particular tip profile with respect to the squealer geometries. The midspan and near-hub area of all the three profiles are equally affected by total pressure gradients which may be attributed to the presence of secondary flow structures affecting the rotor passage flow.

7.3. Phase-Time Analysis

The time-resolved flow field downstream of the HP stage is dominated by the rotor features (i.e. wakes and secondary flows) and by vane-rotor interactions. In order to clarify the importance of the various periodic flow features, a phase-time visualization of the pressure information is generated. As a relevant example, the phase-time contours of total pressure of blade AC06D at 89.7% span are proposed in Fig. 12. The stage periodicity (spatial and temporal) is fully represented in this contour plot by considering five vanes (vertical direction) and five rotor passages (horizontal axis). Similarly, the RMS distribution is represented in Fig. **??**, indicating the random unsteadiness affecting the flow at the same blade span.

The horizontal patterns in these plots are due to stationary structures, i.e. they are uniquely related to the vane blades. The most evident inclined periodic flow feature, propagating from the bottom to the top in both space and time, is represented by the rotor wake. This latter is periodically modulated, in space and time, by the interaction with the vane features. It is therefore possible to distinguish several types of flow non uniformities affecting the outlet pressure distribution, which will be referred to as modes.

By following the theory proposed by [26], it is possible to retrieve the origin of each mode in a stator-only,

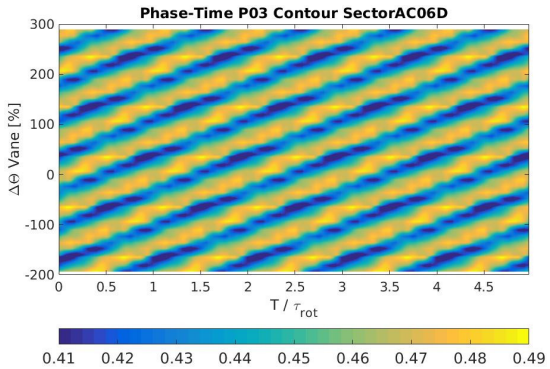

Figure 12: Phase-Time P_{03} Contours at 89.7% Span (AC06D)

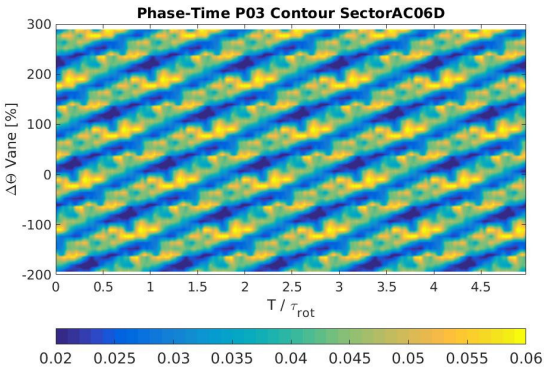

Figure 13: Phase-Time RMS(P_{03})Contours at 89.7% Span (AC06D)

rotor-only or vane-rotor interaction phenomenon, detecting and quantifying the most important sources of unsteadiness.
The decomposition is performed by considering the pressure field as a superposition of infinite circumferential rotating structures, defined as angular modes (m_θ). Each angular mode presents a number of lobes equal to a linear combination of the number of vane and rotor blades of the HP stage, as from eq. 1.

$$m_\theta(n,k) = n \cdot N_R + k \cdot N_V \tag{1}$$

The angular position of these circumferential patterns changes in time according to a propagation equation, allowing to define a rotational speed ω_{m_θ} characterizing each spinning mode.

$$\omega_{m_\theta}(n,k) = \Omega \cdot n \cdot N_R / m_\theta; \tag{2}$$

Following this definition it is possible to detect modes which rotate in the same direction of the rotor (positive inclination in Fig. 12) and modes which rotate in opposite direction (negative inclination in Fig. 12).
In order to represent the evolution in time of the flow unsteadiness, a Fast Fourier Transform is applied in azimuthal direction (i.e. along θ_{vane}) to the fluctuating component of the phase-time plot for each instant in time. This analysis is performed considering a signal sampling frequency equal to the number of samples per rotor revolution, allowing the identification of the azimuthal modes m_θ corresponding to the definition given in eq. 1. The resulting spectrogram (AC06D profile) is presented in Fig. 13.

The spatial modes corresponding to the first harmonics of the blade passing frequency, i.e. $m_\theta(1,0)$=48 and $m_\theta(2,0)$=96, appear clearly visible

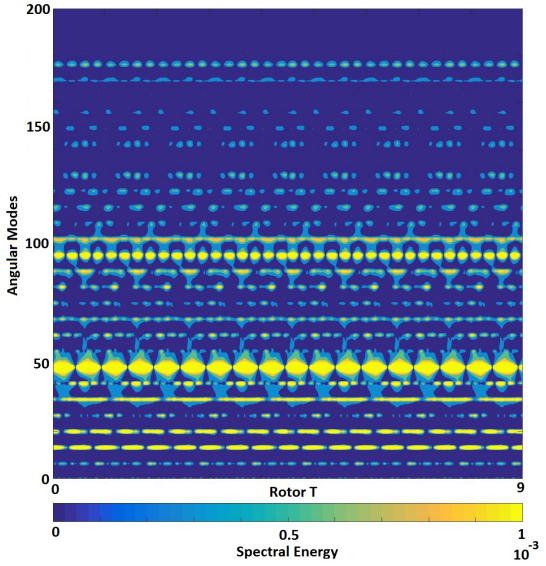

Figure 14: Phase-Time RMS(P_{03})Contours at 89.7% Span (AC06D)

in the plot. As expected, the latter presents a double number of lobes with respect to the former. The stationary influence of the stator-related flow structures, on the other hand, is visible at $m_\theta(0,1)$=34 , $m_\theta(0,2)$=68 and $m_\theta(0,3)$=102, with the second harmonic presenting a smaller amplitude compared to the others.

Following the procedure proposed by [27],in order to identify the temporal modes m_t of each spatial mode m_θ, a further Fast Fourier Transform is applied in the time (i.e. horizontal) direction to the spectrogram exemplified in Fig. 13. It is therefore possible to define a relationship between spatial and temporal

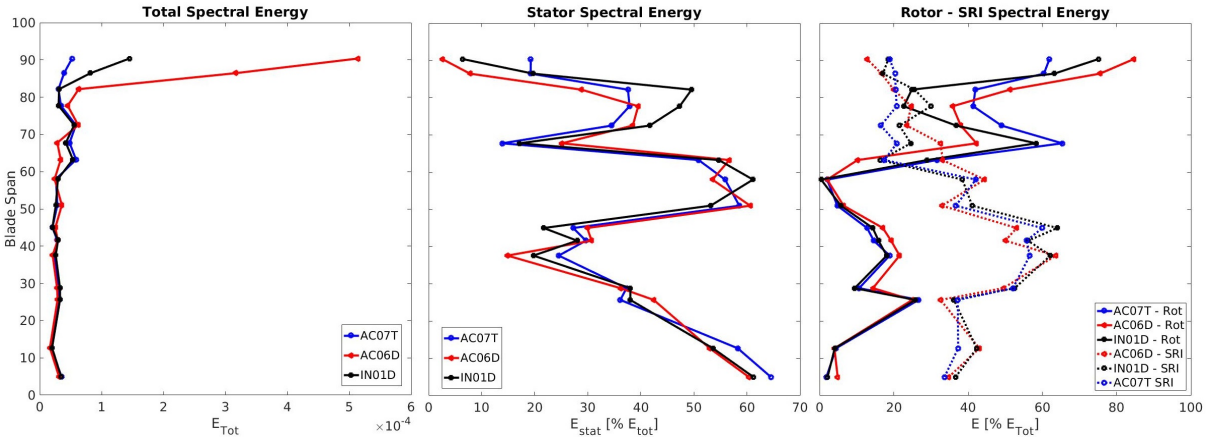

Figure 15: Radial profiles: total (left), stator-only (center) and rotor-only vs. SRI (right) spectral energy

modes (eq. 3).

$$m_t = m_\theta - k \cdot N_V \tag{3}$$

An analysis of the flow in a spatial-/temporal-frequency domain is therefore possible, with each particular flow periodicity represented by a specific set of (m_θ,m_t). For each of these couples, a rotational speed is defined as from eq. 4.

$$\omega_{m_\theta,m_t} = \Omega \cdot m_t/m_\theta \tag{4}$$

The modes which uniquely derive from the stator-rotor interactions can therefore be isolated by subtracting to the modal matrix all those components which are steady in either the stator or rotor frame of reference. Following the definition given in eq. 4, these modes will present rotational speed equal to zero and Ω respectively, i.e. $m_t = 0$ and $m_\theta = m_t$. A computation of the SRI spectral energy can now be performed by applying eq. 5 to the SRI modal matrix.

$$E_{SRI} = \sum_{m_\theta,m_t} A^2_{m_t,m_\theta} \tag{5}$$

where A_{m_t,m_θ} represents the amplitude of the related mode. Iterating this procedure at different radial positions and for different types of modes, it is possible to compute the distributions in Fig. 15

A temporal Inverse Fourier Transform is applied to the SRI modal matrix uniquely, allowing the visualization of the related spatial modes as in Fig. 16.

8. Conclusions

This paper presented the measurement setup employed for the aerodynamic characterization of the flow field downstream of a one-stage HP turbine test rig. The transient character of the facility allows to correctly reproduce engine-like conditions for the duration of a test, typically ranging between 250 and 300 ms.

The time varying pressure distribution was investigated over an entire vane pitch in order to fully resolve the stage spatial and temporal periodicity. For the present campaign, 6 different optimized blade seal geometries were tested at two values of clearance. A ”rainbow rotor” setup was employed in order to simultaneously test the different blade tips performance. This paper presents the aerodynamic characterization of three of them: a classical squealer profile, a high-performance rimmed tip and a carved profile.

Time-average and time-resolved total pressure contours are presented, in order to highlight the influence of the various tip geometries on the outlet flow. A modal decomposition analysis is proposed in order to separate the different contributions that modulate the unsteadiness of the stage outflow. The vane-, rotor- and stator/rotor-periodicities are identified. The energy content of each mode type is evaluated over the entire blade span for the three profiles. This quantitative analysis of the total pressure distribution, performed in the frequency domain, allows to classify the contribution of each unsteadiness source. A further analysis of the results, complemented by time-resolved numerical computations, will ideally

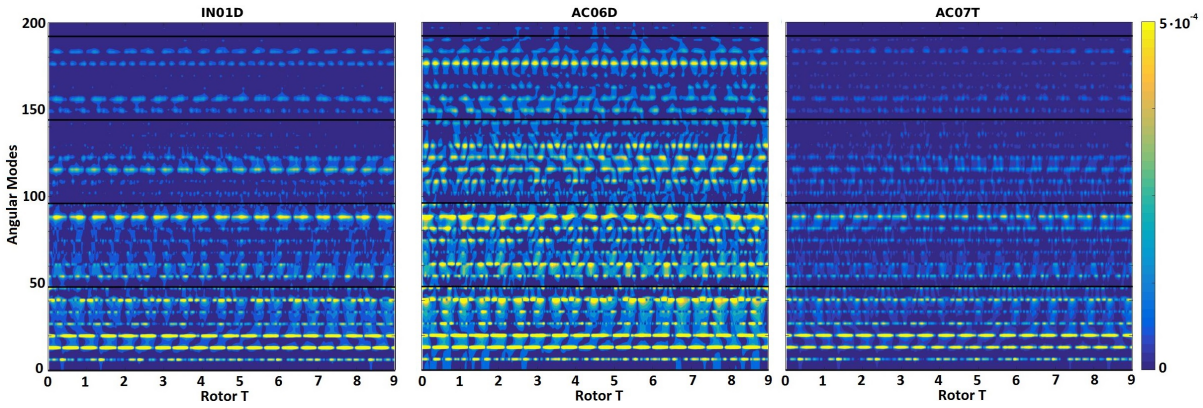

Figure 16: Total Pressure Azimuthal FFT Spectrograms

permit to link these results to the physics of the flow field. This research study should ultimately provide a quantitative assessment of the contribution of each mode to the overall stage aerodynamic losses.

References

[1] J. P. Bindon, Pressure distributions in the tip clearance region of an unshrouded axial turbine as affecting the problem of tip burnout, in: ASME 1987 International Gas Turbine Conference and Exhibition, American Society of Mechanical Engineers, 1987, pp. V001T01A085–V001T01A085.

[2] J. D. Denton, Loss mechanisms in turbomachines, in: ASME 1993 International Gas Turbine and Aeroengine Congress and Exposition, American Society of Mechanical Engineers, 1993, pp. V002T14A001–V002T14A001.

[3] T. Booth, Tip clearance effects in axial turbomachines: Importance of tip clearance flows in turbine design, Von Karmin Institute for Fluid Dynamics Lecture Series 5 (1985) 15–19.

[4] T. Booth, P. Dodge, H. Hepworth, Rotor-tip leakage: Part ibasic methodology, Journal of Engineering for Power 104 (1) (1982) 154–161.

[5] R. S. Bunker, A review of turbine blade tip heat transfer, Annals of the New York Academy of Sciences 934 (1) (2001) 64–79.

[6] N. Cumpsty, A. Heyes, Jet propulsion, Cambridge University Press, 2015.

[7] M. Collins, K. Chana, T. Povey, Improved methodologies for time-resolved heat transfer measurements, demonstrated on an unshrouded transonic turbine casing, Journal of Turbomachinery 138 (11) (2016) 111007.

[8] V. Shyam, A. Ameri, J.-P. Chen, Analysis of unsteady tip and endwall heat transfer in a highly loaded transonic turbine stage, Journal of Turbomachinery 134 (4) (2012) 041022.

[9] T. Hofer, T. Arts, Aerodynamic investigation of the tip leakage flow for blades with different tip squealer geometries at transonic conditions, in: ASME Turbo Expo 2009: Power for Land, Sea, and Air, American Society of Mechanical Engineers, 2009, pp. 1051–1061.

[10] F. Heyes, H. Hodson, G. Dailey, The effect of blade tip geometry on the tip leakage flow in axial turbine cascades, in: ASME 1991 International Gas Turbine and Aeroengine Congress and Exposition, American Society of Mechanical Engineers, 1991, pp. V001T01A052–V001T01A052.

[11] C. De Maesschalck, S. Lavagnoli, G. Paniagua, T. Verstraete, R. Olive, P. Picot, Heterogeneous optimization strategies for carved and squealer-like turbine blade tips, Journal of Turbomachinery 138 (12) (2016) 121011.

[12] V. Shyam, A. Ameri, Comparison of various supersonic turbine tip designs to minimize aerodynamic loss and tip heating, in: ASME 2011 Turbo Expo: Turbine Technical Conference and Exposition, American Society of Mechanical Engineers, 2011, pp. 887–895.

[13] Q. Zhang, L. He, Tip-shaping for hp turbine blade aerothermal performance management, Journal of Turbomachinery 135 (5) (2013) 051025.

[14] P. Newton, G. Lock, S. Krishnababu, H. Hodson, W. Dawes, J. Hannis, C. Whitney, Heat transfer and aerodynamics of turbine blade tips in a linear cascade, Journal of Turbomachinery 128 (2) (2006) 300–309.

[15] R. Dénos, G. Paniagua, Effect of vane-rotor interaction on the unsteady flowfield downstream of a transonic high pressure turbine, Proceedings of the Institution of Mechanical Engineers, Part A: Journal of Power and Energy 219 (6) (2005) 431–442.

[16] R. Miller, R. Moss, R. Ainsworth, C. Horwood, Time-resolved vane-rotor interaction in a high-pressure turbine stage, Transactions-American Society of Mechanical Engineers Journal of Turbomachinery 125 (1) (2003) 1–13.

[17] S. Krishnababu, P. Newton, W. Dawes, G. D. Lock, H. Hodson, J. Hannis, C. Whitney, Aerothermal investigations of tip leakage flow in axial flow turbinespart i: Effect of tip geometry and tip clearance gap, Journal of Turbomachinery 131 (1) (2009) 011006.

[18] S. Thorpe, S. Yoshino, R. Ainsworth, N. Harvey, An investigation of the heat transfer and static pressure on the over-tip casing wall of an axial turbine operating at engine representative flow conditions.(ii). time-resolved results, International journal of heat and fluid flow 25 (6) (2004) 945–960.

[19] C. De Maesschalck, S. Lavagnoli, G. Paniagua, Blade tip shape optimization for enhanced turbine aerothermal performance, in: ASME Turbo Expo 2013: Turbine Technical Conference and Exposition, American Society of Mechanical Engineers, 2013, pp. V03CT14A011–V03CT14A011.

[20] C. De Maesschalck, S. Lavagnoli, G. Paniagua, Blade tip

carving effects on the aerothermal performance of a transonic turbine, Journal of Turbomachinery 137 (2) (2015) 021005.
[21] R. Olive, S. Lavagnoli, C. G. M. De Maesschalck, G. Paniagua, Method for modelling a bathtub of a blade, uS Patent App. 15/324,198 (Jul. 13 2017).
[22] C. Sieverding, T. Arts, The vki compression tube annular cascade facility ct3, in: ASME 1992 International Gas Turbine and Aeroengine Congress and Exposition, American Society of Mechanical Engineers, 1992, pp. V005T16A001–V005T16A001.
[23] G. Paniagua, C. Sieverding, T. Arts, Review of the von karman institute compression tube facility for turbine research, in: ASME Turbo Expo 2013: Turbine Technical Conference and Exposition, American Society of Mechanical Engineers, 2013, pp. V03CT14A031–V03CT14A031.
[24] S. Lavagnoli, C. De Maesschalck, V. Andreoli, Design considerations for tip clearance control and measurement on a turbine rainbow rotor with multiple blade tip geometries, Journal of Engineering for Gas Turbines and Power 139 (4) (2017) 042603.
[25] B. Lakshminarayana, Fluid dynamics and heat transfer of turbomachinery, John Wiley & Sons, 1995.
[26] J. M. Tyler, T. G. Sofrin, Axial flow compressor noise studies, Tech. rep., SAE Technical Paper (1962).
[27] N. Courtiade, X. Ottavy, N. Gourdain, Modal decomposition for the analysis of the rotor-stator interactions in multistage compressors, Journal of Thermal Science 21 (3) (2012) 276–285.

LIF Temperature field Measurement for Internal Forced Convection Blade Cooling

Gian Luca Gori

Turbomachinery and Propulsion Department, von Karman Institute for Fluid Dynamics, Belgium, gian.luca.gori@vki.ac.be

Supervisor: Tony Arts

Professor, Turbomachinery and Propulsion Department, von Karman Institute for Fluid Dynamics, Belgium, arts@vki.ac.be

Abstract

Internal Cooling technology for Gas Turbines, although supported by wide literature, still presents possible important improvements. The classical CFD codes, based on constant Pr_t and isotropic turbulence, present a limited fidelity for the convective heat transfer prediction (at best 10-15%). The innovative contribution of flow temperature data by Laser-Induced Fluorescence will bring important information and likely help the development of the current numerical tools.

Keywords: turbomachinery, convective heat transfer, internal cooling, laser-induced fluorescence

1. Introduction

1.1. Internal cooling

The present research on cooling channels focuses on an aeronautical application (gas turbine), but is of definite interest to many other fields of engineering (oil industry, automotive, nuclear environments ...). The performance, in terms of thermal efficiency and specific power of a gas turbine cycle, increases with the Turbine Inlet Temperature ($\sim$ 1600 °C). The limits are set by the blades and endwalls material resistance ($\sim$1000 °C) against thermal and mechanical loads. The life time of these components will increase by using efficient cooling techniques, cutting down the high costs for the parts replacements. An example of an air-cooled blade and its cross section is given in Fig. 1. A major contribution to the heat extraction is given by forced convection in internal passages.

The main objective of internal cooling channels is to maximize the wall heat transfer while keeping the channel pressure drop as low as possible. Initially designed with smooth walls, their surface has rapidly been equipped with various obstacles to increase the thermal exchange area and the local mixing. The resulting flow field is strongly 3D and unsteady [1] [2]; it becomes even more heterogeneous when the channel is put into rotation (rotor blades application)[3]. The strong assumptions of isotropic turbulence and constant *turbulent Prandtl number* Pr_t limit the accuracy of the heat transfer prediction (at best 10-15%) by commercial *RANS* simulations. The lack of experimental data due to the complexity and the availability of representative facilities, certainly, does not help for numerical improvements. The present research wants to contribute at providing high quality and high resolution experimental data acting directly on the causes of the CFD low fidelity.

Unlike most of the investigations available in literature, not only the wall heat transfer and velocity fields, but also the flow temperature distribution will be the object of this experimental study. Although for velocity and surface heat transfer measurements, Particle Image Velocimetry (PIV) and Liquid Crystal Thermography (LCT) are already consolidated and largely used techniques [4], a few Cold Wire measurements were strongly dependent on the position of the probe [5]. They are also able to measure only temperature fluctuations related to the small vorticies. Therefore, Laser-Induced Fluorescence (LIF) has been selected for planar and non-intrusive temperature measurements.

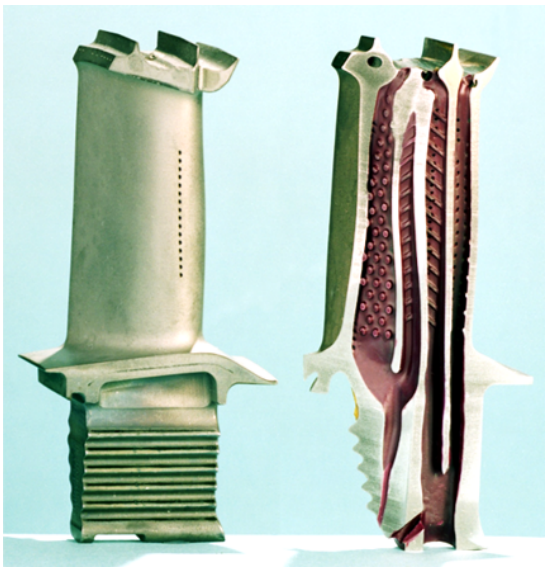

Figure 1: An air-cooled HP turbine blade and its cross-section.

1.2. Laser-Induced Fluorescence

The technique is a spectroscopic method based on the spontaneous emission of certain molecules after the excitation by a laser light. Never applied for internal cooling research so far, it needs to be developed for this specific application. Neglecting the fluorescence re-absorption and the Beer's attenuation, a simplified expression of the signal intensity I_f in function of the emitted wavelength λ and the absolute temperature T is given by Eq. 1 [6] :

$$I_f(\lambda) = K_{opt}(\lambda)K_{spec}(\lambda)V_c I_1 C e^{\beta(\lambda)/T} \quad (1)$$

where K_{opt} is an optical constant, V_c the measuring volume, I_1 the incident laser intensity, C the molecular concentration of the fluorescent tracer, K_{spec} and β spectroscopic constants of the target molecule. More details on the different contributions and parameters dependencies are presented in ref. [7]. The final output, registered by a detector, is an image with a signal given by the integral of the expression in Eq. 1 all over the spectra.

The signal obtained by a single camera, therefore, does not depend only on temperature but also on the intensity of the laser excitation and the concentration of the tracer. Information of the local temperature might be retrieved by the so called single-line approach. However, problems occur if the concentration and/or the laser intensity vary in space and/or in time and in the case these variations cannot be neglected or properly taken into account. The latter issues disappear when two or more ground states are observed. The method is called multi-line approach. It requires two or more excitations and/or two or more spectral channels. A double detection and single excitation, the so-called two-color method, is normally a good compromise for keeping the set-up as simple as possible [7]. Compared to dual-excitation (e.g. [8]), two-color LIF requires only one laser source [9]. The ratio calculated between the intensity recorded of two different spectral bands cancels out the dependence of I_1 and C (Eq. 2).

$$R_f(T) = \frac{I_{f,1}}{I_{f,2}} = \frac{K_{opt,1}}{K_{opt,2}} exp\left(\frac{\beta_1 - \beta_2}{T}\right) \quad (2)$$

The $I_{f,1}$ and $I_{f,2}$ represent the intensities of the two spectral bands observed. A temperature calibration is still required for determining the constants $K_{opt,1}/K_{opt,2}$ and $(\beta_1 - \beta_2)$. The selection of these two spectral bands defines respectively the parameters β_1 and β_2. As discussed in [10], in order to obtain a high temperature dependence of R_f, the difference $(\beta_1 - \beta_2)$ should be as large as possible. Although the two-color approach looks always more convenient than one-color measurements, the relative uncertainty at least doubles due to the lower signals and temperature dependence [11]. Therefore, it is important to evaluate the real need of two ground states, especially looking at the uniformity of the fluorescent molecule within the field of view.

If the flow under investigation does not contain any fluorescent molecules, a proper dye must be added to the main flow. The objective is to create a well-mixed flow which allows the measurements without modifying the physics. For heat transfer and temperature determination both *Re* and *Pr* numbers of the experiments should match the real operating ones. Although *Re* can be easily adjusted by modifying the flow velocity, *Pr* is a property of the working fluid. Different *Pr* cause not only changes on the mean temperature profile but also on the temperature fluctuations [12]. For the specific application of air-cooled HP turbine blades, the working fluid is represented by part of air bled from the compressor. Although in literature liquid-phase PLIF is more developed than gas-phase PLIF, the latter is preferable in order to represent correctly the same physics. Toluene and acetone are the most used tracers for gas-phase LIF thermography (e.g. [13][14][15][16]). The air-tracer mixture *Pr* has been studied numerically by means of the NASA CEA algorithm [17]. Although the code is based on chemical equilibrium, the manual provides the relationship

to compute the mixture properties assuming no reactions between the selected species. Acetone can reach a maximum molecular concentration about 25% in air at ambient conditions. Its influence on Pr is more important than the one of toluene. However, in saturation conditions, variations are lower than 5% and with 15% of concentration (already hard to achieve with a bubbler in a continuous flow) lower than 2%. On the other hand, at ambient conditions toluene has a maximum concentration of about 3% and the amount of tracer inserted into the flow is not able to modify considerably the value of Pr (less than 1%).

Acetone is a ketone and started to be used for its high vapor pressure [18], its low toxicity and low cost [19]. The absorption (between 200 and 350 nm) was measured in 1992 by Lozano [20] and later in 1996 by Thurber [8]. The emission, instead, occurs between 300 and 550 nm [18]. On the other hand organic molecules (as toluene) have a very high signal compared to the one produced by ketones [21]. In particular, toluene has been characterized later in [22] [23] in terms of the absorption (240-290 nm) and the fluorescence emission (250-350 nm) as well as its oxygen quenching (not present for acetone). The red shift of toluene made this tracer also suitable for two-color thermography. For both acetone and toluene, the time required for the vapor sublimation is relatively short which makes the seeding procedure simple [24] [15]. More details of the characteristics of fluorescent tracers used for gas-phase thermography are provided in ref. [25].

Acetone vapor mixed with air was selected as the working fluid for the preliminary study for simplicity as well as for the aforementioned advantages. Toluene present possible re-absorption of the emitted light, quenching by oxygen and deeper UV fluorescence spectra. However, the discussion in section 2.3 will show the low relevance of this drawbacks compared to the possible improvements.

2. Preliminary study

The first studies are performed in a static cell built to investigate suitable LIF tracers (Fig. 2). The test section is $50x50mm^2$, $90mm$ height. A small tap in the bottom allows to introduce the tracer with a syringe. On top of that a fan is placed (black rectangle) in order to mix properly the air with the vaporized tracer. The pressure was monitored by a water manometer to estimate the vapor concentration inside the cell. Four thermocouples probes were installed to monitor the temperature at the same high of the laser beam. The top part is composed by five aluminum walls. The four lateral walls are provided with quartz windows for the laser and the cameras optical accesses. Each of them are sealed with two o-rings and a thin screwed plate. All the external walls were thermally insulated by a 15 mm thickness foam. Higher temperatures are achieved by heating up the bottom aluminum plate with a heat gun.

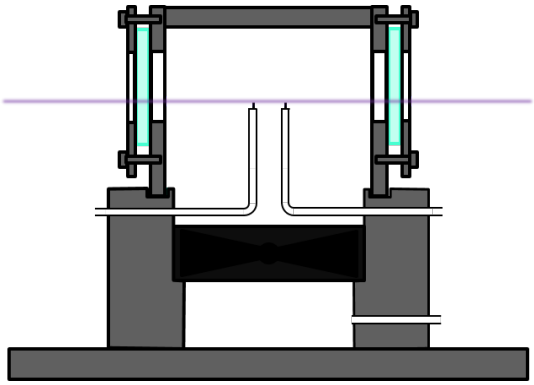

Figure 2: Sketch of the measurement cell section.

2.1. Two-color acetone calibration measurements

The objective of the present campaign is to link an intensity ratio R_f (Eq. 2) to the assumed uniform temperature inside the cell. According to some available data of the emission spectra of acetone and toluene, two-color acetone LIF thermography is performed. Different filters available in the market have been tested numerically. The two spectral bands were chosen in the way suggested in [10] to maximize the temperature sensitivity ($\beta_1 - \beta_2$). The SHX350 and the XUL0385 filters from Asahi Spectra®showed the best performance and were used in the present experimental campaign.

The two-color technique, as mentioned in section 1.2, requires two detectors (Lavision®Imager Intense) and one excitation source (Fig. 3). The latter was provided by a Nd:Yag laser (Quantel®Big Sky Laser) with 266 nm wavelength pulses of 33 mJ and 532 nm wavelength pulses of 180 mJ. Two dichroic mirrors at 45° allow to decrease the green component of the beam entering in the test section. Acetone, as the majority of organic molecules, does not feature absorption at 532 nm and additional high energy light only produces undesirable reflections. After the dichroic mirrors the beam passes through a fused-silica spherical lens in order to focus the beam in the center of the cell. The two cameras should observe

as well as possible the same area of interest. In order to decrease the number of degrees of freedom and to use only one camera lens, the configuration is the one shown in Fig. 3. The light coming from the investigated area is focused by an UV 100 mm lens and splitted by a ND filter positioned at 45°. The two colored filters are mounted directly in front of the 2 sensors. Together with the long pass filter, the related camera is additionally provided with a stopband filter (500-600 nm) in order to cut down the remaining green laser scattered light. A bellow mounted between the splitter cage and one camera allows the proper focusing of both detectors at the same time. A series of 400 pictures are taken at a 3 Hz repetition rate for each investigated temperature inside the cell. Binning of 8 x 8 pixels is used to maximize the signal. In the same conditions an image of target plate for the spatial calibration of the cameras and the background (image without tracer) are acquired.

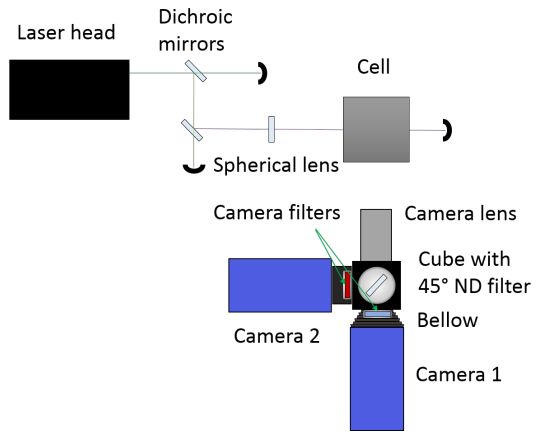

Figure 3: Two-color acetone LIF set-up sketch.

The image processing is performed entirely with Matlab ®. 10 images of the background are averaged for the two cameras and the resulting images are subtracted from the fluorescence intensities. The spatial calibration was applied to match exactly the two fields of view observed. After this operation, the intensity ratio is computed in every location of the laser beam. The mean and the standard deviation are obtained both for spatial and time dimensions. Mean and standard deviation of the thermocouples are also computed in order to assess the spatial uniformity and the variation of temperature during the single experiments.

The results of the experimental campaign are summarized by Fig. 4. The ratio between the two camera intensities is represented in the middle of the cell in function of the mean temperature inside the cell during the specific experiment. The extracted location has been chosen in the middle of the laser beam where the fluorescence intensity is higher and the data are more reliable. Due to the *photon shot noise* the higher the signal, the higher the signal to noise ratio S/N. A strong dependence with temperature can be observed. At the maximum investigated temperature (98°C) the value of the intensity ratio drops by 46% of the one recorded at 48°C.

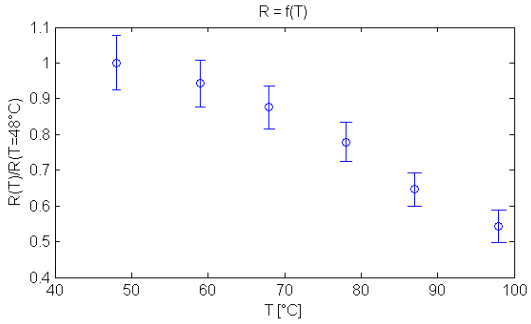

Figure 4: Normalized Intensity Ratio in function of the operating temperature inside the cell.

The uncertainty on the intensity ratio was computed by the standard deviation recorded over the 400 images taken for each experiment. This results in about 7.3% of the intensity ratio for a confidence level of 95%. It turns out that temperature may be determined, inversely, with an uncertainty of ± 8°C. The absolute value of uncertainty needs to be compared with the measurement range in a specific application being a heat transfer phenomena. The bigger the range, the smaller the effect of the uncertainty on the measurements. Thus, for a measured range of 100°C the uncertainty will account 8%. The main contribution on the error is given by the camera noise. Its effect on the measurements can be limited only by increasing the signal itself. The energy fluctuations of the laser pulses were not quantified. However, the method is theoretically not affected by these variations in the range of proportionality. During the experiments the thermocouples have shown variations between 1 and 1.8°C, whereas dis-uniformity in the spatial dimension are at maximum 0.8°C. The presented results represent only a starting point for the final objectives of this research. The presence of an important temperature dependence on the intensity ratio is encouraging for detecting the thermal boundary layer in internal flow applications. Furthermore, the experiments put in evidence some aspects which needs to be deeper

analysed:

- the signal is very low (order of 200/4065) and, therefore, the noise acts an important role for the determination of the measurement uncertainty;
- there is no scientific evidence about the dependence with temperature discovered. The filters applied for these measurements were expected to provide a maximum variation of 10% of the signal within 100°C variation. Data present in literature of the acetone are not sufficient to take important conclusions [18].

In the case of a low signal the main contribution to the image noise is given by the so called *read-out noise*. The latter depends uniquely upon the detector. In order to get rid of its strong effect the signal needs to be enhanced. Either the CCD cameras require two intensifiers or they will be replaced by two ICCDs. Although the *photon shot noise* will be amplified together with the signal, the *read out noise* will account less to the measurement uncertainty. The second point opened the necessity of testing more accurately the acetone emission spectra in order to improve the understanding of the spectroscopic features of the selected tracer.

2.2. Acetone spectral measurements

Concerning the unexpected behavior of acetone during the previous experiments and ignoring possible other physical effects, the investigation of the fluorescence emission spectra of acetone is needed in order to explain what was found in section 2.1. The measurement cell is exactly the same of the previous experiments. The detection system of Fig. 3 is replaced by a spectrometer (PI Acton Sp2750®) connected to an ICCD camera (PI-MAX 3®). In addition to that, a laser energy monitor is added to the system (Fig. 5). A small portion of light (1 to 5%) is reflected by a quartz plate. More attenuation optics are placed in front of a photodiode in order to protect the sensor and avoid the saturation of the latter. A stopband filter is also used to get rid of the remaining green component. The output signal integrated by a Boxcar Averager (Stanford Research Systems®). A reference of the laser power is provided for each pulse and this value is used to normalize the image intensities.

The wavelength full range recorded by the specific grating is about 100 nm. Four ranges are used to cover the entire spectral emission of acetone from 300 nm to 600 nm with an overlap of 20 nm. Binning of 2 x 2 is used leading to a resolution of 0.1 nm and 100

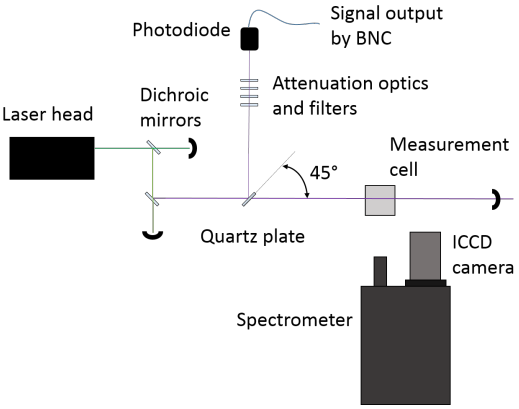

Figure 5: Spectral measurements set-up.

images were averaged. The temperature was kept at the same level while the four sets of data were acquired. Together with the images, temperature from the four thermocouples, pressure and energy levels were recorded. The variation of pressure inside the cell is less than ± 2 Pa and, therefore, its effect on the measurements was neglected. The calibration of the system is performed using a halogen and deuterium lamp. Knowing the theoretical and the recorded signals the spectral calibration is applied after the background subtraction as described by Eq. 3:

$$S = (S_{rec} - BG)\frac{Cali_{rec} - BG}{Cali_{the}} \quad (3)$$

where S and S_{rec} are the calibrated and the recorded fluorescence signals, $Cali_{the}$ the theoretical emission of the calibration lamp, $Cali_{rec}$ its recorded signal and BG the background image taken without tracer.

All the measurement sets are taken to reconstruct the emission spectra of acetone. The plot in Fig. 6 represents the latter normalized with the peak value at each temperature. Except for some errors in the curve of 60°C, all the curves collapse in one. This plot explains that the shape of the fluorescence emission does not change considerably with the temperature and neither a significant red shift (as for tracers like toluene and anisole) was recorded. According to this measurements acetone is not a proper tracer for two-color thermography since it shows the same temperature dependence at every wavelength. On the other hand, it does not explain the behavior observed in the previous experiments.

2.3. Discussion and Conclusions

There is no scientific evidence before these measurements of the encouraging trend of the acetone in-

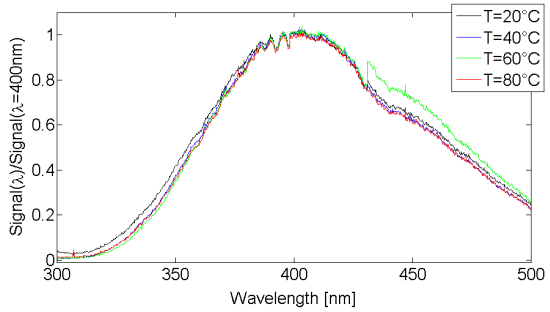

Figure 6: Acetone emission spectra normalized with ambient temperature in function of the cell temperature.

tensity ratio with temperature (Fig. 4). Unfortunately, the experiment is not able to explain the observed phenomena and further assessments are required. However, the latter go out of the specific goal to bring a suitable tool for accurate temperature measurements in a cooling channel. It will be more useful to test the detection set-up for a continuous flow, out of phenomena as tracer aging and significant variation of concentration during the experiments. A calibration in-situ, required for accurate measurements, may reveal its real feasibility. The one-color approach and toluene as a tracer are the alternatives already tested and used in literature. In the first place toluene was not considered being slightly more toxic than acetone, being subjected to oxygen quenching and possible fluorescence re-absorption. Besides, the one-color approach requires to take into account the laser power fluctuations and the possible variation of tracer concentration. However, these difficulties are already overcome by looking at the toluene signal in air (even higher than the one of acetone) and the laser energy monitor built for the present campaign.

3. Facility

According to the conclusions of the preliminary study a more complex set-up was required to test the technique in a continuous flow. The global work of the design is represented by the 3D view of the facility in Fig 7. The purpose is to perform experiments in an internal 2D flow. The test rig is an already existing model which presents a cross section of 240 x 40 mm^2, therefore, with a *channel aspect ratio* of 6. The channel, as the structure of the wind tunnel, is made in aluminum. Four optical windows allow the optical access of the light source and the camera at the entrance of the channel and 1150 mm downstream. The decision of their streamwise location allows characterizing both the inlet and the fully developed region. Originally made in plexiglass, they have been replaced with quartz plates considering the UV components of the laser light and the emitted fluorescence. The bottom wall can be heated up with thin resistances (Minco HAP6949®). The goal is to obtain the temperature profiles in order to compare the data with other experimental means (e.g. thermocouple or cold wire measurements). The *Reynolds number* based on the channel height $Re_H = 6700$ was chosen high enough to produce a fully turbulent, fully developed flow and low enough in order to have a thicker *boundary layer*, easier to measure. The resulted mass-flow needed to be provided is about 30 g/s leading to a bulk velocity of 3 m/s. It is, therefore, required to generate the flow inside the test section including the selected fluorescent dye.

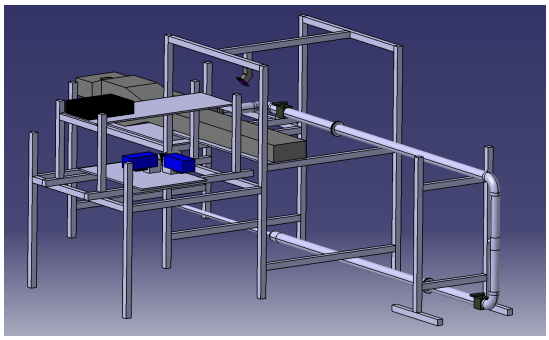

Figure 7: PLIF facility.

Two mass-flow meters are required to control both the mass-flow and the tracer concentration. The LIF flow generator is sketched in Fig. 8. Flow goes from right to left. The air is taken from the 7 bar compressed line of the VKI. The flow splits in two branches. One of those passes through the seeder and the other one has the purpose to dilute the mixture. They merge and are connected to the inlet of the wind tunnel. The pipes are made in PE100 Black, resistant to pressurized air up to 16 bars and able to withstand both acetone and toluene vapors. The internal diameter is a DN50 mm. The length of the pipes is determined by the upstream and downstream constraints for the mass-flow meters given by the British Standards [26]. In order to measure such a low mass-flow, orifice plates with a diameter ratio of 0.6 have been selected [27], producing pressure drops of the order of 10 mbar. The latter are measured by *Differential Pressure Transducers* which also monitor the pressure upstream each orifice plate. Together with the temperature obtained by a thermocouple far downstream,

the air density is computed. The NI cDAQ-9174®, through the modules NI 9215 and NI 9212, acquires all these data. With a home written LabView®code the mass-flow and the tracer concentration can, therefore, be monitored in real time. By changing the position of the valves iteratively these two values are adjusted as desired.

Aluminum profiles supports hold both pipes, test section and the required equipment for the measurements. The laser is mounted on a plate supported by posts fixed to the camera structure. The advantage is, once the set-up is aligned, the illumination moves horizontally with the field of view of the detectors. On the laser support the required optics are placed and the laser beam is projected vertically by a UV enhanced mirror hanged on a horizontal support.

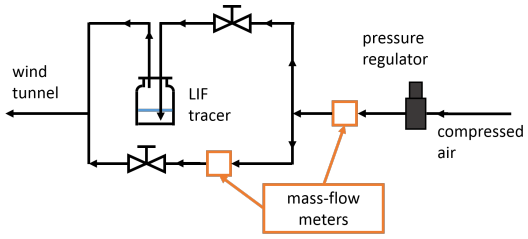

Figure 8: Flow sketch.

In order to characterize the flow inside the test section some PIV measurements have been performed. The streamwise velocity profile have been shown to be symmetric. A shape factor of 1.4 is the confirmation of a fully turbulent boundary layer. In order to see if the flow was fully developed the Reynolds stresses are plotted in Fig. 9. The linear behavior in the main part of the channel verifies the statement. This plot also allowed to determine the friction velocity and to represent the boundary layer with the u^+ and y^+ coordinates. Fig. 10 shows a good agreement with the logarithmic law obtained with typical constants for internal flows (k=0.37, B=5.1).

The facility has been used for one-color toluene LIF thermography and traverse measurements with a thermocouple probe in order to compare immediately the temperature profiles. The results obtained are presented in the following section.

4. LIF measurements and results

The fluorescence produced by the toluene is collected by a Sodern Cerco®UV lens and recorded by the same ICCD camera (PI-MAX 3®) used before for

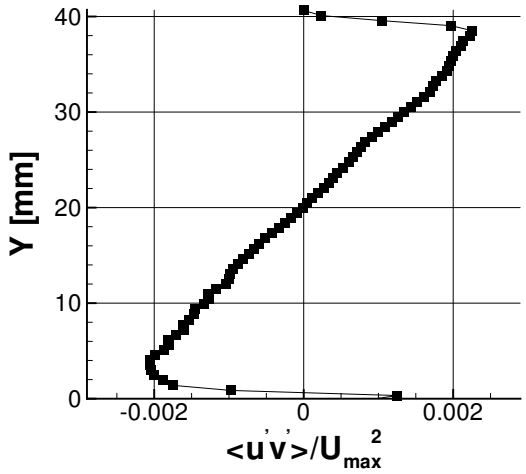

Figure 9: Non-dimensional Reynolds stresses profile inside the channel.

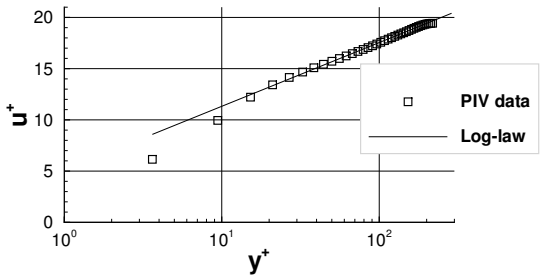

Figure 10: Comparison of the velocity boundary layer with the logaritmic law.

the spectral measurements. In front of the camera a short pass filter of 400 nm is used to cut down the remaining green light of the laser whereas the Semrock 266nm RazorEdge®ultrasteep long-pass filter has the purpose to get rid of the main UV laser frequency reflections on the channel walls. The camera is synchronized with the laser by a Stanford DG535 Digital Delay/Pulse Generator®. 1000 images are taken at 10 Hz at isothermal conditions (ambient temperature) and with the bottom wall heated up to a temperature around 70°C. No binning is applied to use the full resolution of the camera. A series of 50 background images is also acquired without the tracer as well as another series of 50 images of a dotted grid plate in the plane of measurement for the spatial calibration. All of them are imported in Davis®(software for acquisition an image processing by Lavision Gmbh®). By a standard proceeding embedded in the software the dotted plate image, averaged over the 50 samples, is used for the spatial calibration. The output is a distor-

tion correction and a change from pixels to mm in the X and Y axis of the images.

The measurements performed follow the one-color methodology. This means only one ground state is taken into consideration and the signal provided by our tracer might be strongly affected by variations of the laser excitation power and the tracer concentration. Therefore, a proper correction needs to be applied at this moment. Laser beam shape and power distribution change in time are neglected whereas the signal of every image at isothermal and warm conditions as well as the background images are normalized by the photodiode output (Laser power correction). In order to take into account detection non-uniformities and variations in space of laser fluence and concentration a Flat Field correction (FFC) [11] is applied using the image related to an isothermal state as the Flat Field. Therefore, the corrected signal is obtained by the following relationship:

$$I^* = \frac{I_{heated\,wall} - < BG >}{< I_{amb} > - < BG >} \tag{4}$$

where $< BG >$ is the average background image over the 50 samples, subtracted from both images related to the ground states: the isothermal $< I_{amb} >$, averaged over 1000 samples, and the target condition $I_{heated\,wall}$. Whereas $< BG >$ increases the signal recorded independently, the excitation energy and tracer concentration contribute proportionally to the fluorescent signal in which the investigation focuses. As a result, the image related to the ground state of interest (*heated wall*) is divided by the image related to the isothermal state (or the ambient condition).

4.1. Results and discussion

The results of the LIF measurements are shown in Fig. 11 compared with the output of a thermocouple probe traversed along the channel height (black circles). The latter present a non symmetric profile of temperature due to the warmer bottom wall compared to the one on the top. It is important to point out that not only the bottom wall was warmer (~ 70°C) than the fluid (~ 30°C), but also the top wall (~ 40°C). This is due to the conduction trough the aluminum walls of the channel. On the horizontal axis the temperatures in °C are compared. Although the flow has been shown to be fully developed, the heating length (length of the full channel) is not sufficient to produce a flow which is also thermally fully established. When fully established, the temperature profile should be linear between the values on the two walls.

The LIF measurement output I^* was averaged on the 1000 samples recorded and converted to temperature with a two-point calibration using the value obtained with the thermocouple. A 2D Gaussian filter is applied to the profile (red line) and compared with the profile measured with the thermocouple. Although the absolute outputs of temperature are forced to match with the two measurement technique, the trend along the channel height shows a good agreement between them. Some issues appear in the bottom, very close to the wall, where some reflections are the main reason of the two bumps of the red line. In addition, a noisy profile is observed between 25 and 35 mm. Here the reason can be found on the image post processing. The expansion of the aluminum due to the increase of temperature causes a displacement of the walls. A correction is needed to match the two images. This operation introduced a discontinuity. However, the trend of the LIF profile still respects the one measured by the thermocouple.

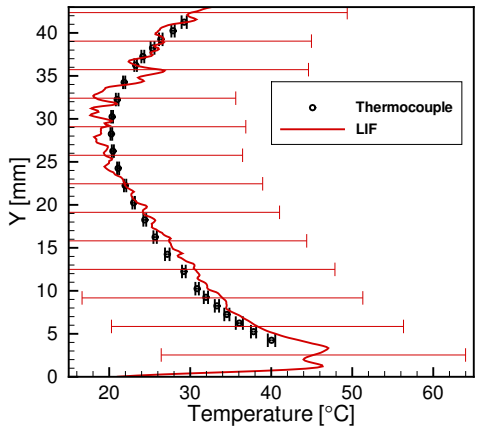

Figure 11: Comparison of the normalized averaged LIF signal I^* and the non-dimensional temperature profile measured by a thermocouple traversed along the channel height.

The temperature dependence of the LIF signal is relatively low in the investigated interval compared to the noise. This is the reason for the large red error bars. They represent the standard deviation of the signal computed for the 95% confidence level. In terms of temperature, it is about ± 19 °C. The possible improvement of the results shown in this picture, therefore, should act on lowering the measurement uncertainty. In order to act on the major contributions of the random error there are two possible options. The first one is to increase the temperature dependence which

is related to the tracer photophysics. The second way is to increase the signal-to-noise ratio S/N of the fluorescence signal. Both results can be obtained at the same time replacing air with nitrogen as the main flow. Indeed, toluene is highly affected by the phenomenon of oxygen quenching. From ref. [25] the signal of toluene in pure nitrogen (zero oxygen content) theoretically increases by a factor of 70. Together with that the fluorescent quantum yield varies one order of magnitude more with temperature in the same temperature range.

For this reason the facility has been equipped with 8 nitrogen cylinders at 200 bar. The flow is controlled by two independent pressure regulators in order to keep the mass-flow constant even when the upstream pressure decreases. The user is allowed to blow nitrogen, air or both together into the test section. Only the LIF measurements will be performed in nitrogen. The action of blowing an inert gas is not expected to eliminate completely the oxygen content. However, the latter will be strongly reduced. At the same time a more detailed and resolved temperature calibration procedure has been design to improve and evaluate the systematic error. Different position on the image will be investigated at different temperatures to take into account possible variations of response inside the field of view.

5. In-situ calibration

Since most of the studies are performed in internal combustion engines or other applications where a calibration in-situ is really difficult to perform, in order to retrieve the correct temperature some alternative methods were developed [28]. The field does not require accurate absolute temperature [29]. For the specific application, instead, a proper temperature calibration needs to be carried out.

The advantage of performing an in-situ calibration is due to the fact that a different configuration of the set-up might change the temperature effect on the signal. It has been shown that the signal recorded in a cell do not present the same behavior with temperature as in the test section of the experiments. Ref. [16] provided a methodology to correct the results by anchor the few points measured with a thermocouple in an IC engine. However, this does not take into account the possibility of a different shape of the curve and uses only two points for the calibration. The idea shown in this section is to create a flow, in the same conditions of the test, at different known temperature in order to build an accurate calibration curve in different regions of the field of view. Indeed, certain areas might behave in different ways due to fluorescence reflections which are not present in the background image. The ideal methodology is to create a flow, in the same conditions of the test in terms of species concentration, at a uniform known temperature. The latter is hard to produce for the large section of the present channel. Therefore, the author decided to produce only a limited portion of the flow at elevated temperature. A sketch of the experimental calibration set-up is represented in Fig. 12. The flow goes from left to right, two lateral fences direct the mass-flow to the center of the cross-section (not represented in the picture). In this way the flow is more constraint to pass through the heater. The latter is a simple pipe provided with electrical resistances. The flow coming out of the tube is warm and its temperature is measured by a thermocouple probe at the same location of the laser sheet. The thermocouple is displaced along the channel height thanks to a traverse system. The sealing is accomplished by three PTFE's bushes installed on the top wall where the probe stem slides smoothly. Therefore, the probe can move both horizontally (three possible positions) and vertically with a traverse system. The heated tube is also able to be traversed vertically in the same way. Three measurements will be done (three horizontal positions of the probe) for each heater position along the channel height. Four vertical positions of the heater will be used to build 4 x 3 calibration curves for the twelve sub-regions. The actual design is performed and measurements will come soon in order to evaluate the absolute error in the measurements.

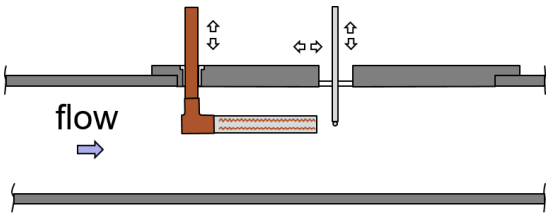

Figure 12: In-situ calibration set-up sketch. A pipe with internal resistances heats the flow passing through. A thermocouple probe measures the temperature in the same location of the laser sheet.

6. Conclusion

In summary, the present investigation will cope with the issues of the heat transfer prediction in the

field of internal cooling by looking directly at the major causes of the numerical and experimental data discrepancies. The aerodynamic and thermal analysis will provide a physical explanation of the complex phenomena of forced convection. The innovative, high quality and high resolution data of the present research will represent a suitable tool for CFD codes validation and modeling improvements.

The importance of flow temperature measurements in cooling technology has been proven in the document. LIF thermography will be introduced as a planar and non intrusive measurement technique. Some preliminary results, in a static and uniform temperature cell, show the feasibility of the method. Remarks and possible improvements of the measurements are largely treated. Constraints and difficulties of the application are discussed identifying suitable alternatives for the next step of the research. A novel facility has been completely designed and built at VKI. The author investigated the thermal boundary layer for a 2D internal flow with the one-color method and using toluene as the fluorescent tracer. The results have shown a really good match of the LIF signal with the measurements of a thermocouple in the lower part of the channel. Some issues are identified where the possible reasons are fluorescence reflections and image processing discontinuity. The high uncertainty registered can be lowered by decreasing the oxygen content in the flow causing the strong quenching of the signal and the change of the temperature dependence. The facility has been modified with the option to blow nitrogen (instead of air) into the test section. Besides, an in-situ calibration set-up has also been designed together with the procedure to follow, ready now to be tested. Results will come soon and the test are expected to improve considerably the results quality and measurement uncertainty. Eventually, the set-up will be embedded with the PIV equipment in order to obtain the turbulent heat transport term $\overline{v'T'}$, required for the determination of Pr_t.

Acknowledgments

The funding of this PhD research project through a FRIA grant, delivered by the Fonds de la Recherche Scientifique (FNRS), is gratefully acknowledged.

References

[1] L. Casarsa, T. Arts, Experimental investigation of the aerothermal performance of a high blockage rib-roughened cooling channel, Journal of Turbomachinery 127 (2005) 580–588.

[2] N. D. Cardwell, P. P. Vlachos, K. A. Thole, Developing and fully developed turbulent flow in ribbed channels, Exp Fluids 50 (2011) 1357–1371.

[3] I. Mayo, G. Luca Gori, A. Lahalle, T. Arts, Aerothermal characterization of a rotating ribbed channel at engine representative conditions–part i: High-resolution particle image velocimetry measurements, Journal of Turbomachinery 138 (10) (2016) 101008–101008–9. doi:10.1115/1.4032926.
URL http://dx.doi.org/10.1115/1.4032926

[4] P. Ligrani, Heat transfer augmentation technologies for internal cooling of turbine components of gas turbine engines, International Journal of Rotating Machinery 2013.

[5] T. Arts, M. T. Abad-Lozano, Y. Kinoue, S. Pierret, The unsteady temperature field in a turbine blade cooling channel, RTO AVT Symposium, 2001.

[6] F. Lemoine, Y. Antoine, M. Wolff and M. Lebouch, Simultaneous temperature and 2D velocity measurements in a turbulent heated jet using combined laser-induced fluorescence and LDA, Experiments in Fluids 26 (1999) 315–323.

[7] A. Y. C. Tropea, J. Foss, Handbook of Experimental Fluid Mechanics, Springer, 2007.

[8] M. C. Thurber, F. Grisch and R. K. Hanson, Temperature imaging with single- and dual-wavelength acetone planar laser-induced fluorescence, Optics Letters 22 (4) (1996) 251–253.

[9] M. Luong, W. Koban and C. Schulz, Novel strategies for imaging temperature distribution using Toluene LIF, Journal of Physics: Conference Series 45 (2006) 133–139.

[10] P. Lavieille, F. Lemoine, G. Lavergne and M. Lebouch, Evaporating and combusting droplet temperature measurements using two-color laser-induced fluorescence, Experiments in Fluids 31 (2001) 45–55.

[11] B. Peterson, E. Baum, B. Böhm, V. Sick, A. Dreizler, Evaluation of toluene lif thermometry detection strategies applied in an internal combustion engine, Applied Physics B 117 (1) (2014) 151–175. doi:10.1007/s00340-014-5815-0.
URL http://dx.doi.org/10.1007/s00340-014-5815-0

[12] Y. Na, D. V. Papavassiliou, T. J. Hanratty, Use of direct numerical simulation to study the effect of prandtl number on temperature fields, International Journal of Heat and Fluid Flow 20 (3) (1999) 187 – 195. doi:https://doi.org/10.1016/S0142-727X(99)00008-9.

[13] S. P. Kearney and F. V. Reyes, Quantitative temperature imaging in gas-phase turbulent thermal convection by laser-induced fluorescence of acetone, Experiments in Fluids 34 (2003) 87–97.

[14] Lei Shi, Xiaoan Mao and Artur J Jaworski, Application of planar laser-induced fluorescence measurement techniques to study the heat transfer characteristics of parallel-plate heat exchangers in thermoacoustic devices, Measurement Science and Technology 21 (2010) 116.

[15] V. A. Miller , M. Gamba, M. G. Mungal and R. K. Hanson, Single- and dual-band collection toluene PLIF thermometry in supersonic flows, Experiments in Fluids 54 (2013) 1539–1551.

[16] C. Gessenhardt, C. Schulz and S.A. Kaiser, Endoscopic temperature imaging in a four-cylinder IC engine via two-color toluene fluorescence, Proceedings of the Combustion Institute 35 (2014) 36973705.

[17] S. G., B. J. McBride, Computer Program for Calculation of Complex Chemical Equilibrium Compositions and Applications, Nasa Reference Pubblication 1311, NASA (1994).

[18] R. A. Bryant, J. M. Donbar, J. F. Driscoll, Acetone laser induced fluorescence for low pressure/low temperature flow visualization, Experiments in Fluids 28 (5) (2000) 471–476.

doi:10.1007/s003480050407.
URL https://doi.org/10.1007/s003480050407

[19] M. C. Thurber, F. Grisch, B. J. Kirby and M. Votsmeier, Measurements and modeling of acetone laser induced fluorescence with implication for temperature imaging diagnostics, Applied Optics 37 (21) (1998) 4963–4978.

[20] A. Lozano, Laser-excited luminescent tracers for planar concentration measurements in gaseous jets, Ph.D. thesis, Stanford University (1992).

[21] C. Schulz, V. Sick, Tracer-lif diagnostics: quantitative measurement of fuel concentration, temperature and fuel/air ratio in practical combustion systems, Progress in Energy and Combustion Science 31 (1) (2005) 75 – 121. doi:https://doi.org/10.1016/j.pecs.2004.08.002.

[22] W. Koban, J. D. Koch, R. K. Hanson and C. Schulz, Absorption and fluorescence of toluene vapor at elevated temperatures, Phys. Chem. Chem. Phys 6 (2004) 2940–2945.

[23] W. Koban, J. D. Koch, R. K. Hanson and C. Schulz, Oxygen quenching of toluene fluorescence at elevated temperatures, Applied Physics B 80 (2005) 777–784.

[24] M. C. Thurber, Acetone Laser-Induced Fluorescence for temperature and multiparameter imaging in gaseous flows, Ph.D. thesis, Stanford University (1999).

[25] S. Faust, M. Goschütz, S. A. Kaiser, T. Dreier, C. Schulz, A comparison of selected organic tracers for quantitative scalar imaging in the gas phase via laser-induced fluorescence, Applied Physics B 117 (2013) 183–194.

[26] B. Standards, Measurements of fluid flow by means of pressure differential devices inserted in circular cross-section conduits running full - Part 1: General principles and requirements, Standard BS EN ISO 5167-1:2003, European Committee for Standardization (2003).

[27] B. Standards, Measurements of fluid flow by means of pressure differential devices inserted in circular cross-section conduits running full - Part 1: Orifice plates, Standard BS EN ISO 5167-2:2003, European Committee for Standardization (2003).

[28] K. Tran, P. Guibert, C. Morin, J. Bonnety, S. Pounkin, G. Legros, Temperature measurements in a rapid compression machine using anisole planar laser-induced fluorescence, Combustion and Flame 162 (10) (2015) 3960 – 3970. doi:http://dx.doi.org/10.1016/j.combustflame.2015.07.033.

[29] S. Kaiser, M. Schild, C. Schulz, Thermal stratification in an internal combustion engine due to wall heat transfer measured by laser-induced fluorescence, Proceedings of the Combustion Institute 34 (2) (2013) 2911 – 2919. doi:http://dx.doi.org/10.1016/j.proci.2012.05.059.

Advanced experimental aero-thermal investigations of wall-bounded swirling flows in three-dimensional ribbed tubes

Marco Virgilio

Turbomachinery and Propulsion Department, von Karman Institute for Fluid Dynamics, Belgium, marco.virgilio@vki.ac.be

Supervisor: Tony Arts

Professor and Head of Department, Turbomachinery and Propulsion Department, von Karman Istitute for Fluid Dynamics, Belgium, tony.arts@vki.ac.be

University Supervisor: Kevin Van Geem

Professor, Laboratory for Chemical Technology, Universiteit Gent, Belgium, Kevin.VanGeem@UGent.be

Abstract

The effects of helical ribs on both the flow field and the heat transfer have been investigated experimentally in circular cross section channels. Stereoscopic Particle Image Velocimetry (S-PIV) was applied in order to measure the 3 components of the mean and turbulent velocities. Moreover, steady-state Liquid Crystal Thermography (LCT) and Infrared Thermography (IRT) were used for studying the forced convection on the wall. In this paper, high turbulent kinetic energy and heat exchange are shown a few rib heights downstream of the obstacles.

Keywords: Helical ribs, Flow Field, Heat Transfer, Stereoscopic Particle Image Velocimetry, Liquid Crystal Thermography

1. Introduction

In processes such as the hydrocarbons steam cracking for the production of ethylene, the reactors expect short residence time for endothermic reactions, so a high rate of heat transfer is required. One of the solutions is likely to be the use of pipe turbulators, as in Fig. 1, whose positive effects have been already tested in commercial plants [1]. Generally speaking, they disrupt the boundary layer at the wall and make the flow temperature profile to be more homogeneous. As a consequence, the coking rate is minimized, the cracking volume maximized and both the run length and the tube life are extended since the wall temperature is kept relatively low. Hence, similarly as in turbomachinery [2], local obstacles help to enhance the heat transfer in the reactor tubes. The knowledge gained from turbomachinery will be useful in this environment. As a matter of fact, there is a massive need to increase the gas turbine efficiency by means of rising the flow temperature. To maintain the blade integrity, at least, internal cooling is needed. To improve the forced convection on the blade walls, the internal channels need to be ribbed in order to enhance the heat transfer. Although it has been demonstrated by several authors that the increase of the Nu number is about more than 1.5 times the one seen in a smooth tube at the same Reynolds and Prandtl numbers [3], the ribbing technique is limited by the rise in the friction losses [4]. Therefore, a multi-objective optimization design is a reasonable method which can find out the best solution to the problem stated before. Anyway, the optimization tool needs the use of a fluid dynamic solver which has to be able to well simulate the turbulent structures generated at the wall. In this case, Large Eddy Simulations (LES) are supposed to be the best choice in terms of quality, in comparison with RANS, and time-saving, instead of DNS. Therefore, the chosen sub-grid scale model needs to be validated by doing measurements of the turbulent swirling flows. Afterward, optimizing techniques can be carried on for the design of chemical reactors, turbines internal cooling channels or heat exchangers in a more general sense.

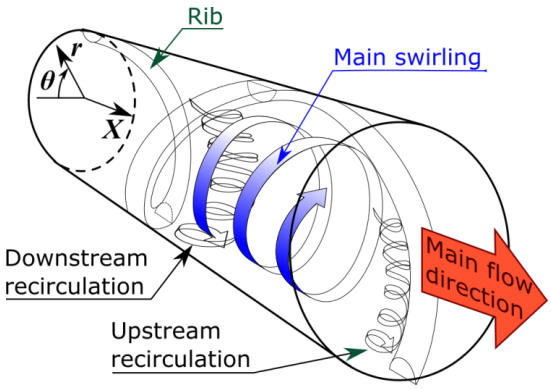

Figure 1: Swirled flow inside helically ribbed pipes [3].

The present experimental investigation focuses on the aero-thermal characterization of a helically corrugated cylindrical cooling channel. Empirical correlations for the evaluation of the friction factor and Nusselt number for ribbed geometries were proposed by Ravigururajan and Bergles [5] and Pethkool et al. [6]. Nevertheless, the correlations are based on heat transfer measurements affected by a significant lack of information, since they are obtained by point-wise techniques. Garcia et al. [7] have already provided 2D-PIV data for helically corrugated ducts but for flows whose regimes are laminar and transient without any detailed info about the heat transfer. On the other hand, Bonanni et al. [8] provided the heat transfer coefficient over the full surface of a rib-roughened circular channel by using transient LCT. In that study, the obstacles were placed perpendicularly to the main flow direction. Recently, LES were performed by Zhu [9] in a configuration similar to the ones studied in the present paper.

The ambition of this Ph.D. research is to continue the work made by Mayo et al.[3] and to extend the investigation also to three-dimensional turbulators, understanding the complexity of wall-bounded turbulent swirling flows. The investigation has been done experimentally with Stereo-Particle Image Velocimetry to measure the flow field. It allows an accurate full-field evaluation of the mean flow quantities together with the turbulence statistics. Moreover, the secondary flows and vortical structures are solved and the results are matched with the associated heat transfer at the inner wall. The latter measurements have been carried out by means of steady-state LCT. Hence, a well-documented test case for high-fidelity computations is provided.

2. Experimental Setup

2.1. Velocity measurement setup

The flow field measurements have been made in the low-speed water tunnel (Fig. 3) placed at the 'Heat and Mass transfer lab' of the von Karman Institute. The flow is accumulated in a settling chamber where the water level is kept constant thanks to an adjustable overflow channel, which works as a by-pass. In such a way, the total inlet pressure can be chosen and kept constant, which means steady boundary conditions. The mass flow, chosen during the experiments, corresponds to a turbulent flow Reynolds number. Anyway, it is kept at low values, which are enough to allow corresponding LES computations. The water is discharged by the settling chamber into the inlet duct. In order to have the flow developed, the inlet section has a length of 15 diameters (internal diameter of 150 mm), according to Incropera [10]. Downstream of the inlet duct, there is the test section which is made of acrylic glass to obtain full optical access to the area of interest. The turbulence generators tested are made of ABS (Acrylonitrile Butadiene Styrene) and they are manufactured according to the stereolithography technique.

Two different kinds of helicoidal turbulator have been inserted in the test section and tested with S-PIV and LCT. The Geometry-A consists of a semi-circle section swept throughout a helical pattern tangentially to the inner surface of the cylinder under test. The helix has a pitch of 63 mm repeated for 10 times, the angle of attack is 80° and the semi-circle section has a constant height-to-diameter ratio of 3.6%. The dimensionless parameters of the geometry are the same as in M. Zhu et al. [9], who simulated the flow with LES. The other geometry explained in this paper is the Geometry-B, which has the same helix parameters stated before but the semicircle-sections have a height which is changing through the helical pattern direction. The maximum semi-circle height is the same as the Geometry-A. This height decreases slightly to a zero value after an angular displacement of 11° in both the directions of the helix. In one pitch of the helix, there are 6 obstacles equally spaced, for a total of 8 full pitches. The concept behind this alternative geometry is to maintain the same enhanced local heat transfer as for Geometry-A but with a lower skin friction. The start of the rib is located 440 mm downstream of the origin of the test section inlet. The S-PIV images are taken for the area between the obstacles far 5 and 6 times the pitch from the rib inlet. This choice has been taken by considering the fact that

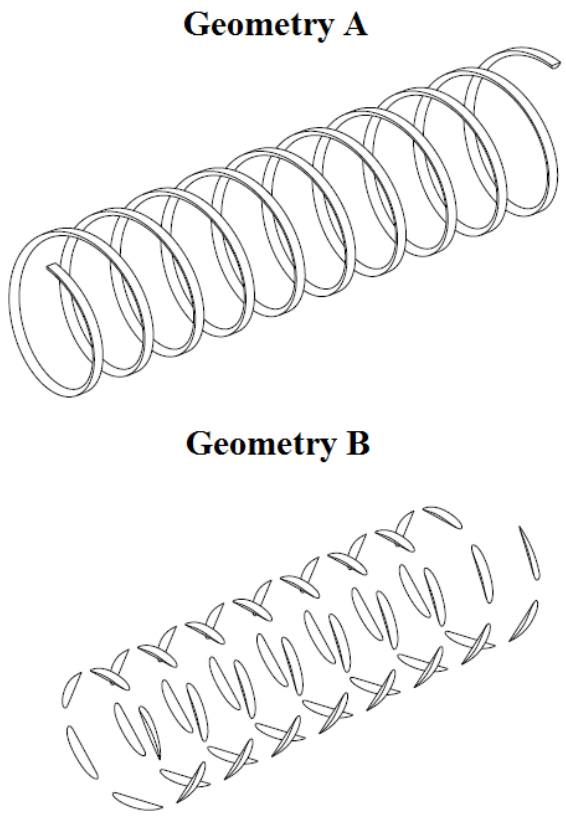

Figure 2: Obstacles of the ribbed channel

the typical development distance in low blockage ratio cooling channels is about 6 rib pitches [11]. To check the periodicity of the phenomenon, the same measurements have been made for the same area as before but switched of 1 pitch towards to the outlet of the ribbed test section. The channel is split longitudinally in two parts, to allow the spatial calibration of the 2 cameras. In order to match the refraction index of the solid wall and to minimize the images deformation, water has been chosen as working fluid. For the same reason as before, the test section is inserted into a transparent reservoir filled with water, in the interest of having a flat interface between the external air and the solid [12]. By measuring the static pressure drop given by an orifice plate, designed according to the ISO 5167 norm [13], it is possible to read the mass flow. The mass flow meter has been put 20 diameters downstream of the test section exit, and its dimensions have been chosen to minimize the relative measurement uncertainty, which turns to be 1.5% of the reading. A spherical valve is placed downstream of the orifice plate, allowing a coarse control of the flow regime. The fluid is finally collected in a large discharge chamber, and driven again to the settling chamber by means of a pump.

The investigated areas are illuminated by a Quantel Tween BSL 200 double pulse Nd:YAG laser which provides 70 mJ per pulse, that is the 33% of the nominal laser power. The combination of a telescope (focal length range of 300mm-2m), a cylindrical lens (20mm) and a mirror makes a focused light sheet of about 1 mm thickness to cover the region of interest between two obstacles. Two double-shutter CCD cameras with a sensor of 2360 x 1776 pix^2 are placed on the same side of the test section and equipped with Nikon Nikkor lenses of 50 mm focal length set to f/8. This choice of the cameras lenses (50 mm) let the image particle sizes to be between the range 3-7 pixels, which is optimal for minimizing the uncertainty coming from the cross-correlation algorithm [14]. In the interest of having a focused image all over the measurement plane, a Scheimpflug mount is used for each camera [15]. Most of the time, the angle between the cameras optical axes and the horizon is chosen to be 45°. Generally, bigger the angle, bigger is the sensitivity to the velocity components perpendicular to the laser sheet. On the other hand, the uncertainty on the other two velocity components gets increased. Hence, the author chose to reduce the angle at 23°(Fig. 4), as suggested by the authors N. J. Lawson and J. Wu [16] and Mayo et al. [3]. The resulting overall Magnification Factor is about 29 pix/mm.

The in-situ calibration of the image acquisition system is performed following the method proposed by Soloff et al. [17]. A dotted calibration grid is put inside the test section and positioned in the middle of the laser sheet by means of an adjustable micrometer support. The calibration plate is then displaced in two steps of 0.25mm each in the out-of-plane direction. The goal is to obtain a classical 3-D mapping function which makes the positions in the image system and in the real system to match. The partial derivatives of the functions in x,y and z are then used by the commercial software Davis 8.2, provided by Lavision, to compute the real particle displacement.

The S-PIV data will be used to validate LES results, so the target has been to investigate the statistics of the turbulent flow field [18]. To reach the convergence of the statistics, 1000 PIV realizations are acquired at a frequency of 1Hz [19], which is the rate of the slowest turbulent structure. In order to have a maximum particle displacement of about 10 pix [19], the separation time between the two frames of each PIV realizations has been set at 2.2 ms. The algorithm for the

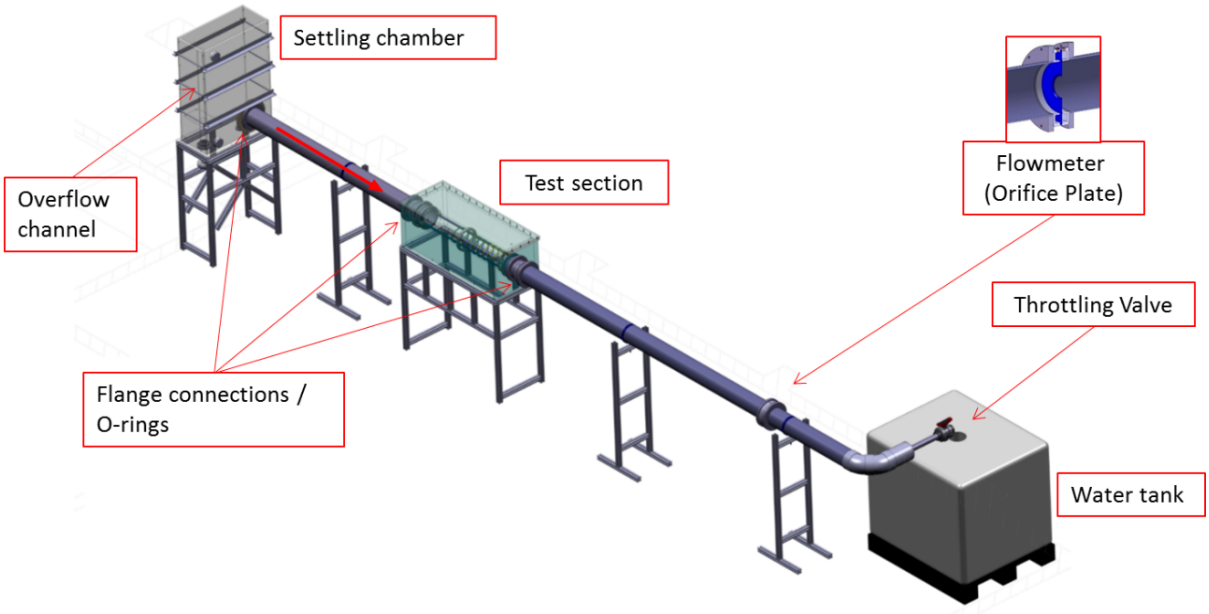

Figure 3: Facility for the S-PIV measurements.

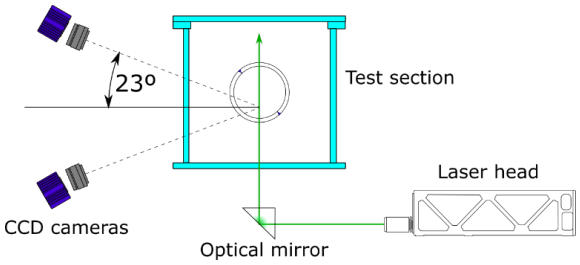

Figure 4: Set up of cameras and laser sheet for Stereo-PIV

stereoscopic system processed the images in three refinement steps, with a final interrogation window size of 32 x 32 pix^2 and an overlap of 75%. In such a configuration, the system has a resolution of 1.1 x 1.1 mm^2. The seeding particles are Chospheric fluorescent polyethylene spheres of 10-45 μm diameter. A 532 nm notch filter is placed in front of each camera sensor in order to cut off the laser light, in such a fashion that only the fluorescent scattered light is recorded. By doing so, the background reflections are minimized and the signal to noise ratio has increased. The concentration of the particles is about 20 g/m^3 in order to have at least with a high probability 10 particles per window.

2.2. *Heat transfer measurement setup*

In heat transfer measurements the tested flow should have the same Prandtl number as in the real applications. Because of the complexity of building a facility with a reacting ethane flow, the chosen fluid has been air since it is the simplest to work with. Anyway, the Large Eddy Simulations are supposed to be made with air as well, to validate how the code solves the energy equation. The facility (Fig. 5) works in the suction mode by operating a centrifugal blower at its exit. In this way, the inlet flow is not affected by the highly turbulent flow generated by the blower. Initially, the air enters the inlet duct, whose length is of 15 diameters. In such a way, the flow develops just before entering the test section, which is the same as the one used for the velocity measurement setup. Two additional K-type thermocouples are placed at the inlet and outlet sections in order to measure the temperature at the centre. The mass flow exiting the test section is directed through a U-bend towards the exit pipe. An orifice plate is placed in the exit pipe at a distance of 30 diameters downstream the U-bend. In this way, the operation of the mass flow meter is in agreement with the ISO 5167 norm [13]. The rotational speed of the blower can be changed so that the static pressure drop across the orifice plate corresponds to the required Reynolds number. Downstream of the mass flow meter, there is a settling chamber where the flow is discharged in. In such a system, it is possible to dump the possible fluctuations generated at the discharge side of the blower.

The inner surface temperature, T_w, has been mea-

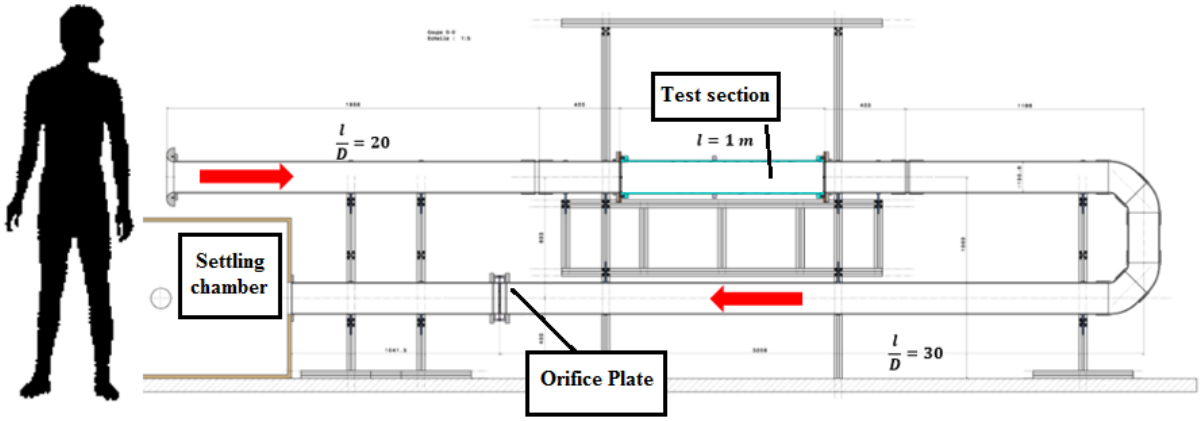

Figure 5: Facility for the TLCs measurements.

sured by using the Liquid Crystal Thermography in the range 35-55 °C. Therefore, a layer of TLCs (Hallcrest Ltd) is firstly deposited on the inner wall of the cylinder under test, followed by a matt black paint layer to enhance the contrast, an acrylic adhesive of 0.06 mm thickness and an Inconel foil 600 of 0.025 mm thickness. The metal sheet extends to the full length of the test section and the obstacles are glued on the top of it. To increase the wall temperature, a DC voltage is applied to the Inconel foil and the heat transfer between the foil and the fluid is started. The Joule heating per unit area, q_{Joule}, is uniform since the metal alloy has a low resistivity temperature coefficient and the spatial variations of it under the present experimental conditions are below the 0.3%. The transparency of the Plexiglas and the black paint allow a Nikon D7100 digital SLR camera to acquire RGB intensities scattered by the TLCs. The camera lens is a Nikon AF DC-Nikkor 105 mm f/2D which allows minimizing the angular aperture of the camera due to its big focal. In such a way, the longitudinal variations of the recorded colours are kept as low as possible and so also the measurement uncertainty. Then, the SLR camera is focused on the test section from a distance of about 850 mm with an angle of 45°with respect to the horizontal. The ISO sensitivity has been set at 100 in order to enhance the signal to noise ratio of the images. The aperture and the shutter speed are set respectively at f/16 and 2 seconds, in order to have the images with the red, blue and green saturations as high as possible. The authors Kodzwa and Eaton [20] advice to work with high saturated images to minimize the temperature uncertainty given by the Liquid Crystals Thermography. The white balance of the camera has set at 4170 K, the same as for the led panel light. In such a fashion, the image colour range in the RGB space and the colour sensitivity of the camera are maximized [21].The test section is placed in a black box (Fig. 6), to avoid reflections coming from the environment, and below a diffusive LED light panel (Pan-70W). The part of the image processed is called Region of Interest (ROI) which consists on a rectangle whose dimensions are one helix pitch in the horizontal direction and 30°in the vertical direction of the image. The location of the Region of Interest in the stream-wise direction is established consistently with the S-PIV measurement area.

To evaluate the heat transfer by convection at the wall, the heat balance in each surface element of the Inconel needs to be solved. To do so, the temperature field at the inner and outer surfaces of the test section need to be measured. As stated before, the internal temperature of the ribbed pipe is given by the TLCs while the external cylinder temperature is provided by the infrared (IR) camera. The ThermaCAM SC3000 (Flir Systems) has a QWIP detector working in the infrared region of 8-9 μm. The IR images are taken with a spatial resolution of 1.1 mrad at a frequency of 50/60Hz. The evaluation of the Slit Response Function and the spatial frequency of the ROI suggest no images restoration. The test section is made of acrylic glass material, so the SLR is able to record the color distribution of the TLCs layer. For a specific temperature, angular position and illumination level on the curved surface, the liquid crystals scatter a predominant wavelength of the incident diffused light [22].

Therefore, the function who matches the TLCs colour properties and the temperature is obtained by doing a calibration in situ. During the calibration, the lower half of the cylinder is removed, to give an access to the infrared thermography. Hence, the IR camera is able to measure the temperature field on the inner surface of the pipe. On the other side, the SLR camera records the behaviour of the TLCs paint on the inner surface of the acrylic glass. With this approach, it is possible to match locally the temperature measured by the IR camera with the colours observed by the SLR camera in the same region (ROI). By means of the Hollingsworth equations [21], the red, blue and green intensities are converted in hue, saturation and intensity. To avoid heat flux reflection of the environment from the metal foil to the IR camera [23], a high emissivity vinyl (thickness of 0.1 mm) covers the inner surface of the cylinder. The IR camera itself has been calibrated both for the Plexiglas and for the vinyl materials, providing respectively ±0.5°C and ±0.4°C extended uncertainties. The final calibration curves of the TLCs have been made for each row of the ROI and they consist in spline curves fitted to 18 calibration points. The corresponding uncertainties, with a level of confidence of 95%, take into account: the spatial variation of the Hue values over each row; the spatial variation of the temperature provided by the IR camera; the digital resolution of the SLC camera and the temperature uncertainty given by the IR camera. The major error source comes from the infrared thermography, which takes into account the errors in the IR camera calibration and the spatial variation of the temperature inside each row. This calibration methodology provides a resulting overall uncertainty on the temperature measurement between $\pm 0.46°C$ and $\pm 0.77°C$, depending on the row position inside the ROI. The extended uncertainty depends also on the temperature, and it results to be $\pm 0.46°C$ in the red region at 38.7°C ; $\pm 0.74°C$ in the green region at 46.5°C and $\pm 0.50°C$ in the blue region at 53.3°C. From this uncertainty analysis, it turns out that the biggest uncertainty is in the green region where the partial derivative $\partial T/\partial Hue$ has the biggest value. The chosen level of confidence is 95% respecting the terms of the ASME uncertainty nomenclature [24].

The Joule power per unit area (q_{Joule}) generated by the Inconel foil is transferred by convection (q_{conv}) to the flow and by conduction (q_{cond}) to the channel. Internal radiation fluxes are not considered since the elementary surfaces of the wall are put in a cavity with very low temperature differences. The equation to be solved is the following:

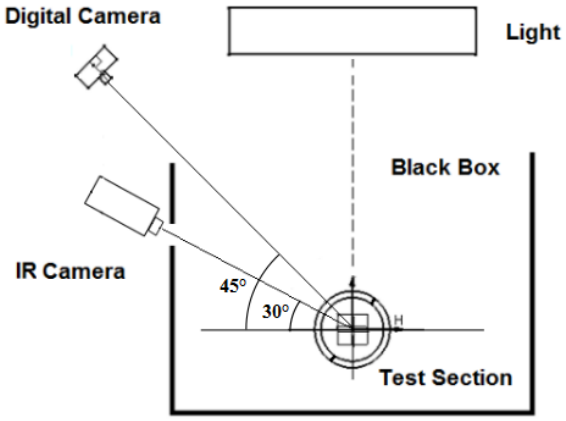

Figure 6: Images acquisition system and IR measurements layout

$$Q_{\text{conv}} = Q_{\text{Joule}} - Q_{\text{cond}} \tag{1}$$

The Q_{cond} takes into account the 3 conductive heat flux components (i.e radial, axial and azimuthal) at each point of the pipe inner wall. Due to the non-uniformity of the conduction losses, the resulting heat transfer by convection per unit area is not perfectly uniform. The standard deviation of the q_{conv} fluxes for each surface element are equal to the 5.5%. The heat transfer coefficient, h, is defined as:

$$h(z,\theta) = \frac{q_{\text{conv}}(z,\theta)}{T_{\text{w}}(z,\theta) - T_{\text{c}}(z,\theta)} \tag{2}$$

where θ and z are the cylindrical coordinates along the pipe surface. Since the evaluation of the bulk Temperature is impossible without knowing its profile inside the swirling flow, all the properties and heat transfer coefficients are evaluated with the temperature of the flow at the centreline of the test section T_c. The latter is assumed to grow linearly from the inlet to the outlet section of the pipe. The dimensionless form of the convective coefficient is the Nusselt number, defined as:

$$Nu(z,\theta) = \frac{hD}{k_{\text{f}}} \tag{3}$$

where D is the pipe diameter and k_f is the thermal conductivity of the flow. It makes sense to compare the heat transfer in the ribbed cylinder with the one for a smooth channel, by means of the Enhancement Factor (EF):

$$EF(z,\theta) = \frac{Nu(z,\theta)}{Nu_0} \tag{4}$$

where Nu_0 is the Nusselt number of a fully developed flow in a smooth circular pipe, estimated from the Dittus-Belter correlation:

$$Nu_0 = 0.023 \times Re^{0.8} \times Pr^{0.4} \quad (5)$$

The reliability of the technique described before for heat transfer measurements has been validated in the work of the authors Mayo et al. [3] who applied the same measurements routine for a smooth channel without any turbulator inside. The results in terms of Nusselt number, for several Reynolds numbers, agree with those given by the correlation of Dittus-Belter. In the worst case, at a Reynolds number of about 2×10^5, the difference between measurements and correlation is of 7.4%.

2.3. Friction coefficient measurement setup

The friction losses evaluations have been made using the air tunnel used for the heat transfer measurements. Actually, this facility has two pressure taps, one upstream and one 2 diameters downstream of the test section. An inductive pressure transducer (Validyne) measures the static differential pressure Δp_{static}. Out of it, the surface average of the wall shear tensor can be computed by using the formula as below:

$$\tau_{\text{wall}} = \frac{\Delta p_{\text{static}} \times r}{2 \times L} \quad (6)$$

where r and L are respectively, the inner radius of the test section and the distance between the two wall pressure taps. The pressure transducer has a Full Scale of ±86 Pa and provides an uncertainty of ±0.2 Pa. This low value has been provided thanks to the Ultra Low Differential Pressure calibrator DPI 610 LP which has a span of 250 Pa and an extended uncertainty of ±0.05% of the span. Therefore, the friction coefficient C_f, averaged on the ribbed surface, is computed according to the formula:

$$C_{\text{f}} = \frac{\tau_{\text{wall}}}{0.5 \times \rho \times u_b^2} \quad (7)$$

where ρ is the flow density and u_b is the bulk velocity given by the orifice plate. To validate the technique, the measurements made for the test section without any turbulator have been compared with the Blasius correlation for turbulent fully developed flows in smooth pipes [18]:

$$C_{\text{f}} = \frac{0.079}{Re^{0.25}} \quad (8)$$

3. Results

As expected, both the turbulators make the friction losses to increase, because of the presence of wall obstacles. Regarding the Geometry-A, the friction factors are quite constant at a level of about 8 times the one given by the Blasius correlation for fully developed flows in smooth pipes. For the case of Geometry-B, the same takes place at lower values. As a matter of fact, the Geometry-B has been designed to decrease the pressure losses of this kind of turbulators.

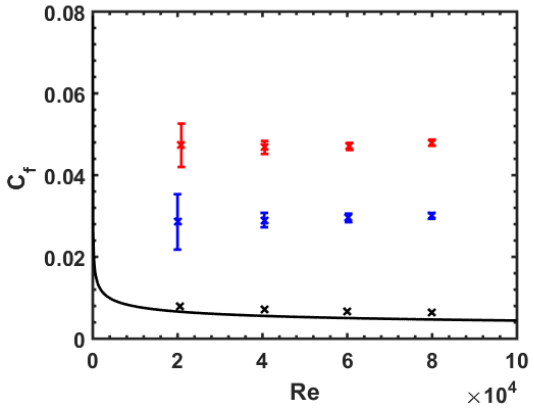

Figure 7: Friction factor as a function of Reynolds number: red crosses, Geometry-A; blue crosses, Geometry-B; black crosses, smooth pipe; solid line, Blasius

The contours of Fig. 8 show the EF distributions plotted between the obstacles of two turbulators, at a same distance in terms of helix pitches. The Geometry-A makes the flow to separate and to reattach where the heat transfer shows its biggest value. This reattachment line follows the helix pattern imposed by the turbulator and it is set at a distance of about 4 times the rib's height. The surface averaged Nusselt number slightly increases with the Reynolds number, showing a maximum EF of about 1.72, with an extended uncertainty of 6% (Tab. 1). When the test section is equipped with the Geometry-B, the same phenomenon as before occurs in the area just downstream the obstacle ($\theta = -22° \div 22°$), but the reattachment lengths are slightly smaller (Fig. 11). The reattachment area does not follow any helix pattern, resulting to be a deformed line downstream the obstacle trailing edge. The higher the Reynolds number, the more is the deformation of the reattachment line. The area where the EF has its maximum value, corresponds to the impingement of the separated flow. This zone tends to get closer to the obstacle at the

edge where $\theta = 20^\circ$ and to get resized with increasing mass flows. The tendency of the surface averaged EF is to stay more or less constant with the Reynolds number at values slightly lower than the other geometry. Nevertheless, the maximum heat transfer enhancement has been shown for Re = 80000 at values comparable with the Geometry-A.

Table 1: Surface averaged EF

Re number	$EF_{\text{geometry A}}$	$EF_{\text{geometry B}}$
20000	1.77±0.14	1.43±0.13
40000	1.77±0.10	1.49±0.10
60000	1.78±0.09	1.48±0.09
80000	1.79±0.09	1.47±0.09

The flow field at the regime of Reynolds number equal to 20000 between the obstacles is provided by the Stereo-PIV measurements. The Fig. 9 plots the axial components of the velocity field at several locations between the obstacles. It is clear from the figure that the blockage provided by the Geometry-A is higher than the one given by the other turbulator.

The separation of the flow, followed by the impingement and recirculation bubble is better shown in the Fig. 10 where the streamlines are plotted on the top of the velocity azimuthal component distribution. The reattachment length results to be equal to the one argued by the EF contours, that is where X/e is about 4, for the Geometry-A and at a lower value, for the Geometry-B. Higher values for the swirl are given by the Geometry-A, since the turbulator has a profile that develops continuously through the helix pattern. The highest values for the azimuthal component are shown at the leading edge of the obstacles. In the case of the Geometry-B, the left side of the recirculation bubble has a negative swirl at the wall close to the trailing edge. This phenomenon is due to the discontinuity of the geometry blockage throughout the helix development.

The dimensionless Turbulent Kinetic Energy (k) fields defined as:

$$k = \frac{0.5 \times (u'^2 + v'^2 + w'^2)}{{U_{\text{bulk}}}^2} \tag{9}$$

where u', v' and w' are the velocity fluctuations in the three dimensions, is shown in Fig. 11, together with the EF plot between the obstacles. The Geometry-A provides a higher k than the Geometry-B, all over the flow field, with a maximum value of about 12.5% of the bulk velocity. The area is where the flow shows a high shear due to the separation from the obstacle. The same value has been measured for the other geometry, in the same position between X/e=2 and X/e=4. The remarkable difference is that, with the Geometry-B the dimensionless TKE, and so the turbulence levels, are lower in the zone far from the wall. Just behind the maximum value of the dimensionless TKE, the EF shows its peak, for both the cases (Fig. 11).

4. Conclusion

Data for the validation of Large Eddy Simulation on chemical reactors has been provided. The way the code solves the Navier-Stokes and the energy equation for the small scales can be verified with the results showed hereby. The measurements outcome, concerning the flow field and the heat transfer, show the importance of turbulators thought as well-performing cooling channels techniques. The induced 3-dimensional separation makes the flow to impinge on the wall allowing the enhanced heat transfer. Anyway, the topology of the flow and the increased turbulence produce more skin friction at the wall. An overall efficiency of the system, which takes into account both the results, can be evaluated by means of the equation below:

$$\eta = \frac{\frac{Nu}{Nu_S}}{\frac{(1+C_f)}{(1+C_f)_S}} \tag{10}$$

Actually, the global energetic efficiency (η) stated before, represents the ratio between the performances of the system with and without turbulator. The Tab. 2 shows its values at different Reynolds number for the two geometries. As a final remark, the geometry-A provides an higher energetic performance in therms of aero-thermal properties. The statistical mean over the several values at different Re number turns to be 1.6 and 1.3, for Geometra-A and Geometry-B respectively. The oncoming work will be concerning the performance evaluation given by dimpled channels in terms of heat transfer and friction losses.

Acknowledgments

The author wishes to thank the Laboratory for Chemical Technology in Gent University and CERFACS, for the initiative in performing the present experimental campaign. Also, the help and expertise of Ignacio Mayo Yage, Julien Desset, Grard Goossens

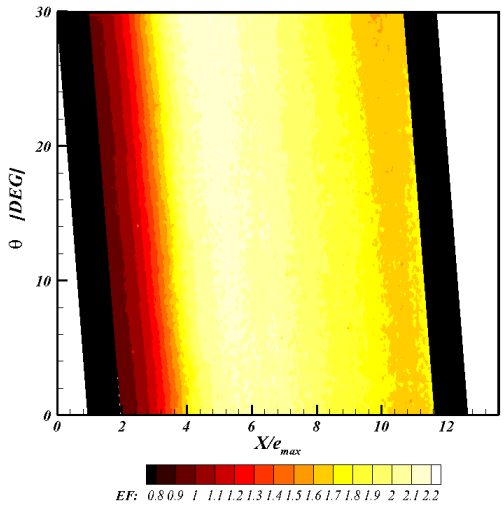

(a) EF field at Re = 20000 (Geometry-A)

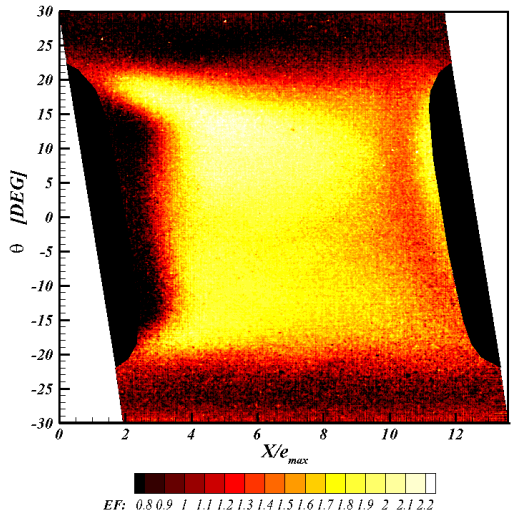

(b) EF field at Re = 20000 (Geometry-B)

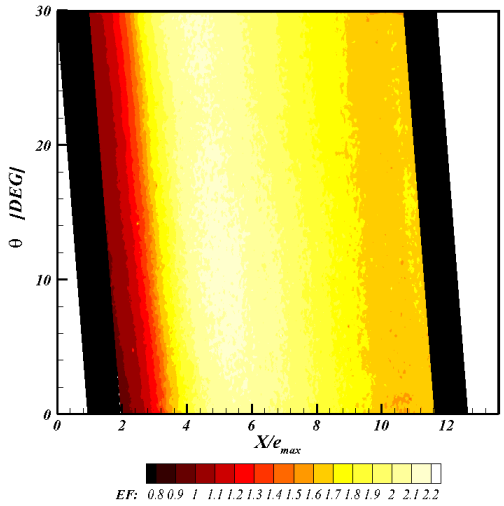

(c) EF field at Re = 40000 (Geometry-A)

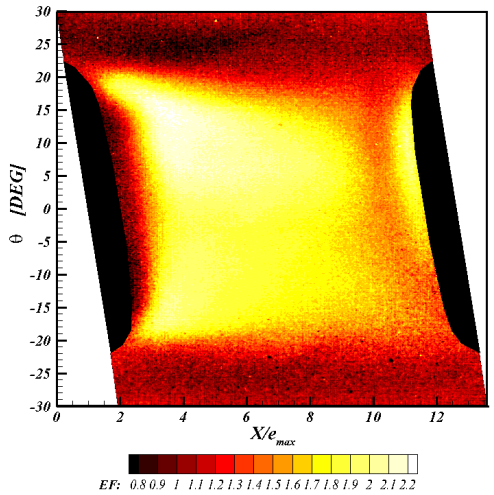

(d) EF field at Re = 40000 (Geometry-B)

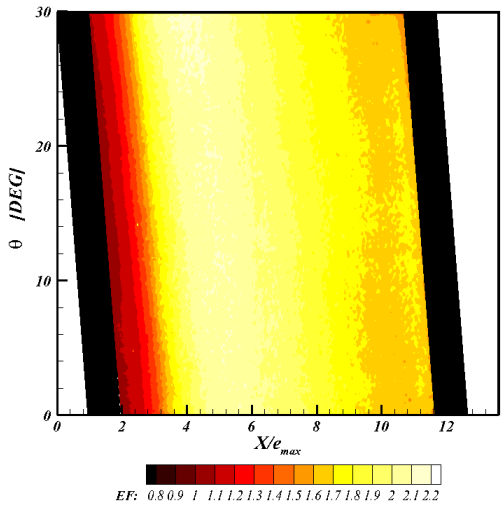

(e) EF field at Re = 60000 (Geometry-A)

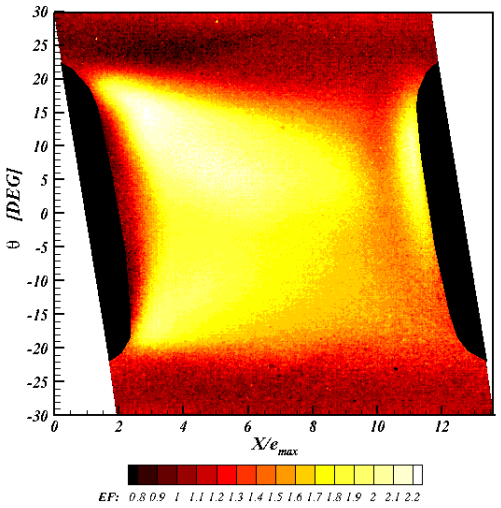

(f) EF field at Re = 60000 (Geometry-B)

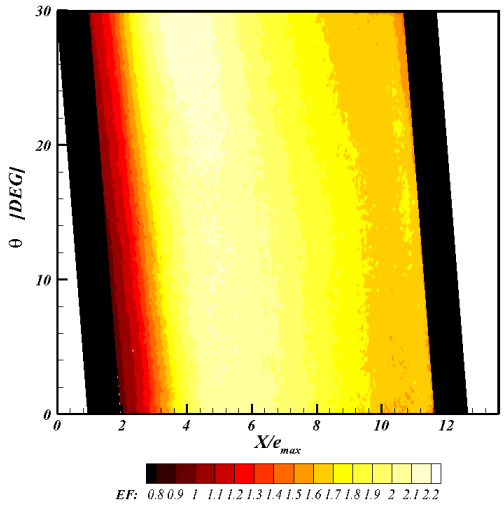

(g) EF field at Re = 80000 (Geometry-A)

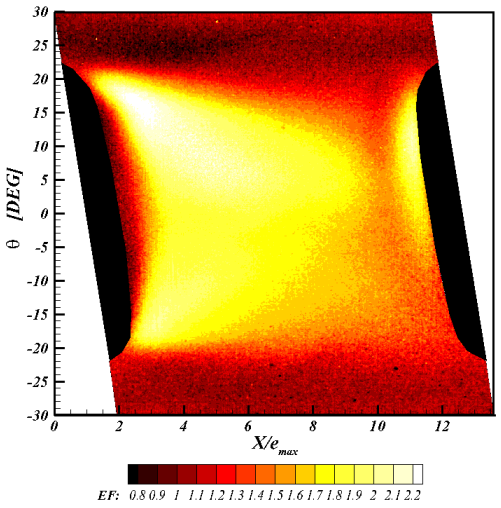

(h) EF field at Re = 80000 (Geometry-B)

Figure 8: EF contours between 2 obstacles of the 2 geometries as a function of Re number

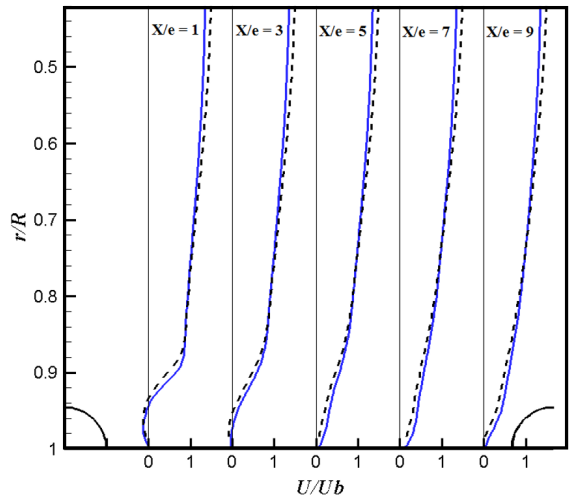

Figure 9: Axial velocity profiles at Re = 20000: blue solid, geometry A; black dashed, geometry B

Table 2: Global efficiency of the two geometries

Re number	$\eta_{\text{geometry A}}$	$\eta_{\text{geometry B}}$
20000	1.70	1.40
40000	1.70	1.46
60000	1.71	1.44
80000	1.72	1.43

and Jean-Christophe Desilve at VKI are highly appreciated.

References

[1] M. Gyrffy, M. Hineno, K. Hashimoto, P. Seong-Hoan and Y. Min-Soo, MERT performance and technology update, AIChE Spring Meeting.

[2] J. C. Han, S. Dutta and S. Ekkad, Gas Turbine Heat Transfer and Cooling Technology, Second Edition, Taylor and Francis, 2012.

[3] I. Mayo, B. C. Cernat, M. Virgilio, A. Pappa, T. Arts, Aerothermal Investigation of the Flow and Heat Transfer in a Helically Corrugated Cooling Channel, no. Proceedings of ASME Turbo Exp: Turbine Technical Conference and Expositiono, Seoul, South Korea, 2016.

[4] P. Ligrani, Heat Transfer Augmentation Technologies for Internal Cooling of Turbine Components of Gas Turbine Engines , International Journal of Rotating Machinery 2013.

[5] T. S. Ravigururajan and A. E. Bergles, Development and verification of general correlations for pressure drop and heat transfer in single-phase turbulent flow in enhanced tubes, Experimental Thermal and Fluid Science 70.

[6] S. Pethkool, S. Eiamsa-ard, S. Kwankaomeng and P. Promvonge, Turbulent heat transfer enhancement in a heat exchanger using helically corrugated tube, International Communications in Heat and Mass Transfer 38 (2011) 340–347.

[7] A. Garcia, J. P. Solano, P. G. Vicente and A. Viedma, Flow pattern assessment in tubes with wire coil inserts in laminar and transition regimes, Int. J. Heat Fluid Flow 28 (2007) 516–525.

[8] L. Bonanni, R. Da Soghe, B. Facchini, M. Micio, M. Pievaroli, L. Tarchi, L. Abba and M. Maritano, Heat transfer and friction in circular ducts with shaped ribs, no. Proceedings of the 10th European Turbomachinery Conference, Lappeenranta, Finland, 2013.

[9] M. Zhu, E. Riber, B. Cuenot, J. Bodart and T. Poinsot, Wall-resolved Large Eddy Simulation in refinery ribbed pipes, no. Center for turbulence research - Proceeding of the Summer program, 2014.

[10] F. P. Incropera, D. P. DeWitt, T. L. Bergman and A. S. Lavine, Foundamentals of Heat and Mass transfer, 6th ed., John Wiley & Sons, 2007.

[11] F. Coletti, T. Maurer, T. Arts and A. Di Sante, Flow Field investigation in rotating rib-roughened channel by means of particle image velocimetry, Experiments in Fluids 52 (2012) 1043–1061.

[12] C. W. H. van Doorne and J. Westerweel, Measurement of laminar, transitional and turbulent pipe flow using stereoscopic-PIV, Experiments in Fluids 42 (2007) 259–279.

[13] ISO 5167 - Measurement of fluid flow by means of pressure differential devices inserted in circular cross-section conduits running full, Tech. rep., International Organization for Standardization (2003).

[14] A. K. Prasad, Stereoscopic particle image velocimetry, Experiments in Fluids 29 (2000) 103–116.

[15] A. K. Prasad and K. Jensen, Scheimpflug stereocamera for particle image velocimetry to liquid flows, Appl. Optics 34 (1995) 7092–7099.

[16] N. J. Lawson and J. Wu, Three-dimensional particle image velocimetry: experimental error analysis of a digital angular stereoscopic system, Meas. Sci. Technol. 8 (1997) 1455–1464.

[17] S. M. Soloff, R. J. Adrian and Z. C. Liu, Distortion Compensation for generalised stereoscopic particle image velocimetry, Meas. Sci. Technol. 8 (1997) 1441–1454.

[18] S. B. Pope, Turbulent flows, Cambridge University Press, 2000.

[19] R. J. Adrian and J. Westerweel, Particle Image Velocimetry, Cambridge University Press, 2000.

[20] P. M. Kodzwa Jr. and J. K. Eaton, Angular effects on thermochromic liquid crystal thermography, Experiments in Fluids 43 (2007) 929–937.

[21] B. Cukurel, C. Selkan and T. Arts, Color theory perception of steady wide band liquid crystal thermometry, Experimental Thermal and Fluid Science 39 (2012) 112–122.

[22] N. Abdullah, A. R. A. Talib, A. A. Jaafar and M. A. M. Salleh, The basics and issues of thermochromic liquid crystal calibration, Experimental Thermal and Fluid Science 34 (2010) 1089–1121.

[23] G. M. Carlomagno and G. Cardone, Infrared thermography for convective heat transfer measurements, Exp. Fluids 49 (2010) 1187–1218.

[24] Test Uncertainty, Tech. rep., American Society of Mechanical Engineers, New York (2005).

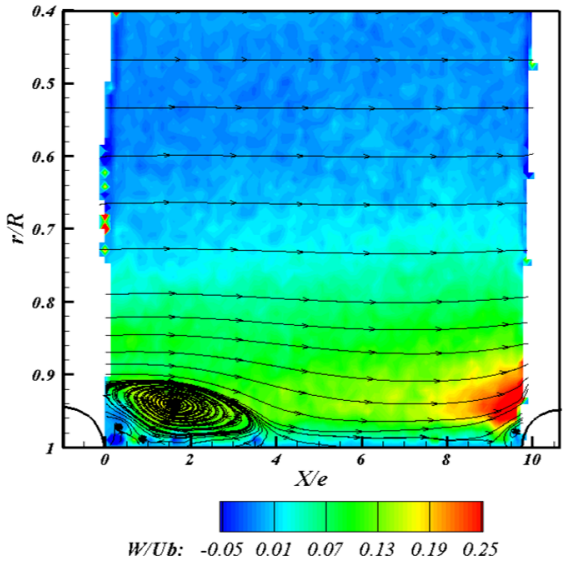

(a) Stream lines and azimuthal velocity field at Re = 20000 (geometry A)

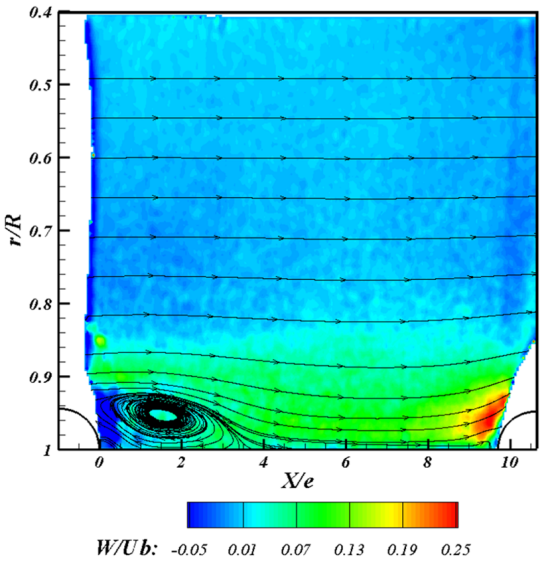

(b) Stream lines and azimuthal velocity field at Re = 20000 (geometry B)

Figure 10: Flow Field between 2 obstacles of the 2 geometries at Re = 20000

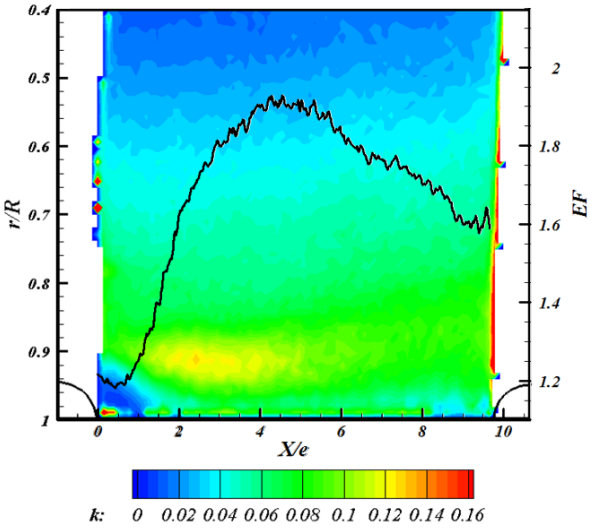

(a) Turbulent Kinetic Energy (k) field at Re = 20000 (geometry A)

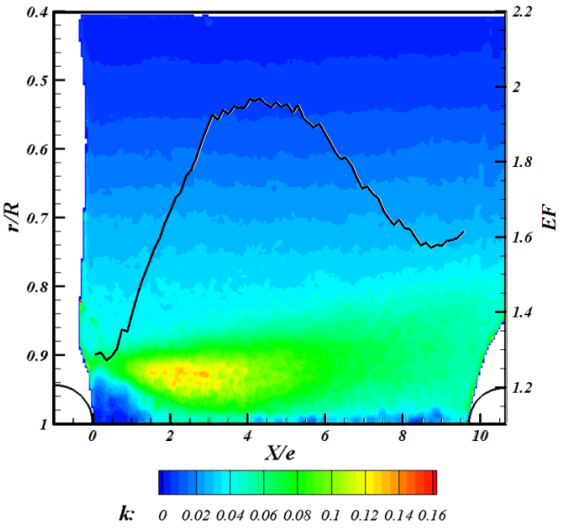

(b) Turbulent Kinetic Energy (k) field at Re = 20000 (geometry B)

Figure 11: TKE distibution between 2 obstacles of the 2 geometries at Re = 20000

DEVELOPMENT OF ADVANCED CFD AND OPTIMIZATION

Adjoint Surface Optimization for Internal and External Aerodynamics Applications by means of OpenFOAM

Giacomo Alessi

Environmental and Applied Fluid Dynamics Department, von Karman Institute for Fluid Dynamics, Belgium, giacomo.alessi@vki.ac.be

Supervisor: Jeroen van Beeck

Professor, Environmental and Applied Fluid Dynamics Department, von Karman Institute for Fluid Dynamics, Belgium, vanbeeck@vki.ac.be

Supervisor: Tom Verstaete

Associate Professor, Turbomachinery and Propulsion Department, von Karman Institute for Fluid Dynamics, Belgium, tom.verstraete@vki.ac.be

University Supervisor: Bert Blocken

Part-Time Full Professor, Civil Engineering Department, Leuven University, Belgium, bert.blocken@bwk.kuleuven.be

Abstract

The pressure loss reduction inside the u-bends of internal cooling channels is of crucial importance to increase the performance of cooling systems of gas turbines. The optimization technique proposed in the present work is based on the continuous adjoint shape method and is implemented in the OpenFOAM open-source framework. The calculated gradients of the objective function are linked to a node-based constrained morphing routine, allowing the modification of the shape towards an optimum design with minimum pressure loss. The integration with a robust mesh morpher solver leads to successive automatic steps towards the design improvement. Design modifications take into account constraints and limitations related to the chosen design. The feasibility of the design is guaranteed by the application of a smoother with the aim to avoid rough external surfaces.

Keywords: surface adjoint optimization, mesh morphing, open-source

1. Introduction

Nowadays, the use of numerical tools to assist design development is of common practice. Thanks to the continuous growth of the computational resources and the increased accuracy of numerical simulation models, it is possible to compare different design prototypes and investigate the influence of several parameters with the aim to improve their performance. However, due to the designs complexity, many different parameters are usually coupled and their effect on the design could be difficult to assess. As a consequence, in the past decades it has been performed a large development of computational routines that autonomously maximize the design performance, i.e. the so-called optimization algorithms. Nonetheless, many design optimization techniques suffer from dimensionality problems, since the numerical effort significantly increases with the degrees of freedom. Especially when costly CFD simulations are required to evaluate the performance, the search for optimal shapes can only be executed effectively with limited design freedom. Gradient based optimization techniques, however, still allow for rich design spaces if the adjoint method is used to compute the sensitivities [1], since its computational cost is independent from the number of design variables. The direction of improvement can be obtained at a fixed cost independently from the size of the design variables space, considerably reducing the overall procedure time and the computational power needed. The adjoint method is becoming more and more the tool of choice for gradient optimizations, whose application can be found

in different fields [2; 3; 4].

An optimization routine based on the adjoint method has been developed in this work and has been tested with an internal aerodynamic application. The optimization test case is linked to turbomachinery industrial applications, in particular to the cooling system of gas turbines [5]. The U-bend shape is particularly representative of the cooling system design, being the major source of thermodynamic efficiency loss. Due to the large number of parameters that plays a role in this application, the adjoint method represents an efficient approach to the problem.

2. The U-bend test case

Cooling systems of gas turbines, in most of the cases, use air bled from the high pressure compressor, leading to a penalty in thermodynamic efficiency. A design of the internal cooling passages for minimal pressure losses would improve the global efficiency of the gas turbine. The U-bends that connect consecutive passages are amongst the largest contributors to the pressure losses in the cooling system and deserve special attention during the design phase. Hence, its design has been considered separated from the rest of the internal cooling structure in this optimization work. The considered design and flow configuration has received particular attention both from research groups and industries, thus various approaches and optimization strategies have been applied to it [6; 7; 8].

The numerical domain considered in the present work is represented by a circular U-bend of square section (hydraulic diameter $D_h = 0.075[m]$), whose geometrical details can be found in Coletti et al. [9]. A velocity profile with a bulk velocity of $U_0 = 8.4[m/s]$ and a turbulence intensity of $T.I. = 5\%$ has been imposed at the inlet [10]. A zero pressure boundary condition is applied to the outlet and a no-slip condition to the wall.

Reynolds-averaged NavierStokes simulations have been performed using a structured grid, assuring a maximum y_+ value of 0.94. The Lauder-Sharma low-Reynolds $k-\epsilon$ turbulence model has been used. The velocity field obtained and its streamlines are shown in Fig. 1, in particular: ((a)) at $z/D_h = 0.5$ and ((b)) at $z/D_h = 0.03$. The flow accelerates approaching the bend, it reaches the maximum velocity around the inner wall while it decelerates along the outer wall. At the symmetry plane, $z/D_h = 0.5$, the flow starts to separate before the end of the bend forming a separation bubble. A longer recirculation bubble is present at $z/D_h = 0.03$. The flow field characteristics obtained

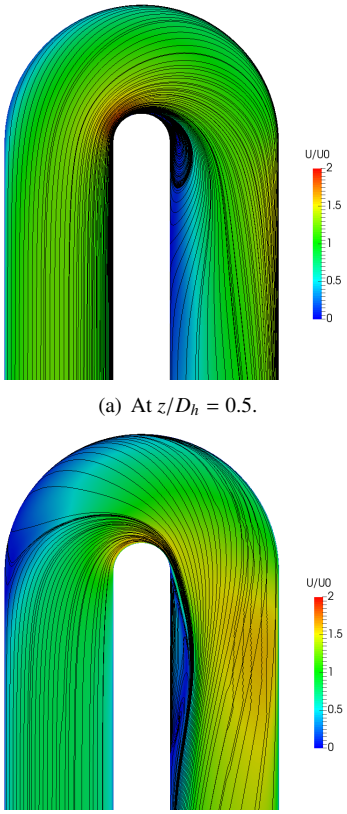

(a) At $z/D_h = 0.5$.

(b) At $z/D_h = 0.03$.

Figure 1: Velocity field and streamlines in the initial 3D U-bend design.

are in agreement with the numerical ones in Coletti et al. [9].

The routine has been first tested with a 2D test case to verify the reliability of the procedure and after applied to the 3D case. The 2D geometry refers to the symmetry plane of the 3D U-bend design, thus the flow field characteristics are similar to it with the exception of the presence of a longer separation bubble than the one obtained in the 3D case at $z/D_h = 0.5$, as shown in Fig. 2.

The aim of the study is the minimization of the total pressure losses, thus the considered cost function J is represented by:

$$J = p_T^{in} - p_T^{out} = \left(p + \frac{1}{2}\rho U^2\right)_{in} - \left(p + \frac{1}{2}\rho U^2\right)_{out} \quad (1)$$

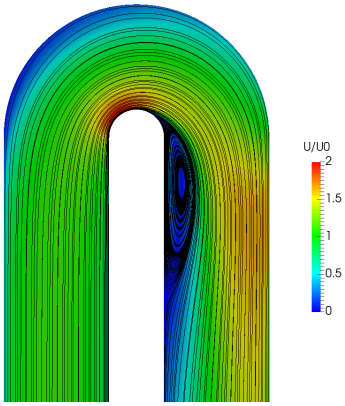

Figure 2: Velocity field and streamlines in the initial 2D U-bend design.

3. The adjoint method in the context of shape optimization

In the adjoint formulation two systems of equations have to be solved, the Navier-Stokes equations and the adjoint equations. The first step of the optimization process is to solve the Navier-Stokes equations (primal system) to obtain convergent flow variables, as shown in Sec. 2; successively the convergence assessment is required for the adjoint variables. By solving both systems of equations, a surface sensitivity map can be extrapolated. The information contained in it suggests the modifications to perform on the body contour to increase the performance. Based on this information the geometry boundary can be modified. Eventually, as proposed in the present work (Sec. 4), a mesh morphing solver can be included in the optimization routine to allow automatic successive steps of the optimization process. A schematic loop of the optimization routine implemented is shown in Fig. 3.

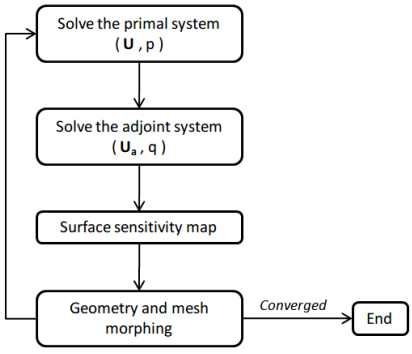

Figure 3: Optimization loop.

3.1. Adjoint equations

The problem to be considered is: minimize J such that the Navier-Stokes equations are satisfied. A general cost function J can be taken into account, dependent on the flow variables $\mathbf{U}$ and p, respectively velocity and pressure, and on the design variables.

Following the derivation in Papoutsis-Kiachagias and Giannakoglou [11], the adjoint equations, continuity and momentum, are:

$$\nabla \cdot \mathbf{U_a} = \frac{\partial J_\Omega}{\partial p} \tag{2}$$

$$\mathbf{U_a}\cdot\nabla\mathbf{U} - \mathbf{U}\cdot(\nabla\cdot\mathbf{U_a}) = \nabla\cdot(2\nu_{eff}D(\mathbf{U_a})) - \nabla q - \frac{\partial J_\Omega}{\partial \mathbf{U}} \tag{3}$$

The boundary conditions, derived for the following specified boundaries, are listed in Tab. 1.

Table 1: Adjoint boundary conditions.

Inlet and walls		
$\mathbf{U_a}_t = 0$	$U_{an} = -\frac{\partial J_\Gamma}{\partial p}$	$n \cdot \nabla q = 0$
Outlet		
$q = U_n U_{an} + \nu_{eff}(\mathbf{n}\cdot(\nabla\cdot U_{an})) + \frac{\partial J_\Gamma}{\partial U_n}$		
$U_n \mathbf{U_a}_t + \nu_{eff}(\mathbf{n}\cdot(\nabla\cdot\mathbf{U_a}_t)) + \frac{\partial J_\Gamma}{\partial \mathbf{U}_t} = 0$		

where: $\mathbf{U}$ and p represent the velocity and the pressure (primal variables); $\mathbf{U_a}$ and q are the adjoint velocity and the adjoint pressure (adjoint variables); ν_{eff} is the effective viscosity; $D(\mathbf{U_a})$ represents the rate of strain tensor; the subscripts Ω and Γ are referred, respectively, to the volume and boundary contributions of the cost function; while the subscripts t and n are referred to the tangential and normal component.

As highlighted by the adjoint equations and their boundary conditions, the adjoint problem needs to be fed with information related to the cost function, making a one-to-one relation between the two. The cost function chosen for the U-bend optimization, i.e. the total pressure loss between inlet and outlet (Eq. 1), gives a contribution only to the boundary conditions, as well as for all the cost functions that are only defined along the boundaries. Those cost functions identify a class for which the adjoint equations do not vary with a cost function variation.

In the present work the variation of the effective turbulent viscosity with a design modification has been considered negligible. The so-called frozen turbulence assumption neglects the change of turbulent

quantities under geometry variations. The use of the frozen turbulence assumption can have a significant influence on the obtained solution [12]. On the other hand, the use of an adjoint turbulence model would increase the complexity of the method. Despite the possible loss of accuracy, the use of this hypothesis leads to an overall validity of the solution obtained.

3.1.1. Surface sensitivity map

The adjoint optimization method uses the information from the derivative of the objective function with respect to the design variables in its search for the minimum. The design variables chosen in the present work are represented by the normal displacement of each surface node, β, resulting in a very rich design space.

The gradient information, also called surface sensitivity map, can be evaluated from the solution of the primal and adjoint equations system, as in Eq. 4.

$$S = \frac{\partial J}{\partial \beta} = -\nu_{eff} \frac{\partial \mathbf{U_a}}{\partial \mathbf{n}} \frac{\partial \mathbf{U}}{\partial \mathbf{n}} \tag{4}$$

The surface sensitivity map is evaluated at the geometry walls and expresses how much the geometry is sensitive to the performance, i.e. how much the objective function would change for a unit movement in the direction of the surface normal. A highly sensitive area entails that only a very small shape modification would already result in a large change of the objective function. The design variable space is composed of the normal nodes displacement, thus the modifications must be performed in the direction normal to the surface itself. The sensitivity map obtained in the 2D U-bend test case is shown in Fig. 4.

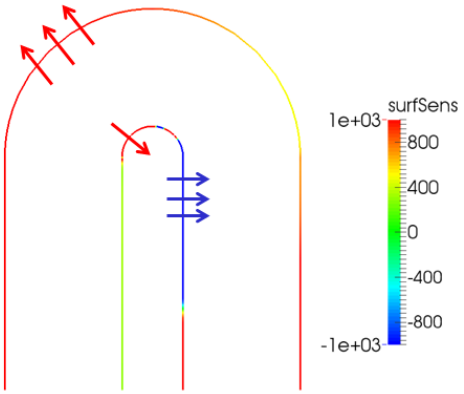

Figure 4: Surface sensitivity map and improvement directions (2D test case).

A positive sensitivity map region has to be moved away from the fluid to increase the performance, while a negative sensitivity value indicates that a performance improvement would be reached by moving those regions towards the fluid. On the other hand, modifications of a zero sensitivity map region will not influence the cost function.

Before converting the gradient information into a real design variation, a preliminary step is needed. The surface sensitivity presents high frequency oscillations that, due to the use of the node based approach, would result in a irregular shape if not treated in a suitable way. Moreover, the high frequency oscillations will amplify during the optimization phases, causing mesh distortion problems and ultimately leading to unrealistic shapes. The attainment of a smooth sensitivity is a crucial point to obtain a valid geometry deformation, and thus an admissible design. Hence, the use of a filter that takes out the high order oscillations is indispensable. The choice of the smoothing strategy requires particular attention: while it is mandatory to get rid of the discontinuities, the main information content of the sensitivity must be preserved.

A weighted average smoothing has been used in the present work for the 2D optimization test case. In particular, the smoothed sensitivity $\overline{S}$ has been evaluated as follow:

$$\overline{S_i} = \sum_j \omega_j \sum_i \omega_i S_i \tag{5}$$

where the weight ω is calculated as:

$$\omega_i = l_i / l_{sum} \tag{6}$$

In Eq. 6, l_i is the inverse distance between face centers and boundary points and l_{sum} is the sum of the inverse distances. The same definition is used for w_j, where the distance to be considered is the one from the boundary points to the face centers. The smoothing strategy used corresponds to successive weighted interpolations of the surface sensitivity from face centers to boundary points and vice versa, resulting in a weighted average that takes into account a stencil of three consecutive nodes.

The importance of the application of a smoothing function is highlighted in Fig. 5(a) and Fig. 5(b), which show the raw and smoothed sensitivity signal along the 2D U-bend inner wall respectively after 1 and 100 iterations. The high frequency oscillations are already present at the first iteration step and become more pronounced with the iterations. Note how

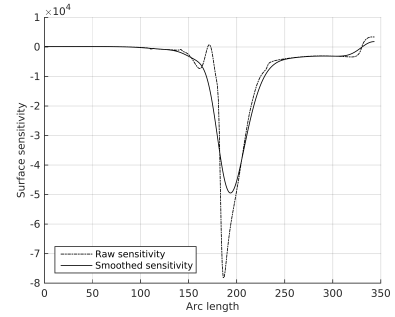

(a) At the first loop iteration.

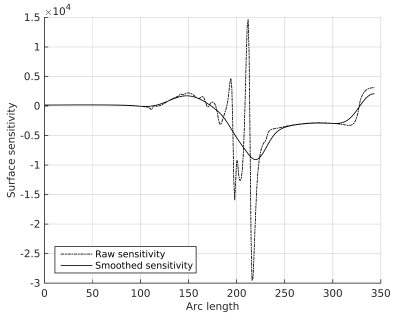

(b) After 100 loop iterations.

Figure 5: Raw and smoothed sensitivity signal along the 2D U-bend inner wall.

the smoothed signal still maintains the main information of the raw sensitivity.

A Gaussian smoothing [13] has been used in the 3D test case, thus the smoothed sensitivity is given by:

$$\overline{S} = (I - \lambda K)S \tag{7}$$

where: I is the identity matrix; λ takes the name of scale factor and it is a bounded positive number $0 < \lambda < 1$; $K = I - \Omega$; Ω represents the weights matrix, whose non-zero elements correspond to the design variables neighbours and are equal to the inverse distance between each node and its neighbour.

Although the performance of the two different smoothing strategies are comparable, the Gaussian smoothing resulted to be more efficient when dealing with high number of design variables and therefore used for the 3D optimization.

4. Constrained morphing routine for an optimal design

The last step of the optimization process implemented includes the modification of the design and a link to a mesh morpher solver to allow successive automatic steps towards the design improvement. This leads to deal with two important issues: 1) the design modifications need to take into account particular limitations intrinsic to the chosen design, e.g. aerodynamic and geometrical constraints, and 2) the surface deformations must lead to a variation of the internal grid of the fluid domain which ensures a sufficient mesh quality to solve the RANS equations further. Moreover, the design feasibility must be guaranteed, hence rough surfaces cannot be accepted.

4.1. Design variation

Once the sensitivity oscillations have been ironed out, as shown in Sec. 3.1.1, it is possible to link its information to a design variation. In the present work the design is updated using a steepest descent algorithm, as in Eq. 8:

$$\mathbf{x_{i+i}} = \mathbf{x_i} + \alpha \overline{S}\,\mathbf{n} \tag{8}$$

where $\mathbf{x_i}$ and $\mathbf{x_{i+i}}$ represent the position vector of each node, respectively, before and after the boundary movement. Each node is displaced in the direction normal to the surface, $\mathbf{n}$, with a magnitude depending on the smoothed surface sensitivity, $\overline{S}$. An additional parameter α is included and is defined as follows:

$$\alpha = \frac{\epsilon}{max\|\overline{S}_1\|} \tag{9}$$

The role of the parameter is to normalize the sensitivity, through its maximum value at the first iteration of the optimization loop, and to fix the maximum step size of the movement, through the parameter ϵ. In the present work, ϵ is kept constant, so it has been used a steepest descent algorithm with fixed step size. Nevertheless, the surface sensitivity decreases its magnitude in its route to the optimum, hence the magnitude of the nodes movement decreases iteration by iteration and eventually becomes null if a local minimum is reached.

The choice of the right value for the parameter α represents a key point of the optimization process. A big value of α could be unsuitable as it could overshoot the optimum and worsen the design straight away. On the other hand a value that is too small would exponentially increase the computational time. The choice of the suitable value to be assigned is left to the user, as it is highly case-dependent. The results shown in the present work refer to a value of $\epsilon = 10^{-4}$ and of $\epsilon = 5 \cdot 10^{-3}$, respectively, for the 2D and 3D

optimization case. A bigger initial deformation has been imposed to the 3D case in order to minimize the number of optimization cycles needed to reach an optimum design, being each 3D flow field evaluation much more computationally expensive than the 2D one.

The algorithm described by Eq. 8 represents a classical steepest descent algorithm and allows a huge degree of freedom in the attainment of the optimized design. However, the majority of the designs must respect constraints, geometrical and aerodynamic, and the optimization is usually required in a limited region of the design. The planar constraints and limitations present in the U-bend test case are shown in Fig. 6. The height of the channel is allowed to change up to $0.1D_h$.

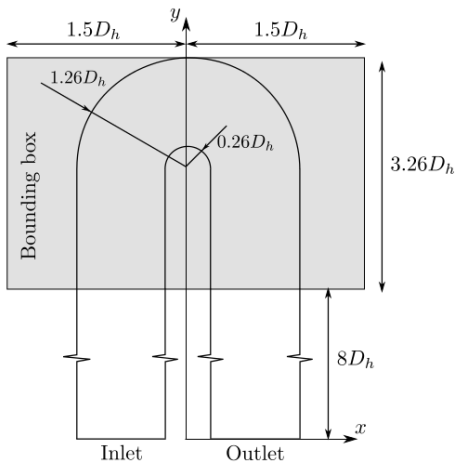

Figure 6: Planar constraints and limitations in the U-bend test case.

The bounding box shown in Fig. 6 indicates the constraints to be satisfied and the zones of the U-bend that can take part in the optimization process. In order to fulfil the requirements, a constrained steepest descent algorithm has been implemented. This has been included in a versatile optimization routine that allows to the user the freedom to choose between unconstrained and constrained optimization. In the latter, the definition of a bounding box is requested. Finally, it is given to the user the possibility to choose whether to perform the optimization in a confined region or in the whole design.

4.2. Mesh morphing strategy

The last step of the optimization process is represented by a link between the boundary movement and the mesh deformation. For the cases where the motion is solution-dependent, can be used a mesh morpher based on the Laplace equation in which the prescribed boundary movement represents the boundary condition for the internal cell motion. Details about the mesh morphing strategy can be found in Jasak [14]. In the present work, a distance-based quadratic method has been chosen, so the diffusivity in the Laplace equation is function of the inverse square distance from the nearest boundary. A distance-based diffusivity improves the mesh quality near the boundaries: it redistributes the movement inside the domain allowing bigger deformations on the center of the domain where bigger cells are present.

Nevertheless, the described strategy in not sufficient to avoid a local worsening of the mesh quality near the moving boundaries. The solver calculates the cell displacement based on a cell-centred approach and interpolates to obtain the points movement. However, boundaries with prescribed movement maintain their imposed value, leading to possible differences between those values and the ones of the internal points and eventually to highly distorted cells, especially for very thin layers. In order to maintain a good mesh quality, a point interpolation method has been used [15]. The method allows to maintain a fixed first layer height by extending the interpolation to the boundaries. The difference between the interpolated value on the boundary and the desired boundary condition is then propagated into the mesh.

The main concern about the use of a mesh movement solver is its capability to preserve the mesh quality. It is indeed of crucial importance for an automatic process to avoid the accumulation of error due to low mesh quality. The strategy described, together with the use of a suitable smoother and an appropriate step size for the boundary movement, allows the fulfilment of the mesh quality criteria. The cancellation of the high frequency noise in the sensitivity map is indeed fundamental in order to avoid overlapping of boundaries. However, the choice of the correct parameters to set is not straightforward and highly case-dependent, thus several attempts could be necessary before finding the most appropriate ones. In order to ensure the correctness of the process, thus avoiding to perform the optimization with a highly distorted mesh, a mesh quality check has been introduced after each mesh morphing step. The additional step assures that the mesh quality criteria are satisfied at each iteration step and decides whether to continue with successive iterations of the optimization loop or to end the process.

5. Optimization results

The application of the steps described outlines an optimization routine that should bring to an improvement of the design with respect to the objective function taken into account. In the present work, the optimization routine has been fed with a U-bend shape with the aim to reduce the total pressure loss in it. In order to verify the reliability of the procedure developed, a 2D optimization corresponding to the symmetry plane of the U-bend design has been firstly performed. The satisfactory results obtained with it, allowed to proceed with the optimization of the 3D design.

5.1. 2D optimization test case

The outcome of the optimization routine is illustrated in Fig. 7, which shows different optimized shapes, their normalized velocity field and their velocity streamlines. Fig. 7(a) shows a rough transition from the design regions subjected to boundaries movement and the regions that are not allowed to take part in the optimization process. Even though an improvement in the pressure drop has been achieved ($\Delta p = -20\%$), the shape obtained cannot be considered during an industrial process because of the highlighted discontinuity. The abrupt variation in the shape takes place over one single cell, hence the obtained result is questionable.

In order to overcome this problem, two approaches are proposed: the assignment of a continuity constraint for the surface sensitivity or for the boundary displacement, respectively in Fig. 7(b) and Fig. 7(c). The constraints allow to obtain smooth optimized designs that could be manufactured in an industrial process. The continuity constraint imposed on the surface sensitivity is less demanding, so bigger design modifications can be reached. Despite the biggest improvement is achieved imposing the constraint on the sensitivity ($\Delta p = -31.5\%$), the constraint on the displacement seems to give results more suitable to an industrial process. Indeed less modifications should be performed on the original geometry, maintaining a remarkable improvement in the design performance ($\Delta p = -28.5\%$). Obviously, the attainment of the continuity constraints allows to reach better improvements, being the discontinuities present in the initial optimization (Fig. 7(a)) a limitation to the capability of the optimizer that remains trapped in a local minimum.

A comparison between the flow field in the original and optimized geometries, Fig. 2 and Fig. 7 respectively, highlights the direction taken by the optimization routine to achieve its objective. The body shape is modified in order to obtain a pressure drop minimization through the reduction of the separation bubble size that takes form after the bend. The separation region is indeed the main source of pressure loss in the proposed design, thus its suppression represents the target of the optimization routine. Analyses of the optimized U-bend shapes verify the characteristics discussed in the previous sections. A flat region is present at the top part of the bend (Fig. 7(a)-7(b)), showing that the geometrical constraints imposed have been reached and satisfied. The external geometries are smooth, proving the effectiveness of the smoothing strategy used on the sensitivity. The mesh morpher has been shown to be robust enough so that the mesh quality criteria were satisfied at each iteration.

The variation of the cost function during the optimization process is shown in Fig. 8. The three different optimizations performed reach a stable minimum, identified from the attainment of a constant value of the cost function. The introduction of the continuity constraints clearly influences the optimization history, resulting in a speed up of the optimization process. The preference for the application of the constraint on the displacement rather than on the sensitivity is confirmed also by the optimization history, since a comparable final improvement is obtained halving the computational time of the process. The optimization history of the case with a continuity constraint on the displacement converges in approximately 2000 iterations. The high number of iterations performed does not imply the use of a computational expensive routine. Indeed, the use of partially converged variables at each iteration step considerably speeds up the process, allowing to reach the minimum in a night-time period. A fully convergent simulation was carried out at the end of the optimization process, confirming the 28.5% improvement in the total pressure loss and thus verifying the validity of the approach used.

5.2. 3D optimization test case

The optimization performed on the 2D test case highlighted the necessity to impose a continuity constraint in the transitional region in order to avoid abrupt variations in the design. The best result in terms of design and computational time has been attained with the assignment of the continuity constraint on the boundary displacement, thus it has been applied also in the 3D optimization case. The optimized

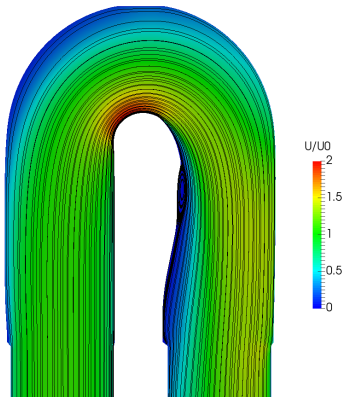

(a) No constraint in the transitional region. ($\Delta p = -20\%$).

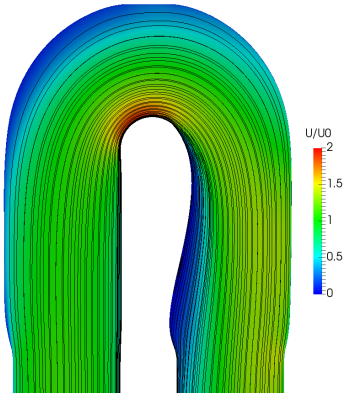

(b) Continuity constraint for the sensitivity. ($\Delta p = -31.5\%$).

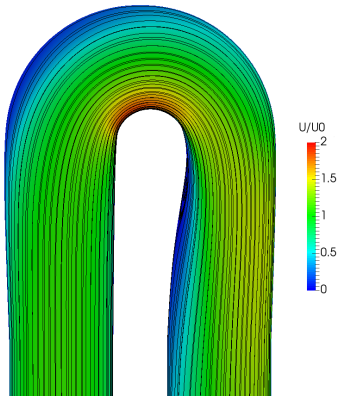

(c) Continuity constraint for the displacement. ($\Delta p = -28.5\%$).

Figure 7: Optimized 2D U-bend shape: velocity field and streamlines.

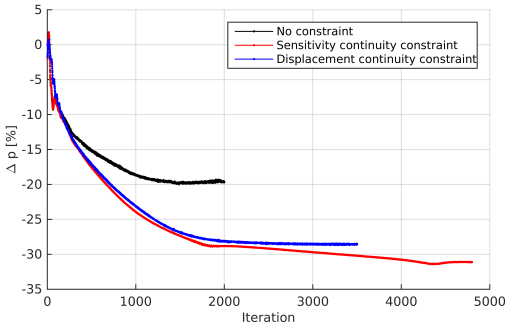

Figure 8: Optimization history 2D U-bend.

U-bend design obtained is shown in Fig. 9, in particular a xz and yz view, ((a)) and ((b)), and a section at x=0 ((c)). The section gradually enlarge in the y-direction until the constraint (Fig. 9(b)). Different xz profiles are present along the y axis as illustrated in the yz section (Fig. 9(c)). The final design obtained would be unpredictable without the use of an optimization routine. A smooth external shape is attained, proving once again the effectiveness of the smoothing strategy proposed. A comparison between the resulting velocity fields, Fig. 10, and the initial ones, Fig. 1, confirms the tendency of the optimizer to modify the design with the aim to suppress the separation bubble, as observed in the 2D optimization case. Moreover, a significant reduction of the maximum velocity inside the geometry is obtained.

The route towards the optimum design is shown in Fig. 11. A stable local minimum has been reached with an improvement on the total pressure loss of the 30%. The initial bigger deformation applied to the 3D case in comparison to the 2D one allows to reach the optimum design in approximately 25 iterations and in a night-time period using 12 processors. The mesh morpher routine has been shown to be robust enough to tolerate the big deformations imposed.

6. Conclusions

The optimization of an internal flow application has been described in the present work, detailing the structure of the routine developed. The U-bend test case has been optimized with respect to the total pressure loss. The use of an adjoint optimization strategy allowed to efficiently approach the problem, given the high number of design variables taken into account. The solution of the primal and adjoint problem gives information on the modifications to perform in order

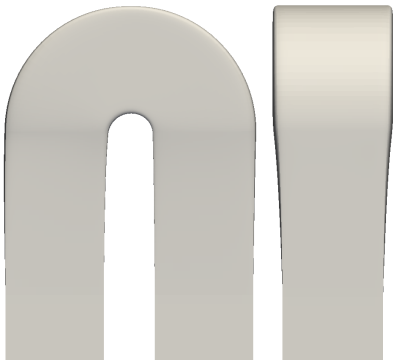

(a) xz view. (b) yz view.



(c) yz section at x=0.

Figure 9: Optimized 3D U-bend shape.

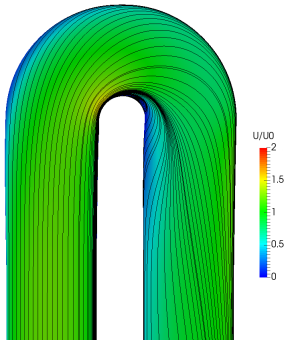

(a) At $z/D_h = 0.5$.

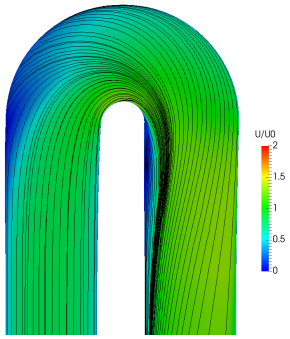

(b) At $z/D_h = 0.03$.

Figure 10: Optimized 3D U-bend: velocity field and streamlines.

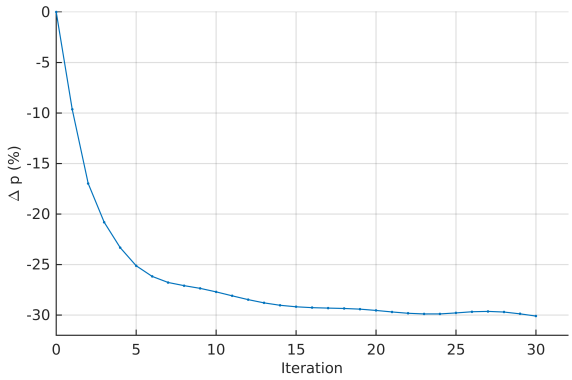

Figure 11: Optimization history 3D U-bend.

to improve the design, which has been attained trough the link to a constrained mesh morphing routine. The optimization has been performed in a restricted area of the design and subjected to geometrical constraints. Limitations on the regions that can be optimized are generally present, however the evaluation of an unfeasible optimization covering the whole geometry could be of interest. Indeed, it would enlarge the design space and it could lead to ideas for further design and for different design strategies.

The optimization routine allowed to obtain an improvement of the cost function of the 28.5%-30%, respectively in the 2D-3D case, through the reduction of the separation bubble size that develops after the bend. Manufacturability of the design is assured by a smooth external geometry.

Acknowledgments

This work was supported by the Fonds Wetenschappelijk Onderzoek Vlaanderen - FWO.

References

[1] O. Pironneau, On optimum design in fluid mechanics, Journal of Fluid Mechanics 64 (part I) (1974) 97–100.

[2] A. Jameson, Aerodynamic design via control theory, Journal of Scientific Computing 3 (3) (1988) 233–260.

[3] C. Othmer, Adjoint methods for car aerodynamics, Journal of Mathematics in Industry 4 (1).

[4] J. Goit and J. Meyers, Optimal control of wind farm power extraction in large eddy simulations, AIAA SciTech 32nd ASME Wind Energy Symposium, AIAA 2014-0709.

[5] S. D. J. Han, S. Ekkad, Gas Turbine Heat Transfer and Cooling Technology, Taylor and Francis, New York, 2000.

[6] T. Verstraete and J. Li, Multi-objective optimization of a u-bend for minimal pressure loss and maximal heat transfer performance in internal cooling channels, ASME Turbo Expo 2013: Turbine Technical Conference and Expositions, 3A: Heat Transfer.

[7] S. Zehner, H. Steinbruck, S. Neumann and B. Weigand, The ice formation method: A natural approach to optimize turbomachinery components, International Journal of Design & Nature 3 (4) (2009) 259–272.
[8] H. Namgoong, C. Son and P. Ireland, U-bend shaped turbine blade cooling passage optimization, 2th AIAA/ISSMO Multidisciplinary Analysis and Optimization Conference, AIAA 2008-5926.
[9] F. Coletti, T. Verstraete, T. Vanderwielen, J. Bulle and T. Arts, Optimization of a u-bend for minimal pressure loss in internal cooling channels - part II: Experimental validation, ASME paper GT2011-46555.
[10] T. Verstraete, F. Coletti, J. Bulle, T. Vanderwielen and T. Arts, Optimization of a u-bend for minimal pressure loss in internal cooling channels - part I: Numerical method, ASME paper GT2011-46541.
[11] E. Papoutsis-Kiachagias and K. Giannakoglou, Continuous adjoint methods for turbulent flows, applied to shape and topology optimization: Industrial applications, Archives of Computational Methods in Engineering 23 (2) (2016) 225–299.
[12] A. Zymaris, D. Papadimitriou, K. Giannakoglou and C. Othmer, Continuous adjoint approach to the spalart-allmaras turbulence model for incompressible flows, Computers & Fluids 38 (2009) 1528–1538.
[13] G. Taubin, Curve and Surface Smoothing Without Shrinkage, Proceedings of the Fifth International Conference on Computer Vision (1995) 852–857.
[14] H. Jasak and Z. Tukovic, Automatic mesh motion for the unstructured finite volume method, Transactions of FAMENA 30 (2) (2006) 1–20.
[15] Mesh motion: new point interpolation methods, https://www.openfoam.com/releases/openfoam-v3.0+/numerics.php.

Single-point optimization of the LS89 turbine cascade using a hybrid algorithm

Arnaud Châtel

Turbomachinery and Propulsion Department, von Karman Institute for Fluid Dynamics, Belgium, arnaud.chatel@vki.ac.be

Supervisor: Tom Verstraete

Associate Professor, Turbomachinery and Propulsion Department, von Karman Institute for Fluid Dynamics, Belgium, tom.verstraete@vki.ac.be

University Supervisor: Grégory Coussement

Professor, Fluids-Machines Unit, University of Mons, Belgium, gregory.coussement@umons.ac.be

Abstract

This paper presents a hybrid optimization algorithm which combines the two main families of optimization methods namely an evolutionary algorithm and a gradient-based method. The better performance of the developed hybrid method, compared to a classical evolutionary algorithm, is first demonstrated on two analitycal functions. Then, the algorithm is used to optimize LS89 turbine cascade, resulting in a new design with about 20 percent lower entropy production. A thorough flow analysis shows that the improvements are largely due to a significant decrease in trailing edge losses.

Keywords: aerodynamic optimization, hybrid algorithm, evolutionary algorithm, gradient-based method, profile losses

1. Introduction

Nowadays, optimization methods are integrated into the design process in various industrial sectors, as they have proven to reduce the design cost and time while at the same time improving product quality [1; 2; 3; 4]. Due to this, they are increasingly used in more elaborate and complex design tasks, which require more efficient and versatile optimization algorithms. Since these optimizations require more computational resources and can be very time-consuming, the improvement of the optimization methods themselves becomes a crucial challenge. This improvement is particularly relevant when the performance of the design is quantified using advanced computational methods. This is the case in aerodynamic design processes where Computational Fluid Dynamics (CFD) are used to predict the flow performance.

Currently, two main families of optimization methods can be distinguished depending on the order of the derivative of the objective function used. Gradient-free methods use only the value of the objective function, while gradient-based methods require additionally the computation of gradient values in order to perform the optimization [5; 6]. Each of these two families has its own advantages and disadvantages. The most prevalent gradient-free methods in the field of shape optimization are evolutionary algorithms which are based on Darwinian evolution [5]. They allow a global exploration of the complete design space using a population of individuals which evolve in the search space. However, because of the so-called ”curse of dimensionality” [7], the convergence performance of these algorithms becomes relatively poor when the number of design variables increases. Even though gradient-free methods can rapidly identify the region of the design space where the global minimum is located, the convergence towards this minimum can be very long [8; 9]. On the contrary, gradient-based methods concentrate

the optimum search in a direction defined by means of the gradients of the objective function. When combined with the adjoint method to compute the gradients efficiently, these methods tend to converge more rapidly and do not suffer to the same extend from the curse of dimensionality [10]. However this family of methods performs a local exploration of the design space and tends to be trapped in local minima.

In this context, hybrid optimization algorithms, which combines both families of methods, benefit from the respective strengths of gradient-free and gradient-based methods. Therefore, the hybrid algorithms have better convergence performance towards the global optimum of the design space. A review of different kinds of hybrid optimization algorithms can be found in [11]. Most of the methods described in the paper are applied on job-shop scheduling problems [12; 13]. In the engineering field, the common hybridization strategy consists in the incorporation of a gradient-based method into the gradient-free method [11]. In this strategy, two different approaches can be distinguished in the literature. First, the gradient-based method can be integrated directly in the loop of the evolutionary algorithm in order to locally improve individuals of each population. This approach is generally called Lamarckian approach or memetic algorithm [14; 9; 15; 8]. In the second approach, the gradient-free method performs a certain number of generations and then gradient-based methods are applied on the most promising individuals of the last population [16].

In this work, we propose an hybrid algorithm which combines an evolutionary algorithm called Differential Evolution [17] and the classical steepest descent method [5]. The hybridization is based on the Lamarckian evolution briefly mentioned above. This hybrid algorithm is tested on the well-known LS89 turbine cascade [18]. A single point optimization of the geometry profile is performed in order to minimize the entropy generated by the flow through the cascade.

This paper is structured as follows: the first section is dedicated to the hybrid optimization algorithm which is extensively presented. Then the proposed method is tested and validated on two analytical functions specially designed to test the performance of optimization algorithms. The third section describes the LS89 application, the geometry parametrization, and the aerodynamic performance parameters used in the optimization process. At the end of this section, the results of the hybrid optimization are compared to the results obtained in a previous study [19] in which the LS89 profile was optimized using a classical gradient-based method. Finally, in the last section, the optimized profile found by the hybrid algorithm is compared to the LS89 profile in order to understand the mechanisms behind the improved performance.

2. Hybrid optimization algorithm

The first part of this section describes the basic principle of the proposed hybrid optimization algorithm. Then, in order to explain the methodology, three different aspects of the hybrid method are discussed namely the position of the hybridization, the selection of the individuals for local improvements and the imposition of constraints.

2.1. Basic principle

The aim of the implemented hybrid optimization algorithm is to combine efficiently a gradient-free and a gradient-based method. This combination should benefit from the respective strengths of both methods, namely the faster convergence of the gradient-based method and the capacity to locate the global optimum of the gradient-free method. The chosen methodology is based on the Lamarckian evolution [8; 15] and consists in incorporating directly the gradient-based method inside the gradient-free algorithm.

In this work, the hybrid algorithm uses the Differential Evolution (DE) algorithm developed by Price and Storn [17] as the gradient-free method and the steepest descent associated with line search method [20; 21] as the gradient-based search. The ideal step length in the descent direction is computed by a line search method based on the Wolfe conditions [21]. The integration of the gradient-based method inside the loop of the evolutionary algorithm is presented in Fig. 1.

The hybrid algorithm starts like the classical DE algorithm with a population of random individuals which are evaluated and reproduced in order to create a new population. The reproduction is composed by two mechanisms called mutation and crossover as described in [17]. Then, the hybridization of the DE algorithm occurs within the generated new population. In this population, the most promising individuals are chosen to be locally improved using

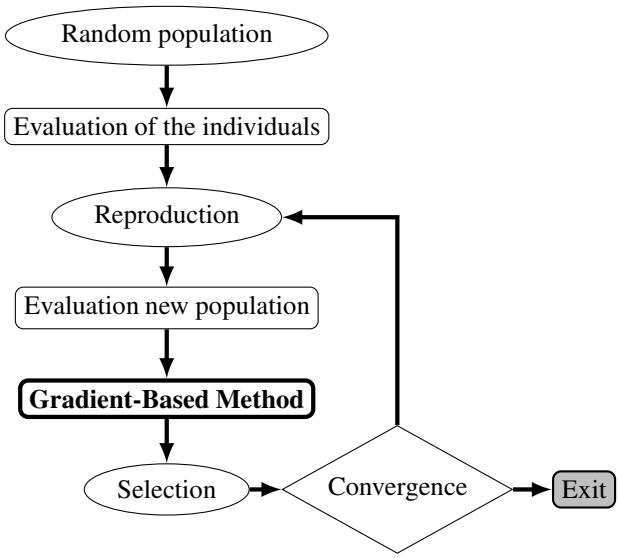

Figure 1: Hybrid Algorithm combining the DE algorithm and the steepest descent method.

the gradient-based method regarding them as starting points for the steepest descent algorithm. Therefore, the gradient values of the objective function with respect to the design parameters are computed only for these promising individuals. For each individual selected for a local search, only one iteration of the steepest descent method is performed because there is no need to bring the individuals exactly to their minimum which could be just local [14; 8]. Continuing the steepest descent method until convergence of each individual can generate a prohibitive computational cost just to locate local minima. Once the selected individuals have been locally improved, they are reintegrated in their original population and the *selection* between this population and the previous one is carried out. Finally, if the stopping criterion are not respected, the evolutionary process restarts.

Hereinafter, three different points of the hybrid algorithm are discussed: the position of the hybridization in the DE algorithm, the selection of the individuals which are locally improved and the imposition of the constraint in the hybrid algorithm.

2.2. Position of the hybridization

The gradient-based methods are always performed before the *selection* of the DE algorithm because it allows to conserve the diversity introduced by the evolutionary algorithm. Indeed, in this situation, the steepest descent algorithm is applied to new created individuals at each generation. In contrast, if the local improvement is performed after the *selection*, an individual with a good potential can be replaced during the *selection* by another on which local searches have already been realized in the previous generations. In that case, the gradient-based method is always applied to the same individuals and, therefore, the algorithm can get stuck in a local minimum during more generations.

2.3. Selection of the individuals for local improvement

The most promising individuals of the new populations are chosen by assigning a probability to be locally improved. In a population, the individual with the lowest value of the objective function has the highest probability value equal to 1. The probability p_i of the other individuals of the population is computed relatively to the objective function of the best individual $f_{obj}|_{BestInd}$ and can be expressed by:

$$p_i = \frac{\frac{1}{f_{obj}|_i}}{\frac{1}{f_{obj}|_{BestInd}}}. \quad (1)$$

Finally, for each new generation, gradient-based methods are applied on all the individuals of the population which have a probability above a certain limit p_{limit} defined beforehand by the user.

2.4. Imposition of constraints

In many optimizations, the aim is to identify a design $\vec{X}$ which minimizes the objective function $f(\vec{X})$ while respecting certain constraints $g(\vec{X})$. Therefore the problem is usually expressed as follows:

$$\text{Minimize:} \quad f(\vec{X}) \quad (2)$$

$$\text{Subject to:} \quad g(\vec{X}) \leq 0. \quad (3)$$

In the DE algorithm, the constraints are imposed by eliminating the individuals which do not respect the Eq. 3 in the *selection* process. Therefore, in the hybrid method, the individuals locally improved have to respect the constraints otherwise they will be directly eliminated in the next *selection* process and the computational cost of the steepest descent method will be lost. For gradient-based methods, however, such simplified handling of the constraints is not possible and more elaborate algorithms are needed. The simplest approach consists in adding a penalty term to the objective function, which penalizes the objective when the constraint is violated [19; 21]. This exterior

penalty method converges in case of active constraints to a design which violates the constraint as a balance between the improvement of the objective and deterioration of the penalty, which is perceived as a serious deficit in the hybrid method as the design will be thrown away in the next round of the DE *selection* process. Therefore, in this work, another method is implemented which corrects the individuals with active constraint. The methodology is called the Projected Gradient method and consists in projecting the concerned individuals on the constrained limit expressed by:

$$g(\vec{X}) = 0 \tag{4}$$

The principle of the projected gradient method is presented in Fig. 2 where the grey area contains all the designs which respect the constraint (expressed by Eq. 3). During the steepest descent, the design $\overrightarrow{X_i}$ is modified in the direction $\vec{S}$ computed using the gradients and, for a certain value of the step length, a design $\overrightarrow{X_{i+1}}$ which does not respect the constraint can be obtained. In this particular case, the design $\overrightarrow{X_{i+1}}$ is projected on the limit of the constraint (expressed by Eq. 4) using the vector $\vec{\delta}$ in order to obtain a new design $\overrightarrow{X_{Cor}}$. The computation of the vector $\vec{\delta}$ starts with the linear approximation of the constraint function around the corrected design $\overrightarrow{X_{Cor}}$:

$$g(\overrightarrow{X_{Cor}}) = g(\overrightarrow{X_{i+1}} + \vec{\delta}) = g(\overrightarrow{X_{i+1}}) + \vec{\delta}.\nabla g(\overrightarrow{X_{i+1}}) = 0 \tag{5}$$

Since the aim of the method is to project the design $\overrightarrow{X_{i+1}}$ on the limit of the constraint where $g(\vec{X}) = 0$, the right hand side of Eq. 5 is equal to 0 and the vector $\vec{\delta}$ can be computed using the final formula 6. In this development, only a linear approximation of the function $g(\vec{X})$ is used, and therefore few iterations of this process could be needed in order to correct properly the design. It can be seen, in the previous development, that the projected gradient method makes use of the gradient values of the constraint (∇g) which have to be computed if a design does not respect the constraint.

$$\vec{\delta} = -\frac{g(\overrightarrow{X_{i+1}})}{\nabla g(\overrightarrow{X_{i+1}})} \tag{6}$$

The projected gradient method is used at two different places in the hybrid optimization algorithm. First, in the obvious case of an individual which does not respect the constraint during the steepest descent method. In that case the design is modified in the direction given by the projected gradient method until the constraint is satisfied. Secondly, the projected gradient method is also applied to correct new promising individuals generated by the evolutionary algorithm which eventually do not respect the constraint. These individuals are first corrected by the projection process and, then, are locally improved by the steepest descent method.

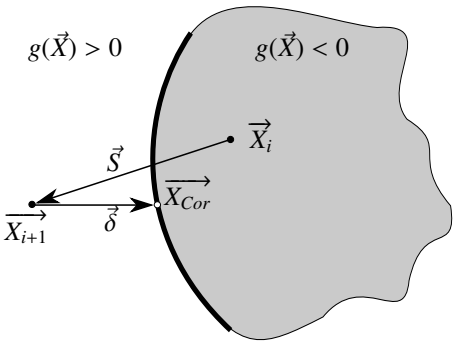

Figure 2: Principle of the projected gradient method

3. Validation on analytical functions

The proposed hybrid algorithm is first validated on two analytical functions specially designed to assess the performance of optimization methods [22]. The functions are called Rastrigin and Rosenbrock and are respectively expressed by Eq. 7 and Eq. 8. Both functions are represented in Fig. 3 and their values at the global minimum are equal to zero.

$$f_{Rastrigin} = 10 + \sum_{i=1}^{N_{Param}} [x_i^2 - 10.cos(2\pi x_i)] \tag{7}$$

$$f_{Rosenbrock} = \sum_{i=1}^{N_{Param}-1} [100.(x_{i+1} - x_i^2)^2 + (1 - x_i)^2] \tag{8}$$

As shown in Fig. 3, the Rastrigin function is highly multimodal which makes the localization of the global minimum relatively complicated. On the opposite, the Rosenbrock function is unimodal but the only minimum is located inside a parabolic and flat valley. This function is used as a benchmark problem in optimization because the valley is easy to find, while the convergence towards the global minimum inside the valley can be difficult even for

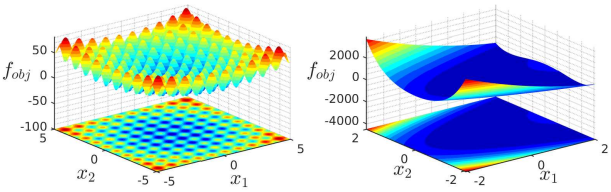

Figure 3: Rastrigin function (left) and Rosenbrock function (right) defined 2 parameters

gradient-based methods. In order to demonstrate the effect of the hybridization on optimizations conducted in larger design spaces, the algorithm is tested on the Rastrigin functions described by 2 and 5 parameters and on the Rosenbrock functions computed by means of 2 and 20 parameters.

The aim of the proposed algorithm is to localize the global minimum of the functions using a limited computational cost. Such a global exploration of the design space is not feasible using gradient-based methods and can only be performed with evolutionary algorithms. Therefore, in this section, the performance of the new hybrid method in terms of number of iterations and number of evaluations of the function is compared to the performance of the classical DE algorithm. Since evolutionary algorithms are non-deterministic methods, the performance of the two different algorithms needs to be statistically analyzed. Due to this, each optimization is performed 40 times and the averaged results are presented in Fig. 4 and in Fig. 5. In these figures, the y-axis represents the ratio between the objective of the best individual of the new populations generated f_{best} and the objective of the best individual taken in the starting population f_{Max}. Generally, the computational cost for the gradients evaluation is of the same order of magnitude than the cost for the objective function evaluation. Indeed, in industrial applications involving CFD analysis, the gradients can be obtained at a similar cost as the CFD using the adjoint method [10]. Hence, in the results, both kinds of evaluations are considered to take one unit of evaluation time.

As shown in Figs. 4 and 5, the hybrid method converges faster than the DE towards the global minimum of the two analytical functions. Moreover, the comparisons represented in the bottom plots of the figures are the most important because they show that the hybridization of the DE algorithm allows to decrease the number of evaluations needed to locate the minimum.

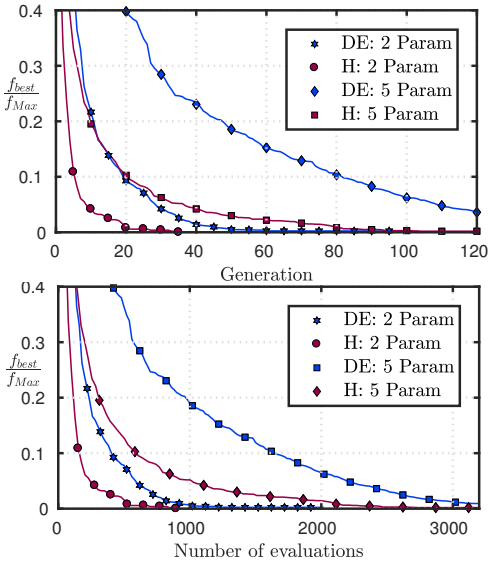

Figure 4: Comparison of the performance of the DE and the hybrid (H) algorithms in terms of number of generations (top) and in terms of number of evaluations (bottom) for the Rastrigin function

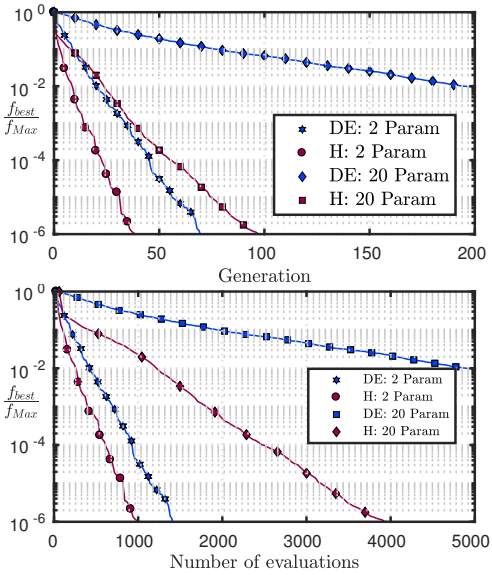

Figure 5: Comparison of the performance of the DE and the hybrid (H) algorithms in terms of number of generations (top) and in terms of number of evaluations (bottom) for the Rosenbrock function

And, in aerodynamic shape optimization, where the objectives are computed by means of CFD, the reduction of this evaluation number is crucial in order to limit the computational cost of the complete optimization. Finally, for both functions, the effect of the curse of dimensionality can be clearly identified in the plots when the number of parameters defining the objective functions increases. Indeed, for the Rastrigin and Rosenbrock functions respectively computed using 5 and 20 parameters, the DE algorithm converges relatively slowly and requires to perform many evaluations. In the case of the hybrid method, the hybridization improves the performance of the evolutionary algorithm and therefore, the proposed algorithm is less affected by the curse of dimensionality.
In conclusion, this section showed that the new hybrid optimization method allows to locate the global minimum of a function at a lower computational cost than classical evolutionary algorithms.

4. Application on a turbomachinery case

In this section, the proposed hybrid algorithm is tested on a typical turbomachinery application: the turbine cascade LS89. The first part of this section describes the different characteristics of the LS89 optimization while the second part presents the results and compares them with those obtained using a classical gradient-based method.

4.1. LS89 Application

In this work, a single point optimization of the LS89 geometry profile is performed in order to minimize the entropy generated by the flow through the cascade. The LS89 turbine blade, represented in Fig. 6, is a highly loaded blade with a flow turning of about 75°. The LS89 cascade has been designed at the Von Karman Institute and extensively tested in various flow operating conditions from the subsonic to the transonic regime [18]. The single point optimization presented in the paper is performed for an operating point characterized by a downstream isentropic Mach number of 0.9. The conditions at the inlet and at the outlet for this operating point are summarized in the Table 1.

Table 1: Definition of the operating point conditions

Inlet	P_0	147 500 Pa
	T_0	420 $°K$
	α_{in}	0 °
Outlet	P	80 000 Pa

4.1.1. Parametrization

In order to enable the geometrical design optimization with regards to its flow performance, the geometry of the cascade is constructed using the parametrization method described in [19; 23]. The turbine is completely defined by 19 design parameters represented in Fig. 6. First the blade camber line is represented with a second order Bézier curve using the control points P_{LE}, P_M and P_{TE}. These control points are obtained using the axial chord c_a, the stagger angle γ and the outlet metal angle β_{out}. Then to define the blade thickness, the control points of the SS and the PS B-Splines are located in the direction normal to the camber line by imposing the distance t_i as shown in Fig. 6. At the LE, the position of the first control points of the SS and the PS is computed in order to obtain a G2 continuity between the SS and PS B-splines, assuring a continuity of the radius of curvature which ensures a smooth flow at the connection. The last control points of the PS and the SS are localized using respectively the angle φ_{PS} and φ_{SS}. Finally, the profile of the blade is closed at the TE by a circular arc. The construction of the cascade is completed by imposing the pitch between two successive blades. During the optimization process, the axial chord and the TE radius remain constant for all the designs. The axial chord is maintained in order to conserve the axial dimension c_a of the cascade and the TE radius r_{TE} is kept fixed in order to respect manufacturing tolerances.

4.1.2. Objective and constraints

The objective of the optimization consists in minimizing the entropy generation J through the cascade while maintaining the flow turning of the original blades in order to achieve at least the same work. This aerodynamic constraint on the outlet flow angle expressed by Eq. 9 is imposed during the optimization process.

$$\frac{\alpha}{\alpha_{LS89}} \geq 1 \tag{9}$$

The exit flow angle α is mass-averaged at the outlet of the computational domain and is equal to $\alpha_{LS89} = 74.89°$ for the original LS89 blade.

The entropy generation (Eq. 10) is computed between the inlet and the outlet of the computational

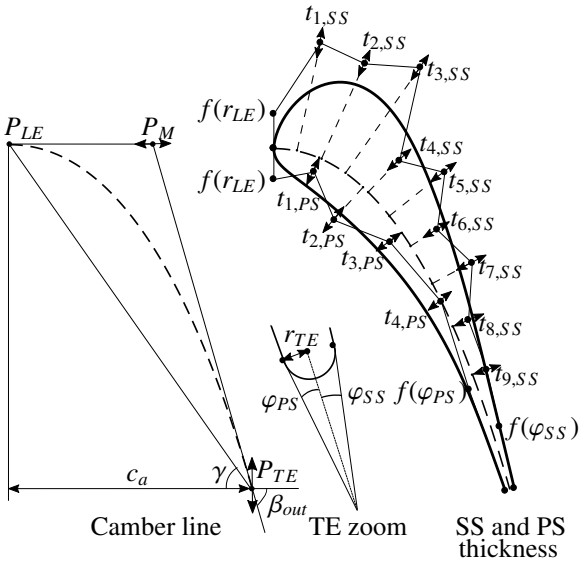

Figure 6: Parametrization of the LS89 turbine cascade

domain using the mass-flow averaged entropy at the respective position.

$$J = S_{out} - S_{in} \tag{10}$$

4.2. Results

In the hybrid method, since the gradients of the objective function and of the constraint can be needed for certain individuals, a complete process chain of tools has been developed at the von Karman Institute, which comprises a geometry generator, a grid generator and a CFD solver. All these tools have been differentiated in order to accurately compute the gradient values of the different functions using a CAD-based adjoint method [2]. The references [19; 23] provide a detailed description of the complete chain of tools and a validation of the gradients computed in the case of the LS89 turbine. In this application, the automatically generated mesh is structured and constructed using one O-grid block around the blade and 6 others H-grid blocks. The mesh generated for the LS89 application is presented in Fig. 7. The numerical simulations are performed by solving the Reynolds-Averaged Navier-Stokes (RANS) equations and using the Spalart-Allmaras equation in order to model the flow turbulence. The validation of the CFD computation is presented in Fig. 8 by comparing the evolution of the isentropic Mach number along the blade obtained numerically with experimental results.

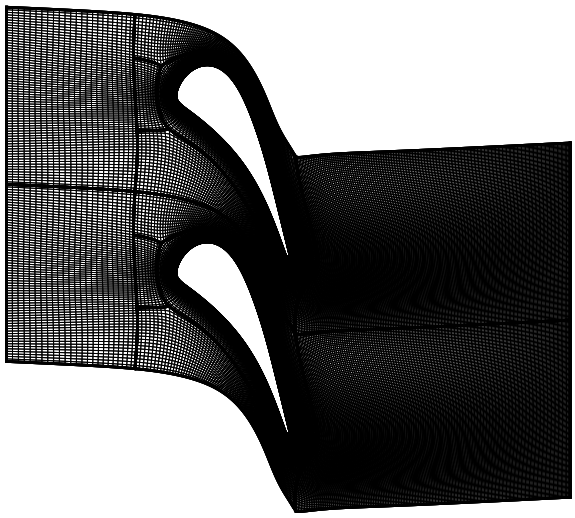

Figure 7: Mesh generated for the LS89 cascade

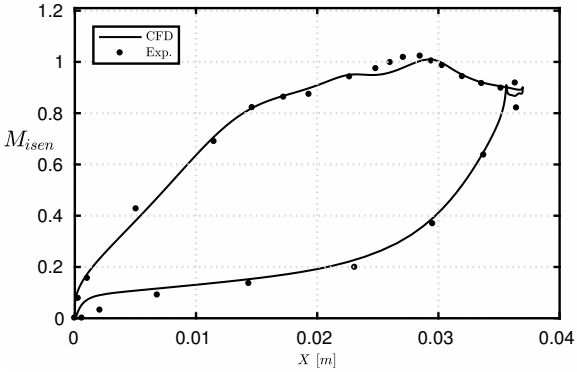

Figure 8: Validation of the CFD solver

The evolution of the population during the hybrid optimization is visualized in Fig. 9. The figure shows for each generation number the composition of the population in terms of objective (top) and constraints (bottom). A very large spread in objective function is present during the first steps of the optimization, but this rapidly reduces with generation number. At the same time, many designs do not satisfy the constraints at the start, but these designs disappear after only 5 iterations through a combination of the selection process of the DE and the gradient-based projection method. Near the end of the optimization process all designs are just satisfying the constraints, meaning that the constraint becomes active and that only an improvement is possible in a direction perpendicular to the constraint gradient. The final population has

still some variation in the objective function, which indicates that some diversity in the population is preserved. This is an essential ingredient in global exploration. Figure 9 shows that the optimization converges towards a population where all the individuals reduce the entropy generation through the cascade by about 20 percent while maintaining the flow turning of the original profile. The evolution of the best individual of each generation is represented in Fig. 10 by a solid line. These are the results of the algorithm after the steepest descent improvement. Also shown in the figure by dots are the designs created by the proceeding evolutionary step which have been improved afterwards by the steepest descent method to the designs represented by the solid line. The figure demonstrates the two main advantages of the hybrid algorithm, namely the acceleration of the convergence by locally improving an individual (arrow A in the figure) and the possibility to correct promising individuals which do not respect the constraint (arrow B in the figure).

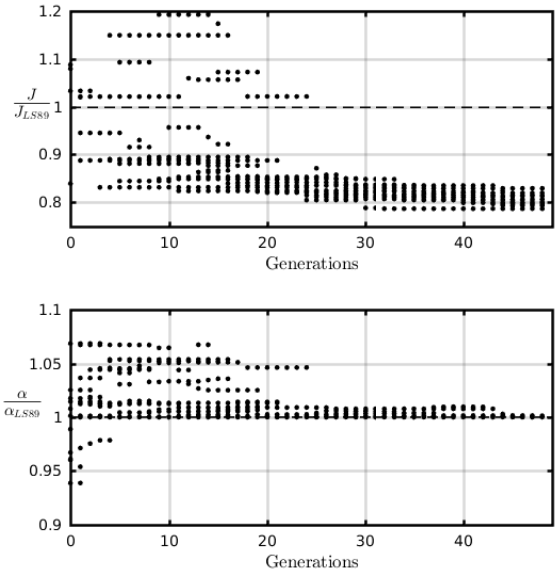

Figure 9: Values of the objective function and the constraint of all the individuals for each generation

The best individual found using the hybrid algorithm reduces the entropy generation through the cascade by 21.3 percent while maintaining exactly the same flow turning. In Ref. [19], based on an identical geometry parametrization, the same single point optimization of the LS89 turbine has been performed

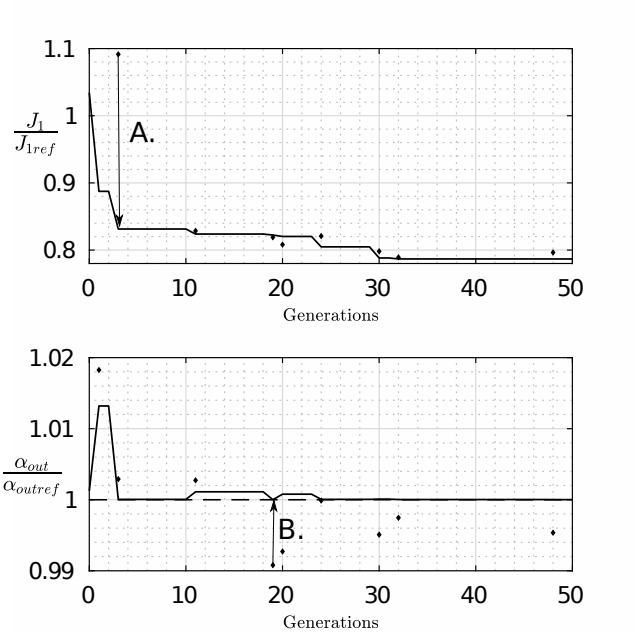

Figure 10: Evolution of the best individual of the populations during the optimization.

using a gradient-based method (GBM). In this optimization, the aerodynamic constraint is imposed by adding a penalty term to the objective function when the inequality Eq. 9 is not satisfied. The results of both optimization methods are compared in Tab. 2. The table shows that the method described in this paper allows to find a much better design improvement of the LS89 turbine cascade (21.3 % compared to 11.6 % improvement respectively). This is due to the fact that the hybrid method performs a global exploration of the design space.

The last row of the Tab. 2 compares the number of evaluations performed during both optimizations where the adjoint computations have the same computational cost than the CFD simulations. It can be seen from this comparison that the GBM needs significantly less evaluations of the objective function to converge. However, the hybrid algorithm allows to perform a global exploration of the design space and therefore, the localization of a better minimum is possible. Moreover, the hybrid method is easily parallelisable by evaluating the different individuals of a population in parallel. Furthermore, between two successive populations, the local improvements of the most promising individuals using the steepest descent method can also be performed in parallel. In terms of computational cost, each CFD and adjoint compu-

tation lasts approximately 20 minutes using two processors. For the overal gradient-based optimization described the Ref [19], two Intel(R) Core(TM) i7-4790K CPU 4.00GHz processors were used for approximately 2 days, while the hybrid method took more or less 10 days using 6 processors of the same type. To conclude, the new algorithm developed allows to find a better minimum than classical optimization methods at a reasonable computational cost.

Table 2: Comparison between GBM results and hybrid results

	LS89	GBM [19] Variation	Hybrid Variation
$J\ [Pa/(kg/m^3)]$	826.7	731 -11.6 %	650.5 -21.3%
$\alpha_{out}[^\circ]$	74.89	74.89 -0 %	74.89 -0%
Evaluations		70	1600

5. Comparison of the profiles

This section describes different characteristics of the new profile obtained at the end of the optimization using the hybrid algorithm. The baseline and the optimized cascades are compared in terms of geometry, isentropic Mach number distribution along the blades, total pressure loss, boundary layer parameters and base pressure.

Comparison of the cascade geometries:. The two geometries of the cascade are compared in Fig. 11. The figure shows that the pitch between two consecutive blades has significantly increased from 0.057 *mm* to 0.076 *mm*. We observe as well an increase in chord length of the blades by lowering the stagger angle (from 54.9° to 59.7°), such that the decrease in solidity remains limited (from 1.11 to 0.96). The leading edge of the new blades is less curved, which leads to a modification of the stagnation point position along the PS. The larger pitch between two consecutive blades and throat area increase the mass-flow through the optimized cascade by about 25% compared to the baseline configuration.

Isentropic Mach number distribution and loading:. The evolution of the isentropic Mach number along the SS and PS of the blades are presented in Fig. 12. Due to the lower curvature on the suction side in the front part of the optimized vane and due to the increase of the mass-flow, the flow is quickly accelerated until X ≈ 0.02m. This acceleration leads to a small supersonic pocket followed by a weak shock on the SS of the blade. In the last part of the SS, the flow is strongly decelerated and reaches a smaller isentropic Mach number than the one obtained downstream of the baseline blades. The comparison of the isentropic Mach numbers clearly illustrates a significantly higher loaded optimized blade, which is in-line with the decreased solidity. The Zweifel coefficient Z_w [24] allows to quantify how efficiently a blade profile is loaded and is expressed as follows:

$$Z_w = \frac{\int_0^1 (P_{PS} - P_{SS}) \frac{dx}{c_a}}{(P_{0in} - P_{out}).c_a}. \tag{11}$$

The Zweifel coefficient of the LS89 turbine cascade is equal to 0.61 [19], while the value of the coefficient computed in the case of the optimized profile is 0.84.

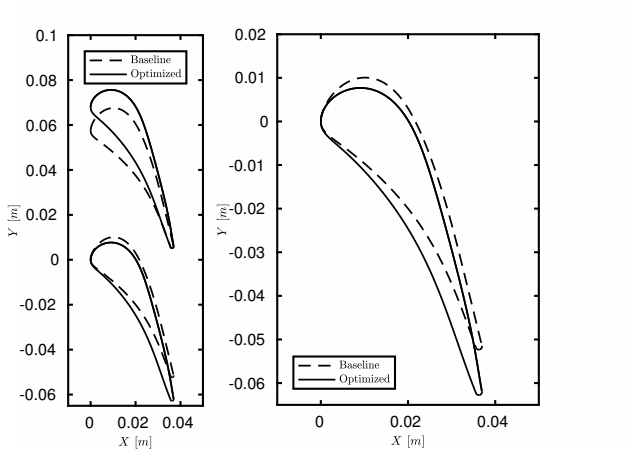

Figure 11: Comparison of the cascade geometries

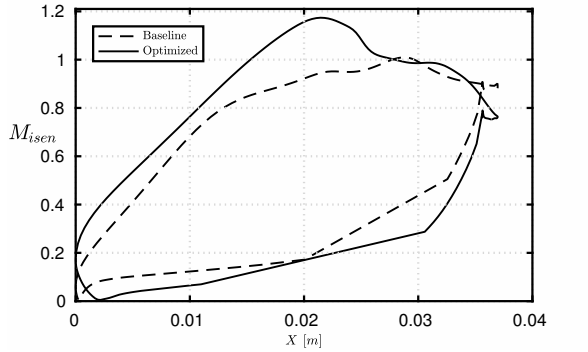

Figure 12: Isentropic Mach Number comparison

The significant difference demonstrates that the new profile is much more efficiently loaded which allows to achieve the same flow turning than the baseline cascade while increasing the pitch.

Total pressure loss:. The evolution of the total pressure loss relatively to the dynamic pressure q in a plane downstream of the blades (in $\frac{X}{C_a} = 1.433$) for the two different cascade geometries is represented on Fig. 13. The figure illustrates that the total pressure losses generated in the wake downstream of the blades is smaller for the optimized geometry. Moreover, the width of the wake compared to the pitch is smaller for the new design. These two factors allow to explain the reduction of the total pressure loss (from 2.665 kPa to 2.07 kPa) between the inlet and the fully mixed-out flow at the outlet which equals to a diminution of about 22.4 percent.

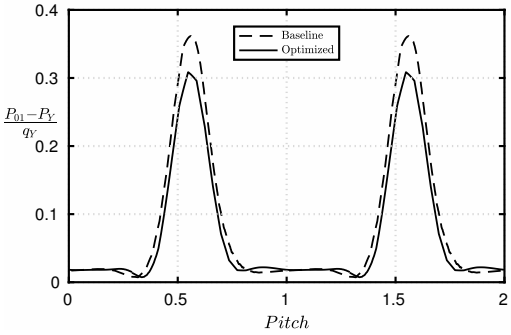

Figure 13: Total pressure loss downstream (at $\frac{X}{C_a} = 1.433$) of the blade

Boundary layer parameters:. The boundary layers have an important impact on the profile losses generated in turbine cascades [25]. Therefore, the boundary layer parameters computed for the baseline and the optimized profiles in two locations along the SS are compared in Tab 3. The first point (1) is placed at 85 percent of the axial chord which represents a location where the strong deceleration starts in the case of the optimized profile. The second point (2) is located closer to the TE at 97 percent of the axial chord. Table 3 shows that, even at the beginning of the deceleration in (1), the boundary layer is thicker in the case of the optimized profile. This is due to the presence of the weak shock at the end of the supersonic bubble on the SS which destabilizes the boundary layer. Moreover, due to the strong deceleration in the last part of SS, the thickness of the boundary layer increases faster along the profile of the new geometry. Comparatively, the boundary layer thickness, displacement thickness and momentum thickness are higher for the optimized cascade which should lead to higher profile losses in that case [25]. However, another term plays a significant role in the loss generation of turbine cascades which is the static pressure at the trailing edge [26; 27; 28; 25].

Table 3: Comparison of the boundary layer parameters along the SS in two different locations (1 and 2 respectively at 85 percent 97 percent of the axial chord)

	$LS89_1$	Opt_1	$LS89_2$	Opt_2
δ $[mm]$	1	1.3	1.3	2
δ* $[mm]$	0.19	0.25	0.25	0.53
θ $[mm]$	0.11	0.14	0.15	0.3
H	1.75	1.74	1.65	1.83

Base pressure:. In turbine cascades, a large part of the blade loss comes from the entropy generated close to the trailing edge. Indeed, at transonic speeds, 70 percent of the losses come from downstream the TE [28]. In this region, the entropy is generated by the mixing of the boundary layers originating of the SS and the PS. As explained in detail in [25; 26; 27; 28], the mixing process leads to a dissipation which is directly linked to the static pressure at the TE of the blades, also called base pressure. The comparison between the base pressure of the LS89 cascade and the one obtained numerically for the optimized geometry is presented in Fig. 14. The figure demonstrates that the pressure distribution at the TE of the optimized profile is higher than the base pressure obtained for the LS89 turbine which eventually leads to lower mixing losses. The difference between the two base pressures is of the order of 12 percent and can be explained by the higher boundary layer thickness just before the TE. Xu and Denton proved in [28] that higher boundary layer thickness upstream the TE leads to larger pressure distribution at the TE. Therefore, the higher base pressure obtained in the case of the optimized profile can be associated to a smaller entropy generation in the TE region. This is illustrated by Fig. 15 which compares the distribution of streamlines around the TE for the baseline and the optimized profiles. The figure shows that the recirculation bubble located in the TE region is smaller in the case of the new geometry which leads to a higher base pressure and, therefore, to a smaller entropy generation

in this region. Therefore, this higher pressure distribution along the TE measured explains the reduction of the entropy generation computed for the new optimized cascade.

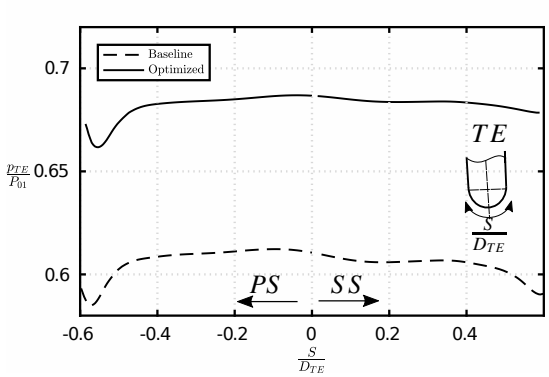

Figure 14: Comparison of the base pressure distributions obtained using RANS simulations

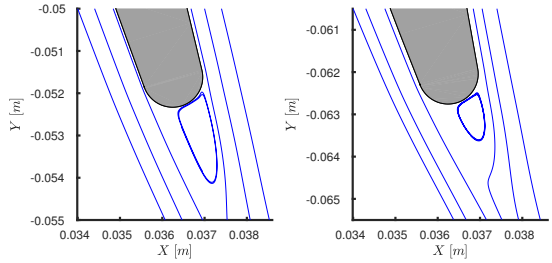

Figure 15: Distribution of the streamlines around the TE for the baseline profile (left) and the optimized profile (right)

6. Conclusion

This paper presents a single point aerodynamic optimization of the LS89 turbine cascade using an hybrid optimization algorithm. The hybrid algorithm combines a classical evolutionary algorithm with a steepest descent method. This algorithm has been developed in order to tackle the most well known disadvantages of both methods and to benefit from their respective strengths. Especially, the hybrid method merges the capacity to perform a global exploration from the evolutionary algorithm with the faster local convergence of the steepest descent method. The hybrid algorithm used in the context of this work is constructed using the Lamarckian evolution approach which consists in incorporating the gradient-based method directly inside the loop of the evolutionary algorithm. Moreover, in this new algorithm, a projected gradient method is combined to the steepest descent method in order to correct the promising individuals which do not respect the aerodynamic constraint.
First, the effectiveness of the new hybrid method is demonstrated on two benchmark problems by comparing its performance with the performance of the classical DE algorithm. Then, the hybrid method is applied to a typical turbomachinery application: the LS89 turbine cascade. The aim of the optimization is to modify the geometry of the cascade in order to minimize the entropy generated inside the cascade while maintaining the flow turning of the original vane. The use of the presented algorithm allows to find a new design which reduces the generated losses by a factor of 21 percent. The optimized geometry is mainly characterized by a larger pitch distance between 2 consecutive blades, a slightly longer chord and the curvature is higher in the front part of the blade. Finally, the analysis of the flow obtained in the optimized cascade in terms of loading, boundary layer parameters and base pressure demonstrates that the reduction of the profile losses are due to a smaller dissipation in the TE region characterized by higher base pressure.

Acknowledgments

This work has been performed in the context of the MOTOR project (http://motor-project.eu/) funded by the European Union Horizon 2020 Framework Programme for Research and Innovation under Grant Agreement No. 678727. Therefore, the authors would like to thanks the European Union for funding the MOTOR project.

References

[1] J. C. Vassberg and A. Jameson, Industrial applications of aerodynamic shape optimization, no. VKI Lecture Series on Introduction to Optimization and Multidisciplinary Design, Brussels, Belgium, 2016.

[2] L. Mueller and T. Verstraete, CAD Integrated Multipoint Adjoint-Based Optimization of a Turbocharger Radial Turbine, Int. J. Turbomach. Propuls. Power.

[3] T. Verstraete, S. Amaral, R. Van den Braembussche and T. Arts, Design and Optimization of the Internal Cooling Channels of a High Pressure Turbine Blade, Part 2 Optimization, J. Turbomach.

[4] S. Shahpar, S. Caloni and L. de Prielle, Automatic Design Optimization of Profiled Endwalls Including Real Geometrical Effects to Minimize Turbine Secondary Flows, Journal of turbomachinery 139(7).
[5] T. Verstraete, Introduction to optimization and multidisciplinary design, no. VKI Lecture Series on Introduction to Optimization and Multidisciplinary Design, Brussels, Belgium, 2016.
[6] J. R. R. A. Martins and J. T. Hwang, Multidisciplinary Design Optimization of Aircraft Configurations - Part 1: A modular coupled adjoint approach, VKI Lecture Series on Introduction to Optimization and Multidisciplinary Design.
[7] S. Chen and J. Montgomery, Measuring the curse of dimensionality and its effects on particle swarm optimization and differential evolution, Applied Intelligence (2015) 514–526.
[8] T. A. El-Mihoub, A. A. Hopgood, L. Nolle and A. Battersby, Hybrid genetic algorithms: A review, no. Engineering Letters, 13:2.
[9] V. Kelner, F. Capitanescu, O. Léonard and L. Wehenkel, A hybrid optimization technique coupling an evolutionary and a local search algorithm, no. Journal of Computational and Applied Mathematics 215, 2008, pp. 448–456.
[10] A. Jameson, Aerodynamic Design via Control Theory, Journal of Scientific Computing (1988) 233–260.
[11] Y. G. Xu, G. R. Li and Z. P. Wu, A novel hybrid genetic algorithm using local optimizer based on heuristic pattern move, Applied Artificial Intelligence: An International Journal (2010) 601–631.
[12] R. Cheng, M. Gen and Y. Tsujimura, A tutorial survey of job-shop scheduling problems using genetic algorithms: Part II Hybrid genetic strategies, Int J. Computers Industrial Engineering 37(1) 51–55.
[13] T. Yamade and R. Nakano, A genetic algorithm applicable to large-scale job-shop problems, In Parallel problem solving from nature:PPSN II, eds. R. Manner and B. Manderick. North-Holland: Elsevier Science Publisher 281–290.
[14] D. Whitley, S. Gordon and K. Mathias, Lamarckian evolution, the Baldwin effect and function optimization, Davidor Y., Schwefel HP., Mnner R. (eds) Parallel Problem Solving from Nature PPSN III. PPSN 1994. Lecture Notes in Computer Science (1994) 6–15.
[15] N. K. W. E. Hart, J. E. Smith, Recent Advances in Memetic Algorithms, Springer, Berlin, 2005.
[16] F. Muyl, L. Dumas and V. Herbert, Hybrid method for aerodynamic shape optimization in automotive industry, Journal of Computers and Fluids, 33(1) (2008) 97–119.
[17] K. Price and N. Storn, Differential Evolution, Dr. Dobb's Journal (16) (1997) 18–24.
[18] M. L. d. R. T. Arts, A. W. Rutherfort, Aero-thermal investigation of a highly loaded transonic linear turbine guide vane cascade. A test case for inviscid and viscous flow computations, Tech. Rep. 174, von Karman Institute for Fluid Dynamics (1990).
[19] I. S. Torreguitart, T. Verstraete and L. Mueller, Optimization of the LS89 axial turbine profile using a CAD and adjoint based aproach, no. 12th European Conference on Turbomachinery Fluid dynamics & Thermodynamics, Stockholm, Sweden, 2017.
[20] T. Verstraete, Multidisciplinary Turbomachinery Component Optimization Considering Performance, Stress and Internal Heat Transfer, Ph.D. thesis, Universiteit Gent (2008).
[21] G. N. Vanderplaats, Numerical Optimization Techniques for Engineering Design.
[22] M. Molga, Test functions for optimization needs.
[23] I. S. Torreguitart, T. Verstraete and L. Mueller, Cad kernel and grid generation algorthmic differentiation for turbomachinery adjoint optimization, no. 7th European Congress on Computational Methods and Applied Sciences and Engineering, Hersonissos, Greece, 2016.
[24] O. Zweifel, The spacing of turbo-machine blading, especially with large angular deflection, Brown Boveri Rev.32 (1945) 436–444.
[25] J. D. Denton, Loss mechanisms in turbomachines, no. ASME 1993 International Gas Turbine and Aeroengine Congress and Exposition, 1993.
[26] C. H. Sieverding, H. Richard and J-M Desse, Turbine blade trailing edge flow characterisics at high subsonic outlet mach number, Journal of turbomachinery 125(2) (2003) 298–309.
[27] C. H. Sieverding, M. Stanislas and J. Snoeck, The base pressure problem in transonic turbine cascade, Journal of Engineering for Power 102 (1980) 711–718.
[28] L. Xu and J. D. Denton, The base pressure and loss of a family of four turbine blades, Journal of turbomachinery 110 (1988) 9–17.
[29] T. Verstraete, CADO: A Computer aided design and optimization tool for turbomachinery applications, no. 2nd Conf. on Engineering Optimization, Lisbon, Portugal, 2010.
[30] J. Nocedal, S. J. Wright, Numerical Optimization, Springer, Berlin, 2006.
[31] T. S. Schobeiri, Turbomachinery flow physics and dynamic performance, Springer, Berlin, 2012.
[32] S. Vagnoli, T. Verstraete, B. Mateos and C.H. Sieverding, Prediction of the unsteady turbine trailing edge wake flow characteristics and comparison with experimental data, Proceedings of the Institution of Mechanical Engineers, Part A: Journal of Power and Energy.
[33] S. Pierret, Designing turbomachinery blades by means of the function approximation concept based on artificial neural networks, genetic algorithm, and the navier-stokes equations, Ph.D. thesis, Faculté Polytechnique de Mons (1999).
[34] J. Kopriva, G.M. Laskowsky, H. Reza and and al., Assessment of high pressure cooled and uncooled turbine blade wakes via RANS and URANS at engine scale conditions, Paper No. GT2013-94285, ASME turbo expo.

Adjoint Method with Thermal Constraints for the Optimization of Fluid Machinery

Maria Faruoli

Environmental and Applied Fluid Dynamics Department, von Karman Institute for Fluid Dynamics, Belgium, School of Engineering, University of Basilicata, Italy, maria.faruoli@vki.ac.be

Supervisor: Jeroen van Beeck

Associate Professor, Environmental and Applied Fluid Dynamics Department, von Karman Institute for Fluid Dynamics, Belgium, vanbeeck@vki.ac.be

Advisors: Giacomo Alessi and Lilla Kapa Koloszár

PhD candidate, Environmental and Applied Fluid Dynamics Department, von Karman Institute for Fluid Dynamics, Belgium, giacomo.alessi@vki.ac.be

Research Engineer, Environmental and Applied Fluid Dynamics Department, von Karman Institute for Fluid Dynamics, Belgium, koloszar@vki.ac.be

University Supervisor: Annarita Viggiano and University Advisor: Vinicio Magi

Assistant Professor, School of Engineering, University of Basilicata, Italy, annarita.viggiano@unibas.it

Professor, School of Engineering, University of Basilicata, Italy, vinicio.magi@unibas.it

Abstract

In geometry optimization process of fluid flow systems, methods that combine CFD and numerical optimization techniques provide a suitable tool to get an optimal configurations.Among the others, the adjoint method represents a valid choice because of its low computational cost. The method is based on the computation of a sensitivity map of the domain that represents how to variate the design variable in order to get the objective function imposed. The computational cost of the optimization process is the same of solving two Navier-Stokes systems, independently on the number of design variables. Although the topological adjoint optimization is applied mostly in Aerodynamics applications, the application of this method to problems with thermal constraints is not widely studied, but its potentialities are evident.

The adjoint system of equations including the temperature equation and the relative boundary conditions were derived and implemented in the open-source software OpenFOAM, by imposing the ”frozen turbulence” hypothesis. The objective of the project is to develop a robust and stable numerical tool to be applied to a wide range of cases, characterized by thermal phenomena, and an adjoint turbulent model for the optimization of turbulent flows. Moreover, multi-objective optimization will be introduced, thus allowing to optimize more objective functions at the same time.

As a first application, a Stirling engine regenerator is considered. The regenerator is a heat-exchanger placed between the hot and cold working streams, usually composed of stacked woven wire. Its design influences heavily the engine performances. Specifically, the pressure drop and the heat transfer are studied, by evaluating the friction coefficient and the thermal efficiency. As a preliminary phase for the optimization, the case is studied by means of OpenFOAM and the results are compared with those obtained in scientific literature in order to tune the numerical model of the regenerator. Firstly, isothermal flows through the regenerator and adiabatic wires are analyzed, by assuming the fluid as incompressible. In the second part, airflows with a temperature of 500 K and wires at a temperature of 300 K are studied, by considering a compressible fluid. The results show a good agreement for the friction coefficient in both compressible and incompressible cases. Instead, the thermal efficiency results are in good agreement with the references in laminar regime (i.e. Re <200), while turbulent flows need further studies.